Measurements of Branching Fraction and CP Violation in B Meson Rare Decays to Final States containing eta or eta' Mesons in the BaBar Experiment at SLAC

Alfio Lazzaro

SLAC-R-862

Prepared for the Department of Energy
under contract number DE-AC02-76SF00515

Printed in the United States of America. Available from the National Technical Information Service, U.S. Department of Commerce, 5285 Port Royal Road, Springfield, VA 22161.

MEASUREMENTS OF BRANCHING FRACTION AND CP VIOLATION IN B MESON RARE DECAYS TO FINAL STATES CONTAINING η OR η' MESONS IN THE *BABAR* EXPERIMENT AT SLAC

ALFIO LAZZARO
PH.D. THESIS, UNIVERSITÀ DEGLI STUDI DI MILANO

SLAC-R-862
APRIL 11, 2007

PREPARED FOR THE DEPARTMENT OF ENERGY
UNDER CONTRACT NUMBER DE-AC02-76SF0015

Published by

Stanford Linear Accelerator Center
Technical Publications MS 68
2575 Sand Hill Road
Menlo Park, CA 94025

Università degli Studi di Milano
Facoltà di Scienze Matematiche, Fisiche e Naturali
Dipartimento di Fisica

Corso di Dottorato di Ricerca in Fisica, Astrofisica e Fisica Applicata
FIS/04 - FISICA NUCLEARE E SUBNUCLEARE
CICLO XIX

Tesi di Dottorato di Ricerca

MEASUREMENTS OF BRANCHING FRACTION AND CP VIOLATION IN B MESON RARE DECAYS TO FINAL STATES CONTAINING η OR η' MESONS IN THE *BABAR* EXPERIMENT AT SLAC

Allievo Alfio Lazzaro

Tutor:	Prof. F. Palombo Università degli Studi di Milano
Co-Tutor:	Prof. W. T. Ford University of Colorado, Boulder
Coordinatore:	Prof. G. Bellini

BABAR-THESIS-07/002
SLAC-R-862

Anno Accademico 2005–2006

Ai miei genitori, alle mie sorelle e a mio fratello:
alla mia famiglia

To my parents, my sisters and my brother:
to my family

Contents

Introduction

This thesis has been realized in the *BABAR* experiment, running on the PEP-II e^+e^- collider at the Stanford Linear Accelerator Center (SLAC), USA. The main goal of the experiment is the study of the CP violation in the B meson system. The CP violation has a central role in the particle physics since his discovery in 1964 [1]. Previously, the observation of the parity violation in the 1950s marks the inception of the discovery of the symmetry-violating properties in weak interaction. In 1956, Lee and Yang showed that parity conservation, while well-tested in strong and electromagnetic interactions, was not experimentally constrained for weak interactions, and proposed a list of experimental tests [2]. C. S. Wu and collaborators performed one of these experiments, and showed that parity was not conserved in nuclear β decay, conclusively demonstrating the uniqueness of the weak interaction among the forces [3]. However the CP transformation was still considered valid. The discovery, eight years later, of the decay of the neutral kaon meson with long lifetime in two pions by Christenson, Cronin, Fitch and Turlay [1] establishes the CP violation in the weak interaction. In 1973 (almost 10 years later), Kobayashi e Maskawa suggested a generalization of the quark mixing matrix, introduced by Cabibbo [4], where the CP violation in the neutral kaons can be explained using a model with three families of quarks and leptons [5] (this happened a year before even the charm quark was discovered). The quarks of the third family, called b per bottom (or beauty) and t per top, were discovered in 1977 [6] and in 1994 [7], respectively. More than 30 years of experimental researches in the kaon system has yielded only in 1999 the observation of direct CP violation [8]. All measurements are consistent with the Standard Model (SM) description given by Cabibbo, Kobayashi, Maskawa (CKM) quark-mixing matrix. However, the smallness of the CP violating effects in the kaon system is an impediment to progress in that sector. The present and the future to constraint the CKM scenario (or to find effects beyond the SM) is in general given by the decays with b quark. A meson with a quark

$\bar{b}$, shown as B meson, is similar to a K meson with a quark $\bar{s}$. His decay modes, as found by *BABAR* and Belle[1], exhibit significant CP asymmetries, as predicted by the SM. After 7 years of running, the two experiments have collected a large sample of B (larger than expected). With the measurements of the CP parameters in the golden channels $b \to c\bar{c}s$ [9] and, more recentely, the observation of the direct CP violation in $B^0 \to K^+\pi^-$ [10], the two main goals of these experiments have been reached. All these results are consistent with the SM prediction. However, Flavor Changing Neutral Current (FCNC) mediated processes are not yet strongly constrained and in this case we can have effect due to New Physics (NP). In particular, the comparison of the time dependent CP asymmetries for $b \to s$ decays and the $b \to c\bar{c}s$ is a good place where to look for contributions from NP. In the $B^0 \to \eta' K^0$ mode we have observed for the first time the CP-asymmetry violation in $b \to s$ dominated B-decays [11]. This measurement is described in this thesis. The $b \to s$ decays occur through loop (penguin) transitions at the leading order, so that the presence of NP effects should produce a deviation from the SM, as given by the tree (NP free) process $b \to c\bar{c}s$ [12]. These decay modes are Cabibbo suppressed with branching fraction of the order of 10^{-4} or less, with respect to the dominant tree decays of the B mesons. For this reason a huge amount of B mesons is needed. The two machines PEP-II and KEK-B have been constructed to have high luminosity (so called b-factories). The energy in center of mass corresponds to $\Upsilon(4S)$ resonance, a resonance composed by a pair of $b\overline{b}$ quark, with mass of about 10.56 GeV, which decays in a pair of B mesons ($\sim 50\%$ B^+B^-, $\sim 50\%$ $B^0\overline{B}^0$). The cross section of $\Upsilon(4S)$ is about 1.1 nb. The two experiments *BABAR* and Belle have recorded together more than 1 ab^{-1} of data in about 7 years of running. To perform measurements of time dependent asymmetry is needed a good measurement of the two B vertex decays coming from $\Upsilon(4S)$. For this reason, PEP-II and KEK-B have asymmetric beams in order to produce $\Upsilon(4S)$ mesons with a certain relativistic boost in laboratory frame. This allows to have measurable distance for the two B vertex decays. In PEP-II we have e^- of 9 GeV and e^+ of 3.1 GeV.

The Milano Group works in the *BABAR* Collaboration studying the charmless decays of the B meson. In particular in this thesis we report the study of the decays with $b \to s$ transition with an η or η' mesons in the final state. For the neutral modes $\eta' K^0$, ηK^0, $\eta\eta$, $\eta'\phi$, $\eta\phi$, $\eta'\eta' K^0$, $\eta K^0\gamma$, $\eta' K^0\gamma$ and for the charged modes $\eta' K^\pm$, $\eta'\eta' K^\pm$, $\eta K^\pm\gamma$, $\eta' K^\pm\gamma$ we have performed a measurement of the branching fraction (or upper

[1] similar experiment to *BABAR* in the KEK-B accelerator (Tsukuba, Japan).

limit at 90% of confidence level in the case where we don't see significant signal). For the modes with a significant number of signal yields we have performed the CP violation measurements. In particular for the decay $B^0 \to \eta' K^0$ we have performed the Time Dependent CP-asymmetries measurement.

Note that the main goal of this thesis work is the measurement of the branching fractions, charge asymmetry, and Time-Dependent CP Violation in $\eta' K^0$ mode. All other measurements are reported here for completion because they are connected by similar physics arguments. They are part of the Milan analysis activity, done by undergraduate students. They should not be considered as done in this thesis work.

The measurements of the two body-modes $\eta\eta$, $\eta\phi$, and $\eta'\phi$ are used to determine a theoretical bound based on SU(3) flavor symmetry for the difference between SM prediction and the experimental measurements of CP violation parameters in $b \to s$ loop-dominated modes. In general for this estimation we need to measure the branching fractions (or upper limits) of neutral B decays to two-body modes with η', η, ϕ, ω, π^0, K^0, K^{*0} [13, 14, 15, 16].

There is an important issue related to the branching fractions of $\eta^{(\prime)} K$ (charged and neutral) modes. Since the discover of $B \to \eta' K$ in 1997 [17] with high branching fraction (higher than expected), it was found that the corresponding mode with η is suppressed. This fact was pointed out by Lipkin in 1991 [18]. In particular, using arguments concerning the $\eta - \eta'$ mixing angle and the parity of K or K^* we can say that $\eta' K$ and ηK^* are enhanced, while ηK and $\eta' K^*$ are suppressed. This scheme is experimentally verified. The branching fraction of all these modes are already measured, but the $B^0 \to \eta K^0$. So it is important to measure also this mode to complete the scenario.

Finally we report on the measurements of the radiative modes $B \to \eta^{(\prime)} K\gamma$ and of the three-body mode $B \to \eta'\eta' K$. Both cases are good candidates to manifest effects due to NP in CP violations [19, 20].

For all measurements we use an unbinned maximum likelihood fit to extract the number of signal yields and CP parameters. To perform these fits we have developed a flexible program in C++ language, called `MiFit`, which has taken a consistent part of the work described in this thesis. This program is used in all Milan analyses.

All these measurements have been presented in conferences and published in Physical Review Letters or Physics Review D (Rapid Comunication). These measurements are official *BABAR* results, approved by the Collaboration.

The thesis is structured in eight chapters. In the first chapter we describe the CP violation and how it is explained in the SM. We give the theoretical description of the modes studied in this thesis. We report also the latest main results for the CP violation. In the second chapter we describe the *BABAR* detector with a description of each sub-detector. In the third chapter we describe the software used by the collaboration, in particular the code used in the events reconstruction, which is described in the fourth chapter. In the fifth chapter we describe the softwares used to selected the events and the `MiFit` program. After that, in the sixth chapter we show the discriminating variables used for the events selection and how the selection is done. In the last two chapters we report the analyses and results of the branching fractions and charge asymmetries measurements and the time-dependent CP asymmetries analysis of the mode $B^0 \to \eta' K^0$, respectively.

Chapter 1

CP Violation in the B Meson System

1.1 Introduction

In the Standard Model (SM) [21] the CP violation is explained by the Kobayashi and Maskawa mechanism [5]. In particular, the source of the CP violation is a single phase in mixing matrix, which is called Cabibbo-Kobayashi-Maskawa (CKM) matrix, which describes the charged current in the weak interaction between quarks. Experimentally the CP violation has been observed in K decays [1] and recently in B decays [9, 10]. So far all measurements are consistent with this scenario. However, there is room for New Physics (NP) if we find a discrepancy from the SM predictions. For this reason it is important to have as many measurements as possible of CP violation in different processes.

In this chapter we will describe the formalism of the CP violation in the B meson system and the CKM mechanism. Furthermore we will report the recent experimental results for the B meson physics.

1.2 Discrete Symmetries

The set of operators on the Hilbert space of state functions on the quantum field contains both discrete and continuous transformations that preserve the Minkowski interval $t^2 - \vec{x}^2$. The set of continuous transformations that preserve this interval are the familiar Lorentz transformations, comprised of the product space of rotations, translations, and Lorentz boosts. The three independent discrete transformations that also preserve $t^2 - \vec{x}^2$ are the charge conjugation operator (C), the parity operator (P),

and the time-reversal operator (T). These form a complete set of discrete Minkowski interval-preserving transformations of the Hilbert space.

1.2.1 Parity

The parity operator P reverses the signs of the 3 spatial elements of a four-vector: $(t, \vec{x}) \rightarrow (t, -\vec{x})$ and $(E, \vec{p}) \rightarrow (E, -\vec{p})$. One can easily visualize parity as a mirror-image plus an 180-degree rotation normal to the plane of the mirror — this reverses the momentum of a particle but leaves its spin unchanged.

Consider the action of parity on the particle and antiparticle annihilation operators of the Dirac field $a^s_{\vec{p}}$ and $b^s_{\vec{p}}$. Parity transforms the states $a^s_{\vec{p}}|0\rangle$ and $b^s_{\vec{p}}|0\rangle$ to $a^s_{-\vec{p}}|0\rangle$ and $b^s_{-\vec{p}}|0\rangle$. This implies

$$Pa^s_{\vec{p}}P^{-1} = \eta_a a^s_{-\vec{p}} \qquad \text{and} \qquad Pb^s_{\vec{p}}P^{-1} = \eta_b b^s_{-\vec{p}}, \tag{1.1}$$

where η_a and η_b are phases. Since $P^2 = \mathbf{1} \Rightarrow \eta_a, \eta_b$ must equal ± 1 (the parity group, as with the other two discrete operators, is idempotent, *i. e.* $P^{-1} = P$).

1.2.2 Time Reversal

The time reversal operator reverses momentum and spin and also flips the sign of the time component of a state. Therefore we want the transformation of the Dirac particle and antiparticle annihilation operators to be:

$$Ta^s_{\vec{p}}T^{-1} = \eta'_a a^{-s}_{-\vec{p}} \qquad \text{and} \qquad Tb^s_{\vec{p}}T^{-1} = \eta'_b b^{-s}_{-\vec{p}}. \tag{1.2}$$

1.2.3 Charge Conjugation

The charge conjugation operator is defined to be the transformation of a particle into its antiparticle without changing momentum or spin. Thus,

$$Ca^s_{\vec{p}}C^{-1} = \eta''_a b^s_{\vec{p}} \qquad \text{and} \qquad Cb^s_{\vec{p}}C^{-1} = \eta''_b a^s_{\vec{p}}. \tag{1.3}$$

1.2.4 CP and CPT

The combination CPT operator has a rather special property: it is guaranteed to be a fundamental symmetry of nature, with only the basic assumptions of Lorentz invariance, locality, and the spin-statistics relation.[1] It's summarized and shown in the Table 1.1 how scalars, pseudoscalars, vectors, pseudovectors, tensors, and derivative operator are affected by the discrete symmetries. It is also shown the effect of the combination CP operator.

	C	P	T	CP	CPT
Scalar	+1	+1	+1	+1	+1
Pseudoscalar	+1	-1	-1	-1	+1
Vector	$-\vec{1}$	$\begin{pmatrix} +1 \\ -1 \\ -1 \\ -1 \end{pmatrix}$	$\begin{pmatrix} +1 \\ -1 \\ -1 \\ -1 \end{pmatrix}$	$\begin{pmatrix} -1 \\ +1 \\ +1 \\ +1 \end{pmatrix}$	$-\vec{1}$
Pseudovector	$+\vec{1}$	$\begin{pmatrix} -1 \\ +1 \\ +1 \\ +1 \end{pmatrix}$	$\begin{pmatrix} +1 \\ -1 \\ -1 \\ -1 \end{pmatrix}$	$\begin{pmatrix} -1 \\ +1 \\ +1 \\ +1 \end{pmatrix}$	$-\vec{1}$
Tensor	-1	$\begin{pmatrix} +1 & -1 & -1 & -1 \\ -1 & +1 & +1 & +1 \\ -1 & +1 & +1 & +1 \\ -1 & +1 & +1 & +1 \end{pmatrix}$	$\begin{pmatrix} -1 & +1 & +1 & +1 \\ +1 & -1 & -1 & -1 \\ +1 & -1 & -1 & -1 \\ +1 & -1 & -1 & -1 \end{pmatrix}$	$\begin{pmatrix} -1 & +1 & +1 & +1 \\ +1 & -1 & -1 & -1 \\ +1 & -1 & -1 & -1 \\ +1 & -1 & -1 & -1 \end{pmatrix}$	$+1$
Derivative Operator	$+\vec{1}$	$\begin{pmatrix} +1 \\ -1 \\ -1 \\ -1 \end{pmatrix}$	$\begin{pmatrix} -1 \\ +1 \\ +1 \\ +1 \end{pmatrix}$	$\begin{pmatrix} +1 \\ -1 \\ -1 \\ -1 \end{pmatrix}$	$-\vec{1}$

Table 1.1: Summary of discrete symmetries for scalars, pseudoscalars, vectors, pseudovectors, tensors, and derivative operator.

It is possible to see that, if we restrict our attention to scalars, pseudoscalars, vectors, and the derivative operator, a Lagrangian formed from only such quantities must remain CP-invariant. It can be also demonstrated that a quantum field of any spin with real coupling constants cannot violate CP. However, particle masses and coupling constants do not transform under CP. If any of these quantities is not purely real, it

[1] Note that the spin-statistics relation itself is implied from Lorentz invariance, positive energies, positive norms, and causality.

will suffer a phase shift relative to the quantities that are transformed by CP, thus potentially violating CP symmetry. Such phase differences must be robust against gauge modifications in order to manifest themselves as CP violation. If simple redefinitions of the phases of any of the fields can remove overall phases in each field coupling, the theory remains CP-conserving. As will be shown in next sections, if only two fermion generations are present, such a redefinition always exists. For a CP violation phase the Kobayashi-Maskawa prediction of a third generation is necessary.

1.3 Neutral Mesons Formalism

1.3.1 Mixing of Neutral Mesons

The four pairs of conjugate neutral mesons that decay weakly, K^0, D^0, B^0, and B_s^0, can each mix with their respective antiparticle. The ability to mix implies that the flavor eigenstates may not be equivalent to the mass eigenstates; the observed presence of mixing (into conjugate flavor-specific decays) implies that the mass and flavor eigenstates are in fact different. Lack of CP symmetry implies a third set of eigenstates, CP eigenstates, which can differ from the mass and flavor eigenstates, as will be seen below.

Consider a weakly-decaying neutral meson X^0 (which could be any of K^0, D^0, B^0 or B_s^0). An arbitrary linear combination of the flavor eigenstates

$$a|X^0\rangle + b|\bar{X}^0\rangle \tag{1.4}$$

mixes according to the time-dependent Schrödinger equation

$$i\frac{\partial}{\partial t}\begin{pmatrix} a \\ b \end{pmatrix} = \mathcal{H}\begin{pmatrix} a \\ b \end{pmatrix}, \tag{1.5}$$

where

$$\mathcal{H} = M - i\frac{\Gamma}{2} \equiv \begin{pmatrix} m_{11} & m_{12} \\ m_{21} & m_{22} \end{pmatrix} - \frac{i}{2}\begin{pmatrix} \gamma_{11} & \gamma_{12} \\ \gamma_{21} & \gamma_{22} \end{pmatrix} \tag{1.6}$$

The m and γ parts represent the mixing and decay parts, respectively, of the time dependence. Each of the off-diagonal elements can be complex: the angle in the complex plane of m_{12} represents the phase of the mixing, and γ_{12} represents the (complex) cou-

pling to common decay modes of X^0 and $\bar{X}^0$ (for example, $B^0/\bar{B}^0 \rightarrow J/\psi K_S^0$ or $\pi^+\pi^-$). We can see that CPT invariance guarantees that $m_{11} = m_{22}$ and $\gamma_{11} = \gamma_{22}$, and that $m_{21} = m_{12}^*$ and $\gamma_{21} = \gamma_{12}^*$.

The mass eigenstates are the eigenvectors of the Hamiltonian:

$$\begin{aligned} |X_L\rangle &= p|X^0\rangle + q|\bar{X}^0\rangle \\ |X_H\rangle &= p|X^0\rangle - q|\bar{X}^0\rangle \end{aligned} \tag{1.7}$$

where $|X_L\rangle$ and $|X_H\rangle$ are the lighter and heavier mass eigenstates, and the coefficients p and q satisfy the relation

$$|q|^2 + |p|^2 = 1. \tag{1.8}$$

The eigenvalues λ_L e λ_H of (1.6) are:

$$\lambda_L = m_L - i\frac{\Gamma_L}{2}, \quad \lambda_H = m_H - i\frac{\Gamma_H}{2}, \tag{1.9}$$

where m_L and m_H are the masses of the eigenstates $|X_L\rangle$ and $|X_H\rangle$, respectively, and Γ_L and Γ_H their decay parts. Requiring the CPT invariance ($\mathcal{H}_{11} = \mathcal{H}_{22}$ and $\mathcal{H}_{21} = \mathcal{H}_{12}^*$) and defining the mass difference $\Delta m = m_H - m_L$ and amplitude difference $\Delta\Gamma = \Gamma_H - \Gamma_L$, we obtain:

$$(\Delta m)^2 - \frac{1}{4}(\Delta\Gamma)^2 = 4(|m_{12}|^2 - \frac{1}{4}|\gamma_{12}|^2), \quad \Delta m\Delta\Gamma = 4\mathrm{Re}(m_{12}\gamma_{12}^*), \tag{1.10}$$

$$\frac{q}{p} = \sqrt{\frac{m_{12}^* - \frac{1}{2}i\gamma_{12}^*}{m_{12} - \frac{1}{2}i\gamma_{12}}} = -\frac{\Delta m - \frac{i}{2}\Delta\Gamma}{2(m_{12} - \frac{i}{2}\gamma_{12})}. \tag{1.11}$$

1.3.2 The Neutral K System

Mixing between the two neutral K weak eigenstates K^0 and $\bar{K}^0$ was first predicted in 1955 by Gell-Mann and Pais [22]. The two physical states, $|K_1\rangle = \frac{1}{\sqrt{2}}(K^0 + \bar{K}^0)$ and $|K_2\rangle = \frac{1}{\sqrt{2}}(K^0 - \bar{K}^0)$, would thus be CP eigenstates with eigenvalues $+1$ and -1. The dominant decay of neutral K mesons is $\pi^+\pi^-$, due to helicity constraints and the fact the 3-body phase space is strongly suppressed at these mass scales (due to the well-known $(\Delta m)^5$ scaling rule). However, $\pi^+\pi^-$ is itself a CP eigenstate with eigenvalue $+1$. Thus, if CP were exactly conserved, *only the* $|K_1\rangle$ *physical state could decay into it*.

The limited phase space to decays other than $\pi^+\pi^-$ forces the lifetime of the eigenstate with opposite CP, K_2, to be far larger (3 orders of magnitude) than the lifetime of the K_1. Thus the nomenclature K_S^0 and K_L^0 (for short and long lifetimes) is used. The lifetime difference is very convenient since it allows for simple experimental separation of the two physical states.

In 1964, Fitch and Cronin made their discovery that K_L^0 can in fact decay into $\pi^+\pi^-$ with a branching fraction of 2×10^{-3} [1]. Since CP is thus not strictly conserved, the general formalism detailed in the previous subsection must be used. Thus we have

$$\begin{aligned} |K_S\rangle &= p|K^0\rangle + q|\bar{K}^0\rangle \\ |K_L\rangle &= p|K^0\rangle - q|\bar{K}^0\rangle \end{aligned} \tag{1.12}$$

where p and q are commonly parameterized as:

$$p = \frac{1+\epsilon}{\sqrt{2(1+|\epsilon|^2)}}; \qquad q = \frac{1-\epsilon}{\sqrt{2(1+|\epsilon|^2)}} \tag{1.13}$$

The real part of ϵ is a measure of CP violation purely in mixing whereas the imaginary part is a measure of CP violation in the interference between mixing and decay (see the following section). The former is the simplest one to be measured experimentally and was the effect seen in the original 1964 discovery. Since, in the K system, $\Delta\Gamma$ is of the same order as Δm, these effects are of similar magnitude, quite unlike the neutral B system, where the latter is far more prevalent.

1.3.3 The Neutral B System

The B^0 meson can mix with its respective antiparticle via a pair of box diagrams shown in fig. 1.1. In 1987 this mixing was established, with contributions from experiments at both proton-antiproton and electron-positron colliders. Some indication for $B^0 - \overline{B}^0$ mixing, contributed by both $B_d = (\bar{b}d)$ and $B_s = (\bar{b}s)$, was found by UA-1 at the $Sp\bar{p}S$ collider [23]; clear convincing evidence was first obtained by the ARGUS Collaboration at DORIS [24], at the $\Upsilon(4S)$, where only B_d is produced.

For neutral B mesons, in contrast with the neutral K system, the lifetime difference $\Delta\Gamma$ between the two mass eigenstates is *small* compared with the mixing frequency due to the difference in masses Δm. This difference in behavior of the K and B is due to the larger mass of the B meson and thus far greater phase space for flavor-specific

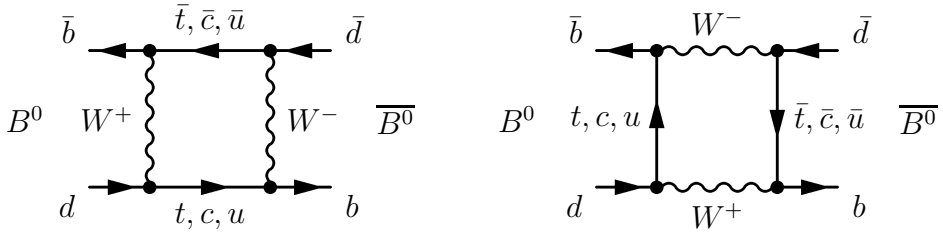

Figure 1.1: Feynman diagrams mixing $B^0 - \overline{B}^0$.

decays in the B system, which dominates the partial width (in contrast to the K system) and gives equivalent contributions (by CPT symmetry) to the width of both neutral B eigenstates. The resulting lack of decay suppression of either eigenstate implies nearly equivalent lifetimes.

Due to this simplification in formalism, the time evolution of neutral B mesons which are initially created (at time $t = 0$) as pure flavor eigenstates can be written as:

$$|B^0_{phys}(t)\rangle = f_+(t)|B^0\rangle + (q/p)f_-(t)|\overline{B}^0\rangle \tag{1.14}$$

$$|\overline{B}^0_{phys}(t)\rangle = f_+(t)|B^0\rangle + (q/p)f_-(t)|\overline{B}^0\rangle \tag{1.15}$$

where

$$f_+(t) = e^{-imt}e^{-\Gamma t/2}\cos(\Delta m t/2) \tag{1.16}$$

$$f_-(t) = e^{-imt}e^{-\Gamma t/2} i \sin(\Delta m t/2), \tag{1.17}$$

with $m = (m_H + m_L)/2$, $\Gamma = (\Gamma_H + \Gamma_L)/2$. This approximation holds up to the condition that

$$\Delta\Gamma \ll \Delta m \tag{1.18}$$

Since $\Delta\Gamma = \mathcal{O}(10^{-3})\Delta m$ in the B system, corrections to it are not considered in CP asymmetry measurements with the current statistics.

1.4 Three Types of CP Violation

Three types of CP violation can potentially be observed at B physics experiments:[2]

[2]There can be other manifestations of *CP* violation, *e. g.* CP violation in interaction. However observable *CP* violation at B-factories can all be classified into the 3 categories.

1. CP violation in decay (often referred to as direct CP violation): this occurs when multiple amplitudes with different weak phases as well as different strong phases contribute to a given final state, the result is visible as differing magnitude of the amplitude to a decay versus its CP conjugate.

2. CP violation purely in mixing: this occurs when the mass eigenstates of a neutral meson are different from the CP eigenstates.

3. CP violation in the interference between decays of mixed and unmixed mesons: this occurs for decays which are common to a neutral meson and its antiparticle.

1.4.1 CP Violation in Decay (Direct CP Violation)

Direct CP violation manifests itself as a difference in the magnitude of the amplitude to a given decay as compared with its CP conjugate, thus resulting in differing rates to the two elements of the CP conjugate pair (see fig. 1.2). It can occur for both neutral and charged decays.[3] Amplitudes from B^0 and $\overline{B}^0$ to a final state f and its CP conjugate may be written as

$$A_f = \sum_i A_i e^{i(\phi_i+\delta_i)} \qquad \text{and} \qquad \bar{A}_{\bar{f}} = \eta_{CP} \sum_i A_i e^{i(-\phi_i+\delta_i)} \tag{1.19}$$

where η_{CP} is the CP eigenvalue (multiplied by a convention-dependent phase) if f is a CP eigenstate, ϕ_i are the weak phases, and δ_i are the strong phases. CP violation can only occur when the different weak phase contributions also have different strong phases (otherwise a simple rotation can remove the strong phase and thus the ratio would clearly have unit magnitude). It can also only occur when weak phases are nontrivial, *i. e.* when exists a relative phase between them (that is therefore irreducible by a rotation of the Lagrangian). Only when both different weak phases *and* different strong phases are present, we may have the condition:

$$|\bar{A}_{\bar{f}}/A_f| \neq 1 \tag{1.20}$$

This is CP violation in decay. CP violation in decay has been observed in the kaon system and recently in the B system too. Since the strong phases that enter into measurements of CP violation in decay involve hadronic uncertainties, the relation of such

[3] For charged decays, it is the *only* potential manifestation of CP violation.

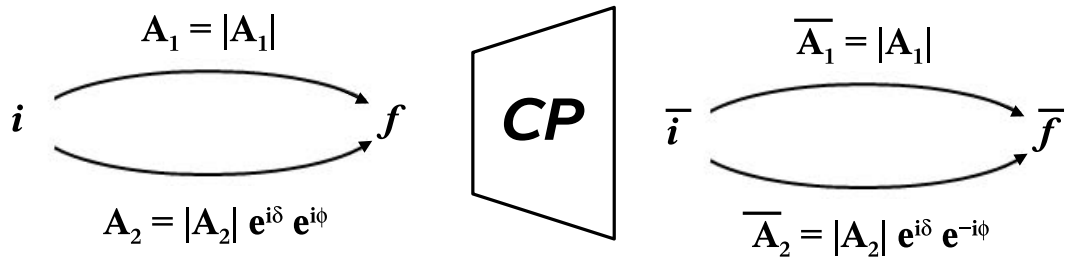

Figure 1.2: Effect of the "CP mirror" on interfering decay amplitudes for the transition between an initial state i and a final state f. The direct CP asymmetry is due to the interference between two amplitudes A_1 and A_2 with a relative CP-conservating phase δ and a CP-violating phase ϕ.

measurements to CKM factors (see next section) cannot be calculated from first principles. However, the strong phases may themselves be measured if the CKM factors are known from other measurements. These strong phase measurements can then be used as inputs to other measurements which have equivalent strong phases (thus allowing the extraction of other parameters), and thus measurements of CP violation in decay can (indirectly) provide a useful handle on fundamental quantities.

1.4.2 CP Violation Purely in Mixing

From section 1.3.1, the mass eigenstates of the neutral meson system are the eigenvectors of the Hamiltonian:

$$\begin{aligned} |B_L\rangle &= p|B^0\rangle + q|\overline{B}^0\rangle \\ |B_H\rangle &= p|B^0\rangle - q|\overline{B}^0\rangle \end{aligned} \tag{1.21}$$

where

$$\frac{q}{p} = \sqrt{\frac{m_{12}^* - \frac{1}{2}i\gamma_{12}^*}{m_{12} - \frac{1}{2}i\gamma_{12}}} \tag{1.22}$$

If q and p have different magnitudes, the CP conjugates of the mass eigenstates clearly will differ from the mass eigenstates themselves by more than a trivial phase. Thus the mass eigenstates will not be CP eigenstates and CP violation will be manifest. CP violation from

$$|q/p| \neq 1 \tag{1.23}$$

is purely an effect of mixing and is independent of decay mode. Thus it may be referred to as CP violation purely in mixing.

In neutral B decays, as discussed in section 1.3.3, this effect is expected to be very small. Since

$$\Delta m = \mathcal{O}(10^3)\Delta\Gamma \tag{1.24}$$

this implies that

$$|m_{12}| \gg |\gamma_{12}| \tag{1.25}$$

and thus the factor in eq. 1.11 simplifies to a near-phase. CP violation purely in mixing should thus only enter the neutral B system at the 10^{-3} level. An asymmetry in the measurements of the overall rate to flavor tagged B^0 vs. $\overline{B}^0$ would be a signature of CP violation purely in mixing. With greater statistics, evidence for this may be seen; at present, experimental limits exist. It has been clearly observed, however, in the neutral kaon system (where it is the prevalent effect); the discovery of CP violation in 1964 was a detection of CP violation purely in mixing.

1.4.3 CP Violation in Interference Between Decays of Mixed and Unmixed Mesons

Final states which may be reached from either B^0 or $\overline{B}^0$ decays can exhibit a third type of CP violation, which results from the interference between the decays of mixed and of unmixed neutral B mesons which both decay to the final state (see fig. 1.3).

Consider the CP-violating asymmetry in rates between B^0 and $\overline{B}^0$ as a function of

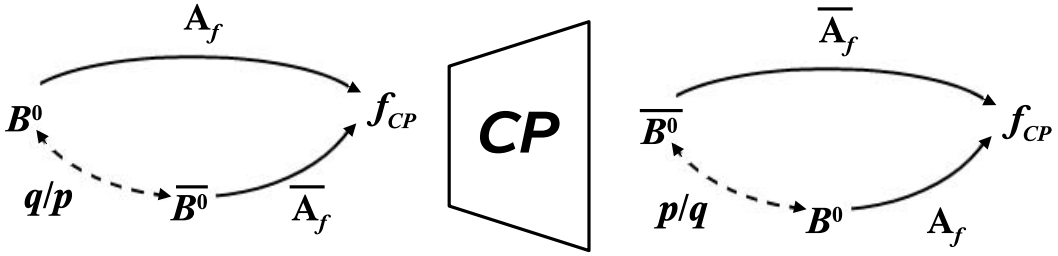

Figure 1.3: Effect of the "CP mirror" on B^0 decay to a CP eigenstate f_{CP}. The CP asymmetry is due to the interference between mixing, described by parameters p and q, and the decay amplitudes A_f and $\bar{A}_f$.

time:

$$a_{CP}(t) = \frac{\Gamma(B^0_{phys}(t) \to f) - \Gamma(\bar{B}^0_{phys}(t) \to f)}{\Gamma(B^0_{phys}(t) \to f) + \Gamma(\bar{B}^0_{phys}(t) \to f)} \tag{1.26}$$

To calculate each of the time-dependent rates $\Gamma(t)$, one can form the inner product of eqs. 1.14 and 1.15 with the final state f and then take the magnitude squared of the resulting amplitudes:

$$\begin{aligned}
&\Gamma(B^0(t) \to f) \propto \\
&|\langle f|\mathcal{H}|B^0(t)\rangle|^2 = \quad e^{-\Gamma t} \quad &\left\{\cos^2\left(\frac{\Delta m t}{2}\right)|\langle f|\mathcal{H}|B^0\rangle|^2\right. \\
&&+\sin^2\left(\frac{\Delta m t}{2}\right)\left|\frac{q}{p}\right|^2|\langle f|\mathcal{H}|\overline{B}^0\rangle|^2 \\
&&-\frac{i}{2}\left|\frac{q}{p}\right|e^{-2i\phi_M}\sin(\Delta m t)\langle f|\mathcal{H}|B^0\rangle\langle f|\mathcal{H}|\overline{B}^0\rangle^* \\
&&\left.+\frac{i}{2}\left|\frac{q}{p}\right|e^{2i\phi_M}\sin(\Delta m t)\langle f|\mathcal{H}|B^0\rangle^*\langle f|\mathcal{H}|\overline{B}^0\rangle\right\}
\end{aligned} \tag{1.27a}$$

$$\begin{aligned}
&\Gamma(\overline{B}^0(t) \to f) \propto \\
&|\langle f|\mathcal{H}|\overline{B}^0(t)\rangle|^2 = \quad e^{-\Gamma t} \quad &\left\{\cos^2\left(\frac{\Delta m t}{2}\right)|\langle f|\mathcal{H}|\overline{B}^0\rangle|^2\right. \\
&&+\sin^2\left(\frac{\Delta m t}{2}\right)\left|\frac{p}{q}\right|^2|\langle f|\mathcal{H}|B^0\rangle|^2 \\
&&+\frac{i}{2}\left|\frac{p}{q}\right|e^{-2i\phi_M}\sin(\Delta m t)\langle f|\mathcal{H}|B^0\rangle\langle f|\mathcal{H}|\overline{B}^0\rangle^* \\
&&\left.-\frac{i}{2}\left|\frac{p}{q}\right|e^{2i\phi_M}\sin(\Delta m t)\langle f|\mathcal{H}|B^0\rangle^*\langle f|\mathcal{H}|\overline{B}^0\rangle\right\}
\end{aligned} \tag{1.27b}$$

where $2\phi_M$ is the phase of q/p. Since, as shown above, for the B system $|q/p| \approx 1$, we can thus write

$$\langle f|\mathcal{H}|\overline{B}^0(t)\rangle = \eta_{CP}e^{-2i\phi_D}|\lambda|\langle f|\mathcal{H}|B^0(t)\rangle \tag{1.28}$$

where ϕ_D is the phase of the decay, η_{CP} is the CP eigenvalue of f, and

$$\lambda = \frac{q}{p}\frac{\langle f|\mathcal{H}|\overline{B}^0\rangle}{\langle f|\mathcal{H}|B^0\rangle} = \frac{q}{p}\frac{\overline{A}_f}{A_f} = |\lambda|e^{-2i(\phi_M+\phi_D)}. \tag{1.29}$$

In this way the expressions 1.27a and 1.27b greatly simplify:

$$|\langle f|\mathcal{H}|B^0(t)\rangle|^2 = A^2 e^{-\Gamma t}\{1 - C\cos(\Delta m t) - S\sin(\Delta m t)\} \quad (1.30)$$

$$|\langle f|\mathcal{H}|\overline{B}^0(t)\rangle|^2 = A^2 e^{-\Gamma t}\{1 + C\cos(\Delta m t) + S\sin(\Delta m t)\} \quad (1.31)$$

where $A^2 = |\langle f|\mathcal{H}|B^0\rangle|^2$ and

$$C = \frac{1-|\lambda|^2}{1+|\lambda|^2} \qquad \text{and} \qquad S = \eta_{CP}\frac{-2\sin(2(\phi_M+\phi_D))}{1+|\lambda|^2} = \frac{2\,\mathrm{Im}\,\lambda}{1+|\lambda|^2} \quad (1.32)$$

Thus the time-dependent asymmetry

$$a_{CP}(t) = \frac{\Gamma(B^0_{phys}(t)\to f) - \Gamma(\overline{B}^0_{phys}(t)\to f)}{\Gamma(B^0_{phys}(t)\to f) + \Gamma(\overline{B}^0_{phys}(t)\to f)} = C\cos(\Delta m t) - S\sin(\Delta m t) \quad (1.33)$$

In the absence of CP violation, S and C must both go to zero, since they occur only when weak phases do not cancel. C is only nonzero when the ratio of the amplitude norms differs from unity, which is the signature of direct CP violation (detailed in section 1.4.1). However, it is possible that $|q/p| = 1$ and $|\lambda| = 1$, *i. e.*, there is no CP violation in either mixing or decay, but the CP asymmetry in eq. 1.33 is nonzero, because $\mathrm{Im}\lambda \neq 0$. In this case, from the definitions in 1.32, S is nonzero. This represents a distinct type of CP violation. It results from the interference of the decays of mixed mesons with those of unmixed mesons (*CP violation in the interference between decay with and without mixing*, or *mixing-induced CP violation*); if the mixing contains a phase that is not cancelled by the decay itself, this observable time-dependent asymmetry above will result. Unlike CP violation in decay, no nontrivial strong phases are required.

As will be seen in the next section, CP violation in interference between decays of mixed and unmixed mesons is a large effect in the SM picture of the neutral B system. Since this is a measurement of an asymmetry rather than an absolute rate, many experimental and model-dependent uncertainties (such as reconstruction efficiency) that would otherwise contribute to experimental error, instead cancel out in the ratio. Thus it provides an excellent mechanism for precision measurements of CP violation and the study of the SM picture of CP asymmetry.

1.5 CP Violation in the Standard Model

CP violation within the context of the Standard Model $\mathrm{SU}(2) \times \mathrm{U}(1)$ electroweak symmetry was introduced by Kobayashi and Maskawa in 1973 via the postulation of a third family of quarks. This occurred a year prior to the discovery of charm; only 3 quarks existed at the time, so the prediction was quite prescient. The b-quark was then first observed in 1977. The prediction of additional quarks did not occur entirely without precedent, however. Theoretical interpretation of quark mixing via the weak interaction has closely followed experimental result, and the development of the 3 x 3 CKM matrix and its CP violating phase was a steady and piecewise process.

1.5.1 The CKM Matrix

The observed suppression of flavor-changing neutral current decays indicates that the quark sector is separated into families, similar to the lepton sector. However, lepton flavor is conserved[4], whereas quark generation is manifestly violated (*e. g.* in weak decays of kaons). However, strangeness-changing decays have an additional suppression compared with strangeness-conserving weak decays. This "Cabibbo factor" may be accounted for by considering that, similar to neutral mesons, the quark mass eigenstates differ from the weak eigenstates. Thus a mixing matrix describing transitions between quark generations is necessary.

Such a matrix must be unitary since quark number is manifestly conserved. With 2 generations, a unitary matrix can be described by a single parameter θ_C:

$$\begin{pmatrix} d_{mass} \\ s_{mass} \end{pmatrix} = \begin{pmatrix} \cos\theta_C & \sin\theta_C \\ -\sin\theta_C & \cos\theta_C \end{pmatrix} \begin{pmatrix} d \\ s \end{pmatrix} \tag{1.34}$$

where d_{mass} and s_{mass} are the mass eigenstates nearest to the flavor eigenstates d and s respectively. The Cabibbo quark-mixing angle θ_C, was introduced in 1963 [4] to explain the small weak-interaction decay rates for particles carrying strangeness. When CP violation was discovered in 1964 by the observation of the CP-odd decay $K_L^0 \rightarrow \pi^+\pi^-$ [1], researchers had not yet perceived the intimate relation between the dynamical rules of quark-flavor mixing and the phenomenon of CP violation. Hence the terrain was open for speculations. In 1970, Glashow, Iliopoulos and Maiani (GIM) [25] used the unitary quark-mixing ansatz to postulate the existence of a fourth

[4] not considering the recently discovered neutrino oscillations and thus lepton mixing.

quark with quantum number charm to explain the observed suppression of strangeness-changing neutral currents (*e. g.*, $K_L^0 \to \mu^+\mu^-$). This mechanism yields the absence of tree-level Flavor-Changing Neutral Currents (FCNC) in the SM. The same matrix 1.34 (experimentally) holds for the (u, c) quark pair. The Cabbibo angle θ_C is thus a full description of 2-generation mixing.

In 1973 the concept of quark-flavor mixing and CP violation were unified when Kobayashi and Maskawa showed that for at least three generations of quarks, there would be enough physical degrees of freedom left in the quark-flavor mixing matrix to allow for a nonzero phase [5]. The subsequent discovery of bottom and top quarks, and even a third lepton generation, as well as the observation of direct CP violation in the kaon system backed the KM idea. For three quarks families the Yukawa interaction of the quarks is given by

$$\mathcal{L}_Y = -Y_{ij}^d \, \overline{Q_{Li}^I} \, \phi \, d_{Rj}^I - Y_{ij}^u \, \overline{Q_{Li}^I} \, \varepsilon \, \phi^* u_{Rj}^I + \text{h.c.}, \tag{1.35}$$

where $Y^{u,d}$ are 3×3 complex matrices, ϕ is the Higgs field, i and j are generation labels, and ε is the 2×2 antisymmetric tensor. The Q_L^I are left-handed quark doublets, and d_R^I and u_R^I are right-handed down- and up-type quark singlets, respectively, in the weak-eigenstate basis. When ϕ acquires a vacuum expectation value, $\langle\phi\rangle = (0, v/\sqrt{2})$, eq. (1.35) yields Dirac mass terms for quarks with 3×3 mass matrices

$$M^u = \frac{vY^u}{\sqrt{2}}, \qquad M^d = \frac{vY^d}{\sqrt{2}}. \tag{1.36}$$

To move from the basis of the flavor eigenstates to the basis of the mass eigenstates, one performs the transformation

$$U_L^{u(d)} M^{u(d)} U_R^{u(d)\dagger} = \text{diag}\Big(m_{u(d)}, m_{c(s)}, m_{t(b)}\Big), \tag{1.37}$$

where $U_L^{u,d}$ and $U_R^{u,d}$ are unitary matrices and the masses m_q are real. The quark mass matrices are diagonalized by different transformations for the left-handed up- and down-quarks, which are part of the same $\text{SU}(2)_L$ doublet,

$$Q_L^I = \begin{pmatrix} u_{Li}^I & d_{Li}^I \end{pmatrix} = (U_L^{u\dagger})_{ij} \begin{pmatrix} u_{Lj} & (U_L^u U_L^{d\dagger})_{jk} \, d_{Lk} \end{pmatrix}. \tag{1.38}$$

By convention, we pulled out $(U_L^{u\dagger})_{ij}$, so that the “misalignment" between the two

transformations operates on the down-type quark mass eigenstates. Thus the charged-current weak interaction is modified by the product of the diagonalizing matrices of the up- and down-type quark mass matrices, the so-called Cabibbo-Kobayashi-Maskawa (CKM) matrix,

$$V = U_L^u U_L^{d\dagger} = \begin{pmatrix} V_{ud} & V_{us} & V_{ub} \\ V_{cd} & V_{cs} & V_{cb} \\ V_{td} & V_{ts} & V_{tb} \end{pmatrix} . \tag{1.39}$$

However, the neutral-current part of the Lagrangian in the mass eigenstate basis remains unchanged, *i. e.* there are no flavor-changing neutral currents at tree level.

Being the product of unitary matrices, V itself is unitary, $VV^\dagger = \mathrm{I}$. This requirement and the freedom to arbitrarily choose the global phases of the quark fields reduce the initial nine unknown complex elements of V to three real numbers and one phase, where the latter accounts for CP violation. Because these four numbers effectively govern the rates of all tree- and loop-level electroweak transitions (see section 1.5.3 for a description of these transitions) that involve the charged current, it is a compelling exercise to overconstrain V. If inconsistencies among different measurements occur, it would reveal the existence of physics beyond the SM.

1.5.2 Unitarity Conditions and the Unitarity Triangle

Unitarity of the CKM matrix V requires that

$$V^\dagger V = VV^\dagger = \mathrm{I} \quad \Rightarrow \quad \sum_{\mathrm{j}} V_{ji}^* V_{jk} = \sum_j V_{ij} V_{kj}^* = \delta_{ik} \tag{1.40}$$

This results in 9 independent equations, 3 of which (for the diagonal of the product unit matrix) equal one and 6 of which equal zero. The equations for the off-diagonal elements, each containing a sum of 3 complex numbers which equals 0, will each

describe a triangle in the complex plane:

$$V_{cd}V_{ud}^* + V_{cs}V_{us}^* + V_{cb}V_{ub}^* = 0 \tag{1.41a}$$
$$V_{cd}V_{td}^* + V_{cs}V_{ts}^* + V_{cb}V_{tb}^* = 0 \tag{1.41b}$$
$$V_{ud}V_{td}^* + V_{us}V_{ts}^* + V_{ub}V_{tb}^* = 0 \tag{1.41c}$$
$$V_{us}^*V_{ud} + V_{cs}^*V_{cd} + V_{ts}^*V_{td} = 0 \tag{1.41d}$$
$$V_{ub}^*V_{us} + V_{cb}^*V_{cs} + V_{tb}^*V_{ts} = 0 \tag{1.41e}$$
$$V_{ub}^*V_{ud} + V_{cb}^*V_{cd} + V_{tb}^*V_{td} = 0 \tag{1.41f}$$

The differences between these 6 triangles are purely empirical. There is no theoretical motivation at present for the fact that 4 of them are nearly degenerate and only 2 describe triangles that have each of their sides being the same order of magnitude in length. It is empirically the case that only eqs. 1.41c and 1.41f above describe triangles which are not nearly degenerate. The triangle corresponding to the last equation, 1.41f, is the one that is used to pictorially represent the irreducible CP violating phase and is referred to as the Unitarity Triangle (UT).

The number of free parameters of V can be greatly reduced by very general considerations. Unitarity and the freedom to arbitrarily choose the global phase of a quark field, reduce the original $2n_g^2$ unknowns (where $n_g = 3$ is the number of generations) to $(n_g - 1)^2$ unknowns. Among these $n_g(n_g - 1)/2$ are rotation angles and $(n_g - 1)(n_g - 2)/2$ phases describe CP violation. Three generations allow for only a single CP-violating phase, in total four independent parameters.

They exist many CKM parameterizations. Chau and Keung [26] proposed the "standard parameterization" of V. It is obtained by the product of three (complex) rotation matrices, where the rotations are characterized by the Euler angles θ_{12}, θ_{13} and θ_{23}, which are the mixing angles between the generations, and one overall phase δ,

$$V = \begin{pmatrix} c_{12}c_{13} & s_{12}c_{13} & s_{13}e^{-i\delta} \\ -s_{12}c_{23} - c_{12}s_{23}s_{13}e^{i\delta} & c_{12}c_{23} - s_{12}s_{23}s_{13}e^{i\delta} & s_{23}c_{13} \\ s_{12}s_{23} - c_{12}c_{23}s_{13}e^{i\delta} & -c_{12}s_{23} - s_{12}c_{23}s_{13}e^{i\delta} & c_{23}c_{13} \end{pmatrix}, \tag{1.42}$$

where $c_{ij} = \cos\theta_{ij}$ and $s_{ij} = \sin\theta_{ij}$ for $i < j = 1, 2, 3$. This parameterization satisfies exactly the unitarity relation.

Following the observation of a hierarchy between the mixing angles, $s_{13} \ll s_{23} \ll$

$s_{12} \ll 1$, Wolfenstein [27] proposed an expansion of the CKM matrix in terms of the four parameters λ, A, ρ and η ($\lambda \simeq |V_{us}| \approx 0.23$ being the expansion parameter, that is the Cabibbo parameter $\lambda \equiv \sin\theta_C$), which is widely used in the contemporary literature. We use the definitions to *all orders* [28]

$$\begin{aligned} s_{12} &\equiv \lambda\,, \\ s_{23} &\equiv A\lambda^2\,, \\ s_{13}e^{-i\delta} &\equiv A\lambda^3(\rho - i\eta)\,. \end{aligned} \tag{1.43}$$

Inserting the above definitions into eq. (1.42), we have the expressions for all CKM elements. We can truncate at third order in λ:

$$V = \begin{pmatrix} 1-\frac{\lambda^2}{2} & \lambda & A\lambda^3(\rho - i\eta) \\ -\lambda & 1-\frac{\lambda^2}{2} & A\lambda^2 \\ A\lambda^3(1-\rho-i\eta) & -A\lambda^2 & 1 \end{pmatrix} + \mathcal{O}(\lambda^4) \tag{1.44}$$

with (λ, A, ρ, η) as the 4 real parameters describing the CKM matrix, the latter 3 being of order 1.

Unitary triangle obtained by eq. 1.41f can be rotated and scaled choosing a conventional phase in a way that $V_{cb}^* V_{cd}$ is real, and so aligning related side to real axis, and dividing length of all sides for $|V_{cd}V_{cb}^*|$ so length is normalized to 1. The triangle (show in fig. 1.4) will have two fixed vertexes at (0,0) and at (1,0) and coordinates of the remaining vertices will depends by (ρ,η) corresponding to Wolfenstein's parameters; lengths of sides become:

$$R_u \equiv \left|\frac{V_{ub}^* V_{ud}}{V_{cb}^* V_{cd}}\right| = \sqrt{\rho^2+\eta^2}, \qquad R_t \equiv \left|\frac{V_{tb}^* V_{td}}{V_{cb}^* V_{cd}}\right| = \sqrt{(1-\rho)^2+\eta^2}. \tag{1.45}$$

The three angles of out unitary triangle, denoted with α, β and γ, are:

$$\alpha \equiv \arg\left[-\frac{V_{td}V_{tb}^*}{V_{ud}V_{ub}^*}\right], \quad \beta \equiv \arg\left[-\frac{V_{cd}V_{cb}^*}{V_{td}V_{tb}^*}\right], \quad \gamma \equiv \arg\left[-\frac{V_{ud}V_{ub}^*}{V_{cd}V_{cb}^*}\right]. \tag{1.46}$$

These quantities are physical and can be measured from CP asymmetries in B decays. Consistency among different experimental values helps in the verification of the SM.

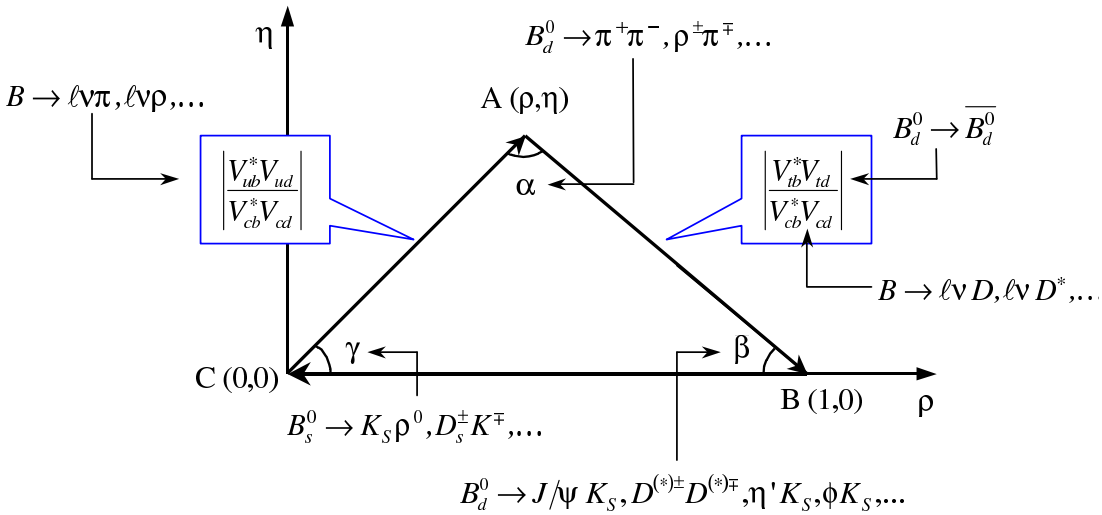

Figure 1.4: Unitary triangle and main decays to measure the sides and the angles.

1.5.3 Tree and penguin processes

For the CP asymmetries it is important to consider both weak phases difference and strong phases difference. So, we need to distinguish which diagrams give a contribution to total amplitude with different phases. Generally, amplitudes for mesons composed by a heavy quark and a light quark are divided in two classes, so called *tree* and *loop* (also known as *penguin*). If all complications due to long distance strong interactions, final state interactions or hadron-hadron interactions are negligible, this split is easily explained through weak diagrams.

In the penguin diagrams the W boson is emitted and reabsorbed in the same line of emitter quark (fig. 1.5), while all other diagrams are tree, *i. e.* they have no loop in weak diagram (fig. 1.6). Tree diagrams are further split in *spectator* (light quark of the starting meson is disconnected in the weak diagram), *exchange* (W boson is swapped between starting meson quarks) and *annihilation* (starting meson quarks are annihilated to make W). However, this separation between different kinds of tree diagram is not important in CP violation because two kinds of tree diagrams, that contribute to decay amplitude, have the same CKM matrix element and so the same weak phase. Differently from tree diagram, in $b \to q$ process with $q = \{d, s\}$, penguin terms contribute with different combinations of CKM elements $V_{ib}^* V_{iq}$ depending by the quark within loop $i = \{u, c, t\}$. So the differences of weak phase, which contribute to the CP-asymmetries, are due to the different penguin and tree contributions; therefore it becomes important to know intensities and weak phases related to both kinds of dia-

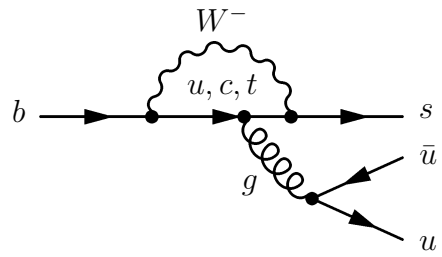

Figure 1.5: Penguin diagram for $b \to sg^*$ process.

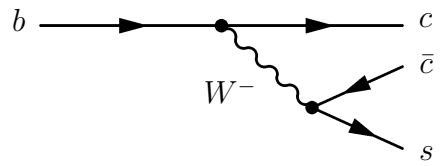

Figure 1.6: Tree diagram for $b \to cW^-$ process.

gram.

Penguin diagrams include strong interactions too. The quark in the loop emits a gluon to compensate for mass difference between initial and final quark. Gluon can produce a quark-antiquark pair or be reabsorbed and re-issued from other gluons that can be found in this kind of process. The differences of strong phase of these processes are the base for the direct CP asymmetry.

The FCNC transitions, $b \to s$ and $b \to d$, are forbidden at tree level in SM. They can only occur at the loop level. In these loop diagrams, the SM particles can be replaced with new particles. As a result, the rates and kinematic distributions of FCNC decays can significantly deviate from the SM predictions. Therefore the FCNC decays serve as a sensitive probe of the new physics.

1.5.4 Extraction of CKM matrix elements

With the remarkable exception of the UT angles, the experimental observables presently used to constrain (ρ, η) vertex depend on hadronic matrix elements. QCD is well established as the theory of strong interaction, and it has been tested to high precision in

the perturbative regime where the coupling constant α_s is small. However, presently it is difficult to obtain quantitative predictions in the low-energy regime, except for a few special cases. In this section we recall briefly a few general techniques to evaluate the matrix elements relevant to quark-flavor physics. These methods give controllable systematic errors, that is the uncertainties can be incrementally improved in a well-defined way, expanding in small parameters order by order. Most of the model-independent theoretical tools utilize that some quark masses are smaller while others are greater than $\Lambda_{\rm QCD}$ (here $\Lambda_{\rm QCD}$ denotes a typical hadronic scale, of order 500 MeV).

Effective Hamiltonians for Weak Decays

All flavor-changing interactions (except that of the top quark) are due to tree and loop diagrams involving heavy virtual particles: W bosons in the SM, or not-yet-discovered particles in its extensions. These particles propagate over much shorter distances than $1/m_b$, so their interactions can be described by local operators. In principle, there is an infinite number of such operators. The contributions of the higher dimensional ones are however suppressed by increasing powers of m_b/m_W, so it is sufficient to consider the first few operators. The effective weak Hamiltonian can be written as $H_W = \sum C_i(\mu)\, O_i(\mu)$, where O_i are the lowest dimensional operators contributing to a certain process and C_i are their Wilson coefficients, with perturbatively calculable scale dependences. The simplest examples where this methods is applied are the semileptonic decays (like $b \to c\ell\bar{\nu}$) while semileptonic decays involving a $\bar{\ell}\ell$ pair and nonleptonic decays are more complicated. For more details see ref. [29].

Chiral Symmetry

The u, d and s-quark masses are small compared with $\Lambda_{\rm QCD}$, so it is useful to consider the $m_q \to 0$ limit ($q = u, d, s$) and treat corrections perturbatively. This is known as the chiral limit, because the Lagrangian for the light quarks has a $\mathrm{SU}(3)_{\rm L} \times \mathrm{SU}(3)_{\rm R}$ chiral symmetry, under which the left- and right-handed quarks transform differently. This symmetry is spontaneously broken to $\mathrm{SU}(3)_{\rm V}$ by the vacuum expectation value of the quark families. Chiral symmetry relates different hadronic matrix elements to one another, and has very diverse applications in flavor physics.

Because the u and d-quark masses are small, the $\mathrm{SU}(2)$ isospin symmetry between the u and d is usually a very good approximation. The corrections to the chiral limit are suppressed by $(m_d - m_u)/\Lambda_{\chi\rm SB}$, where $\Lambda_{\chi\rm SB} \approx 1\,\mathrm{GeV}$ is the chiral symmetry

breaking scale, and are usually not larger than a few percent at the amplitude level. There are also explicit violations of chiral symmetry, for example, due to weak or electromagnetic interactions. The full $\mathrm{SU}(3)$ symmetry is broken by $m_s/\Lambda_{\chi\mathrm{SB}}$, and is known to have typically $20-30\%$ corrections.

Some of the most prominent cases of isospin symmetry in the context of the CKM matrix include relations between amplitudes involving charged and neutral pions, the determination of $|V_{ud}|$, and the extraction of the UT angle α from $B \to \pi\pi$ decays. Similarly, $\mathrm{SU}(3)$ symmetry and chiral perturbation theory are key ingredients in determining $|V_{us}|$. $\mathrm{SU}(3)$ has also been used as a bound on the SM-induced deviations of the time-dependent CP asymmetries from $\sin 2\alpha$ or $\sin 2\beta$ in the penguin-dominated modes (see section 1.5.7).

Heavy-Quark Symmetry and Heavy-Quark Effective Theory

In mesons composed of a heavy quark and a light antiquark the energy scale of strong interactions is small compared with the heavy-quark mass. The heavy quark acts as a static point-like color source with fixed four-velocity, which cannot be altered by the soft gluons responsible for confinement. Hence the configuration of the light degrees of freedom becomes independent of the spin and flavor (mass) of the heavy quark, which, for N_f heavy-quark flavors, results in a $\mathrm{SU}(2\mathrm{N_f})$ heavy-quark spin-flavor symmetry [30].

Heavy-quark spin-flavor symmetry has many important implications for the spectroscopy and strong decays of B and D mesons (for details see [31]). It is especially predictive for exclusive $B \to D^{(*)}\ell\overline{\nu}$ semileptonic decays, which are relevant for the determination of $|V_{cb}|$.

Deviations from the heavy-quark limit can be included using the heavy-quark effective theory (HQET) [32], which provides a systematic expansion in powers of $\alpha_s(m_Q)$ and $\Lambda_{\mathrm{QCD}}/m_Q$ ($Q = b, c$). The former type of corrections is calculable perturbatively, whereas the latter ones can be parameterized by a minimal set of hadronic matrix elements that can be extracted from data and/or estimated using nonperturbative techniques.

Factorization and Soft-Collinear Effective Theory

In the decay $B \to M_1 M_2$, if the meson M_1 that inherits the spectator quark from the B is heavy and M_2 is light then “color transparency" can justify factorization [33, 34].

Traditionally, naive factorization refers to the hypothesis that matrix elements of the four-quark operators can be estimated by grouping the quark fields into a pair that can mediate $B \to M_1$ transition and into another pair that describes vacuum $\to M_2$ transition.

These ideas are the base of the recent development of the Soft Collinear Effective Theory (SCET) [35]. SCET is designed to describe the interactions of energetic and low invariant-mass partons in the $Q \gg \Lambda_{\rm QCD}$ limit. It introduces distinct fields for the relevant degrees of freedom, and a power-counting parameter λ. There are two distinct theories, $\rm SCET_I$ in which $\lambda = \sqrt{\Lambda_{\rm QCD}/Q}$ and $\rm SCET_{II}$ in which $\lambda = \Lambda_{\rm QCD}/Q$. They are appropriate for final states with invariant mass $Q\lambda$, like jets and inclusive $B \to X_s\gamma$, $X_u\ell\overline{\nu}$, $X_s\ell^+\ell^-$ decays ($m_X^2 \sim \Lambda_{\rm QCD}Q$) for $\rm SCET_I$, and exclusive hadronic final states ($m^2 \sim \Lambda_{\rm QCD}^2$) for $\rm SCET_{II}$.

1.5.5 Magnitudes of CKM matrix elements

We report in this section the measurements of the magnitude of CKM elements. More informations can be found in ref. [36].

$|V_{ud}|$

The most precise determination comes from the study of superallowed $0^+ \to 0^+$ nuclear β decays:

$$|V_{ud}| = 0.97377 \pm 0.00027. \tag{1.47}$$

$|V_{us}|$

The magnitude of V_{us} has been extracted traditionally from semileptonic kaon decays:

$$|V_{us}| = 0.2257 \pm 0.0021. \tag{1.48}$$

$|V_{cd}|$

The most precise measurement of $|V_{cd}|$ is based on neutrino and antineutrino interactions. The difference of the ratio of double-muon to single-muon production by neutrino and antineutrino beams is proportional to the charm cross section off valence

d-quarks, which allows to obtain:

$$|V_{cd}| = 0.230 \pm 0.011. \tag{1.49}$$

$|V_{cs}|$

The direct determination of $|V_{cs}|$ is possible from semileptonic D or leptonic D_s decays, relying on the calculations of the hadronic matrix elements. We obtain

$$|V_{cs}| = 0.957 \pm 0.017 \pm 0.093, \tag{1.50}$$

where the first error is experimental and the second one, which is dominant, is from the theoretical error of the form factor.

$|V_{cb}|$

This matrix element can be determined from exclusive and inclusive semileptonic decays of B mesons to charm:

$$|V_{cb}| = (41.6 \pm 0.6) \times 10^{-3}. \tag{1.51}$$

$|V_{ub}|$

The determination of $|V_{ub}|$ has been obtained combining measurements from inclusive and exclusive $B \to X_u \ell \bar{\nu}$ decays:

$$|V_{ub}| = (4.31 \pm 0.30) \times 10^{-3}, \tag{1.52}$$

which is dominated by the inclusive measurement. This measurement is somewhat above the range favored by the measurement of the $\sin 2\beta$ discussed below.

$|V_{td}|$ and $|V_{ts}|$

The CKM elements $|V_{td}|$ and $V_{ts}|$ cannot be measured from tree-level decays of the top quark, so one has to rely on determinations from $B - \overline{B}$ oscillations mediated by box diagrams or loop-mediated rare K and B decays. Theoretical uncertainties in hadronic effects limit the accuracy of the current determinations. These can be reduced by taking ratios of processes that are equal in the flavor $\mathrm{SU}(3)$ limit to determine $|V_{td}/V_{ts}|$.

For these last measurements a new theoretically clean and significantly improved constraint is provided by the measurements of the mass difference of the two neutral B_s meson by CDF Collaboration, $\Delta m_s = (17.77 \pm 0.10 \pm 0.07)$ ps^{-1} [37].

$$|V_{td}| = (7.4 \pm 0.8) \times 10^{-3} \quad (1.53)$$

$$|V_{ts}| = (40.6 \pm 2.7) \times 10^{-3} \quad (1.54)$$

$$|V_{td}/V_{ts}| = 0.206^{+0.008}_{-0.006} \quad (1.55)$$

$|V_{tb}|$

The direct determination of $|V_{tb}|$ from top decays uses the ratio of branching fractions $R = \mathcal{B}(t \to Wb)/\mathcal{B}(t \to Wq) = |V_{tb}|^2$, where $q = b, s, d$. The measurements give a 95% CL lower limit

$$|V_{tb}| > 0.78. \quad (1.56)$$

1.5.6 Unitarity Triangle Angle Measurements

The UT angles α, β and γ (defined in eq. 1.46) are all accessible from the B sector, albeit with different sensitivity and purity. Whereas the measurements of β (the leading experimental observable here is $\sin 2\beta$) and γ, through B decays in charmonium and open charm, respectively, are theoretically clean, the measurement of α in charmless B decays relies on theoretical assumptions. Because the measurements of α and γ involve interference with transitions governed by the small CKM matrix element V_{ub}, they require larger data samples than when measuring $\sin 2\beta$. The $\sin 2\beta$ can be also measured in penguin dominated modes with $b \to s$ transitions (see section 1.5.7), where, also in this case, due to the small branching fractions of the modes involved, a larger data sample is required than when measuring $\sin 2\beta$ in charmonium.

The experimental techniques to measure the UT angles also change radically from one to another. The measurements of α and β require $B^0\overline{B}^0$ mixing and therefore use neutral B mesons, whereas the measurements of γ use interference between $b \to u$ and $b \to c$ decay amplitudes, and can be done with both neutral and charged B decays.

Concerning the CP violation in B^0 mixing, which has been searched for with both flavor-specific and inclusive B^0 decays in samples where the initial flavor state is tagged, the current world average is $|q/p| = 1.0018 \pm 0.0017$ [38, 39], whereas the deviation from unity is expected to be $|q/p| - 1 \approx 0.0003$ [40]. For this reason we will

neglect it in the following.

In this section we will briefly report techniques and measurements of the UT angles. More informations can be found in ref. [36].

β from B Decays to Charmonium Final States

In $b \to c\bar{c}s$ quark-level decays, the time-dependent CP violation parameters measured from the interference between decays with and without mixing are S and C defined in eq. 1.32. In the SM, with a very good approximation, we expect for these decays $S = -\eta_{CP}\,\sin 2\beta$ and $C = 0$ for the transition $B^0 \to f$, where $\eta_{CP} = \pm 1$ is the CP eigenvalue of f and 2β is the phase difference between the $B^0 \to f$ and $B^0 \to \overline{B}^0 \to f$ decay paths. The $b \to sq\bar{q}$ penguin amplitudes have dominantly the same weak phase as the $b \to c\bar{c}s$ tree amplitude. Since only λ^2-suppressed penguin amplitudes introduce a new CP-violation phase, amplitudes with a single weak phase dominate these decays.

The theoretically cleanest case is $B \to J/\psi K^0_{S,L}$, but several other charmonium modes have been measured by *BABAR* and Belle: $J/\psi\, K^0_S$, $\psi(2S)K^0_S$, $\chi_{c1}K^0_S$ and $\eta_c K^0_S$ modes with $\eta_{CP} = -1$, as well as $J/\psi\, K^0_L$, which has $\eta_{CP} = +1$. In the latest result from Belle, only $J/\psi\, K^0_S$ and $J/\psi\, K^0_L$ are used. The world average reads [41]

$$\sin 2\beta = 0.675 \pm 0.026. \tag{1.57}$$

This measurement has a four-fold ambiguity in β, which can be resolved by a global CKM fit mentioned below. Experimentally, the two-fold ambiguity $\beta \to \pi/2 - \beta$ (but not $\beta \to \pi + \beta$) can be resolved by a time-dependent angular analysis of $B^0 \to J/\psi\, K^{*0}(892)$ [42] or a time-dependent Dalitz plot analysis of $B^0 \to \overline{D}^0 h^0$ ($h^0 = \pi^0, \eta, \omega$) with $\overline{D}^0 \to K^0_S\pi^+\pi^-$ [43]. The latter gives the better sensitivity and disfavors the solutions with $\cos 2\beta < 0$ at the 98.3% CL, consistent with the global CKM fit result. In fact from the result 1.57 we obtain for the angle β within $[0, \pi]$ the solutions $(21.2 \pm 1.0)^\circ$ and $(68.8 \pm 1.0)^\circ$, where the first number is compatible with the result from the global CKM fit without the measurement of β, $(27.70^{+0.78}_{-3.94})^\circ$ and $\sin 2\beta_{\rm CKM} = 0.823\,^{+0.016}_{-0.085}$ [44].

In $b \to c\bar{c}d$ quark-level decays, such as $B^0 \to J/\psi\,\pi^0$ or $B^0 \to D^{(*)}D^{(*)}$, unknown contributions from (not CKM suppressed) penguin-type diagrams, carrying a different weak phase than the tree-level diagram, compromises the clean extraction of $\sin 2\beta$. Consequently, they are not included in the $\sin 2\beta$ average.

The β angle can be also measured using $b \to s\bar{q}q$ penguin dominated decays. These decays have the same CKM phase as the $b \to c\bar{c}s$ tree level decays, up to corrections suppressed by λ^2, since $V_{tb}^* V_{ts} = -V_{cb}^* V_{cs}[1 + \mathcal{O}(\lambda^2)]$. If new physics contributes to the $b \to s$ loop diagrams and has a different weak phase, it would give rise to $S \neq -\eta_{CP} \sin 2\beta$ and possibly $C \neq 0$. Therefore, the main interest in these modes is not simply to measure $\sin 2\beta$, but to search for the new physics. The $B^0 \to \eta' K^0$ is one of these modes. Details of the measurements of CP violation time-dependent for these modes are given in section 1.5.7.

As expected in the SM, no direct CP violation has been observed in all these modes.

α from Charmless B Decays

Unlike $B^0 \to J/\psi K^0$, for which amplitudes with weak phases different from the dominant tree phase are doubly CKM suppressed, multiple weak phases must be considered in most of the analyses of B decays to final states without charm. Since α is the angle between $V_{tb}^* V_{td}$ and $V_{ub}^* V_{ud}$, only time-dependent CP asymmetries in $b \to u\bar{u}d$ dominated tree modes can directly measure $\sin 2\alpha$, in contrast to $\sin 2\beta$, where several different transitions can be used. Since $b \to u\bar{u}d$ penguin amplitudes have a different CKM phase than $b \to u\bar{u}d$ tree amplitudes, and their magnitudes are the same order in λ, the penguin contribution can be sizable and makes the α determination complicated. This complication makes the extraction of the CKM couplings from the experimental observables considerably more difficult, although richer. The decays most sensitive to α are $B^0 \to \pi^+\pi^-$, $\rho^\pm\pi^\mp$, and $\rho^+\rho^-$. The extraction of α in the presence of unknown penguin amplitudes requires an isospin analysis [45] for $\pi\pi$, $\rho\rho$, and a Dalitz-plot analysis [46] for $\rho^\pm\pi^\mp$. The goal is to estimate the penguin contribution (*penguin pollution*) with respect to tree contribution. Relying on flavor symmetries, in particular $\mathrm{SU}(2)$, does not represent a severe theoretical limitation. However, it certainly creates model-dependent uncertainties from flavor-symmetry breaking so that — neglecting statistical considerations — the measurement of α is not of the same quality as the measurements of $\sin 2\beta$ and γ. A new promising mode to extract α is the $B^0 \to a_1^\pm\pi^\mp$. This is not a CP eigenstate, like $B^0 \to \rho^\pm\pi^\mp$. So far there is no a CP-violation measurement of this mode, but the branching fractions is well measured [47]. Differently from $\rho^\pm\pi^\mp$, here a Dalitz plot analysis is not easy because of the four bodies in the final state. Furthermore, the a_1 meson has a large width which is not well known [36].

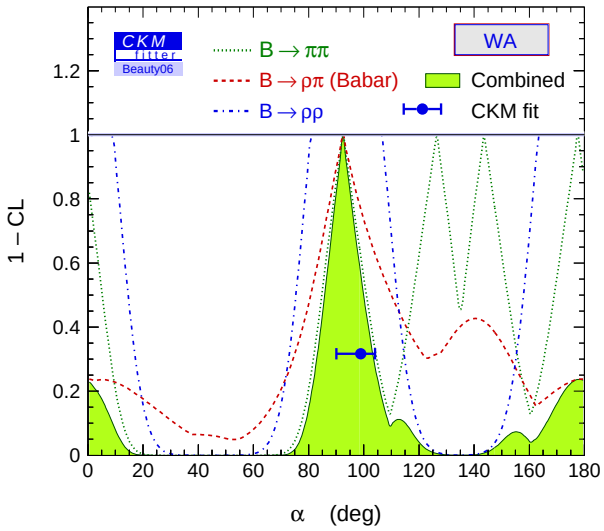

Figure 1.7: Constraints on α from the modes $\pi\pi$ (World Average), $\rho^{\pm}\pi^{\mp}$ (*BABAR*), $\rho\rho$ (WA), compared to the prediction from the CKM fit (not including these measurements) [44].

Anyway, it is possible to perform an analysis using a quasi-two-body approximation, using $\mathrm{SU}(3)$ symmetry to estimate the penguin pollution [48].

Combining the three measurements of the modes $\pi\pi$, $\rho^{\pm}\pi^{\mp}$, and $\rho\rho$ from *BABAR* and Belle experiments, α is constrained as:

$$\alpha = \left(92.6\,^{+10.7}_{-9.3}\right)^{\circ}. \tag{1.58}$$

This measurement is in agreement with the expectation $\alpha_{\mathrm{CKM}} = (100.0\,^{+4.5}_{-7.3})^{\circ}$ from the global CKM fit (where the direct α measurement has been excluded from the fit) [44]. The results are shown in the fig. 1.7. A different statistical approach gives similar constraint from the combination of these measurements [49].

γ from B Decays to Open Charm

By virtue of eq. 1.46, γ does not dependent on CKM elements involving the top quark, so it can be measured in tree level B decays. This is an important distinction from the measurements of α and β, and implies that the direct measurements of γ are unlikely to be affected by physics beyond the SM.

The golden methods to determine γ at the B-factories utilize the measurement of

direct CP violation in $B^+ \to DK^+$ decays, where the neutral D meson can be both D^0 and $\overline{D}^0$ (and where D^0 also stands for D^{*0}). The D^0 corresponds to the leading $\overline{b} \to \overline{c}$ transition, whereas the $\overline{D}^0$ is produced by a CKM- and color-suppressed $\overline{b} \to \overline{u}$ transition. If the final state is chosen so that both D^0 and $\overline{D}^0$ can contribute, the two amplitudes interfere, and the resulting observables are sensitive to the UT angle γ, the relative weak phase between the two B decay amplitudes.

Among the many methods that exploit this interference, the experiments concentrate on the reconstruction of the neutral D in a CP eigenstate (GLW) [50], in other final states common to D^0 and $\overline{D}^0$ such as $K^{\mp}\pi^{\pm}$ (ADS) [51], or in the self-conjugate three-body final state $K^0_S\pi^+\pi^-$ (GGSZ) [52]. For this last method, the analysis can be optimized by studying the Dalitz plot dependence of the interferences. The best present determination of γ comes from this method. All variations are sensitive to the same B decay parameters and can therefore be treated in a combined fit to extract γ.

Combining the GLW, ADS, and Dalitz analyses [44], γ is constrained as

$$\gamma = \left(60^{+38}_{-24}\right)^{\circ}. \tag{1.59}$$

The likelihood function of γ is not Gaussian, and the 95% CL range is $21^{\circ} < \gamma < 122^{\circ}$. This measurement is in agreement with the expectation $\gamma_{\rm CKM} = (59.0\,^{+9.3}_{-3.8})^{\circ}$ from the global CKM fit (where the direct γ measurement has been excluded from the fit) [44]. The results are shown in the fig. 1.8. Similar results are found in [49].

There is another way to measure γ. Similar to the decay $B^0 \to \rho^{\pm}\pi^{\mp}$, which is not a CP eigenstate but sensitive to α because both final states can be reached by both neutral B flavors, interference between decays with and without mixing can occur in $B^0 \to D^{(*)\pm}\pi^{\mp}(\rho^{\pm})$. A time-dependent analysis of these decays is sensitive to $\sin(2\beta+\gamma)$, because the CKM-favored $\overline{b} \to \overline{c}$ decay amplitude interferes with the CKM-suppressed $b \to u$ decay amplitude with a relative weak-phase shift γ. In these $\overline{b} \to \overline{c}(u\overline{d}),\ \overline{u}(c\overline{d})$ quark-level transitions no penguin contributions are possible, because all quarks in the final state are different. Hence there is no direct CP violation. Combining the $D^{\pm}\pi^{\mp}$, $D^{*\pm}\pi^{\mp}$, and $D^{\pm}\rho^{\mp}$ measurements [53] gives $\sin(2\beta+\gamma) = 0.8^{+0.18}_{-0.24}$, consistent with the previously discussed results for β and γ. The $2\beta+\gamma$ measurements help to exclude large values of γ.

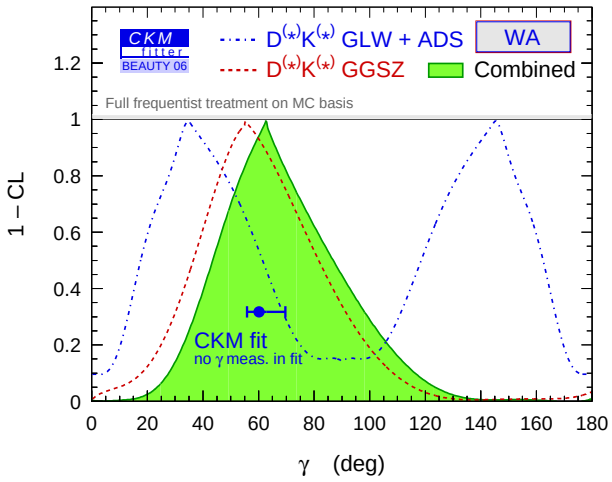

Figure 1.8: Constraints on γ from World Average $D^{(*)}K^{(*)}$ decays (GLW+ADS) and Dalitz analyses compared to the prediction from the global CKM fit (not including these measurements) [44].

1.5.7 CP Asymmetries in Loop-Dominated $b \to s$ and $b \to s\gamma$ Modes

The FCNC $b \to s$ transition is mediated by penguin diagrams. It can have any up-type quark in the loop, so its amplitude can be written as

$$\begin{aligned} A_{b\to s} &= m_t V_{tb} V_{ts}^* + m_c V_{cb} V_{cs}^* + m_u V_{ub} V_{us}^* \\ &= (m_c - m_t) V_{cb} V_{cs}^* + (m_u - m_t) V_{ub} V_{us}^* = \mathcal{O}(\lambda^2) + \mathcal{O}(\lambda^4)\,, \end{aligned} \quad (1.60)$$

where the unitarity of the CKM matrix has been used in the second step. In the SM, the amplitude is dominated by the first, $V_{cb}V_{cs}^*$, term, which has the same weak phase as the amplitude in $B^0 \to J/\psi K^0$ decay. We expect $||\bar{A}/A| - 1| = \mathcal{O}(\lambda^2)$, and the time-dependent CP asymmetry parameters are given to a similar accuracy by $S_{b\to sq\overline{q}} \approx -\eta_{CP} \sin 2\beta$ and $C_{b\to sq\overline{q}} \approx 0$.

Owing to the large mass scale of the virtual particles that can occur in the loops, additional diagrams from physics beyond the SM, with heavy particles in the loops, may contribute. The measurement of CP violation in these channels and the comparison with the B-to-charmonium reference value is therefore a sensitive probe for physics beyond the SM. A discrepancy between $S_{b\to sq\overline{q}}$ and $\sin 2\beta$ can provide an indication of new physics. If the SM and new physics contributions are both significant,

the deviations of the CP asymmetries from $\sin 2\beta$ become mode dependent, because they depend on the relative size and phase of the contributing amplitudes, which are determined by the quantum numbers of the new physics and by strong interactions.

The important question is how well can we bound the contribution of the second, CKM-suppressed, term to the $b \to sq\overline{q}$ transition in eq. 1.60? This term has a different weak phase than the dominant first term, so its impact on $S_{b\to sq\overline{q}}$ depends on both its magnitude and relative strong phase. Naive factorization suggests that for $q = s$ the λ^2 suppression of the second term is likely to hold because it would require an enhancement of rescattering effects to upset this. However, for $q = u$, there is a color-suppressed $b \to u$ tree diagram, which has a different weak (and possibly strong) phase than the leading λ^2 penguin amplitude. For $q = d$, any light neutral meson formed from $d\overline{d}$ also has a $u\overline{u}$ component, and there is "tree pollution" again. The B^0 decays to $\pi^0 K_S^0$ and ωK_S^0 belong to this category. The mesons η' and $f_0(980)$ have significant $s\overline{s}$ components, which may reduce the tree pollution. Neglecting rescattering, the three-body final state $K^0\overline{K}^0 K^0$ (reconstructed as $K_S^0 K_S^0 K_S^0$) has no tree pollution (pure-penguin mode), whereas $B^0 \to K^+K^-K^0$ (excluding ϕK^0, which is a pure-penguin mode) does.

As a consequence, only an effective $S = -\eta_{CP} \sin 2\beta_{\rm eff}$ is determined. Recently QCD factorization (QCDF) [15, 54, 55] and SCET [56] was used to calculate the deviations $\Delta S = \sin 2\beta_{\rm eff} - \sin 2\beta$ in some of the two-body penguin modes. It was found that the deviations are the smallest ($\lesssim 0.05$) for ϕK^0 and $\eta' K^0$. This is fortunate because these are also the modes in which the experimental errors are the smallest. The SM shifts enhance $-\eta_f S_f$ (except for ρK_S^0) using [54, 55], while suppress $S_{\eta' K_S}$ using [56]. SU(3) flavor symmetry has also been used to bound the SM-induced deviations ΔS [13, 14, 57]. Owing to the lack of information on strong phases and the weak experimental bounds on some $b \to dq\overline{q}$ mediated rates, the resulting bounds tend to be weak. An exception is $\pi^0 K_S^0$, where SU(3) relates the relevant amplitudes to $\pi^0\pi^0$ and K^+K^- [14]. The theoretical understanding of factorization in three-body decays does not yet allow accurate bounds on ΔS to be computed.

There has been considerable excitement about these measurements in the past few years. Before ICHEP 2006 conference, if one restricted the modes to those with the potentially smallest theoretical uncertainties, *i. e.* the final states ϕK^0, $\eta' K^0$, and $K^0\overline{K}^0 K^0$, and attempted to average the $\sin 2\beta_{\rm eff}$ results, $\langle \sin 2\beta_{\rm eff} \rangle = 0.50 \pm 0.08$,[5]

[5] All s-penguin average reported here are, in fact, doubly naïve since it neglects both the theoretical

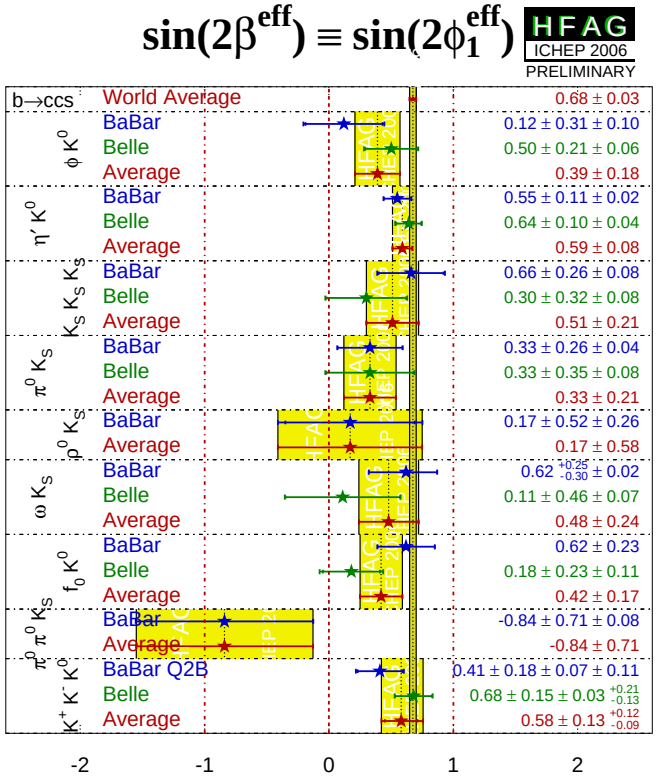

Figure 1.9: Comparison of world average $\sin 2\beta_{(\text{eff})}$ results from penguin-dominated decays, and the charmonium reference value [41].

which is within 2.2σ reach of the charmonium reference value. Beginning of 2005, this s-penguin average was 0.40 ± 0.09, and because the charmonium result was larger at that time, the discrepancy between the $\sin 2\beta$ numbers was at the 3.2σ level, which explains the popularity of the results. Most recent results for the measurement of $\sin 2\beta_{\text{eff}}$ from the various penguin modes presented at ICHEP 2006 conference are compiled in fig. 1.9. Using these measurements, the s-penguin average for the final states ϕK^0, $\eta' K^0$, and $K^0 \overline{K}^0 K^0$ becomes 0.55 ± 0.07, at the 1.7σ level from charmonium $\sin 2\beta$ numbers. Considering the measurements of all s-penguin modes, the average is 0.52 ± 0.05, which is 2.6σ from charmonium $\sin 2\beta$. The simple conclusion is that better statistics are required to clarify the situation.

uncertainty discussed above, and the fact that experimental systematic uncertainties are correlated between the measurements of individual modes. For these reasons, they are to consider only for academic interest, to use with extreme caution, if at all.

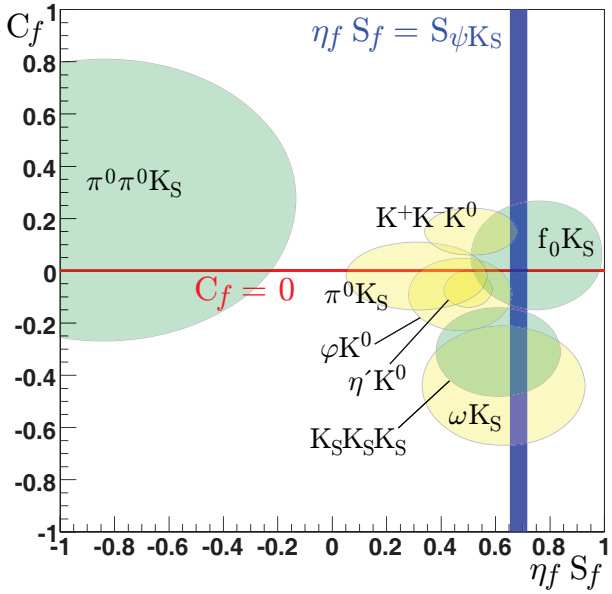

Figure 1.10: 2D comparisons of averages in the different $b \to s$ modes [41]. This plot (and the averages) assume no correlations between the S and C measurements in each mode.

As expected in the SM, no direct CP violation has been observed in all these modes, *i. e.* C is consistent with zero. A 2D comparisons plot of averages for C and $\eta_{CP}S$ in the different $b \to s$ modes is shown in fig. 1.10.

Another interesting measurement in the penguin sector is the time-dependent CP asymmetry in $b \to s\gamma$ exclusive modes, which probes the polarization of the photon. In the SM, b-quarks mainly decay to $s\gamma_L$ and $\overline{b}$-quarks to $\overline{s}\gamma_R$, so their interference is suppressed, proportional to $r_{f_s} = A(\overline{B}^0 \to X_{f_s}\gamma_R)/A(\overline{B}^0 \to X_{f_s}\gamma_L)$. Although the $B \to X_s\gamma$ rate is correctly predicted by the SM at the 10% level, where the measurement sums over the rates to left- and right-handed photons, the ratio r_{f_s} is sensitive to new physics. So far only the time-dependent CP asymmetry for the mode $B \to K^0_S\pi^0(K^{*0})\gamma$ has been measured. *BABAR* and Belle have measured it exclusively and inclusively, with the averages $S_{K^*\gamma} = -0.28 \pm 0.26$ and $S_{K_S\pi^0\gamma} = -0.09 \pm 0.24$ [41]. If only the electromagnetic penguin operator, $O_7 \sim \overline{s}\,\sigma^{\mu\nu}F_{\mu\nu}(m_bP_R + m_sP_L)b$ contributed to the rate, it would give $S_{K^*\gamma} = -2(m_s/m_b)\sin 2\beta$ [58]. This also holds in the nonresonant $B \to K^0_S\pi^0\gamma$ case [59]. In general in [59] the authors point out that for B_d or B_s to $P_1P_2\gamma$ (where P_1 and P_2 are pseudoscalar mesons), through a

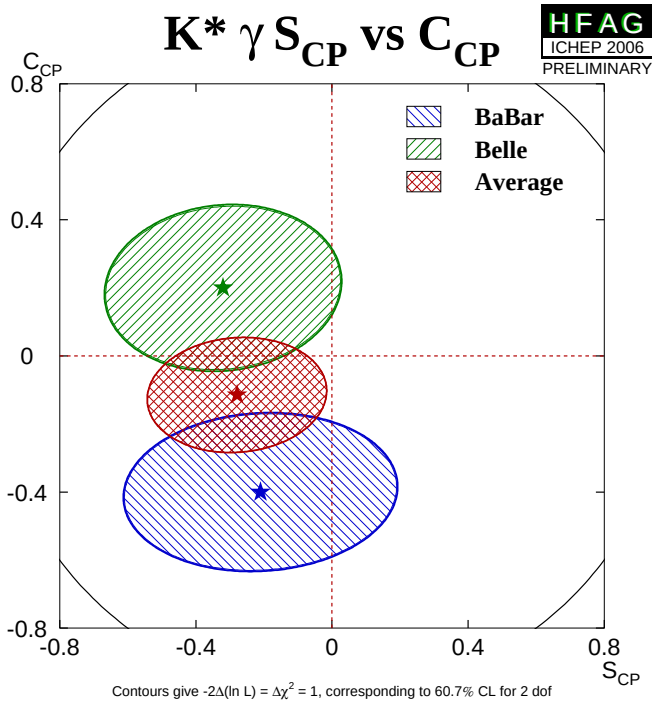

Figure 1.11: 2D comparison of averages for $B \to K^0_S\pi^0(K^{*0})\gamma$ mode [41]. This plot (and the averages) assume no correlations between the S and C measurements in each mode.

flavor changing dipole transition, time-dependent oscillations can reveal the presence of physics beyond the SM. They suggest other modes to study, like $B \to \eta K^0_S\gamma$ or $B \to \eta' K^0_S\gamma$. Grinstein *et al.* [60] recently realized that four-quark operators contribute to r that are not suppressed by m_s/m_b. The numerically dominant term is due to the matrix element of $O_2 = (\overline{c}\,\gamma^\mu P_L b)(\overline{s}\,\gamma_\mu P_L c)$, and its contribution to the inclusive rate can be calculated reliably, $\Gamma(\overline{B}^0 \to X_s\gamma_R)/\Gamma(\overline{B}^0 \to X_s\gamma_L) \approx 0.01$ [60]. This suggests that for most final states, on average, $r \sim 0.1$ should be expected. A SCET analysis of the exclusive decay proved the power suppression of the amplitude ratio, $A(\overline{B}^0 \to \overline{K}^{0*}\gamma_R)/A(\overline{B}^0 \to \overline{K}^{0*}\gamma_L) = \mathcal{O}[(C_2/3C_7)\,(\Lambda_{\rm QCD}/m_b)] \sim 0.1$ [60], but the uncertainties are sizable.

Also in $B \to K^0_S\pi^0(K^{*0})\gamma$ no direct CP violation has been observed. A 2D comparison plot of averages for C and S is shown in fig. 1.11.

1.5.8 Weak-Phase Information from Direct CP Violation in B Decays

The CKM mechanism causes "direct" CP violation in the decay, as soon as at least two amplitudes with different strong and weak phases contribute. Because virtual loops are present in all meson decays, "some" (possibly unobservable) amount of direct CP violation occurs. Owing to the large weak phases arising in B decays, direct CP violation should be more prominent here than, *e. g.*, in the kaon system. This has been confirmed by the measurement of the direct CP asymmetry $A_{K^+\pi^-} = -0.093 \pm 0.015$ in $B^0 \to K^+\pi^-$ decays [41]. Evidence for direct CP violation in neutral B decays also exists for $B^0 \to \pi^+\pi^-$ (5.6σ significance) [41]. Recently, the first evidence for direct CP violation in charged B decays emerged from the mode $B^+ \to K^+\rho^0$ with a charge asymmetry of $0.31\,^{+0.11}_{-0.10}$ [41]. With the data samples at the B-factories increasing, we expect the discovery of more and more rare-decay modes with significant CP violation in the decay.

From the point of view of the weak-phase extraction, the required conspiracy between competing amplitudes of similar size and the occurrence of strong phases, represent serious obstacles. A reliable and model-independent calculation of direct CP violation is not possible at present, and estimates based on factorization are plagued by large uncertainties. However, flavor symmetries in particular isospin can be exploited to (essentially) assess model independently direct CP violation. In B decays to $\pi\pi$, $\rho\pi$ and $\rho\rho$, the measurements of direct CP-violating asymmetries (independent of whether they are compatible with zero or not) are essential inputs to the isospin analyses. In the $K\pi$ system the corresponding isospin analysis used to extract γ [61] is fruitless at present, and affected by possibly large isospin-breaking corrections from electroweak penguins, which cannot be taken into account model independently as is the case in the $\pi\pi$ and $\rho\rho$ isospin analyses.

Although a quantitative prediction is difficult, direct CP violation can be a powerful probe for new physics in decays where negligible CP asymmetries are expected. This is the case for all B decays dominated by a single decay amplitude. Prominent examples are penguin-dominated decays, such as $b \to s\gamma$ or $B \to K^{(*)}\ell^+\ell^-$, where a significant nonzero direct CP violation would unambiguously indicate new physics.

1.5.9 The Global CKM Fit

Using the independently measured CKM elements mentioned in the previous sections, the unitarity of the CKM matrix can be checked. We obtain $|V_{ud}|^2 + |V_{us}|^2 + |V_{ub}|^2 = 0.9992 \pm 0.0011$ (first row), $|V_{cd}|^2 + |V_{cs}|^2 + |V_{cb}|^2 = 0.968 \pm 0.181$ (second row), and $|V_{ud}|^2 + |V_{cd}|^2 + |V_{td}|^2 = 1.001 \pm 0.005$ (first column), respectively. These provide strong tests of the unitarity of the CKM matrix. The sum of the three angles of the unitarity triangle, $\alpha+\beta+\gamma = (173.8\,^{+39.5}_{-25.8})^\circ$, is also consistent with the SM expectation.

The CKM matrix elements can be most precisely determined by a global fit that consists of maximizing a likelihood built upon relevant experimental measurements and their SM predictions, which depend on the parameters of the theory, and imposes the SM constraints (*i. e.*, three generation unitarity). Some of the parameters of the theory, such as quark masses or matrix elements, are experimentally or theoretically constrained, whereas others are unknown. These unknowns contain the four Wolfenstein parameters (defined in eq. 1.43), but also, for instance, hadronic quantities that occur in the determination of the UT angles α and γ. There are several approaches to combining the experimental data and to consider the free parameters of the theory. CKMfitter [44] use frequentist statistics, while UTfit [49] uses a Bayesian approach. These approaches provide similar results.

The constraints implied by the unitarity of the three generation CKM matrix significantly reduce the allowed range of some of the CKM elements. The fit for the Wolfenstein parameters, as obtained in ref. [44], gives

$$\begin{aligned} \lambda &= 0.22717^{+0.00100}_{-0.00101}, & A &= 0.806^{+0.014}_{-0.014}, \\ \rho &= 0.195^{+0.022}_{-0.055}, & \eta &= 0.326^{+0.027}_{-0.015}. \end{aligned}$$

Once the Wolfenstein parameters are fit, determining fully consistent confidence levels for all related observables is straightforward. The results of the fit are shown in the ρ, η plane in fig. 1.12. The outer contour of the combined fit corresponds to 95% CL exclusion. Also shown are the 95% CL regions for the individual constraints entering the fit (the constraint from $B^+ \to \tau^+\nu_\tau$ is not shown, although it is included in the fit). This global CKM fit contains all relevant information collected by the experiments. From the new physics perspective, it is interesting to confront the measurements according to their sensitivity to new physics contributions. Fig. 1.13 shows on the left plot the constraints that originate from mainly tree-level processes, together with their combined fit. The right plot shows the constraints from loop-induced processes. To fix

the length scale of the UT and the constraints on λ and A from the tree-level determinations of the CKM elements $|V_{ud}|$, $|V_{us}|$ and $|V_{cb}|$ are used. If γ is extracted from the measurement of α using β from mixing-induced CP violation as input, it is effectively a tree-level quantity, because the isospin analysis isolates the $\Delta I = 3/2$ component in the decay amplitude, which is assumed to be standard [44]. Consequently, the constraint for γ that enters the tree-level plot is the average of the direct measurement of γ via open-charm processes, and the value obtained from $\pi - \alpha - \beta$, from which new physics in mixing cancels. This provides the first determination of ρ, η from (effectively) tree-level processes. Good agreement is observed between the tree-level and loop-induced constrained fits.

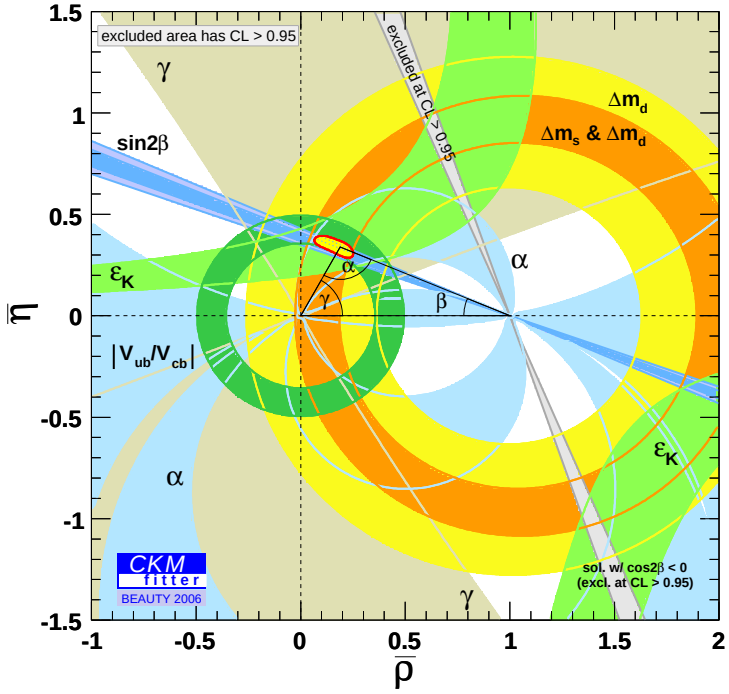

Figure 1.12: Confidence levels in the ρ, η plane for the global CKM fit. The shaded areas indicate 95% CL allowed regions [44].

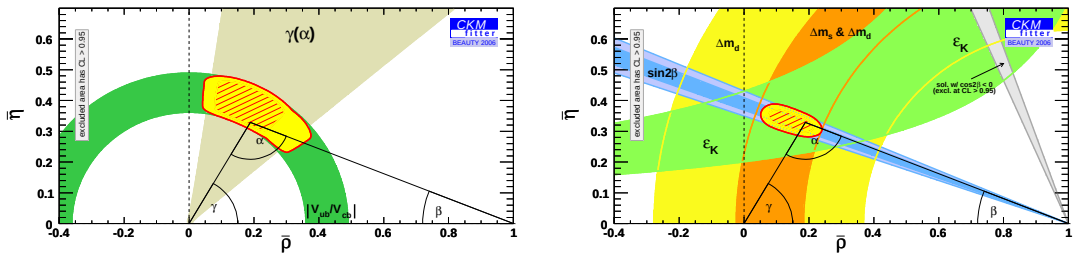

Figure 1.13: Confidence levels in the ρ, η plane for global CKM fits using only tree-level (left) and loop-induced (right) inputs. The shaded areas indicate 95% CL allowed regions [44].

Chapter 2

The *BABAR* Detector

2.1 Overview — B-Factories

Exploring CP violation in the B system and its potential impact on the Standard Model, baryogenesis, and cosmology, requires copious production of B mesons, accurate measurement of the B time of flight and flavor, and reasonably low background in the reconstruction. There are several potential options for experiments which can fulfill these criteria:

1. Hadron colliders ($\overset{(-)}{p}p$): The cross section for $B\overline{B}$ production at TeV hadron colliders is very high compared with e^+e^- B factories, approximately 100 μb vs. 1.2 nb. This large advantage does compete with several disadvantages, however. Hadronic collisions have far more background, making reconstruction of final states which do not contain a J/ψ very challenging. Purely hadronic final states with non-negligible background in e^+e^- colliders at the $\Upsilon(4S)$, such as $\pi^0\pi^0$, may be extremely difficult at a hadronic collider and it is not clear that it will be possible to reconstruct such decays. Nevertheless, these experiments do have a statistical advantage and also have the potential for observing CP violation in the B_s system, which is beyond the reach of $\Upsilon(4S)$ experiments. LHC-b at CERN is a new experiment currently under construction.

2. Fixed target proton beam experiments: Fixed-target experiments also offer the potential of a higher rate of B production, but have even greater levels of backgrounds, superimposed interactions, and boost which compresses all tracks in a small solid angle. A significant effort was undertaken at DESY to build such an

experiment, HERA-B.

3. e^+e^- colliders at the Z-pole: The Z-pole presents a relatively clean environment for B-physics with a relatively large cross section ($\sim$ 6 nb). However, the luminosities achieved at this energy are low, the only two colliders in the world which can reach it, LEP and SLD, are both dismantled, and the cost of building new experiments at this energy prevents this from being a viable option.

4. Symmetric and asymmetric e^+e^- B-factories: The $\Upsilon(4S)$ resonance provides a very clean environment for B reconstruction, with a very favorable ratio of $b\overline{b}$ production from e^+ and e^- beams compared to lighter quark pairs ($\sigma(b\overline{b})/\sigma(q\overline{q}) \simeq 0.28$). Asymmetric e^+ and e^- beams provide a boost to the B meson pair that is produced, allowing for reconstruction of B flavor as a function of time of flight through the separation of the B vertices in the lab frame, Δz. The concept of asymmetric B-factories was first proposed in 1987 by Pier Oddone [62]. He proposed that the best way to produce and study B particles would be to construct an asymmetric collider that could create a separation in space between the decay products of individual B and $\overline{B}$ mesons. In fact, unlike symmetric beams, the B particles are carried downstream in the direction of the higher energy beam and this forward boost enables the decay products to separate, allowing to observe the distances between their points of decay. This condition is required to measure the time-dependent CP asymmetries (see sections 2.3 and 2.4). Statistical limitations, of which luminosity is the critical factor, are the dominant source of error for time-dependent CP asymmetries. Two asymmetric B-factories have been built and are currently producing physics: PEP-II/*BABAR* [63] and KEK-B/Belle [64]. Previously, the symmetric B-factory CLEO (at the CESR ring at Cornell) was able to produce precision B physics results, however the symmetric design and the limited statistics precluded measurement of time-dependent CP-violating asymmetries.

The *BABAR* and Belle experiments are very similar, with the following important differences: the KEK-B/Belle B factory has a nonzero beam crossing angle (4.2 mr) at the interaction point (IP), whereas the PEP-II/*BABAR* B factory has a more traditional collinear IP. The KEK design potentially allows a greater number of beam bunches to be stored in the ring, due to absence of parasitic crossings at $\pm$ 1m, as are present in the PEP-II design. However KEK-B is a highly non-traditional design; concerns

over higher-order mode resonances at the IP led the PEP-II B factory to use a collinear crossing. So far, both KEK-B and PEP-II have performed well. At the time of writing, PEP-II has integrated 406.28 fb^{-1} and KEK-B has integrated 649.1 fb^{-1}.

The particle identification method also differs between *BABAR* and Belle: as will be described in section 2.7, *BABAR* uses quartz bars to internally reflect Cherenkov light to a backward-mounted detector (the DIRC), whereas Belle uses an aerogel Cherenkov detector. In addition, *BABAR* has a 5-layer silicon vertex detector (SVT, see section 2.5) that can do standalone tracking, whereas Belle uses a 3-layer silicon vertex detector. More details on *BABAR* and Belle detectors can been found in refs. [65] and [66], respectively. In the following sections we will focus on *BABAR* detector description. In fig. 2.1 we show the cartoon of *BABAR* detector, where we indicate each subdetector. The longitudinal section is shown in fig 2.2.

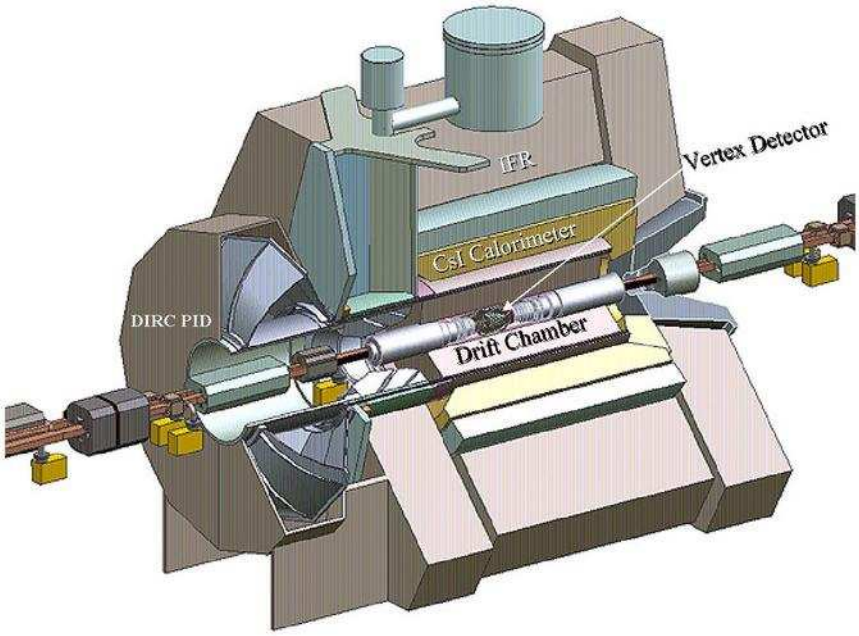

Figure 2.1: *BABAR* detector where each subdetector is indicated.

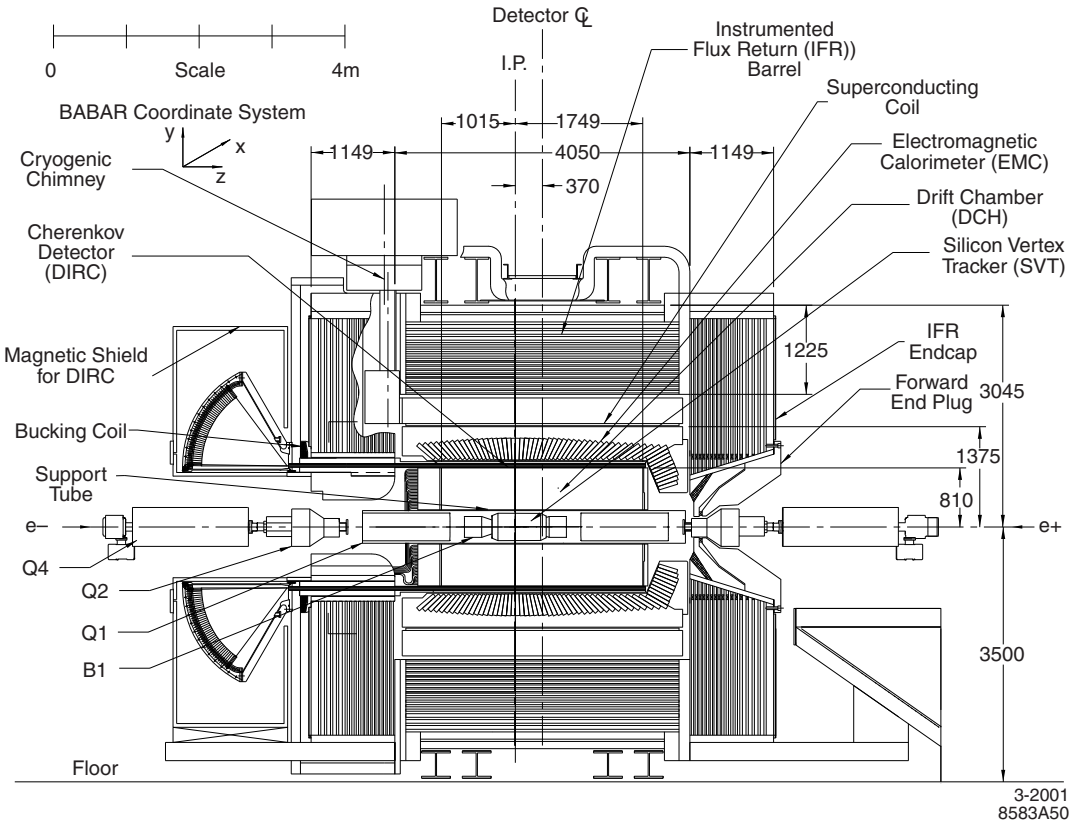

Figure 2.2: *BABAR* detector longitudinal section.

2.2 The PEP-II Asymmetric Collider

The design of PEP-II is shown in fig. 2.3. The 9.0 GeV electrons and 3.1 GeV positrons are injected in PEP-II from the SLAC linac via bypass lines in the linac gallery. They collide in the single interaction point of PEP-II, where *BABAR* is situated. The collisions are inside a beam-pipe of beryllium with diameter of 2.5 cm. The beam parameters are listed in table 2.1. PEP-II has surpassed design goals both in instantaneous and in average integrated luminosity.

The energy in the center-of-mass system (CMS) is $\sqrt{s} = 10.58$ GeV, which corresponds to $\Upsilon(4S)$ resonance. With this configuration, the CMS moves in laboratory frame with a relativist boost of $\beta\gamma = 0.56$, which gives an average separation between the two B (coming from $\Upsilon(4S)$ decay) vertexes of $\beta\gamma c\tau = 270\,\mu$m. The cross sections of production of fermionic pairs at CMS energy are shown in table 2.2.

Most of the data is taken at the $\Upsilon(4S)$ resonance (on-peak). However approxi-

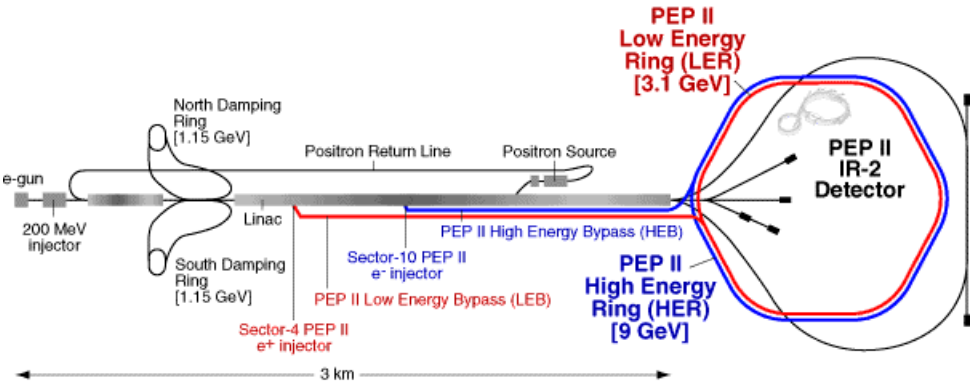

Figure 2.3: The PEP-II asymmetric storage ring and the SLAC linear accelerator. The SLAC linac is the injector for PEP-II. The single interaction point of PEP-II is at Interaction Region 2, where *BABAR* is situated.

Parameters	Design	Typical
Energy HER/LER (GeV)	9.0/3.1	9.0/3.1
Current HER/LER (A)	0.75/2.15	1.88/2.90
# of bunches	1658	1732
σ_{Lx} (μm)	110	120
σ_{Ly} (μm)	3.3	4.1
σ_{Lz} (mm)	9	1.75
Luminosity ($10^{33}\,\mathrm{cm}^{-2}\mathrm{s}^{-1}$)	3	11-12
Luminosity (pb^{-1}/d)	135	891

Table 2.1: PEP-II beam parameters. Values are given for the design and for colliding beam operation at time of writing. HER and LER refer to the high energy e^- and low energy e^+ ring, respectively. σ_{Lx}, σ_{Ly}, and σ_{Lz} refer to the R.M.S. horizontal, vertical, and longitudinal bunch size at the IP.

$e^+e^- \rightarrow$	Cross Section (nb)
$b\bar{b}$ ($\sigma_{b\bar{b}}$)	1.05
$c\bar{c}$ ($\sigma_{c\bar{c}}$)	1.30
$s\bar{s}$ ($\sigma_{s\bar{s}}$)	0.35
$u\bar{u}$ ($\sigma_{u\bar{u}}$)	1.39
$d\bar{d}$ ($\sigma_{d\bar{d}}$)	0.35
$\tau^+\tau^-$ (σ_τ)	0.94
$\mu^+\mu^-$ (σ_μ)	1.16
e^+e^- (σ_e)	$\sim$40

Table 2.2: Cross sections σ of production of fermionic pairs at $\Upsilon(4S)$ mass energy in nb $= 10^{-33}$cm^2.

mately 10% are taken at 40 MeV below the resonance peak (off-peak), where there is not $\Upsilon(4S)$ resonance production, to allow studies of non-resonant background in data (see fig. 2.4). A plot of PEP-II integrated luminosity and *BABAR* recorded integrated luminosity as a function of time is shown in fig. 2.5. In fig. 2.6 we show the integrated luminosity per day. At the time of writing, PEP-II has integrated 406.28 fb^{-1}, while *BABAR* has recorded 390.85 fb^{-1} (which corresponds to an efficiency of 96.2%). It is important to note that the data has been collected in five different periods (so called runs), so the actual dataset corresponds to run 1 to run 5 periods.

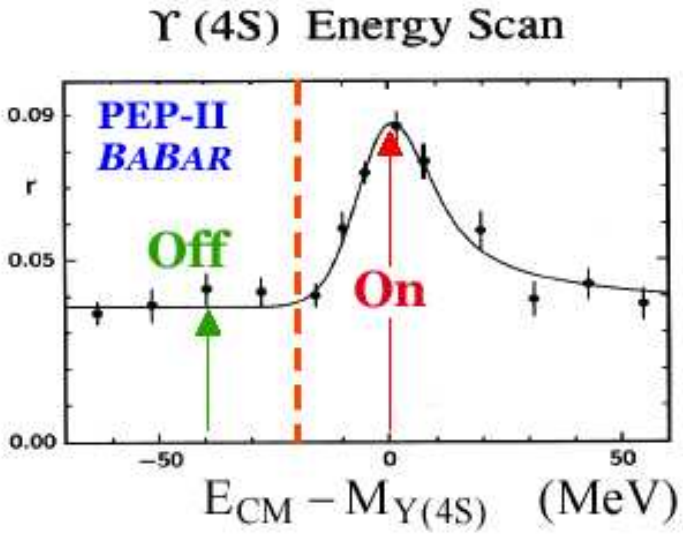

Figure 2.4: Plot of the cross section as function of $\Upsilon(4S)$ resonance mass and PEP-II CMS energy. We show the two regions corresponding to on-peak and off-peak energies.

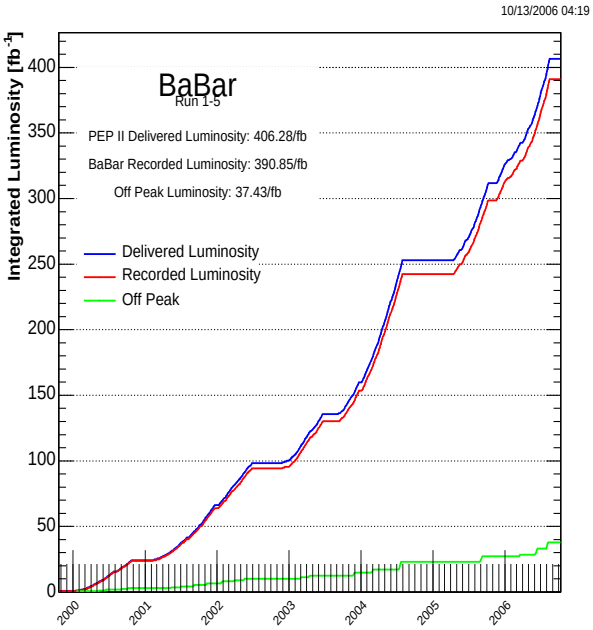

Figure 2.5: PEP-II -*BABAR* integrated luminosity since startup.

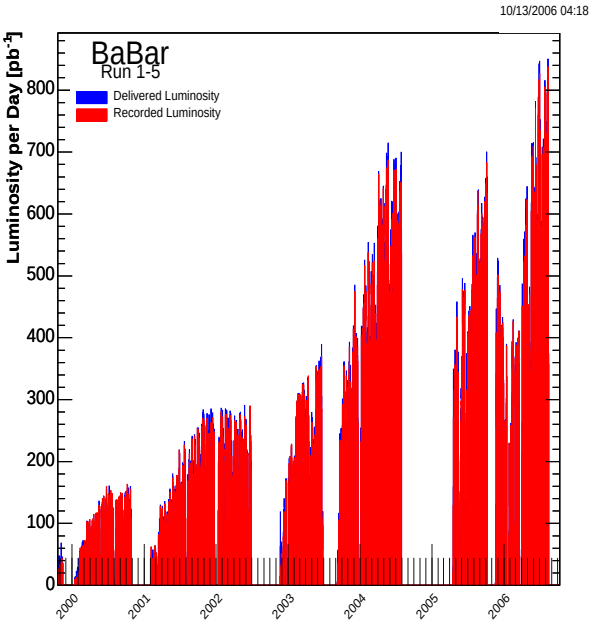

Figure 2.6: PEP-II -*BABAR* integrated luminosity per day.

2.3 Formalism for $\Upsilon(4S) \to B\overline{B}$ coherent states

B^0 and $\overline{B}^0$ mesons produced by $\Upsilon(4S)$ decay are in a coherent $L = 1$ state (P-wave). One way to view this state is that each of the two particles evolve in time as described in section 1.3.3. However they evolve in phase, so that at any time, until one particle decays, there is always exactly one B^0 and one $\overline{B}^0$ present [1]. However once one of the particles decays the other continues to evolve, and thus there are possible events with two B^0 or two $\overline{B}^0$ decays, whose probability is governed by the time between the two decays.

Two mesons produced in $\Upsilon(4S)$ decay are identified by the θ angle that form with electrons beam direction in Υ rest frame. Coherent state is described by antisymmetric function:

$$\begin{aligned} S(\tau_1,\tau_2) \quad &= \tfrac{1}{\sqrt{2}}\{B^0_{phys}(\tau_1,\theta,\phi)\overline{B}^0_{phys}(\tau_2,\pi-\theta,\phi+\pi) \\ &\quad -\overline{B}^0_{phys}(\tau_1,\theta,\phi)B^0_{phys}(\tau_2,\pi-\theta,\phi+\theta)\}\sin(\theta) \end{aligned} \tag{2.1}$$

and replacing eqs. 1.14 and 1.15, we can write as

$$\begin{aligned} S(\tau_1,\tau_2) \quad &= \tfrac{1}{\sqrt{2}}e^{-(\Gamma/2+im)(\tau_1+\tau_2)}\{\cos[\Delta m(\tau_1-\tau_2)/2](B^0_1\overline{B}^0_2-\overline{B}^0_1B^0_2) \\ &\quad -i\sin[\Delta m(\tau_1-\tau_2)/2]\left(\tfrac{p}{q}B^0_1B^0_2-\tfrac{q}{p}\overline{B}^0_1\overline{B}^0_2\right)\}\sin(\theta_1). \end{aligned} \tag{2.2}$$

where τ_1 is B_1 proper time, which we identify with B meson decaying forward ($\theta_1 < \pi/2$), and τ_2 is B_2 proper time moving in the opposite direction. Since in Υ rest frame the two B mesons have equal but opposite momenta, we can consider, until one of two mesons will decay, $\tau_1 = \tau_2$, and eq. 2.2 contains one B^0 and one $\overline{B}^0$. When one of the two particles decays, its proper timer stops, so proportional terms to $\sin[\Delta m(\tau_1-\tau_2)/2]$ assume importance.

From eq. 2.2 one can derive the amplitude in which one of two mesons decays in a final state f_1 at t_1 time while the other one decays in a state f_2 at t_2 time:

$$\begin{aligned} A(t_1,t_2) \quad &= \tfrac{1}{\sqrt{2}}e^{-(\Gamma/2+im)(t_1+t_2)}\zeta(t_1,t_2)\{\cos[\Delta m(t_1-t_2)/2](A_1\bar{A}_2-\bar{A}_1A_2) \\ &\quad -i\sin[\Delta m(t_1-t_2)/2]\left(\tfrac{p}{q}A_1A_2-\tfrac{q}{p}\bar{A}_1\bar{A}_2\right)\}\sin(\theta_1), \end{aligned} \tag{2.3}$$

[1] This is yet one more particle physics case of the classic Einstein-Podolsky-Rosen situation.

where A_i means B^0 decay amplitude in a f_i state, and $\bar{A}_i$ is $\overline{B}^0$ decay amplitude in the same state f_i. Any state that allows us to identify such flavor of the parent B meson (*tagging decays*) has one of two amplitudes A_f or $\bar{A}_f$ equal to zero. In the eq. 2.3 we introduce the following brief notation to mantain same signs with 2.2:

$$\zeta(t_1, t_2) = \begin{cases} +1 & t_1 = \tau_1,\ t_2 = \tau_2 \\ -1 & t_1 = \tau_2,\ t_2 = \tau_1 \end{cases}$$

but this factor vanishes in decay rate calculation.

It is now straightforward to calculate the time-dependent rate for producing the combined final states f_1, f_2. One finds:

$$\begin{aligned} R(t_1, t_2) = Ne^{-\Gamma(t_1+t_2)}\{&(|A_1|^2 + |\bar{A}_1|^2)(|A_2|^2 + |\bar{A}_2|^2) - 4\text{Re}(\tfrac{q}{p}A_1^*\bar{A}_1)\text{Re}(\tfrac{q}{p}A_2^*\bar{A}_2) \\ &- \cos(\Delta m_B(t_1 - t_2))[(|A_1|^2 - |\bar{A}_1|^2)(|A_2|^2 - |\bar{A}_2|^2) + 4\text{Im}(\tfrac{q}{p}A_1^*\bar{A}_1)\text{Im}(\tfrac{q}{p}A_2^*\bar{A}_2)] \\ &+ 2\sin(\Delta m_B(t_1 - t_2))[\text{Im}(\tfrac{q}{p}A_1^*\bar{A}_1)(|A_2|^2 - |\bar{A}_2|^2) - (|A_1|^2 - |\bar{A}_1|^2)\text{Im}(\tfrac{q}{p}A_2^*\bar{A}_2)]\} \end{aligned} \tag{2.4}$$

In this formula, it was performed an integral on all possible directions of both B mesons, so we could delete angular dependence, and an overall normalization factor N has appeared. We used also the approximation $|q/p| = 1$.

To measure CP asymmetries we look for events in which a B (B_{CP}) decays in a CP eigenstate f_{CP} at $t_{f_{CP}}$ time, while the other meson (B_{tag}) decays in a way that allows us to identify its flavor, so called *tagging* mode, at t_{tag} time. For example, take a tagging mode with with $A_2 = 0$, $\bar{A}_2 = \bar{A}_{\text{tag}}$. This identifies the B_{tag} meson as a B^0 at $t_2 = t_{\text{tag}}$ time at which the tagging decay occurs. Note that this is true even when the taggin decay occurs after the CP eigenstate decay. In this case the state of the B_{tag} at any time $t_{f_{CP}} < t_{\text{tag}}$ must be just that mixture which, if it had not decayed, would have evolved to become a B^0 at time $t_{f_{CP}} = t_{\text{tag}}$. So, the expression 2.4 reduces to

$$\begin{aligned} R(t_{\text{tag}}, t_{f_{CP}}) = Ne^{-\Gamma(t_{\text{tag}}+t_{f_{CP}})}|\bar{A}_{\text{tag}}|^2|A_{f_{CP}}|^2\{&1 + |\lambda_{f_{CP}}|^2 \\ &+ \cos[\Delta m_B(t_{f_{CP}} - t_{\text{tag}})](1 - |\lambda_{f_{CP}}|^2) \\ &- 2\sin[\Delta m_B(t_{f_{CP}} - t_{\text{tag}})]\text{Im}(\lambda_{f_{CP}})\} \end{aligned} \tag{2.5}$$

with $\lambda_{f_{CP}}$ defined in eq. 1.29.

If the final tagging state has $\bar{A}_2 = 0$, $A_2 = A_{\text{tag}}$, that identifies B_{tag} as a $\overline{B}^0$ at t_{tag} time, an expression similar to eq. 2.5 applies, except that the signs of both the cosine

and the sine terms are reversed. Hypothesis $|q/p| = 1$ guarantees us that amplitudes for opposite tags are the same. With these rates, we can evaluate time-dependent CP asymmetry that results to be equal to expression 1.33, where $t = \Delta t = t_{f_{CP}} - t_{\rm tag}$:

$$a_{CP}(\Delta t) = C\cos(\Delta m \Delta t) - S\sin(\Delta m \Delta t). \tag{2.6}$$

Expression 2.5 is function of two temporal variables $t_{\rm tag}$ and $t_{f_{CP}}$ which represent the times since $B^0\overline{B}^0$ pair creation for $B_{\rm tag}$ and B_{CP}, respectively. This requires the reconstruction of pair creation time but it is practically impossible to realize it. So, to solve this problem, we replace variables

$$\{t_{\rm tag}, t_{f_{CP}}\} \rightarrow \{s = t_{\rm tag} + t_{f_{CP}}, \Delta t = t_{f_{CP}} - t_{\rm tag}\}$$

with these new ones, assuming values:

$$\begin{array}{c} -\infty < \Delta t < +\infty \\ |\Delta t| < s < +\infty \end{array} \tag{2.7}$$

Integrating on s, we obtain relationship between decay rate for $B_{CP} \rightarrow f_{CP}$ and Δt:

$$R(\Delta t) \propto e^{-\Gamma|\Delta t|}[1 \pm S\sin(\Delta m \Delta t) \mp C\cos(\Delta m \Delta t)] \tag{2.8}$$

where the upper (lower) sign denotes a $B_{\rm tag}$ as B^0 ($\overline{B}^0$). Finally, the Δt distributions is given by:

$$F(\Delta t) = \frac{e^{-|\Delta t|/\tau}}{4\tau}[1 \pm S\sin(\Delta m \Delta t) \mp C\cos(\Delta m \Delta t)], \tag{2.9}$$

where the upper (lower) sign denotes a decay accompanied by a B^0 ($\overline{B}^0$) tag, τ is the mean B^0 lifetime, Δm is the $B^0\overline{B}^0$ mixing frequency.

2.4 Overview of Experimental Technique at the $\Upsilon(4S)$

In order to measure time-dependent CP-violating asymmetries at the $\Upsilon(4S)$, one must (of course) first reconstruct a neutral B decay mode that can exhibit CP violation, such as $B^0 \rightarrow J/\psi K^0_S$. However, that is merely the first step. After signal event reconstruction, the additional tracks in the event (which are to the decay products of

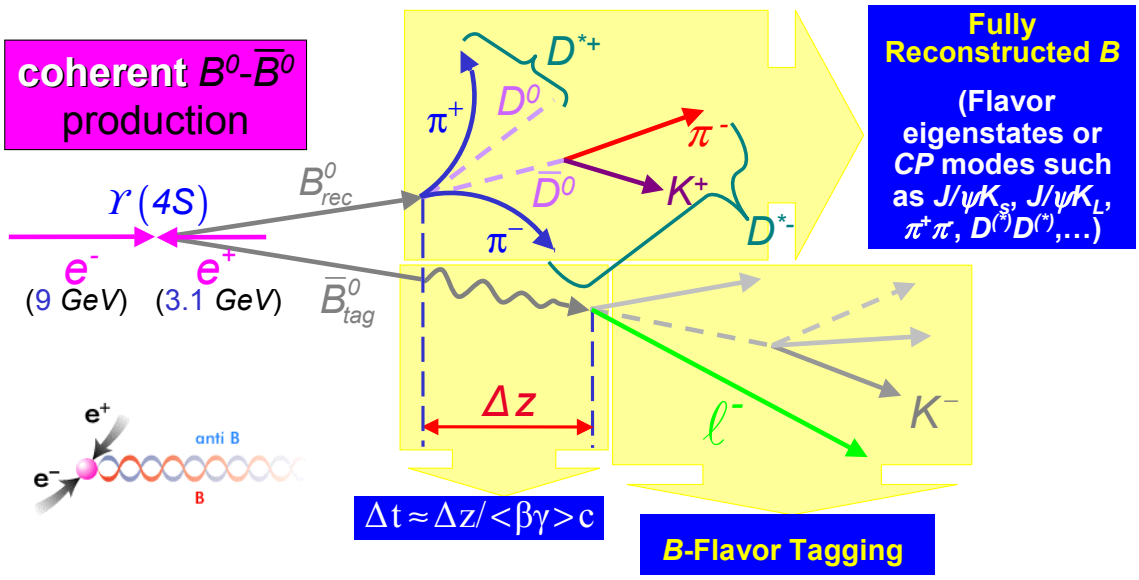

Figure 2.7: Experimental reconstruction technique used for measuring time-dependent CP-violating asymmetries at an $\Upsilon(4S)$ asymmetric collider. A coherent $B\overline{B}$ pair is produced from the $\Upsilon(4S)$ decay, which allows determination of reconstructed neutral B flavor as a function of decay time.

the other B [the "tag side B"]) must be used to determine whether the other B in the event was a B^0 or $\overline{B}^0$, due to the fact that the decay rate is different for B^0 and $\overline{B}^0$ (see eq. 2.9).

After both the event reconstruction and the flavor tagging are completed, the difference in vertex z-position[2] between the reconstructed B vertex and the tag side B vertex must be determined. This difference, Δz, is (very nearly) proportional to the decay time difference Δt between the two B decays. Δt is the time measurement over which the CP-violating asymmetry can occur, and it is input in eq. 2.9. Figure 2.7 gives an overview of this reconstruction method.

2.4.1 The flavor tagging algorithm

As said above, a key ingredient in the measurement of the time-dependent CP asymmetries is to determine whether at $\Delta t = 0$ the meson decaying to a CP final state was a B^0 or a $\overline{B}^0$. This 'flavor tagging' is achieved with the analysis of the decay products

[2]The z-axis in *BABAR* is along the direction of the beam line, with electrons (and the center-of-mass boost) pointing toward $+z$ in the lab frame.

of the recoiling meson $B_{\rm tag}$. The overwhelming majority of $B_{\rm tag}$ decays to a final state that is flavor-specific, *i. e.* only accessible from either a B^0 or a $\overline{B}^0$, but not from both.

An example is the semileptonic decay $B^0 \to D^{*-}\ell^+\nu_\ell$ (or $\overline{B}^0 \to D^{*+}\ell^-\bar{\nu}_\ell$) with an appreciable branching fraction of 5.35% [36]. Here the charge of the lepton unambiguously identifies the decay as from a B^0 or a $\overline{B}^0$. The subsequent decays of $D^{*+} \to D^0\pi^+$ and $D^0 \to K^-X^+$ give a soft pion and a kaon in the final state whose charges also uniquely identify the flavor of $B_{\rm tag}$. Another example is the self-tagging decay $B^0 \to D^{*-}\pi^+$. This decay gives an energetic π^+ and a low-momentum π^- in the final state, and the $B_{\rm tag}$ flavor can be inferred from the charges of both.

The purpose of the flavor tagging algorithm is to determine the flavor of $B_{\rm tag}$ with the highest possible efficiency $\epsilon_{\rm tag}$ and lowest possible probability w of assigning a wrong flavor to $B_{\rm tag}$. In the presence of a finite mistag probability w and a difference of mistag probability for $B_{\rm tag}$ tagged as B^0 or $\overline{B}^0$, $\Delta w = w_{B^0} - w_{\overline{B}^0}$, the CP asymmetry (eq. 2.9) is reduced by a dilution factor $D = (1-2w)$:

$$f(\Delta t) = \frac{e^{-|\Delta t|/\tau}}{4\tau}\left[1 \mp \Delta w \pm (1-2w)\left[S\sin(\Delta m \Delta t) - C\cos(\Delta m \Delta t)\right]\right] \quad (2.10)$$

The figure of merit for the performance of the tagging algorithm is the effective tagging efficiency (or "tagging power")

$$Q = \epsilon_{\rm tag}(1-2w)^2, \quad (2.11)$$

which is related to the statistical uncertainty σ in the coefficients S and C through

$$\sigma \propto \frac{1}{\sqrt{Q}} \quad (2.12)$$

The *BABAR* tagging algorithm is a modular, multivariate flavor-tagging algorithm that analyses charged tracks on the tag side to assign a flavor and associated probability w to $B_{\rm tag}$. The flavor of $B_{\rm tag}$ is determined from a combination of nine different tag signatures, such as the properties of charged leptons, kaons, and pions. For each of these signatures, properties such as charge, momentum and decay angles are used as input to a Neural Network (NN) or "sub-tagger". These sub-taggers are combined in a single Neural Network (`Tag04`), or "Committee of Networks" [67, 68], trained to assign the correct flavor to $B_{\rm tag}$. Based on the output of this Neural Network and on the sub-taggers that contributed to it, each event is assigned to one of six mutually

exclusive tag categories.

This modular approach, that keeps track of the underlying physics of each event, allows for detailed study of systematics. In particular it allows to separate semi-leptonic B decays, assigned to the `Lepton` tag category, from other decays. These `Lepton` tags do not only have a low w, but have more precisely reconstructed $B_{\rm tag}$ vertices, are less sensitive to the bias from the charm on the tag side and are immune from the intrinsic mis-tag associated with Doubly Cabibbo Suppressed Decays [69].

The `Tag04` NN output is mapped to values between -1 and 1. The output value NN corresponds approximately [67] to the probability p of correct assignment through

$$p = (1 + |NN|)/2. \tag{2.13}$$

The NN value is used for the final classification in the six hierarchical and mutually exclusive tag categories: `Lepton`, `Kaon I`, `Kaon II`, `Kaon-Pion`, `Pion` or `Other`. The events where the informations are not enough to have a clear identification are classified as `Untagged` and are unsuitable for the measurement of CP asymmetries. The name given to each category indicates the dominant physics processes (or subtagger) contributing to the flavor identification.

Since the tagging is mostly independent of the reconstructed B decay mode, the tagging parameters $\epsilon_{\rm tag}$, w, and Δw can be taken from a fit to samples of fully reconstructed B events (so called BReco) which have definite flavor (such as $B^0 \to D^{*-}\pi^+$ or $D^{*-}\rho^+$) (see section 8.8 for a description of this fit). The overall efficiency of tagging is 74.6% and the fraction of tagged events with an incorrect tag is 15.5%. The taggin power Q is 30.5%.

2.4.2 Tag vertex reconstruction

All reconstructed charged tracks that are not part of the fully reconstructed B_{CP} candidate are assigned to $B_{\rm tag}$. A set of loose track criteria is applied to these in order to reject ghost tracks. Each track must be successfully fit and its momentum is required to be below 10 GeV/c. Furthermore the distance of closest approach (DOCA) to the beam spot (luminous region) must be less than 4 cm along the beam axis and less than 0.4 cm in the transverse direction.

To improve the vertex resolution, K^0_S or Λ^0 candidates are used as input to the vertex fit in place of their daughters. Furthermore, track pairs that are consistent with

photon conversions ($\gamma \to e^+e^-$) are excluded from the fit.

The remaining candidates are used in a geometrical fit to a common vertex, taking into account the beam energies, the beam spot position and the flight direction of the other, fully reconstructed B candidate. The track with the highest χ^2 contribution is removed if its exceeds $\chi^2 > 6$ and the vertex fit is redone until no track fails this χ^2 requirement.

In all but 1.3% of events, a tag side vertex is successfully fit from on average 3.5 tracks. The resolution in $\Delta z = z_{CP} - z_{\rm tag}$ is approximately $190\ \mu$m, corresponding to a resolution in Δt of 1.1 ps, when excluding less than 1% of misreconstructed "outlier" vertices. It is dominated by the precision in the tag side vertex position $z_{\rm tag}$, and is slightly biased towards negative values due to the presence of charmed particles on the tag side. Figure 2.8 briefly describes the Δt measurement and resolution function. CP violation manifests itself as a difference in Δt distribution 2.10, depending on whether the flavor tag is B^0 or $\overline{B}^0$. This decay time distribution is convolved by the error of Δt (*i. e.* the resolution function). Vertex resolution is mostly independent from the reconstructed B decay mode and small differences are reflected in the assigned Δt errors. So parameters of the Δt resolution function can be taken from fit to the BReco sample, as well as the tagging parameters (see section 8.8 for a description of this fit).

2.5 The Silicon Vertex Tracker (SVT)

The SVT contains 5 layers of silicon, double sided with conductive strip sensors. Strips on the opposite sides of each layer are orthogonal: ϕ strips run parallel to the beam axis and z strips run transverse to the beam direction. An image of fully assembled SVT is shown fig. 2.9.

Together, the SVT and the central tracking drift chamber (DCH) form the charged particle tracking system (see also section 2.11.2). Precise and efficient measurement of track 4-momentum is necessary for full reconstruction of B meson decays, which tend to have multiple charged decay products. In addition, good vertex (and Δz) resolution and accurate extrapolation to the outer subdetectors is essential for reconstruction and background subtraction. Thus, accurate charged particle tracking and vertexing is required.

The 5 layers and relatively long radial separation between SVT detector layers provide both standalone track pattern recognition and refinement of drift chamber tracks

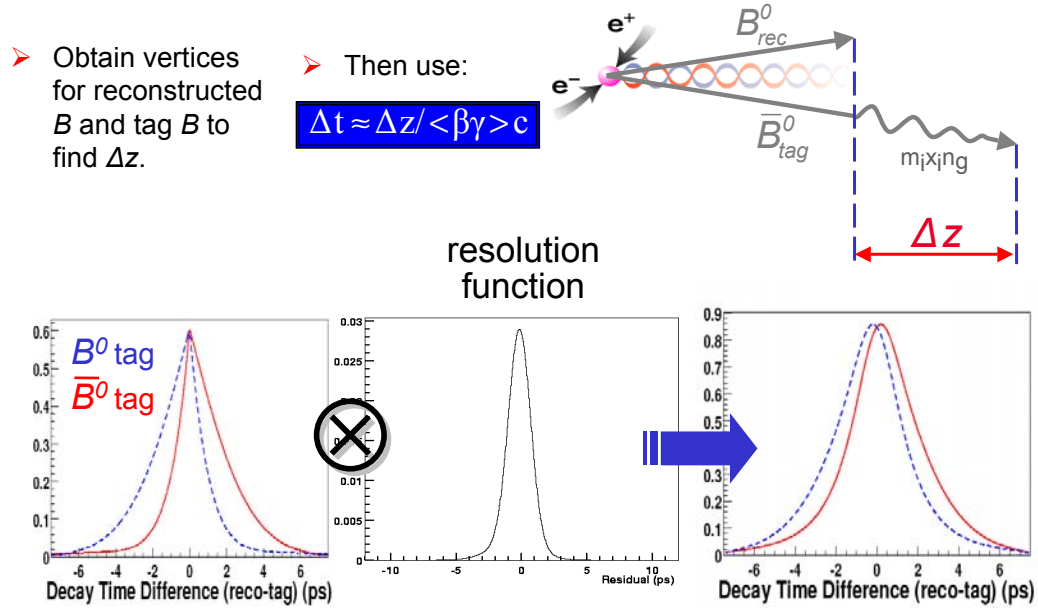

Figure 2.8: Δt measurement and resolution function. The difference in reconstructed z-position of the tag and reconstructed B decay vertices is used to determine the time difference Δt.

via addition of SVT hits. The necessity of precise measurements close to the interaction point for Δz measurement and for background rejection using vertex quality, and for efficient reconstruction of low momentum tracks (such as slow pions from D^* decays), drive the requirements for the SVT.

The SVT silicon is composed of n-type substrate with p^+ and n^+ strips on opposite sides. The bias voltage ranges from 25-35 V. The layers of the SVT are divided radially into modules, shown as line segments in fig. 2.10. The modules in the inner 3 layers are straight along the z-axis, while those in layers 4 and 5 are arch-shaped, as shown in fig. 2.11. The arch design was chosen to minimize the amount of silicon as well as increase the angle of incidence of tracks originating at the IP which cross the arch "lampshades" near the edges of acceptance. The total active silicon area is 0.96 m^2. The parameters of the layout of the SVT are shown in table 2.3.

The strip pitch (width) varies from 50 to 210 μm depending on the layer (inner layers are more closely bonded). The strips are AC-coupled to the electronic readout. Only approximately half the strips are read out; most have an unconnected "floating strip" between each pair of active strips (to reduce cost of readout electronics without adversely impacting performance). Digitization is performed by an ATOM ("A Time-

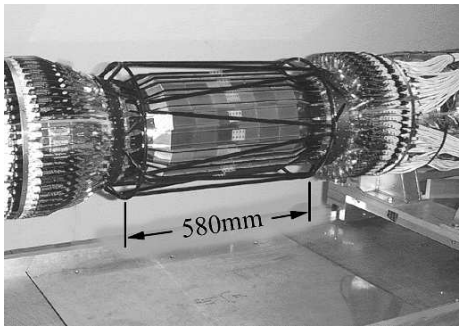

Figure 2.9: Fully assembled SVT. The silicon sensors of the outer layer are visible, as is the carbon-fiber space frame (black structure) that surrounds the silicon.

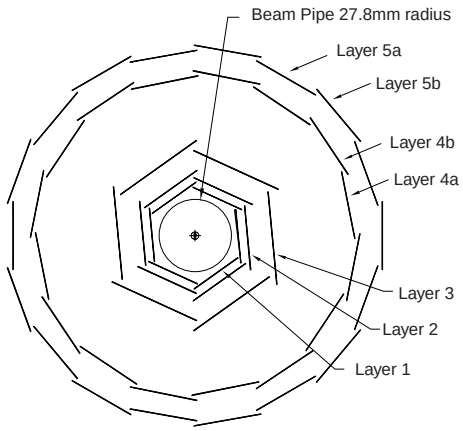

Figure 2.10: Transverse section of the SVT.

Over-Threshold Machine") chip at the end of each set of 128 strips, which amplifies, digitizes, and buffers the signal from each channel. The ATOM chip compares the charge accumulated on each strip with an (adjustable) threshold of 0.95 fC, and records the time in clock intervals (30 MHz for the SVT) for which each strip is over threshold. This information is then delivered to a computer farm for further processing upon an accept signal from the Level 1 Trigger (see section 2.10).

A variety of monitoring checks and calibrations must be performed on the SVT to maintain data quality. Perhaps the most important of these from an avoidance-of-equipment-damage perspective is radiation protection. Twelve silicon PIN diodes surround the support cones and monitor both instantaneous radiation and accumulated dose. The beam is automatically aborted if radiation levels are above 1 Rad/s threshold. So far, the SVT is well below the operational limit of 4 MRad integrated dose. The silicon PIN diodes have a temperature-dependent leakage current that increases with absorbed radiation dose. Due to absorbed doses of over 2 MRad in some diodes, the leakage current in these diodes is much higher than the current induced by the radiation. The temperature is monitored very precisely but it is a challenge to correct for the temperature dependence of the leakage current, and the annealing and reverse-annealing effects due to radiation damage. During the 2002 summer shutdown a system of two diamond sensors has been installed inside the SVT. These diamond sensors, grown by chemical vapor deposition (CVD), have no significant leakage cur-

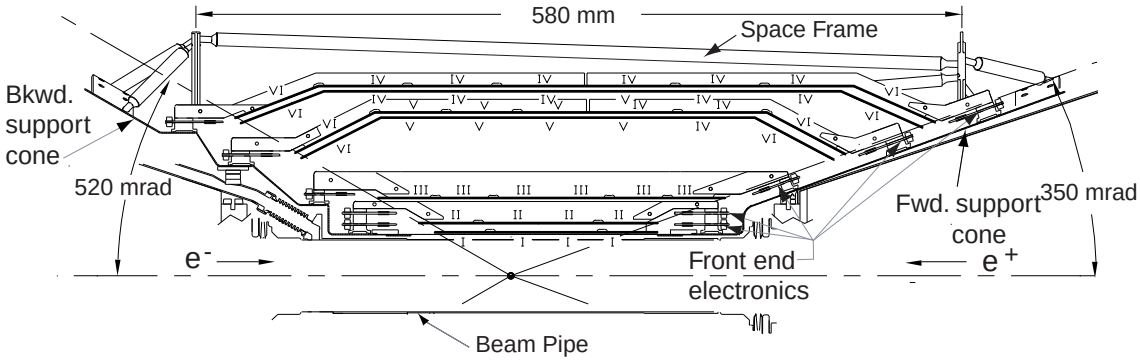

Figure 2.11: Longitudinal section of the SVT.

rent and are much more radiation hard than silicon PIN diodes. With a bias voltage of 500V applied across a 500-μm-thick polycrystalline CVD diamond sensor, the size of the signal due to a minimum-ionizing particle is more than 50% of that for a signal from a 300-μm-thick silicon sensor. The two diamond sensors augment (rather than replace) the primary existing silicon PIN-diode radiation sensors.

For data quality calibration, channel gains and noise must be individually calibrated, and these are done online via an integrated pulse generator and calibration electronics. The offline reconstruction has the responsibility for calibration of the alignment of each SVT module. Alignment is critical for accuracy of vertexing and of tracking reconstruction, and is done in two steps. The local SVT alignment uses dimuon and cosmic ray events to calibrate the relative position of each of the 340 wafers. The global alignment then determines the overall position and rotation of the SVT with respect to the DCH.

The SVT has performed according to design essentially since its inception. A combined hardware and software hit-finding efficiency greater than 95% is observed, excluding the 4 (out of 208) readout sections which are defective. Single hit resolution for tracks originating from the IP averages 20 μm in both z and ϕ for hits on the inner 3 layers and 40 μm in z and 20 in ϕ for hits in the outer 2 layers. Before the summer 2002 shutdown there were 9 readout sections out of 208 that were not used in the DAQ. During the shutdown it was recabled the SVT and there was the possibility to inspect closely all the modules with problems. This allowed us to fix 5 of the 9 problems and

Quantity	Layer 1	Layer 2	Layer 3	Layer 4a	Layer 4b	Layer 5a	Layer 5b
Radius (mm)	32	40	54	124	127	140	144
Wafers/Module	4	4	6	7	7	8	8
Modules/Layer	6	6	6	8	8	9	9
ICs/Readout	7	7	10	5		5	
Length Strip, b/f :							
ϕ (mm)	82	88	127	230/189	230/203	270/257	270/270
z (mm)	40	48	70	104	104	104	104
z Ganging % (f/b):				34/67	48/67	88/98	98/98
Readout pitch (μm):							
ϕ	50	55	55	80–100		80–100	
z	100	100	100	210		210	
Floating Strips:							
ϕ	—	—	—	1		1	
z	1	1	1	1		1	
Intrinsic Resolution (μm):							
ϕ	10	10	10	10–12		10–12	
z	12	12	12	25		25	

Table 2.3: Parameters of the SVT layout.

the last 4 sections do not have significantly impact on performances.

2.6 The Drift Chamber (DCH)

The DCH contains 40 layers of gold-coated tungsten-rhenium sense wires and gold-coated aluminium field wires in a mixture of 80% helium and 20% isobutane gas. There are a total of 7,104 sense wires and 21,664 field wires, with one wire per electronics channel. Wires are each tensioned (30 grams for sense wires, 155 grams for field wires) and pass through the aluminium endplates via feedthroughs made from Celenex insulating plastic around a copper wire jacket. The layers are grouped by four into 10 superlayers, with the wires in each superlayer oriented as either axial (directly parallel to the z-axis) or "stereo" (at a small angle in ϕ with respect to the z-axis, in order to obtain longitudinal position information). 6 of the 10 superlayers are stereo,

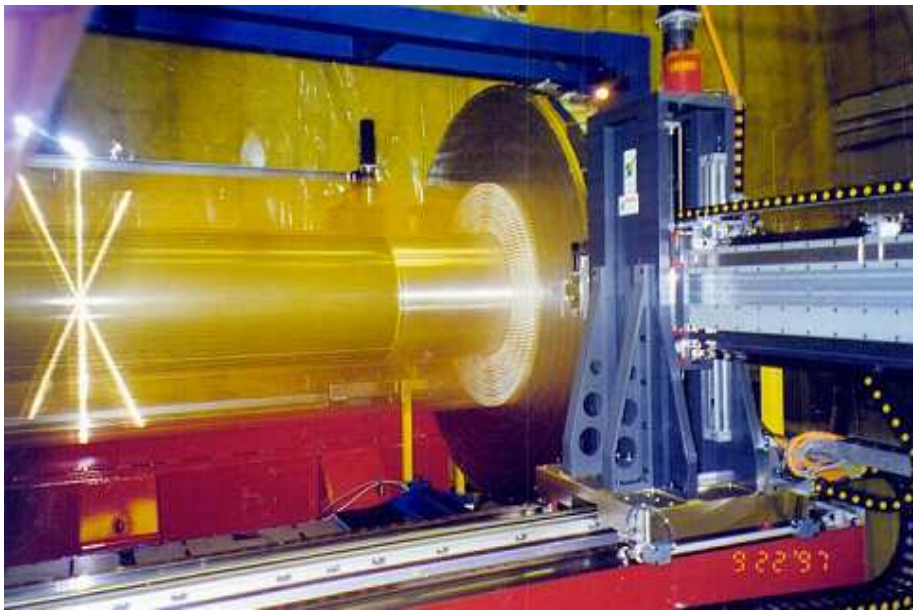

Figure 2.12: DCH wire stringing at TRIUMF (September 1997).

and the other 4 are axial.[3] An image of assembled DCH is shown fig. 2.12. The DCH is asymmetric in z about the interaction point, as shown in fig. 2.13, to accommodate the forward boost of the center of mass of physics events.

The endplates are 24 mm thick aluminium, except for the outer 33.1 cm of the for-

[3]The arrangement is, from inner to outer, AUVAUVAUVA (A = axial, U = u stereo ($+\phi$), V = v stereo ($-\phi$)).

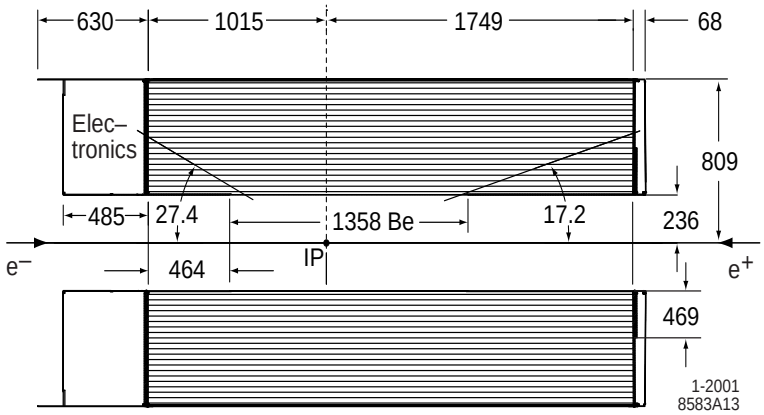

Figure 2.13: Longitudinal section of the drift chamber.

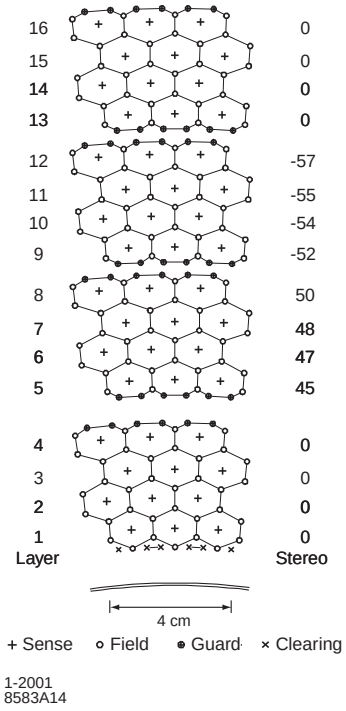

Figure 2.14: DCH cell pattern (for a section of the inner 16 [of 40] layers).

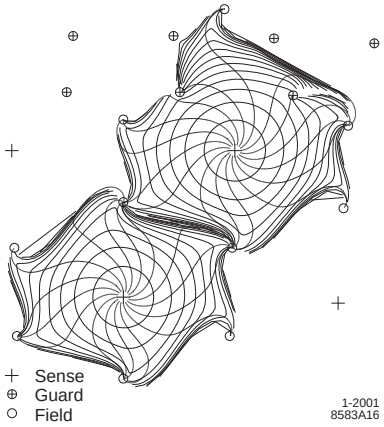

Figure 2.15: DCH cell drift isochrones for cells in layers 3 and 4 (axial). Isochrones are at 100 ns intervals.

ward endplate, which is reduced to 12 cm to minimize the amount of material in front of the forward calorimeter endcap. The inner cylinder is fabricated from beryllium (to minimize the multiple scattering for the section of inner cylinder within the tracking fiducial volume) and aluminium (for the rest). The outer cylinder is 1.6 mm carbon fiber on 6 mm thick honeycomb Nomex core. The total thickness of the DCH is 1.08% X_0.

The cells are arranged in a hexagonal pattern, each with a sense wire at the center and field wires at the corners, as shown in fig. 2.14. Cells on a superlayer boundary have a slightly different arrangement, with two guard wires taking the place of a single field wire. The nominal operating voltage is 1930 V. Isochrones and drift paths, calculated using the GARFIELD simulation, are shown in fig. 2.15.

The DCH electronics are designed to provide accurate measurements of signal time and integrated charge (as well as providing information to the Level 1 Trigger, see section 2.10). Service boards plug directly onto the wire feedthroughs on the rear endplate. These boards distribute the high voltages as well as pass signal and ground

to the front-end electronics assemblies. The front-end assemblies (FEAs) plug into the service boards and amplify, digitize, and buffer (for 12.9 μs) the signals. The digital data is sent, upon receipt of a level 1 trigger accept signal, via 59.5 MHz serial link to a data I/O module which transmits the signal to the external electronics via fiber-optic cable. Extraction of hit time and integrated charge from the digital waveform takes place in the readout modules (ROMs) in external electronics.

Online calibrations of channel gain and threshold are performed daily via internal pulse generation. The data are monitored online to check for FEA or other electronics failure or for miscalibrated output. Monitoring and control of high voltage, radiation protection (using silicon PIN diodes similar to the SVT, as well as RadFETs for integrated dose measurement), the gas system, and temperature are performed, similar to other subsystems, via a slow control system based on EPICS.

Offline calibrations of the time-to-distance relation within cells, as well as of the deposited charge used for particle identification via $\mathrm{d}E/\mathrm{d}x$ measurement, are performed. The time-to-distance relation is determined from two-prong events (Bhabha scattering events and dimuons) and is fit to a sixth-order Chebychev polynomial for each cell layer, with separate fits to right and left sides of wires (to account for $E \times B$ asymmetries). A correction for time-to-distance variations as a function of track entrance angle to the cell is determined via simulation (not calibration) and added to the calibrated entrance-angle-averaged relation. The design goal for the average drift distance resolution was 140 μm. An average resolution of 110 μm is achieved. The drift distance resolution as a function of drift distance can be seen from the offline monitoring plot shown in fig. 2.16 (left side).

The energy loss per unit length of tracks, $\mathrm{d}E/\mathrm{d}x$, contains particle type information due to the dependence of $\mathrm{d}E/\mathrm{d}x$ on particle velocity (Bethe-Bloch relation), and is derived from measurements of integrated charge deposited in each cell along the track path. An overall multiplicative correction to the charge measurements due to gas pressure and temperature variations is performed once per run; additional calibrations due to variations with track entrance angle in ϕ and in θ are performed only when high-voltage settings are changed. Particle identification using the drift chamber provides significant information up to high momenta, as can be seen in fig. 2.16 (right side).

Cell-by-cell channel efficiency is also monitored; typical efficiency is 90-95%.

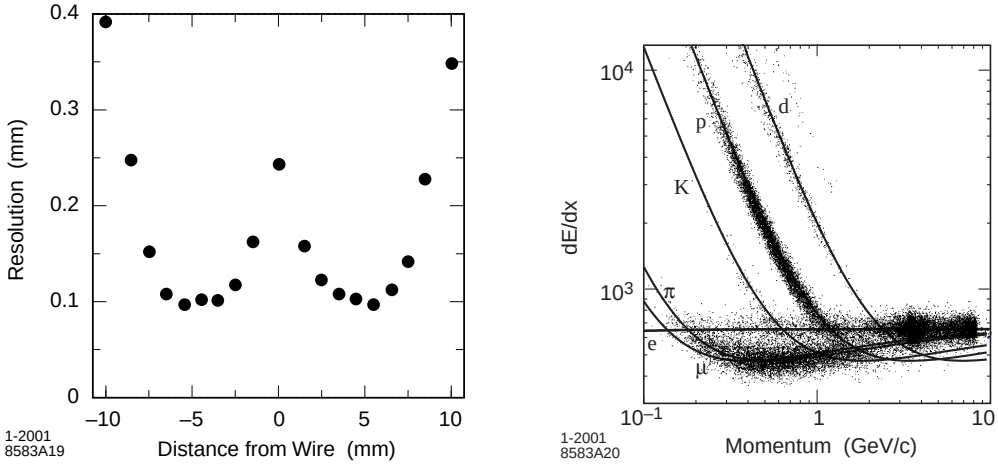

Figure 2.16: DCH drift distance resolution as a function of the drift distance in the cell (left); DCH particle identification as a function of momentum using $\mathrm{d}E/\mathrm{d}x$ (right).

2.7 The Cherenkov Detector (DIRC)

BABAR has stringent requirements for $\pi - K$ separation over a large momentum range. At the lower end of the range, primarily at momenta < 1 GeV, flavor tagging using kaons from cascade decays is an efficient way of determining B flavor. At the high end of the range, reconstructing $B^0 \to \pi^+\pi^-$ and $B^0 \to K^\pm\pi^\mp$ requires separation at momenta up to 4.2 GeV in the lab frame. At intermediate energies, $\pi - K$ is necessary to reduce background in charmless decays such as $B^+ \to \eta' K^+$. The particle identification device must exhibit sufficient $\pi - K$ separation throughout this wide range of momentum with a minimum of material in order to avoid adversely impacting calorimeter resolution.

The DIRC (Detector of Internally Reflected Cherenkov light) principle uses internal reflection within quartz bars to propagate Cherenkov light to readout phototubes while preserving the Cherenkov angle. This requires extremely flat surfaces in order to avoid dispersing the reflected angles. Fused, synthetic silica quartz is used due to the excellent optical surface it allows through polishing, as well as other favorable properties such as long attenuation length, low chromatic dispersion, small radiation length, and radiation hardness. Schematic views of DIRC are shown in figs. 2.17 and 2.18. Figure 2.19 shows as the light is internally reflected down to a wedge to reflect photons into a water-filled "standoff box". The standoff box (SOB) is enclosed by an array of 10752 photomultiplier tubes (PMTs), which are each 29 mm in diameter. The Cherenkov light from a particle passing through the DIRC forms a ring (essentially a conic section) imaged on the phototubes. The opening angle of this conic section contains information on particle type via the typical relation $\cos\theta_c = 1/n\beta$, with β being the particle velocity normalized to the speed of light, and n being the mean index of refraction ($= 1.473$ for fused silica).

Both efficiency and the timing of the electronics are critical for DIRC performance. Timing is critical for two reasons: one, for background hit rejection, resolving ambiguities, and separation of hits from differing tracks within an event; and two, timing gives information on the photon propagation angles, allowing an independent measurement of the Cherenkov angle. The intrinsic timing resolution of the PMTs is limited to 1.5 ns by transit time spread. Data from the phototubes is read out to front-end electronics, which performs the amplification, digitization, and buffering. Reduction of data from out-of-time or noisy PMTs is performed in in the external electronics and reduces the data volume by 50% using rough timing cuts. Online calibration of PMT efficiency,

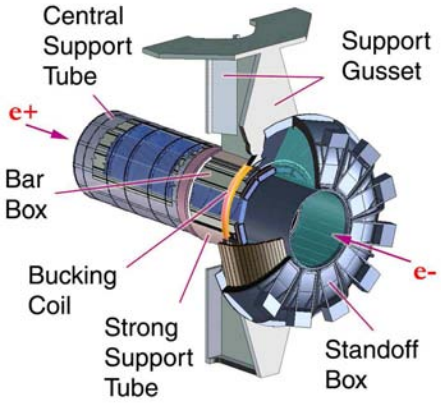

Figure 2.17: View of DIRC mechanical structure.

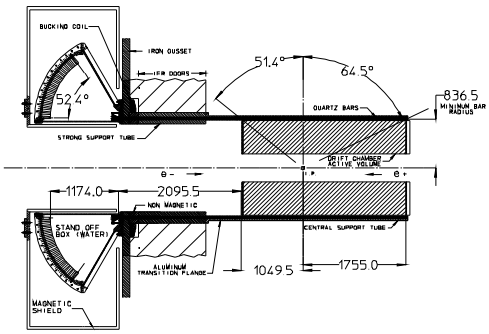

Figure 2.18: Longitudinal section of the DIRC. Length units are mm.

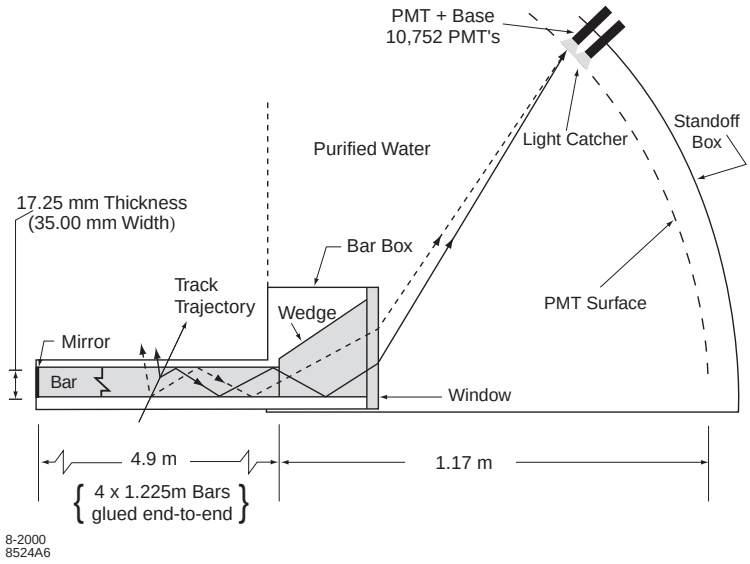

Figure 2.19: DIRC schematic showing the principle behind PID measurements. The Cherenkov angle is preserved through specular internal reflection.

timing response, and electronics delays uses a light pulser system which generates precise 1 ns flashes from blue LEDs inside the SOB.

The DIRC has performed well throughout *BABAR*'s operational lifetime: 99.7% of PMTs are operating with design performance. The measured time resolution is 1.7 ns, very close to the intrinsic resolution of the PMTs. The Cherenkov angle resolution for dimuon events is 2.5 mrad, close to the design goal of 2.2 mrad. This results in $\pi - K$ separation at 3 GeV of 4.2σ. The distributions of the Cherenkov angle, as function of the momentum, for a sample of π and a sample of K are shown in fig. 2.20. The mean kaon selection efficiency and pion misidentification for a "loose" selection are 96.2% and 2.1% respectively, as can be seen in fig. 2.21. This results in dramatic background rejection with little signal loss for charm reconstruction, as may be seen in fig. 2.22.

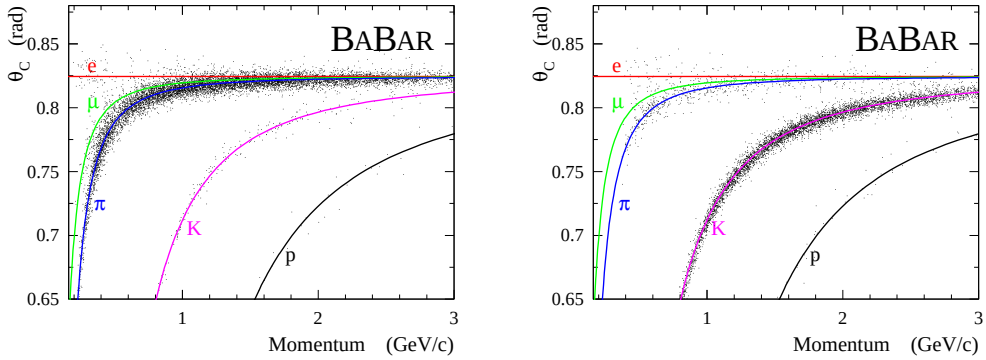

Figure 2.20: Cherenkov angle distributions, as function of the momentum, for a sample of π (left) and a sample of K (right). The samples come from the reconstruction of decay $D^{*+} \to D^0 \left(\to K^- \pi^+\right) \pi^+$.

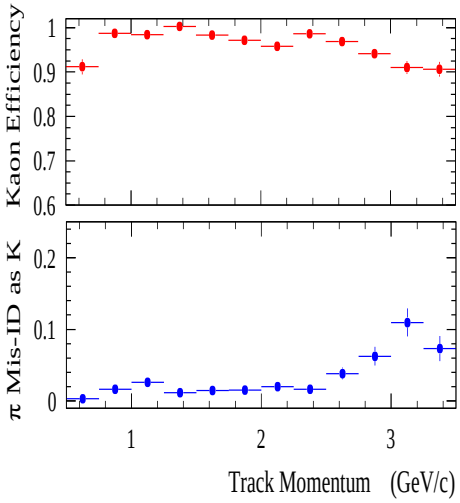

Figure 2.21: Kaon selection efficiency (top) and pion misidentification probabilities (bottom) as a function of momentum.

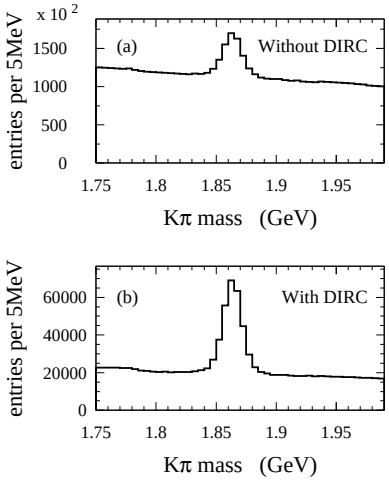

Figure 2.22: Inclusive $K\pi$ invariant mass spectrum (a) without and (b) with the use of the DIRC for kaon identification.

2.8 The Electromagnetic Calorimeter (EMC)

The design parameters for the *BABAR* EMC are driven by the requirements of precisely measuring energies over a spectrum from 20 MeV to 9 GeV in a 1.5 T magnetic field and a high radiation environment. At the high end of the spectrum, measurements of QED processes such as Bhabha and two-photon scattering, as well as (at slightly lower energies) photons from the critical physics processes $B^0 \rightarrow \pi^0\pi^0$ and $B^0 \rightarrow K^*\gamma$ decays, present the motivating incentive. The need for efficient detection of photons from high multiplicity B decays containing π^0's determines the requirement for the low end of the spectrum. *BABAR* uses a thallium-doped cesium iodide (CsI(Tl)) crystal calorimeter in order to achieve the necessary energy and angular resolution to meet these physics requirements.

The EMC contains a cylindrical barrel and a conical endcap containing a total of 6580 CsI(Tl) crystals. The crystals have nearly square front and rear faces with a trapezoidal longitudinal cross-section. They range in length from 29.6 to 32.4 cm with a typical front face dimension of 4.7 x 4.7 cm. A diagram can be seen in fig. 2.23. The crystals are mounted in thin (300 μm) carbon-fiber composite housings which are mounted on an aluminium strong-back (see fig. 2.24). Although light incident on the crystal boundary is internally reflected, the small part that is emitted is reflected back with a coating of white reflective TYVEK on the outer surface. Surrounding that are thin layers of aluminium and mylar to act as RF shielding and electrical insula-

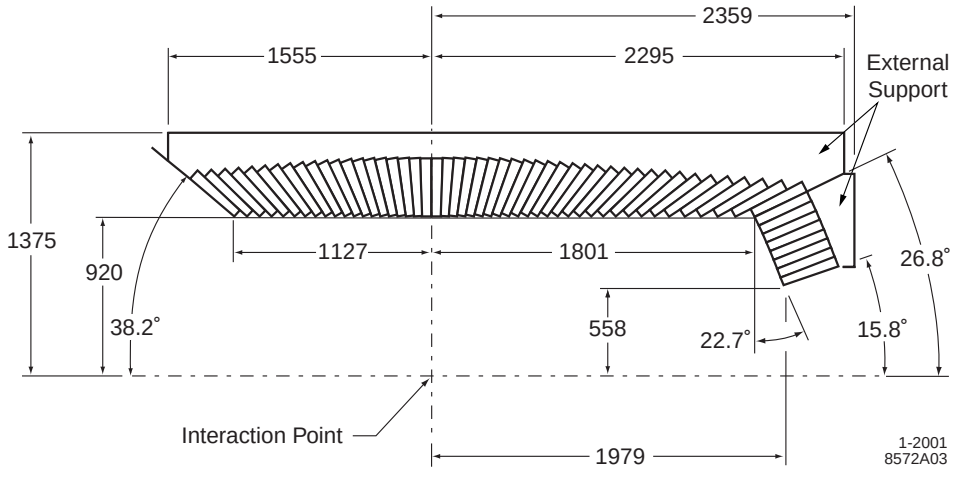

Figure 2.23: Longitudinal section of the EMC. Length units are mm.

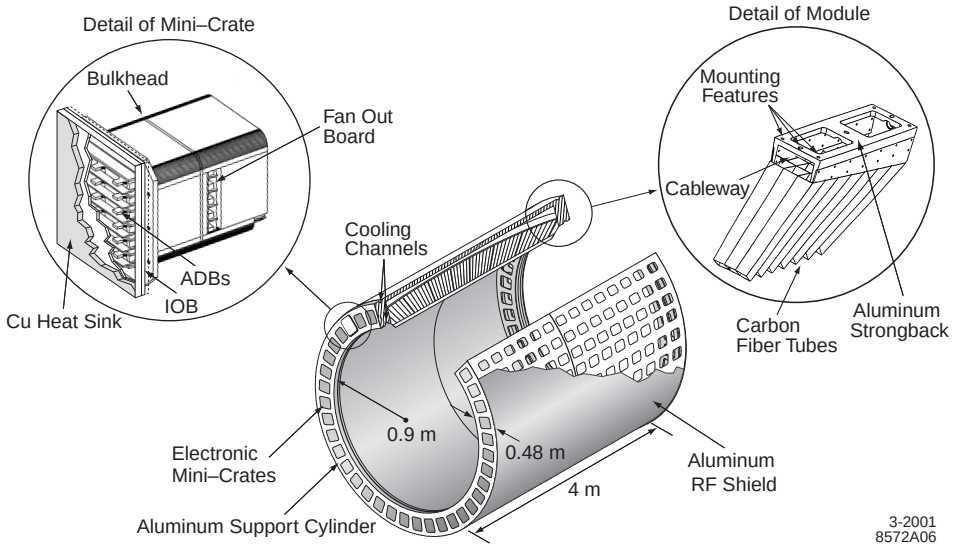

Figure 2.24: The EMC barrel support structure, modules, and mini-crates.

tion respectively. On the rear face of the crystal, two 1 cm^2 silicon PIN diodes with quantum efficiency of 85% for CsI(Tl) scintillation light are mounted via transparent polystyrene substrate.

Each diode is connected to a low-noise preamplifier which shapes and amplifies the signal by a factor between 1 and 32. The signal is then transmitted to mini-crates at the end of the barrel (see fig. 2.24) where a digitization CARE ("custom auto-range encoding") chip provides an additional variable amplification factor. Unlike other subsystems (except for the IFR), the EMC does not buffer the data on front-end electronics; rather it outputs the full digital datastream to the read-out modules in external electronics, which perform, on receipt of a level 1 accept signal, a parabolic fit to the digitally filtered datastream to derive energy and time measurements.

A variety of online calibrations and checks is performed, including a neutron source which produces a monoenergetic 6.13 MeV calibration signal and a xenon flash light pulser system. Offline energy calibrations are necessary for higher energy corrections. The relation between polar angle and energy of Bhabha and radiative Bhabha scattering events is used to calibrate the 0.8-9 GeV range. The middle range is covered by π^0 calibration, which constrains the mass of a sample of π^0's to the known value, extracting correction coefficients.

The clustering pattern recognition uses a seed crystal algorithm to establish energy clusters. Local energy maxima within a cluster are used (if there are more than 1) to

separate the cluster into bumps. Charged particle tracks are associated with bumps using a χ^2 consistency cut. In an average hadronic event, 15.8 clusters are detected, of which 10.2 are not associated to a track.

Energy resolution is determined using $\chi_{c1} \rightarrow J/\psi\gamma$ and Bhabha scattering events to be

$$\frac{\sigma_E}{E} = \frac{(2.32 \pm 0.30)\%}{\sqrt[4]{E(\,\mathrm{GeV})}} \oplus (1.85 \pm 0.12)\% \tag{2.14}$$

and angular resolution is determined using π^0 and η decays to be

$$\left(\frac{3.87 \pm 0.07}{\sqrt{E(\,\mathrm{GeV})}} + 0.00 \pm 0.04 \right) \text{mrad.} \tag{2.15}$$

As can be seen in fig. 2.25, the reconstructed π^0 average width is 6.9 MeV. The EMC allows a good separation between electrons and charged hadrons using the ratio of shower energy to track momentum (E/p) and other variables which describe the shower shape. These last variables are also used to discriminate K_L^0 mesons from photons.

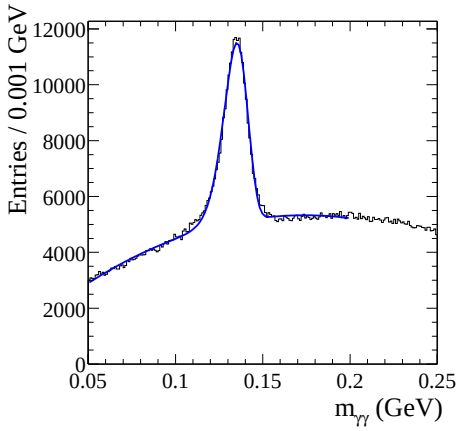

Figure 2.25: Two photon invariant mass, using photons between 30 and 300 MeV.

2.9 The Instrumented Flux Return (IFR)

Detection of neutral hadrons (primarily K_L^0's) and muons is necessary for several *BABAR* analyses and analysis techniques. Muons provide a very clean B flavor tag, extremely useful for increased efficiency in tagging the opposite-side B for time-dependent CP violation measurements. Muons are also necessary for reconstructing $J/\psi \rightarrow \mu^+\mu^-$, as well as for measuring semileptonic branching fractions, required for extracting magnitudes of CKM elements. K_L^0 reconstruction is critical for the $B^0 \rightarrow J/\psi K_L^0$ and $B^0 \rightarrow \eta' K_L^0$ channels. Initially, *BABAR* used an Instrumented Flux Return (IFR) composed of layers of resistive plate chambers (RPCs) and steel plates in order to provide enough material to separate pions and kaons from muons and to efficiently detect the presence and position of both μ and K_L^0 over a large solid angle. Due to some inefficiencies of some RPCs, during Summer 2004 shutdown a part of the RPCs of the barrel region (see fig. 2.26) has been replaced with plastic Limited Streamer Tubes (LSTs). The remaining part of RPCs of the barrel region will be replaced during the Summer 2006 shutdown.

As shown in fig. 2.26, the IFR consists of layers of planar RPCs/LSTs in a barrel and endcap [4] (red lines) as well as 2 layers of cylindrical RPCs (green lines) between the EMC and the magnet. Between the RPC/LST layers are steel plates of thickness varying between 2 cm (inner plates) to 10 cm (outer plates). The total mass of the IFR is 870 metric tons.

Planar RPCs contain a 2 mm Bakelite gap with ~ 8 kV across it. Ionizing particles which cross the gap create streamers of ions and electrons in the gas mixture (which is typically 56.7% Argon, 38.8% Freon, and 4.5% isobutane) which in turn creates signals via capacitive coupling on the "x-strips" and "y-strips" on opposite sides of the RPC. Strip width varies between 16 mm and 38.5 mm. The 2 mm gap is kept constant using polycarbonate spacers spread at 10 cm intervals and glued to the Bakelite. The Bakelite surface is smoothed with an application of linseed oil. Cylindrical RPCs are composed of a special thin and flexible plastic, rather than Bakelite, and have no linseed oil or other surface treatment. They are laminated to cylindrical fiberglass boards.

A "standard" LST configuration consists of a silver plated wire 100 μm in diameter, located at the center of a cell 9x9 mm^2 section. A plastic (PVC) extruded

[4] In the endcap regions there are only RPCs.

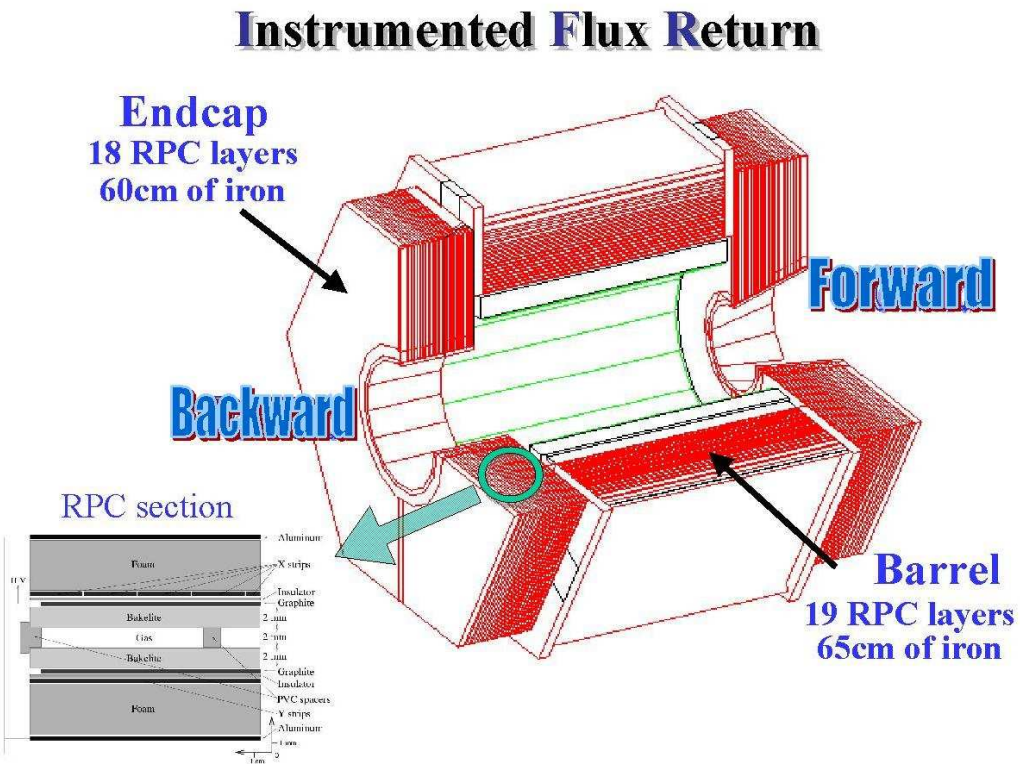

Figure 2.26: The instrumented flux return modules, structure, and RPCs/LSTs.

structure, or "profile", contains 8 such cells, open on one side, as shown in fig. 2.27. The profile is coated with a resistive layer of graphite, having a typical surface resistivity between 0.2 and 1 MΩ/square. The profiles, coated with graphite and strung with wires, are inserted in plastic tubes ("sleeves") of matching dimensions for gas containment. The signals for the measurement of one coordinate can be read directly from the wires, but it has become customary instead to read both coordinates with strip planes, thereby avoiding the complications of feedthroughs and DC-blocking capacitors. For such tubes the operating voltage is typically 4.7 kV; the efficiency plateaus are at least 200 V wide; the signals on the wire are of the order of 200/300 mV (into 50 Ω), typically 50 ns at the base, sometimes with an afterpulse. The gas mixtures are strongly quenching: the original one (25% Ar, 75% n-pentane) being explosive has been replaced in accelerator use by a non-flammable one based on CO_2. The LST geometrical efficiency is limited by the ratio of active versus total volume in the cell. The effect is mitigated by the fact that most tracks do not impinge perpendicularly. In the gap between iron slabs is wide enough, the inefficiency can be greatly reduced by using larger cells or, alternatively, a double-layer geometry.

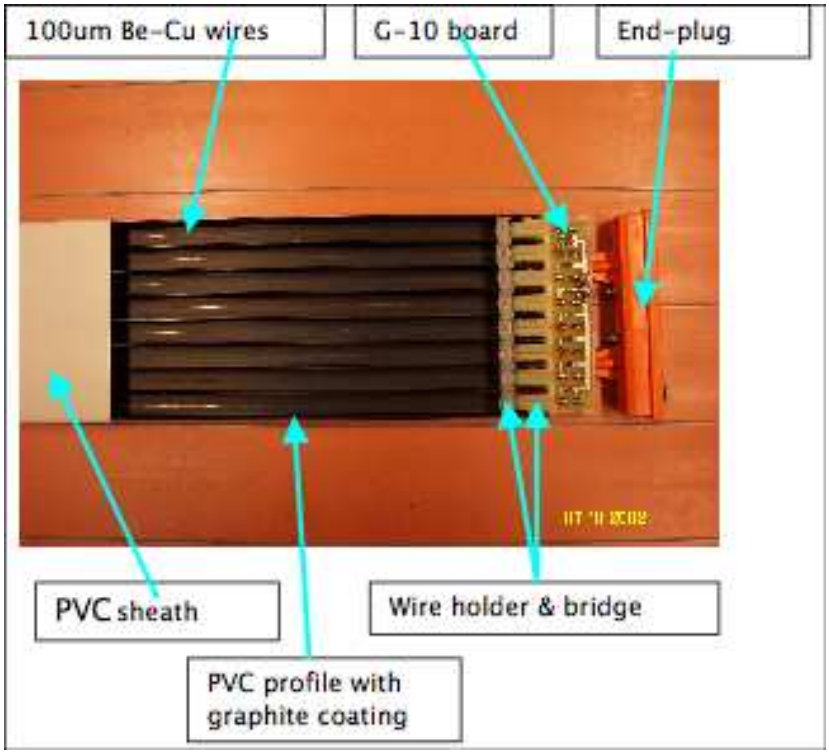

Figure 2.27: Photo of a standard LST, partially inserted in the sleeves.

The RPC strips are connected to front-end cards (FECs) containing the amplification and digitization electronics, which are primarily sandwiched between the iron plates. FECs shape the signal and perform a comparison with an adjustable threshold. For LST, instead of recycling the existing FECs, it has been decided to build new FECs. These FECs have a different input section but with the same interface to the existing IFR-FIFO boards, which is used for the readout of the LST's and are well integrated in the *BABAR* Data Acquisition (DAQ). The data format is the same as in the RPC system. This choice allows us to use the present DAQ software and electronics also with the LST system. Compared to the RPC FECs, two new functions are provided: front-end amplification and a settable threshold.

Similar to the EMC, the IFR does not buffer its data on the detector, so the full digital datastream is output to front-end crates (located beside the detector) which contain TDC timing as well as buffering and calibration electronics. Data is read out to the ROMs on receipt of a level 1 accept signal. Online calibration is performed using test pulse generators integrated in the front-end crates. Offline efficiency calibration

is also necessary for muon ID (in order to determine the expected hits for the muon hypothesis), and this is done using cosmic rays.

Reconstruction of clusters proceeds via two methods: a standalone method where groups of hits along 1 dimension within a module are joined to form one-dimensional clusters, which are then combined with opposite-side hits to form two-dimensional clusters, and then with other modules to form 3D clusters; and a "swimmer" method, where charged tracks are propagated to the IFR — 1D clusters within 12 cm of the expected path are combined to form 2D or 3D clusters. Clusters which are not matched to a charged track are considered as neutral clusters. Muon identification uses variables such as number of expected vs. actual interaction lengths transverse and the χ^2 match to the charged track.

2.10 The Trigger

The *BABAR* trigger needs to provide high efficiency that is well-understood and stable for physics events. Since the events which pass the trigger must be fully reconstructed in the offline event reconstruction, the output rate must be no higher than 120 Hz to satisfy computing limitations of the offline processing farm. Since events with either a DCH track or a > 100 MeV EMC cluster occur at 20 kHz, the trigger is responsible for scaling this rate down by a factor of > 150 while accepting over 99% of B events, over 95% of hadronic continuum, and over 90% of $\tau^+\tau^-$ events. It also must be flexible enough to deal with changing background conditions, as this can happen at any given time at *BABAR*, without impact on physics or increase in online dead time (which must be $< 1\%$). The *BABAR* trigger is implemented in two levels, a Level 1 hardware trigger (called L1), and a Level 3 software trigger (called L3); a Level 2 trigger is used in some other high energy particle physics experiments, but was not needed for *BABAR*.

The Level 1 trigger consists of four subsystems: the Drift Chamber Trigger (DCT) a trigger for charged particles, the Calorimeter Trigger (EMT) for neutral particles, an IFR Trigger used for calibration and works as cosmic trigger (IFT), and global electronics for producing the final L1 accept signal (GLT stands for Global Level Trigger). A scheme of the L1 trigger is shown in fig. 2.28. The DCT is further subdivided azimuthally into track segment finders (TSF), a binary link tracker for producing tracks from the segments (BLT), and a p_t discriminator (PTD). The 24 TSF modules sample each DCH cell in axial layers for signals every 269 ns (64 clock ticks of the PEP-II-

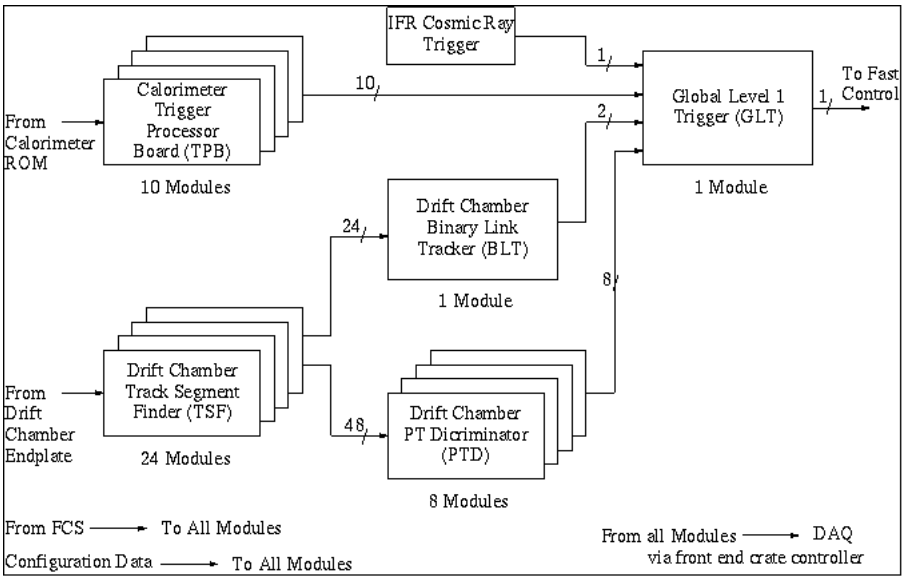

Figure 2.28: Trigger L1 scheme.

BABAR 4.2 ns clock interval). The DCT and EMT receive information from the DCH and EMC detectors, respectively, process it, and send condensed data to the Global Trigger.

The axial DCH cells are arranged into 1776 "pivot groups" (see fig. 2.29) and segments are constructed from hits within a pivot group. The cells in a pivot group are numbered 0 through 7, as shown in fig. 2.29 (cell 4 is the pivot cell). Note that if the pivot group template (the black circles in the figure) were to move one cell to the right, a new pivot cell (cell 4a) and a new pivot group would be defined. In the first version, only axial layers were used to avoid the complication of accounting for stereo layer within hardware electronics. Since 2004, the DCT trigger has been upgraded with a new system which performs 3D tracking using stereo wire information from the DCH to obtain ~ 4 cm resolution in track z (along beamline) coordinates of tracks to improve background rejection. Each cell contributes a 2 bit quantity (containing very rough information on the time, as well as the presence, of a hit on that cell) per sample, thus each pivot group outputs 16 bits. The TSF look-up table then determines if a given 16-bit quantity corresponds to a valid segment or not. The binary link tracker (BLT) receives this information and determines whether segments lie in a road defined by "supercells," which are sectors of a superlayer covering to 1/32 of the DCH in ϕ. Patterns of segment-containing supercells that appear to correspond to tracks (according

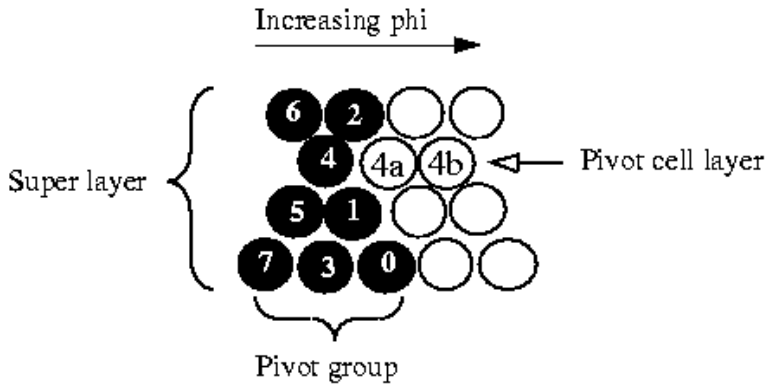

Figure 2.29: Showing the definitions of pivot cell and pivot group. Numbers indicate the cell number within a pivot group; the pivot cell is number 4. 4a and 4b indicate adjacent pivot cells.

to the BLT look-up table) are output to the L1 global trigger. In parallel with the BLT, the p_t discriminator (PTD) checks TSF segments in axial superlayers to see if they are consistent with a track having a greater p_t than a configurable minimum cutoff value. This information is also output to the GLT.

The level 1 calorimeter trigger (EMT) divides the EMC into 280 "towers" of 24 crystals each (22 for the endcap). All crystal energies within a tower which are above a 20 MeV threshold are summed and supplied to the EMT trigger processor boards (TPBs). The TPBs digitally filter the energy deposition (to smooth the output waveform of noise) and compare neighboring towers to look for clusters which span more than one tower. Trigger line "primitives" (bytes corresponding to trigger type and information) are output to the GLT corresponding to the energy and placement of found clusters.

The GLT attempts to match the angular locations of calorimeter towers and drift chamber tracks, and flexibly generates Level 1 triggers and sends them on to the Fast Control and Timing system (FCTS), based on the results of the processing. The GLT also uses the IFT information to independently trigger on cosmic ray and mu-pair events. The Level 1 trigger rates are typically 2.5 kHz at a luminosity of $L = 8 \times 10^{33}\text{cm}^{-2}\text{s}^{-1}$. The various stages of the L1 system operate at 4 MHz to 15 MHz intervals with a total L1 trigger latency of $\sim 11\mu$s. The combined L1 trigger efficiency is $> 99.9\%$ for generic $B\overline{B}$ events, 99% for continuum, and 94.5% for $\tau^+\tau^-$ events.

The Level 3 trigger analyzes the event data from the DCH and EMC sub-systems

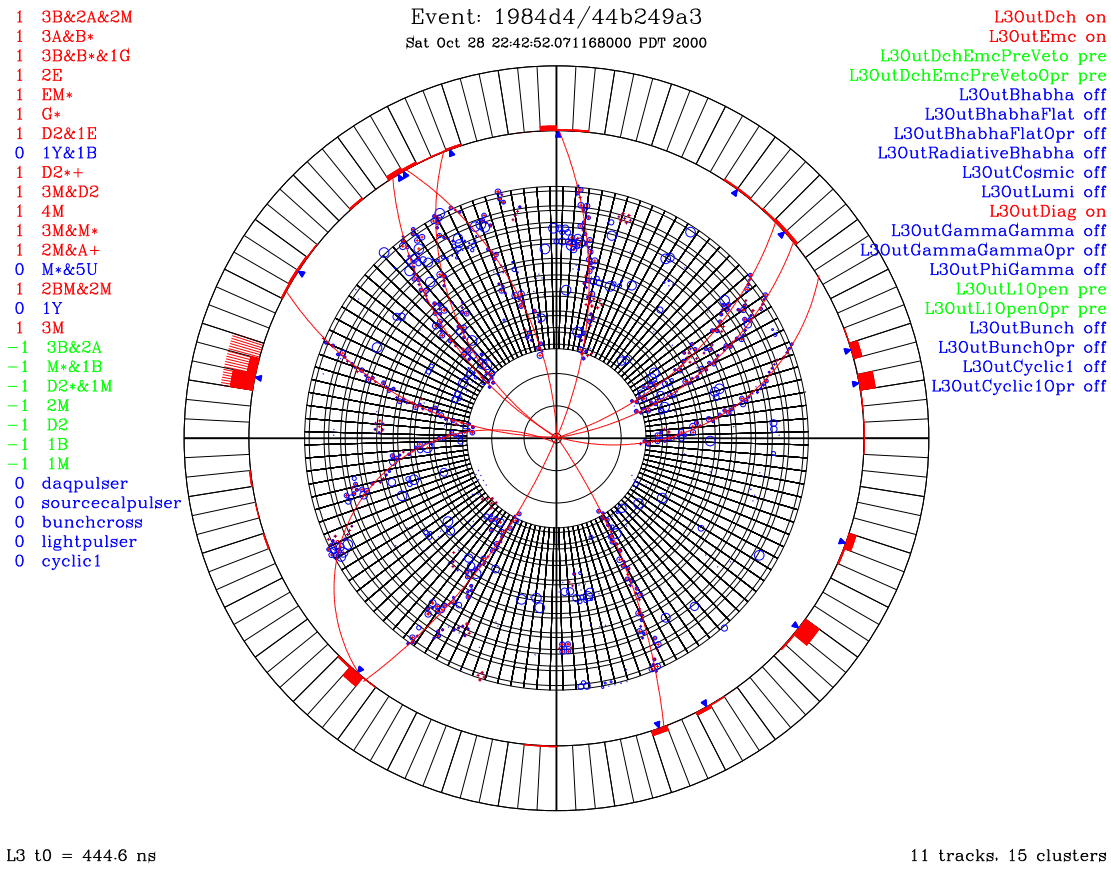

Figure 2.30: A level 3 trigger event display for a multihadron event.

in conjunction with the L1 trigger information to further reduce background events. An event display reconstruction from L3 trigger is shown in fig. 2.30. The level 3 DCH algorithm fits L1 tracks to helices and is able to determine the z_0 of tracks, which is important information for rejecting background. The dominant source of events accepted by level 1 is beam-gas or beam-wall interaction background, as well as cosmic rays, which can be separated from physics events using the point of closest approach of tracks to the interaction point(IP). L3 trigger also performs Bhabha veto, selection of various calibration events and critical general online monitoring tasks. The L3 operates on an online farm which consists of 28 Dell 1650 (dual Pentium-III 1.4 GHz) computers with fast algorithms processing at $\sim$4 ms per event. The L1 triggers are reduced by typically a factor of $\sim$ 10 after the L3 filtering, before logging to the data storage system.

2.11 Track Reconstruction

Complete reconstruction of B decays (in addition to other major *BABAR* analysis techniques, such as tagging) requires precise and efficient charged particle tracking. As will be seen later, separation of B decays from combinatoric background requires precise determination of mass and energy, which in turn requires precision measurement of track momentum. Data from the SVT and DCH is combined to satisfy the stringent charged particle tracking requirements of *BABAR*.

Charged tracks are parameterized by the 5 variables $d_0, \phi_0, \omega, z_0, \tan\lambda$ and their error matrix. The parameters are defined as: d_0 is the distance of the track to the z-axis at the track's point of closest approach to the z-axis, z_0 is the distance along the z-axis of that point to the origin, ϕ_0 is the azimuthal angle of the track at that point, λ is the dip angle with respect to the transverse plane, and ω is the curvature of the track and is proportional to $1/p_t$. After tracks are recognized by the pattern recognition algorithms, these 5 variables are fitted, and error matrices are extracted.

Offline track reconstruction begins with tracking and event time information from the L3 trigger. L3 trigger provides both tracks and an estimate of the time at which the interaction occurred (with a resolution of approximately 5 ns), referred to as the t_0.[5] Reconstruction continues by building track segments of 4 hits on four layers within a superlayer and using a linear fit to estimate and improve the L3 t_0 to a precision of about 3 ns. Next, the level 3 DCH tracks are refitted using the more precise offline time-to-distance calibration and placed on the list of reconstructed tracks. The t_0 value is refined further (to 3 ns resolution) by finding the best t_0 fit to the tracks themselves. Following that, two additional DCH track pattern recognition algorithms are run which select tracks with hits not used in L3 tracks. The t_0 is improved again (to < 2 ns resolution) using these extra tracks. The DCH tracks are then fit using a Kalman filter algorithm. DCH tracks are then extrapolated into the SVT via a hit-adding algorithm, and then two standalone SVT track pattern recognition algorithms add any remaining SVT tracks. Finally, SVT tracks are extrapolated into the DCH to pick up any remaining DCH hits. This sequence will be discussed in detail in the following subsections.

[5] The e^+e^- interaction time is referred to as the "bunch t_0," often shortened to "t_0."

2.11.1 t_0 Reconstruction

Reconstruction of the event interaction time, or t_0, is necessary for both fitting DCH tracks (since the DCH time-to-distance relation is necessary for position information of a track within a given cell, a time must be provided as input) and for rejecting out-of-time hits within the SVT to reduce background. t_0 reconstruction takes place in several steps, iterated with track pattern recognition since the two are interdependent, during offline reconstruction.

The initial measurement of the event time is provided by the L1 Trigger in hardware electronics. The L1 trigger looks for track segments in the DCH and clusters in the EMC, and sends an accept that includes all data in each subsystem's latency buffer to be read out. The trigger timing is tuned such that this buffer typically starts about 450 ns before the event, with a resolution of about 50 ns. That estimate, with an error of approximately 50 ns, forms the first event t_0 estimate. The L3 Trigger uses the level 1 DCH segments and a fast, rudimentary time-to-distance function to fit tracks. The fit produces an event time measurement that is accurate to approximately 5 ns. This estimate is then given to offline reconstruction as input.

Offline t_0 reconstruction begins with the DCH segment-based t_0 finder. Four consecutive hits on adjacent layers within a superlayer form a DCH segment. A t_0 value is fit for each segment such that the corresponding isochrone on each cell is tangent to a line segment passing through the superlayer. This requires a 3×3 matrix inversion corresponding to the two parameters of the line segment in addition to the t_0. The event t_0 estimate must then be obtained by combining these fitted segment t_0s. There are several different segment cell patterns corresponding to different angles of the track through the superlayer, and segments are weighted according to type (highly-angled segments give lower-quality information than radial ones, since they tend to be from lower-momentum tracks). The segment t_0's are sorted according to time and the weighted average is taken of the middle third of this list. Using only the middle third provides robustness against out-of-time background segments. The weighted average segment t_0 is used as input to the Level 3 track converter, which then outputs a list of tracks to the event.

The tracks are then used to provide a more precise estimate of the t_0 using the DCH track-based t_0 finder. The DCH track-based t_0 finder takes a list of tracks as input and finds the best fit t_0 from the list of tracks. For each track, an average of the time residuals from each hit, weighted by the error on the residual taken from the time-

to-distance resolution function, is calculated. This average is then added to the prior t_0 estimate in order to obtain the best-fit t_0 from that track, along with its associated error. The weighted average of these track t_0s is then taken, with the track t_0 with the largest χ^2 from the initial average dropped from the final average (for robustness against the occasional background track). This forms the track-based event t_0.

The track-based t_0 is calculated once after both the offline L3 track converter and the first DCH pattern recognition algorithm have run, and again after the two additional DCH pattern recognition algorithms have run. The final DCH t_0 is used for all final track fits and is provided to the DRC for background rejection, after which the DRC is able to refine the t_0 further.

2.11.2 Track fitting

BABAR tracks would be exact helices if not for 3 effects: multiple scattering, energy loss in material, and inhomogeneities in the magnetic field. Although these effects are fairly small in *BABAR* due to the small amount of material in the tracking volume and the $< 5\%$ inhomogeneities in the field, they nevertheless are important for the level of precision needed for accurate Δz and vertex fit quality. Thus a Kalman filter is used to propagate tracks accounting for each of those three effects and create a piecewise helix trajectory. For initial fits (and for input to the Kalman algorithm), a simple helix fit will suffice. Track fitting is done using both helix fits (for initial fitting) and a piecewise-helix Kalman fit algorithm (for the final fit). The DCH and SVT standalone track fitters (and DCH-specific hit-adder) use a helix fit for the initial fit which is replaced by a Kalman fit later in reconstruction, whereas the DCH $\rightarrow$ SVT and SVT $\rightarrow$ DCH hit-adders are integrated with the Kalman fitter to perform a piecewise helix fit as the hits are added.

The helix fit algorithm performs a least-squares fit to a list of hits. It assumes the weight matrix is diagonal, *i. e.* that the hits are uncorrelated. The fit iterates and removes the hit with largest "pull" (residual divided by error) on each iteration if it lies more than 3 sigma from the fit. Removed hits which return to within 3 sigma after an iteration are added back. Convergence occurs either when the change in total χ^2 is less than 0.01 or if the fit reaches 12 iterations. If the latter occurs before the former, it is considered a failed fit.

The Kalman fit takes into account the effects of material and inhomogeneous magnetic field to create a piecewise helix fit. The parameters of a track can be transformed

into "weight space" where:

$$\gamma \equiv C^{-1}, \quad \beta \equiv \gamma P \tag{2.16}$$

where P is the vector of 5 track parameters (taken as input from a preliminary helix fit) and C is the corresponding covariance matrix. The effect of adding a hit on these parameters is:

$$\gamma_H \equiv L^T w^2 L, \quad \beta_H \equiv L^T w(LR - r) \tag{2.17}$$

where r is the residual of the hit, R is the hit's position, and $L \equiv \frac{\delta r}{\delta P}|_R$. These act as additive corrections to the weights:

$$\gamma_{new} = \gamma_{old} + \gamma_H, \quad \beta_{new} = \beta_{old} + \beta_H \tag{2.18}$$

These are the Kalman filter equations.

Performing the fit in weight space also allows for simple equations describing magnetic field inhomogeneities, energy loss, and multiple scattering. The materials and magnetic field map are kept in the *BABAR* conditions database (the database used for storage of detector calibration constants) allowing for their use directly in the fit. Both an inwards and an outwards fit are done, with the final weights β and γ being the sum of the inner and outer fits (this is referred to as "smoothing"). A resolution of $\sigma(p_t)/p_t = 0.13\% \times p_t + 0.45\%$ is obtained.

Chapter 3

BABAR Software

3.1 Introduction

In this chapter we will present *BABAR* framework and software tools used during this thesis work. This section includes a presentation of the simulation and the reconstruction programs used in *BABAR* collaboration.

The *BABAR* software system includes two parts: *online* system (data acquisition, checking and monitoring) and *offline* system (reconstruction, simulation and data analysis). It is implemented on PC with commercial Unix operative systems (SunOS e OSF/1) and Linux.

3.2 Programming choices

The software used in the *BABAR* experiment is developed using *Object Oriented* programming [70] implemented on Unix machines.

There is a big choice of object oriented programming languages; among all possibilities, the *BABAR* collaboration has chosen the C++ [71] for its specific demands, like large availability for compilers, distributed with free open-source licenses, compatibility with different platforms, efficiency of the code and tools for development and debugging, and large availability of libraries.

3.2.1 Object oriented programming

The main feature of object oriented coding can be simplified through an analogy with real world: utilization of an object is not linked to knowledge, for an user, of its internal operation. For example, to drive a car we could not know how engine is and how it works, but this (substantial) difference doesn't influence our driving. This is an example of separation between *what* an object offers in functionality terms and *how* it realizes this functionality; the way to interface with an user should be constant in the time, but system can be modified, expanded and optimized. This feature is fundamental in complex software system codes, as what used in *BABAR*.

In C++, the tool that allows us to use object oriented programming is the *class*, data type defined by programmer; it is composed by a public interface that gives us functions to operate on contained data, and a hidden, private, structure that typically includes both internal representation of data and utility functions to operate on themselves. This way to hide the effective implementation is called *encapsulation* and it's typical for object oriented programming. So, classes can be thought as boxes that speak each other with messages: we can operate on data for a class (that is most the interesting thing for an user) only through some function in public interface; these functions are called *methods*. Such a way to operate can give us some advantages because we can shield data from illegal operations and verify finished operations (*e. g.*, verification on variation interval of a quantity, as in data input stage). Furthermore, it allows a re-utilization of the code (*e. g.*, a set of classes to operate on vectors and matrices with usual addition and product operations) and it reduces the development and software debugging times.

Another object oriented feature is *objects hierarchy*, which we can illustrate with a real world example: it's possible to define some abstract data types with certain very general properties; in fact we are able to think to abstract objects, like a particle, and to derive from these ones other objects with more definite properties, "boson or fermion?". Continuing in this hierarchy, we can specify more detailed properties, "if fermion: lepton or quark?" and reach up for more internal levels maintaining general class properties, leaving them as before or modifying parts of them. This feature is called *heredity* and we can have single heredity (if it is derived by only one more general class) or multiple heredity (if derived by more classes).

The third concept of object oriented language is the *polymorphism*, which is strictly linked to heredity. It is the language ability to use some specific objects (derived by

more generic classes) as generic class objects. For example, it would be possible to have a list with all particles with a fixed momentum, independently if they are bosons or leptons, and to use them in a uniform way (for a fixed particles class definition). This propriety is typical of the containers, like lists of objects.

3.3 Code Organization

The *BABAR* software is accessible to all registered users through NFS system file (*Networked File System*) or AFS (*Andrew File System*), mounted on every UNIX workstation at SLAC. The scheme is replied in all calculus labs in the countries that collaborate to the experiment: USA, France, England, Italy and Germany.

3.3.1 *BABAR* Framework

The *BABAR* software is organized like a framework for the reconstruction of events recorded by the detector. To figure out what programming inside a framework means, it's possible to compare it with reality: in every home we find water, electricity, telephones, etc. and these services are supplied without worrying about how they are realized. The full set of the services is the framework.

In software engineering, a framework supplies base services, like I/O, graphic management, data scheme management. The obvious advantage is: low-level function problems have already been solved and generally in a very efficient way with few faults. So, the user can only work in his specific domain; in this way, it is favored a re-use of the code (a well written code can be re-used to solve similar problems even if not identical).

3.3.2 Package

The *BABAR* framework is completely modular, and his base element is the *package*, defined as a set of classes planned to solve certain exact problems very close among them (for example a selectors package, where his classes are planned to assign a specific identity to a candidate particle). In every package we can find classes with same tasks, that differ for chosen approach or chosen operative technique.

Many dozens of packages are available, to cover a large spectrum of possibilities and requests coming from events reconstruction and analysis.

3.3.3 Release

We define *release* the set of all packages, each defined in his specific version. If packages are updated with new classes, releases are updated with new packages. Particularly, we can distinguish releases in two kinds: testing releases for code implementation and testing and stable releases used for official analyses.

3.3.4 Module

The *BABAR* framework base unity is defined as *module* and it can be either a class of a package or an user defined class based on other package classes. The modules hold code that draws data for every event, runs specific algorithms and it can eventually give back results that can be used in next phases.

An executable analysis program is formed by one or more compiled and linked modules; each of them can be enabled or disabled during execution if it is useful or not in data processing. Framework functionality management is left to TCL (*Tool Command Language*) language that has two features: it can interpret commands, so it can be an interface among user and framework, and it can be used as a scripting language to check exactly the operations for every module, in a similar way with a Unix shell. It can be used on many platforms.

Modules can be added in a *sequence* in which they are executed in apparition order. Modules and sequences can be combined in a *path*, a completed sequence which begins with an input module and ends with an output module. The presence of particular filter modules can allow that a path will be finished before exiting and so a processed event won't reach output module. Multiple paths can be specified and each of them can be enabled or disabled.

3.4 Online System

The *BABAR* Online software comprehends detector check and monitoring systems, processes related to data flow, from front-end electronics to storaging in database, and the run checking programs. These tasks are solved by main Online system components: *Data Flow*, *Run Control*, *Online Event Processing* (OEP) and *Prompt Reconstruction*. There is another component, *Detector Control*, but it is not joined to events acquisition: it checks software and hardware detector components (*e. g.*, for example DCH

high tension system).

3.4.1 Online Data Flow (ODF)

The data acquisition system is composed by a software and a hardware component; the former is called *Data Flow*, the latter is called *Platform*. Often, we refer to both as *BABAR Data Flow*.

Data Flow has the task of joining all data coming from front-end electronics, processing them in a preliminary way (so called *feature-extraction*) and delivering them to OEP.

Main Platform elements are: checking masters that give the trigger interface, the distribute clock, and the command system; the read-out modules (ROM); particular modules that catch data from front-end electronics and execute feature-extraction; and the *bulk data fabric* which transports data inside-outside the platform. Every platform needs a clock and an external trigger system; it has 32 input lines for the trigger that produce level 1 trigger acceptance signal (L1 accept). Then this signal is propagated to all the platforms. A platform can manage electronics for more than one sub-detector. In this way, the sub-detectors can't be independent if they are on a same platform, unless they are on different platforms. To maximize resources, such platforms are *partitioned*: in this way operations related to different sub-detectors are done in parallel. Data Flow platform has been drawn considering rigorous conditions due to experiment for dimensions and events frequency. Components are organized in a hierarchy that permits to execute operations with a high-grade of parallelism.

3.4.2 Online Event Processing (OEP)

OEP receives completed events from Data Flow's Event Builder, executes level 3 trigger algorithms, checks data quality through so called *Fast Monitoring* processes and develops other tasks as supporting functions to calibration activities. Furthermore, OEP provides avaliable events for the reconstruction to *Prompt Reconstruction*.

Work done by OEP is distributed among knots of a farm composed by Unix machines. On every machine are solved identical processes in parallel.

3.4.3 Prompt Reconstruction

The tasks of Prompt Reconstruction are to reconstruct, in short time, all events that passed level 3 trigger filter and to furnish calibration constraints and informations on data quality. This allows us to diagnose immediately detector problems in such a way that they can be solved without losing integrated luminosity. In particular, this function has been important in the preliminary phases of the experiment. Many calibration constraints, like pedestals and electronics component gain, are evaluated through special runs. Others, like DCH time-distance relationship and relative corrections of alignment between chamber and vertex detector, need a large number of reconstructed events. Prompt Reconstruction receives these quantities from a previous (but recent) calibration, stored in the dataset, and applies them to current data. Generated constraints per every reconstructed events block are storage in the Condition Database to be read again during the following reconstruction block.

The Prompt Reconstruction results are monitored by *Prompt Monitoring* that checks, for example, DCH performances, data quality, and reconstruction and calibration algorithms of reconstruction. Unlike Fast Monitoring, Prompt Monitoring analyzes reconstructed events and has a large number of informations on tracks.

3.5 Monte Carlo Simulation

Completed simulation of the detector is formed by three parts: events generation, particles tracing through the detector, and detector reply simulation.

3.5.1 Generators

Simulation process starts with event generation, using one of the available different generators: generator of $B\overline{B}$ events with the corresponding decay channels; $q\bar{q}$, with $q = u, d, s, c$, background events; e^+e^- diffusion events; and other backgrounds linked with accelerator operation. Furthermore, energies of beams and the interaction point position smearing are simulated. For each beam is used a Gaussian with width 5.5 MeV for the high energy beam, and 3.1 MeV for the low energy beam. Smearing for interaction point is in the x and y coordinates of 160 μm and 6 μm, respectively, and it is simulated with a Gaussian for each coordinate. The z beam position is modelled on a flat distribution 1 cm long.

Most important events generator for $B\overline{B}$ is EvtGen. This generator furnishes a scheme in which specific decay channels can be implemented as modules. Such modules, called EvtGen *patterns*, can solve different functions, *e. g.* they can evaluate decay amplitudes. EvtGen introduces the $B - \overline{B}$ mixing, generating $\Upsilon(4S)$ decays in a user defined proportion of $B^0\overline{B}^0$, $\overline{B}^0\overline{B}^0$ and B^0B^0 final states with correct Δt distributions. The CP asymmetries are generated with modules which modify the B mesons lifetime distributions.

There are available generic patterns to simulate two-body decays to combinations of scalar, vector and tensor mesons. There are also generic patterns to simulate three-body decays or radiative decays. Decay features (branching ratio, numbers of sons and patterns) are inserted in an ASCII file called `DECAY.DEC`.

Generator manages only exclusive final states; for quarks to hadrons fragmentation we use Jetset7.4, which is used for $q\bar{q}$ background generation and weak baryons decays. Jetset7.4 decay table has been updated to latest measurements.

3.5.2 BOGUS

BOGUS simulator (*Babar Object-oriented Geant4-based Unified Simulation*), using Geant4 [72] package developed by CERN, provides an unified simulation, since it permits either a complete simulation or a faster simulation.

Geant4 includes tools to simulate detector geometry, charged and neutral tracks revelation through the detector, interactions and decays of every kind of particle, magnetic field and detector reply.

BOGUS is composed by several packages, one for each subdetector. In each of them are contained standard routines recalled in different simulation phases. Geometries of each subdetector are re-created starting from parameters hold in a format ASCII data bank, in which they are specified materials, dimensions, positions, and orientations for every enabled and disabled subdetector.

Monte Carlo tracks hits are called in the *BABAR* terminology *GHits*. These contain all needed informations to obtain detector reply simulation in a second phase. Monte Carlo truth informations and *GHits* are stored for next analyses.

3.5.3 Detector reply

Tracks hits digitalization happens in another process called *SimApp*. This process takes *GHit* input information and produces digitalized data as output in the same format of those producted by real detector. At the end of such a process, Monte Carlo data are processed by same code of real data. This code is organized like a subsystems packages set. These packages contain routines to give simulated data sample as most similar as data coming from detector. Another function of SimApp packages code is to add background hits: rather than simulate background in the detector, it is preferred to catch a random trigger sample and mix (using correct luminosity factors) them with Monte Carlo simulated events.

3.6 *BABAR* Database

The original *BABAR* Event Store used two data-storage formats: *Objectivity* database and *Kanga* (“Kind ANd Gentler Analysis”) datasets. In a second stage, *BABAR*’s data storage has changed to a completely new system. The new model is called *CM2* (“Computing Model 2”).

The Objectivity database was a large object-oriented database with several levels of detail stored for each event. It could be used for almost any analysis or detector study. The Objectivity database had four levels of detail: *raw*, *reco*, *micro* and *nano* (or "tag"). *Raw* and *reco* were very big databases that kept virtually all of the details for every event. The original idea was to keep *raw* and *reco* informations for jobs like detector studies. They were infrequently used, and only a small part of the information was ever accessed. *Micro* was a smaller and more user-friendly database, where the informations were more useful for physics analyses, rather than detector studies, or more refined analysis tasks. *Nano* ("tag") contained even less details, and was used only to skim data for few given key characteristics to save loading time of the whole event information for each event (a time-consuming process).

The Kanga datasets stored only the micro level information in ROOT-type files (architecture for object oriented data analysis developed by CERN) [73]. This is the level of detail required for most physics analysis jobs, avoiding the complication of interacting with the full Objectivity database.

The idea was to have Objectivity as the main database, and use Kanga files at remote sites.

The new CM2 Event Store has just one database, the *Mini*. The *Mini* database is basically an extended version of the *micro*, however with the additional capability to store information written into "skims" by users (“user data”), *i. e.* user-defined composite candidate lists and user-calculated quantities. The *Mini* contains all of the informations from the old *Micro* database, plus a small part of *Raw* and *Reco*.

The new data storage format is more like *Kanga* than anything else, so we may refer to the CM2 Mini database as "CM2 Kanga," "new Kanga" or (since old-kanga is obsolete) just "Kanga". In the tab. 3.1 we summarize the differences between the old Objectivity/Kanga system and the new CM2/Mini system.

	Old Objectivity/Kanga	**New CM2/Mini/Kanga**
Level of detail	Objectivity: high detail Old Kanga: low detail	Mini: intermediate detail
Portability	Objectivity: central Old Kanga: portable	Mini: central, but easily skimmed to make portable collections
User data	Objectivity: None (central database) Old Kanga: Lots (small, user-defined collections)	Mini: some user data in central database

Table 3.1: Differences between the old system database and CM2.

3.7 Reconstruction Software

We already gave prominence to packages as base element of *BABAR* software; in the following sections we will describe the main *packages* used for analyses presented in this thesis work.

3.7.1 `Beta` package

`Beta` is a data analysis program developed for *BABAR*, and it is the base interface for data reconstruction. `Beta` main task is to furnish a solid and simple basement to write detailed physical analysis programs; to do that it gives the needed tools for particles identification, B flavor tagging, vertexes reconstruction, etc.

All the `Beta` structure, and so the reconstruction mechanism, is based on four fundamental concepts:

- *Candidate*. A candidate is the representation that `Beta` gives to the particle that could be existed in the considered event. There are many kinds of candidates, like charged tracks, reconstructed by SVT and DCH, which can be, for example, pions or kaons, or calorimeter neutral clusters, which can be photons. The important thing is that all candidates have same interface (they are `BtaCandidate` objects) and they can be used in a general way.

- *Operator*. An operator acts on one or more candidates, combining them in new candidates (for example, defining a mother particle by two charged tracks) or extracting informations as mass, energy, charge etc. by them.

- *Selector*. A selector is a particular structure that creates candidates with certain features starting by avaliable candidates lists. For example a selector for π^0 selection can seek, in a list of photons, pairs of photons with invariant mass close to nominal π^0 mass and combine them with a right operator in π^0 candidates. Selectors can be generic or destined to a specific physical analysis, and they can be used in different analyses (for different decay channels) without modifying anything.

- *Combiner*. It creates an agreement between two candidates. For example, reconstructed candidates can be combined to respective Monte Carlo generated candidates.

For every *BABAR* event, reconstructed `BtaCandidate` objects are gathered in lists. Each list has a different identity hypothesis and different selection criteria. In tab. 3.2 are listed some default lists avaliable in the Micro database level.

3.7.2 `CompositionTools` and `SimpleComposition` packages

These packages contain functions for the creation of `BtaCandidate` lists that describe a fixed decay reaction, for example $\pi^0 \rightarrow \gamma\gamma$, starting by `BtaCandidate` existing lists.

Candidates obtained are tree-like decay. For these trees we can impose kinetical and geometrical constraints and cuts, like masses, energies, momenta, and composite candidate reconstruction probability cuts. So, composite candidates are decay trees that combine tracks, neutral clusters, PID and fitting. In this way, using all the infor-

Name of the list	Description
`ChargedTracks`	Candidates with charge not equal to zero. Pion mass hypothesis is assigned.
`CalorNeutral`	Candidates are single bumps not associated to any tracks. Photon mass hypothesis is assigned.
`CalorClusterNeutral`	Candidates that correspond to multi-bump neutral or single bumps not associated to any cluster related to a track.
`NeutralHad`	Candidates that correspond neutral clusters in hadronic calorimeter not associated to any tracks.
`GoodTracksVeryLoose`	`ChargedTracks` list candidate with: • Min Transverse Momentum: 0.0 GeV • Max Momentum: 10 GeV • DCH min # hit: 0 • Max DOCA in xy plane: 1.5 cm • Min z DOCA: -10 cm • Max z DOCA: 10 cm
`GoodTracksLoose`	Same cuts as `GoodTracksVeryLoose` with: • Min momentum: 0.1 GeV • DCH min # hit: 12
`GoodPhotonLoose`	`CalorNeutral` list candidate with: • Min energy: 0.030 GeV • Min # of crystals: 0 • Max "lateral momentum": 0.8 Gev

Table 3.2: Main avaliable lists in Micro database.

mations given by detector, `CompositionTools` and `SimpleComposition` are the packages for the reconstruction of every kind of composite particle.

Chapter 4

Events Reconstruction

4.1 Introduction

The neutral B modes studied in this thesis work are reconstructed in the final states ηK^0_S, $\eta\phi$, $\eta\eta$, $\eta K^0_S\gamma$, $\eta' K^0_S$, $\eta' K^0_L$, $\eta'\phi$, $\eta' K^0_S\gamma$, and $\eta'\eta' K^0_S$. For the charged B modes, we consider the final states $\eta K^\pm\gamma$, $\eta' K^\pm$, $\eta' K^\pm\gamma$, and $\eta'\eta' K^\pm$. Then, the B daughter resonances are reconstructed in:

- $\eta \to \gamma\gamma$ ($\eta_{\gamma\gamma}$), $\eta \to \pi^+\pi^-\pi^0$ ($\eta_{3\pi}$);
- $\pi^0 \to \gamma\gamma$;
- $K^0_S \to \pi^+\pi^-$ (K^0_{S+-}), $K^0_S \to \pi^0\pi^0$ (K^0_{S00});
- $\phi \to K^+K^-$;
- $\eta' \to \rho^0\gamma$ ($\eta'_{\rho\gamma}$), $\eta' \to \eta\pi^+\pi^-$ ($\eta'_{\eta\pi\pi}$);
- $\rho^0 \to \pi^+\pi^-$.

The K^0_L meson candidates are identified either as an unassociated cluster of energy in the EMC or as a cluster of hits in the IFR. We use the informations from the tracking system, the EMC and the DIRC to identify charged pions and kaons in the final state. The photon candidates are identified in the EMC.

In this chapter we will describe the methods used to identify particles inside *BABAR* and to verify the detector reply. After that, we will describe the resonances and B mesons reconstruction.

4.2 Particles Reconstruction and Identification

The charged tracks reconstruction is described in section 2.11. Once that the tracks are reconstructed, their identification is realized using particular selectors. They take all informations for each track and give the probability that a track is a specific kind of particle. The informations are combined using a likelihood technique. We have selectors for kaons, pions, electrons, muons, and protons identification. Each selector has different levels for the identification: very tight, tight, loose, and very loose, respectively to have from high probability to low probability of identification. It is possible to use the selectors as veto for the charged tracks selection, *e. g.* we want select pions among the reconstructed charged tracks and for this reason we apply veto for kaons, protons, electrons, and muons using their respective selectors. In our analysis described in this thesis work we do not use the muon selector.

It is important to note that the selectors for the charged tracks are verified using specific data sample, so called control sample, with high signal purity and statistics. In general a control sample is used for several goals:

- study of the reply for the subdetectors,
- evaluate the performance of the algorithms for the particles identifications,
- estimate systematic uncertainties.

Pure samples of a particle are selected using only kinematical informations. For example, a pure pions sample is selected using $K^0_S \to \pi^+\pi^-$ decay channel and applying tighter cuts on several variables as: angle between K^0_S candidate direction and the directions of his daughters, the distance of the vertex from interaction point and the mass of reconstructed K^0_S candidate. Invariant mass distribution of $\pi^-\pi^+$ pairs is shown in the fig. 4.1: purity of the sample is greater than 99%.

For K mesons data sample with a very high purity, we can use selected tracks coming from the decay chain $D^{*+} \to \pi^+ D^0$, $D^0 \to \pi^+ K^-$ and its charge conjugation. In the fig. 4.2 we show the distribution of the mass difference between $K\pi\pi$ and $K\pi$, $0.139 < \Delta M < 0.162$ GeV/c^2. With a tight cut on this variable, the combinatorial background is equal to 13% for a kaons sample with 90% of purity.

For the electrons identification, they are separated from charged hadrons through energy, lateral momentum of the shower and tracks momentum. To obtain a better precision, we have to check that energy loss $\mathrm{d}E/\mathrm{d}x$ in DCH and the Cherenkov angle of

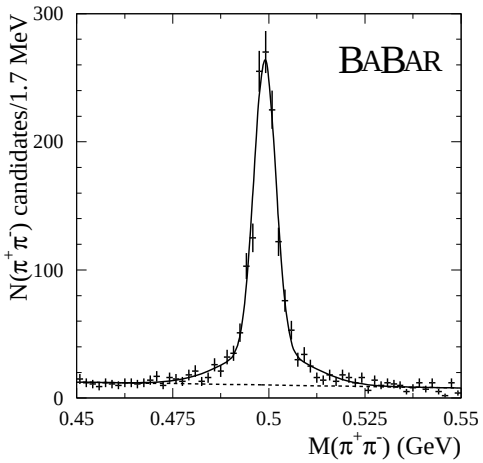

Figure 4.1: Mass distribution for K^0_S candidates used to select pions control sample.

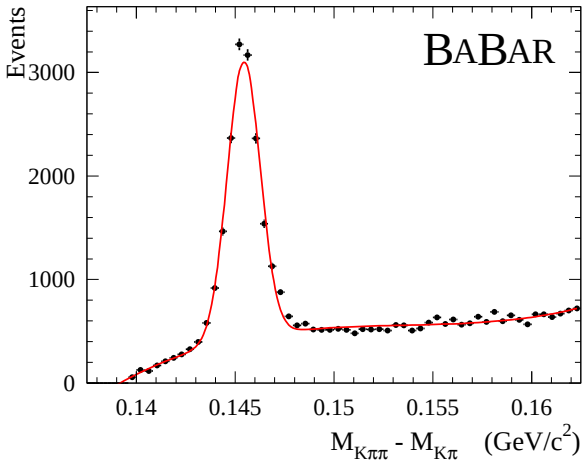

Figure 4.2: Distribution of mass difference for D^* and D^0 candidates, used to select kaons control samples.

DIRC are consistent with electron hypothesis. One of the most important variables for hadrons discrimination is the ratio between the energy left in the calorimeter and track momentum (E/p). Figure 4.3 shows efficiency for the electrons identification and probability of a misidentification of pions; both of them are function of the momentum and the polar angle, measured in the lab frame. Efficiency for electrons identification has been studied using electrons coming from radiative Bhabha and events $\gamma\gamma \rightarrow 4e$. Probability of misidentification of pions is measured using τ three body decays and charged pions coming from K_S^0 decay. Selection tight criteria has an average efficiency of 94.8% in the momentum interval $0.5 < p < 2$ GeV/c while probability of misidentification of $\sim 0.3\%$. With very tight criteria, the efficiency is 88.1% with an average uncorrected pions identification of 0.15%.

Leaving the charged particles, we describe now the photons identification. Usually an EMC electro-magnetic shower is distributed on many adjacent crystals forming a *cluster* of a certain left energy. We can distinguish two kinds: single *cluster* with a single energy maximum and *merged cluster* where we have more local energy maxima, called *bumps*. The reconstruction and the identification algorithm has been developed in a way to identify efficiently the *clusters*, distinguish them from *bumps* and determine if they are generated by a neutral or charged track. A *cluster* has at least one crystal with energy greater than 10 MeV and the adjacent crystals are considered part of a *cluster* if their energy exceeds the 1 MeV threshold. To establish the local energy maxima inside a *cluster* it's requested that candidate crystal would have an energy, $E_{LocalMax}$, greater than every adjacent crystal. Furthermore it must be verified the following condition: $0.5(N - 2.5) > \frac{E_{NMax}}{E_{LocalMax}}$ where E_{NMax} is the maximum energy for N adjacent crystals with energy greater than 2 MeV. All the clusters are divided in many *bumps* in the same number of local maxima. The energy for every crystal is associated with each *bump* with a simultaneous adjustment, starting from the shape of electro-magnetic shower, the centers and energies of the *bumps*. Then all the reconstructed charged tracks in the tracking volume are extrapolated until the EMC entrance and for every track-bump pairs is evaluated the association probability. All the *bumps* with a low probability are considered photons candidates. A little percentage of these candidates is rejected if the shape is not compatible with the one expected for an electro-magnetic shower. To check the photons reconstruction, we consider the reconstruction of the control samples with $\pi^0 \rightarrow \gamma\gamma$ and $\eta \rightarrow \gamma\gamma$. We assume as their origin the primary interaction point. The spectrum of the invariant mass for the $\gamma\gamma$ pairs is

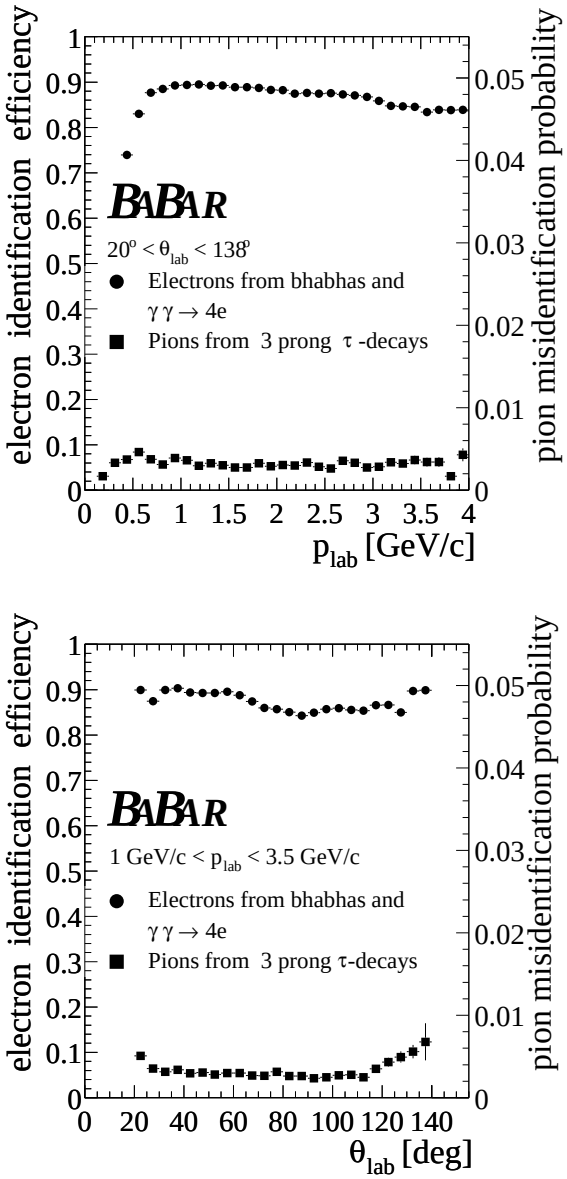

Figure 4.3: Efficiency of the electrons identification and probability of a incorrect pions identification vs momentum (top) and polar angle (bottom).

shown in fig. 4.4 for different E_γ and $E_{\gamma\gamma}$ ranges; it's possible to distinguish peaks for π^0 and η. The mass resolution for π^0 is 6.9 MeV in the multi-hadronic events while 6.5 MeV for $\tau\tau$ events. The detector segmentation and the spatial resolution allow to reconstruct π^0 with the EMC photons separation until 5 cm without a significative worsening in the mass resolution. The little fraction of high energy π^0 in which we cannot separate the photons, about 10% in the 4-6 GeV region, are distinguished through single photons with the help of the cluster shape.

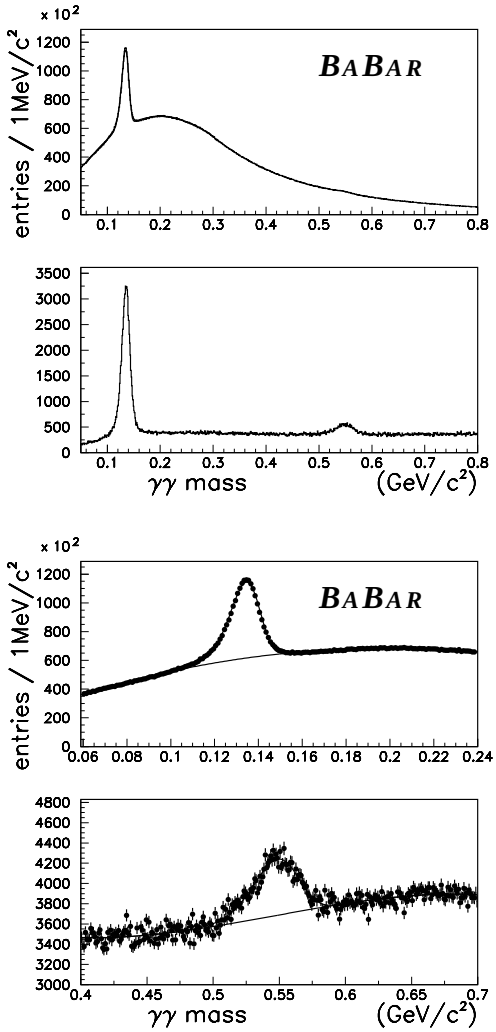

Figure 4.4: Mass spectrum for $\gamma\gamma$ pairs in the hadronic events in the π^0 and η regions. $E_\gamma > 30\,\mathrm{MeV}$, $E_{\gamma\gamma} > 300\,\mathrm{MeV}$ (top), $E_\gamma > 100\,\mathrm{MeV}$, $E_{\gamma\gamma} > 1\,\mathrm{GeV}$(bottom).

4.3 Daughter Particles Reconstruction

Charged tracks and electromagnetic showers identified by the detector are organized in lists, as shown in tab. 3.2. The elements from these lists are combined to form particle candidates using tools from the `CompositionTools` and `SimpleComposition` packages (see section 3.7.2 for a description of these packages). The reconstruction is the same for both MC and data samples.

The cuts described in the following sections 4.3.1 – 4.3.10 are done at reconstruction level (so called preliminary cuts). Tighter cuts are applied later during the events selection, described in the chapter 6.

4.3.1 π^0

Two photons taken from the `GoodPhotonLoose` list are combined to form a π^0 candidate, kinematically fitted to the true pion mass [36], using the standard tool from `CompositionTools`. We make a cut on unfitted mass between 0.10 and 0.16 GeV/c^2.

4.3.2 ρ^0

The ρ^0 mesons have been reconstructed using the `SimpleComposition` tools. As input list we used `GoodTracksVeryLoose`, expected for $B^0 \to \eta'_{\rho\gamma}\phi$ and $B \to \eta'_{\rho\gamma}K\gamma$ modes where we use `GoodTracksLoose`, with all the charged particles considered as pions. ρ^0 candidate mass was required to be between 0.4 and 1.1 GeV/c^2 around nominal value.

4.3.3 ϕ

The ϕ meson has been reconstructed in $\phi \to K^+K^-$ decay channel by using the `SimpleComposition` tools. As input list we have `GoodTracksLoose` with all the charged particles considered as kaons. We made a cut on mass between 0.99 and 1.05 GeV/c^2.

4.3.4 $\eta_{\gamma\gamma}$

The η mesons have been reconstructed in $\eta \rightarrow \gamma\gamma$ decay channel by using the `CompositionTools` tools. Input list is the `GoodPhotonLoose` for the two photons. The $\eta_{\gamma\gamma}$ mass is kinematically fitted to the true η mass [36], and the unfitted mass is cut between 0.470 and 0.620 GeV/c^2.

4.3.5 $\eta_{3\pi}$

The η mesons have been reconstructed in $\eta \rightarrow \pi^+\pi^-\pi^0$ decay channel by using the `CompositionTools` tools. Input list for charged tracks is the `GoodTracksLoose` list with all the charged particles considered as pions. The $\eta_{3\pi}$ mass is kinematically fitted to the true η mass [36], and the unfitted mass is cut between 0.470 and 0.620 GeV/c^2.

4.3.6 $\eta'_{\rho\gamma}$

The η' mesons have been reconstructed in $\eta' \rightarrow \rho^0\gamma$ decay channel by using the `SimpleComposition` tools. The photons have been taken from `GoodPhotonLoose` list. The $\eta'_{\rho\gamma}$ mass is kinematically fitted to the true η' mass [36], and the unfitted mass is cut between 0.900 and 1.010 GeV/c^2.

4.3.7 $\eta'_{\eta\pi\pi}$

The η' mesons have been reconstructed in $\eta' \rightarrow \eta\pi^+\pi^-$ decay channel with $\eta_{\gamma\gamma}$ or $\eta_{3\pi}$ by using the `SimpleComposition` tools. Input list for charged tracks is the `GoodTracksLoose` list with all the charged particles considered as pions. The $\eta'_{\rho\gamma}$ mass is kinematically fitted to the true η' mass [36], and the unfitted mass is cut between 0.900 and 1.010 GeV/c^2.

4.3.8 K^0_L

The K^0_L selection is similar to what done in the other *BABAR* analyses with K^0_L meson, like $B^0 \rightarrow J/\psi K^0_L$ [74] and $B^0 \rightarrow \phi K^0_L$ [75]. We indentify a K^0_L candidate either as a cluster of energy deposited in the EMC or as a cluster of hits in two or more layers of the IFR that cannot be associated with any charged track in the event. We use the

`CalorClusterNeutral` list and `NeutralHad` list for EMC and IFR reconstruction, respectively, as input lists to `CompositionTools` tools. About 60% of the K_L^0 is detected in the EMC while 40% is detected in the IFR.

We cannot measure the magnitude of K_L^0 meson momentum ($|\mathbf{p}_{K_L^0}|$) with the detector. Following the same procedure used in $B^0 \to J/\psi\, K_L^0$ analysis [74], we measure the direction of K_L^0 momentum, taken from the η' vertex to the centroid of the EMC or IFR candidate, then from the η' four-momentum and fixing the mass of B candidates and K_L^0 candidates to PDG values [36], we can extract $\mathbf{p}_{K_L^0}$. We obtain two solutions, but we take the greatest one (in general only one solution is positive).

K_L^0 selection from EMC

The selection in the EMC is performed according to the following requirements:

- The centroid of the cluster has $\cos\theta < 0.935$, where θ is the polar angle of the cluster center of gravity.
- The cluster energy is at least 200 MeV and smaller than 2 GeV.
- The `CalorClusterNeutral` list includes candidates with a track-shower match probability of less than 1%.
- We require the K_L^0 not to form a $\gamma\gamma$ invariant mass between 100 MeV/c^2 and 150 MeV/c^2 together with another cluster, for events with at least 30 MeV of energy (the requirement is not applied if the Zernike moment $|Z_{20}|$ is less then 0.8).
- We reject two-bump clusters if the cluster energy is larger than 1 GeV and they are consistent with a merged π^0 (M(2 bumps)) $> 110\ \mathrm{MeV}/c^2$).

K_L^0 selection from IFR

The requirements for K_L^0 candidates from IFR are:

- At least two planar IFR layers.
- The cluster center of gravity (cog) must have $-0.75 < \cos\theta < 0.93$, where θ is the polar angle of the cog.

- For any track with a momentum larger than 0.75 GeV/c, the relative position between the cluster centroid in the IFR (θ_{K_L}, ϕ_{K_L}) and the position of the charged tracks in the EMC ($\theta_{track}, \phi_{track}$) must not satisfy $|\theta_{K_L} - \theta_{track}| < 350$ mrad; as well as $-750 < (\phi_{K_L} - \phi_{track}) < 300$ mrad for positively charged tracks and $-300 < (\phi_{K_L} - \phi_{track}) < 750$ mrad for negatively charged tracks.

4.3.9 K^0_{s+-}

The K^0_S mesons have been reconstructed in $K^0_S \to \pi^+\pi^-$ decay channel combining oppositely charged tracks from `ChargedTracks` list, with all the charged particles considered as pions, by using the `SimpleComposition` tools. We use `TreeFitter` algorithm to extract the decay vertex, with constraint of the K^0_S production point to the beamspot (see section 4.4 for a description of `TreeFitter` algorithm and beamspot constraint). We applied a cut of 0.45 – 0.55 GeV/c^2 on the mass of K^0_S.

4.3.10 K^0_{s00}

The K^0_S mesons have been reconstructed in $K^0_S \to \pi^0\pi^0$ decay channel combining two π^0 candidates by using the `CompositionTools` tools. We use `WalkFit` algorithm to extract the decay vertex, with constraint of the K^0_S production point to the beamspot. Essentially in a first step the decay vertex is chosen at the beamspot, so the angles between gammas are underestimated which leads to too low invariant masses for π^0. In this way we determine the momentum direction. After that the K^0_S decay vertex is fitted along this direction, requiring a π^0 mass constraint. We applied a cut of 0.34 – 0.61 GeV/c^2 on the mass of K^0_S.

4.4 B Candidates Reconstruction

B candidates have been formed combining their daughter candidates. In particular, in case of daughter resonances with reconstructed multiple decays, we consider the cases shown in tab. 4.1 and tab. 4.2 for neutral and charged B candidates, respectively. The primary photons in $\eta^{(\prime)}K\gamma$ modes are taken from the `GoodPhotonLoose` list, requiring a preliminary cut on their energy in CMS between 1.5 and 3.5 GeV. The charged primary kaons in the charged B candidates are taken from the `GoodTrackLoose` list.

We combine the B daughters and determine the B decays vertex using a particular algorithm, `TreeFitter`, which performs the vertex fit of the B candidates with a global decay chain fit based on a Kalman filter (see section 2.11.2 for a description of the Kalman filter). For this fit we apply geometrical and kinematical (on the momentum) constraints. We consider also a "beamspot" constraint, which forces the B to originate from the interaction point, taking the error in that point into account. The beamspot is calculated event by event and his errors are the size of the interaction point, which is about 10 μm in y, 200 μm in x and 8 mm in z. In the reconstruction of modes with K^0_L we use also a B mass constraint [36].

As additional preliminary cuts we apply a cut between 4.99 and 5.59 GeV on the energy of the B candidate in CMS frame and a cut on B mass between 4.7 and 5.7 GeV/c^2. Other cuts for the analysis will be described in detail in the chapter 6.

The variables of the reconstructed B candidates are saved in a ROOT file using a particular package, called `MiReco`, developed during this thesis work.

Main Decay	Daughter Resonances Sub-Decays	Labels
$B^0 \to \eta K^0_S$	$\eta_{\gamma\gamma}$, $\eta_{3\pi}$, K^0_{S+-}	$B^0 \to \eta_{\gamma\gamma} K^0_S$ $B^0 \to \eta_{3\pi} K^0_S$
$B^0 \to \eta\phi$	$\eta_{\gamma\gamma}$, $\eta_{3\pi}$	$B^0 \to \eta_{\gamma\gamma}\phi$ $B^0 \to \eta_{3\pi}\phi$
$B^0 \to \eta\eta$	$\eta_{\gamma\gamma}$, $\eta_{3\pi}$	$B^0 \to \eta_{\gamma\gamma}\eta_{\gamma\gamma}$ $B^0 \to \eta_{\gamma\gamma}\eta_{3\pi}$ $B^0 \to \eta_{3\pi}\eta_{3\pi}$
$B^0 \to \eta K^0_S\gamma$	$\eta_{\gamma\gamma}$, $\eta_{3\pi}$, K^0_{S+-}	$B^0 \to \eta_{\gamma\gamma} K^0_S\gamma$ $B^0 \to \eta_{3\pi} K^0_S\gamma$
$B^0 \to \eta' K^0_S$	$\eta_{\gamma\gamma}$, $\eta_{3\pi}$, $\eta'_{\rho\gamma}$, $\eta'_{\eta\pi\pi}$, K^0_{S+-}	$B^0 \to \eta'_{\rho\gamma} K^0_{S+-}$ $B^0 \to \eta'_{\eta(\gamma\gamma)\pi\pi} K^0_{S+-}$ $B^0 \to \eta'_{\eta(3\pi)\pi\pi} K^0_{S+-}$
	$\eta_{\gamma\gamma}$, $\eta'_{\rho\gamma}$, $\eta'_{\eta\pi\pi}$, K^0_{S00}	$B^0 \to \eta'_{\rho\gamma} K^0_{S00}$ $B^0 \to \eta'_{\eta\pi\pi} K^0_{S00}$
$B^0 \to \eta' K^0_L$	$\eta_{\gamma\gamma}$, $\eta'_{\eta\pi\pi}$	$B^0 \to \eta'_{\eta\pi\pi} K^0_L$
$B^0 \to \eta'\phi$	$\eta_{\gamma\gamma}$, $\eta'_{\eta\pi\pi}$, $\eta'_{\rho\gamma}$	$B^0 \to \eta'_{\eta\pi\pi}\phi$ $B^0 \to \eta'_{\rho\gamma}\phi$
$B^0 \to \eta' K^0_S\gamma$	$\eta_{\gamma\gamma}$, $\eta'_{\eta\pi\pi}$, $\eta'_{\rho\gamma}$, K^0_{S+-}	$B^0 \to \eta'_{\eta\pi\pi} K^0_S\gamma$ $B^0 \to \eta'_{\rho\gamma} K^0_S\gamma$
$B^0 \to \eta'\eta' K^0_S$	$\eta_{\gamma\gamma}$, $\eta'_{\eta\pi\pi}$, $\eta'_{\rho\gamma}$, K^0_{S+-}	$B^0 \to \eta'_{\eta\pi\pi}\eta'_{\eta\pi\pi} K^0_S$ $B^0 \to \eta'_{\eta\pi\pi}\eta'_{\rho\gamma} K^0_S$

Table 4.1: Neutral B decay modes and their subdecays studied in this thesis work. In the right column we show the labels used to indicate these modes, reconstructed in their specific subdecays, in the following chapters.

Main Decay	Daughter Resonances Sub-Decays	Labels
$B^{\pm} \to \eta K^{\pm}\gamma$	$\eta_{\gamma\gamma}$, $\eta_{3\pi}$	$B^{\pm} \to \eta_{\gamma\gamma} K^{\pm}\gamma$ $B^{\pm} \to \eta_{3\pi} K^{\pm}\gamma$
$B^{\pm} \to \eta' K^{\pm}$	$\eta_{\gamma\gamma}$, $\eta_{3\pi}$, $\eta'_{\eta\pi\pi}$, $\eta'_{\rho\gamma}$	$B^{\pm} \to \eta'_{\eta(\gamma\gamma)\pi\pi} K^{\pm}$ $B^{\pm} \to \eta'_{\eta(3\pi)\pi\pi} K^{\pm}$ $B^{\pm} \to \eta'_{\rho\gamma} K^{\pm}$
$B^{\pm} \to \eta' K^{\pm}\gamma$	$\eta_{\gamma\gamma}$, $\eta'_{\eta\pi\pi}$, $\eta'_{\rho\gamma}$	$B^{\pm} \to \eta'_{\eta\pi\pi} K^{\pm}\gamma$ $B^{\pm} \to \eta'_{\rho\gamma} K^{\pm}\gamma$
$B^{\pm} \to \eta'\eta' K^{\pm}$	$\eta_{\gamma\gamma}$, $\eta'_{\eta\pi\pi}$, $\eta'_{\rho\gamma}$	$B^{\pm} \to \eta'_{\eta\pi\pi}\eta'_{\eta\pi\pi} K^{\pm}$ $B^{\pm} \to \eta'_{\eta\pi\pi}\eta'_{\rho\gamma} K^{\pm}$

Table 4.2: Charged B decay modes and their subdecays studied in this thesis work. In the right column we show the labels used to indicate these modes, reconstructed in their specific subdecays, in the following chapters.

Chapter 5

Statistical technique and software for physical analysis

5.1 Introduction

In this chapter we will describe the software developed to do the analyses presented in this thesis work.

In the first part we will show the analysis technique based on unbinned maximum likelihood fit (ML fit), chosen by *BABAR* collaboration as the official one. This kind of analysis allows high efficiency and the possibility to take in account errors with a better precisions and to consider correlations between the variables.

Then we will present the procedures that allow us to pass through reconstructed events to the ones which we fit, starting from identification of the problems and showing identified solutions.

In the end, we will describe the fitting software, illustrating features and functionalities. To develop the analysis software has been chosen an object oriented coding technique (C++ language) using the ROOT framework classes and a particular classes package for the unbinned ML fit, called RooFit. We will briefly present features of both.

5.2 Maximum Likelihood Technique

The extraction of the results in the analyses has been done using unbinned extended maximum likelihood fits. We explain in this section which are the characteristics of a

such method.

We consider a random variable x (or a multidimensional random vector $\hat{x} = (x_1, \ldots, x_n)$) distributed with a distribution function $f(x;\theta)$. We suppose the expression $f(x;\theta)$ well-known, but at least a parameter θ (or parameters $\hat{\theta} = (\theta_1, \ldots, \theta_n)$) is unknown. So, $f(x;\theta)$ expression represents, after normalizing it, hypothezed probability density function (PDF) for the x variable. Then, we suppose to perform an experiment where a measurement has been repeated N times, supplying $x_1, \ldots, x_N$ values. The probability of x_i included between the interval $[x_i, x_i + \mathrm{d}x_i]$ for every i is

$$P(\theta) = \prod_{i=1}^{N} f(x_i;\theta)\mathrm{d}x_i. \tag{5.1}$$

If the hypothezed expression $f(x;\theta)$ for PDF and the parameter θ are correct, this probability will have a large value for measured data. Vice versa, a parameter value very different by real one gives us a small probability for realized measurements. The maximum likelihood method is a technique to estimate the parameter value for a finite data sample. Since $\mathrm{d}x_i$ does not depend by parameter, same considerations done for $P(\theta)$ can be effected for the function $\mathcal{L}$, defined as:

$$\mathcal{L}(\theta) = \prod_{i=1}^{N} f(x_i;\theta) \tag{5.2}$$

called *likelihood function*. It is clear that to estimate the parameter value we have to maximize this function (*i. e. maximum likelihood*). We should underline that x_i are measured and the $f(x;\theta)$ function is well-known, so $\mathcal{L}$ only depends by parameter we want to fit. The evaluation of maximum for likelihood $\mathcal{L}$ as function of the unknown parameter, or equivalently the minimum of $-\ln(\mathcal{L})$ [1], can be done in a numeric way.

It is often the case that the number of observations N in the sample is itself a Poisson random variable with a mean value n. So, the result of the experiment can be defined as the number N and the N values $x_1, \ldots, x_N$. The likelihood function is then given by the product of the Poisson probability to find N and the function 5.2 for the N values of x,

$$\mathcal{L}(n,\theta) = \frac{e^{-n}}{N!} \prod_{i=1}^{N} n f(x_i;\theta). \tag{5.3}$$

[1] So called negative log-likelihood (NLL). In some case is used also to minimize the function $\chi^2 = -2\ln(\mathcal{L})$.

This function is called *extended likelihood function*. It is really the usual likelihood function, however, only now with the sample size N defined to be part of the result of the experiment. In this case we have to maximize $\mathcal{L}(n, \theta)$ as function of n value and θ parameter (*i. e. extended maximum likelihood*).

Now we see how extended maximum likelihood technique allows us to measure the number of signal events and the number of background events in a data sample where every event has constituted by h observable quantities $\hat{x} = (x_1, \ldots, x_h)$ (*e. g.* mass, energy, angular helicity). We suppose that parameters we have to evaluate are the number of events $n_1, \ldots, n_s$, each one corresponding to a particular specie of events (like signal, continuum background, non-continuum background). To distinguish the events of each specie between them, we determine the distributions for each observable quantity that present a high discriminant power between those species. We fit these distributions with corresponding PDFs, indexed with $f_j^1, \ldots, f_j^h$, with $j = 1, \ldots, s$. So, we have a PDF for each observable quantity and for each specie, which means h PDFs for each specie and h times s PDFs in total. If the observable quantities are independent (otherwise we should consider correlation terms), we can define the total PDF for event i with observable quantities $\hat{x}^i = (x_1^i, \ldots, x_h^i)$ and the specie j as

$$\mathcal{P}_j^i = \prod_{l=1}^{h} f_j^l(x_l^i) \tag{5.4}$$

and the extended likelihood function becomes:

$$\mathcal{L} = \frac{e^{-\sum_{j=1}^{s} n_j}}{N!} \prod_{i=1}^{N} \sum_{j=1}^{s} n_j \mathcal{P}_j^i. \tag{5.5}$$

5.3 ROOT

BABAR software uses ROOT, an object oriented framework dedicated to scientific data analysis [73]. The project was born in CERN in the middle of '90s to furnish tools for data analyses that would offer a better stability with respect to FORTRAN traditional tools. At the same time, people need a programming that allow them to manage quickly big projects, realized by huge and mixed groups, using advanced software programming techniques: it has been chosen the object oriented programming, that in the 90s stood out as optimal choice to realize complex projects.

ROOT framework has been developed using a liberal and informal style [76] where it is necessary an interaction between developers and users, roles very similar and often superimposed: this allows to maintain a continuous evolving project. ROOT architecture is really portable: released version for more common commercial Unix versions (SunOS/Solaris, IBM AIX, HP-UX, SGI IRIX, Compaq/DEC OSF1), for Linux, for Windows, and for MacOs are avaliable. Furthermore the availability of the source code gives adaption to specific necessities of operative system possible.

The ROOT basic structure is formed by a hierarchy of over 300 classes, divided in 14 categories and organized as a tree with one common root, where a large part of classes inherits from common class `TObject`. Among categories we find:

- *container classes* that implement a series of complex data structures as vectors, lists, sets and maps used very often in ROOT;
- *histogram classes* and *minimization* procedure that offer advanced functionalities for statistical data analysis as histograms in one, two or three dimensions, profiles, fitting, minimization and evaluation of mathematical formulas;
- *tree classes* and *ntuple* that extend potentialities of PAW[2] n-tuples, 2D and 3D graphical classes and classes for both graphical and textual interface for the user;
- *operative system interface* that represents the only link with Operative System and favours framework portability;
- *classes for the documentation* that allows a careful and complete documentation generation during project developments.

ROOT is based on C/C++ interpreter called CINT [78]; his goal is to process programs (*script*) which do not need high performance but allowing a quick development. CINT supports about 95% of ANSI C code and about 85% of C++.

5.4 RooFit

RooFit package is formed by a set of classes constructed on ROOT framework dedicated to unbinned maximum likelihood fit, and uses a natural and intuitive notation, that not needs a direct knowledge of ROOT programming [79].

[2] Framework for statistical analysis developed in FORTRAN [77].

RooFit is composed by two packages: RooFitModels and RooFitCore. Former contains all the classes for the PDFs definition and complex models (as sum or product of PDFs). Latter puts at everybody disposal a set of classes to define fitting models and fitting methods; it extends ROOT graphical functions allowing to project fitting models as function of several parameters; it allows data and both discrete and continuous variables management.

5.4.1 Main classes

Variables: `RooRealVar` and `RooCategory`

The first operation we have to do when we create a fit model is to define variables and parameters: it is not done a type distinction between them because they are all objects of `RooRealVar` class. A `RooRealVar` object is featured with a value, a minimum and maximum limit, an error, a name, an unit of measurement, a description and other attributes (for example, to establish if the object defines a constant or a variable).

The `RooRealVar` objects can be used to construct more complex structures as vectors, matrices or lists in the C/C++ traditional way. However, RooFit offers container classes adapted to multidimensional structures called `RooArgList` and `RooArgSet`. They allow to create a list of different variables to use them with other classes (for example as PDFs parameters).

If `RooRealVar` are used to describe continuous variables, `RooCategory` permit to manage discrete variables. Examples of discrete variables can be the B tagging (B^0 or $\overline{B}^0$ and the different tagging categories), the run number of the events, or a naive identification between different channels in a combined fit. In the last case the `RooCategory` allows to do simultaneous fits to different samples for each different channels.

Data sets: `RooDataSet`

A useful class to manage complex data structure is called `RooDataSet`. It permits to organize the data as a matrix, in which single variables are represented in columns while in the rows the single events. The variables are provided in the constructor using a `RooArgSet` object. Data are read through `read()` method. This method allows to access to both text-like files (ASCII) and binary-like ones with ROOT *tree* format.

Distributions: `RooAbsPdf`

The most common distributions used in the analyses are Gaussians (`RooGaussian`), asymmetric Gaussians (`RooBifurGauss`), polynomials (`RooPolynomial`), Argus functions [80] (`RooArgusBG`), Breit-Wigner functions (`RooBreitWigner`), and time-dependent CP asymmetries model (`RooBCPEffDecay`). The single classes inherits from the abstract class `RooAbsPdf` and we can define new functions in a quick and simple way.

The `RooAbsPdf` class puts at the people's disposal a series of generic methods for the events random generation based on a *try–reject* technique that can be redefined in a more efficient way for the subclasses. This class offers a fundamental method `fitTo()` that effects a fit creating a specific object `TMinuit`. It perform the fits using the Minuit algorithm [81], minimizing the likelihood function in several steps (`MIGRAD, MINOS, HESSE`). The `RooAbsPdf` class offers also some other options for plotting and drawing. It is useful to note that `RooAbsPdf` distributions are automatically normalized (they are PDFs).

Furthermore we can compose single PDFs through sum (`RooAddPdf`), product (`RooProdPdf`), and convolution (`RooConvPdf`). A particular constructor of `RooAddPdf` class permits to declare the extended likelihood functions.

5.5 Software for the events selection: the *Selector*

The variables determined for each event during the events reconstruction are saved in ROOT files contained in particular structures called *tree*. These files represent the output of the events reconstruction process. During this stage loose cuts are applied on the variables to effect a first discrimination betweet signal and background (*preliminary* cuts). This permits to reduce files dimension.

After the reconstruction, we can optimize the values of the cuts (obviously using tighter cuts). To do that, it is necessary a program that allows us to read values of the variables, held in the trees, and to apply the new cuts. Then, the new survived events are saved in ROOT files for later analysis (ML fit). ROOT realizes that with a solid and flexible method, using the so called *selector*. This procedure is based on the realization of an user's personalized class (*i .e.* depending on the analyses to realize) that is derived from the `TSelector` class. The following methods are implemented in it:

- `TSelector::Begin`: This function is called before to read the values of the first event stored in the trees. It is possible to furnish a configuration parameter that permits to effect several kind of operations for a fixed selector, like saving events for the ML fit, to perform cut and count analysis, to draw variables distributions. Configuration parameter is an alfanumeric string: reading of this parameter and the identification of the operation requested is performed in this function `Begin`.

- `TSelector::Process`: This function is called for every single event. It contains the definition of the cuts to be applied on variables' values. After each cut we have a counter that allows us to determine the number of the events that pass it. If the variable values of an event pass all the cuts, the event is counted in all the counters and saved. Vice versa, if a determined cut is not respected, the event is rejected and the counting operation is interrupted in the last passed cut.

- `TSelector::Terminate`: This function is called at the end of variables reading of all the events. It performs the conclusive operations, *i. e.* closing the output file, drawing histograms, showing at screen the number of the events after all the cuts.

Cause different analyses differ essentially for the variables and for the cut values, from the description above, we can guess that the method which is more specific for each analysis is `Process`. For all the other methods is possible to realize a template which we can refer to.

5.6 Fitting Program: `MiFit`

As explained in the section 5.2, we use an unbinned extended maximum likelihood (ML) fit to extract the results in our analyses. The reconstructed events, after the selection done with the procedures described in section 5.5, are saved in a ROOT file. These events are the input to the ML program.

The development of this program, called `MiFit`, is an important part of this thesis work. It is developed in C++, and we use the ROOT and RooFit classes in a standalone executable code. During the thesis work there were several updates on the program, depending of the new analysis requests. Each update is tagged with a version and the actual version is 3.1. All analyses in the Milan *BABAR* group use `MiFit`.

The main goal of `MiFit` is to provide a very simple interface to perform several operations used in the different analyses. It is not requested any skills about ROOT and RooFit, but any configuration of the program is given using intuitive configuration text files: `mipdf.cfg` and `mifit.cfg`. The former is used when we make the PDF fits of the variables, while the latter for any other function of the program. The structure of the two files is very similar. However, we have decided to consider the operation of PDF fit as different from the other ones and therefore we use two different files.

`MiFit` is based on four main classes:

1. **MFConfiguration**: the goal of this class is to read the configuration file (mipdf.cfg or mifit.cfg) and to interpret it line by line. If no errors occur (there is a syntax spelling and declarations consistency check), it provides to other classes the necessary informations to declare objects requested in the configuration reading. The configuration file is divided in different parts:

   - *config*: some features are fixed, such as the title for each PDF, best candidate choice selection criteria, number of $B\overline{B}$ pairs, blind procedure parameters.
   - *embedded tree*: some tests (called MC toy experiments) require the generation of a sample of data from PDFs and the embedding of events taken from external samples. In this part we declare these external samples and the number of events to embed to the generated sample.
   - *input*: here all fitting variables are listed. Definition syntax is given by: name (same name of the variable in the tree), description, definition interval used to normalize the PDF and eventually unity of measurement.
   - *category*: it contains the discrete variables used for tagging informations (tag and category) and indices of different sub-decays for the simultaneous fits.
   - *correction*: the PDFs obtained fitting on MC data have small discrepancies with respect to what we could obtain from the real data. This is due to a not good MC simulation. For example, in some cases the resonances masses have a small difference in the central value and in the width. Using a control sample, we study this effect and we take it in account applying corrections to the parameters. In some cases, these corrections are run-

dependent, *i. e.* they are different for each run of data. In this part of the configuration file we declare these corrections.

- *pdfparam*: here we declare the PDFs parameters which can be fixed or floating in the fit. There are some options that we can consider for each parameter: *constant*, if we want that the floating parameter does not change from the initial value, and *blind*, if we want that parameter is blinded.
- *KEYSpdf*: in this section we declare the KEYS PDFs (aka "Kernel Estimating Your Shapes") which are non-parametric PDFs that describe a distribution empirically, *i. e.* without referring to any model of the expected shape. In some cases it is difficult to fit a distribution with a standard PDF so this kind of PDF helps us in doing it.
- *pdf*: here we define the PDFs used to fit variables. They exist several kinds of avaliable PDFs, like Gaussians, asymmetric Gaussians, polynomials and Chebychev polynomials, and combinations of these (for example Gaussian plus a first degree polynomial). For each PDF we must give the name of the variable to fit (declared in *input* section) and the names of the parameters (declared in *pdfparam*).
- *CPpdf*: here we declare the PDFs for the time-dependent CP asymmetries model. These are special PDFs because they have as input parameters also the B tagging discrete variable (declared in *category* section) and the resolution model (declared in *pdf*).
- *yieldvar*: here we declare the variables which correspond to the numbers of the events for each species (signals and backgrounds).
- *extendedpdf*: in this section we consider the product of the PDFs declared in *KEYSpdf*, *pdf*, and *CPpdf* sections to obtain the total PDF for each species (signals and backgrounds) times the correspondent yield variable, declared in *yieldvar*.
- *fitpdf*: the PDFs declared in *extendedpdf* are summed to obtain the final extended PDF for the fit.
- *simfitpdf*: in this section we declare special PDFs for simultaneous fits, *i. e.* fits of different categories of events where each one is fitted with a different *fitpdf* PDF. This is the case of the fit for different sub-decays. To do that we assign each PDF to the value of a discrete variable (the label).

2. **MFDataFile**: this class performs the reading of input events from the ROOT files. It verifies the correspondence between declared variables in *input* and *category* sections and the variables of the tree in the ROOT file. If no errors occur, it performs final cuts on such input variables, the best candidate choice selection (if requested) for events with multiple candidates (we can make a random selection or using a best χ^2 selection), calculate the correlation matrix for the input variables, write in an output file two samples: one for events after the cuts and the other one after the best choice selection (corresponding to the final sample for the fit).

3. **MFModels**: this class instances all PDFs declared in the section *KEYSpdf*, *pdf*, *CPpdf*, *extendedpdf*, *fitpdf*, and *simfitpdf*. It controls if the number of parameters for each PDF is correct. This class performs also the generation of events from PDFs and the drawing of a PDF.

4. **MFFits**: the goals of this class is to perform the ML fits for a single variable or the extended ML fits for the yields extraction. In this class we also have defined the MC toy experiment procedures, branching fractions and upper limits calculations, likelihood function plots, contour plots of the likelihood function, and output of the fit results.

Now we will describe some functions of `MiFit`. Further description can be found in the web page

`http://pcbabar1.mi.infn.it/lazzaro/MiFit`

5.6.1 Making PDFs

After launching `MiFit` executable, the program shows a text menu with different options. The option "1" allows us to perform the fit of the distribution of one variable. After reading the configuration file (in this case mipdf.cfg), if no errors occur during the configuration file reading, the program asks which variable we want to fit and which PDF we want to use. At the end of the fit, a plot is visualized of the distribution of the variable with overimposed the PDF. In the plot are shown also the values of the PDF parameters and the χ^2 value calculated between the distribution and the PDF. We can choose the number of bins for the distribution (just a graphical reason because the

fit is unbinned) and the logarithmic scale for the y-axis. The parameters of the PDF can be copied in the file mifit.cfg to perform the rest of the analysis.

5.6.2 Making Fit

The option "2" of `MiFit` is used to perform extended ML fits. In these fits we extract the numbers of yields of each event hypothesis and the values of PDFs parameters which are floating (like the time-dependent CP parameters S and C). After choosing the option "2", `MiFit` asks (in order):

- if we want to apply correction for MC/data matching. This facility is requested if in the configuration file we have declared PDF parameters with MC/data corrections.

- if we want the results of the fit in blind or unblind mode.

- the extended PDF (declared in *fitpdf* or *simfitpdf*) to use.

When the fit is completed, the results are shown. After that, it is possible to have the statistical significance, the branching fraction and the 90% CL upper limit for the yield variables, and the scan of likelihood function for a specific fit variable.

5.6.3 Making MC Toy Experiments

The third option of `MiFit` is useful to study the causes for biases and correlations with respect to the results. In other words, we want to verify all the hypotheses done on the PDFs and the lack of knowledge on the parameters. That's why we use a statistical technique called "MC toy experiments" generation. In this method we generate several samples of data (with the data generated from PDFs and/or taken from MC data samples) and we fit on them. Since we know the composition of the sample (how many signal and background events are inside it), we expect that the distribution of the results of the fits should be a Gaussian distribution with central value as used in the generation of the events. Eventually, biases obtained between the mean of this Gaussian and the values used in the generation of the events are considered as systematic effects. We can decide also to correct the final results in the fit on real data to take in account these biases. These studies are applied to yields results and to the parameters S and C.

5.6.4 Making Projections

The option "4" of `MiFit` allows to draw projections or $sPlots$ of variables.

In case of the projections, it is necessary to work in two steps. First of all, if we want to project a variable x, we need to emphasize the signal in the data sample with respect to the background. For this reason we apply a cut on likelihood function $\mathcal{L}$, evaluated without the x variable. So, the first step consists in the evaluation of the cut value on $\mathcal{L}$: we use a sample of signal and background events generated from PDFs to optimize this cut. After that, the second step is to apply the cut to the data and then show the distribution of the variable x with its signal and background PDFs superimposed.

The $sPlot$ consists of an event-weighting technique where we use the covariance matrix and PDFs from the ML fit to determine a probability for each event [82]. We use these probabilities to draw the distributions of the variables where their points with errors are normalized to the yield results. For this case, after choosing the variable we want to draw, an extended ML fit is performed on the data, where the likelihood function is evaluated without the variable to draw. The results of this fit are used to draw the $sPlot$.

Chapter 6

Discriminating variables and Events Selection

6.1 Introduction

In this chapter we will describe the discriminating variables used to separate signal from background events. We will consider both kinematical and topological variables. The analyses show two different kinds of background: continuum background $e^+e^- \rightarrow q\overline{q}$ ($q = u, d, s, c$) and the background coming from other $e^+e^- \rightarrow b\overline{b} \rightarrow B\overline{B}$ events with charm or charmless final states (non-continuum background).

At $\Upsilon(4S)$ resonance energy, we have a number of $e^+e^- \rightarrow q\overline{q}$ events about three times with respect to $B\overline{B}$ events. The $q\overline{q}$ continuum background can be studied using collected data under the resonance (off-peak data), while for the study of $B\overline{B}$ background simulated Monte Carlo data is used.

Topological variables describe the spatial structure of the events and furnish a separation between $B\overline{B}$ events and the continuum background ones; kinematical variables allow us to discriminate signal from non-continuum background and further from the continuous one.

6.2 Topological variables

From the kinematical study of $e^+e^- \rightarrow q\overline{q}$ we deduce that background and signal events have a different geometry. Since beam energy in the center of mass (CM) is equal to 10.580 GeV, kinetical energy at $u\bar{u}$, $d\bar{d}$, $s\bar{s}$, $c\bar{c}$ ($udsc$) pairs' disposal is very

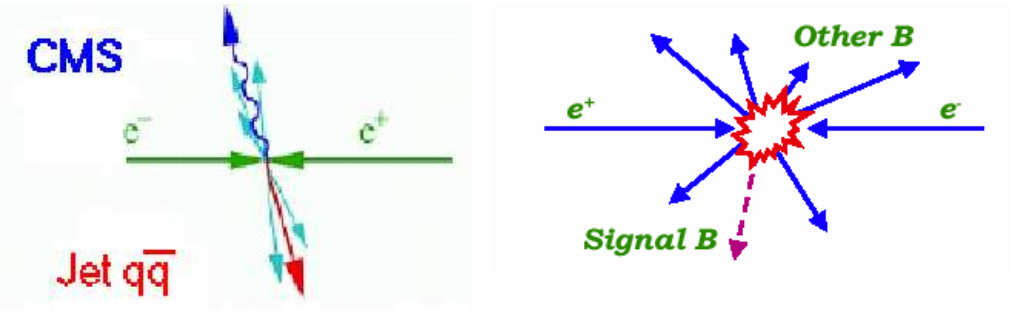

Figure 6.1: Schematic topological rappresentations of $e^+e^- \rightarrow q\overline{q}$ (left) and $e^+e^- \rightarrow \Upsilon(4S) \rightarrow B\overline{B}$ (right).

high: the event jets will be almost anti-parallel. In the case of a process $e^+e^- \rightarrow \Upsilon(4S) \rightarrow B\overline{B}$ the kinetical energy for B mesons will be low, so, the event will be much more isotropic. This fact is illustrated in fig. 6.1.

These different spatial distributions of the particles in the final states allow us to define some topological variables used for background suppression. In particular, in our analyses we use:

- the cosine of angle between the thrust axis of the B candidate and the thrust axis of the other-B in the event, $\cos\theta_{\rm T}$;
- the Fisher discriminant.

Both variables are described in the following sections.

6.2.1 The $\theta_{\rm T}$ angle

The thrust axis is defined as the versor $\vec{n}$ which maximizes the value of variable T, the thrust, defined in the following expression:

$$T = \max_{|\vec{n}|=1} \frac{\sum_i |\vec{n}\vec{p}_i|}{\sum_i |\vec{p}_i|}. \tag{6.1}$$

where p_i are the particles momenta used to calculate it. We consider the $\theta_{\rm T}$, which is the angle between the thrust axis of the B candidate and the thrust axis of the rest of the event (the particles not belonging to the reconstructed B candidate), calculated in CMS frame. For the thrust axis determination we use the informations from neutral and charged particles of the event. The $|\cos\theta_{\rm T}|$ variable has a nearly flat distribution for

$B\overline{B}$ events while it is sharply peaked at 1 for continuum background events (fig. 6.2), for the reason explained above. So this variable gives a strong discrimination power between signal and background events. Usually the cut $|\cos\theta_{\mathrm{T}}| < 0.9$ is applied, but in some cases of high continuum background contribution we use a tighter cut value.

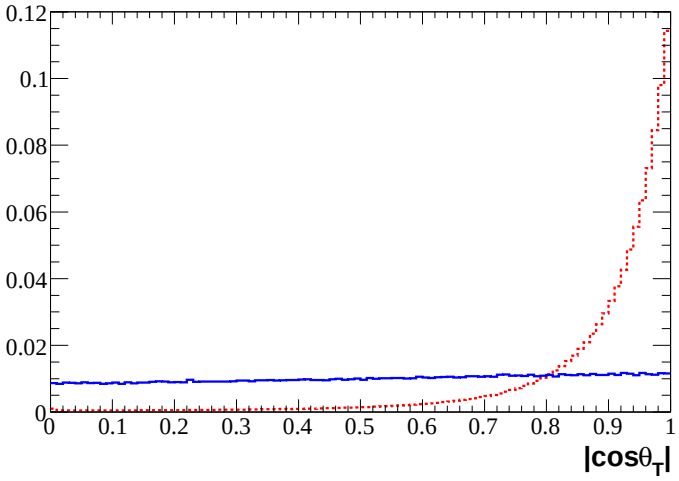

Figure 6.2: Comparison of $|\cos\theta_{\mathrm{T}}|$ variable calculated for $B\overline{B}$ MC signal events (blue solid line) and off-peak data (red dashed line).

6.2.2 $\mathcal{F}$ Fisher Discriminant

The $\mathcal{F}$ Fisher discriminant is a statistical method used to discriminate the events in two hypotheses, signal and background. In general, for every reconstructed event we need to decide if it agrees better with signal or background hypothesis. To do that, we introduce a *statistical test* **t(x)**, function of several **x** event variables. Such a function will have different distributions for those two hypotheses. The simplest choice is represented by Fisher discriminant that is a linear combinations of more variables:

$$\mathcal{F} = \sum_i \alpha_i x_i \tag{6.2}$$

where α_i coefficients are chosen in the way to maximize the separation between $\mathcal{F}$ distributions in signal and background hypotheses [83, 84].

In the variables choice we consider quantities that furnish us informations on topological shape of the event. In our case we use 4 variables: the absolute value of the cosine of the angle between the reconstructed B candidate direction and the beam axis

($|\cos\theta_B|$), the absolute value of the cosine of the angle between the thrust axis of the reconstructed B candidate and the beam axis ($|\cos\theta_C|$), and the two monomials L_0 and L_2 with L_n defined as:

$$L_n = \sum_{i=ROE} p_i \times |\cos(\theta_i)|^n \tag{6.3}$$

where the sum is over the list of the rest of event (all tracks and neutrals which do not belong to the B candidate), p_i is the momentum of particle i, and θ_i is the angle between the direction of particle i and the thrust axis of the B candidate. These variables are shown in fig. 6.3.

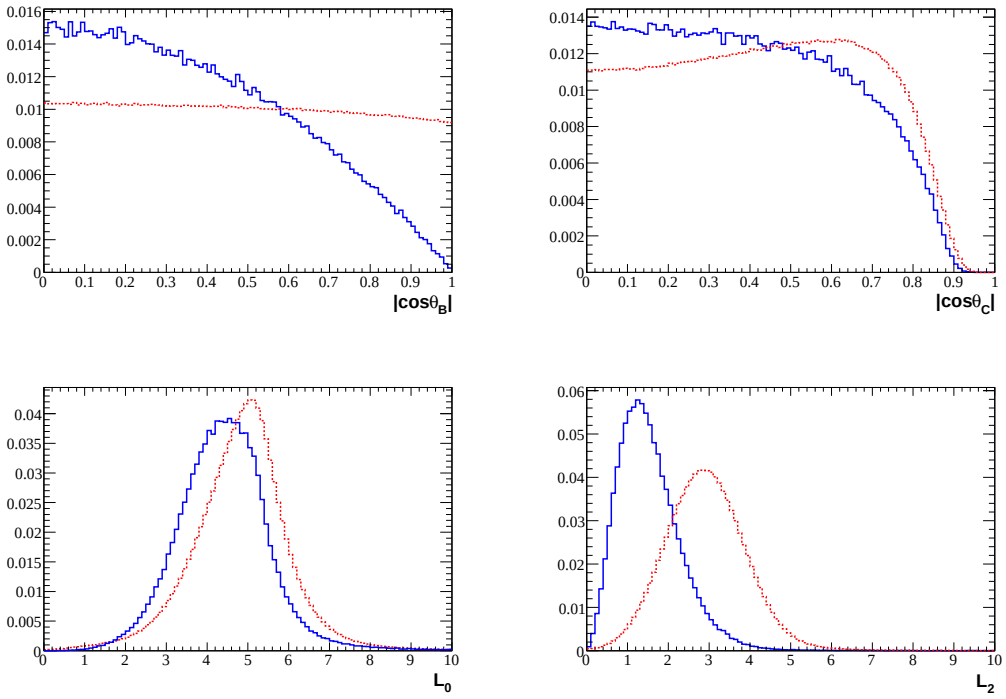

Figure 6.3: Variables used in the $\mathcal{F}$ calculated for $B\overline{B}$ MC signal events (blue solid line) and off-peak data (red dashed line): $|\cos\theta_B|$), top left; $|\cos\theta_C|$, top right; L_0, bottom left; L_2, bottom left.

Our Fisher discriminant has the following form:

$$\mathcal{F} = 0.367 \cdot (1.60287 \cdot |\cos\theta_C| + 1.89495 \cdot |\cos\theta_B| - 0.66531 \cdot L_0 + 2.6685 \cdot L_2) - 1.3 \tag{6.4}$$

where the coefficients are optimized on samples of MC signal events and off-peak data, and they are chosen in order to have the signal and background distribution of $\mathcal{F}$ with

average in -1 and $+1$, respectively.

It was noticed that $\mathcal{F}$ defined in eq. 6.4 is correlated with the tagging category. We recall that our tagging algorithm, `Tag04`, described in section 2.4.1, divides the events in six categories, plus untagged events. We identify these categories with the numbers from 63 to 69, respectively. The correlation is illustrated in fig. 6.4 for the mode $B^{\pm} \to \eta'_{\rho\gamma} K^{\pm}$. The plots show the fitted mean of a bifurcated Gaussian to the $\mathcal{F}$ distribution for each `Tag04` tagging category, for signal and continuum background. A linear polynomial is fitted to the distributions, showing the different slope for signal Monte Carlo and off-peak events.

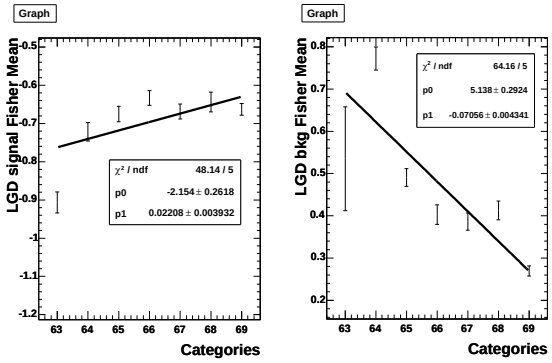

Figure 6.4: Variation of the mean of a bifurcated Gaussian fitted to the $\mathcal{F}$ distribution for each tagging category, for signal MC (left) and off-peak events (right).

Since in our measurements the reconstructed data samples are dominated by continuum background events, the correlation in continuum is most important to remove. We therefore use the parameters from the off-peak sample to reduce the first order of the correlation between the shape of the Fisher distribution and the tagging category, applying a correction on $\mathcal{F}$ done on a category by category basis. For each tagging category, we shift the value of $\mathcal{F}$ such that the distribution for all category have the same average. We define the new Fisher variable $\mathcal{F}'$ [1] as

$$\mathcal{F}' = \mathcal{F} + \delta(\mathrm{Cat}_{\mathrm{Tag04}}), \tag{6.5}$$

[1] In the following chapters we will use the simple $\mathcal{F}$ notation to indicate $\mathcal{F}'$.

where

$$\begin{aligned}
\delta(\mathrm{Cat}_{\mathrm{Tag04}} = 63) &= +0.010, \\
\delta(\mathrm{Cat}_{\mathrm{Tag04}} = 64) &= -0.294, \\
\delta(\mathrm{Cat}_{\mathrm{Tag04}} = 65) &= -0.070, \\
\delta(\mathrm{Cat}_{\mathrm{Tag04}} = 66) &= -0.005, \\
\delta(\mathrm{Cat}_{\mathrm{Tag04}} = 67) &= -0.024, \\
\delta(\mathrm{Cat}_{\mathrm{Tag04}} = 68) &= +0.008, \\
\delta(\mathrm{Cat}_{\mathrm{Tag04}} = 69) &= +0.106.
\end{aligned}$$

The values of the corrections are obtained from an average of the central values of distributions for each category of different modes ($\eta' K$ modes). The distribution of $\mathcal{F}'$ is shown in fig. 6.5.

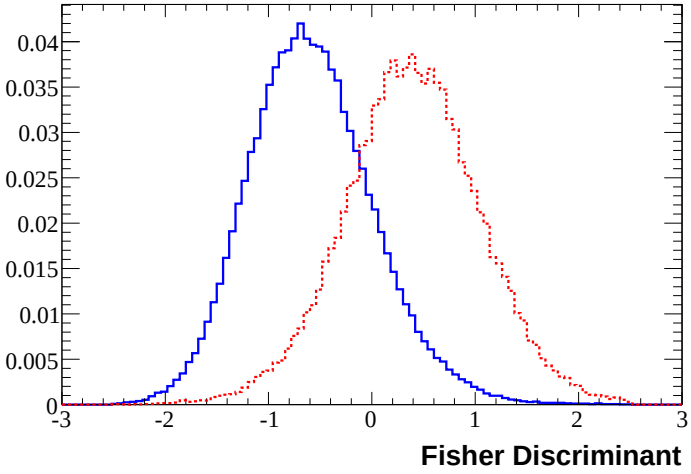

Figure 6.5: Comparison of $\mathcal{F}'$ variable calculated for $B\overline{B}$ MC signal events (blue solid line) and off-peak data (red dashed line).

We checked that the correlation between the $\mathcal{F}'$ mean and the tagging category was reduced for continuum. Figure 6.6 shows the fitted mean of a bifurcated Gaussian to the $\mathcal{F}'$ distribution versus the `Tag04` tagging category. The correlation for continuum is clearly small compared to that of $\mathcal{F}$ and the mean is also more constant over categories than it is for $\mathcal{F}$. The residual variations come from the fact that the plot shows the mean of a fitted bifurcated Gaussian while the correction was obtained from

an average of several distributions for each category of different modes. Finally, we determined directly from the signal and off-peak data the correlation between $\mathcal{F}'$ and the `Tag04` tagging category. For $\eta'_{\rho\gamma}K^0_{S+-}$ mode we obtain the raw correlations given in tab. 6.1. We conclude that the dominant correlation between the Fisher discriminant and the tagging category better removed with the variable $\mathcal{F}'$.

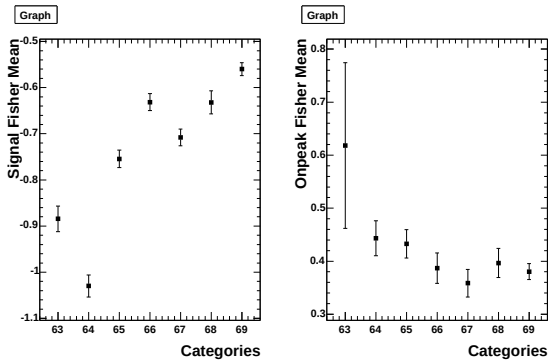

Figure 6.6: Variation of the mean of a bifurcated Gaussian fitted to the $\mathcal{F}'$ distribution for each category, for signal MC (left) and off-peak data (right).

Mode	Data	Correlation of $\mathrm{Cat(Tag04)}$ and $\mathcal{F}$	Correlation of $\mathrm{Cat(Tag04)}$ and $\mathcal{F}'$
$\eta'_{\rho\gamma}K^0_{S+-}$	SIGMC	$+1.6\%$	$+14.8\%$
	OFF	-13.7%	$+1.0\%$

Table 6.1: Correlation between $\mathcal{F}$ or $\mathcal{F}'$ and the tagging category $\mathrm{Cat(Tag04)}$, for signal MC (SIGMC) and off-peak data (OFF).

6.3 Kinematical variables

The B candidates are characterized kinematically by ΔE and m_{ES}. These two variables are defined in order to minimize the correlation between them.

The invariant ΔE is defined as:

$$\Delta E = \frac{2q_{\Upsilon(4S)}q_B - s}{2\sqrt{s}} \tag{6.6}$$

where $q_{\Upsilon(4S)}$ and q_B are four-momenta of the $\Upsilon(4S)$ and the B candidate. We require $|\Delta E| < 0.2$ GeV ($-0.01 < \Delta E < 0.04$ GeV for $B^0 \to \eta' K^0_L$ analysis). In the fig. 6.7

we can see that ΔE presents essentially a Gaussian distribution for the signal events while a linear polynomial is used for the continuum background. In $B^0 \to \eta' K^0_L$ mode, where we apply a B mass constraint to reconstruct the events, the background shape of ΔE is described by an Argus function [80], defined as:

$$F(x) = C\, x\sqrt{1-x^2}\;\; e^{-\xi(1-x^2)}, \tag{6.7}$$

where C is a normalization factor, $x \equiv 2\Delta E/\sqrt{s}$, and ξ is a shape parameter. Also this distribution is shown in fig. 6.7.

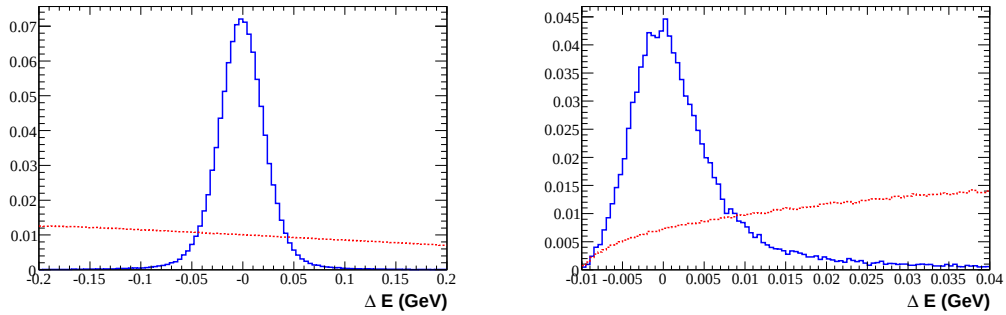

Figure 6.7: Comparison of ΔE distributions for modes without K^0_L meson (left) and $B^0 \to \eta' K^0_L$ mode (right) for $B\overline{B}$ MC signal events (blue solid line) and off-peak data (red dashed line).

The $m_{\rm ES}$ is the beam-energy substituted mass, computed in the LAB frame and independent of mass hypotheses assigned to B candidate daughters:

$$m_{\rm ES} \;= \sqrt{\frac{(s/2 + \vec{p}_{\Upsilon(4S)} \cdot \vec{p}_B)^2}{E^2_{\Upsilon(4S)}} - \vec{p}^{\,2}_B} \tag{6.8}$$

where $s \equiv (q_{\Upsilon(4S)})^2$ is the square of the CM energy, $p_{\Upsilon(4S)}$ and p_B are three-momenta of the $\Upsilon(4S)$ and the B candidate in the LAB frame and $E_{\Upsilon(4S)} \equiv q^0_{\Upsilon(4S)}$ is the energy of the $\Upsilon(4S)$ in the LAB frame. We require $5.25 < m_{\rm ES} < 5.2893$ GeV/c^2. Because of reconstruction technique used in K^0_L analysis, there is a strong correlation between ΔE and $m_{\rm ES}$ in $B^0 \to \eta' K^0_L$ modes. For this reason in this analysis we don't use $m_{\rm ES}$ variable. The comparison between $m_{\rm ES}$ distributions for signal and background is shown in fig. 6.8; essentially the signal is described by a Gaussian distribution while an Argus function is for the continuum background.

The selection cuts for ΔE and $m_{\rm ES}$ are in general quite loose to allow a high effi-

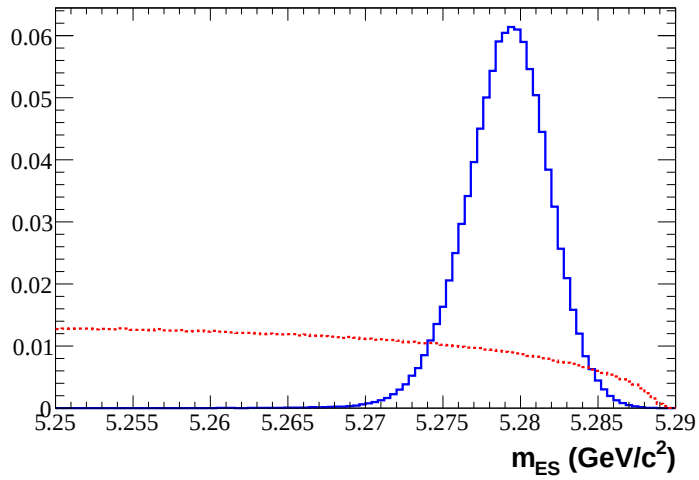

Figure 6.8: $m_{\rm ES}$ variable distributions for $B\overline{B}$ MC signal events (blue solid line) and off-peak data (red dashed line).

ciency and to provide sufficient events in the sidebands to characterise the backgrounds well.

6.4 Events selection

After the cuts applied during the reconstruction (preliminary cuts), described in the section 4.4, tighter cuts are applied to produce the input to maximum likelihood fit. We can distinguish between common cuts applied to all analyses and specific cuts for the selection of the events for a particular analysis. In the following we will describe all these cuts. The efficiency for each cut can be found in sections 7.4.1 and 8.5.1 for the branching fraction and time-dependent CP asymmetries measurements, respectively.

6.4.1 Preliminary Cuts

The preliminary cuts are applied during the events reconstruction, described in the section 4.4. We show here further cuts applied during the reconstruction not mentioned in that section.

- A minimum number of charged tracks in the event (from `GoodTracksVeryLoose` list) $\geq \max[3, N_{\text{tracks in the } B \text{ decay mode}} + 1]$. This cut allows to reduce the background from $e^+e^- \rightarrow \tau^+\tau^-$ events.

- $|\cos\theta_{\rm T}| < 0.9$ ($|\cos\theta_{\rm T}| < 0.7$ for $\eta'_{\eta\pi\pi}\eta'_{\rho\gamma}K^{\pm}$ analysis).
- $E_{\gamma} > 0.050$ GeV for $\eta_{\gamma\gamma}$; $E_{\gamma} > 0.100$ GeV for $\eta'_{\rho\gamma}$.
- $5.25 < m_{\rm ES} < 5.29$ GeV/c^2 (not applied in $B^0 \to \eta' K^0_L$ modes).
- $|\Delta E| < 0.2$ GeV ($-0.01 < \Delta E < 0.04$ GeV in $B^0 \to \eta' K^0_L$ mode).
- Reject events with zero χ^2 B vertex probability;

6.4.2 Selection Cuts

The reconstructed events are selected with further cuts to discriminate signal from background events. Most of these cuts are common to all analyses, like charged particles indentification and daughter resonances mass cuts. However, some analyses require further specific cuts, like for primary γ selection in $\eta^{(\prime)}K\gamma$ analysis, K^0_L selection in $\eta' K^0_L$ analysis, $K^{\pm}$ selection in $\eta' K^{\pm}$ analysis. Further cuts are specific for the TD analysis of $\eta' K^0$. In the following sections we will report the value of common and specific cuts for each analysis.

Common Selection Cuts

These are the common selection cuts applied to all analyses.

- **Event-wide cuts**
  - Charged tracks from $\eta_{3\pi}$, $\eta'_{\eta\pi\pi}$, and ρ^0 candidates satisfy electron, kaon and proton vetoes, by using particles indentification (PID) selectors with criteria `tight` for electrons and kaons, and `veryTight` for protons.
  - Both charged tracks from ϕ candidates satisfy electron, pion and proton vetoes, by using PID selectors with criteria `tight` for electrons and pions, and `veryTight` for protons.
  - Primary kaons in B charged modes satisfy electron and proton vetoes, by using PID selectors with criteria `tight` for electrons and `veryTight` for protons.
  - Primary kaons in B charged modes are identified as kaon by using PID selector with criteria `tight`. This selection is not applied in the $\eta' K^{\pm}$ analysis, where the selection is described below.

- $E_\gamma > 0.030$ GeV for π^0 ($E_\gamma > 0.050$ GeV for π^0 in $\eta K\gamma$ analysis).
- $E_\gamma > 0.100$ GeV for $\eta_{\gamma\gamma}$ ($E_\gamma > 0.030$ GeV for $\eta_{\gamma\gamma}$ in $\eta'\eta'K$ analysis; $E_\gamma > 0.050$ GeV for $\eta_{\gamma\gamma}$ in $\eta'\phi$, $\eta' K_S^0$, $\eta' K_L^0$, $\eta^{(\prime)} K\gamma$ analyses).
- $E_\gamma > 0.200$ GeV for $\eta'_{\rho\gamma}$ ($E_\gamma > 0.100$ GeV for $\eta'_{\rho\gamma}K$ analysis).
- $-4 < \mathcal{F} < 5$.

- **Daughter resonances cuts**
  - ρ^0mass between 0.510 and 1.000 GeV/c^2 (between 0.470 and 1.000 GeV/c^2 for $\eta'_{\rho\gamma}K_S^0$ time-dependent CP asymmetries analysis).
  - The ρ^0 helicity $\mathcal{H}_\rho = \cos\theta_H$ (cosine of the ρ^0's rest frame decay angle of a pion with respect to η' flight direction) with $|\mathcal{H}_\rho| < 0.9$. This variable has a $(1-\mathcal{H}_\rho^2)$ distribution for the true ρ^0 candidates, while it is flat for the combinatorial background.
  - π^0 mass between 0.120 and 0.150 GeV/c^2 (between 0.120 and 0.155 GeV/c^2 for π^0 from K_S^0).
  - η mass between 0.490 and 0.600 GeV/c^2 for $\eta_{\gamma\gamma}$ (resolution 0.013 GeV/c^2) and between 0.520 and 0.570 GeV/c^2 for $\eta_{3\pi}$ (resolution 0.004 GeV/c^2).
  - For primary $\eta_{\gamma\gamma}$ from B we apply a cut on helicity $\mathcal{H}_\eta = \cos\theta_H$ (cosine of the angle between the direction of an η daugther with respect to the flight direction of B in the η meson rest frame) of $|\mathcal{H}_\eta| < 0.9$. This cut reduces the asymmetric $\eta_{\gamma\gamma}$, *i. e.* to remove random combinations of η reconstructed with soft photons.
  - $\eta'_{\rho\gamma}$ mass between 0.930 and 0.990 GeV/c^2 (between 0.910 and 1.000 GeV/c^2 for $\eta'_{\rho\gamma}K\gamma$ analysis; between 0.910 and 0.990 GeV/c^2 for $\eta'_{\rho\gamma}\phi$ analysis; between 0.930 and 0.980 GeV/c^2 for $\eta'_{\rho\gamma}K$ analysis) (resolution 0.008 GeV/c^2).
  - $\eta'_{\eta\pi\pi}$ mass between 0.930 and 0.990 GeV/c^2 (between 0.945 and 0.970 GeV/c^2 for $\eta'_{\eta\pi\pi}K$ analysis) (resolution 0.004 GeV/c^2).
  - ϕ mass between 1.005 and 1.035 GeV/c^2.
  - For K^0_{S+-} we consider K_S^0 mass between 0.486 and 0.510 GeV/c^2, fit vertex probability $\chi^2 > 0.001$ and flight length $> 3\sigma$.
  - For K^0_{S00} we apply the cut on mass between 0.468 and 0.528 GeV/c^2.

Specific Selection Cuts for $\eta^{(\prime)}K\gamma$ analysis

- **Primary photon cuts**
  - Energy of the primary photon in CMS system: $1.6 < E^*_\gamma < 2.7$ GeV (see fig. 6.9 for examples of the photon spectrum in our modes).
  - Cluster without noisy or dead crystals.
  - Primary photon cluster second moment < 0.002.
  - Cosine of primary photon θ angle (laboratory) in the interval: $-0.74,\ 0.93$.
  - Distance of primary photon bump from all other neutral bumps and tracks in B candidate > 25 cm.
  - π^0 veto: the photon combining with all other neutral cluster ($E > 50$ MeV) should not make a π^0 with mass between 0.115 and 0.155 GeV/c^2.
  - η veto: the photon combining with all other neutral cluster ($E > 250$ MeV) should not make an η meson with mass between 0.507 and 0.587 GeV/c^2.
- **Daughter resonances cuts**
  - π^0 veto for $\eta_{\gamma\gamma}$: to suppress background from π^0 in the decays $\eta_{\gamma\gamma}K\gamma$ we used a π^0-veto. Using the π^0 candidate list, we cut an η candidate in the event if in the same event we have a fast enough π^0 ($p^* > 0.8$ GeV/c) which overlaps with the η candidate. This cut allows to reduce the background from $K^*(892)\gamma$ ($K^*(892) \to K\pi^0$) of about 40% and to reduce the efficiency of about 12%;
  - Momentum of η or η' in CMS frame greater than 0.9 GeV/c (0.6 GeV/c in modes with $\eta'_{\eta\pi\pi}$). Examples of distribution of this variable for our modes are shown in fig. 6.10. This cut has been optimized using the maximization of statistical significance. A plot of this optimization is show in fig. 6.11.
  - We have calculated the efficiency as a function of the X_s invariant mass (where X_s represents the system $\eta^{(\prime)}K$) for the given MC simulated events. The distribution of the reconstructed X_s invariant mass has been divided (bin per bin) by the distribution of the same invariant mass obtained directly from MC list. The results of this procedure is shown in the figs. 6.12–6.15. Drops in efficiency at large ηK and $\eta' K$ masses reflect the effect of

the reconstruction and the 1.6 GeV cut in CMS on the energy of primary photon. To limit the phase space to values of X_s invariant mass for which the efficiency is reasonably high we cut just below the point where the efficiency drops (last bin): $m_{X_s} < 3.25\,\mathrm{GeV}/c^2$. Examples of distribution of this variable for our modes are shown in fig. 6.16.

– The decay modes $\eta' K\gamma$ have an irreducible background from the decay $J/\psi K$ with $J/\psi \to \eta'\gamma$ (see section 7.6.3 for a discussion about this background). We introduce a veto to reduce this background, cutting on invariant $\eta'\gamma$ mass between 2.919 and 3.275 GeV/c^2 which is about 3 σ (σ of the reconstructed J/ψ mass, see fig. 7.2) around the nominal value of the J/ψ mass.

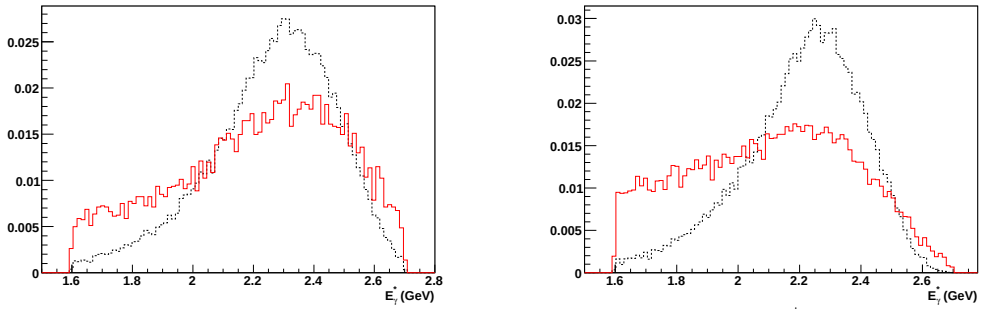

Figure 6.9: Energy photon spectrum in CMS frame for $\eta_{\gamma\gamma}K^{\pm}\gamma$ mode (left) and $\eta'_{\rho\gamma}K^{\pm}\gamma$ mode (right): black dashed line refers to MC signal events, red solid line to on-peak data.

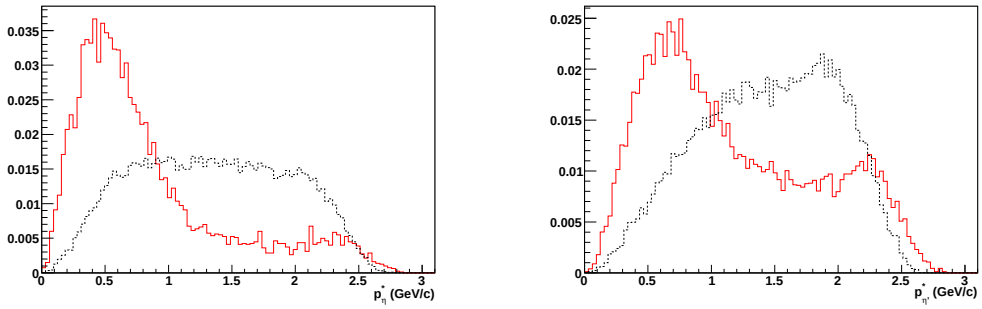

Figure 6.10: Momentum of $\eta^{(\prime)}$ in CMS frame for $\eta_{\gamma\gamma}K^{\pm}\gamma$ mode (left) and $\eta'_{\rho\gamma}K^{\pm}\gamma$ mode (right): black dashed line refers to MC signal events, red solid line to on-peak data.

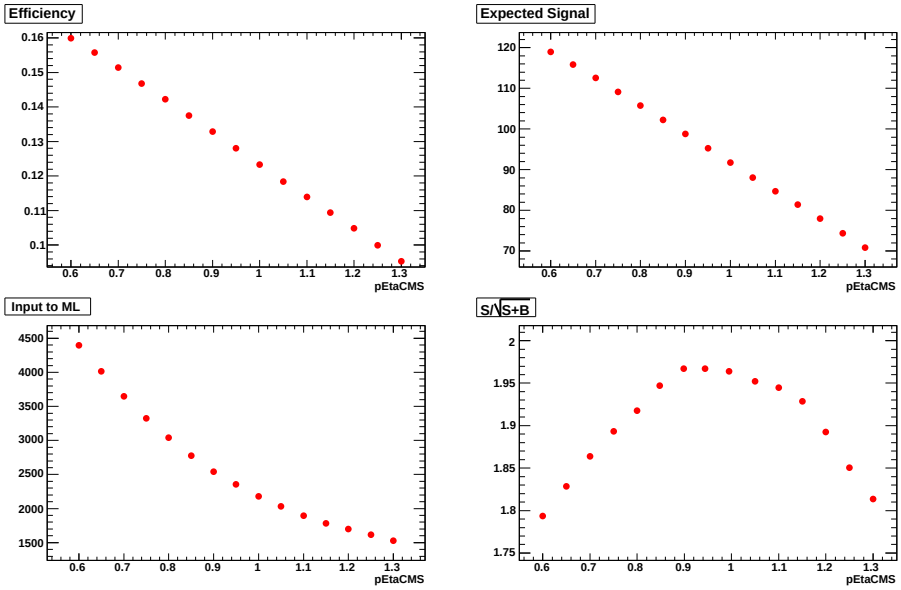

Figure 6.11: Optimization of the cut on momentum of η in CMS frame for $\eta K\gamma$ analysis, using the maximization of statistical significance (in this case we show the optimization for the $\eta_{\gamma\gamma}K^{\pm}\gamma$ mode, but similar analysis has been performed for all modes). We show the efficiency (left upper plot), the expected number of signal yield (right upper plot), the number of events of on-peak sample as input to ML (left lower plot), and the statistical significance (right lower plot), defined as $S/\sqrt{S+B}$, where S and B are the number of expected signal and background yields, when we vary the cut on momentum of η in CMS frame.

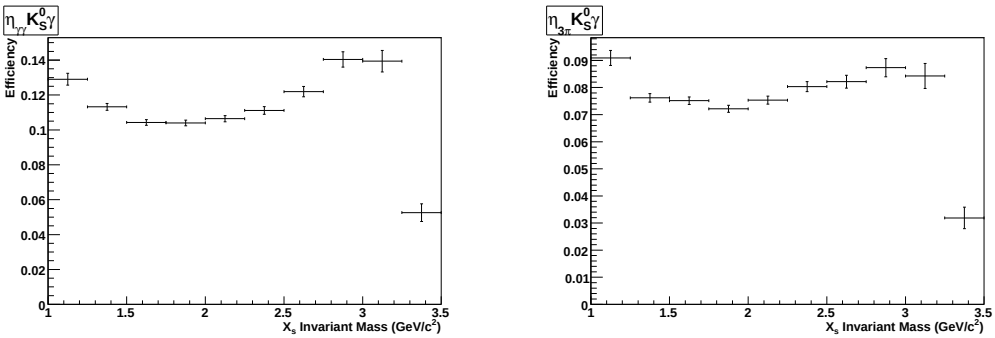

Figure 6.12: Efficiency as a function of $X_s(\eta K^0_S)$ effective mass in the decay mode $B^0 \to \eta K^0_S\gamma$: left $\eta \to \gamma\gamma$, right $\eta \to \pi^+\pi^-\pi^0$.

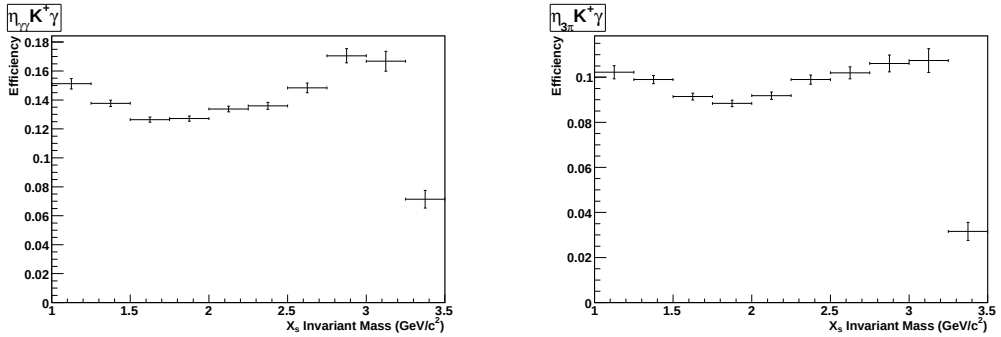

Figure 6.13: Efficiency as a function of $X_s(\eta K^{\pm})$ effective mass in the decay mode $B^{\pm} \to \eta K^{\pm}\gamma$: left $\eta \to \gamma\gamma$, right $\eta \to \pi^+\pi^-\pi^0$.

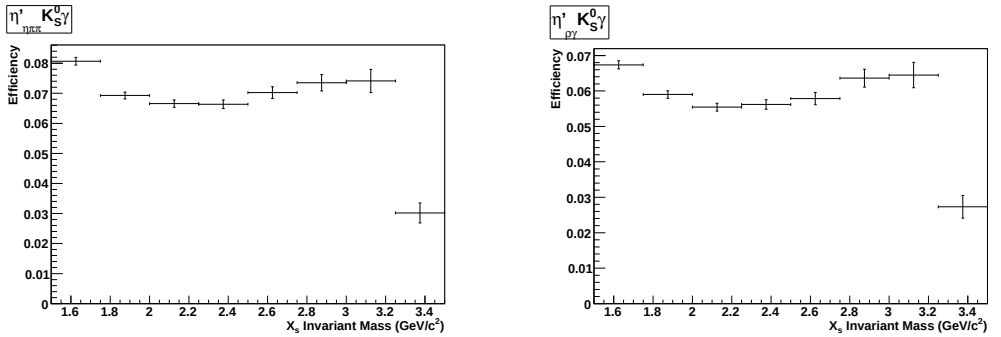

Figure 6.14: Efficiency as a function of $X_s(\eta' K^0_S)$ effective mass in the decay mode $B^0 \to \eta' K^0_S\gamma$: left $\eta' \to \eta\pi^+\pi^-$, right $\eta' \to \rho^0\gamma$.

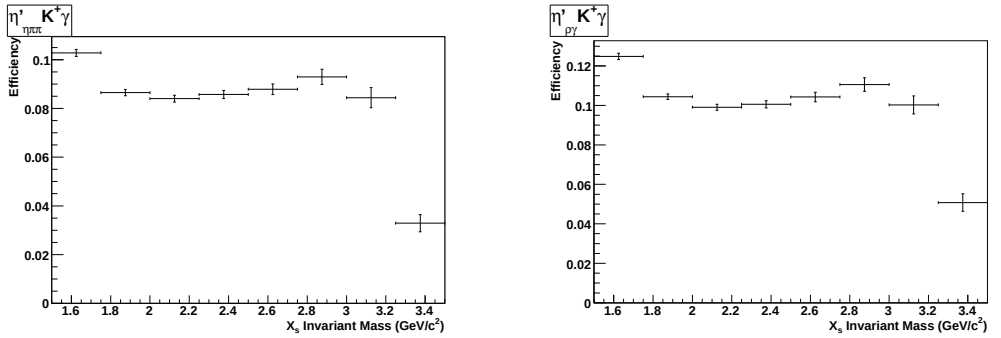

Figure 6.15: Efficiency as a function of $X_s(\eta' K^{\pm})$ effective mass in the decay mode $B^{\pm} \to \eta' K^{\pm}\gamma$: left $\eta' \to \eta\pi^+\pi^-$, right $\eta' \to \rho^0\gamma$.

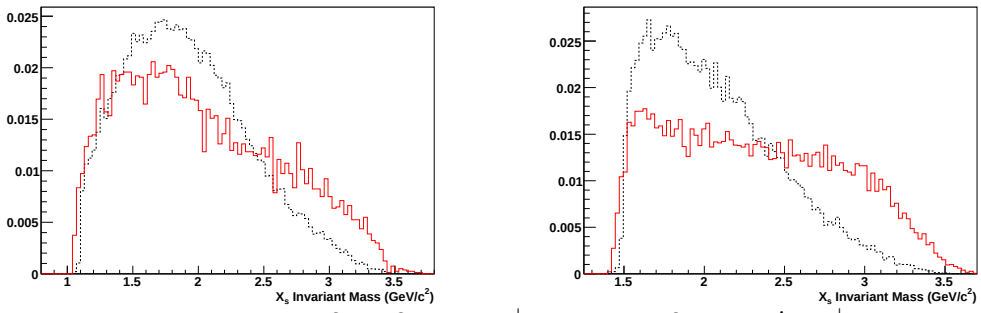

Figure 6.16: Invariant mass of X_s for $\eta_{\gamma\gamma}K^{\pm}\gamma$ mode (left) and $\eta'_{\rho\gamma}K^{\pm}\gamma$ mode (right): black dashed line refers to MC signal events, red solid line to on-peak data.

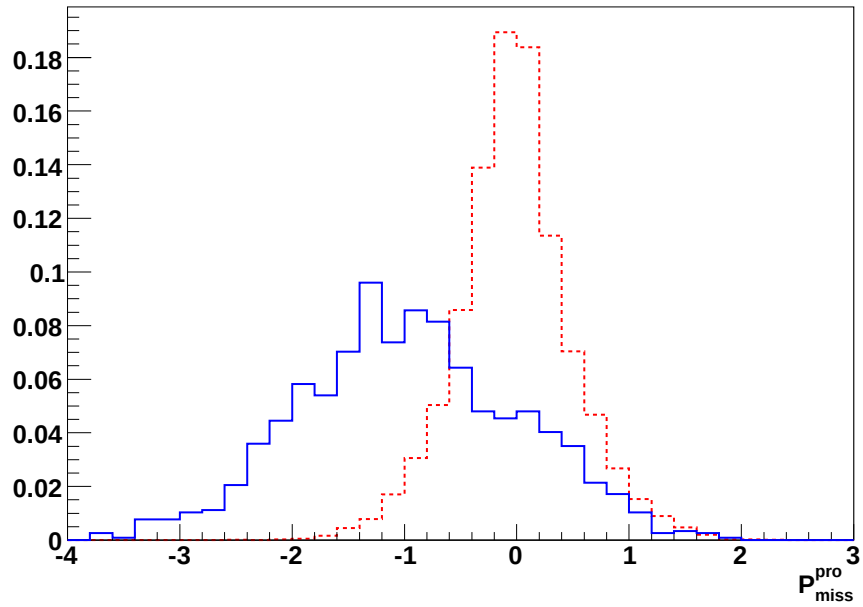

Figure 6.17: P^{pro}_{miss}: comparison between MC signal events (red dashed line) and off-peak data (blue solid line) for the $\eta'_{\eta\pi\pi}K^0_L$ mode.

Specific Selection Cuts for $\eta' K^0_L$ analysis

For $\eta' K^0_L$ mode, we consider specific further cuts to suppress the background.

- cut on transverse Missing Momentum P^{pro}_{miss}. We calculate the K^0_L missing momentum P_{miss} from all tracks (`GoodTracksLoose`) and EMC clusters (`CalorClusterNeutral`) excluding the K^0_L candidate. Then we project it onto the axis of the K^0_L candidate in the transverse plane to the beam direction and we subtract from this projection the transverse momentum of the K^0_L candidate. In this way we obtain the transverse missing projected momentum P^{pro}_{miss}. We show in fig. 6.17 the comparison between the distribution of P^{pro}_{miss} for off-peak data and MC signal events. We optimize the value of the cut using the statistical significance. We use MC signal events as signal events and off-peak data as background events. The optimization is shown in fig. 6.18. The best cut is -0.5.

- cut on $\cos\theta_{P_{miss}} < 0.95$, defined as the cosine of the polar angle of missing momentum with respect to the beam direction in the laboratory frame. The variable distribution is shown in fig. 6.19.

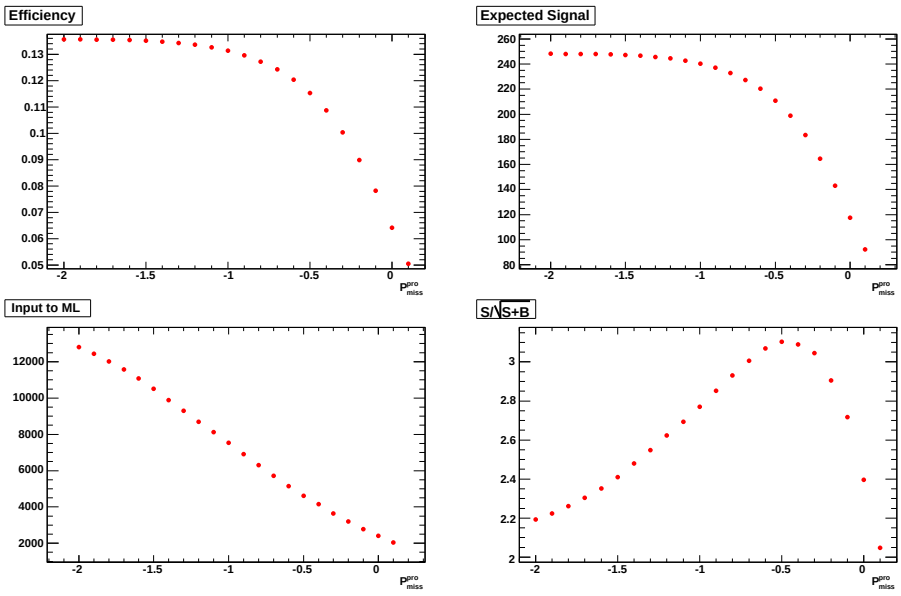

Figure 6.18: Optimization procedure for the cut on P^{pro}_{miss}, referred to $\eta'_{\eta\pi\pi}K^0_L$ mode (see fig. 6.11 caption for a description of the plots).

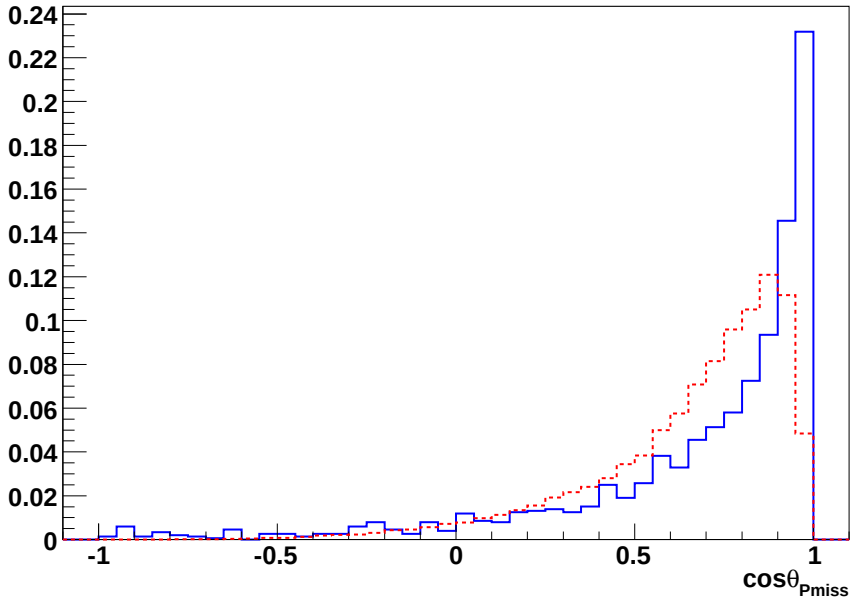

Figure 6.19: $\cos\theta_{P_{miss}}$: comparison between MC signal events (red dashed line) and off-peak data (blue solid line) for $\eta'_{\eta\pi\pi}K^0_L$ mode.

- we cut on the output of a Neural Network (NN) to suppress the background from fake K_L^0 in EMC. We use the TNeuNet package [85], which gives small feed forward networks using the common learning method of vanilla back propagation and working in the ROOT framework. The net has 7 input variables, 1 layer with 10 hidden units and only one ouput, trained to give 0 for background events and 1 for signal events. The input variables used are:
  - *Number of crystals*
  - *Second moment:*
    $$\frac{\sum E_i \cdot r_i^2}{\sum E_i},$$
    where E_i is the energy of crystal i and r_i is the distance of crystal i to the cluster center.
  - *Lateral moment:*
    $$\frac{\sum_{i=2,n} E_i \cdot r_i^2}{(\sum_{i=2,n} E_i \cdot r_i^2) + 25(E_0 + E_1)},$$
    with the crystals in descending energy order.
  - *S1/S9:* The energy of the most energetic crystal (S1) divided by the energy sum of the 3x3 crystal block (S9) with the most energetic crystal in it's center.
  - *S9/S25:* The energy sum of the 3x3 crystal block (S9) with the most energetic crystal in it's center, divided by the energy sum of the 5x5 crystal block (S25) with the most energetic crystal in it's center.
  - *Zernike moments* $|Z_{20}|$, $|Z_{42}|$. The spatial energy distribution of a cluster can be developed as a serie of Zernike polynomials:
    $$E(xE, y) \rightarrow \sum_{n,m} Z_{n,m} \cdot \zeta_{n,m}(r, \phi),$$
    where r is a dimensionless parameter between 0 and 1.

  The variables are shown in fig. 6.20 for MC signal and off-peak events.

  For the training we use events of $\eta'_{\eta\pi\pi} K_L^0$ mode. The training configuration is the following: 1000 events for both signal and background samples as training samples and independent samples of 400 signal events and 400 background events

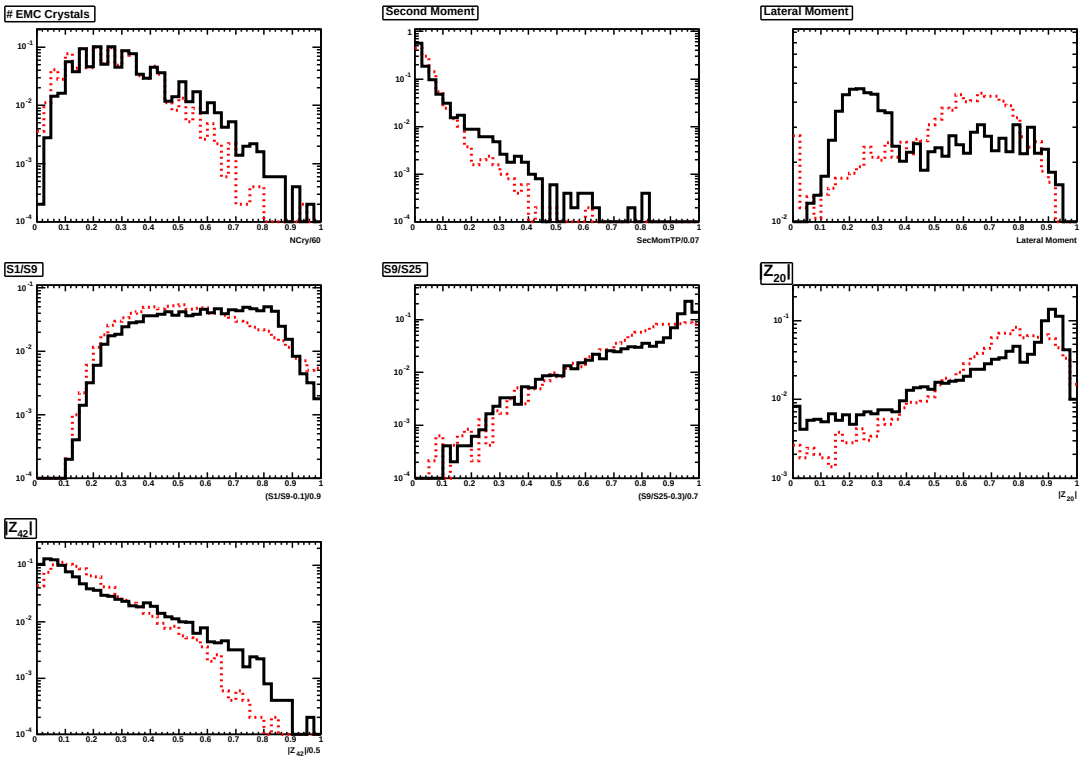

Figure 6.20: Comparison between Neural Network variables for MC signal (black solid line) and continuum background (red dashed line) for K_L^0 selection in $\eta' K_L^0$ analysis.

for validation. We use off-peak events for background events and MC signal events as signal events. The learning parameter is 0.05 and we have performed 5000 cycles for the training. In fig. 6.21 we show the NN errors and the efficiency versus background rejection power plot. The output of the NN is shown in fig. 6.22. We apply a lower cut on the NN output in order to increase the purity of the K_L^0 sample, and this selection has been optimized according to the statistical significance. The results of this study are shown in fig. 6.23. The best cut is found to be 0.4. This cut retains 88% of the EMC events (from MC signal events) and rejects 50% of EMC events of the on-peak samples. If we consider also IFR events, the effect of the cut for the signal events is to retain 92% of events.

To check our NN, we have reconstructed $B^0 \to J/\psi\, K_L^0$ events as control sample. We use the same events selection as in the standard analysis of this mode [112],

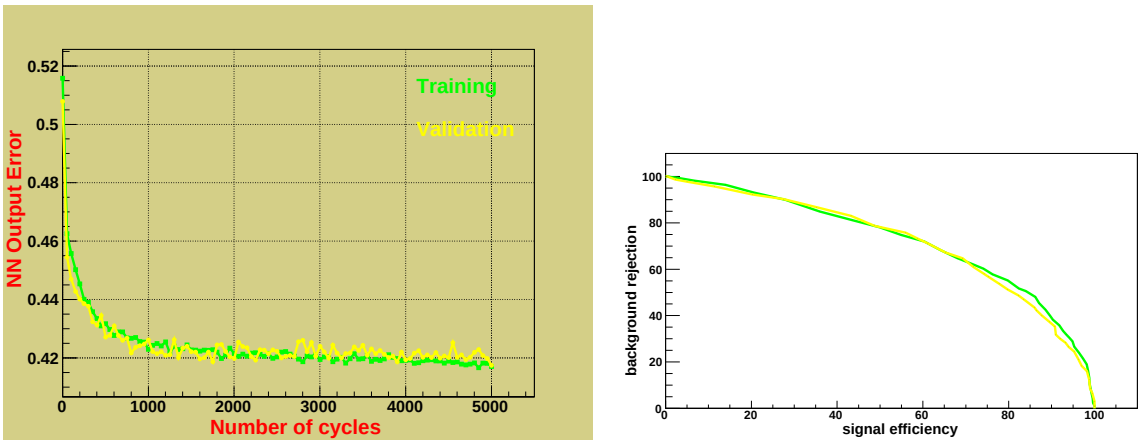

Figure 6.21: Left: Neural Network Error as a function of the number of training cycles. Right: MC signal efficiency versus background rejection plot.

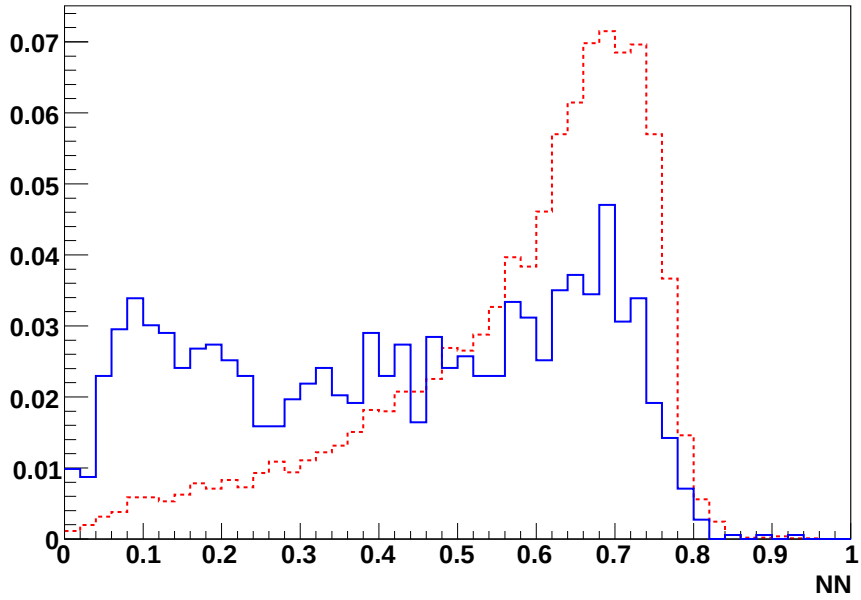

Figure 6.22: Neural network output for MC signal events (red dashed line) and on-peak data (blue solid line) for $\eta'_{\eta\pi\pi}K^0_L$ mode.

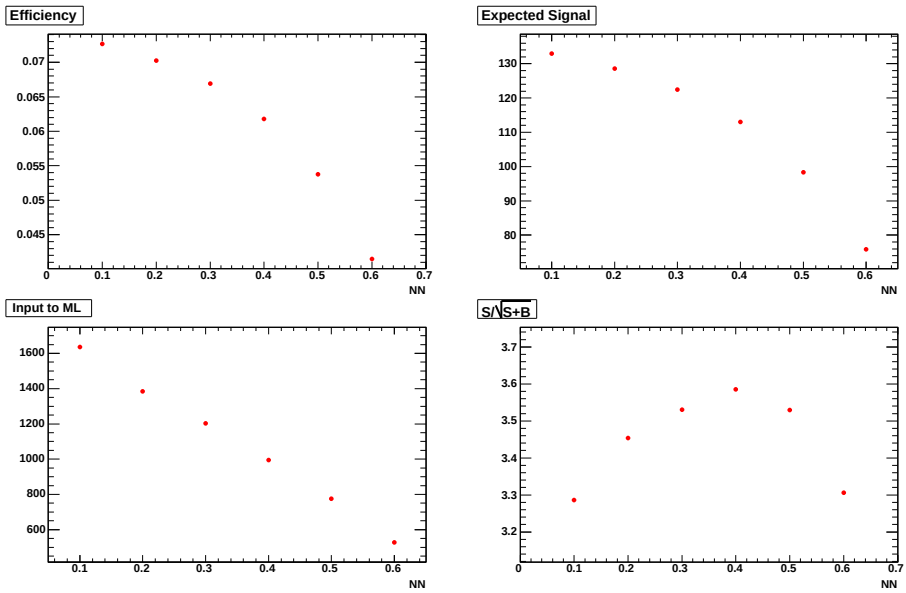

Figure 6.23: Studies of Neural Network variables for the Neural Network optimization (only EMC events) for $\eta'_{\eta\pi\pi}K^0_L$ mode.

but a tight cut on $J/\psi \rightarrow l^+l^-$ invariant mass in order to reduce the combinatoric background and to improve the K^0_L purity of the sample: $3.040 < m(l^+l^-) < 3.162$ GeV/c^2 (about 4.0σ from nominal mass). For the K^0_L selection we use our reconstruction technique. Most of the background comes from other B decays, especially $B^{(0,+)} \rightarrow J/\psi\, K^{*(0,+)}$, with K^* decaying into $K^0_L\pi$ [112]. These events therefore are good candidates for our K^0_L control sample. Of course, we are interested to the events where the K^0_L is reconstructed in EMC. We show in the fig. 6.24 the ΔE distribution for these events after the selection. In the figs. 6.25 and 6.26 we show the comparison between the input variables of NN and the output of NN for $\eta'_{\eta\pi\pi}K^0_L$ MC signal events, $J/\psi\, K^0_L$ MC signal events and $J/\psi\, K^0_L$ on-peak events. For the last sample we require $|\Delta E| < 0.01$ GeV. We fit the ΔE variable using a Crystal Ball PDF [2] for signal events and an Argus PDF for background events in order to extract the fraction of $J/\psi\, K^0_L$ signal events in the input sample. In this way we don't consider properly the background because we should consider two components of background: the inclusive-J/ψ background component (dominant) and the non-J/ψ background component. However we want to have just an estimation of the signal events

[2] A Crystal Ball function is a Gaussian with an exponential tail.

fraction. In the fig. 6.27 we show an example of such a fit. The parameters of the exponential tail are taken from a fit to $J/\psi K_L^0$ MC events using only a Crystal Ball PDF (fig. 6.27). The parameters of the Gaussian are free in the fit to real data, in which we don't use any cut on NN. Then we fix them in the other fits, in which we cut on NN. The Argus parameter and the signal fraction are determinated for every fit with different NN cuts. In the tab. 6.2 we show the signal fraction when we apply different cuts on NN output. We can see how the signal fraction increases applying tighter cuts. This can be also seen in the fig. 6.28.

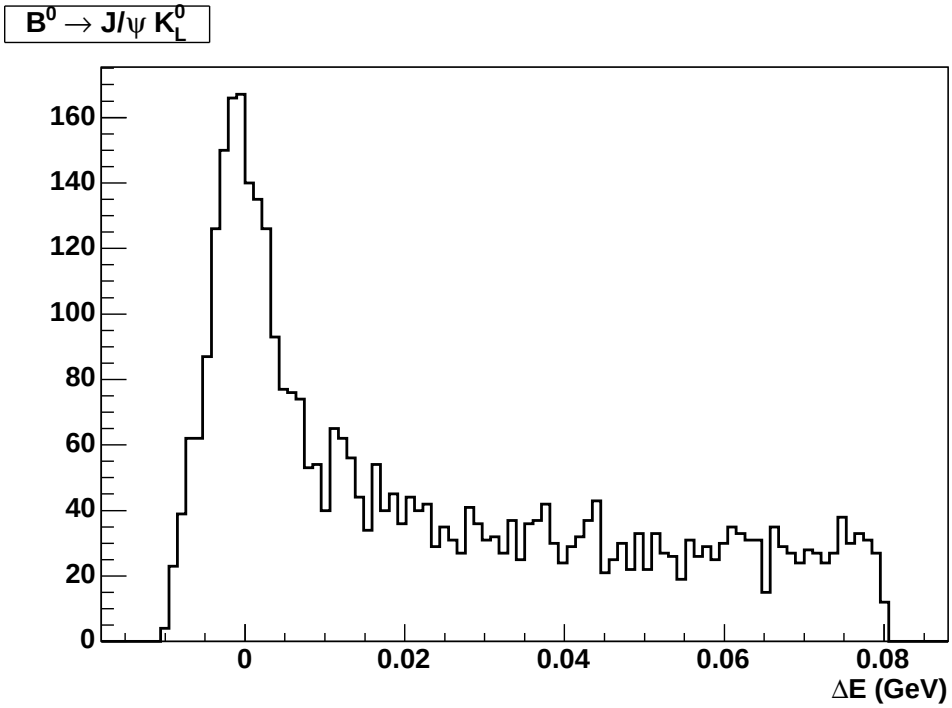

Figure 6.24: ΔE distribution for $B^0 \rightarrow J/\psi K_L^0$ events. The sample is composed of 3913 events.

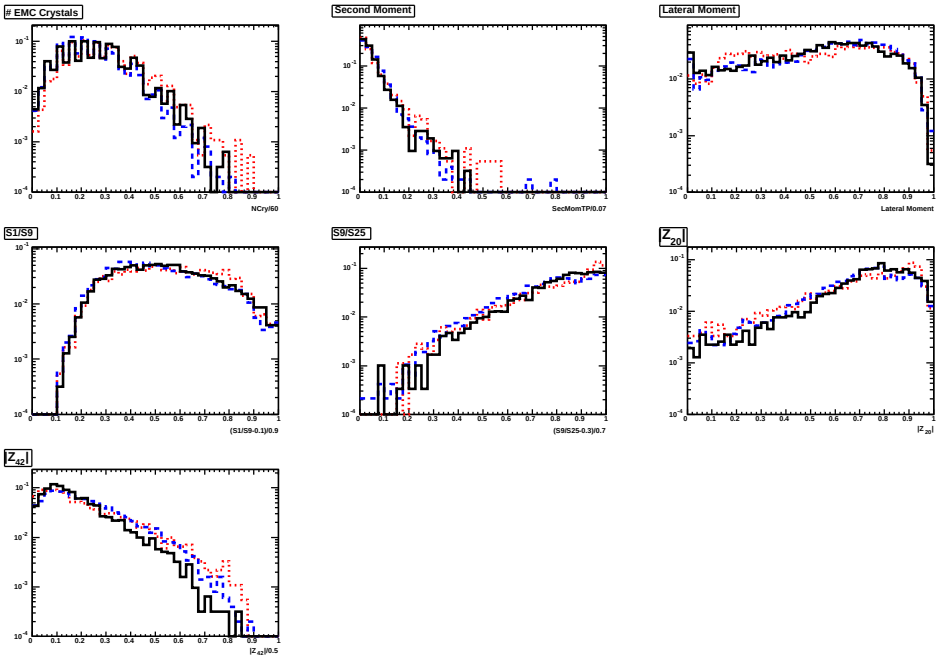

Figure 6.25: Comparison between Neural Network variables for $\eta'_{\eta\pi\pi}K^0_L$ MC signal events (black solid line), $J/\psi\,K^0_L$ MC signal events (blue dashed line) and $J/\psi\,K^0_L$ on-peak events (red dotted line). For the last sample we require $|\Delta E| < 0.01$ GeV.

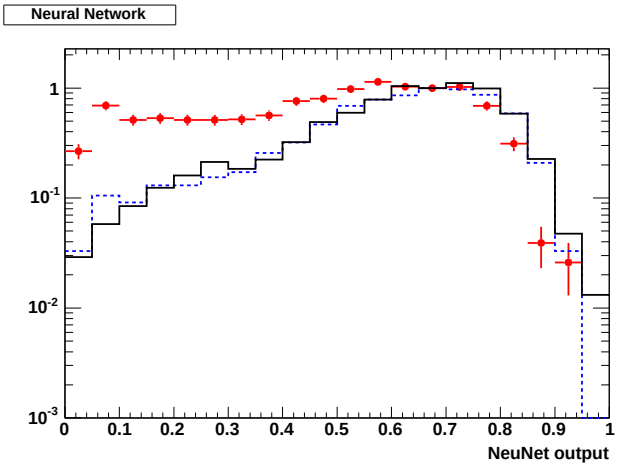

Figure 6.26: Comparison between Neural Network output for $\eta'_{\eta\pi\pi}K^0_L$ MC signal events (black solid line), $J/\psi\,K^0_L$ MC signal events (blue dashed line) and $J/\psi\,K^0_L$ on-peak events (red dotted line). For the last sample we require $|\Delta E| < 0.01$ GeV. The three distributions are normalized to the values of the bin corrisponding to 0.7.

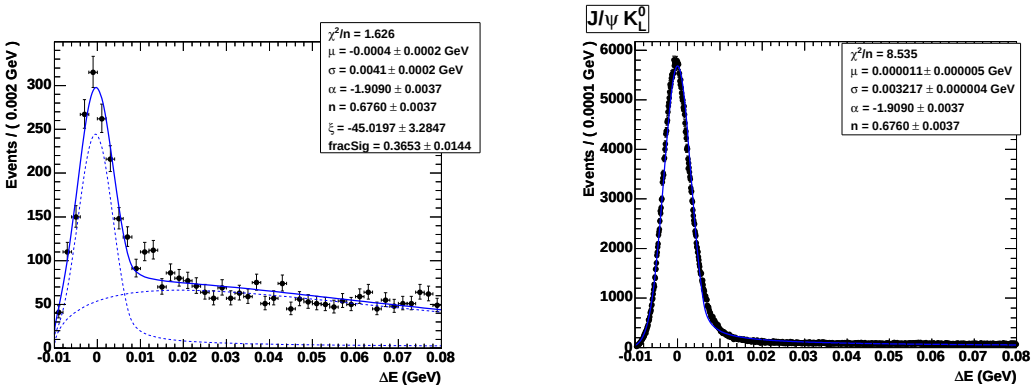

Figure 6.27: Left: ΔE fit of $J/\psi\, K_L^0$ data using a Crystal Ball PDF and an Argus PDF. No cut on Neural Network output is applied. Right: ΔE fit of $J/\psi\, K_L^0$ MC signal events using a Crystal Ball PDF.

NN output cut	# on-peak events	Signal fraction (%)
No cut	3913	36.5 ± 1.4
0.05	3827	36.6 ± 1.5
0.10	3609	36.9 ± 1.6
0.15	3410	37.7 ± 1.6
0.20	3244	37.7 ± 1.6
0.25	3064	38.3 ± 1.6
0.30	2882	38.4 ± 1.8
0.35	2690	38.8 ± 1.8
0.40	2480	39.7 ± 1.9
0.45	2244	40.0 ± 2.0
0.50	1946	42.0 ± 2.1
0.55	1639	42.6 ± 2.3

Table 6.2: $J/\psi\, K_L^0$ signal fraction when we apply different cut on Neural Network output.

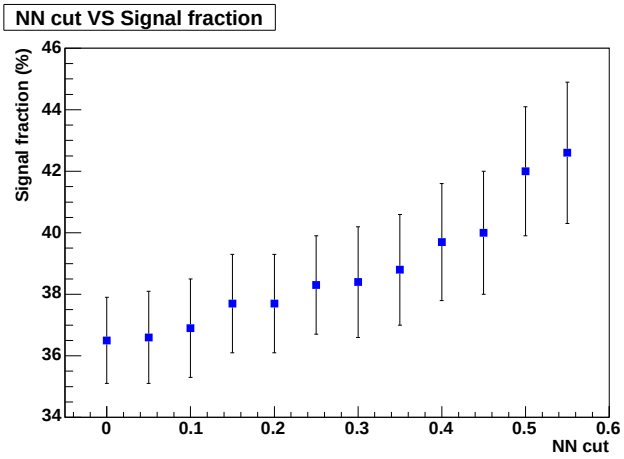

Figure 6.28: $J/\psi\, K^0_L$ signal fraction as function of the cut on Neural Network output.

Specific Selection Cuts for $\eta' K^{\pm}$ analysis

For the charged kaon in $B^{\pm} \to \eta' K^{\pm}$ decay, besides the electron and proton vetoes, we have also done the following requirements:

- number of measured DIRC Cherenkov photons at least equal to 5.
- We measure the DIRC Cherenkov angle θ_C with his error σ_{θ_C} and expected values for kaon hypotheses (θ_K), and we calculate the pull, defined as:

$$pull_K = \frac{\theta_C - \theta_K}{\sigma_{\theta_C}}. \tag{6.9}$$

  The pull is corrected for momentum, polar angle, charge and event run number dependences with a prescription for θ_C resolutions and offsets from expected values for kaons and pions. The distributions of the pull for $\eta'_{\rho\gamma} K^{\pm}$ and $\eta'_{\rho\gamma} \pi^{\pm}$ MC signal events are shown in fig. 6.29. We require the pull to be inside the range $[-5, +2]$ for pion and badly reconstructed candidates rejection. We should note that the branching fraction of the $B^{\pm} \to \eta' \pi^{\pm}$ mode is about 20 times smaller than $B^{\pm} \to \eta' K^{\pm}$ one. We will take in account the background arising from the misidentification of the kaon in pion as systematic effect.

Specific Selection Cuts for $\eta' K^0$ TD analysis

The following cuts are specific for TD analysis:

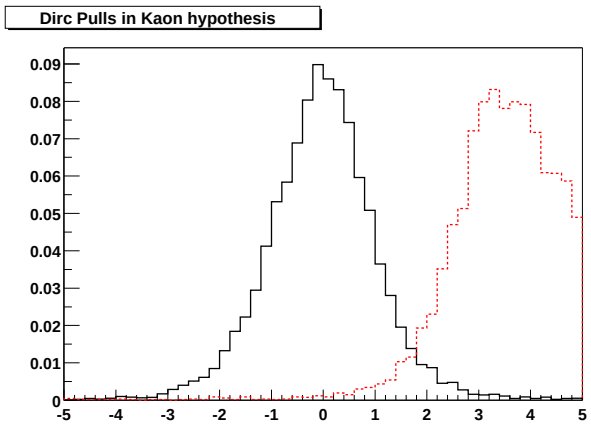

Figure 6.29: Distributions of the pull of DIRC Cherenkov angle in kaon hypothesis for the primary charged track of $\eta'_{\rho\gamma}K^{\pm}$ (black solid line) and $\eta'_{\rho\gamma}\pi^{\pm}$ (red dashed line) MC signal events.

- $|\Delta t| < 20$ ps;
- Δt per-event error $\sigma_{\Delta t} < 2.5$ ps;
- We consider only tagged events.

Chapter 7

Branching Fractions and Direct CP Asymmetry Measurements

7.1 Introduction

We describe in this chapter measurements of branching fractions and charge asymmetries in charmless B meson decays to $\eta' K^0$, $\eta' K^\pm$, $\eta K^0\gamma$, $\eta K^\pm\gamma$, and the results of a search for charmless quasi-two-body B^0 meson decays to ηK^0, $\eta\eta$, $\eta\phi$, $\eta'\phi$, for charmless radiative B meson decays to $\eta' K^0\gamma$, $\eta' K^\pm\gamma$, and for charmless three-body B meson decays to $\eta'\eta' K^0$, $\eta'\eta' K^\pm$, all through the decay modes shown in tab. 4.1 and tab. 4.2.[1] We extract the signal yields and the charge asymmetries using a maximum likelihood (ML) fit.

The large amount of data already accumulated by *BABAR* allows the study of rare charmless B decays to pseudoscalar–pseudoscalar (PP) mesons and pseudoscalar–vector (PV) mesons. Several groups studied these decays and made theoretical predictions for branching fractions under different hypotheses. Some groups study these decays using flavor SU(3) symmetry [14, 86]. Other groups base their calculation using the factorization approach [87]. Recently two QCD approaches have been proposed: perturbative QCD [88] and QCD factorization [15, 89]. The rates of some to these modes appear also in the calculation of upper bounds on the deviation of the S parameter, measured in the time-dependent analysis of $b \to s$ decay modes, from the $\sin 2\beta$ value [13, 14]. In particular, the $B^0 \to \eta\eta$ rate, studied here, appears in the

[1] For the $\eta' K$ modes we use the dominant decay modes with $\eta' \to \eta_{\gamma\gamma}\pi^+\pi^-$, $\eta' \to \rho^0\gamma$, $K^0 \to K^0_s \to \pi^+\pi^-$.

calculation of upper bound on the deviation of the S parameter measured in $\eta' K^0$ (see section 8.2 for a description of this upper bound measurement).

There is an important issue related to the branching fractions of $\eta^{(\prime)} K$ (charged and neutral) modes. Since the discovery of $B \to \eta' K$ in 1997 [17] with high branching fraction (higher than expected), it was found that the corresponding mode with η is suppressed. This fact was pointed out by Lipkin in 1991 [18]. In particular, using arguments concerning the $\eta - \eta'$ mixing angle and the parity of K or K^* we can say that $\eta' K$ and ηK^* are enhanced, while ηK and $\eta' K^*$ are suppressed. This scheme is experimentally verified. The branching fraction of all these modes has been already measured, but the $B^0 \to \eta K^0$. So it is important to measure also this mode to complete the scenario.

Radiative B decays have an important role in the test of the Standard Model of electroweak interactions. Inclusive radiative B decays, proceeding mainly trough $b \to s\gamma$, have already been measured [36]. Only a few exclusive final states have been considered so far [41]. Such decays are interesting also for the possibility to study mixing-induced CP violation [19]. Here we study the radiative B decays to $\eta K \gamma$ and $\eta' K \gamma$.

As shown by T. Gershon and M. Hazumi [20] time-dependent CP asymmetries can be measured in all $B^0 \to P^0 P^0 X^0$ where P^0 and X^0 are CP eigenstate, spin 0, neutral particles. So far the time-dependent CP asymmetries have been measured only in the modes $B^0 \to \pi^0 \pi^0 K^0_S$ and $B^0 \to K^0_S K^0_S K^0_S$ [41]. Here we report the search of $B \to \eta' \eta' K$ modes.

In the charged channels direct CP violation can be detected as a charge asymmetry from the time-integrated decay rate differences between the two charged modes:

$$\mathcal{A}_{ch} = \frac{\Gamma(B^- \to f^-) - \Gamma(B^+ \to f^+)}{\Gamma(B^- \to f^-) + \Gamma(B^+ \to f^+)} \tag{7.1}$$

In this thesis work we measure the charged asymmetries for $f^\pm = \eta' K^\pm$ and $f^\pm = \eta K^\pm \gamma$. Standard Model estimates are quite small however [89, 90].

7.2 Previous Results

The measurements for the $\eta' K$ modes are updates of previous *BABAR* measurements with an integrated luminosity of 82 fb^{-1} [91]. These previous measurements are sum-

Mode	Sig. Yield	$\epsilon \times \prod \mathcal{B}_i$(%)	$\mathcal{B} \times 10^{-6}$	$\mathcal{A}_{ch}$ (%)
$\eta'_{\rho\gamma}K^0$	155 ± 17	2.32	76 ± 8	
$\eta'_{\eta\pi\pi}K^0$	48 ± 8	1.32	42 ± 7	
$\eta' K^0$			61 ± 6	
$\eta'_{\rho\gamma}K^\pm$	514 ± 31	7.08	82 ± 5	6.3 ± 5.9
$\eta'_{\eta\pi\pi}K^\pm$	268 ± 19	4.35	71 ± 5	-0.1 ± 6.8
$\eta' K^\pm$			77 ± 4	3.7 ± 4.5

Table 7.1: Previous *BABAR* results for B decays to $\eta' K$. We report number of signal yields, detection efficiency ϵ, daughter branching fraction product $\prod \mathcal{B}_i$, measured branching fraction $\mathcal{B}$, and charge asymmetry (only charge modes) with statistical error for each decay mode. For the combined measurements we give the branching fraction and charge asymmetry with statistical uncertainty.

marized in tab. 7.1.

The previous *BABAR* results for the other PP and PV modes studied here are summarized in tab. 7.2. The measurements have been done using an integrated luminosity of 82 fb^{-1} for $\eta\eta$, $\eta\phi$, $\eta'\phi$ [92] modes and 211 fb^{-1} for ηK^0 mode [93].

There are not previous *BABAR* measurements for $B \to \eta K\gamma$ modes. Previous measurements have been published by Belle Collaboration [96], using 253 fb^{-1}, which observed these modes for the first time. The results are shown in tab. 7.3.

There are not previous measurements for B decays to $\eta' K\gamma$ and $\eta'\eta' K$, which are measured for the first time.

7.3 Data and Monte Carlo Samples

The analyses presented in this document are based on the data taken by *BABAR* in the period 1999-2006 (`Run1-Run5`). We processed both the data and Monte Carlo samples. The reconstruction is described in chapter 4. Depending on the modes, we use different integrated luminosities for on-peak data:

- $\eta'\eta' K$: 207 fb^{-1}, 228 ± 3 million of $B\overline{B}$ pairs.
- $\eta' K$, $\eta^{(\prime)} K\gamma$: 211 fb^{-1}, 232 ± 3 million $B\overline{B}$ pairs.
- ηK^0_S, $\eta\eta$, $\eta\phi$, $\eta'\phi$: 288 fb^{-1}, 324 ± 4 million of $B\overline{B}$ pairs.

Mode	Sig. Yield	ϵ(%)	$\prod \mathcal{B}_i$(%)	$\mathcal{S}$	$\mathcal{B}$	90% CL U.L.	Th. Pred.
$\eta_{\gamma\gamma}K^0$	$14.1^{+8.5}_{-7.3}$	27.5	13.5	2.3	$1.6^{+1.0}_{-0.9}$		
$\eta_{3\pi}K^0$	$4.2^{+4.8}_{-3.4}$	21.0	7.8	1.4	$1.1^{+1.3}_{-0.9}$		
ηK^0				2.6	$1.5 \pm 0.7 \pm 0.1$	2.5	$1-2$
$\eta_{\gamma\gamma}\eta_{\gamma\gamma}$	$-7.5^{+6.9}_{-5.9}$	21.6	15.5	0.0	$-2.4^{+2.3}_{-2.0}$		
$\eta_{\gamma\gamma}\eta_{3\pi}$	$0.6^{+6.8}_{-5.8}$	16.9	17.9	0.1	$0.4^{+2.5}_{-2.2}$		
$\eta_{3\pi}\eta_{3\pi}$	$-0.1^{+3.5}_{-2.3}$	12.3	5.1	0.0	$-0.4^{+6.2}_{-4.2}$		
$\eta\eta$				0.0	$-0.9^{+1.6}_{-1.4} \pm 0.7$	2.8	$0.06-14$
$\eta_{\gamma\gamma}\phi$	$-10.1^{+5.0}_{-3.9}$	29.7	19.4	0.0	$-2.0^{+1.0}_{-0.7}$		
$\eta_{3\pi}\phi$	$-2.0^{+2.9}_{-1.6}$	20.9	11.1	0.0	$-0.9^{+1.4}_{-0.8}$		
$\eta\phi$	$-$	$-$	$-$	0.0	$-1.4^{+0.7}_{-0.4} \pm 0.2$	1.0	$0.001-0.1$
$\eta'_{\eta\pi\pi}\phi$	$0.5^{+4.0}_{-3.0}$	23.2	8.6	0.1	$0.3^{+2.2}_{-1.7}$		
$\eta'_{\rho\gamma}\phi$	$8.0^{+8.1}_{-6.9}$	22.0	14.5	1.2	$2.8^{+2.9}_{-2.4}$		
$\eta'\phi$	$-$	$-$	$-$	0.8	$1.5^{+1.8}_{-1.5} \pm 0.4$	4.5	$0.001-0.1$

Table 7.2: Previous *BABAR* results for B^0 decays to ηK^0, $\eta\eta$, $\eta\phi$, $\eta'\phi$. We report number of signal yields, detection efficiency ϵ, daughter branching fraction product $\prod \mathcal{B}_i$, significance $\mathcal{S}$, and measured branching fraction $\mathcal{B}$ with statistical error for each decay mode. For the combined measurements we give the significance (with systematic uncertainties included), the branching fraction with statistical and systematic uncertainty, the 90% CL upper limit (U.L.), and theoretical predictions. Branching fractions, 90% CL U.L. and theoretical predictions are in units of 10^{-6}. For the ranges of theoretical predictions see refs. [94] and [95].

MC signal statistics used for the different modes can be seen in tab. 7.4. For the $\eta^{(\prime)}K\gamma$ modes we use in the generation the Kagan-Neubert model [97] (with $m_b = 462$ and $\lambda_1 = -0.39$).

Several million of generic $B\overline{B}$ MC events (charged and neutral) are used for background studies (about 5 times than the on-peak statistics). For more accurate background studies, we reconstruct specific exclusive $B\overline{B}$ MC events (see section 7.6).

7.4 Preparation of the input to ML fit

The events for each mode are reconstructed (chapter 4) and selected (chapter 6). For each event we can have more candidates due to the possible different combinations of the reconstructed particles of the event. To prepare the samples for the input to ML fits, we have to choose one of these candidates per event (of course, in the case of multiple candidates per event). In this way we obtain the final input to ML fits. In this sections

Mode	Sig. Yield	$\epsilon \times \prod \mathcal{B}_i$(%)	$\mathcal{S}$	$\mathcal{B} \times 10^{-6}$
$B^{\pm} \to K^{\pm}\eta\gamma$	$81 \pm 14^{+10}_{-6}$	3.50 ± 0.27	6.8	$8.4 \pm 1.5^{+1.2}_{-0.9}$
$B^0 \to K^0\eta\gamma$	$20.9^{+7.3+4.2}_{-6.5-3.2}$	0.87 ± 0.08	3.4	$8.7^{+3.1+1.9}_{-2.7-1.6}$
$B \to K\eta\gamma$	$102 \pm 16^{+13}_{-8}$	4.37 ± 0.31	7.7	$8.5 \pm 1.3^{+1.2}_{-0.9}$

Table 7.3: Belle results for B decays to $\eta K\gamma$. We report number of signal yields, detection efficiency ϵ, daughter branching fraction product $\prod \mathcal{B}_i$, significance $\mathcal{S}$, and measured branching fraction $\mathcal{B}$. The first errors are statistical, the seconds systematic.

we will report the events selection efficiencies and multiple candidates selection. The reconstruction and selection of the events for $\eta' K$ analysis have been done by another group of the *BABAR* collaboration which has participated to this analysis.

7.4.1 Selection Cut Efficiencies

We report in the tables 7.5–7.14 the selection efficiencies for each cut applied to the reconstructed events of on-peak data and MC signal. Explanation of the cuts is given in section 6.4.2. The efficiencies for each row of the tables are computed after applying all the cuts in the previous rows. For the signal MC samples we give in the final row the raw efficiency, calculated as the ratio of the number of events input to ML and the number of generated MC signal events (table 7.4). Results for the MC events are shown in tables 7.5–7.9. The same informations for on-peak data are shown in tables 7.10–7.14. For these tables the last row gives the number of candidates surviving to all cuts and entering in the input to ML fit.

$\eta'_{\eta\pi\pi}\eta'_{\eta\pi\pi}K^0_S$ 117K	$\eta'_{\eta\pi\pi}\eta'_{\rho\gamma}K^0_S$ 117K	$\eta'_{\eta\pi\pi}\eta'_{\eta\pi\pi}K^\pm$ 117K	$\eta'_{\eta\pi\pi}\eta'_{\rho\gamma}K^\pm$ 117K
$\eta'_{\rho\gamma}K^0_{S+-}$ 896K	$\eta'_{\eta\pi\pi}K^0_{S+-}$ 1105K	$\eta'_{\rho\gamma}K^\pm$ 145K	$\eta'_{\eta\pi\pi}K^\pm$ 127K
$\eta_{\gamma\gamma}K^0_S\gamma$ 232K	$\eta_{3\pi}K^0_S\gamma$ 232K	$\eta_{\gamma\gamma}K^0_S\gamma$ 234K	$\eta_{3\pi}K^0_S\gamma$ 234K
$\eta'_{\rho\gamma}K^0_S\gamma$ 234K	$\eta'_{\eta\pi\pi}K^0_S\gamma$ 234K	$\eta'_{\rho\gamma}K^\pm\gamma$ 232K	$\eta'_{\eta\pi\pi}K^\pm\gamma$ 234K
$\eta_{\gamma\gamma}K^0_S$ 134K	$\eta_{3\pi}K^0_S$ 134K		
$\eta_{\gamma\gamma}\eta_{\gamma\gamma}$ 148K	$\eta_{\gamma\gamma}\eta_{3\pi}$ 148K	$\eta_{3\pi}\eta_{3\pi}$ 148K	
$\eta_{\gamma\gamma}\phi$ 74K	$\eta_{3\pi}\phi$ 74K	$\eta'_{\eta\pi\pi}\phi$ 74K	$\eta'_{\rho\gamma}\phi$ 74K

Table 7.4: Monte Carlo signal events used for the different modes.

Table 7.5: Efficiency (%) and selection cuts (all candidates per event) in $\eta'\eta'K$ MC samples (see text for details).

	$\eta'_{\eta\pi\pi}\eta'_{\eta\pi\pi}K^0_S$	$\eta'_{\eta\pi\pi}\eta'_{\rho\gamma}K^0_S$	$\eta'_{\eta\pi\pi}\eta'_{\eta\pi\pi}K^\pm$	$\eta'_{\eta\pi\pi}\eta'_{\rho\gamma}K^\pm$
Generated	117000	117000	117000	117000
Preliminary cuts	33205	60053	42409	62288
PID vetoes	93.9	90.2	91.9	80.1
PID Fast Particle			75.9	75.2
γ energy		58.2		58.3
η (1) mass	86.1	85.0	86.6	85.8
η (2) mass	85.1		85.0	
ρ^0 mass		96.3		96.6
ρ^0 Helicity		94.8		94.5
$\eta'_{\eta\pi\pi}$ (1) mass	82.9	81.1	83.1	82.8
$\eta'_{\eta\pi\pi}$ (2) or $\eta'_{\rho\gamma}$ mass	80.3	76.2	81.3	78.0
K^0_S mass	95.2	95.9		
K^0_S cuts	93.1	94.7		
Fisher cut	99.4	99.4	99.5	99.6
Raw efficiency	5.7	7.1	6.5	5.9

Table 7.6: Efficiency (%) and selection cuts (all candidates per event) in $\eta K\gamma$ MC samples (see text for details).

	$\eta_{\gamma\gamma}K^0_S\gamma$	$\eta_{3\pi}K^0_S\gamma$	$\eta_{\gamma\gamma}K^\pm\gamma$	$\eta_{3\pi}K^\pm\gamma$
Generated	232000	232000	234000	234000
Preliminary cuts	118293	60066	159635	85616
Fast Gamma cuts:				
Energy	91.8	98.3	92.7	98.5
Second Moment	99.1	99.1	99.1	99.1
Cosine of theta angle	97.6	98.3	97.6	98.3
π^0 and η veto	86.4	88.2	86.8	88.6
Isolation from neutral bumps	94.1	94.6	94.6	94.2
Isolation from tracks	98.1	97.9	97.9	98.0
PID vetoes		97.3		96.3
PID Fast Particle			72.2	72.2
π^0 mass		74.9		75.0
η mass	87.5	97.0	87.2	97.3
η helicity	82.2		82.3	
K^0_S mass	87.6	90.1		
K^0_S cuts	92.0	93.3		
Fisher cut	99.6	99.6	99.7	99.6
π^0 veto for $\eta_{\gamma\gamma}$	88.5		88.4	
η momentum cut	67.0	78.6	68.2	79.8
X_s mass	99.5	99.6	99.5	99.7
Raw efficiency	11.0	7.6	13.4	9.3

Table 7.7: Efficiency (%) and selection cuts (all candidates per event) in $\eta' K\gamma$ MC samples (see text for details).

	$\eta'_{\eta\pi\pi}K^0_S\gamma$	$\eta'_{\rho\gamma}K^0_S\gamma$	$\eta'_{\eta\pi\pi}K^\pm\gamma$	$\eta'_{\rho\gamma}K^\pm\gamma$
Generated	234000	234000	234000	232000
Preliminary cuts	48237	40356	75461	95233
Fast Gamma cuts:				
Energy	98.3	98.7	98.6	98.9
Second Moment	99.2	99.1	99.2	99.1
Cosine of theta angle	98.6	98.3	98.3	98.0
π^0 and η veto	87.0	87.9	87.4	87.9
Isolation from neutral bumps	94.2	94.5	94.4	94.4
Isolation from tracks	97.8	97.7	97.9	97.9
PID vetoes	98.4	94.7	96.3	82.7
PID Fast Particle			63.8	65.6
η or ρ mass	91.5	99.3	91.4	99.4
ρ helicity		95.3		95.6
η' mass	98.3	100.0	98.7	100.0
K^0_S mass	84.9	84.1		
K^0_S cuts	91.0	91.0		
Fisher cut	99.5	99.5	99.6	99.6
η' momentum cut	81.2	76.0	81.1	76.9
X_s mass	99.5	99.5	99.5	99.4
$\eta'\gamma$ mass veto	95.8	91.3	96.5	92.3
Raw efficiency	6.8	5.5	8.6	9.9

Table 7.8: Efficiency (%) and selection cuts (all candidates per event) in ηK^0_S and $\eta\eta$ MC samples (see text for details).

	$\eta_{3\pi}K^0_S$	$\eta_{\gamma\gamma}K^0_S$	$\eta_{\gamma\gamma}\eta_{\gamma\gamma}$	$\eta_{\gamma\gamma}\eta_{3\pi}$	$\eta_{3\pi}\eta_{3\pi}$
Generated	134000	134000	148000	148000	148000
Preliminary cuts	39457	54063	50503	53267	37928
PID vetoes for pions	97.0			97.5	94.7
γ energy		90.6	84.8	91.3	
π^0 (1) mass	80.6				82.2
π^0 (2) mass				81.26	81.2
η (1) mass	98.7	95.6	97.6	96.0	98.7
η (2) mass			97.5	91.0	99.7
η (1) helicity		90.6	91.4	90.9	
η (2) helicity			91.7		
K^0_S mass	96.6	96.1			
K^0_S cuts	96.6	99.6			
Fisher cut	99.9	100.0	100.0	99.9	99.7
Raw efficiency	18.7	28.4	22.1	19.7	12.6

Table 7.9: Efficiency (%) and selection cuts (all candidates per event) in $\eta\phi$ and $\eta'\phi$ MC samples (see text for details).

	$\eta_{3\pi}\phi$	$\eta_{\gamma\gamma}\phi$	$\eta'_{\eta\pi\pi}\phi$	$\eta'_{\rho\gamma}\phi$
Generated	74000	74000	74000	74000
Preliminary cuts	25105	33965	24742	28433
PID vetoes for pions	97.4		99.08	96.1
PID vetoes for kaons	99.2	99.3	99.1	99.3
γ energy		90.4		78.2
ϕ mass	94.7	94.6	94.8	94.9
π^0 mass	73.9			
ρ^0 helicity				97.2
ρ^0 mass				96.8
η helicity		91.8		
η mass	72.8	96.8	92.4	
η' mass			99.1	95.8
Fisher cut	99.9	99.8	100.0	99.9
Raw efficiency	21.9	33.7	24.4	23.1

Table 7.10: Efficiency (%) and selection cuts (all candidates per event) in $\eta'\eta'K$ on-peak data samples (see text for details).

	$\eta'_{\eta\pi\pi}\eta'_{\eta\pi\pi}K^0_S$	$\eta'_{\eta\pi\pi}\eta'_{\rho\gamma}K^0_S$	$\eta'_{\eta\pi\pi}\eta'_{\eta\pi\pi}K^\pm$	$\eta'_{\eta\pi\pi}\eta'_{\rho\gamma}K^\pm$
Preliminary cuts	28037	823999	103728	1096567
PID vetoes	70.3	61.2	70.3	57.7
PID Fast Particle			18.5	19.5
γ energy		57.8		56.4
η (1) mass	74.6	74.4	73.8	74.6
η (2) mass	74.7		73.1	
ρ^0 mass		90.5		90.5
ρ^0 Helicity		88.9		88.6
$\eta'_{\eta\pi\pi}$ (1) mass	57.7	57.5	57.5	57.4
$\eta'_{\eta\pi\pi}$ (2) or $\eta'_{\rho\gamma}$ mass	57.9	55.2	58.1	55.2
K^0_S mass	60.2	58.9		
K^0_S cuts	38.4	40.0		
Fisher cut	98.9	98.7	99.0	98.7
Events to fit	467	8741	1390	8913

Table 7.11: Efficiency (%) and selection cuts (all candidates per event) in $\eta K\gamma$ on-peak data samples (see text for details).

	$\eta_{\gamma\gamma}K^0_S\gamma$	$\eta_{3\pi}K^0_S\gamma$	$\eta_{\gamma\gamma}K^\pm\gamma$	$\eta_{3\pi}K^\pm\gamma$
Preliminary cuts	294720	47624	794904	134579
Fast Gamma cuts:				
Energy	81.3	89.5	81.9	90.5
Second Moment	91.9	89.9	92.2	90.5
Cosine of theta angle	95.9	97.1	95.2	96.6
π^0 and η veto	34.1	39.6	34.1	39.2
Isolation from neutral bumps	76.1	81.3	77.0	81.4
Isolation from tracks	92.6	91.0	91.9	91.0
PID vetoes		78.9		77.5
PID Fast Particle			17.2	15.7
π^0 mass		66.3		65.0
η mass	74.6	91.0	74.1	91.6
η helicity	71.5		73.3	
K^0_S mass	33.1	33.3		
K^0_S cuts	42.1	39.8		
Fisher cut	99.1	99.3	99.3	99.5
π^0 veto for $\eta_{\gamma\gamma}$	74.8		74.0	
η momentum cut	32.7	59.1	29.4	60.9
X_s mass	93.8	90.6	92.8	92.7
Events fo fit	786	310	2391	1108

Table 7.12: Efficiency (%) and selection cuts in $\eta' K\gamma$ on-peak data samples (see text for details).

	$\eta'_{\eta\pi\pi}K^0_S\gamma$	$\eta'_{\rho\gamma}K^0_S\gamma$	$\eta'_{\eta\pi\pi}K^\pm\gamma$	$\eta'_{\rho\gamma}K^\pm\gamma$
Preliminary cuts	22028	323605	62344	980341
Fast Gamma cuts:				
Energy	86.4	92.3	88.3	92.8
Second Moment	91.5	91.0	91.5	91.1
Cosine of theta angle	97.1	96.6	96.5	96.1
π^0 and η veto	36.4	38.8	37.3	38.5
Isolation from neutral bumps	78.9	81.3	78.8	81.1
Isolation from tracks	91.9	91.1	90.7	90.7
PID vetoes	84.5	77.4	83.3	76.0
PID Fast Particle			12.2	14.5
η or ρ mass	77.0	97.8	79.4	97.8
ρ helicity		89.2		89.5
η' mass	94.1	100.0	93.4	100.0
K^0_S mass	31.3	31.9		
K^0_S cuts	33.5	34.6		
Fisher cut	100.0	99.4	99.2	99.4
η' momentum cut	56.4	55.8	55.3	52.6
X_s mass	90.1	93.9	92.0	93.9
$\eta'\gamma$ mass veto	96.6	92.5	94.2	91.3
Events to fit	119	2464	401	8792

Table 7.13: Efficiency (%) and selection cuts (all candidates per event) in ηK^0_S and $\eta\eta$ on-peak data samples (see text for details).

	$\eta_{3\pi}K^0_S$	$\eta_{\gamma\gamma}K^0_S$	$\eta_{\gamma\gamma}\eta_{\gamma\gamma}$	$\eta_{\gamma\gamma}\eta_{3\pi}$	$\eta_{3\pi}\eta_{3\pi}$
Preliminary cuts	12700	28826	9238	10748	2177
PID vetoes for pions	66.6			71.9	51.4
γ energy		70.1	50.1	68.3	
π^0_1 mass	68.6				73.2
π^0_2 mass				70.6	73.4
η_1 mass	93.4	79.3	84.5	81.8	95.0
η_2 mass			83.0	94.4	93.1
η_1 helicity		79.7	85.5	79.3	
η_2 helicity			78.5		
K^0_S mass	60.7	59.5			
K^0_S cuts	47.2	45.1			
Fisher cut	100.0	99.8	99.7	99.8	99.8
Events to fit	1392	3333	2054	1990	421

Table 7.14: Efficiency (%) and selection cuts (all candidates per event) in $\eta\phi$ and $\eta'\phi$ on-peak data samples (see text for details).

	$\eta_{3\pi}\phi$	$\eta_{\gamma\gamma}\phi$	$\eta'_{\eta\pi\pi}\phi$	$\eta'_{\rho\gamma}\phi$
Preliminary cuts	10174	23322	4335	138109
PID vetoes for pions	69.0		78.1	65.4
PID vetoes for kaons	91.5	91.2	92.5	91.6
γ energy		70.8		62.0
ϕ mass	57.1	56.5	56.6	56.3
π^0 mass	69.0			
ρ^0 helicity				89.2
ρ^0 mass				90.5
η helicity		78.8		
η mass	93.0	81.2	79.1	
η' mass			95.3	77.7
Fisher cut	99.9	99.9	100.0	99.9
Events to fit	2066	5231	1169	17111

7.4.2 Multiple Candidate per Event

We have analyzed the problem of multiple candidates per event. As we said above, for each event we can have more candidates due to the possible different combinations of the reconstructed particles of the event. We have to choose one of these candidates per event (the "best" candidate). To do that, in our analyses we use an algorithm based on the best χ^2 quantity computed with η' mass, and also η mass in the $\eta'_{\eta\pi\pi}K$ modes, or the B vertex probability for $\eta'K$ analysis and all other analyses, respectively. Note that all these variables are not used in the likelihood for the ML fit (to avoid bias) (section 7.7).

In this section we will report the efficiencies of the best candidate selection. We first make the choice of the best candidate and then look for events with MC truth [2] or without MC truth. In some modes with multiple particles in the final state we consider as MC truth also events where there is a permutation of the particles (PP) inside the B candidate. Events where the B exchanges a track with the rest of the event are called self-crossfeed (SCF) events. Efficiency of the candidate selection algorithm refers to events which have one candidate with MC truth or which have at least one PP event.

We summarize in tab. 7.15 the number of combinations per event for data and MC signal events, the efficiency of the algorithm of selection (considering MC truth events and MC truth plus PP ones) and the fraction of SCF events after the best candidate

[2] Events with MC truth are reconstructed with the same structure of the generation.

Mode	# combs/event (data)	#combs/event (MC signal)	efficiency (%)		SCF (%)
			MCtruth	MCtruth+PP	
$\eta'_{\eta\pi\pi}\eta'_{\eta\pi\pi}K^0_S$	1.78	2.00	80.3	82.7	42.6
$\eta'_{\eta\pi\pi}\eta'_{\rho\gamma}K^0_S$	1.48	1.66	82.3	84.0	42.7
$\eta'_{\eta\pi\pi}\eta'_{\eta\pi\pi}K^\pm$	1.74	1.92	82.1	84.1	40.9
$\eta'_{\eta\pi\pi}\eta'_{\rho\gamma}K^\pm$	1.47	1.59	85.3	86.6	39.8
$\eta_{\gamma\gamma}K^0_S\gamma$	1.09	1.13	96.7	–	18.7
$\eta_{3\pi}K^0_S\gamma$	1.19	1.24	96.7	–	27.2
$\eta_{\gamma\gamma}K^\pm\gamma$	1.09	1.14	95.6	–	19.0
$\eta_{3\pi}K^\pm\gamma$	1.13	1.24	96.4	–	26.5
$\eta'_{\eta\pi\pi}K^0_S\gamma$	1.17	1.24	96.6	–	20.9
$\eta'_{\rho\gamma}K^0_S\gamma$	1.10	1.17	92.9	–	29.3
$\eta'_{\eta\pi\pi}K^\pm\gamma$	1.17	1.26	96.2	–	21.2
$\eta'_{\rho\gamma}K^\pm\gamma$	1.11	1.18	92.7	–	29.1
$\eta_{\gamma\gamma}K^0_S$	1.02	1.02	99.4	–	8.4
$\eta_{3\pi}K^0_S$	1.10	1.13	98.1	–	22.5
$\eta_{\gamma\gamma}\eta_{\gamma\gamma}$	1.06	1.04	98.6	98.6	9.8
$\eta_{\gamma\gamma}\eta_{3\pi}$	1.14	1.14	97.8	98.0	13.1
$\eta_{3\pi}\eta_{3\pi}$	1.25	1.25	97.0	97.5	16.6
$\eta_{3\pi}\phi$	1.13	1.13	98.3	–	19.2
$\eta_{\gamma\gamma}\phi$	1.03	1.03	99.3	–	5.8
$\eta'_{\eta\pi\pi}\phi$	1.18	1.20	94.9	–	13.6
$\eta'_{\rho\gamma}\phi$	1.08	1.13	92.3	–	13.5

Table 7.15: Results of "best candidate" selection algorithm. We show, in order, the number of combinations per event for data and MC signal events, the efficiency of the algorithm of selection (considering MC truth events and MC truth plus PP ones) and the fraction of SCF events after the best candidate selection.

selection.

In $\eta_{\gamma\gamma}\eta_{\gamma\gamma}$ mode, where we have all neutrals in the final state, we have verified that the selection algorithm with B vertex probability has a little bit higher efficiency than the algorithm based on the daughters mass.

For the $\eta'\eta'K$ modes we observe a high fraction of SCF events as input to ML fits. So we consider in different way events with MCtruth+PP and SCF ones. In particular for branching fraction measurements we consider only events with MCtruth+PP. The reason is that the SCF events are more similar to continuum ones and this effect may produce bias in ML signal yield (see MC toy experiments section 7.8). In fig. 7.1 we

show distributions of ΔE and $m_{\rm ES}$ variables for MC signal events where we compare MCtruth, MCtruth+PP and all events. It is possible to see the effect of SCF events in the tails of the distributions.

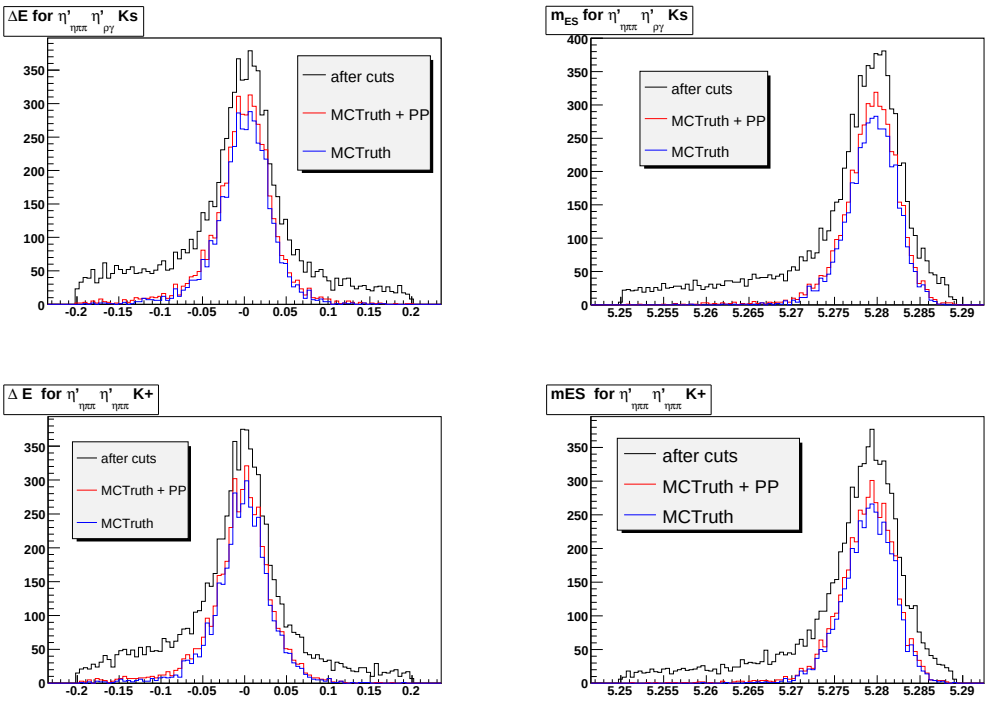

Figure 7.1: Distribution of ΔE (left) and $m_{\rm ES}$ (right) for $\eta'_{\eta\pi\pi}\eta'_{\rho\gamma}K^0_S$ (top) and $\eta'_{\eta\pi\pi}\eta'_{\eta\pi\pi}K^{\pm}$ (bottom): black line referes to all MC signal events(in the legenda indicated as after cuts), red line to MCtruth+PP events and blue line to MCtruth events.

7.5 Efficiency

The MC efficiency (MC ϵ) is calculated as the ratio of the number of signal events in input to ML fit to the number of generated MC signal events. For $\eta'\eta'K$ analysis MC ϵ is calculated as the ratio of the number of the only signal events with MCtruth+PP (see 7.4.2 for a discussion of what is MCtruth+PP) in input to ML fit to the number of generated MC signal events. In all other analyses we consider all signal events, independently of Monte Carlo truth, in input to ML fit. The values of the efficiencies and the products of B daughters branching fractions ($\prod \mathcal{B}_i$) are shown in tab. 7.16.

From control sample studies we note that the MC events disagree from real data. Specific groups in *BABAR* study the corrections to apply to the MC ϵ to match with real data. Tracking efficiency tables provided by the tracking efficiency task force give a

correction of -0.6% and an associated systematic error of 0.8% per track, except the tracks coming from K_S^0. For K_S^0 we follow the recipe described by tracking efficiency task force and we apply a correction of -4.3% and a systematic error of 2.1%. For π^0 and $\eta_{\gamma\gamma}$ we have applied a correction of -3.2% and -2.9%, respectively, suggested by Neutral group. No correction is applied for gamma because we use a particular neutral smearing procedure during the reconstruction of MC events. The corresponding systematic errors are 3% for π^0, η and 1.8% for γ. Considering these corrections we obtain the corrected reconstruction efficiency (corr. ϵ). The summaries of the corrections and systematic errors are in results tables (section 7.10) and systematics tables (section 7.9), respectively.

Mode	$\eta'_{\eta\pi\pi}\eta'_{\eta\pi\pi}K_S^0$	$\eta'_{\eta\pi\pi}\eta'_{\rho\gamma}K_S^0$	$\eta'_{\eta\pi\pi}\eta'_{\eta\pi\pi}K^{\pm}$	$\eta'_{\eta\pi\pi}\eta'_{\rho\gamma}K^{\pm}$
MC ϵ (%)	3.3	4.1	3.8	3.6
$\prod \mathcal{B}_i$ (%)	1.1	3.6	3.1	10.4
Mode	$\eta'_{\eta\pi\pi}K_S^0$	$\eta'_{\rho\gamma}K_S^0$	$\eta'_{\eta\pi\pi}K^{\pm}$	$\eta'_{\rho\gamma}K^{\pm}$
MC ϵ (%)	25.4	27.2	23.9	27.1
$\prod \mathcal{B}_i$ (%)	6.0	10.2	17.5	29.5
Mode	$\eta_{\gamma\gamma}K_S^0\gamma$	$\eta_{3\pi}K_S^0\gamma$	$\eta_{\gamma\gamma}K^{\pm}\gamma$	$\eta_{3\pi}K^{\pm}\gamma$
MC ϵ (%)	11.0	7.6	13.4	9.3
$\prod \mathcal{B}_i$ (%)	13.6	7.8	39.4	22.6
Mode	$\eta'_{\eta\pi\pi}K_S^0\gamma$	$\eta'_{\rho\gamma}K_S^0\gamma$	$\eta'_{\eta\pi\pi}K^{\pm}\gamma$	$\eta'_{\rho\gamma}K^{\pm}\gamma$
MC ϵ (%)	6.8	5.6	8.6	10.1
$\prod \mathcal{B}_i$ (%)	6.0	10.2	17.5	29.5
Mode	$\eta_{\gamma\gamma}K_S^0$	$\eta_{3\pi}K_S^0$		
MC ϵ (%)	28.4	18.7		
$\prod \mathcal{B}_i$ (%)	13.5	7.8		
Mode	$\eta_{\gamma\gamma}\eta_{\gamma\gamma}$	$\eta_{\gamma\gamma}\eta_{3\pi}$	$\eta_{3\pi}\eta_{3\pi}$	
MC ϵ (%)	22.1	19.7	12.6	
$\prod \mathcal{B}_i$ (%)	15.5	17.9	5.1	
Mode	$\eta_{3\pi}\phi$	$\eta_{\gamma\gamma}\phi$	$\eta'_{\eta\pi\pi}\phi$	$\eta'_{\rho\gamma}\phi$
MC ϵ (%)	21.9	33.7	24.4	23.1
$\prod \mathcal{B}_i$ (%)	11.1	19.4	8.6	14.5

Table 7.16: MC efficiency (MC ϵ) and products of B daughters branching fractions ($\prod \mathcal{B}_i$) in each subdecay mode. For modes with K_S^0 we have also included the fraction for $K^0 \to K_S^0$.

7.6 Background Sources

For the background studies, we distinguish the case of analyses already done in *BABAR* ($\eta' K$, ηK^0_s, $\eta\eta$, $\eta\phi$, $\eta'\phi$) and the case of analyses done for the first time now ($\eta'\eta' K$, $\eta^{(\prime)} K\gamma$). For the former it has been verified that in all our target decays we have background contribution only from continuum $udsc$ production with negligible $B\overline{B}$ non continuum crossfeed. For the latter we apply the same considerations (essentially they are decays with the same kinematics).

The continuum background is easily removed in our ML fit using the ΔE, $m_{\rm ES}$, and $\mathcal{F}$ PDFs. So we focus our attention on the $B\overline{B}$ non continuum background. For this kind of background we perform a detailed analysis in all our decay modes. In fact it is strictly connected to the particular decay mode. We can distinguish the background coming from *charm* $B\overline{B}$ decays and from *charmless* $B\overline{B}$ decays. The charm $B\overline{B}$ background is continuum-like background where, essentially, we have a lot of particles in the final state (coming from D defragmentation). In this case we are able to reconstruct B candidates from this background for our modes, but the ΔE and $m_{\rm ES}$ are similar to continuum background PDFs. Furthermore, we allow the parameters of the continuum background PDFs to float in the fits so that any unmodelled B background can be absorbed into this category (especially due to the $\mathcal{F}$ PDF). The remaining charmless $B\overline{B}$ background is the most troublesome and it could be source of bias in our yield results. In general we take care of this background adding a specific component in our ML fits.

In the following sections we will describe the $B\overline{B}$ background studies for each analysis.

7.6.1 $B\overline{B}$ Background studies for $\eta'\eta' K$ analysis

We have done a detailed analysis of $B\overline{B}$ background in all $\eta'\eta' K$ decay modes. Our procedure is realized in two steps. First we apply the full analysis selection to MC generic $B\overline{B}$ samples. In this first step we are interested in finding categories of events which could contribute to background. We look at all the MC events separating possible $B\overline{B}$ crossfeed from charm decays and charmless decays. We find that in our modes there is no charmless contribution. Main charm contribution comes from B decays to many bodies final states, normaly due to a Jetset defragmentation. We focus our study on B decays to maximum 4 bodies. There is no particular category in these decays.

Mode	$B^0\overline{B}^0$	B^+B^-
$\eta'_{\eta\pi\pi}\eta'_{\eta\pi\pi}K^0_S$	44	34
$\eta'_{\eta\pi\pi}\eta'_{\rho\gamma}K^0_S$	928	590
$\eta'_{\eta\pi\pi}\eta'_{\eta\pi\pi}K^\pm$	49	62
$\eta'_{\eta\pi\pi}\eta'_{\rho\gamma}K^\pm$	1304	1939

Table 7.17: Estimated input to ML at our integrated luminosity for $B\overline{B}$ events for $\eta'\eta'K$ decay modes.

We show in tab. 7.17 for each decay mode and for each sample $B^0\overline{B}^0$ and B^+B^-, the number of events passing the full selection, normalized to the integrated luminosity of data.

As a second step in our analysis we perform MC toy experiments with our ML fit (see section 7.7 for the definition of the likelihood function) where the samples are composed by all MC $B^0\overline{B}^0$ or B^+B^- generic sample, embedded signal events (MC-truth+PP) randomly chosen from fully simulated MC signal sample, a right fraction of embedded SCF signal events, and the correspondent $q\overline{q}$ events generated from PDFs, in order to have a sample composition as expected in data. Of course we consider that in these MC toy experiments the statistics is 5.1 times the one in data when considering B^+B^- and 4.6 times for $B^0\overline{B}^0$, so we normalized their results to the integrated luminosity of data. We perform 10 MC toy experiments with different MC signal events and with different $q\overline{q}$ for each one . These different toys have been done to take into account variations due to the particular MC embedded signal events and to $q\overline{q}$. Results of these studies are shown in tab. 7.18 for toys when we embed $B^0\overline{B}^0$ and tab. 7.19 for B^+B^-. The yield mean and yield error are the average value of the 10 repeated toy experiments. In these toys we allow the parameters of the $q\overline{q}$ backgrounds PDFs to float in the fit (as done in final fit on data), so that any unmodelled B background can be absorbed into this category. In the modes with two $\eta'_{\eta\pi\pi}$ the bias is small, while in the modes with $\eta'_{\rho\gamma}$ the bias is large. This effect is reasonable because the former modes have smaller estimated input to ML fit for $B\overline{B}$ and it is absorbed by the $q\overline{q}$ component. Eventually further bias are considered as correction to final results. For the latter modes we decide to add a $B\overline{B}$ component in the fit. We use half of $B^0\overline{B}^0$ and B^+B^- MC generic samples to model the PDFs. Then we repeat our toys using the second half of the samples. Results of these fits are also shown in the previous tables. We can see that the $B\overline{B}$ component in the fit helps to reduce the bias.

Events Type	# Events	Yield Mean	Yield Error	Bias
$\eta'_{\eta\pi\pi}\eta'_{\eta\pi\pi}K^0_S$				
Signal	0	0.1	2.8	+0.1
$q\overline{q}$	423	464.0	24.5	
$B\overline{B}$	44	0 (fixed)		
SCF	0	2.6	12.9	
Signal	10	11.0	5.2	+1.0
$q\overline{q}$	406	447.8	25.0	
$B\overline{B}$	44	0 (fixed)		
SCF	7	7.9	16.0	
$\eta'_{\eta\pi\pi}\eta'_{\rho\gamma}K^0_S$				
Signal	0	20.2	16.9	+20.2
$q\overline{q}$	7813	8651.7	112.4	
$B\overline{B}$	928	0 (fixed)		
SCF	0	69.5	66.5	
Signal	10	39.3	18.8	+29.3
$q\overline{q}$	7796	8604.8	113.5	
$B\overline{B}$	928	0 (fixed)		
SCF	7	96.5	69.7	
Signal	0	−3.2	6.1	−3.2
$q\overline{q}$	7813	8076.0	477.0	
$B\overline{B}$	928	585.0	471.8	
SCF	0	84.0	64.1	
Signal	10	10.9	9.3	+0.9
$q\overline{q}$	7796	8138.0	525.9	
$B\overline{B}$	928	504.6	522.2	
SCF	7	87.5	69.6	
$\eta'_{\eta\pi\pi}\eta'_{\eta\pi\pi}K^{\pm}$				
Signal	0	0.2	3.3	+0.2
$q\overline{q}$	1341	1383.9	41.5	
$B\overline{B}$	49	0 (fixed)		
SCF	0	5.8	18.4	
Signal	10	11.9	6.1	+1.9
$q\overline{q}$	1324	1375.9	41.5	
$B\overline{B}$	49	0 (fixed)		
SCF	7	2.3	21.2	
$\eta'_{\eta\pi\pi}\eta'_{\rho\gamma}K^{\pm}$				
Signal	0	18.1	17.9	+18.1
$q\overline{q}$	7609	8803.9	124.8	
$B\overline{B}$	1304	0 (fixed)		
SCF	0	90.5	86.2	
Signal	10	39.2	20.3	+29.2
$q\overline{q}$	7592	8790.9	127.0	
$B\overline{B}$	1304	0 (fixed)		
SCF	7	83.2	90.4	
Signal	0	−3.2	8.2	−3.2
$q\overline{q}$	7609	7527.9	807.8	
$B\overline{B}$	1304	1298.8	802.0	
SCF	0	90.4	85.5	
Signal	10	10.2	10.5	0.2
$q\overline{q}$	7592	7579.0	883.0	
$B\overline{B}$	1304	1209.8	877.2	
SCF	7	114.2	89.7	

Table 7.18: Results of 10 MC toy experiments for each $\eta'\eta'K$ decay mode where we embed the generic MC $B^0\overline{B}^0$ sample (see the text).

Events Type	# Events	Yield Mean	Yield Error	Bias
$\eta'_{\eta\pi\pi}\eta'_{\eta\pi\pi}K^0_S$				
Signal	0	-1.1	1.9	-1.1
$q\overline{q}$	433	463.7	23.6	
$B\overline{B}$	34	0 (fixed)		
SCF	0	4.0	10.6	
Signal	10	10.8	4.9	-0.8
$q\overline{q}$	416	444.1	25.1	
$B\overline{B}$	34	0 (fixed)		
SCF	7	11.9	15.8	
$\eta'_{\eta\pi\pi}\eta'_{\rho\gamma}K^0_S$				
Signal	0	13.0	14.8	$+13.0$
$q\overline{q}$	8151	8648.7	110.8	
$B\overline{B}$	590	0 (fixed)		
SCF	0	79.6	63.4	
Signal	10	22.6	16.4	$+12.6$
$q\overline{q}$	8134	8666.4	113.0	
$B\overline{B}$	590	0 (fixed)		
SCF	7	52.3	68.1	
Signal	0	1.4	6.1	$+1.4$
$q\overline{q}$	8151	8202.0	420.6	
$B\overline{B}$	590	498.6	413.2	
SCF	0	42.1	61.6	
Signal	10	9.4	8.4	-0.6
$q\overline{q}$	8134	8325.5	38.0	
$B\overline{B}$	590	364.0	430.8	
SCF	7	43.0	67.3	
$\eta'_{\eta\pi\pi}\eta'_{\eta\pi\pi}K^{\pm}$				
Signal	0	1.2	3.1	1.2
$q\overline{q}$	1328	1395.4	40.6	
$B\overline{B}$	62	0 (fixed)		
SCF	0	-6.6	17.2	
Signal	10	9.9	5.9	-0.1
$q\overline{q}$	1311	1372.7	41.9	
$B\overline{B}$	62	0 (fixed)		
SCF	7	7.4	22.4	
$\eta'_{\eta\pi\pi}\eta'_{\rho\gamma}K^{\pm}$				
Signal	0	15.5	16.7	$+15.5$
$q\overline{q}$	6974	8787.8	128.0	
$B\overline{B}$	1939	0 (fixed)		
SCF	0	109.8	89.6	
Signal	10	29.7	18.5	$+19.7$
$q\overline{q}$	6957	8812.3	128.5	
$B\overline{B}$	1939	0 (fixed)		
SCF	7	71.0	92.6	
Signal	0	-1.5	8.4	-1.5
$q\overline{q}$	6974	7028.1	760.3	
$B\overline{B}$	1939	1782.4	756.0	
SCF	0	104.0	86.6	
Signal	10	10.1	11.0	$+0.1$
$q\overline{q}$	6957	6966.7	742.4	
$B\overline{B}$	1939	1795.3	742.4	
SCF	7	140.9	92.4	

Table 7.19: Results of 10 MC toy experiments for each $\eta'\eta'K$ decay mode where we embed the generic MC B^+B^- sample (see the text).

7.6.2 Charmless $B\overline{B}$ Background studies for $\eta' K$ analysis

We have applied the full analysis selection to $B\overline{B}$ sample, removing $b \to c$ and signal backgrounds in order to focus on the most troublesome charmless backgrounds. These studies provide a list of modes for further study. We consider only the $\eta'_{\rho\gamma}$ channels since the $B\overline{B}$ background is further suppressed by nearly an order of magnitude for the $\eta'_{\eta\pi\pi}$ modes. We obtain signal MC samples of $\gtrsim$100K events for each of the significant $B\overline{B}$ background samples. This procedure is shown in tab. 7.20 for the $\eta'_{\rho\gamma}K^0_{S+-}$ decay and in tab. 7.21 for the $\eta'_{\rho\gamma}K^{\pm}$ decay. The branching fractions of the background $B\overline{B}$ modes studied are taken from HFAG tables [98] and PDG [99].

Following the experience obtained with these backgrounds in the previous analysis we add a single $B\overline{B}$ background component to the fit to properly account for these small backgrounds. We obtain the PDFs for this component fitting the distributions of the mix of these events in appropriate proportions.

7.6.3 $B\overline{B}$ Background studies for $\eta^{(\prime)}K\gamma$ analysis

We have done a detailed analysis of $B\overline{B}$ background in all $\eta^{(\prime)}K\gamma$ decay modes. Our procedure is realized in three steps. First we apply the full analysis selection to MC $B\overline{B}$ generic samples and to $b \to s\gamma$ inclusive radiative samples [3]. We look at all the MC events separating possible $B\overline{B}$ crossfeed from charm decays, charmless decays and radiative decays. In this first step we are interested in finding categories of events which could contribute to background. In the second step we reconstruct large samples of MC signal events of candidate crossfeed modes and we evaluate reconstruction efficiency and number of expected candidates (normalized to our integrated luminosity) in ML input. Finally, we perform MC toy experiment studies for the ML fit where we embed these events, taken from MC events, as expected in the ML fit input (see MC toy experiments section 7.8). In this way we see if the candidate is a real candidate for background or not. If it is a real candidate, then we use these MC events to prepare the PDFs to introduce in the fit. If background comes from several decay modes, the PDFs are prepared using weighted numbers of events from each decay mode. PDFs are prepared with all events surviving cuts and best candidate selection. Because charmless events are the peaking contribution to our background, the PDFs are prepared using

[3] $b \to s\gamma$ inclusive radiative samples are simulated with Kagan-Neubert model [97], with $m_b = 465$, and Jetset defragmentation.

Table 7.20: Potential $B\overline{B}$ background for the $\eta'_{\rho\gamma}K^0_{S+-}$ mode from exclusive charmless B decays included in the feed component. We show efficiency for the mode to pass selection cuts, the measured or estimated branching fraction, the appropriate product branching fraction given how the MC was produced, the estimated background normalized to 232 million $B\overline{B}$ events and the number of events we include in the file we use for making PDFs.

Cross Feed channel	MC ϵ (%)	Est. $\mathcal{B}$ (10^{-6})	$\prod \mathcal{B}_i$ (%)	# evts in ML	# evts in PDF Bkg. file
$B^0 \to \rho^0 K^0$	2.98	5	0.500	17.2	556
$B^\pm \to a_1^\pm K^0$	0.91	15	0.500	15.8	510
$B^\pm \to \rho^0 K^{*\pm}_{K_S\pi^\pm}$	1.47	10	0.229	7.8	251
$B^0 \to f_0 K^0$	1.06	6	0.500	7.3	237
$B^0 \to \phi_{3\pi} K^0$	5.38	8	0.053	5.2	170
$B^\pm \to \eta'_{\rho\gamma} K^{*\pm}_{K_S\pi^\pm}$	2.7	6	0.067	2.5	81
$B^0 \to \rho^- K^{*+}_{K_S\pi^+}$	0.22	20	0.229	2.3	76
$B^0 \to \omega\ K^0$	0.46	6	0.306	1.9	63
$B^\pm \to \rho^\pm K^0$	0.52	3	0.500	1.8	59
$B^0 \to K^{*+}_{K_S\pi^+}\pi^-$	0.13	15	0.333	1.6	52
$B^0 \to \eta'_{\eta\pi\pi} K^0$	0.11	65	0.060	0.9	32
$B^\pm \to \phi_{3\pi} K^{*\pm}_{K_S\pi^\pm}$	0.14	10	0.035	0.1	3
$B^\pm \to K^0 K^{*\pm}_{K_S\pi^\pm}$	0.21	1	0.167	0	2
$B^0 \to \phi_{3\pi} K^{*0}_{K_S\pi^0}$	0.14	11	0.018	0	2
$B^\pm \to \omega\ K^{*\pm}_{K_S\pi^\pm}$	0.02	4	0.204	0	1
$B^\pm \to a_0^\pm(\eta_{3\pi}\pi^\pm) K^0$	0.15	1	0.135	0	1
$B^\pm \to K^0 K^{*\pm}_{K^\pm\pi^0}$	0.1	1	0.167	0	1
$B^0 \to \eta'_{\rho\gamma} K^{*0}_{K^+\pi^-}$	0.01	4	0.197	0	0
$B^0 \to \rho^0 K^{*0}_{K^+\pi^-}$	0	10	0.667	0	0
$B^0 \to K^{*+}_{K^+\pi^0}\pi^-$	0	15	0.333	0	0
$B^0 \to \omega\rho^0$	0	1	0.891	0	0
Total				64.4	2097

Table 7.21: Potential $B\overline{B}$ background for the $\eta'_{\rho\gamma}K^{\pm}$ mode from exclusive charmless B decays included in the feed component. We show efficiency for the mode to pass selection cuts, the measured or estimated branching fraction, the appropriate product branching fraction given how the MC was produced, the estimated background normalized to 232 million $B\overline{B}$ events and the number of events we include in the file we use for making PDFs.

Cross Feed channel	MC ϵ (%)	Est. $\mathcal{B}$ (10^{-6})	$\prod \mathcal{B}_i$ (%)	# evts in ML	# evts in PDF Bkg. file
$B^{\pm} \to \rho^0 K^{\pm}$	4.48	4	1.000	41.5	1163
$B^0 \to \rho^0 K^{*0}_{K^+\pi^-}$	1.43	10	0.667	22.2	622
$B^0 \to \rho^+ K^-$	0.82	9	1.000	17.2	483
$B^{\pm} \to \phi_{3\pi} K^{\pm}$	5.17	9	0.155	16.7	468
$B^{\pm} \to \rho^0 K^{*\pm}_{K^{\pm}\pi^0}$	1.52	10	0.333	11.7	328
$B^0 \to a_1^+ \pi^-$	0.14	40	0.667	9	253
$B^{\pm} \to a_1^0 \pi^{\pm}$	0.15	20	1.000	7.2	202
$B^0 \to \rho^0 \pi^+$	0.3	9	1.000	6.3	178
$B^{\pm} \to \rho^{\pm} \rho^0$	0.08	26	1.000	5.3	150
$B^0 \to \eta'_{\rho\gamma} K^{*0}_{K^+\pi^-}$	2.58	4	0.197	4.7	132
$B^{\pm} \to \omega\ K^{\pm}$	0.44	5	0.891	4.5	128
$B^{\pm} \to \eta'_{\rho\gamma} K^{*\pm}_{K^{\pm}\pi^0}$	2.88	6	0.098	3.9	110
$B^0 \to \rho^- K^{*+}_{K^+\pi^0}$	0.23	20	0.333	3.6	100
$B^{\pm} \to \eta'_{\eta\pi\pi} K^{\pm}$	0.08	78	0.174	2.7	76
$B^0 \to K^{*+}_{K^+\pi^0} \pi^-$	0.2	15	0.333	2.4	67
$B^{\pm} \to \eta'_{\rho\gamma} \rho^{\pm}$	0.16	13	0.295	1.4	40
$B^0 \to \rho^+ \rho^-$	0.02	30	1.000	1.4	39
$B^{\pm} \to \omega \pi^{\pm}$	0.04	6	0.891	0.6	16
$B^0 \to \eta'_{\rho\gamma} K^0$	0.02	65	0.101	0.3	10
$B^0 \to a_0^-(\eta_{\gamma\gamma}\pi^-) K^+$	0.36	1	0.394	0.3	9
$B^0 \to K^{*+}_{K_S\pi^+} \pi^-$	0.02	15	0.333	0.3	8
$B^0 \to \eta'_{\rho\gamma} \rho^0$	0.33	1	0.295	0.2	6
$B^0 \to a_0^+(\eta_{\gamma\gamma}\pi^+)\pi^-$	0.03	3	0.394	0	2
$B^{\pm} \to \eta_{3\pi} \pi^{\pm}$	0.01	5	0.226	0	1
$B^{\pm} \to \eta'_{\eta\pi\pi} \pi^{\pm}$	0	3	0.174	0	0
$B^0 \to a_0^+(\eta_{\gamma\gamma}\pi^+)\rho^-$	0	6	0.394	0	0
$B^0 \to \omega\ K^0$	0	6	0.306	0	0
Total				163.4	4591

only these events.

This analysis is based on samples of generic $B\overline{B}$ about 3.2 times the statistics expected at the integrated luminosity used in this analysis and on MC samples of radiative charged and neutral B decays of 328000 and 330000, respectively. Using a branching fraction of 339×10^{-6} (from HFAG tables [100]) for the process $b \to s\gamma$, we estimate that our MC samples of radiative B mesons are about 4.2 times the statistics expected at the integrated luminosity used in this analysis. We show in tab. 7.22 for each decay mode and for each of the four samples $B^0\overline{B}^0$, B^+B^-, $B^+ \to X_{su}\gamma$ and $B^0 \to X_{sd}\gamma$ the total number of events passing the full selection. In the $B\overline{B}$ generic events we have eliminated all radiative $B \to X_s\gamma$ decays while in $B \to X_s\gamma$ we have eliminated all signal events. In this table the numbers related to $B^0\overline{B}^0$ and B^+B^- are normalized to the integrated luminosity of data. Note that the numbers of $B\overline{B}$ input events are not those used later in MC toy experiments.

Mode	$B^0\overline{B}^0$	B^+B^-	$B^0 \to X_{sd}\gamma$	$B^+ \to X_{su}\gamma$
$\eta_{\gamma\gamma}K^0_S\gamma$	36	16	105	38
$\eta_{3\pi}K^0_S\gamma$	14	11	65	31
$\eta'_{\eta\pi\pi}K^0_S\gamma$	9	5	20	20
$\eta'_{\rho\gamma}K^0_S\gamma$	155	119	390	235
$\eta_{\gamma\gamma}K^\pm\gamma$	31	98	145	426
$\eta_{3\pi}K^\pm\gamma$	27	48	117	157
$\eta'_{\eta\pi\pi}K^\pm\gamma$	20	26	51	78
$\eta'_{\rho\gamma}K^\pm\gamma$	353	612	863	1222

Table 7.22: Input to ML for each $\eta^{(\prime)}K\gamma$ target decay mode. Generic $B\overline{B}$ statistics is normalized to the integrated luminosity of data.

In the following we report the results of the $B\overline{B}$ studies for each $\eta^{(\prime)}K\gamma$ decay mode. The branching fractions of the background $B\overline{B}$ modes studied are taken from PDG [99] and HFAG tables [100].

The decay modes $\eta' K\gamma$ have an irreducible background from the decay $J/\psi K$ with $J/\psi \to \eta'\gamma$. The expected background contribution is shown in tab. 7.23. We have reconstructed MC signal events of these radiative J/ψ background modes. We show in fig. 7.2 the distribution of $\eta'\gamma$ invariant mass for the J/ψ radiative decays and for the target mode $\eta'_{\rho\gamma}K^\pm\gamma$. In all the four target modes with an η' in the final state we have applied a veto, cutting a region of about 3 σ around the nominal mass of J/ψ. We have applied the same veto for both the sub-decay modes with $\eta'_{\rho\gamma}$ and $\eta'_{\eta\pi\pi}$.

Cross Feed channel	MC ϵ (%)	$\mathcal{B}$ (10^{-4})	$\prod \mathcal{B}_i$ (10^{-4})	# evts in ML fit input
		$\eta'_{\eta\pi\pi}K^{\pm}\gamma$		
$J/\psi\,K^+$ ($J/\psi \to \eta'_{\eta\pi\pi}\gamma$)	3.1	10.0 ± 0.4	7.5 ± 0.6	5.3 ± 0.2
		$\eta'_{\eta\pi\pi}K^0_S\gamma$		
$J/\psi\,K^0$ ($J/\psi \to \eta'_{\eta\pi\pi}\gamma$)	3.1	8.5 ± 0.5	2.6 ± 0.2	1.6 ± 0.1
		$\eta'_{\rho\gamma}K^{\pm}\gamma$		
$J/\psi\,K^+$ ($J/\psi \to \eta'_{\rho\gamma}\gamma$)	4.9	10 ± 0.4	12.7 ± 1.0	14.6 ± 0.6
		$\eta'_{\rho\gamma}K^0_S\gamma$		
$J/\psi\,K^0$ ($J/\psi \to \eta'_{\rho\gamma}\gamma$)	4.0	8.5 ± 0.5	4.4 ± 0.3	3.5 ± 0.2

Table 7.23: $J/\psi\,K$ (with $J/\psi \to \eta'\gamma$) crossfeed channel, MC reconstruction efficiency ϵ, measured branching fraction ($\mathcal{B}$), daughter branching fraction product, estimate background (normalized to our integrated luminosity) in ML input for $\eta' K\gamma$ decays without veto applied.

In the tables 7.24–7.29 we show the possible crossfeed modes from other $B\overline{B}$ decays for our $\eta^{(\prime)}K\gamma$ decay modes. For the modes $\eta_{3\pi}K^0_S\gamma$ and $\eta'_{\eta\pi\pi}K^0_S\gamma$, due to the combined and strong requirements on $\eta_{3\pi}$, $\eta'_{\eta\pi\pi}$ and K^0_S mesons, we do not find possible crossfeed in $B\overline{B}$ samples and in radiative samples.

We see that, essentially, the main contributions come from the radiative B decays. We use these MC reconstructed events to prepare PDFs for the $B\overline{B}$ components in the ML fits for $\eta_{\gamma\gamma}K^0_S\gamma$, $\eta_{\gamma\gamma}K^{\pm}\gamma$, $\eta_{3\pi}K^{\pm}\gamma$, $\eta'_{\rho\gamma}K^0_S\gamma$, and $\eta'_{\rho\gamma}K^{\pm}\gamma$ modes. MC toy

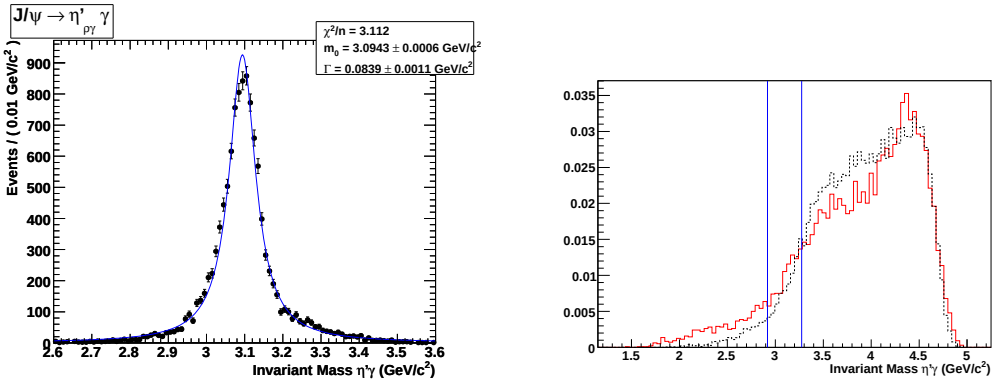

Figure 7.2: Invariant mass of $\eta'\gamma$. Left: distribution and fit with a Breit-Wigner function for MC $J/\psi\,K^+$ ($J/\psi \to \eta'_{\rho\gamma}\gamma$) events reconstructed as $\eta'_{\rho\gamma}K^{\pm}\gamma$. Right: same distribution for $\eta'_{\rho\gamma}K^{\pm}\gamma$ mode where black dashed line refers to MC signal events, red solid line to on-peak data. The region between the blue solid vertical lines has been vetoed.

Cross Feed Channel	MC ϵ (%)	Est. $\mathcal{B}$ (10^{-6})	$\prod \mathcal{B}_i$ (%)	# evts in ML
$B^0 \to K^*(892)\gamma$ ($K^0_S\pi^0$)	0.64	40.1	11.5	6.8 ± 0.1
$B^0 \to K_1(1270)\gamma$	0.02	58	100	3.0 ± 0.4
$B^\pm \to K_1(1270)\gamma$	0.03	43	100	2.6 ± 0.3
$B^\pm \to \eta_{\gamma\gamma}K^\pm\gamma$	0.19	8.7	13.6	1.5 ± 0.1
$B^0 \to K^*_2(1430)\gamma$	0.04	12.4	100	1.2 ± 0.1
$B^0 \to J/\psi K^0_S$ ($J/\psi \to$ hadrons)	0.002	850	30.2	1.0 ± 0.5
$B^\pm \to K^*(892)\gamma$	0.005	40.3	100	0.5 ± 0.1
$B^\pm \to K^*_2(1430)\gamma$	0.01	14.5	100	0.5 ± 0.1
Total				17.1 ± 0.7

Table 7.24: Potential $B\overline{B}$ background for the $\eta_{\gamma\gamma}K^0_S\gamma$ mode. For each decay mode we give the MC reconstruction efficiency ϵ, branching fraction ($\mathcal{B}$), daughter branching fraction product, estimate background (normalized to our integrated luminosity) in ML input. The error for the latter is computed considering only the error on efficiency estimation (related to the number of reconstructed MC events).

Cross Feed Channel	MC ϵ (%)	Est. $\mathcal{B}$ (10^{-6})	$\prod \mathcal{B}_i$ (%)	# evts in ML
$B^\pm \to K^*(892)\gamma$	0.29	40.3	100	27.6 ± 0.8
$B^0 \to K_1(1270)\gamma$	0.08	43	100	10.6 ± 0.8
$B^\pm \to K_1(1270)\gamma$	0.07	58	100	6.5 ± 0.5
$B^\pm \to K^*_2(1430)\gamma$	0.14	12.4	100	4.8 ± 0.3
$B^\pm \to \eta_{\gamma\gamma}K^{*\pm}(\pi^0K^\pm)$	0.35	24.3	13.1	2.6 ± 0.1
$B^0 \to D^{*+}\rho^-$ ($D^{*+} \to D^0\pi^+$)	0.0002	6800	67.7	2.1 ± 1.5
$B^0 \to K^*(892)\gamma$	0.02	40.1	100	2.0 ± 0.2
$B^0 \to \eta_{\gamma\gamma}K^0_S\gamma$	0.55	8.7	13.6	1.5 ± 0.1
$B^0 \to K^*_2(1430)\gamma$	0.05	14.5	100	1.4 ± 0.1
$B^\pm \to \eta'_{\eta\pi\pi}K^\pm\gamma$	0.12	8.4	17.5	0.4 ± 0.1
$B^\pm \to J\psi K^\pm$ ($J/\psi \to$ hadrons)	0.0002	1000	87.7	0.3 ± 0.2
Total				59.8 ± 2.0

Table 7.25: Potential $B\overline{B}$ background for the $\eta_{\gamma\gamma}K^\pm\gamma$ mode. For each decay mode we give the MC reconstruction efficiency ϵ, branching fraction ($\mathcal{B}$), daughter branching fraction product, estimate background (normalized to our integrated luminosity) in ML input. The error for the latter is computed considering only the error on efficiency estimation (related to the number of reconstructed MC events).

Cross Feed Channel	MC ϵ (%)	Est. $\mathcal{B}$ (10^{-6})	$\prod \mathcal{B}_i$ (%)	# evts in ML
$B^{\pm} \rightarrow D^0\rho^{\pm}$ $(D^0 \rightarrow K^+\pi^-\pi^0)$	0.001	13400	13.0	4.3 ± 2.5
$B^{\pm} \rightarrow K_2^*(1430)\gamma$	0.08	14.5	100	2.6 ± 0.2
$B^{\pm} \rightarrow \eta'_{\eta\pi\pi}K^{\pm}$	0.08	69.4	17.5	2.2 ± 0.1
$B^0 \rightarrow K_2^*(1430)\gamma$	0.05	12.4	100	1.5 ± 0.2
$B^0 \rightarrow K^*(892)\gamma$ $(K^+\pi^-)$	0.009	40.1	66.6	0.6 ± 0.1
$B^0 \rightarrow \eta_{3\pi}K_S^0\gamma$	0.38	8.7	7.8	0.6 ± 0.1
$B^{\pm} \rightarrow \eta'_{\eta\pi\pi}K^{\pm}\gamma$	0.19	8.4	17.5	0.6 ± 0.1
$B^{\pm} \rightarrow \eta'_{\rho\gamma}K^{\pm}\gamma$	0.05	8.4	29.5	0.3 ± 0.1
Total				12.7 ± 2.5

Table 7.26: Potential $B\overline{B}$ background for the $\eta_{3\pi}K^{\pm}\gamma$ mode. For each decay mode we give the MC reconstruction efficiency ϵ, branching fraction ($\mathcal{B}$), daughter branching fraction product, estimate background (normalized to our integrated luminosity) in ML input. The error for the latter is computed considering only the error on efficiency estimation (related to the number of reconstructed MC events).

Cross Feed Channel	MC ϵ (%)	Est. $\mathcal{B}$ (10^{-6})	$\prod \mathcal{B}_i$ (%)	# evts in ML
$B^{\pm} \rightarrow \eta_{3\pi}K^{\pm}\gamma$	0.26	8.4	22.6	1.1 ± 0.1
$B^0 \rightarrow \eta'_{\eta\pi\pi}K_S^0\,\gamma$	0.52	8.7	6.0	0.6 ± 0.1
Total				1.7 ± 0.1

Table 7.27: Potential $B\overline{B}$ background for the $\eta'_{\eta\pi\pi}K^{\pm}\gamma$ mode. For each decay mode we give the MC reconstruction efficiency ϵ, branching fraction ($\mathcal{B}$), daughter branching fraction product, estimate background (normalized to our integrated luminosity) in ML input. The error for the latter is computed considering only the error on efficiency estimation (related to the number of reconstructed MC events).

Cross Feed Channel	MC ϵ (%)	Est. $\mathcal{B}$ (10^{-6})	$\prod \mathcal{B}_i$ (%)	# evts in ML
$B^0 \to K_1(1270)\gamma$	0.30	58	100	40.4 ± 1.5
$B^\pm \to K_1(1270)\gamma$	0.22	43	100	21.6 ± 1.0
$B^0 \to D^{*+}\rho^-$ $(D^{*+} \to D^0\pi^+)$	0.0009	6800	67.7	9.5 ± 3.2
$B^0 \to D^+\rho^-$ $(D^+ \to K^0_S\pi^0\pi^+)$	0.01	7700	3.3	8.9 ± 2.2
$B^0 \to K_1(1400)\gamma$	0.30	12	100	8.2 ± 0.3
$B^\pm \to D^0\rho^\pm$ $(D^0 \to K^0_S\pi^+\pi^-)$	0.01	13400	2.1	7.9 ± 2.1
$B^\pm \to K_1(1400)\gamma$	0.18	15	100	6.1 ± 0.3
$B^0 \to K^*_2(1430)\gamma$	0.15	12.4	100	4.3 ± 0.3
$B^\pm \to K^*_2(1430)\gamma$	0.10	14.5	100	3.4 ± 0.2
$B^0 \to D^+\rho^-$ $(D^+ \to K^0_S\pi^+)$	0.02	7700	1.0	2.8 ± 0.4
$B^\pm \to K^*(892)\gamma$	0.02	40.3	100	1.7 ± 0.2
$B^\pm \to \eta'_{\rho\gamma}K^\pm\gamma$	0.21	8.4	29.5	1.2 ± 0.1
$B^0 \to K^*(892)\gamma$ $(K^0_S\pi^0)$	0.08	40.1	11.5	0.9 ± 0.1
$B^0 \to \eta_{3\pi}K^0_S\gamma$	0.49	8.7	7.8	0.8 ± 0.1
$B^0 \to K^{*0}(892)\gamma$ $(K^+\pi^-)$	0.009	40.1	66.6	0.6 ± 0.2
$B^0 \to D^{*+}\rho^-$ $(D^{*+} \to D^0(K^0_S\pi^+\pi^-)\pi^+)$	0.01	6800	1.4	0.6 ± 0.3
$B^0 \to D^{*+}\rho^-$ $(D^{*+} \to D^0(K^0_S\pi^0)\pi^+)$	0.01	6800	0.5	0.5 ± 0.1
$B^0 \to D^{*+}\rho^-$ $(D^{*+} \to D^+(K^0_S\pi^+)\pi^0)$	0.01	6800	0.3	0.5 ± 0.1
$B^0 \to \eta'_{\eta\pi\pi}K^0_S\gamma$	0.45	8.7	6.0	0.5 ± 0.1
Total				120.4 ± 4.8

Table 7.28: Potential $B\overline{B}$ background for the $\eta'_{\rho\gamma}K^0_S\gamma$ mode. For each decay mode we give the MC reconstruction efficiency ϵ, branching fraction ($\mathcal{B}$), daughter branching fraction product, estimate background (normalized to our integrated luminosity) in ML input. The error for the latter is computed considering only the error on efficiency estimation (related to the number of reconstructed MC events).

Cross Feed Channel	MC ϵ (%)	Est. $\mathcal{B}$ (10^{-6})	$\prod \mathcal{B}_i$ (%)	# evts in ML
$B^0 \to K_1(1270)\gamma$	0.83	58	100	111.5 ± 2.5
$B^\pm \to K_1(1270)\gamma$	0.98	43	100	97.2 ± 2.0
$B^\pm \to D^0\rho^\pm\ (D^0 \to K^-\pi^+\pi^0)$	0.02	13400	13.0	89.7 ± 11.4
$B^\pm \to K_1(1400)\gamma$	0.88	15	100	30.5 ± 0.7
$B^\pm \to D^0\rho^\pm\ (D^0 \to K^-\pi^+)$	0.03	13400	3.8	30.1 ± 3.4
$B^0 \to K_1(1400)\gamma$	0.67	12	100	18.8 ± 0.5
$B^\pm \to K_2^*(1430)\gamma$	0.43	14.5	100	14.6 ± 0.5
$B^0 \to K_2^*(1430)\gamma$	0.39	12.4	100	11.2 ± 0.4
$B^0 \to D^{*+}\rho^+\ (D^{*+} \to D^0(K^+\pi^-)\pi^+)$	0.02	6800	2.6	8.2 ± 1.7
$B^0 \to D^{*0}\pi^0\ (D^{*0} \to D^0\pi^0, D^0\gamma)$ $(D^0 \to K^+\pi^-, K^-\pi^+\pi^0, K^-\pi^+\pi^-\pi^+)$	0.07	270	18.5	7.9 ± 0.6
$B^\pm \to K^*(892)\gamma$	0.07	40.3	100	6.6 ± 0.4
$B^0 \to K^*(892)\gamma\ (K^+\pi^-)$	0.08	40.1	66.6	5.2 ± 0.6
$B^0 \to D^-\rho^+\ (D^- \to K^-\pi^+\pi^-)$	0.002	7700	9.2	4.0 ± 2.8
$B^\pm \to \eta_{3\pi}K^\pm\gamma$	0.57	8.4	22.6	2.5 ± 0.1
$B^\pm \to \eta'_{\eta\pi\pi}K^\pm\gamma$	0.53	8.4	17.5	1.8 ± 0.1
$B^0 \to \eta'_{\rho\gamma}K_S^0\gamma$	0.60	8.7	10.2	1.2 ± 0.1
$B^\pm \to \eta_{\gamma\gamma}K^\pm\gamma$	0.13	8.4	39.4	1.0 ± 0.1
Total				442.0 ± 12.8

Table 7.29: Potential $B\overline{B}$ background for the $\eta'_{\rho\gamma}K^\pm\gamma$ mode. For each decay mode we give the MC reconstruction efficiency ϵ, branching fraction ($\mathcal{B}$), daughter branching fraction product, estimate background (normalized to our integrated luminosity) in ML input. The error for the latter is computed considering only the error on efficiency estimation (related to the number of reconstructed MC events).

experiments (see section 7.8) show a fit bias also including these $B\overline{B}$ components in the fits (of course the $B\overline{B}$ components help to reduce the biases). We will correct the signal fit yields for the fit biases and we will apply a systematics (one half of the fit bias corrections). For $\eta'_{\eta\pi\pi}K^{\pm}\gamma$, MC toy experiments show a small bias from $B\overline{B}$ crossfeed and therefore we do not include any $B\overline{B}$ component in the fit, but we will correct the signal fit yield for the fit bias and we will apply a systematics as well as the other modes.

7.6.4 $B\overline{B}$ Background studies for ηK^0_S, $\eta\eta$, $\eta\phi$, $\eta'\phi$ analyses

We analyze here in detail the background coming from charmless $B\overline{B}$ events. These events in fact could be source of bias in our yield results. Our procedure is realized in three steps. First we apply the full analysis selection to MC $B\overline{B}$ generic samples. We show in tab. 7.30 the input to the maximum likelihood in B^+B^- and $B^0\overline{B}^0$ (results are normalized to our integrated luminosity). Signal MC events have been removed from these samples. Note that we have reconstrutected about 3.3 times of generic $B\overline{B}$ with respect to the statistics expected at integrated luminosity of data. We look at all the MC events separating possible $B\overline{B}$ crossfeed from charm decays and charmless decay. We focus our attention to charmless events because they are the peaking contribution to our background. In this first step we are interested in finding categories of events which could contribute to background.

In the second step we reconstruct large samples of MC signal events of candidate

Mode	$B^0\overline{B}^0$	B^+B^-
$\eta_{\gamma\gamma}K^0_S$	39	34
$\eta_{3\pi}K^0_S$	9	8
$\eta_{\gamma\gamma}\eta_{\gamma\gamma}$	7	3
$\eta_{\gamma\gamma}\eta_{3\pi}$	3	3
$\eta_{3\pi}\eta_{3\pi}$	2	1
$\eta_{\gamma\gamma}\phi$	26	14
$\eta_{3\pi}\phi$	9	9
$\eta'_{\eta\pi\pi}\phi$	19	7
$\eta'_{\rho\gamma}\phi$	215	231

Table 7.30: Estimated input to ML at our integrated luminosity for $B\overline{B}$ events for each target decay mode.

crossfeed modes and we evaluate reconstruction efficiency and number of expected candidates (normalized to our integrated luminosity) in ML fit input. Finally, we perform MC toy experiment studies (see section 7.8) where we embed these events, taken from MC events, as expected in the ML input. In this way we see if the candidate is a real candidate for background or not. If it is a real candidate, then we use these MC events to prepare the PDFs to introduce in the fit. If background comes from several decay modes, the PDFs are prepared using weighted numbers of events from each decay mode. PDFs are prepared with all events surviving cuts and with the best candidate selection.

In the tables 7.31–7.37 we show the possible crossfeed modes from other charmless $B\overline{B}$ modes in our target decay modes. The branching fractions of the background $B\overline{B}$ modes are taken from PDG [99] and HFAG tables [100]).

In the $\eta'_{\rho\gamma}\phi$ the main $B\overline{B}$ contribution comes from charm events (as you can see from the comparison of the numbers in table 7.30 and table 7.37). Essentially the background is due to random combination in charm B decays. In our previous analyses of this mode we have found that this background is continuum-like. We allow the parameters of the $q\overline{q}$ backgrounds PDFs to float in the fit (as done in final fit on data), so that any unmodelled B background can be absorbed into this category. We show in fig. 7.3 the distributions of the variables used in the ML fit (see section 7.7 for the likelihood definition for this mode) for $B\overline{B}$ generic events.

We add a $B\overline{B}$ component in the ML fit for the decay modes $\eta_{\gamma\gamma}K^0_S$ and $\eta_{\gamma\gamma}\phi$. PDFs for this component are prepared using reconstructed MC events of the decay modes listed in tab. 7.31 and in tab. 7.35, respectively.

We will correct the ML fit results of the signal yields using the bias found in MC toy experiments analysis and we will give a systematic error.

Cross Feed Channel	MC ϵ (%)	Est. $\mathcal{B}$ (10^{-6})	$\prod \mathcal{B}_i$ (%)	# evts in ML
$B^0 \to \pi^0 K^0_S$	1.3	11.5 ± 1.0	34.5	17
$B^\pm \to \eta_{\gamma\gamma} K^{*\pm}(K^{*\pm} \to \pi^\pm K^0_S)$	2.2	$24.3^{+3.0}_{-2.9}$	9.0	15
$B^0 \to \eta_{\gamma\gamma} K^{*0}(K^{*0} \to \pi^0 K^0_S)$	2.6	18.7 ± 1.7	4.5	7
$B^\pm \to K^{*\pm}\gamma(K^{*\pm} \to \pi^+ K^0_S)$	0.15	40.3 ± 2.6	23.0	5
$B^0 \to K^{*0}\gamma(K^{*0} \to \pi^0 K^0_S)$	0.15	40.1 ± 2.0	11.5	2
Total				46

Table 7.31: Potential $B\overline{B}$ background for the $\eta_{\gamma\gamma}K^0_S$ mode. For each decay mode we give the MC reconstruction efficiency ϵ, branching fraction ($\mathcal{B}$), daughter branching fraction product, estimate background (normalized to our integrated luminosity) in ML input.

Cross Feed Channel	MC ϵ (%)	Est. $\mathcal{B}$ (10^{-6})	$\prod \mathcal{B}_i$ (%)	# evts in ML
$B^\pm \to \eta_{3\pi} K^{*\pm}(K^{*\pm} \to \pi^\pm K^0_S)$	1.7	$24.3^{+3.0}_{-2.9}$	5.2	7
$B^0 \to \eta_{3\pi} K^{*0}(K^{*0} \to \pi^0 K^0_S)$	2.0	18.7 ± 1.7	2.6	3
$B^0 \to \eta'_{\eta\pi\pi} K^0_S$	0.13	64.9 ± 3.5	6.0	2
Total				12

Table 7.32: Potential $B\overline{B}$ background for the $\eta_{3\pi}K^0_S$ mode. For each decay mode we give the MC reconstruction efficiency ϵ, branching fraction ($\mathcal{B}$), daughter branching fraction product, estimate background (normalized to our integrated luminosity) in ML input.

Cross Feed Channel	MC ϵ (%)	Est. $\mathcal{B}$ (10^{-6})	$\prod \mathcal{B}_i$ (%)	# evts in ML
$B^0 \to \eta_{\gamma\gamma}\pi^0$	0.87	$0.6^{+0.5}_{-0.4}$	39.4	1
$B^\pm \to \eta_{\gamma\gamma}\rho^\pm$	0.14	$8.1^{+1.7}_{-1.5}$	39.4	1
$B^0 \to \pi^0\pi^0$	0.05	1.45 ± 0.29	100.0	0
Total				2

Table 7.33: Potential $B\overline{B}$ background for the $\eta_{\gamma\gamma}\eta_{\gamma\gamma}$ mode. For each decay mode we give the MC reconstruction efficiency ϵ, branching fraction ($\mathcal{B}$), daughter branching fraction product, estimate background (normalized to our integrated luminosity) in ML input.

Cross Feed Channel	MC ϵ (%)	Est. $\mathcal{B}$ (10^{-6})	$\prod \mathcal{B}_i$ (%)	# evts in ML
$B^{\pm} \to \eta_{3\pi}\rho^{+}$	0.13	$8.1^{+1.7}_{-1.5}$	22.6	1
$B^{0} \to \eta_{3\pi}\pi^{0}$	0.90	$0.6^{+0.5}_{-0.4}$	22.6	0
Total				1

Table 7.34: Potential $B\overline{B}$ background for the $\eta_{\gamma\gamma}\eta_{3\pi}$ mode. For each decay mode we give the MC reconstruction efficiency ϵ, branching fraction ($\mathcal{B}$), daughter branching fraction product, estimate background (normalized to our integrated luminosity) in ML input.

Cross Feed Channel	MC ϵ (%)	Est. $\mathcal{B}$ (10^{-6})	$\prod \mathcal{B}_i$ (%)	# evts in ML
$B^{0} \to \eta_{\gamma\gamma}K^{*0}$ $(K^{*0} \to \pi^{+}K^{-})$	0.56	18.7 ± 1.7	26.2	9
$B^{0} \to \phi\pi^{0}$	1.5	0.14 ± 0.14	49.1	0
Total				9

Table 7.35: Potential $B\overline{B}$ background for the $\eta_{\gamma\gamma}\phi$ mode. For each decay mode we give the MC reconstruction efficiency ϵ, branching fraction ($\mathcal{B}$), daughter branching fraction product, estimate background (normalized to our integrated luminosity) in ML input.

Cross Feed Channel	MC ϵ (%)	Est. $\mathcal{B}$ (10^{-6})	$\prod \mathcal{B}_i$ (%)	# evts in ML
$B^{0} \to \eta_{3\pi}K^{*0}$ $(K^{*0} \to \pi^{+}K^{-})$	0.35	18.7 ± 1.7	15.1	3

Table 7.36: Potential $B\overline{B}$ background for the $\eta_{3\pi}\phi$ mode. For each decay mode we give the MC reconstruction efficiency ϵ, branching fraction ($\mathcal{B}$), daughter branching fraction product, estimate background (normalized to our integrated luminosity) in ML input.

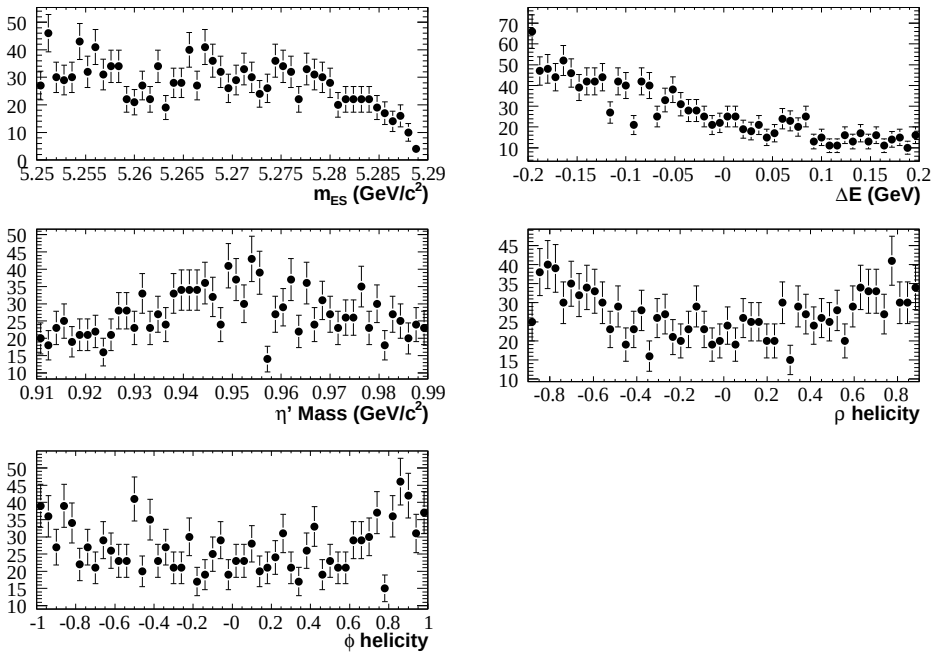

Figure 7.3: Distrbution of ML fit variables for $B\overline{B}$ generic events for $\eta'_{\rho\gamma}\phi$ mode.

Cross Feed Channel	MC ϵ (%)	Est. $\mathcal{B}$ (10^{-6})	$\prod \mathcal{B}_i$ (%)	# evts in ML
$B^0 \to \phi K^{*0}(L, f_L = 1)$ $(K^{*+} \to K^+\pi^+)$	0.43	4.75 ± 0.45	32.7	2
$B^0 \to \phi K^{*0}(T, f_T = 1)$ $(K^{*+} \to K^+\pi^+)$	0.47	4.75 ± 0.45	32.7	2
$B^\pm \to \phi K^{*\pm}(L, f_L = 1)$ $(K^{*\pm} \to K^\pm\pi^0)$	0.18	4.85 ± 0.75	33.3	1
$B^\pm \to \phi K^{*\pm}(T, f_T = 1)$ $(K^{*\pm} \to K^\pm\pi^0)$	0.25	4.85 ± 0.75	33.3	1
$B^0 \to a_1^0 K^{*0}$ $(L, f_L = 0.7)$	0.03	10^*	46.7	1
$B^0 \to a_1^0 \rho^0 (L, f_L = 1)$	0.04	1^*	100.0	0
Total				7

Table 7.37: Potential $B\overline{B}$ background for the $\eta'_{\rho\gamma}\phi$ mode. For each decay mode we give the MC reconstruction efficiency ϵ, branching fraction ($\mathcal{B}$), daughter branching fraction product, estimate background (normalized to our integrated luminosity) in ML input. BF with a $*$ are estimations.

7.7 Maximum Likelihood Fit

7.7.1 Overview

The reconstructed and selected events are ready for the ML fit analysis. In our samples of events we have considered three components: signal (sg), continuum background ($q\overline{q}$), and $B\overline{B}$ background ($b\bar{b}$). In the $\eta'\eta'K$ modes we split the signal component in MCtruth+PP signal (sg) and self-crossfeed signal (SCF) (see section 7.4.2). The $B\overline{B}$ background component (for charmless or charm B background events) is not used in all modes (as discussed in section 7.6). Table 7.38 shows the fit components used for each mode.

For each input event i, the likelihood ($\mathcal{L}_i$) is defined as [4]:

$$\mathcal{L}_i = n_{sg}\mathcal{P}^i_{sg} + n_{SCF}\mathcal{P}^i_{SCF} + n_{q\bar{q}}\mathcal{P}^i_{q\bar{q}} + n_{b\bar{b}}\mathcal{P}^i_{b\bar{b}} \tag{7.2}$$

where $\mathcal{P}^i_{sg}$, $\mathcal{P}^i_{SCF}$, $\mathcal{P}^i_{q\bar{q}}$ and $\mathcal{P}^i_{b\bar{b}}$ are the probability for signal, SCF, continuum background and $B\overline{B}$ background, evaluated with the observables of the ith event as the product of the probability density functions (PDFs) for each of the observable. n_{sg} (number of signal events), n_{SCF} (number of SCF events), $n_{q\bar{q}}$ (number of continuum events) and $n_{b\bar{b}}$ (number of $B\overline{B}$ events) are free parameters in the fit. For branching fractions measurements we consider only the signal events n_{sg}.

For N input events, the overall likelihood is:

$$\mathcal{L} = \frac{\exp\left(-\sum_j n_j\right)}{N!}\prod_i^N \mathcal{L}_i \tag{7.3}$$

where n_j is the number of events found by the fitter for j-component. Our fitter minimizes the expression $-\ln\mathcal{L}$ with respect to a set of free parameters.

When we fit for charge asymmetry for $\eta' K^{\pm}$ and $\eta K^{\pm}\gamma$ modes, we split the likelihood function depending on the charge of the B meson:

$$\mathcal{L}^k_i = n^k_{sg}\mathcal{P}^i_{sg} + n^k_{q\bar{q}}\mathcal{P}^i_{q\bar{q}} + n^k_{b\bar{b}}\mathcal{P}^i_{b\bar{b}} \tag{7.4}$$

[4] Of course considering the components for each mode as in tab. 7.38.

where $k = 1$ for B^- and $k = 2$ for B^+. The yields n_j^k are written as:

$$\begin{aligned} n_j^1 &= n_j \cdot (1 + \mathcal{A}_j)/2 \\ n_j^2 &= n_j \cdot (1 - \mathcal{A}_j)/2 \end{aligned} \tag{7.5}$$

where $\mathcal{A}_j$ is the charge asymmetry as defined in eq. 7.1. Then the total likelihood for the event i is:

$$\mathcal{L}_i = \prod_{k=1}^{2} \mathcal{L}_i^k \tag{7.6}$$

The n_j and $\mathcal{A}_j$ are free parameters in the fit.

7.7.2 Discriminating Variables and their Probability Distribution Functions

We describe in this section PDFs of the discriminating variables for the components used in the ML fit. We show in tab. 7.38 which discriminating variables are used in the ML fits for each B decay mode. We choose the variables to use following the requirement that they should have a good discriminating power between signal and background and they should be uncorrelated because of the definition of our likelihood function (we study the effect of the correlations using MC toy experiments). The ϕ helicity $\mathcal{H}_\phi = \cos\theta_H$ is defined as cosine of the ϕ's rest frame decay angle of a kaon respect to ϕ flight direction. The shape of the distributions of this variable is parabolic polynomial for signal events and linear polynomial for continuum background events.

PDFs for signal, SCF, and $B\overline{B}$ have been done using Monte Carlo simulated events. PDFs for background have been done using on-peak sidebands, defined as:

- *Grand Side Band* (GSB): $5.25 < m_{\rm ES} < 5.27 \ {\rm GeV}/c^2$
- ΔE *Side Band* (DESB): $0.1 < |\Delta E| < 0.2 \ {\rm GeV}$

The parameters for the $m_{\rm ES}$ background distributions are determined by fits to DESB sidebands, while the other parameters are determined from GSB data.

Table 8.19 reports the general parameterizations chosen for the different PDFs.

Most of the background parameters are floated in the fit: Argus parameter for $m_{\rm ES}$; coefficient of Chebyshev polynomial for ΔE; mean, $\sigma_{\rm left}$ and $\sigma_{\rm right}$ of aymmetric Gaussian for $\mathcal{F}$; coefficients of Chebyshev polynomial and fraction for daughter

resonance masses; coefficient of Chebyshev polynomial for ρ helicity and ϕ helicity. Appendix A shows PDFs plots, correlations between input variables for all decay modes, and the values of the background parameters left floating in the final fits.

We deal with uncertainties in PDFs parameters in the systematics section 7.9.

7.7.3 MC/data Matching

The MC simulation does not reproduce very well the real data. In particular we can have small differences in the signal PDFs, done with MC events, with respect to the real data distributions. From control samples, we determine shifts and scale factors to apply to $m_{\rm ES}$ and ΔE core distributions. Data and Monte Carlo control sample $B^- \to D^0\pi^-$ have been used to measure systematic difference for these variables. Our studies show that corrections for $m_{\rm ES}$ are different for Runs1-5 data so we determine separate corrections. For η and η' masses we determine the scale factor and shift parameters by allowing them to float in our on-peak data sample (for η parameters we use ηK^0_S samples and for η' parameters we use $\eta' K^\pm$ samples). For the $\mathcal{F}$ parameters we don't apply any corrections. We show shifts and scale factors in tab. 7.40. We consider a systematic error for these corrections.

In $\eta' K$ analysis, we modify the fit procedure in order to take into account the uncertainties of the signal PDF parameters directly in the fit. We do this because we can (the data samples are now large enough) and the precision of the branching fraction for the charged mode is now $\sim$3%; we wish to account for these uncertainties in signal parameters as rigorously as possible. Our procedure is to float in the yield fits the ΔE scale factor, the $m_{\rm ES}$ offset (four separate offset for Runs1-4), and the three asymmetric Gaussian parameters for $\mathcal{F}$. For the modes with $\eta'_{\rho\gamma}$, we fit the $\eta'_{\eta\pi\pi}$ and $\eta'_{\rho\gamma}$ simultaneously, with only the $\mathcal{F}$ parameters in common in order to more precisely determine these parameters for these modes which have higher background (and hence $\mathcal{F}$ is more important). The fit values of the floated signal parameters are in good agreement with expectations from the control sample studies.

Decay Mode	Fit Components	Discriminating Variables
$\eta'_{\eta\pi\pi}\eta'_{\eta\pi\pi}K^0_S$	sg, SCF, $q\overline{q}$	$m_{\rm ES}$, ΔE, $\mathcal{F}$, both η' mass
$\eta'_{\eta\pi\pi}\eta'_{\rho\gamma}K^0_S$	sg, SCF, $q\overline{q}$, $b\overline{b}$	$m_{\rm ES}$, ΔE, $\mathcal{F}$, $\eta'_{\eta\pi\pi}$ mass, η mass, $\mathcal{H}_\rho$
$\eta'_{\eta\pi\pi}\eta'_{\eta\pi\pi}K^\pm$	sg, SCF, $q\overline{q}$	$m_{\rm ES}$, ΔE, $\mathcal{F}$, both η' mass
$\eta'_{\eta\pi\pi}\eta'_{\rho\gamma}K^\pm$	sg, SCF, $q\overline{q}$, $b\overline{b}$	$m_{\rm ES}$, ΔE, $\mathcal{F}$, $\eta'_{\eta\pi\pi}$ mass, η mass, $\mathcal{H}_\rho$
$\eta'_{\eta\pi\pi}K^0_{S+-}$	sg, $q\overline{q}$	$m_{\rm ES}$, ΔE, $\mathcal{F}$
$\eta'_{\rho\gamma}K^0_{S+-}$	sg, $q\overline{q}$, $b\overline{b}$	$m_{\rm ES}$, ΔE, $\mathcal{F}$
$\eta'_{\eta\pi\pi}K^\pm$	sg, $q\overline{q}$	$m_{\rm ES}$, ΔE, $\mathcal{F}$
$\eta'_{\rho\gamma}K^\pm$	sg, $q\overline{q}$, $b\overline{b}$	$m_{\rm ES}$, ΔE, $\mathcal{F}$
$\eta_{\gamma\gamma}K^0_S\gamma$	sg, $q\overline{q}$, $b\overline{b}$	$m_{\rm ES}$, ΔE, $\mathcal{F}$, η mass
$\eta_{3\pi}K^0_S\gamma$	sg, $q\overline{q}$	$m_{\rm ES}$, ΔE, $\mathcal{F}$, η mass
$\eta_{\gamma\gamma}K^\pm\gamma$	sg, $q\overline{q}$, $b\overline{b}$	$m_{\rm ES}$, ΔE, $\mathcal{F}$, η mass
$\eta_{3\pi}K^\pm\gamma$	sg, $q\overline{q}$, $b\overline{b}$	$m_{\rm ES}$, ΔE, $\mathcal{F}$, η mass
$\eta'_{\eta\pi\pi}K^0_S\gamma$	sg, $q\overline{q}$	$m_{\rm ES}$, ΔE, $\mathcal{F}$, η' mass, η mass
$\eta'_{\rho\gamma}K^0_S\gamma$	sg, $q\overline{q}$, $b\overline{b}$	$m_{\rm ES}$, ΔE, $\mathcal{F}$, η' mass, $\mathcal{H}_\rho$
$\eta'_{\eta\pi\pi}K^\pm\gamma$	sg, $q\overline{q}$	$m_{\rm ES}$, ΔE, $\mathcal{F}$, η' mass, η mass
$\eta'_{\rho\gamma}K^\pm\gamma$	sg, $q\overline{q}$, $b\overline{b}$	$m_{\rm ES}$, ΔE, $\mathcal{F}$, η' mass, $\mathcal{H}_\rho$
$\eta_{\gamma\gamma}K^0_S$	sg, $q\overline{q}$, $b\overline{b}$	$m_{\rm ES}$, ΔE, $\mathcal{F}$, η mass
$\eta_{3\pi}K^0_S$	sg, $q\overline{q}$	$m_{\rm ES}$, ΔE, $\mathcal{F}$, η mass
$\eta_{\gamma\gamma}\eta_{\gamma\gamma}$	sg, $q\overline{q}$	$m_{\rm ES}$, ΔE, $\mathcal{F}$, both $\eta_{\gamma\gamma}$ mass
$\eta_{\gamma\gamma}\eta_{3\pi}$	sg, $q\overline{q}$	$m_{\rm ES}$, ΔE, $\mathcal{F}$, $\eta_{\gamma\gamma}$ mass, $\eta_{3\pi}$ mass
$\eta_{3\pi}\eta_{3\pi}$	sg, $q\overline{q}$	$m_{\rm ES}$, ΔE, $\mathcal{F}$, both $\eta_{3\pi}$ mass
$\eta_{\gamma\gamma}\phi$	sg, $q\overline{q}$, $b\overline{b}$	$m_{\rm ES}$, ΔE, $\mathcal{F}$, η mass, $\mathcal{H}_\phi$
$\eta_{3\pi}\phi$	sg, $q\overline{q}$	$m_{\rm ES}$, ΔE, $\mathcal{F}$, η mass, $\mathcal{H}_\phi$
$\eta'_{\eta\pi\pi}\phi$	sg, $q\overline{q}$	$m_{\rm ES}$, ΔE, $\mathcal{F}$, η' mass, η mass, $\mathcal{H}_\phi$
$\eta'_{\rho\gamma}\phi$	sg, $q\overline{q}$	$m_{\rm ES}$, ΔE, $\mathcal{F}$, η' mass, $\mathcal{H}_\rho$, $\mathcal{H}_\phi$

Table 7.38: Fit components and discriminating variables in the fit for each decay: sg, signal (or MCtruth+PP signal in $\eta'\eta'K$ modes); SCF, self-crossfeed signal; $q\overline{q}$, continuum background; $b\overline{b}$, $B\overline{B}$ background. See text for a description of the variables.

Fit Component	ΔE	$m_{\rm ES}$	$\mathcal{F}$	η mass	$\eta'_{\eta\pi\pi}$ mass	$\eta'_{\rho\gamma}$mass	$\mathcal{H}_\rho$	$\mathcal{H}_\phi$
sg	DG/TG	CB/TG	G + AG	DG	DG	DG	CH2	CH2
SCF	G + CH2	CB	G + AG	DG	G + CH2	–	CH2	–
$q\overline{q}$	CH1	A	AG + CH1	MCG + CH1	MCG + CH1	MCG + CH1	CH1	CH1
$b\overline{b}$	CH4/K	A/K	G + AG	G + CH1	G + CH1	CH1	CH1	CH2

Table 7.39: PDF parameterizations used for signal, SCF signal, $q\overline{q}$ background and $B\overline{B}$ background (G = Gaussian, MCG = Gaussian from MC, DG = double Gaussian, TG = triple Gaussian, AG = asymmetric Gausssian, CB = Crystal Ball, A = Argus, CHn = n^{th} order Chebyshev polynomial, K = KEYS.

	Shift (MeV)	Scale Factor
ΔE		
run1-5	0 ± 5	1.05 ± 0.05
$m_{\rm ES}$		
run1	0.8 ± 0.2	1.00 ± 0.04
run2	0.6 ± 0.2	1.00 ± 0.04
run3	0.4 ± 0.2	1.00 ± 0.04
run4	0.1 ± 0.2	1.00 ± 0.04
run5	-0.3 ± 0.2	1.00 ± 0.06
$\eta \to \gamma\gamma$		
run1-5	0.9 ± 0.8	1.07 ± 0.12
$\eta \to \pi^+\pi^-\pi^0$		
run1-5	0.0 ± 0.3	1.06 ± 0.11
$\eta' \to \rho^0\gamma$		
run1-5	0.0 ± 0.9	1.10 ± 0.13
$\eta' \to \eta\pi^+\pi^-$		
run1-5	0.2 ± 0.2	1.02 ± 0.08

Table 7.40: Shifts and scale factors for MC/data matching to apply to the core Gaussians used to fit signal distributions. The corrections are given for the data of different runs.

7.8 Verification Tests

7.8.1 Charge Asymmetry Measurements on MC samples

We have determined the charge asymmetry for the Monte Carlo simulated events for charged decay modes. These events have been generated with 0 charge asymmetry. Results are shown in tab. 7.41.

Decay Mode	Signal yields	$\mathcal{A}_{sig}$ (10^{-2})
$\eta'_{\eta\pi\pi}K^{\pm}$	30059 ± 174	-1.0 ± 0.6
$\eta'_{\rho\gamma}K^{\pm}$	37739 ± 198	-0.8 ± 0.5
$\eta_{\gamma\gamma}K^{\pm}\gamma$	30530 ± 179	-1.0 ± 0.6
$\eta_{3\pi}K^{\pm}\gamma$	21256 ± 149	-1.2 ± 0.7

Table 7.41: Charge asymmetry for signal Monte Carlo simulated events.

7.8.2 MC Toy experiments

We performed 500 MC toy experiments for each decay mode in order to validate the ability of our fitter to extract correctly the signal yields and charge asymmetry present in data and Monte Carlo simulated events. In particular we check for the presence of any possible bias in the fit results. The events are taken from the MC for signal and SCF events and generated from PDFs for continuum background. The $B\overline{B}$ background events are generated from PDFs for $\eta'\eta'K$ modes and taken from MC events for the other modes. Numbers of signal, $B\overline{B}$ and continuum events in each experiment are as expected in data. The numbers of $B\overline{B}$ events are those shown in the tables of section 7.6.

We perform several trials with different numbers of signal and $B\overline{B}$ events. In this way, we can study, for example, the effect of the $B\overline{B}$ events fitting with or without the $B\overline{B}$ events in the samples. We study also the effect of fitting with $B\overline{B}$ component or forcing $B\overline{B}$ component to zero. If no signal events are embedded, we know that there is a small negative bias of a few events visible; this is mostly an artifact of the low signal yields and small sample sizes. This effect has been extensively studied in previous analysis in *BABAR* and is understood [101].

Results of the toy experiments are shown in tables 7.42–7.49 for all the decay modes. In tab. 7.49 we report the results of toy experiments for $\eta' K^{\pm}$ modes where we

fit also the charge asymmetry. We fit the distributions of the toy experiments results and their errors with Gaussians and the central values are reported in the tables. We calculate also the pulls variables for the results and we fit their distributions with Gaussians. The central values and sigmas of these Gaussians are also shown in the tables. Distributions for $\eta' K$ modes are shown in the fig. 7.4 for signal yields and fig. 7.5 for charge asymmetry values.

The biases obtained in these MC toy experiments studies are used to correct the results fitted in on-peak data. For the modes ηK^0_S, $\eta\eta$, $\eta\phi$, $\eta'\phi$, where we are performing an update of the measurements and we need higher precision, we have also generated the signal events from PDFs and the values of the biases are taken as difference between the results of toys with signal events taken from MC and the results of toys with signal events generated from PDFs. In this way we take in account the effect of the low signal yields and small sample sizes (mentioned above).

We introduce a systematic uncertainty for the fit biases.

Component	# Events	Yield Mean	Yield Error	Pull Mean	Pull σ
$\eta'_{\eta\pi\pi}\eta'_{\eta\pi\pi}K^0_S$					
sg	0	-3.5 ± 0.4	3.0 ± 0.1	-0.55 ± 0.14	1.02 ± 0.10
SCF	0	3.1 ± 0.9	12.4 ± 0.1	0.18 ± 0.06	1.01 ± 0.06
$q\overline{q}$	467	468.2 ± 0.7	24.2 ± 0.1		
sg	10	11.1 ± 0.2	5.0 ± 0.1	0.21 ± 0.03	1.04 ± 0.02
SCF	7	3.6 ± 0.7	14.4 ± 0.1	-0.36 ± 0.06	1.04 ± 0.05
$q\overline{q}$	450	452.2 ± 0.6	24.5 ± 0.1		
$\eta'_{\eta\pi\pi}\eta'_{\rho\gamma}K^0_S$					
sg	0	-1.6 ± 0.4	6.4 ± 0.1	-0.20 ± 0.06	1.06 ± 0.05
SCF	0	2.0 ± 2.7	56.5 ± 0.3	0.04 ± 0.05	1.06 ± 0.04
$q\overline{q}$	8741	8737.0 ± 2.5	107.7 ± 0.1		
$b\overline{b}$	0	0 (fixed)			
sg	10	11.0 ± 0.4	8.3 ± 0.1	0.09 ± 0.05	0.99 ± 0.04
SCF	7	6.8 ± 2.8	60.6 ± 0.2	-0.08 ± 0.05	1.00 ± 0.04
$q\overline{q}$	8724	8723.0 ± 2.6	109.3 ± 0.1		
$b\overline{b}$	0	0 (fixed)			
sg	0	-1.1 ± 0.3	6.4 ± 0.1	-0.20 ± 0.06	1.10 ± 0.06
SCF	0	-1.8 ± 0.3	3.5 ± 0.1	-0.37 ± 0.08	1.12 ± 0.09
$q\overline{q}$	8741	8762.0 ± 18.9	380.1 ± 1.5		
$b\overline{b}$	0	-18.1 ± 9.2	369.8 ± 1.5	0.03 ± 0.05	1.10 ± 0.04
sg	10	11.4 ± 0.4	8.3 ± 0.1	0.13 ± 0.05	1.03 ± 0.04
SCF	7	4.7 ± 2.8	3.9 ± 0.1	-0.07 ± 0.05	0.97 ± 0.04
$q\overline{q}$	8724	8757.0 ± 18.3	382.2 ± 1.5		
$b\overline{b}$	0	-32.2 ± 8.4	372.9 ± 1.6	-0.07 ± 0.05	1.07 ± 0.05
sg	0	-1.4 ± 0.5	7.0 ± 0.1	-0.21 ± 0.08	1.1 ± 0.06
SCF	0	-1.8 ± 0.3	3.5 ± 0.1	-0.37 ± 0.08	1.12 ± 0.09
$q\overline{q}$	7223	7237.0 ± 20.5	402.7 ± 1.9		
$b\overline{b}$	1518	1507.0 ± 21.2	398.1 ± 1.9	-0.01 ± 0.05	1.05 ± 0.05
sg	10	10.7 ± 0.4	9.0 ± 0.1	0.11 ± 0.04	0.96 ± 0.04
SCF	7	11.1 ± 3.1	67.4 ± 0.2	0.01 ± 0.05	1.00 ± 0.04
$q\overline{q}$	7206	7239.0 ± 20.0	402.6 ± 2.0		
$b\overline{b}$	1518	1480.0 ± 20.1	398.5 ± 2.0	-0.05 ± 0.05	1.07 ± 0.04

Table 7.42: Results of 500 MC Toy experiments for $\eta'\eta' K^0_S$ modes. We show MC signal and SCF embedded yields, $B\overline{B}$ and continuum background generated events, means of the reconstructed yields, means of the error of the reconstructed yiels, means of the signal and $B\overline{B}$ pull, σ of the signal and $B\overline{B}$ pull (see text for more details).

Component	# Events	Yield Mean	Yield Error	Pull Mean	Pull σ
$\eta'_{\eta\pi\pi}\eta'_{\eta\pi\pi}K^{\pm}$					
sg	0	-2.2 ± 0.4	3.9 ± 0.4	-0.52 ± 0.11	1.02 ± 0.06
SCF	0	3.5 ± 1.1	18.2 ± 0.2	-0.17 ± 0.05	1.07 ± 0.04
$q\overline{q}$	1390	1390.0 ± 0.9	40.7 ± 0.1		
sg	10	11.6 ± 0.2	6.1 ± 0.1	0.40 ± 0.03	0.98 ± 0.03
SCF	7	3.4 ± 1.0	20.8 ± 0.1	-0.43 ± 0.05	1.02 ± 0.04
$q\overline{q}$	1373	1375.0 ± 0.9	41.3 ± 0.1		
$\eta'_{\eta\pi\pi}\eta'_{\rho\gamma}K^{\pm}$					
sg	0	-1.3 ± 0.5	8.4 ± 0.1	-0.12 ± 0.06	1.04 ± 0.05
SCF	0	-7.4 ± 4.3	81.2 ± 0.3	-0.03 ± 0.04	1.01 ± 0.03
$q\overline{q}$	8913	8919.0 ± 3.8	121.8 ± 0.1		
$b\overline{b}$	0	0 (fixed)			
sg	10	12.2 ± 0.4	10.1 ± 0.1	0.18 ± 0.04	1.00 ± 0.03
SCF	7	-2.8 ± 4.0	83.5 ± 0.2	-0.08 ± 0.04	1.01 ± 0.04
$q\overline{q}$	8896	8898.0 ± 3.8	122.8 ± 0.1		
$b\overline{b}$	0	0 (fixed)			
sg	0	-0.2 ± 0.4	8.6 ± 0.1	-0.05 ± 0.05	1.00 ± 0.01
SCF	0	6.5 ± 3.8	80.5 ± 0.2	0.07 ± 0.05	1.01 ± 0.04
$q\overline{q}$	8913	8895.0 ± 36.7	618.3 ± 1.4		
$b\overline{b}$	0	13.1 ± 35.1	609.7 ± 1.3	0.01 ± 0.05	1.09 ± 0.05
sg	10	11.4 ± 0.5	10.1 ± 0.1	0.15 ± 0.05	0.95 ± 0.04
SCF	7	-2.8 ± 4.1	83.3 ± 0.2	0.01 ± 0.04	0.94 ± 0.04
$q\overline{q}$	8896	8909.0 ± 37.9	621.7 ± 1.4		
$b\overline{b}$	0	-3.9 ± 37.7	612.6 ± 1.3	-0.05 ± 0.05	1.10 ± 0.05
sg	0	-0.9 ± 0.4	9.0 ± 0.1	-0.10 ± 0.05	1.07 ± 0.04
SCF	0	1.3 ± 4.1	85.4 ± 0.3	0.03 ± 0.05	1.01 ± 0.04
$q\overline{q}$	5661	5705.0 ± 35.7	678.2 ± 3.3		
$b\overline{b}$	3252	3206.0 ± 35.5	670.6 ± 3.8	-0.05 ± 0.05	1.11 ± 0.05
sg	10	11.8 ± 0.5	10.6 ± 0.1	0.15 ± 0.04	0.98 ± 0.04
SCF	7	-0.3 ± 4.3	88.0 ± 0.2	-0.06 ± 0.05	1.00 ± 0.04
$q\overline{q}$	5644	5590.0 ± 36.9	679.2 ± 3.2		
$b\overline{b}$	3252	3309.0 ± 36.9	670.7 ± 3.2	0.10 ± 0.05	1.06 ± 0.04

Table 7.43: Results of 500 MC Toy experiments for $\eta'\eta' K^{\pm}$ modes. We show MC signal and SCF embedded yields, $B\overline{B}$ and continuum background generated events, means of the reconstructed yields, means of the error of the reconstructed yiels, means of the signal and $B\overline{B}$ pull, σ of the signal and $B\overline{B}$ pull (see text for more details).

Component	# Events	Yield Mean	Yield Error	Pull Mean	Pull σ
$\eta_{\gamma\gamma} K^0_S \gamma$					
sg	30	32.3 ± 0.5	11.2 ± 0.1	0.19 ± 0.04	0.94 ± 0.03
$q\overline{q}$	806	803.9 ± 0.5	29.9 ± 0.1		
$b\overline{b}$	0	0 (fixed)			
sg	30	32.0 ± 0.5	11.7 ± 0.1	0.14 ± 0.04	1.07 ± 0.04
$q\overline{q}$	806	807.4 ± 2.3	53.0 ± 0.2		
$b\overline{b}$	0	-3.0 ± 2.4	47.6 ± 0.2	-0.04 ± 0.05	1.05 ± 0.04
sg	30	34.5 ± 0.5	11.5 ± 0.1	0.38 ± 0.04	0.96 ± 0.03
$q\overline{q}$	787	801.6 ± 0.5	30.0 ± 0.1		
$b\overline{b}$	19	0 (fixed)			
sg	30	33.9 ± 0.5	12.2 ± 0.1	0.29 ± 0.04	0.95 ± 0.03
$q\overline{q}$	787	795.5 ± 2.1	53.6 ± 0.2		
$b\overline{b}$	19	6.8 ± 2.3	48.5 ± 0.3	-0.23 ± 0.05	0.97 ± 0.04
sg	30	33.6 ± 0.5	11.5 ± 0.1	0.35 ± 0.04	0.93 ± 0.04
$q\overline{q}$	787	783.1 ± 0.5	30.0 ± 0.2		
$b\overline{b}$	19	19 (fixed)			
$\eta_{3\pi} K^0_S \gamma$					
sg	12	13.0 ± 0.2	6.6 ± 0.1	0.12 ± 0.04	0.94 ± 0.03
$q\overline{q}$	328	327.1 ± 0.2	18.9 ± 0.1		
$\eta_{\gamma\gamma} K^{\pm} \gamma$					
sg	103	110.0 ± 0.8	19.4 ± 0.1	0.35 ± 0.04	1.00 ± 0.03
$q\overline{q}$	2469	2462.0 ± 0.8	52.2 ± 0.1		
$b\overline{b}$	0	0 (fixed)			
sg	103	109.6 ± 0.8	20.4 ± 0.1	0.27 ± 0.04	0.98 ± 0.03
$q\overline{q}$	2469	2476.0 ± 2.9	88.7 ± 0.2		
$b\overline{b}$	0	-14.9 ± 3.1	75.3 ± 0.2	-0.17 ± 0.04	0.88 ± 0.03
sg	103	116.9 ± 0.9	19.8 ± 0.1	0.70 ± 0.04	0.99 ± 0.03
$q\overline{q}$	2407	2455.0 ± 0.8	52.2 ± 0.1		
$b\overline{b}$	62	0 (fixed)			
sg	103	114.9 ± 0.9	20.9 ± 0.1	0.59 ± 0.04	0.96 ± 0.03
$q\overline{q}$	2407	2414.0 ± 3.6	87.9 ± 0.2		
$b\overline{b}$	62	43.6 ± 3.8	77.8 ± 0.2	-0.25 ± 0.05	1.02 ± 0.04
sg	103	109.7 ± 0.8	19.8 ± 0.1	0.36 ± 0.04	0.92 ± 0.03
$q\overline{q}$	2407	2400.0 ± 0.9	52.2 ± 0.1		
$b\overline{b}$	62	62 (fixed)			
$\eta_{3\pi} K^{\pm} \gamma$					
sg	41	42.9 ± 0.4	11.7 ± 0.1	0.19 ± 0.04	0.99 ± 0.03
$q\overline{q}$	1155	1153.0 ± 0.4	35.3 ± 0.1		
$b\overline{b}$	0	0 (fixed)			
sg	41	42.5 ± 0.5	13.2 ± 0.1	0.12 ± 0.04	1.00 ± 0.03
$q\overline{q}$	1155	1161.0 ± 2.1	56.8 ± 0.1		
$b\overline{b}$	0	-8.4 ± 2.3	50.1 ± 0.2	-0.21 ± 0.05	0.98 ± 0.04
sg	41	45.8 ± 0.5	12.0 ± 0.1	0.39 ± 0.03	0.95 ± 0.03
$q\overline{q}$	1140	1150.0 ± 0.4	35.3 ± 0.1		
$b\overline{b}$	15	0 (fixed)			
sg	41	44.3 ± 0.5	13.4 ± 0.1	0.23 ± 0.04	0.95 ± 0.04
$q\overline{q}$	1140	1157.0 ± 2.1	57.3 ± 0.1		
$b\overline{b}$	15	-5.1 ± 2.3	51.0 ± 0.1	-0.40 ± 0.05	1.02 ± 0.04
sg	41	41.6 ± 0.5	11.9 ± 0.1	0.06 ± 0.04	0.98 ± 0.04
$q\overline{q}$	1140	1139.0 ± 0.5	35.3 ± 0.1		
$b\overline{b}$	15	15 (fixed)			

Table 7.44: Results of 500 MC Toy experiments for $\eta K \gamma$ modes. We show MC signal embedded yield, MC $B\overline{B}$ embedded, mean of the reconstructed yields, mean of the error of the reconstructed yields, mean of the signal pull, σ of the signal pull (see text for more details).

Component	# Events	Yield Mean	Yield Error	Pull Mean	Pull σ
$\eta'_{\eta\pi\pi}K^0_S\gamma$					
sg	9	9.2 ± 0.2	4.3 ± 0.1	0.02 ± 0.04	1.02 ± 0.03
$q\overline{q}$	129	128.8 ± 0.2	11.8 ± 0.1		
$\eta'_{\rho\gamma}K^0_S\gamma$					
sg	12	14.1 ± 0.7	14.9 ± 0.1	0.19 ± 0.05	0.93 ± 0.04
$q\overline{q}$	2819	2817.0 ± 0.7	54.9 ± 0.1		
$b\overline{b}$	0	0 (fixed)			
sg	12	13.8 ± 0.8	15.0 ± 0.1	0.18 ± 0.05	0.98 ± 0.04
$q\overline{q}$	2819	2825.0 ± 4.3	109.5 ± 0.3		
$b\overline{b}$	0	-14.9 ± 4.5	96.9 ± 0.4	-0.08 ± 0.05	0.97 ± 0.04
sg	12	16.6 ± 0.7	15.6 ± 0.1	0.28 ± 0.04	0.91 ± 0.04
$q\overline{q}$	2696	2815.0 ± 0.7	55.1 ± 0.1		
$b\overline{b}$	123	0 (fixed)			
sg	12	13.6 ± 0.7	15.4 ± 0.1	0.08 ± 0.04	0.97 ± 0.04
$q\overline{q}$	2696	2711.0 ± 4.7	110.9 ± 0.3		
$b\overline{b}$	123	107.3 ± 4.6	99.8 ± 0.3	-0.17 ± 0.04	0.96 ± 0.03
sg	12	12.4 ± 0.6	15.1 ± 0.1	0.04 ± 0.04	0.97 ± 0.04
$q\overline{q}$	2696	2696.0 ± 0.7	55.0 ± 0.1		
$b\overline{b}$	123	123 (fixed)			
$\eta'_{\eta\pi\pi}K^{\pm}\gamma$					
sg	30	31.6 ± 0.3	8.0 ± 0.1	0.19 ± 0.03	0.98 ± 0.03
$q\overline{q}$	432	430.6 ± 0.3	21.5 ± 0.1		
$b\overline{b}$	0				
sg	30	31.6 ± 0.3	8.0 ± 0.1	0.11 ± 0.03	0.97 ± 0.03
$q\overline{q}$	430	430.5 ± 0.3	21.5 ± 0.1		
$b\overline{b}$	2				
$\eta'_{\rho\gamma}K^{\pm}\gamma$					
sg	61	78.2 ± 1.3	29.8 ± 0.1	0.52 ± 0.04	0.90 ± 0.03
$q\overline{q}$	10150	10133 ± 1.3	104.6 ± 0.1		
$b\overline{b}$	0	0 (fixed)			
sg	61	71.8 ± 1.4	30.3 ± 0.1	0.34 ± 0.05	0.97 ± 0.04
$q\overline{q}$	10150	10139.1 ± 10.1	214.2 ± 0.3		
$b\overline{b}$	0	0.0 ± 10.3	193.1 ± 0.3	-0.00 ± 0.05	1.00 ± 0.04
sg	61	93.6 ± 1.4	31.6 ± 0.1	1.01 ± 0.04	0.94 ± 0.03
$q\overline{q}$	9706	10117.4 ± 1.4	105.0 ± 0.1		
$b\overline{b}$	444	0 (fixed)			
sg	61	75.5 ± 1.5	31.5 ± 0.1	0.61 ± 0.05	1.02 ± 0.03
$q\overline{q}$	9706	9747.0 ± 9.7	218.3 ± 0.3		
$b\overline{b}$	444	390.4 ± 10.1	199.6 ± 0.3	-0.32 ± 0.05	0.98 ± 0.04
sg	61	74.6 ± 1.3	31.0 ± 0.1	0.44 ± 0.04	0.95 ± 0.03
$q\overline{q}$	9706	9693.0 ± 1.3	104.8 ± 0.1		
$b\overline{b}$	444	444 (fixed)			

Table 7.45: Results of 500 MC Toy experiments for $\eta' K\gamma$ modes. We show MC signal embedded yield, MC $B\overline{B}$ embedded, mean of the reconstructed yields, mean of the error of the reconstructed yiels, mean of the signal pull, σ of the signal pull (see text for more details).

Component	# Events	Yield Mean	Yield Error	Pull Mean	Pull σ
		$\eta_{3\pi}K^0_S$			
sg	11 (from PDFs)	10.4 ± 0.3	5.7 ± 0.1	-0.16 ± 0.05	1.04 ± 0.04
$q\overline{q}$	1369	1381.6 ± 0.3	37.4 ± 0.1		
$b\overline{b}$	12 (from MC)				
sg	11 (from MC)	11.5 ± 0.2	5.5 ± 0.1	-0.16 ± 0.04	1.01 ± 0.03
$q\overline{q}$	1369	1380.5 ± 0.2	37.4 ± 0.1		
$b\overline{b}$	12 (from MC)				
		$\eta_{\gamma\gamma}K^0_S$			
sg	19 (from PDFs)	18.6 ± 0.4	10.1 ± 0.1	-0.05 ± 0.05	1.01 ± 0.05
$q\overline{q}$	3290	3292.3 ± 1.4	60.8 ± 0.1		
$b\overline{b}$	24 (from PDFs)	19.9 ± 1.1	20.2 ± 0.1	-0.12 ± 0.05	1.06 ± 0.05
sg	19 (from MC)	19.4 ± 0.4	10.0 ± 0.1	0.05 ± 0.04	1.02 ± 0.03
$q\overline{q}$	3290	3295.4 ± 1.1	60.8 ± 0.1		
$b\overline{b}$	24 (from MC)	19.7 ± 1.0	20.2 ± 0.1	-0.26 ± 0.05	1.05 ± 0.05
		$\eta_{\gamma\gamma}\eta_{\gamma\gamma}$			
sg	17 (from PDFs)	15.8 ± 0.5	10.0 ± 0.1	-0.10 ± 0.05	1.06 ± 0.04
$q\overline{q}$	2035	2037.6 ± 0.5	46.0 ± 0.1		
$b\overline{b}$	2 (from MC)				
sg	17 (from MC)	19.7 ± 0.4	10.0 ± 0.1	0.26 ± 0.04	0.92 ± 0.03
$q\overline{q}$	2035	2034.3 ± 0.4	46.0 ± 0.1		
$b\overline{b}$	2 (from MC)				
		$\eta_{\gamma\gamma}\eta_{3\pi}$			
sg	10 (from PDFs)	10.3 ± 0.3	6.3 ± 0.1	-0.03 ± 0.05	1.06 ± 0.04
$q\overline{q}$	1979	1979.9 ± 0.3	44.8 ± 0.1		
$b\overline{b}$	1 (from MC)				
sg	10 (from MC)	10.8 ± 0.3	6.2 ± 0.1	0.04 ± 0.04	0.98 ± 0.03
$q\overline{q}$	1979	1979.0 ± 0.3	44.8 ± 0.1		
$b\overline{b}$	1 (from MC)				
		$\eta_{3\pi}\eta_{3\pi}$			
sg	2 (from PDFs)	2.0 ± 0.2	2.8 ± 0.1	0.04 ± 0.06	1.02 ± 0.06
$q\overline{q}$	419	419.0 ± 0.2	20.6 ± 0.1		
sg	2 (from MC)	2.3 ± 0.1	2.7 ± 0.1	0.04 ± 0.04	0.97 ± 0.04
$q\overline{q}$	419	418.7 ± 0.1	20.6 ± 0.1		

Table 7.46: Results of 500 MC Toy experiments for ηK^0_S and $\eta\eta$ modes. We show MC signal and $B\overline{B}$ embedded/generated events, continuum background generated events, means of the reconstructed yields, means of the error of the reconstructed yields, means of the signal pull, σ of the signal pull (see text for more details).

Component	# Events	Yield Mean	Yield Error	Pull Mean	Pull σ
		$\eta_{3\pi}\phi$			
sg	6 (from PDFs)	6.4 ± 0.2	4.3 ± 0.1	0.14 ± 0.05	1.02 ± 0.04
$q\overline{q}$	2057	2059.5 ± 0.2	45.5 ± 0.1		
$b\overline{b}$	3 (from MC)				
sg	6 (from MC)	7.2 ± 0.2	4.3 ± 0.1	0.23 ± 0.04	0.96 ± 0.03
$q\overline{q}$	2057	2058.9 ± 0.2	45.5 ± 0.1		
$b\overline{b}$	3 (from MC)				
		$\eta_{\gamma\gamma}\phi$			
sg	0	0.5 ± 0.4	7.7 ± 0.1	-0.03 ± 0.05	1.02 ± 0.05
$q\overline{q}$	5198	5198.1 ± 0.7	73.1 ± 0.1		
$b\overline{b}$	44 (from PDFs)	44.5 ± 0.9	16.0 ± 0.1	0.05 ± 0.05	1.09 ± 0.04
sg	0	-1.9 ± 0.4	7.5 ± 0.1	-0.31 ± 0.07	1.12 ± 0.06
$q\overline{q}$	5198	5186.7 ± 0.6	73.1 ± 0.1		
$b\overline{b}$	44 (from MC)	59.0 ± 0.9	16.4 ± 0.1	0.86 ± 0.05	1.04 ± 0.04
		$\eta'_{\eta\pi\pi}\phi$			
sg	1 (from PDFs)	0.8 ± 0.2	2.7 ± 0.1	-0.19 ± 0.09	1.13 ± 0.10
$q\overline{q}$	1168	1168.2 ± 0.2	34.3 ± 0.1		
sg	1 (from MC)	0.2 ± 0.2	2.7 ± 0.1	-0.26 ± 0.08	0.99 ± 0.07
$q\overline{q}$	1168	1168.8 ± 0.2	34.3 ± 0.1		
		$\eta'_{\rho\gamma}\phi$			
sg	0	-1.0 ± 0.4	6.0 ± 0.1	-0.04 ± 0.07	0.97 ± 0.06
$q\overline{q}$	17107	17113.1 ± 0.4	131.0 ± 0.1		
$b\overline{b}$	7 (from MC)				

Table 7.47: Results of 500 MC Toy experiments for $\eta\phi$ and $\eta'\phi$ modes. We show MC signal and $B\overline{B}$ embedded/generated events, continuum background generated events, means of the reconstructed yields, means of the error of the reconstructed yields, means of the signal pull, σ of the signal pull (see text for more details).

$\eta'_{\rho\gamma}K^0$		
Signal events	460	
Bkg. events	9245	
$B\overline{B}$ events	0	
	Sg	$B\overline{B}$
Value	474.3 ± 0.8	-27.1 ± 2.0
Value Error	27.64 ± 0.02	38.14 ± 0.11

$\eta'_{\eta\pi\pi}K^0$	
Signal events	194
Bkg. events	438
	Sg
Value	193.6 ± 0.3
Value Error	15.20 ± 0.01

Table 7.48: Mean values of signal yield parameters and their errors for 500 embedded toy MC experiments for $\eta' K^0_{S+-}$ modes.

$\eta'_{\rho\gamma}K^+$			
Signal events	1343		
Bkg. events	37663		
$B\overline{B}$ events	776		
	Sg	$B\overline{B}$	$\mathcal{A}_{ch}$ (%)
Value	1389.9 ± 1.5	710.1 ± 3.9	-1.5 ± 0.2
Value Error	50.44 ± 0.02	85.41 ± 0.07	3.5 ± 0.1

$\eta'_{\eta\pi\pi}K^+$		
Signal events	606	
Bkg. events	1277	
	Sg	$\mathcal{A}_{ch}$ (%)
Value	605.1 ± 0.5	-0.4 ± 0.2
Value Error	26.60 ± 0.01	4.4 ± 0.1

Table 7.49: Mean values of of signal yield and charge asymmetry parameters and their errors for 500 embedded toy MC experiments for $\eta' K^{\pm}$ modes.

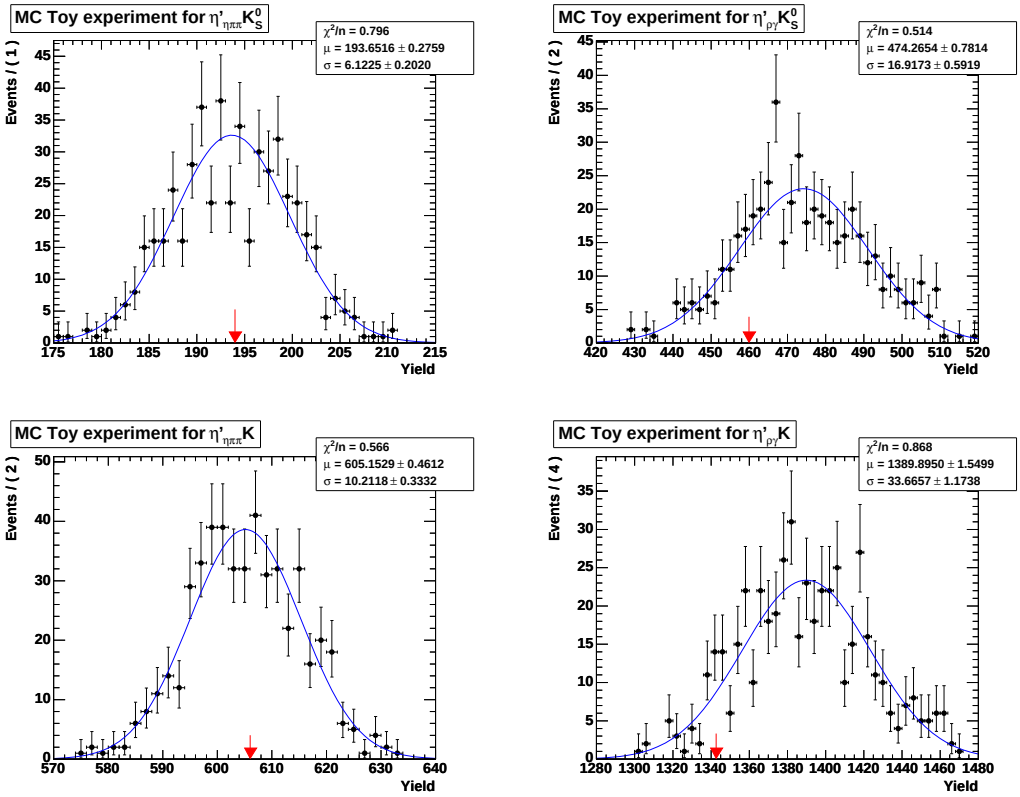

Figure 7.4: MC toy-experiments for yields in: $\eta'_{\eta\pi\pi}K^0_{S+-}$ (upper left); $\eta'_{\rho\gamma}K^0_{S+-}$ (upper right); $\eta'_{\eta\pi\pi}K^{\pm}$ (bottom left); $\eta'_{\rho\gamma}K^{\pm}$ (bottom right). Arrow indicates the value obtained in the data fit.

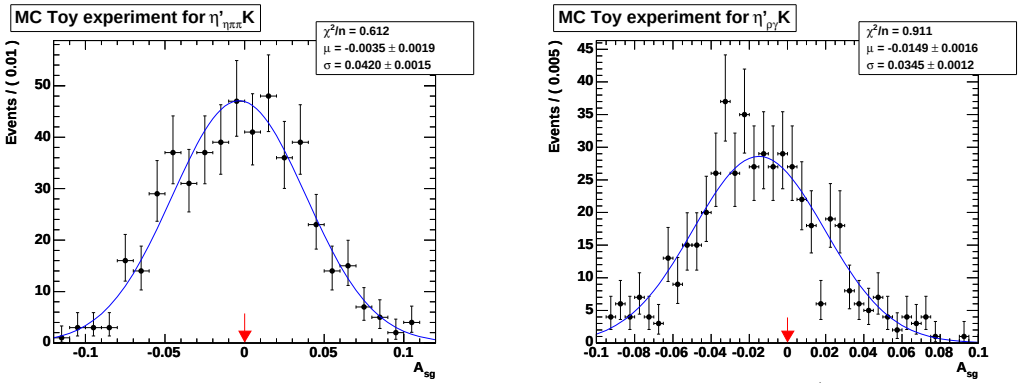

Figure 7.5: MC toy-experiments for charge asymmetry in $\eta'_{\eta\pi\pi}K^{\pm}$ (left) and $\eta'_{\rho\gamma}K^{\pm}$ (right). Arrow indicates the value of MC signal events $A = 0$.

7.9 Systematic Errors

We present here the main sources of systematic uncertainties in the measurement of branching fractions and charge asymmetries.

7.9.1 Branching Fraction Systematics

We consider systematic errors from the fit yield and efficiency. The former are mostly additive while the latter are multiplicative. The results are summarized in tables 7.50–7.53 and described below. Some of the systematics sources refer to specific modes, like the photon spectrum in $\eta^{(\prime)}K\gamma$ analyses, but most of them are common to all modes.

- ML fit bias: We determine the fit bias, from toy MC studies (see section. 7.8.2). This bias is due to the fact that we neglect correlations in the fit and the small feed due to the $B\overline{B}$ background. We quote the systematic uncertainty summing in quadrature half of the fit bias and the statistical uncertainty of the bias itself. For the modes ηK^0_S, $\eta\eta$, $\eta\phi$, and $\eta'\phi$ we consider an additional effect due to the small sample size, obtained from toy experiments where all events are generated from PDFs.

- MC/data corrections: In section 7.7.3 we have described the shifts and scale factors to apply to our signal PDFs. We use the errors of these values to calculate a systematics effect due to the variation of these correction factors when we vary them of $\pm 1\sigma$. In this way, we apply these variations, one at a time, to our signal PDFs and re-run the ML fit. In the $\eta' K$ modes, since we vary the main signal PDF parameters in the fits, this uncertainty is included in the statistical error and no systematic uncertainty is assigned.

- $B\overline{B}$ background: We quote a systematic effect due to the $B\overline{B}$ background only for the $\eta' K$ modes, where we want a precise measurement. We investigate the effect of neglecting $B\overline{B}$ background for the $\eta'_{\eta\pi\pi}$ modes with generic $B\overline{B}$ MC. The scaled expectation for input to the fit for the $\eta'_{\eta\pi\pi}K^{\pm}$ mode is 24 events from which we estimate the signal-yield systematic uncertainties given in tab. 7.51. For the $\eta'_{\rho\gamma}K^{\pm}$ mode, we have performed a study by embedding the expected number of $b \to c$ events into data and refit to determine the resulting bias in the yield from this source. Three such samples give yield shifts of -2, 4, and 10

events. We take the largest of these as the systematic uncertainty in the effect of including $b \to c$ in the $q\overline{q}$ PDF component and scale this for the $\eta'_{\rho\gamma}K^0$ mode. The uncertainty for charmless background is already included in the fit bias uncertainty (see above), where more than one-half of the bias is due to the $B\overline{B}$ component in the fit.

- Track multiplicity: We have requested the reconstruction of at least 1 charged tracks in the rest of the event. Signal MC inefficiency for this cut is of the order of about 2 %. We assign an uncertainty of 1.0%.

- Track finding efficiency: Study of absolute tracking efficiency provides a systematic error associated with the tables for `GoodTracksLoose` tracks of 0.8%.

- K^0_S finding/efficiency: We have determined K^0_S efficiency correction and associated systematic error for the MC events, following the description of the *BABAR* tracking working group. We assign a 2.1% systematic error;

- Single photons, π^0 and $\eta_{\gamma\gamma}$ efficiency: Following the efficiency corrections procedures described by *BABAR* neutral working group, we assign a systematic error of 3% per π^0 and $\eta_{\gamma\gamma}$ and 1.8% for single photons.

- Luminosity, B counting: The B counting group recommends a systematic uncertainty of 1.1 %.

- Daughter branching fractions: This value is taken directly from PDG [99].

- MC statistics: This is calculated for the number of MC signal events simulated for each decay.

- $\cos\theta_{\rm T}$ cut: A systematic uncertainty of 0.5% for modes where we cut at 0.9 and 2.0% for the $\eta'_{\eta\pi\pi}\eta'_{\rho\gamma}K^{\pm}$ mode, where we cut at 0.7, is assigned as found from $D\pi$ control sample looking at the variation of the shape of signal MC events before and after the $\cos\theta_{\rm T}$ cut.

- PID: We have evaluated the systematic error due to PID vetoes and selection. This is about 1%. For $\eta' K^{\pm}$, where we require a cut on the pull Cherenkov angle, conservatively we estimate that the efficiency correction for this cut to be 0.5%.

- Photon spectrum in $\eta^{(\prime)}K\gamma$ modes: The photon spectrum is not known. Different models predict different photon spectra. Our MC event have been simulated with the Kagan-Neubert model [97]. A different photon spectrum has been obtained from $B \rightarrow X_s\gamma$ generated with Jetset fragmentation. There is a systematic uncertainty due to the different shape of the photon spectrum and a systematic uncertainty due to the cuts applied in the event selection. These two systematic errors have been added in quadrature. We show in fig. 7.6, as examples, the photon spectra in the two modellization for the decays $\eta_{\gamma\gamma}K^{\pm}\gamma$ and $\eta'_{\rho\gamma}K^{\pm}\gamma$ as generated in MC simulation. For the same decays we show the X_s mass in fig. 7.7. Using the X_s mass distributions for the two models and the efficiency distributions shown in the fig. 6.12–6.15, we calculate the MC efficiencies for each model and we estimate the systematic error from their ratio.

Branching fraction and asymmetry results from different decay sub-modes are combined using their log-likelihood curves. These curves are adjusted to consider the effects of systematic uncertainties. Three types of systematic uncertainties are considered:

- *Additive Systematic Uncertainties* affect the fit yield and thus the statistical significance of a result. For example, a bias in the maximum likelihood fitter could systematically increase or decrease the number of events reported.

- *Uncorrelated Systematic Uncertainties* are mode-independent. Generally these are a superset of the additive systematic uncertainties and they include multiplicative systematic uncertainties on quantities which can affect the central value of the final result but not the statistical significance. *e.g.*, uncertainties in the daughter particle branching fractions affect the conversion of the fit yield into a branching fraction, but not the statistical significance of the fit yield itself.

- *Correlated Systematic Uncertainties* affect all modes in the same direction. For example, a Monte Carlo PID selection efficiency correction could bias all modes which use the selector up or down.

Additive systematic uncertainties are included in the quoted statistical significance of individual and combined results. The final combined branching fractions and asymmetries include both uncorrelated and correlated systematic uncertainties.

7.9.2 Charge Asymmetry Systematics

Most of the systematic uncertainties found for branching fraction measurements cancel for the charge asymmetry measurement. The primary sources of bias could be due to tracking differences between opposite charged tracks, PID differences or differences due to the interaction cross sections in the detector. The $\mathcal{A}_{ch}$ bias has been estimated to be -0.005 ± 0.010 or -0.16 ± 0.05 for $\eta K^{\pm}\gamma$ or $\eta' K^{\pm}$ modes, respectively, from the studies of signal Monte Carlo, control samples, and calculation of the asymmetry due to particles intereacting in the detector. We correct for these biases and assign a systematic uncertainty equal to their error.

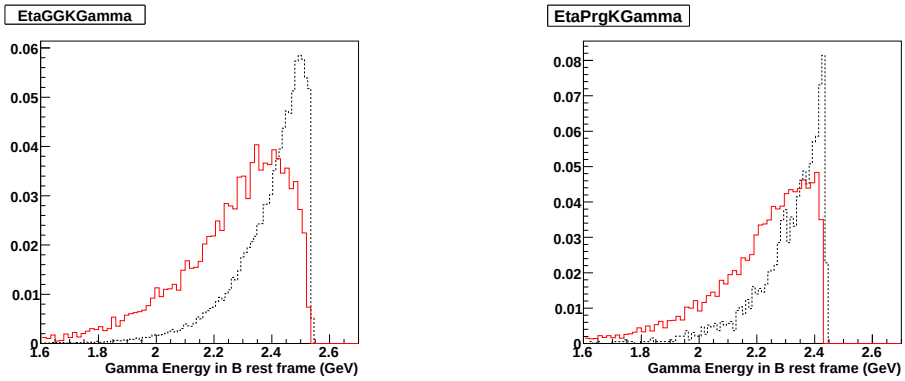

Figure 7.6: Generated energy photon spectrum in B rest frame for $\eta_{\gamma\gamma}K^{\pm}\gamma$ mode (left) and $\eta'_{\rho\gamma}K^{\pm}\gamma$ mode (right): black dashed line refers to events generated with Jetset, red solid line to events generated with Kagan-Neubert model.

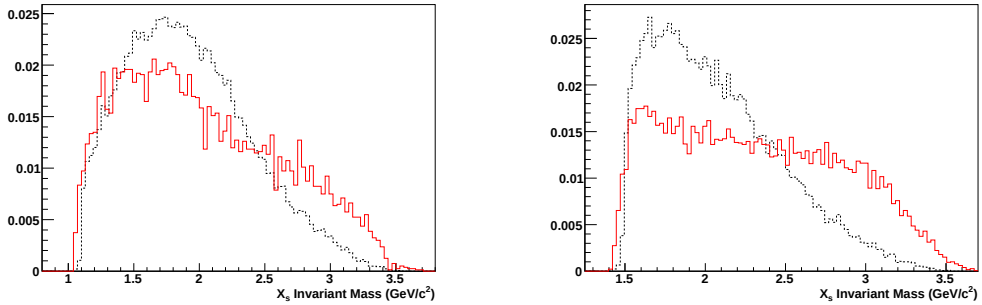

Figure 7.7: Generated X_s invariant mass for $\eta_{\gamma\gamma}K^{\pm}\gamma$ mode (left) and $\eta'_{\rho\gamma}K^{\pm}\gamma$ mode (right): black dashed line refers to events generated with jetset, red solid line to events generated with Kagan-Neubert model.

Quantity	$\eta'_{\eta\pi\pi}\eta'_{\eta\pi\pi}K^0_S$	$\eta'_{\eta\pi\pi}\eta'_{\rho\gamma}K^0_S$	$\eta'_{\eta\pi\pi}\eta'_{\eta\pi\pi}K^\pm$	$\eta'_{\eta\pi\pi}\eta'_{\rho\gamma}K^\pm$
ML Fit bias (A)	0.2	1.9	0.3	4.3
MC/data Corr. (A)	0.1	0.2	0.1	0.8
MC statistics (M)	1.3	1.1	1.2	1.2
Branching frac. (M)	4.9	3.5	4.9	3.5
Track multip. (M)	1.0	1.0	1.0	1.0
Tracking eff/qual (M)	3.2	3.2	4.0	4.0
$\eta_{\gamma\gamma}$ eff.(M)	6.0	3.0	6.0	3.0
γ eff.(M)	–	1.8	–	1.8
K^0_S eff. (M)	2.1	2.1	–	–
Number $B\overline{B}$ (M)	1.1	1.1	1.1	1.1
$\cos\theta_{\rm T}$ (M)	0.5	0.5	0.5	2.0
Particle ID (M)	1.0	1.0	1.0	1.0
Total Uncorr. (events) (A)	0.2	1.9	0.3	4.4
Total Uncorr. (%) (M)	5.1	3.7	5.0	3.7
Total Corr. (%)	7.4	5.5	7.4	5.9

Table 7.50: Estimates of systematic errors. We divide the systematics in two parts: uncorrelated errors (first part of the table) and correlated errors (second part of the table). Uncorrelated and correlated refer to the different daughter decays of the same mode. Some of these errors are additive (A) and given in events, others are multiplicative (M) and given in % . Contributions are combined in quadrature.

Quantity	$\eta'_{\rho\gamma}K^0_{S+-}$	$\eta'_{\eta\pi\pi}K^0_{S+-}$	$\eta'_{\rho\gamma}K^{\pm}$	$\eta'_{\eta\pi\pi}K^{\pm}$
ML Fit bias (A)	7.2	0.2	23.5	0.5
$B\overline{B}$ Bkg (A)	3.0	1.0	10.0	3.0
Branching fractions (M)	3.4	3.4	3.4	3.4
MC statistics (M)	0.2	0.2	0.4	0.4
Track multip. (M)	1.0	1.0	1.0	1.0
Tracking eff/qual (M)	1.6	1.6	2.4	2.4
γ, $\eta_{\gamma\gamma}$ eff. (M)	1.5	3.0	1.5	3.0
K^0_S efficiency (M)	2.1	2.1	–	–
Number $B\overline{B}$ (M)	1.1	1.1	1.1	1.1
$\cos\theta_{\rm T}$(M)	0.5	0.5	0.5	0.5
Track PID (M)	–	–	0.5	0.5
Total Uncorr. (events) (A)	7.8	1.0	25.5	3.0
Total Uncorr. (%) (M)	3.4	3.4	3.4	3.4
Total Corr. (%)	3.4	4.3	3.3	4.2

Table 7.51: Estimates of systematic errors. We divide the systematics in two parts: uncorrelated errors (first part of the table) and correlated errors (second part of the table). Uncorrelated and correlated refer to the different daughter decays of the same mode. Some of these errors are additive (A) and given in events, others are multiplicative (M) and given in % . Contributions are combined in quadrature.

Quantity	$\eta_{\gamma\gamma}K^0_S\gamma$	$\eta_{3\pi}K^0_S\gamma$	$\eta_{\gamma\gamma}K^\pm\gamma$	$\eta_{3\pi}K^\pm\gamma$	$\eta'_{\eta\pi\pi}K^0_S\gamma$	$\eta'_{\rho\gamma}K^0_S\gamma$	$\eta'_{\eta\pi\pi}K^\pm\gamma$	$\eta'_{\rho\gamma}K^\pm\gamma$
ML Fit bias (A)	1.9	0.4	4.3	0.9	2.9	2.7	0.3	3.4
MC/data Corr. (A)	0.9	0.1	0.4	0.2	1.3	1.9	0.2	2.0
MC statistics (M)	0.7	0.8	0.6	0.7	0.8	0.9	0.7	0.7
Branching frac. (M)	0.7	1.8	0.7	1.8	3.4	3.4	3.4	3.4
Track multip. (M)	1.0	1.0	1.0	1.0	1.0	1.0	1.0	1.0
MC ρ^0 lineshape (M)	–	–	–	–	–	2.0	–	2.0
Tracking eff/qual (M)	–	1.6	0.8	2.4	1.6	1.6	2.4	2.4
$\pi^0/\eta_{\gamma\gamma}$ eff.(M)	3.0	3.0	3.0	3.0	3.0	–	3.0	–
γ eff.(M)	1.8	1.8	1.8	1.8	1.8	3.6	1.8	3.6
K^0_S eff. (M)	2.1	2.1	–	–	2.1	2.1	–	–
Number $B\overline{B}$ (M)	1.1	1.1	1.1	1.1	1.1	1.1	1.1	1.1
$\cos\theta_{\rm T}$(M)	1.0	1.0	1.0	1.0	1.0	1.0	1.0	1.0
Particle ID (M)	–	1.0	1.0	1.0	1.0	1.0	1.0	1.0
Photon spectrum (M)	2.6	2.7	1.8	2.0	4.5	5.6	5.2	5.6
Total Uncorr. (events) (A)	2.1	0.4	4.3	0.9	3.2	3.3	0.4	3.9
Total Uncorr. (%) (M)	1.0	2.0	0.9	1.9	3.5	3.5	3.5	3.5
Total Corr. (%)	5.2	5.5	4.5	5.1	6.6	7.7	7.0	7.6

Table 7.52: Estimates of systematic errors. We divide the systematics in two parts: uncorrelated errors (first part of the table) and correlated errors (second part of the table). Uncorrelated and correlated refer to the different daughter decays of the same mode. Some of these errors are additive (A) and given in events, others are multiplicative (M) and given in % . Contributions are combined in quadrature.

Quantity	$\eta_{\gamma\gamma}\eta_{\gamma\gamma}$	$\eta_{\gamma\gamma}\eta_{3\pi}$	$\eta_{3\pi}\eta_{3\pi}$	$\eta'_{\eta\pi\pi}\phi$	$\eta'_{\rho\gamma}\phi$	$\eta_{\gamma\gamma}\phi$	$\eta_{3\pi}\phi$	$\eta_{\gamma\gamma}K^0_S$	$\eta_{3\pi}K^0_S$
Fit bias (A)	2.4	0.6	0.4	0.5	0.6	1.4	0.6	0.8	0.9
MC/data corr. (A)	0.2	0.5	0.2	0.3	0.6	0.8	0.1	1.1	0.4
Branch. frac. (M)	1.0	1.9	2.5	3.6	3.6	1.4	2.2	0.7	1.8
MC statistics (M)	0.6	0.6	0.7	0.7	0.8	0.6	0.8	0.5	0.6
Track multiplicity (M)	1.0	1.0	1.0	1.0	1.0	1.0	1.0	1.0	1.0
Tracking eff/qual (M)	–	1.6	3.2	3.2	3.2	1.6	3.2	–	1.6
π^0,$\eta_{\gamma\gamma}$, γ eff (M)	6.0	6.0	6.0	3.0	1.8	3.0	3.0	3.0	3.0
K^0_S eff. (M)	–	–	–	–	–	–	–	2.1	2.1
Number $B\overline{B}$ (M)	1.1	1.1	1.1	1.1	1.1	1.1	1.1	1.1	1.1
$\cos\theta_{\rm T}$(M)	0.5	0.5	0.5	0.5	0.5	0.5	0.5	0.5	0.5
Total Uncorr. (events) (A)	2.4	0.8	0.5	0.6	0.8	1.6	0.6	1.4	1.0
Total Uncorr. (%) (M)	1.2	2.0	2.6	3.7	3.7	1.5	2.3	0.9	1.9
Total Corr. (%)	6.2	6.4	7.0	4.7	4.0	3.7	4.7	4.0	4.3

Table 7.53: Estimates of systematic errors. We divide the systematics in two parts: uncorrelated errors (first part of the table) and correlated errors (second part of the table). Uncorrelated and correlated refer to the different daughter decays of the same mode. Some of these errors are additive (A) and given in events, others are multiplicative (M) and given in % . Contributions are combined in quadrature.

7.10 Results

In this section we will present the results of branching fraction and charge asymmetry measurements. Summary of all results of ML fit is shown in tables 7.54–7.59. We give the number of events to fit, the signal yield, the various efficiencies and product of daughter branching fractions (where we consider also the $K^0 \to K^0_S$), the fit bias, the statistical significance and 90% confidence level (CL) upper limit (for the modes where the statistical significance is lower than 5 σ). The statistical error on the number of events and the charge asymmetry is taken as the change in the central value when the quantity $\chi^2 = -2\ln\mathcal{L}$ changes by one unit. The statistical significance is taken as the square root of the difference between the value of χ^2 for zero signal events and the value at its minimum. The 90% C.L. upper limit is taken to be the branching fraction below which lies 90% of the total likelihood integral in the positive branching fraction region.

Statistically combining the results of different sub-decays is equivalent to multiplying likelihood curves, *i. e.*, adding the log-likelihood curves and adjusting the minimum back to 0. Including a systematic uncertainty σ_{syst} involves convoluting the likelihood with a Gaussian of width σ_{syst}. If the original likelihood curve is Gaussian with width σ_{stat}, this produces a new Gaussian likelihood curve with $\sigma^2 = \sigma^2_{syst} + \sigma^2_{stat}$. Equivalently, this adjusts the log-likelihood curve by:

$$\chi^2 = \frac{\chi^2_{stat}\chi^2_{syst}}{\chi^2_{stat} + \chi^2_{syst}} \tag{7.7}$$

where χ^2_{stat} is the result of the fit with only statistical error, and $\chi^2_{syst} = (x-\mu)^2/\sigma^2_{stat}$ where x is the quantity the we combine with μ as fit result. This has the effect of broadening the log-likelihood curve to account for the systematic uncertainty.

We show in figs. 7.8–7.14 the $-\ln\mathcal{L}$ for the branching fraction of the sub-decay modes and for the their combination. In figs. 7.15 and 7.16 we show the same plots for the charge asymmetries. These figures are done fixing in the fit all parameters to the values obtained in final fit and varying only the parameter (the signal yield and charge asymmetry in our case) for which we do the $-2\ln\mathcal{L}$ scan.

In figs. 7.17 and 7.18 we show the $sPlot$ of invariant mass ηK and of η energy in CMS for the sub-decay modes of $\eta K\gamma$, respectively.

Table 7.54: Branching fractions results for $\eta'\eta'K$ modes.

ML Fit Quantity	$\eta'_{\eta\pi\pi}\eta'_{\eta\pi\pi}K^0_S$	$\eta'_{\eta\pi\pi}\eta'_{\rho\gamma}K^0_S$	$\eta'_{\eta\pi\pi}\eta'_{\eta\pi\pi}K^\pm$	$\eta'_{\eta\pi\pi}\eta'_{\rho\gamma}K^\pm$
Events to fit	467	8741	1390	8913
Signal yield	1^{+1}_{-1}	4^{+8}_{-7}	4^{+4}_{-3}	14^{+12}_{-10}
$B\overline{B}$ yield	–	965^{+308}_{-325}	–	4670^{+73}_{-71}
SCF yield	-9^{+11}_{-10}	108^{+64}_{-62}	-4^{+16}_{-13}	117^{+73}_{-71}
# Data combs/event	1.78	1.48	1.74	1.47
# MC combs/event	2.00	1.66	1.92	1.59
SCF(%)	42.6	42.7	40.9	39.8
ML-fit bias (events)	+0.5	+3.8	+0.5	+8.5
MC ϵ (%)	3.3	4.1	3.8	3.6
Track corr. (%)	97.6	97.6	97.0	97.0
$\eta_{\gamma\gamma}$ corr. (%)	94.2	97.1	94.2	97.1
K^0_S corr. (%)	95.7	95.7	–	–
$\prod \mathcal{B}_i$ (%)	1.1	3.6	3.1	10.4
Corr. $\epsilon \times \prod \mathcal{B}_i$ (%)	0.032	0.134	0.108	0.353
Stat. sign. (σ)	0.5	0.0	2.1	0.5
$\mathcal{B}(\times 10^{-6})$	$6.2^{+19.7}_{-10.1}$	$1.0^{+26.5}_{-21.9}$	$14.9^{+15.0}_{-11.2}$	$6.4^{+14.6}_{-12.6}$
90% CL UL($\times 10^{-6}$)	50.2	45.0	39.2	27.1
Combined $\mathcal{B}(\times 10^{-6})$	$4.7^{+13.8}_{-8.6} \pm 0.3$		$11.2^{+8.8}_{-6.9} \pm 1.0$	
Stat. sign. (incl. syst.) (σ)	0.5		2.0	
90% CL UL($\times 10^{-6}$) (incl. syst.)	30.7		24.8	

Table 7.55: Branching fractions and Charge asymmetry results for $\eta' K$ modes.

Analysis	$\eta'_{\eta\pi\pi}K^{\pm}$	$\eta'_{\rho\gamma}K^{\pm}$	$\eta'_{\eta\pi\pi}K^{0}$	$\eta'_{\rho\gamma}K^{0}$
Events to fit	1883	39782	632	9705
Signal yield	609 ± 28	1347 ± 57	198 ± 16	457 ± 30
$B\overline{B}$ yield	–	797 ± 115	–	-10 ± 59
# Data combs/event	1.050	1.067	1.103	1.070
# MC combs/event	1.056	1.081	1.109	1.084
ML-fit bias (events)	-0.9 ± 0.5	46.9 ± 1.5	-0.4 ± 0.3	14.3 ± 0.8
MC ϵ (%)	23.9	27.1	25.4	27.2
Tracking corr. (%)	98.2	98.2	98.8	98.8
Neutrals corr. (%)	97.1	99.0	97.1	99.0
K^0_S corr. (%)	–	–	95.7	95.7
Corr. ϵ (%)	22.8	26.3	23.3	25.5
$\prod \mathcal{B}_i$ (%)	17.5	29.5	6.02	10.2
Corr. $\epsilon \times \prod \mathcal{B}_i$ (%)	3.99	7.76	1.40	2.60
$\mathcal{B}(\times 10^{-6})$	66 ± 3	72 ± 3	61 ± 5	73 ± 5
Combined $\mathcal{B}(\times 10^{-6})$	$68.9 \pm 2.0 \pm 3.2$		$67.4 \pm 3.3 \pm 3.2$	
Background $\mathcal{A}_{ch}$	-0.026 ± 0.029	-0.016 ± 0.005	–	–
Corr. Signal $\mathcal{A}_{ch}$	-0.001 ± 0.044	0.055 ± 0.036	–	–
Combined Signal $\mathcal{A}_{ch}$	$0.033 \pm 0.028 \pm 0.005$		–	
90% CL interval	$[-0.012, 0.078]$		–	

Table 7.56: Branching fractions results for $\eta K\gamma$ modes.

ML Fit Quantity	$\eta_{\gamma\gamma}K^0\gamma$	$\eta_{3\pi}K^0\gamma$	$\eta_{\gamma\gamma}K^\pm\gamma$	$\eta_{3\pi}K^\pm\gamma$
Events to fit	786	310	2391	1108
Signal yield	40^{+13}_{-12}	15^{+8}_{-7}	119^{+22}_{-21}	55^{+14}_{-13}
$B\overline{B}$ yield	-16^{+39}_{-39}	$-$	38^{+76}_{-73}	-45^{+50}_{-48}
# Data Combs/event	1.09	1.19	1.09	1.13
# MC Combs/event	1.13	1.24	1.14	1.24
SCF(%)	18.7	27.2	19.0	26.5
Fit bias (events)	$+3.7$	$+0.7$	$+8.6$	$+1.8$
MC ϵ (%)	11.0	7.6	13.4	9.3
Track corr. (%)	$-$	98.8	99.4	98.2
$\pi^0/\eta_{\gamma\gamma}$ corr. (%)	97.1	96.8	97.1	96.8
K^0_S corr. (%)	95.7	95.7	$-$	$-$
$\prod \mathcal{B}_i$ (%)	13.6	7.8	39.4	22.6
Corr. $\epsilon \times \prod \mathcal{B}_i$ (%)	1.39	0.54	5.10	2.00
Stat. sign. (σ)	4.6	2.9	8.0	6.6
$\mathcal{B}(\times 10^{-6})$	$11.2^{+4.0}_{-3.7}$	$11.5^{+6.1}_{-5.3}$	$9.4^{+1.8}_{-1.7}$	$11.4^{+3.0}_{-2.8}$
90 CL % UL ($\times 10^{-6}$)	15.9	19.4	$-$	$-$
Combined $\mathcal{B}$ ($\times 10^{-6}$)	$11.3^{+2.8}_{-2.6} \pm 0.6$		$10.0 \pm 1.3 \pm 0.5$	
Stat. sign. with syst. (σ)	5.3		10.0	
Background $\mathcal{A}_{ch}$	$-$	$-$	0.014 ± 0.022	-0.028 ± 0.031
Corr. Signal $\mathcal{A}_{ch}$	$-$	$-$	-0.013 ± 0.153	-0.219 ± 0.205
Combined Signal $\mathcal{A}_{ch}$	$-$		$-0.086 \pm 0.120 \pm 0.010$	
90% CL interval	$-$		$[-0.282, 0.113]$	

Table 7.57: Branching fractions results for $\eta' K\gamma$ modes.

ML Fit Quantity	$\eta'_{\eta\pi\pi}K^0\gamma$	$\eta'_{\rho\gamma}K^0\gamma$	$\eta'_{\eta\pi\pi}K^\pm\gamma$	$\eta'_{\rho\gamma}K^\pm\gamma$
Events to fit	119	2464	401	8792
Signal yield	-5^{+2}_{-2}	19^{+16}_{-14}	7^{+6}_{-5}	17^{+27}_{-24}
$B\overline{B}$ yield	–	17^{+82}_{-82}	–	527^{+157}_{-158}
# Data Combs/event	1.17	1.10	1.17	1.11
# MC Combs/event	1.24	1.17	1.26	1.18
SCF(%)	20.9	29.3	21.2	29.1
Fit bias (events)	-5.8	$+5.3$	$+0.5$	$+6.7$
MC ϵ (%)	6.8	5.6	8.6	10.1
Track corr. (%)	98.8	98.8	98.2	98.2
$\eta_{\gamma\gamma}$ corr. (%)	97.1	–	97.1	–
K^0_S corr. (%)	95.7	95.7	–	–
$\prod \mathcal{B}_i$ (%)	6.0	10.2	17.5	29.5
Corr. $\epsilon \times \prod \mathcal{B}_i$ (%)	0.37	0.54	1.44	2.93
Stat. sign. (σ)	0.4	1.2	1.6	0.5
$\mathcal{B}(\times 10^{-6})$	$0.6^{+2.8}_{-2.0}$	$11.2^{+12.8}_{-11.0}$	$1.9^{+1.8}_{-1.4}$	$1.5^{+3.9}_{-3.6}$
90 CL % UL ($\times 10^{-6}$)	5.9	27.4	4.6	7.0
Combined $\mathcal{B}$ ($\times 10^{-6}$)	$1.1^{+2.8}_{-2.0} \pm 0.1$		$1.9^{+1.5}_{-1.2} \pm 0.1$	
Stat. sign. w syst. (σ)	0.6		1.7	
90% C.L. UL ($\times 10^{-6}$) (incl. syst.)	6.6		4.2	

Table 7.58: Summary of ML fit results of $\eta\eta$ and ηK^0 modes.

Quantity	$\eta_{\gamma\gamma}\eta_{\gamma\gamma}$	$\eta_{\gamma\gamma}\eta_{3\pi}$	$\eta_{3\pi}\eta_{3\pi}$	$\eta_{\gamma\gamma}K^0$	$\eta_{3\pi}K^0$
Events to fit	2054	1990	421	3333	1392
Signal yield	17^{+10}_{-9}	10^{+7}_{-5}	2^{+3}_{-2}	19^{+10}_{-9}	11^{+6}_{-5}
$B\overline{B}$ yield	–	–	–	24 ± 20	–
# Data Combs/event	1.06	1.14	1.25	1.02	1.10
# MC Combs/event	1.04	1.14	1.25	1.02	1.13
SCF (%)	9.8	13.1	16.6	8.4	22.5
ML-fit bias (events)	$+3.9 \pm 0.6$	$+0.5 \pm 0.4$	$+0.3 \pm 0.4$	$+0.8 \pm 0.6$	$+1.1 \pm 0.4$
MC ϵ (%)	22.1	19.7	12.6	28.4	18.7
Track corr. (%)	100.0	98.8	97.6	100.0	98.8
K^0_S corr. (%)	–	–	–	96.7	96.7
$\pi^0/\eta_{\gamma\gamma}$ corr. (%)	94.2	93.9	93.6	97.1	96.8
$\prod \mathcal{B}_i$ (%)	15.5	17.9	5.1	13.5	7.8
Corr. $\epsilon \times \prod \mathcal{B}_i$ (%)	3.23	3.27	0.59	3.60	1.35
Stat. sign. (σ)	1.9	2.1	1.1	2.6	2.7
$\mathcal{B}(\times 10^{-6})$	$1.3^{+1.0}_{-0.9}$	$0.9^{+0.6}_{-0.5}$	$1.1^{+1.6}_{-1.0}$	$1.5^{+0.9}_{-0.8}$	$2.4^{+1.4}_{-1.1}$
90 CL % UL ($\times 10^{-6}$)	2.6	1.9	4.0	2.8	4.5
Combined $\mathcal{B}$ ($\times 10^{-6}$)		$1.1^{+0.5}_{-0.4} \pm 0.1$		$1.8^{+0.7}_{-0.6} \pm 0.1$	
Stat. sign. w syst. (σ)		3.0		3.5	
90% C.L. UL ($\times 10^{-6}$) (incl. syst.)		1.8		2.9	

Table 7.59: Summary of ML fit results of $\eta\phi$ and $\eta'\phi$ modes.

Quantity	$\eta_{\gamma\gamma}\phi$	$\eta_{3\pi}\phi$	$\eta'_{\eta\pi\pi}\phi$	$\eta'_{\rho\gamma}\phi$
Events to fit	5231	2066	1169	17111
Signal yield	-11^{+7}_{-5}	6^{+5}_{-4}	1^{+3}_{-2}	-3^{+9}_{-8}
$B\overline{B}$ yield	44 ± 15	–	–	–
# Data Combs/event	1.03	1.13	1.18	1.08
# MC Combs/event	1.03	1.13	1.20	1.13
SCF (%)	5.8	19.2	13.6	13.5
ML-fit bias (events)	-2.4 ± 0.6	$+0.8 \pm 0.3$	-0.6 ± 0.3	-1.0 ± 0.4
MC ϵ (%)	33.7	21.9	24.4	23.1
Track corr. (%)	98.8	97.6	97.6	97.6
$\pi^0/\eta_{\gamma\gamma}$ corr. (%)	97.1	96.8	97.1	–
$\prod \mathcal{B}_i$ (%)	19.4	11.1	8.6	14.5
Corr. $\epsilon \times \prod \mathcal{B}_i$ (%)	6.27	2.30	1.99	3.27
Stat. sign. (σ)	0.0	1.5	0.8	0.0
$\mathcal{B}(\times 10^{-6})$	$-0.4^{+0.3}_{-0.2}$	$0.7^{+0.7}_{-0.5}$	$0.3^{+0.5}_{-0.3}$	$-0.2^{+0.9}_{-0.7}$
90 CL % UL ($\times 10^{-6}$)	0.4	1.9	1.3	1.6
Combined $\mathcal{B}$ ($\times 10^{-6}$)	$0.07^{+0.25}_{-0.18} \pm 0.01$		$0.16^{+0.44}_{-0.29} \pm 0.01$	
Stat. sign. (σ)	0.0		0.5	
90% C.L. UL ($\times 10^{-6}$) (incl. syst.)	0.55		0.98	

7.10.1 Projections

We draw the $m_{\rm ES}$ and ΔE projection plots for our decays. To reduce the contribution of background, we make a cut on the quantity:

$$R = \frac{P_{sig}}{P_{sig} + P_{bkg}} \tag{7.8}$$

where P_{sig} and P_{bkg} are the probability for the event to be signal or background, respectively. These probabilities are calculated from PDFs, excluding in the computation the variable being plotted. These projections are shown in figs. 7.19–7.23. Fit curves shown are not a fit to the data in the histogram but the projection of the overall fit scaled to take into account the effect of the cut on R.

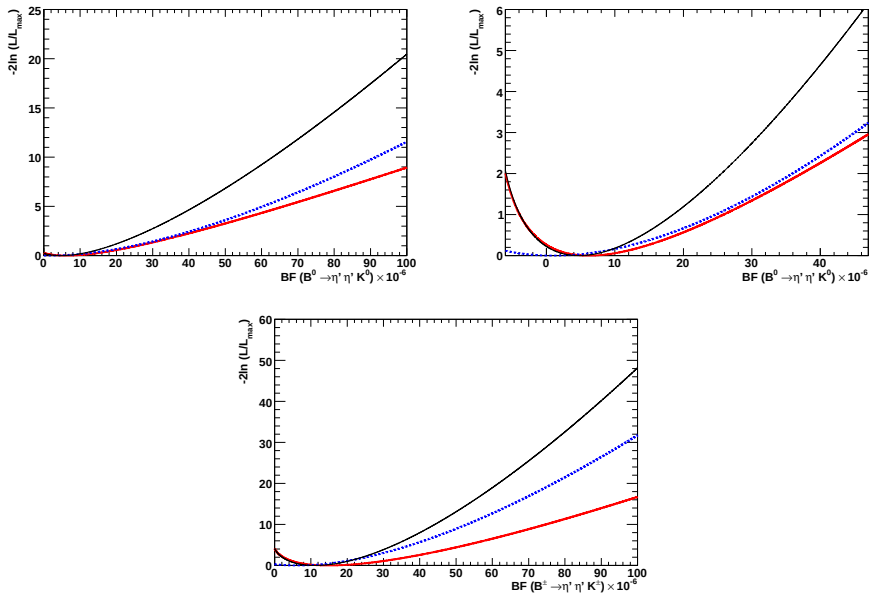

Figure 7.8: $-2\ln\mathcal{L}$ as a function of the branching fraction. Plots are for $\eta'\eta'K$ modes: top, neutral mode (right plot is a zoom near zero); bottom, charged mode. Blue dashed line for $\eta'_{\eta\pi\pi}\eta'_{\rho\gamma}K$; red dotted-dashed line for the subdecays with $\eta'_{\eta\pi\pi}\eta'_{\eta\pi\pi}K$; black solid line combined.

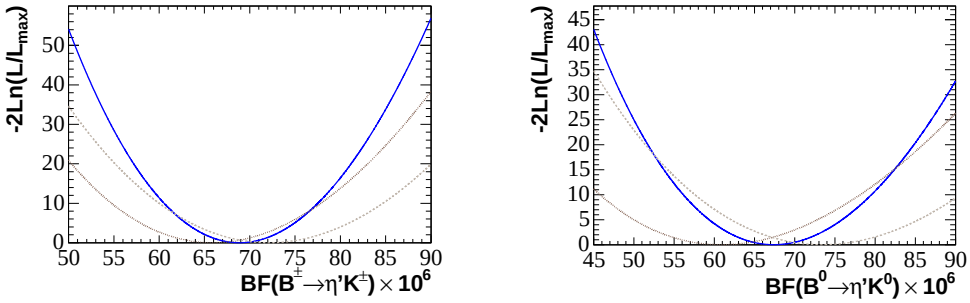

Figure 7.9: $-2\ln\mathcal{L}$ as a function of the branching fraction. Plots are for $\eta' K$ modes: left, charged mode; right, neutral mode. The solid blue line refers to combined sub-decays, the dotted line to the $\eta'_{\eta\pi\pi}$ sub-decay and the dashed line to the $\eta'_{\rho\gamma}$ sub-decay.

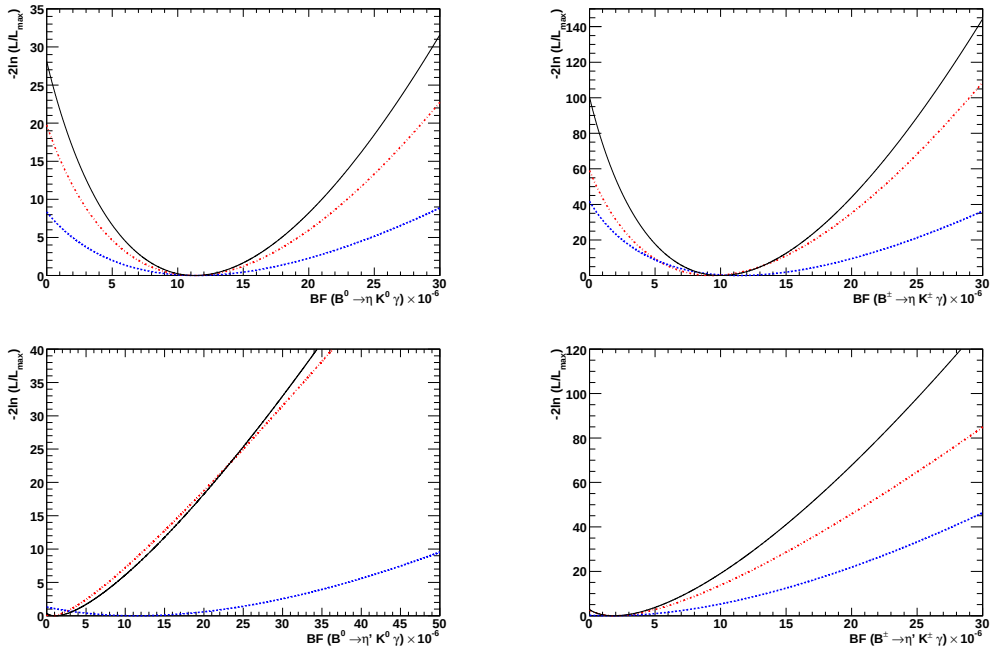

Figure 7.10: $-2ln\,\mathcal{L}$ as a function of the branching fraction. Plots on top are for $\eta K\gamma$ modes: left, neutral modes; right, charged modes. Blue dashed line for the subdecays with $\eta_{3\pi}$; red dotted-dashed line for the subdecays with $\eta_{\gamma\gamma}$; black solid line combined. Plots on bottom are for $\eta' K\gamma$ modes: left, neutral modes; right, charged modes. Blue dashed line for the subdecays with $\eta'_{\rho\gamma}$; red dotted-dashed line for the subdecays with $\eta'_{\eta\pi\pi}$; black solid line combined.

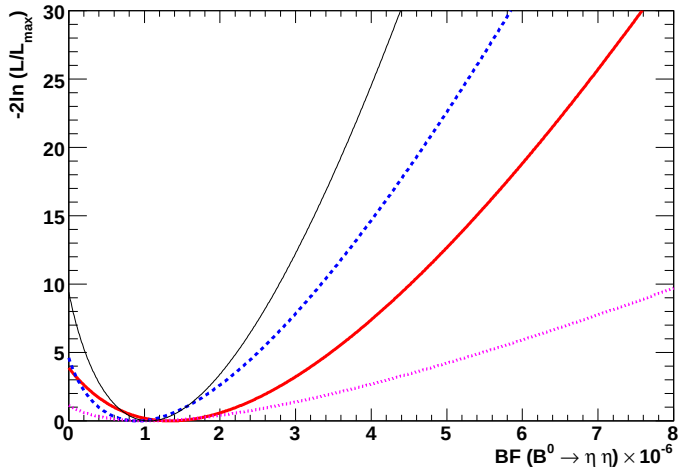

Figure 7.11: Distributions of $-\ln\mathcal{L}$ convolved with uncorrelated systematic errors for $\eta\eta$ modes: $\eta_{\gamma\gamma}\eta_{\gamma\gamma}$ red solid line, $\eta_{\gamma\gamma}\eta_{3\pi}$ blue dashed line, $\eta_{3\pi}\eta_{3\pi}$ pink dotted line, combined modes black line.

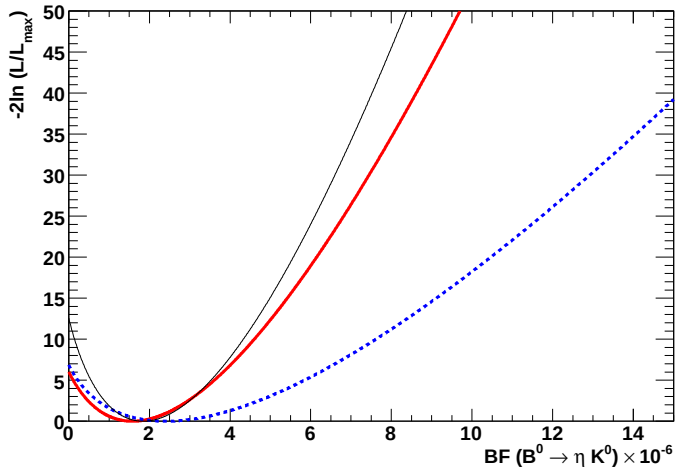

Figure 7.12: Distributions of $-\ln\mathcal{L}$ convolved with uncorrelated systematic errors for ηK^0_S modes: $\eta_{\gamma\gamma}K^0_S$ red solid line, $\eta_{3\pi}K^0_S$ blue dashed line, combined modes black line.

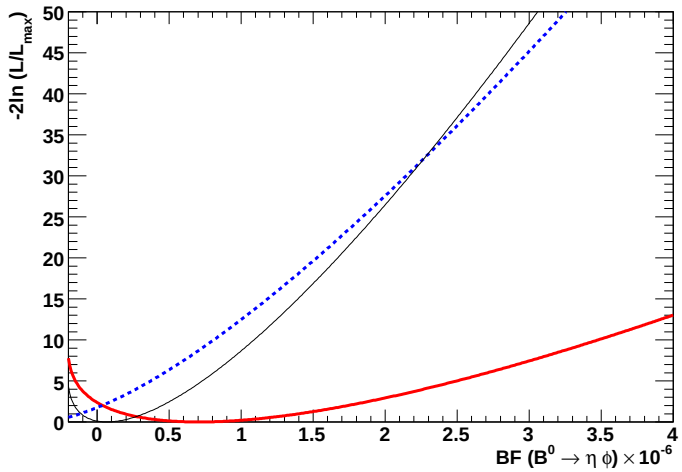

Figure 7.13: Distributions of $-\ln\mathcal{L}$ convolved with uncorrelated systematic errors for $\eta\phi$ modes: $\eta_{3\pi}\phi$ red solid line, $\eta_{\gamma\gamma}\phi$ blue dashed line, combined modes black line.

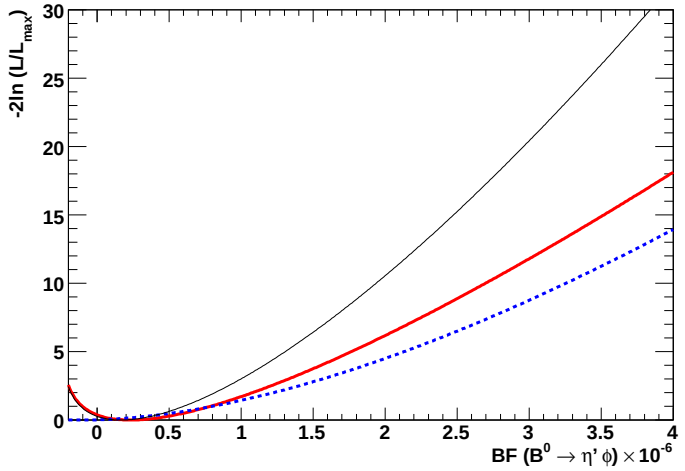

Figure 7.14: Distributions of $-\ln\mathcal{L}$ convolved with uncorrelated systematic errors for $\eta'\phi$ modes: $\eta'_{\eta\pi\pi}\phi$ red solid line, $\eta'_{\rho\gamma}\phi$ blue dashed line, combined modes black line.

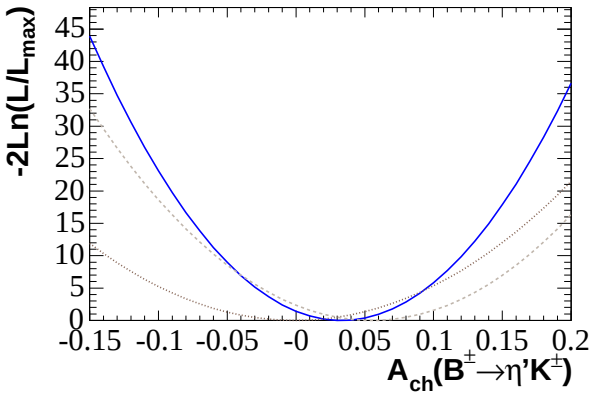

Figure 7.15: $-2\ln\mathcal{L}$ scan as a function of $\mathcal{A}_{ch}$ for the $\eta' K^{\pm}$ modes: dotted line $\eta' \to \eta\pi^+\pi^- K^{\pm}$; dashed line $\eta'_{\rho\gamma} K^{\pm}$; solid blue line combined.

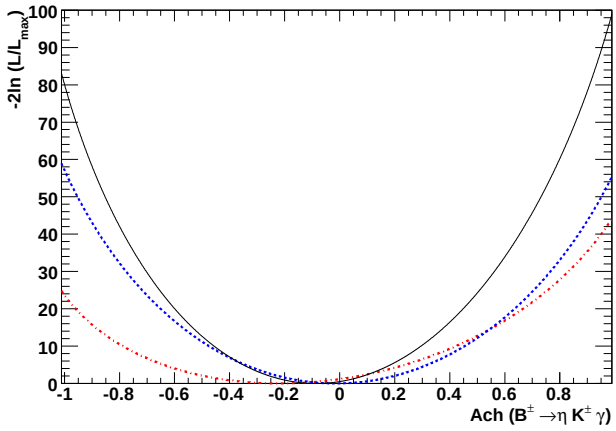

Figure 7.16: $-2ln\ \mathcal{L}$ scan as a function of $\mathcal{A}_{ch}$ for the $\eta K^{\pm}\gamma$ modes: blue dashed line $\eta_{3\pi} K^{\pm}\gamma$; red dotted-dashed line $\eta_{\gamma\gamma} K^{\pm}\gamma$; black solid line combined.

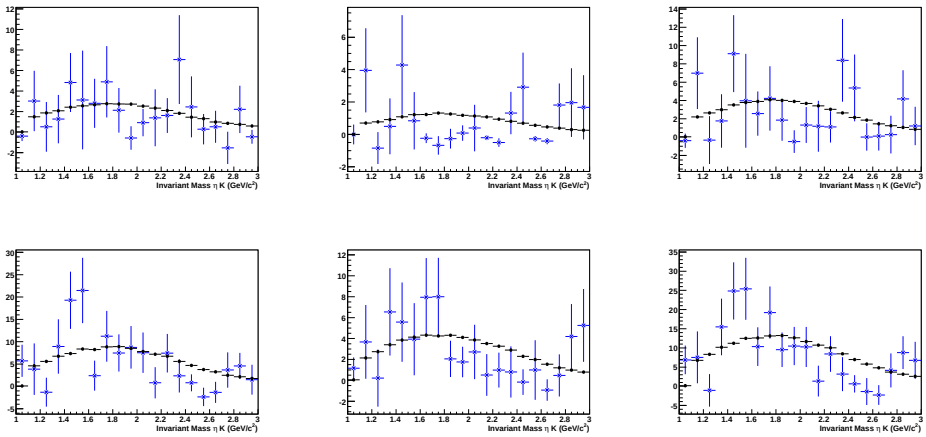

Figure 7.17: sPlots of invariant mass ηK for the sub-decay modes of $\eta K\gamma$ (neutral on top, charged on bottom): left for the subdecays with $\eta_{\gamma\gamma}$; center for the subdecays with $\eta_{3\pi}$; right for the two sub-decays added. The blue points represent the on-resonance data, the black points are for signal MC. The points are normalized to on-resonance ones.

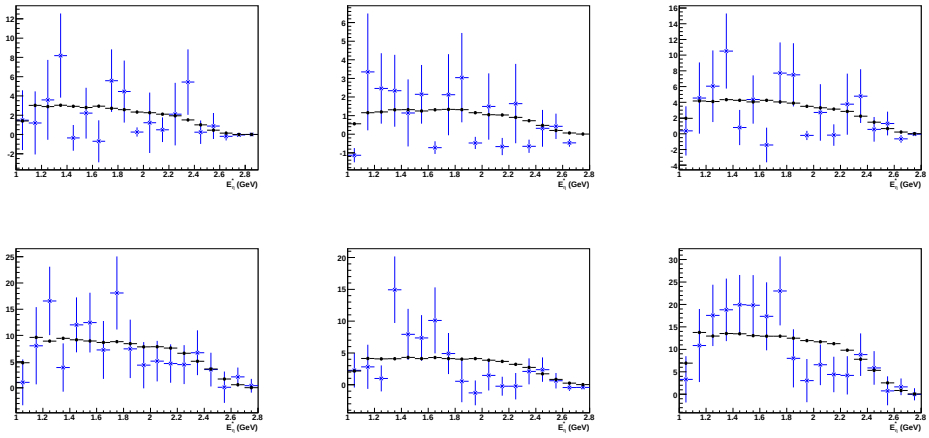

Figure 7.18: sPlots of η energy in CMS for the sub-decay modes of $\eta K\gamma$ (neutral on top, charged on bottom): left for the subdecays with $\eta_{\gamma\gamma}$; center for the subdecays with $\eta_{3\pi}$; right for the two sub-decays added. The blue points represent the on-resonance data, the black points are for signal MC. The points are normalized to on-resonance ones.

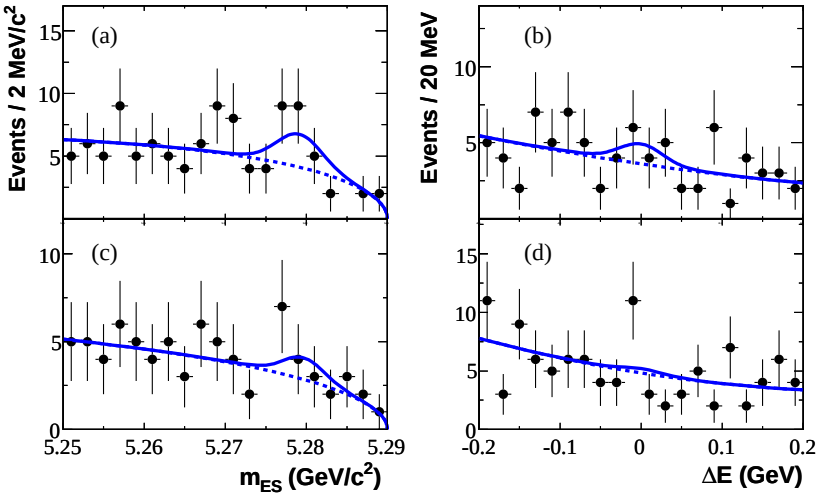

Figure 7.19: The B candidate $m_{\rm ES}$ and ΔE projections for $\eta'\eta' K^{\pm}$ (a, b) and $\eta'\eta' K^0$ (c, d) for the two η' sub-decays together. Points with errors represent the data, solid curves the full fit functions, and dashed curves the background functions.

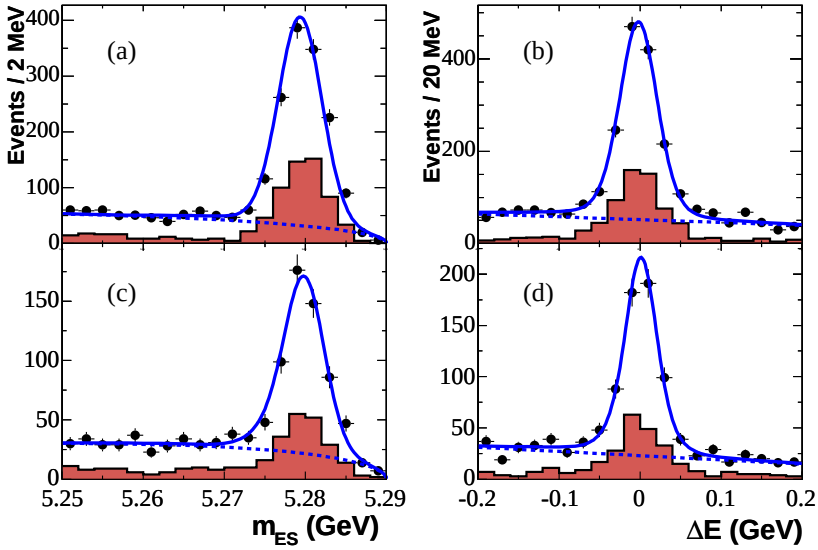

Figure 7.20: The B candidate $m_{\rm ES}$ and ΔE projections for $B^+ \to \eta' K^+$ (a, b) and $B^0 \to \eta' K^0$(c, d) for main sub-decays modes. Points with errors represent the data, solid curves the full fit functions, and dashed curves the background functions; the shaded histogram represents the $\eta'_{\eta\pi\pi} K$ subset.

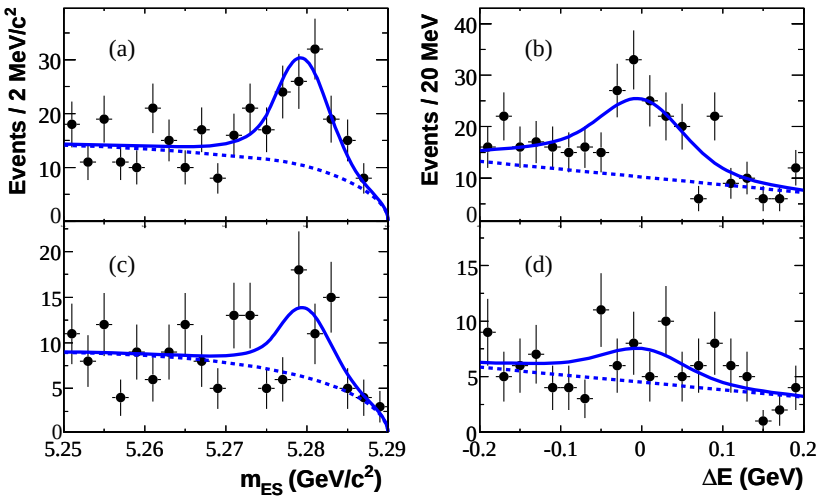

Figure 7.21: The B candidate $m_{\rm ES}$ and ΔE projections for $\eta K^{\pm}\gamma$ (a, b) and $B^0 \to \eta K^0\gamma$ (c, d) for the two η sub-decays together. Points with errors represent the data, solid curves the full fit functions, and dashed curves the background functions.

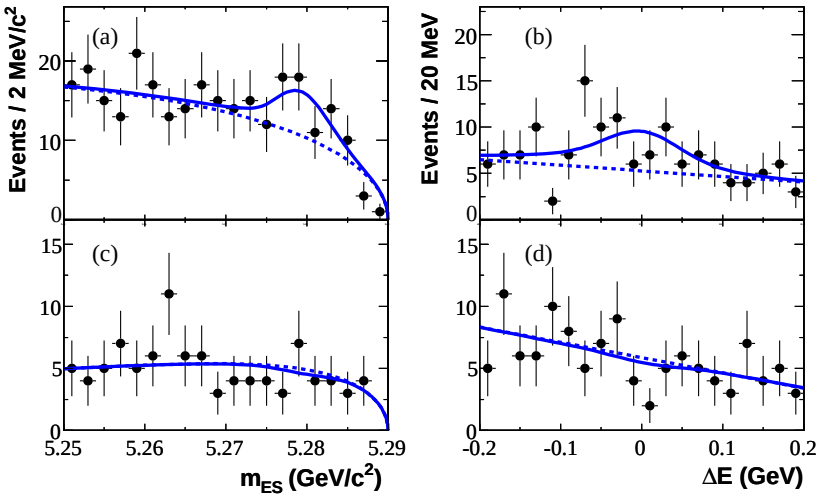

Figure 7.22: The B candidate $m_{\rm ES}$ and ΔE projections for $\eta' K^{\pm}\gamma$ (a, b) and $\eta' K^0\gamma$ (c, d) for the two η' sub-decays together. Points with errors represent the data, solid curves the full fit functions, and dashed curves the background functions.

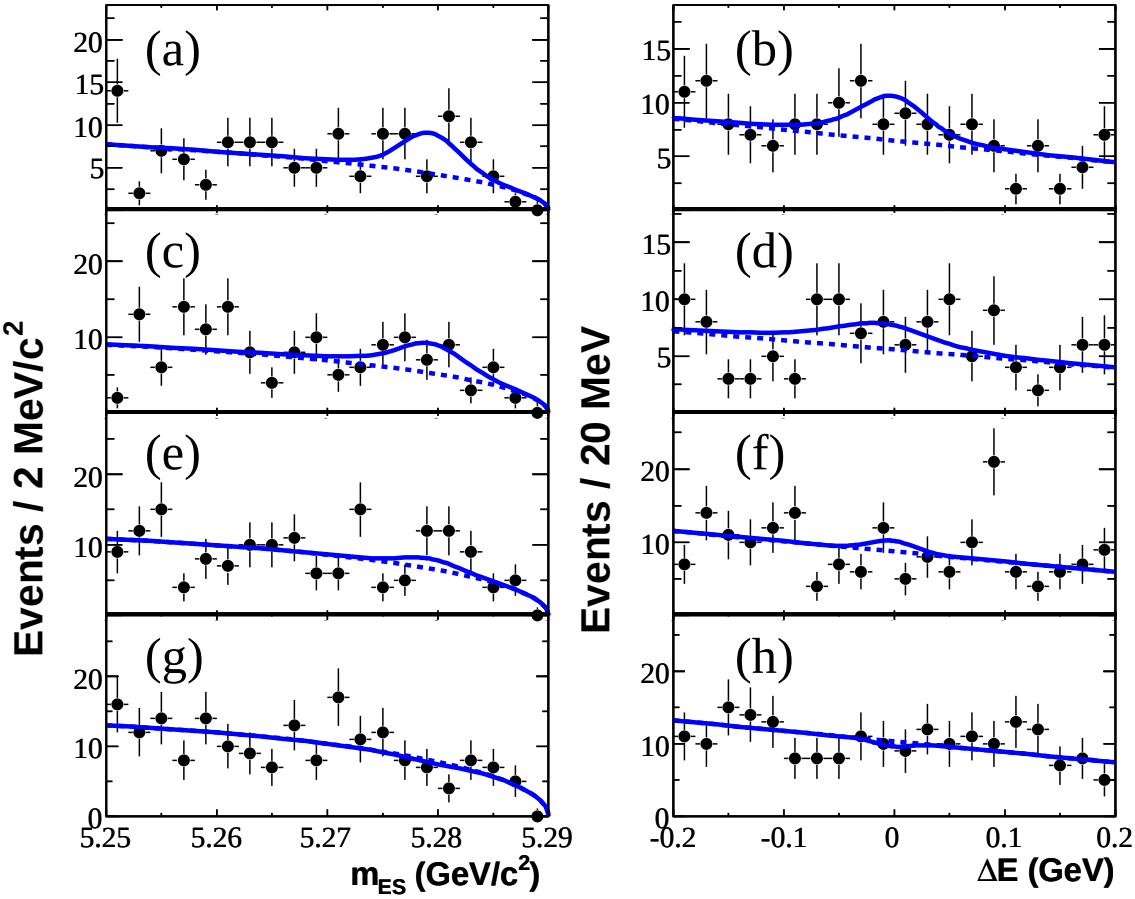

Figure 7.23: Projections on $m_{\rm ES}$ (left) and ΔE (right) in the dacays: (a, b) ηK^0_S, (c, d) $\eta\eta$, (e, f) $\eta\phi$, (g, h) $\eta'\phi$. Points with error bars (statistical only) represent the data, the solid line the full fit function, and the dashed line its background component.

Chapter 8

Time-Dependent CP asymmetries measurements in $B^0 \to \eta' K^0$

8.1 Introduction

We describe in this chapter the measurement of the time-dependent CP asymmetries in the charmless B^0 meson decays to $\eta' K^0_S$ and $\eta' K^0_L$ through the decay modes shown in tab. 4.1 and tab. 4.2.[1] We extract the parameters of CP violating asymmetry S and C from a combined maximum likelihood fit to the time evolution of $\eta' K^0_S$ and $\eta' K^0_L$ (see section 1.4.3 for definitions of these quantities).

8.2 Theoretical Overview and SU(3) Upper Bounds on $S - \sin 2\beta$

Decays of B^0 mesons to $\eta' K^0$ proceed mostly via a single penguin (loop) amplitude with the same weak phase [12] present in B^0 meson decays through a Cabibbo-Kobayashi-Maskawa (CKM) favored $b \to c\bar{c}s$. However CKM-suppressed amplitudes and multiple particles in the loop introduce other weak phases whose contribution is not negligible [13, 14, 15, 16].

Figure 8.1 shows the $B^0 - \overline{B}^0$ mixing diagram (a), together with some possible decay amplitudes for $B^0 \to \eta' K^0$. The diagrams (b-d), together with electroweak coun-

[1] The time-dependent measurements is also performed in $B^\pm \to \eta' K^\pm$ modes, where we expect $S = C = 0$, as a check.

terparts and other variants, all contribute in principle. All are CKM suppressed. However the tree (fig. 8.1b) is also Cabibbo (and for the neutral mode color) suppressed, and expected to be small [12, 15]. The observed branching fraction is larger than at least initially expected [102], spawning a variety of conjectures by way of explanation. These include flavor singlet [103], charm enhanced [104], and constructively interfering internal penguin diagrams (fig. 8.1c,d) [18, 102]. The last is reinforced by a recent NLO QCD factorization calculation [15], which finds that the singlet mechanisms do not enhance the rate significantly, which is in fact adequately predicted by constructive interference of the $b \to \eta'$ and $b \to K$ diagrams (fig. 8.1c,d). Both penguin amplitudes have, like the Golden mode, vanishing weak phases. Thus a time-dependent asymmetry measurement should, in the absence of new physics, yield an alternative measurement of $\sin 2\beta$. That is, with the usual additional assumption that CP is conserved in the mixing itself, the predictions for our asymmetry measurements are $-\eta_{CP} S = \sin 2\beta$ and $C = 0$.

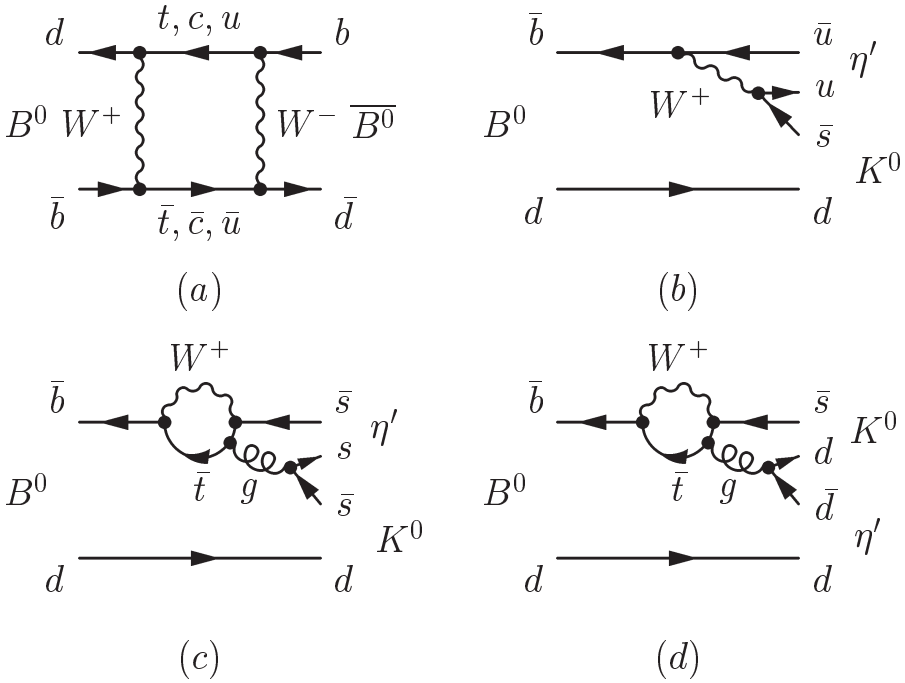

Figure 8.1: Feynman diagrams describing (a) $B^0 - \overline{B}^0$ mixing; the decay $B^0 \to \eta' K^0$ via (b) color-suppressed tree, (c, d) internal gluonic penguin. For the charged mode the corresponding tree diagram is external, not color suppressed.

Additional higher-order amplitudes with different weak phases would lead to deviations of $-\eta_{CP}S$ from $\sin2\beta$ For the $B^0 \to \eta' K^0$ mode, so the time-dependent asymmetry measurement for this decay provides an approximate measurement of $\sin2\beta$. Theoretical bounds for the small deviation $\Delta S = (-\eta_{CP}S) - \sin2\beta$ have been calculated with an SU(3) analysis [13, 14, 105], which uses the branching fractions of the π^0, η, and η' two-body combinations from B^0 decays. Such bounds were improved by last measurements [41], like our measurement of $B^0 \to \eta\eta$ mode reported in this thesis work. QCD factorization calculations [15] conclude that ΔS is smaller than what found in these SU(3) based upper bounds. A deviation ΔS superior to this limit can be considered an effect of phases coming from new physics [16].

We have calculated SU(3) based bounds using new recent measurements from *BABAR* [106, 107] and Belle taken from HFAG [41]. The SU(3) based upper bound calculation has been done using a macro written by Denis Dujmic [108]. This macro allows calculation of upper bounds for 10 different final states, including also $\eta' K^0$ which we have used. We have updated the relevant experimental information now available. The relevant theoretical formalism with all details for the calculation of these bounds can be found in [13, 14]. Here we mention only a few items to make more clear what we have done.

Constraints on CP asymmetries in $\eta' K^0$ can be written in terms of rates of other SU(3) related processes in different superpositions, depending on the level of approximation chosen. In one of these combinations, amplitudes of isoscalar pairs including π^0, η and η' mesons in final state are involved:

$$\begin{aligned}&\frac{1}{4\sqrt{3}}A(\pi^0\pi^0) - \frac{1}{3}A(\pi^0\eta) + \frac{5}{6\sqrt{2}}A(\pi^0\eta') \\ &+\frac{2}{3\sqrt{3}}A(\eta\eta) - \frac{11}{12\sqrt{3}}A(\eta'\eta') - \frac{5}{3\sqrt{3}}A(\eta\eta')\end{aligned} \tag{8.1}$$

Another combination is based on the assumption that a single SU(3) amplitudes dominates decays into a singlet and an octet pseudoscalar [14]. It involves four decay processes:

$$\frac{1}{3\sqrt{3}}A(\pi^0\pi^0) + \frac{1}{3\sqrt{6}}A(K^+K^-) - \frac{2}{3}A(\pi^0\eta) - \frac{2}{\sqrt{3}}A(\eta\eta') \tag{8.2}$$

Another combination, valid in the approximation of no exchange and no penguin annihilation contributions [14], involves only three strangeness-conserving am-

Mode	$\eta' K^0$	$\pi^0\pi^0$	$\pi^0\eta$	$\pi^0\eta'$	$\eta\eta$	$\eta'\eta'$	$\eta\eta'$	K^+K^-
$\mathcal{B}$	64.9 ± 3.5	1.45 ± 0.29	< 1.3	$1.5^{+0.7}_{-0.6}$	< 1.8	< 2.4	< 1.7	0.05 ± 0.09

Table 8.1: Branching fractions $\mathcal{B}$ and 90% CL upper limits (in units of 10^{-6}) for the modes used in SU(3) based upper bound calculation for ΔS in $B^0 \to \eta' K^0$ mode (see text for more details).

plitudes:

$$-\frac{5}{6}A(\pi^0\eta) + \frac{1}{3\sqrt{2}}A(\pi^0\eta') - \frac{\sqrt{3}}{2}A(\eta\eta') \tag{8.3}$$

Branching fractions (or upper limit at 90% confidence level (CL)) used here are given in tab. 8.1.

In "Denis" analysis program one can choose between a Bayesian and a frequentist approach. We have followed a frequentist approach. The weak angle γ has been generated following an asymmetric Gaussian with mean 59.8° and widths 4.9° and 4.1°. The $\eta - \eta'$ mixing angle has been taken 20°. The cosine of the strong phase (which is unknown) is taken flat between -1 and 1. We have generated 4000 MC simulated experiments and obtained the 90% CL upper limit for the ΔS bound.

For the combination in eq. 8.1, we find:

$$\Delta S = 0.15$$

For the combination in eq. 8.2, we find

$$\Delta S = 0.09$$

For the combination in eq. 8.3, we find

$$\Delta S = 0.08$$

There upper bounds were 0.23, 0.15, and 0.12, respectively, with previous branching fractions values [14].

These bounds are affected by a theoretical error (due to approximations and flavor SU(3) considerations) of order 20 or 30 %. We have to note however that such bounds are certainly overestimated because all amplitudes in the combinations 8.1, 8.2, and 8.3 carry different strong phases and we should not expect that they all add up coherently

(which is what is done in the calculation of ΔS).

The bounds for ΔS have been calculated in other different theoretical approaches as QCD factorization [15, 55], QCD factorization with modeled rescattering [109], Soft Collinear Effective Theory (SCET) [56]. These models estimate $|\Delta S|$ to be of the order 0.01, and with uncertainties give bounds $|\Delta S| \lesssim 0.05$. A new correlated bounds on the CP asymmetries parameters in $\mathcal{B}(B^0 \to \eta' K^0)$ using SU(3) have been recently updated: $-0.05 < \Delta S < 0.09$ [57].

8.3 Previous Results

The measurement of time-dependent (TD) CP asymmetry parameters for $B^0 \to \eta' K^0$ decay reported in this thesis work is an update of the measurements we sent to HEP2005 conference [110] based on an integrated luminosity of 211 fb^{-1}. In such a measurement we have included for the first time the $\eta' K^0_L$ modes, with $\eta'_{\eta(\gamma\gamma)\pi\pi}$ and $\eta'_{\rho\gamma}$. The latter mode has an high background and gives a negligible contribution to the final measurement of S and C, but an additional systematics, and for this reason we decide to not use in the new update. The results for the $\eta' K^0_S$ modes are based on the same integrated luminosity of $\eta' K^0_L$ modes and have been published in 2005 [111]. In this analysis we had added the modes with $\eta'_{\eta(3\pi)\pi\pi}$ and K^0_{S00} in order to increase the statistics with respect to the first *BABAR* measurements, based on an integrated luminosity of 82 fb^{-1}, where only the modes with $\eta'_{\eta(\gamma\gamma)\pi\pi}$, $\eta'_{\rho\gamma}$, and K^0_{S+-} were considered [91].

The results sent to HEP2005 conference are shows in tab. 8.2. The combined result for S is 2.8 standard deviations (only statistical error) from the $\sin 2\beta = 0.722 \pm 0.046$ value measured by *BABAR* at that time [112].

Mode	$-\eta_{CP} S$	C
$\eta' K^0_S$	$+0.30 \pm 0.14$	-0.21 ± 0.10
$\eta' K^0_L$	$+0.60 \pm 0.31$	$+0.10 \pm 0.21$
$\eta' K^0$	$+0.36 \pm 0.13 \pm 0.03$	$-0.16 \pm 0.09 \pm 0.02$

Table 8.2: *BABAR* results presented at HEP2005 conference for S and C from the $B^0 \to \eta' K^0_S$ and $B^0 \to \eta' K^0_L$ time-dependent fits with statistical error only and results from combined fits with statistical and systematic errors.

8.4 Data and Monte Carlo Samples

The analysis presented in this document is based on the data taken by *BABAR* in the period 1999-2006 (`Run1-Run5`). Results in this version of the note are based on the following samples:

- On-peak data:
  - 349.0 fb^{-1}, (383.6 ± 3.8) million of $B\bar{B}$ pairs.
- Off-peak data:
  - 27.2 fb^{-1}
- generic $B\overline{B}$ Monte Carlo:
  - 471.6 million events for generic $B^0\bar{B}^0$.
  - 469.2 million events for generic B^+B^-.
- Signal Monte Carlo: Statistics used for the different modes can be seen in tab. 8.3.

$\eta'_{\eta(\gamma\gamma)\pi\pi}K^0_{S+-}$ 675K	$\eta'_{\rho\gamma}K^0_{S+-}$ 675K	$\eta'_{\eta(3\pi)\pi\pi}K^0_{S+-}$ 117K	$\eta'_{\eta(\gamma\gamma)\pi\pi}K^0_{S00}$ 134K	$\eta'_{\rho\gamma}K^0_{S00}$ 103K
$\eta'_{\eta(\gamma\gamma)\pi\pi}K^{\pm}$ 675K	$\eta'_{\rho\gamma}K^{\pm}$ 675K	$\eta'_{\eta(3\pi)\pi\pi}K^{\pm}$ 134K	$\eta'_{\eta\pi\pi}K^0_L$ 143K	

Table 8.3: Monte Carlo signal events.

8.5 Preparation of the input to ML fit

The events for each mode are reconstructed (chapter 4) and selected (chapter 6). For each event we can have more candidates due to the possible different combinations of the reconstructed particles of the event. To prepare the samples for the input to ML fits, we have to choose one of these candidates per event (of course, in the case of multiple candidates per event). In this way we obtain the final input to ML fits. In this sections we will report the events selection efficiencies and multiple candidates selection. The

reconstruction and selection of the on-peak data events for $\eta'_{\eta(\gamma\gamma)\pi\pi}K^0_{S+-}$, $\eta'_{\rho\gamma}K^0_{S+-}$, $\eta'_{\eta(\gamma\gamma)\pi\pi}K^{\pm}$, and $\eta'_{\rho\gamma}K^{\pm}$ modes have been done by another group of the *BABAR* collaboration which has participated to this analysis.

8.5.1 Selection Cut Efficiencies

We report in the tables 8.4–8.11 the selection efficiencies for each cut applied to the reconstructed events of on-peak data and MC signal. Explanation of the cuts is given in section 6.4.2. The efficiencies for each row of the tables are computed after applying all the cuts in the previous rows. For the signal MC samples we give in the final row the raw efficiency, calculated as the ratio of the number of events input to ML and the number of generated MC signal events (table 8.3). Results for the MC events are shown in tables 8.4–8.7. The same informations for on-peak data are shown in tables 8.8–8.11. For these tables the last row gives the number of candidates surviving to all cuts and entering in the input to ML fit.

Table 8.4: Efficiency (%) and selection cuts (all candidates per event) in $\eta' K^0_S(\pi^+\pi^-)$ MC sample. Efficiencies for each row are computed after applying all the cuts in the previous rows. The last row gives the raw efficiency calculated as ratio of the number of events surviving all cuts, including the best candidate selection, and the number of generated events.

	$\eta'_{\eta(\gamma\gamma)\pi\pi}K^0_{S+-}$	$\eta'_{\rho\gamma}K^0_{S+-}$	$\eta'_{\eta(3\pi)\pi\pi}K^0_{S+-}$
Generated	675000	675000	117000
Preliminary cuts	238909	295818	37476
PID vetoes for pions	98.9	96.3	98.0
π^0 mass			78.3
η mass	92.8		98.2
ρ^0 mass		97.2	
ρ^0 hel.		97.3	
η' mass	89.9	81.7	95.3
K^0_S mass	97.6	97.6	97.5
K^0_S cuts	96.8	96.9	97.4
Δt cuts	98.8	98.9	98.5
$\sigma_{\Delta t}$ cuts	97.3	97.9	97.7
tagged events	75.1	75.1	74.7
Raw efficiency	18.1	20.9	8.8

Table 8.5: Efficiency (%) and selection cuts (all candidates per event) in $\eta' K^+$ MC sample. Efficiencies for each row are computed after applying all the cuts in the previous rows. The last row gives the raw efficiency calculated as ratio of the number of events surviving all cuts, including the best candidate selection, and the number of generated events.

	$\eta'_{\eta(\gamma\gamma)\pi\pi}K^\pm$	$\eta'_{\rho\gamma}K^\pm$	$\eta'_{\eta(3\pi)\pi\pi}K^\pm$
Generated	675000	675000	134000
Preliminary cuts	248565	356827	50164
PID vetoes for pions	98.9	95.9	97.2
Veto fast particle	98.4	98.3	98.6
π^0 mass			78.5
η mass	94.5		98.4
ρ^0 mass		97.2	
ρ^0 hel.		97.3	
η' mass	92.3	81.8	96.3
# DIRC photon	86.7	85.7	87.8
DIRC angle pull	95.5	95.2	95.4
Δt cuts	98.9	98.9	98.7
$\sigma_{\Delta t}$ cuts	98.3	97.9	98.0
tagged events	76.6	76.4	74.7
Raw efficiency	18.2	21.8	9.3

Table 8.6: Efficiency (%) and selection cuts (all candidates per event) in $\eta' K^0_{S00}$ MC sample. Efficiencies for each row are computed after applying all the cuts in the previous rows. The last row gives the raw efficiency calculated as ratio of the number of events surviving all cuts, including the best candidate selection, and the number of generated events.

	$\eta'_{\eta\pi\pi}K^0_{S00}$	$\eta'_{\rho\gamma}K^0_{S00}$
Generated	134000	103000
Preliminary cuts	32112	31511
PID vetoes for pions	99.1	96.2
η mass	93.3	
ρ^0 mass		98.6
ρ^0 hel.		97.0
η' mass	90.1	82.3
π^0 mass	97.6	97.2
K^0_S mass	88.8	89.2
Δt cuts	98.8	98.8
$\sigma_{\Delta t}$ cuts	95.0	97.5
tagged events	75.6	75.3
Raw efficiency	10.0	11.9

Table 8.7: Efficiency (%) and selection cuts (all candidates per event) in $\eta' K^0_L$ MC sample. Efficiencies for each row are computed after applying all the cuts in the previous rows. The last row gives the raw efficiency calculated as ratio of the number of events surviving all cuts, including the best candidate selection, and the number of generated events.

	$\eta'_{\eta\pi\pi} K^0_L$
Generated	143000
Preliminary cuts	49153
PID vetoes for pions	98.7
η mass	92.0
η' mass	86.5
$\cos\theta_{P_{miss}}$ cut	94.9
P^{pro}_{miss} cut	83.6
Δt cuts	98.3
$\sigma_{\Delta t}$ cuts	94.0
tagged events	74.9
Neural Network cut	90.1
Raw efficiency	11.6

Table 8.8: Efficiency (%) and selection cuts (all candidates per event) in $\eta' K^0_S(\pi^+\pi^-)$ data. Efficiencies for each row are computed after applying all the cuts in the previous rows. The last row gives the raw efficiency calculated as ratio of the number of events surviving all cuts, including the best candidate selection, and the number of generated events.

	$\eta'_{\eta(3\pi)\pi\pi} K^0_{S+-}$
Preliminary cuts	2173
PID vetoes for pions	73.8
π^0 mass	70.7
η mass	97.3
η' mass	93.6
K^0_S mass	73.7
K^0_S cuts	63.4
Δt cuts	98.8
$\sigma_{\Delta t}$ cuts	97.3
tagged events	64.2
Events to fit	177

Table 8.9: Efficiency (%) and selection cuts (all candidates per event) in $\eta' K^+$ data. Efficiencies for each row are computed after applying all the cuts in the previous rows. The last row gives the raw efficiency calculated as ratio of the number of events surviving all cuts, including the best candidate selection, and the number of generated events.

	$\eta'_{\eta(3\pi)\pi\pi} K^\pm$
Preliminary cuts	7534
PID vetoes for pions	73.7
Veto fast particle	95.2
π^0 mass	70.6
η mass	96.0
η' mass	92.4
# DIRC photon	85.0
DIRC angle pull	51.8
Δt cuts	98.6
$\sigma_{\Delta t}$ cuts	98.3
tagged events	67.3
Events to fit	581

Table 8.10: Efficiency (%) and selection cuts (all candidates per event) in $\eta' K^0_S(\pi^0\pi^0)$ data. Efficiencies for each row are computed after applying all the cuts in the previous rows. The last row gives the raw efficiency calculated as ratio of the number of events surviving all cuts, including the best candidate selection, and the number of generated events.

	$\eta'_{\eta\pi\pi} K^0_{S00}$	$\eta'_{\rho\gamma} K^0_{S00}$
Preliminary cuts	4224	164526
PID vetoes for pions	77.5	65.5
η mass	81.4	
ρ^0 mass		96.7
ρ^0 hel.		88.7
η' mass	62.5	50.0
π^0 mass	93.2	91.6
K^0_S mass	76.1	76.2
Δt cuts	97.6	97.7
$\sigma_{\Delta t}$ cuts	93.5	96.4
tagged events	56.5	58.0
Events to fit	490	13915

Table 8.11: Efficiency (%) and selection cuts (all candidates per event) in $\eta' K^0_L$ data. Efficiencies for each row are computed after applying all the cuts in the previous rows. The last row gives the raw efficiency calculated as ratio of the number of events surviving all cuts, including the best candidate selection, and the number of generated events.

	$\eta'_{\eta\pi\pi} K^0_L$
Preliminary cuts	149154
PID vetoes for pions	71.8
η mass	80.7
η' mass	55.3
$\cos\theta_{P_{miss}}$ cut	80.1
P^{pro}_{miss} cut	35.0
Δt cuts	95.0
$\sigma_{\Delta t}$ cuts	89.7
tagged events	62.3
Neural Network cut	66.8
Events to fit	4199

8.5.2 Multiple Candidate per Event

We have analyzed the problem of multiple signal candidates per event. We first make the choice of the best candidate and then look for events with MC truth or without MC truth. In some modes with multiple particles in the final state we consider as MC truth also events where there is a permutation of the particles (PP) inside the B candidate. Events where the B exchanges a track with the rest of the event are called self-crossfeed (SCF) events. Efficiency of the candidate selection refers to events which have one candidate with MC truth or which have one PP event. In selecting the best candidate we have applied an algorithm based on B vertex probability. Efficiency of this algorithm is in the range 95–98%.

In K^0_L modes we distinguish the candidates in two categories, depending on the sub-detector where the K^0_L candidate informations are taken: EMC and IFR. If the direction of IFR candidate is compatible with a candidate of EMC, we consider the two candidates as the same candidate (category EMC+IFR) and we drop the IFR one. We use the B vertex probability to select the best candidate. If several candidates have the same B vertex probability, we choose the candidate with the K^0_L coming from (in order): EMC+IFR, EMC, IFR.

We summarize in tab. 8.12 the number of combinations per event for data and MC

events, the efficiency of the algorithm of selection (considering MC truth events and MC truth plus PP ones) and the fraction of SCF events.

Mode	# combs/event (data)	#combs/event (MC signal)	efficiency (%)		SCF (%)
			MCtruth	MCtruth+PP	
$\eta'_{\eta(\gamma\gamma)\pi\pi}K^0_{S+-}$	1.09	1.10	98.2		13.8
$\eta'_{\rho\gamma}K^0_{S+-}$	1.08	1.07	97.8		15.2
$\eta'_{\eta(3\pi)\pi\pi}K^0_{S+-}$	1.64	1.77	91.5	98.1	16.2
$\eta'_{\eta(\gamma\gamma)\pi\pi}K^{\pm}$	1.04	1.06	98.9		13.2
$\eta' \to \rho^0\gamma K^{\pm}$	1.07	1.07	97.9		15.8
$\eta'_{\eta(3\pi)\pi\pi}K^{\pm}$	1.61	1.73	92.3	98.4	15.8
$\eta'_{\eta\pi\pi}K^0_{S00}$	1.22	1.23	94.7	95.7	20.4
$\eta'_{\rho\gamma}K^0_{S00}$	1.24	1.22	94.1	95.0	21.5
$\eta'_{\eta\pi\pi}K^0_L$	1.13	1.17	95.6		27.7

Table 8.12: Results of "best candidate" selection algorithm.

8.6 Background Sources

In our previous analyses of the modes studied in this document, we have verified that in all our target decays we have background contribution only from continuum $udsc$ production with negligible $B\overline{B}$ non continuum crossfeed. Infact most of our target decay modes are clean or very clean. In the modes with $\eta'_{\rho\gamma}$, there is a possible background coming from charmless $B\overline{B}$ events. These events in fact could be source of bias in our yield results. In the modes with K^0_L there is a small contribution from the same modes with K^0_S or charged kaon instead of K^0_L.

Our procedure in the $B\overline{B}$ analysis is realized in three steps. First we apply the full analysis selection to MC $B\overline{B}$ generic samples. We show in tab. 8.13 the input to the maximum likelihood in B^+B^- and $B^0\overline{B}^0$ (results are normalized to the integrated luminosity). Signal MC events have been removed from these samples. Note that we have reconstructed about 2.4 times of generic $B\overline{B}$ with respect to the statistics expected at the integrated luminosity of data.

We look at all the MC events separating possible $B\overline{B}$ crossfeed from charm and charmless decay. We focus our attention to charmless events because they are the peaking contribution to our background. In this first step we are interested in finding categories of events which could contribute to background. We find that the decay

Mode	$B^0\overline{B}^0$	B^+B^-
$\eta'_{\eta(\gamma\gamma)\pi\pi}K^0_{S+-}$	6	1
$\eta'_{\rho\gamma}K^0_{S+-}$	329	174
$\eta'_{\eta(3\pi)\pi\pi}K^0_{S+-}$	3	1
$\eta'_{\eta\pi\pi}K^0_{S00}$	1	3
$\eta'_{\rho\gamma}K^0_{S00}$	117	129
$\eta'_{\eta(\gamma\gamma)\pi\pi}K^{\pm}$	5	17
$\eta'_{\rho\gamma}K^{\pm}$	430	1470
$\eta'_{\eta(3\pi)\pi\pi}K^{\pm}$	1	14
$\eta'_{\eta\pi\pi}K^0_L$	128	71

Table 8.13: Estimated input to ML at the integrated luminosity for $B\overline{B}$ events for each target decay mode.

modes which need a detailed control of crossfeed are modes with $\eta' \to \rho^0\gamma$ and modes with K^0_L. In the second step we reconstruct large samples of MC signal events of candidate crossfeed modes and we evaluate reconstruction efficiency and number of expected candidates (normalized to our integrated luminosity) in ML input. In modes with $\eta' \to \rho^0\gamma$ we use these MC events to prepare the PDFs to introduce in the fit, prepared using weighted numbers of events from each decay mode. PDFs are prepared with the events surviving all cuts and with the best candidate selection. Finally, we perform toy-experiment studies where we embed a number of these events, taken from MC events, as expected in the ML input. In this way we control if the candidate is a source of bias or not.

In the tables 8.14, 8.15 and 8.16 we report the results of the $B\overline{B}$ studies for the decay modes $\eta'_{\rho\gamma}K^0_{S+-}$, $\eta'_{\rho\gamma}K^0_{S00}$, and $\eta'_{\rho\gamma}K^{\pm}$, respectively. In the Table 8.17 we report the results of the $B\overline{B}$ studies for mode with K^0_L. The branching fractions of the background $B\overline{B}$ modes studied are taken from PDG [99] and HFAG tables [100].

8.7 Maximum Likelihood Fit

8.7.1 Overview

An unbinned multivariate maximum likelihood (ML) analysis has been done, using MiFit. The events are selected with the cuts described in the section 6.4.2. If an event has multiple combinations, the program selects the best one using a the best B vertex

Cross Feed Channel	MC ϵ (%)	Est. $\mathcal{B}$ (10^{-6})	$\prod \mathcal{B}_i$	# evts in ML
$B^0 \to \pi^+\pi^- K^0_{S+-}$	1.017	$44.8^{+2.6}_{-2.5}$	0.343	60
$B^0 \to a_1^0(\rho^+\pi^-)K^0_{S+-}$	1.518	$15^{\dagger}$	0.172	30
$B^\pm \to a_1^\pm K^0_S$	0.715	$15^{\dagger}$	0.500	21
$B^0 \to \phi_{3\pi} K^0_{S+-}$	4.704	$8.3^{+1.2}_{-1.0}$	0.053	8
$B^\pm \to \rho^\pm K^0_S$	0.595	$5.6^{\dagger}$	0.500	6
$B^\pm \to \rho\, K^*(1430)$	0.033	$40^{\dagger}$	1.000	5
$B^\pm \to \rho^0 K^{*\pm}_{K^0_{S+-}\pi^\pm}$ (Long.)	1.288	$3.6^{+1.9}_{-1.8}$	0.229	4
$B^0 \to \rho\, K^*(1430)$	0.039	$20^{\dagger}$	1.000	4
$B^\pm \to \eta'_{\rho\gamma} K^{*\pm}_{K^0_{S+-}\pi^\pm}$	2.275	$4.9^{+2.1}_{-1.9}$	0.067	3
$B^0 \to K^+K^- K^0_{S+-}$	0.081	$24.7^{+2.3}_{-2.3}$	0.343	3
$B^0 \to K^{*+}_{K^0_S\pi^+}\pi^-$	0.222	$9.8^{+1.1}_{-1.1}$	0.333	3
$B^0 \to \omega K^0_{S+-}$	0.426	$4.8^{+0.6}_{-0.6}$	0.306	2
$B^0 \to \eta'_{\eta\pi\pi} K^0_{S+-}$	0.128	$64.9^{+3.5}_{-3.5}$	0.060	2
$B^\pm \to \pi^\pm K^0_{S+-}$	0.048	$24^{+1.3}_{-1.3}$	0.343	1
$B^0 \to K^0_S K^{*0}_{K^+\pi^-}$	0.652	$0.95^{+0.95}_{-0.95}$	0.230	1
$B^0 \to \rho^- K^{*+}_{K^0_{S+-}\pi^+}$ (Long.)	0.260	$2^{\dagger}$	0.229	0
$B^\pm \to \phi_{3\pi} K^{*\pm}_{K^0_{S+-}\pi^\pm}$	0.150	$9.7^{+1.5}_{-1.5}$	0.035	0
$B^\pm \to K^0_S K^{*\pm}_{K^0_S\pi^\pm}$	0.245	$0.95^{\dagger}$	0.167	0
Total				153

Table 8.14: Potential $B\overline{B}$ background for the $\eta'_{\rho\gamma}K^0_{S+-}$ mode. For each decay mode we give the MC reconstruction efficiency ϵ, branching fraction ($\mathcal{B}$), daughter branching fraction product, estimate background (normalized to the integrated luminosity) in ML input. Branching fractions with † are estimated since no measurement exists.

Cross Feed Channel	MC ϵ (%)	Est. $\mathcal{B}$ (10^{-6})	$\prod \mathcal{B}_i$	# evts in ML
$B^0 \to \pi^+\pi^- K^0_{S00}$	0.502	$44.8^{+2.6}_{-2.5}$	0.155	13
$B^\pm \to a_1^\pm K^0_S$	0.154	$15^\dagger$	0.500	4
$B^\pm \to \rho^\pm\rho^0$ (Long.)	0.059	$18.3^{+3.4}_{-3.4}$	0.96	4
$B^0 \to \rho^+\rho^-$ (Long.)	0.028	$24.2^{+3.5}_{-3.6}$	0.96	3
$B^0 \to a_1^+(\rho^0\pi^+)\pi^0$	0.061	$20^\dagger$	0.500	2
$B^\pm \to \eta'_{\rho\gamma}\rho^\pm$	0.236	$6.8^{+5.0}_{-3.2}$	0.295	2
$B^\pm \to \rho^\pm K^0_S$	0.154	$5.6^\dagger$	0.500	2
$B^0 \to \rho^0\pi^0\pi^0$	0.041	$5.0^\dagger$	1.000	1
$B^0 \to K^{*+}_{K^0_S\pi^+}\pi^-$	0.046	$9.8^{+1.1}_{-1.1}$	0.333	1
$B^0 \to \rho^+ K^{*-}_{\pi^0 K^-}$	0.004	$10^\dagger$	1.000	0
$B^0 \to \pi^0\pi^0 K^{*0}_{\pi^- K^+}$	0.008	$1^\dagger$	0.666	0
$B^\pm \to a_1^\pm(\rho^\pm\pi^0)\pi^0$	0.016	$17^\dagger$	0.500	0
$B^\pm \to K^0_S K^{*\pm}_{K^0_S\pi^\pm}$	0.136	$0.95^\dagger$	0.167	0
$B^0 \to K^0_S K^{*0}_{K^+\pi^-}$	0.052	$0.95^{+0.95}_{-0.95}$	0.230	0
Total				32

Table 8.15: Potential $B\overline{B}$ background for the $\eta'_{\rho\gamma}K^0_{S00}$ mode. For each decay mode we give the MC reconstruction efficiency ϵ, branching fraction ($\mathcal{B}$), daughter branching fraction product, estimate background (normalized to the integrated luminosity) in ML input. Branching fractions with † are estimated since no measurement exists.

Cross Feed Channel	MC ϵ (%)	Est. $\mathcal{B}$ (10^{-6})	$\prod \mathcal{B}_i$	# evts in ML
$B^\pm \to K^\pm\pi^+\pi^-$	1.212	$54.8^{+2.9}_{-2.9}$	1.000	255
$B^0 \to a_1^-(\rho^0\pi^-)K^+$	1.606	$17^\dagger$	0.500	52
$B^\pm \to a_1^0 K^\pm$	1.362	$9.0^\dagger$	1.000	47
$B^0 \to \rho^+ K^-$	1.051	$9.9^{+1.6}_{-1.5}$	1.000	40
$B^\pm \to \phi_{3\pi} K^\pm$	4.537	$8.3^{+0.65}_{-0.65}$	0.155	22
$B^\pm \to \rho K^*(1430)$	0.114	$40^\dagger$	1.000	17
$B^\pm \to K^\pm K^- K^+$	0.082	$33.7^{+1.5}_{-1.5}$	1.000	10
$B^\pm \to \omega K^\pm$	0.369	$6.7^{+0.6}_{-0.6}$	0.891	9
$B^\pm \to \rho^0\pi^\pm$	0.270	$8.7^{+1.0}_{-1.1}$	1.000	9
$B^0 \to a_1^+(\rho^0\pi^+)\pi^-$	0.118	$39.7^{+3.7}_{-3.7}$	0.500	9
$B^0 \to a_1^-(\rho^-\pi^0)K^+$	0.296	$15^\dagger$	0.500	8
$B^0 \to \rho K^*(1430)$	0.102	$20^\dagger$	1.000	8
$B^0 \to \pi^- K^{*+}_{K^+\pi^0}(1430)$	0.136	$46.6^{+5.6}_{-6.6}$	0.310	8
$B^\pm \to a_1^0\pi^\pm$	0.088	$20^\dagger$	1.000	7
$B^0 \to K^+\pi^-$	0.086	$18.9^{+0.7}_{-0.7}$	1.000	6
$B^\pm \to \rho^0 K^{*\pm}_{K^\pm\pi^0}$ (Long.)	1.318	$3.6^{+1.9}_{-1.8}$	0.333	6
$B^0 \to \eta'_{\rho\gamma} K^{*0}_{K^+\pi^-}$	2.122	$3.8^{+1.2}_{-1.2}$	0.197	6
$B^\pm \to \rho^\pm\rho^0$ (Long.)	0.075	$18.3^{+3.4}_{-3.4}$	0.96	5
$B^\pm \to \eta'_{\rho\gamma}\pi^\pm$	1.625	$2.6^{+0.6}_{-0.5}$	0.295	5
$B^\pm \to \eta'_{\eta\pi\pi} K^\pm$	0.086	$69.7^{+2.8}_{-2.7}$	0.174	4
$B^0 \to K^{*+}_{K^+\pi^0}\pi^-$	0.331	$9.8^{+1.1}_{-1.1}$	0.333	4
$B^\pm \to \eta'_{\rho\gamma} K^{*\pm}_{K^\pm\pi^0}$	2.224	$4.9^{+2.1}_{-1.9}$	0.098	4
$B^\pm \to \rho^\pm K^{*0}_{K^+\pi^-}$ (Long.)	0.228	$4.65^{+0.85}_{-0.85}$	0.666	3
$B^0 \to \rho^0 K^{*0}_{K^+\pi^-}$ (Long.)	1.253	$0.65^{+0.65}_{-0.65}$	0.667	2
$B^\pm \to a_1^\pm(\rho^0\pi^\pm)K^{*0}_{K^+\pi^-}$ (Long.)	0.089	$20^\dagger$	0.233	2
$B^0 \to \rho^+\rho^-$ (Long.)	0.019	$24.2^{+3.5}_{-3.6}$	0.96	2
$B^\pm \to \pi^\pm\pi^+\pi^-$ (N.R.)	0.160	$3.0^{+3.0}_{-3.0}$	1.000	2
$B^0 \to f_0 K^{*0}_{K^+\pi^-}$	0.419	$2.0^\dagger$	0.444	1
$B^0 \to a_1^0 K^{*0}_{K^+\pi^-}$ (Long.)	0.052	$10^\dagger$	0.467	1
$B^0 \to \rho^- K^{*+}_{K^+\pi^0}$ (Long.)	0.236	$2.0^\dagger$	0.333	1
$B^0 \to \pi^0\pi^+\pi^-$	0.011	$30^\dagger$	1.000	1
$B^\pm \to \rho^\pm\pi^+\pi^+$	0.008	$5.0^\dagger$	1.000	0
$B^0 \to \eta_{\gamma\gamma} K^{*0}_{K^+\pi^-}$	0.002	$18.7^{+1.7}_{-1.7}$	0.262	0
$B^0 \to \phi_{3\pi} K^{*0}_{K^+\pi^-}$ (Long.)	0.136	$4.75^{+0.45}_{-0.45}$	0.103	0
Total				556

Table 8.16: Potential $B\overline{B}$ background for the $\eta'_{\rho\gamma}K^\pm$ mode. For each decay mode we give the MC reconstruction efficiency ϵ, branching fraction ($\mathcal{B}$), daughter branching fraction product, estimate background (normalized to the integrated luminosity) in ML input. Branching fractions with † are estimated since no measurement exists.

Cross Feed Channel	MC ϵ (%)	Est. $\mathcal{B}$ (10^{-6})	$\prod \mathcal{B}_i$	# evts in ML
$B^0 \to \eta'_{\eta(\gamma\gamma)\pi\pi} K^0_{S+-}$	0.480	$64.9^{+3.5}_{-3.5}$	0.060	6
$B^\pm \to \eta'_{\eta(\gamma\gamma)\pi\pi} K^\pm$	0.063	$69.7^{+2.8}_{-2.7}$	0.174	2
Total				8

Table 8.17: Potential $B\overline{B}$ background for $\eta'_{\eta\pi\pi}K^0_L$ mode. For each decay mode we give the MC reconstruction efficiency ϵ, branching fraction ($\mathcal{B}$), daughter branching fraction product, estimate background (normalized to the integrated luminosity) in ML input.

probability as described in section 8.5.2.

In our fit we have considered three components: signal, continuum background, and $B\overline{B}$ background (the last one only for the modes with $\eta' \to \rho^0\gamma$). In the Tag04 tagger we have 6 tagging categories. We use the index c = (1, 2, 3, 4 ,5 ,6) to indicate that the event belongs to one specific category. For each input event i and category c, the likelihood ($\mathcal{L}_{i,c}$) is defined as:

$$\mathcal{L}_{i,c} = n_{sg} f_{sig,c} \mathcal{P}^{i,c}_{sg} + n_{q\bar{q}} f_{q\bar{q},c} \mathcal{P}^{i}_{q\bar{q}} + n_{b\bar{b}} f_{sig,c} \mathcal{P}^{i}_{b\bar{b}} \tag{8.4}$$

where $\mathcal{P}^{i,c}_{sg}$, $\mathcal{P}^{i}_{q\bar{q}}$ and $\mathcal{P}^{i}_{b\bar{b}}$ are the probability for signal, continuum background and $B\overline{B}$ background, evaluated with the observables of the ith event as the product of the probability density functions (PDFs) for each of the observable. With $f_{sig,c}$ and $f_{q\bar{q},c}$ we indicate the fraction of events for each category for each specie (we consider the fractions for $B\overline{B}$ background egual to signal ones). n_{sg} (number of signal events), $n_{q\bar{q}}$ (number of continuum events) and $n_{b\bar{b}}$ (number of $B\overline{B}$ events) are free parameters in the fit.

The extended likelihood function for all events belonging to category c is:

$$\mathcal{L}_c = \exp\left(-n_{sg} f_{sig,c} - n_{q\bar{q}} f_{q\bar{q},c} - n_{b\bar{b}} f_{sig,c}\right) \prod_{i}^{N_c} \mathcal{L}_{i,c} \tag{8.5}$$

where N_c is the total number of input events in category c. Finally the total likelihood

function for all categories can be written as:

$$\mathcal{L} = \prod_{c=1}^{6} \mathcal{L}_c \tag{8.6}$$

To fit two (or more) different sub-decay modes, the total likelihood becomes:

$$\mathcal{L} = \prod_{d} \mathcal{L}^d \tag{8.7}$$

where the index d runs over the fitted sub-decay modes. Our fitter minimizes the expression $-\ln \mathcal{L}$ with respect to a set of free parameters.

8.7.2 Probability Distribution Functions for Discriminating Variables

We describe in this section PDFs of the discriminating variables for signal and background. We show in tab. 8.18 which discriminating variables are used in the ML fits for each B decay mode.

Mode	PDFs
$\eta' K^0_S$	$m_{\rm ES}$, ΔE, $\mathcal{F}$, Δt
$\eta'_{\eta\pi\pi} K^0_L$	ΔE, $\mathcal{F}$, Δt

Table 8.18: Variables used in ML fits.

PDFs for signal and $B\overline{B}$ have been done using Monte Carlo simulated events and using all events independently from Monte Carlo truth. PDFs for background have been done using off-peak events (for K^0_L modes) or on-peak sidebands (for K^0_S modes), defined as:

- *Grand Side Band* (GSB): $5.25 < m_{\rm ES} < 5.27$ GeV/c^2
- ΔE *Side Band* (DESB): $0.1 < |\Delta E| < 0.2$ GeV

The tab. 8.19 reports the parameterization chosen for the different PDFs. For the $\mathcal{F}$ PDFs and $m_{\rm ES}$ $B\overline{B}$ PDFs, we use asymmetric Gaussians, i.e. Gaussians with different widths on the left and right sides of its peak. Instead of the usual parametrization which uses a mean and two sigmas (left and right sigma, $\sigma_{\rm L}$ and $\sigma_{\rm R}$), we use a new

parametrization which uses a mean, a sigma $\sigma = (\sigma_{\rm L} + \sigma_{\rm R})/2$, and an parameter $A = (\sigma_{\rm L} - \sigma_{\rm R})/(\sigma_{\rm L} + \sigma_{\rm R})$.

The goal of the new parametrization is to reduce the correlation between the parameters of the asymmetric Gaussian.

From our study we found that the $m_{\rm ES}$ endpoint in the Argus distribution is shifted to 5.2893 GeV/c^2 (previously was 5.29 GeV/c^2) as shown in fig. 8.2. We use this value in the fit.

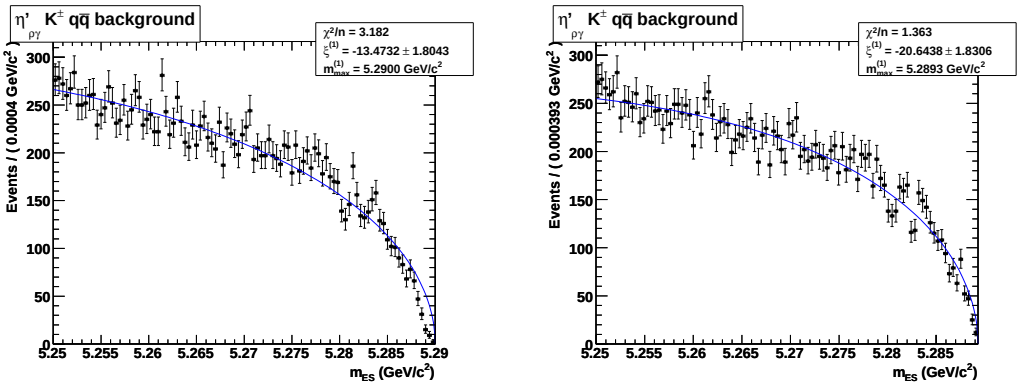

Figure 8.2: Fit to $m_{\rm ES}$ $q\overline{q}$ distribution for $\eta'_{\rho\gamma}K^{\pm}$: on left with endpoint fixed 5.29 GeV/c^2 and on right fixed to 5.2893 GeV/c^2.

Vertex resolution is mostly independent of the reconstructed B decay mode and small differences are reflected in the assigned Δt errors so parameters of the Δt resolution function can be taken from fit to the BReco sample. For our CP sample we use the CP model PDF convoluted with the resolution function described in eq. 8.8. The resolution function $\mathcal{R}_{\rm sig}(t)$ is the same triple Gaussian as described for BReco (naturally since the parameters are in common):

$$\begin{aligned}\mathcal{R}_{\rm sig}(t) &= f_{\rm core}\, G\left(t, s^{\mu}_{\rm core}\sigma_t, s^{\sigma}_{\rm core}\sigma_t\right) + \left(1 - f_{\rm core} - f_{\rm out}\right) G\left(t, s^{\mu}_{\rm tail}\sigma_t, s^{\sigma}_{\rm tail}\sigma_t\right) \\ &+ f_{\rm out}\, G\left(t, \mu_{\rm out}, \sigma_{\rm out}\right) \end{aligned} \tag{8.8}$$

where $G(x, x_0, \sigma)$ is a Gaussian with bias x_0 and standard deviation σ. The $q\overline{q}$ background Δt distribution is modeled using on-peak sideband data. It is parameterized with a triple Gaussian where we use $\Delta t/\sigma_{\Delta t}$ as in signal Δt resolution model.

Most of the background parameters are left floating in the fit: Argus parameter for $m_{\rm ES}$ (ΔE in K^0_L modes); coefficient of Chebyshev polynomial for ΔE; mean, $\sigma_{\rm left}$ and $\sigma_{\rm right}$ of aymmetric Gaussian for $\mathcal{F}$; all Δt PDF parameters. For the $m_{\rm ES}$ and $\mathcal{F}$ background parameters in charged modes and modes with K^0_S, we have decided to

put them in common in the simultaneous fit for all modes, in order to have a better determination of these parameters in the modes with a small input to ML. The values obtained in this way are then used in the fit for each single mode.

Appendix B shows PDFs plots and the correlations between input variables for all decay modes. We deal with uncertainties in PDFs parameters in the systematic section.

Fit Component	ΔE	$m_{\rm ES}$	$\mathcal{F}$	Δt
Signal	DG (CB in K^0_L)	CB	AG + G	CP model
$q\overline{q}$ Background	CH1 (A in K^0_L)	A	AG + CH1	TG
$B\overline{B}$ Background	G + CH3	AG + A	DG	TG

Table 8.19: PDF parameterization used for signal, $q\overline{q}$ background and $B\overline{B}$ background (G = Gaussian, DG = double Gaussian, TG = triple Gaussian, CB = Crystal Ball, AG = asymmetric Gausssian, A = Argus, CHn = n^{th} order Chebyshev polynomial).

8.7.3 MC/data Matching Corrections

We have to correct MC signal events in order to have a better matching with data. For shifts and scale factors of ΔE in neutral modes with K^0_S and in the charged modes we use data and Monte Carlo control sample $B^- \to D^0\pi^-$ to measure systematic difference for these variables. For $m_{\rm ES}$ the shifts are included in the conditions database and is thus included in our reconstruction for Runs1-4. For $m_{\rm ES}$ and ΔE corrections in Run5 data, because we have enough signal events, we determine them by allowing them to float in our on-peak data sample of $\eta'_{\rho\gamma}K^\pm$. For ΔE corrections in K^0_L modes we use the values suggested in $J/\psi\, K^0_L$ analysis. We show shifts and scale factors in tab. 8.20.

8.8 BReco Fits

We fit the BReco data sample to obtain the signal fraction, mistag fractions and mistag differences, and the parameters of signal Δt resolution model, in order to fix them in our CP fit for our decay modes. The BReco modes are self-tagging fully reconstructed B decays. These modes are reconstructed by a specific group in *BABAR*, which provides the data for the fits.

	Shift (MeV)	Scale Factor
ΔE in K^0_S modes		
run1-5	0 ± 5	1.05 ± 0.05
ΔE in K^0_L modes		
run1-5	-0.40 ± 0.25	–
$m_{\rm ES}$		
run1	–	–
run2	–	–
run3	–	–
run4	–	–
run5	-0.3 ± 0.2	1.00 ± 0.06

Table 8.20: Shifts and scale factor to apply to the core Gaussian used to fit signal for MC/data matching. The corrections is given for the data of different runs.

In our fits we fix the values of Δm_d and the B lifetimes to the PDG values [36]: $\Delta m_d = 0.507 \pm 0.005$ ps^{-1}, $\tau_{B^\pm} = 1.638 \pm 0.011$ ps, and $\tau_{B^0} = 1.530 \pm 0.009$ ps.

In order to tag the flavor of the "tag" side of the event, we use the `Tag04` tagger with six tagging categories (we do not consider untagged events). We split several quantities according to these tagging categories: signal fraction, mistag fractions and mistag differences, tag efficiency differences, background yields, and core offset of the signal Δt resolution function.

We use the $m_{\rm ES}$ distribution to discriminate between signal and background events. As signal PDF we use a double Gaussian obtained from fit on MC signal events, while for background we use an Argus function. We find the Argus shape parameter separately for each tagging category, and leave them floating in the fit. We fit the Δt for both signal and background using the B mixing physics model convoluted with a resolution model. The B mixing physics model uses as parameters six quantities: lifetime, Δm_d, mistag fraction, mistag difference, tag and reco efficiency differences. We have four components for Δt:

- **signal**

  The lifetime and Δm_d are fixed to their PDG values for neutral B. We use a triple Gaussian as resolution model (core, tail and outlier), where the core and tail biases and resolutions are scaled to $\sigma_{\Delta t}$ (with the tail scale factor fixed at 3.0), and the outlier Gaussian has mean value fixed at zero and width fixed at 8 ps. The

signal efficiency, mistag fraction, mistag difference, tag efficiency difference for each tagging category are listed in tab. 8.21 for real data and tab. 8.22 for MC events. The signal resolution parameters are given in tab. 8.23 for real data and tab. 8.24 for MC events.

- **peaking background**
  The lifetime is fixed to the PDG value for charged B and Δm_d is fixed to zero. The mistag differences are fixed at zero. We fix the fraction of peaking background to signal component at 1.5%. The resolution model, tag and reco efficiency differences are the same of the signal component.

- **lifetime background**
  The mistag differences, Δm_d and tag and reco efficiency differences are fixed to zero. The mistag fractions and the background lifetime are listed in tab. 8.25. We use a double Gaussian resolution model (core and outlier) where the core bias and resolution are scaled to $\sigma_{\Delta t}$ and the outlier Gaussian again has a fixed mean and width. The background resolution parameters are shown in tab. 8.26.

- **prompt background** (*i. e.* zero lifetime)
  The lifetime, mistag differences, Δm_d and tag and reco efficiency differences are fixed to zero. The resolution model is the same as the lifetime background component. The fraction of prompt background and background mistag fractions are listed in tab. 8.25.

Table 8.21: BReco signal tagging fractions (f), mistag fractions ($\langle w \rangle$), mistag differences (Δw), and tag efficiency differences (μ) for each tagging category determined from fit to the neutral BReco sample.

Category	f_{sig}	$\langle w \rangle$	Δw	μ
`Lepton`	0.1162 ± 0.0008	0.0297 ± 0.0033	-0.0015 ± 0.0064	0.0056 ± 0.0113
`KaonI`	0.1469 ± 0.0009	0.0535 ± 0.0038	-0.0057 ± 0.0071	0.0025 ± 0.0110
`KaonII`	0.2307 ± 0.0010	0.1546 ± 0.0039	-0.0044 ± 0.0066	0.0027 ± 0.0096
`KorPI`	0.1846 ± 0.0010	0.2349 ± 0.0048	-0.0237 ± 0.0078	-0.0167 ± 0.0107
`Pions`	0.1928 ± 0.0010	0.3295 ± 0.0051	0.0524 ± 0.0078	-0.0284 ± 0.0107
`Other`	0.1288 ± 0.0008	0.4193 ± 0.0063	0.0459 ± 0.0094	0.0245 ± 0.0124

Table 8.22: MC BReco signal tagging fractions (f), mistag fractions ($\langle w \rangle$), mistag differences (Δw), and tag efficiency differences (μ) for each tagging category determined from fit to the neutral MC BReco sample.

Category	f_{sig}	$\langle w \rangle$	Δw	μ
`Lepton`	0.1162 ± 0.0008	0.0294 ± 0.0006	0.0016 ± 0.0011	-0.0041 ± 0.0022
`KaonI`	0.1469 ± 0.0009	0.0655 ± 0.0007	0.0016 ± 0.0013	0.0010 ± 0.0022
`KaonII`	0.2307 ± 0.0010	0.1651 ± 0.0007	-0.0022 ± 0.0012	0.0041 ± 0.0020
`KorPI`	0.1846 ± 0.0010	0.2626 ± 0.0009	-0.0186 ± 0.0014	0.0106 ± 0.0022
`Pions`	0.1928 ± 0.0010	0.3507 ± 0.0009	0.0604 ± 0.0014	-0.0221 ± 0.0022
`Other`	0.1288 ± 0.0008	0.4235 ± 0.0011	0.0463 ± 0.0017	0.0072 ± 0.0026

Table 8.23: Summary of BReco signal resolution function parameters.

Parameter	B^0
Scale `Lepton` (core)	1.0631 ± 0.0489
Scale `Not Lepton` (core)	1.0985 ± 0.0235
$\delta(\Delta t)$ `Lepton` (core)	-0.0709 ± 0.0321
$\delta(\Delta t)$ `No Lepton` (core)	-0.1805 ± 0.0145
f (core)	0.8888 ± 0.0092
Scale (tail)	3.0 (fixed)
$\delta(\Delta t)$ (tail)	-1.1140 ± 0.1380
f (outlier)	0.0033 ± 0.0006
Scale (outlier)	8.0 (fixed)
$\delta(\Delta t)$ (outlier) (ps)	0.0 (fixed)

Table 8.24: Summary of MC BReco signal resolution function parameters.

Parameter	B^0
Scale `Lepton` (core)	0.9952 ± 0.0098
Scale `Not Lepton` (core)	1.0898 ± 0.0047
$\delta(\Delta t)$ `Lepton` (core)	-0.0618 ± 0.0061
$\delta(\Delta t)$ `No Lepton` (core)	-0.2472 ± 0.0028
f (core)	0.8894 ± 0.0019
Scale (tail)	3.0 (fixed)
$\delta(\Delta t)$ (tail)	-1.1782 ± 0.0290
f (outlier)	0.0041 ± 0.0001
Scale (outlier)	8.0 (fixed)
$\delta(\Delta t)$ (outlier) (ps)	0.0 (fixed)

Table 8.25: Fit results for BReco prompt background and lifetime mistag fractions and the fraction of prompt background for the neutral BReco sample. The fit background lifetime is 1.202 ± 0.032 ps.

Category	f_P	$\langle w_L \rangle$	$\langle w_P \rangle$
`Lepton`	0.3067 ± 0.0942	0.4788 ± 0.0758	0.0774 ± 0.1350
`KaonI`	0.6738 ± 0.0222	0.2377 ± 0.0276	0.1880 ± 0.0133
`KaonII`	0.6850 ± 0.0166	0.3097 ± 0.0201	0.2457 ± 0.0096
`KorPI`	0.6728 ± 0.0190	0.3595 ± 0.0235	0.3435 ± 0.0119
`Pions`	0.6892 ± 0.0173	0.4550 ± 0.0233	0.4255 ± 0.0111
`Other`	0.7311 ± 0.0182	0.4930 ± 0.0295	0.4613 ± 0.0118

Table 8.26: Summary of BReco background resolution function parameters.

Parameter	B^0
Scale (core)	1.3147 ± 0.0093
$\delta(\Delta t)$ (core)	-0.0205 ± 0.0070
f (core)	0.9802 ± 0.0012
Scale (outlier)	8.0 (fixed)
$\delta(\Delta t)$ (outlier) (ps)	0.0 (fixed)

8.9 Verification Tests

8.9.1 Vertexing Validation for $\eta' K^0_{S00}$ and $\eta'_{\eta(3\pi)\pi\pi} K^0_{S+-}$ modes

To check and validate the K^0_S vertexing reconstruction we made a comparison on vertexing resolution between charged and neutral K^0_S decay mode (K^0_{S00} and K^0_{S+-}) using MC truth signal events. We fit the distributions of the z position of the reconstructed B, z_{CP}, and its pull distributions, on MC truth events with a triple gaussian for z_{CP}. The results are shown in tab. 8.9.1 and 8.9.1.

The results for neutral K^0_S decay are in good agreement with the ones for the charged K^0_S decay, so we verify that the vertexing reconstruction depends mostly from the informations on the η' meson.

		$\eta'_{\eta\pi\pi} K^0_{S00}$	$\eta'_{\eta(\gamma\gamma)\pi\pi} K^0_{S+-}$
B_{CP}	$\mu_{\rm core}$	-0.0009 ± 0.0006	-0.0001 ± 0.0001
	$\sigma_{\rm core}$	0.0099 ± 0.0013	0.0062 ± 0.0002
B_{CP} Pull	$\mu_{\rm core}$	0.0056 ± 0.0161	-0.0006 ± 0.0094
	$\sigma_{\rm core}$	0.8605 ± 0.0166	0.9708 ± 0.0096
Δt Pull	$\mu_{\rm core}$	-0.1612 ± 0.0198	-0.2100 ± 0.0111
	$\sigma_{\rm core}$	1.0555 ± 0.0188	1.0409 ± 0.0119

Table 8.27: Results for vertexing validation.

		$\eta'_{\rho\gamma} K^0_{S00}$	$\eta'_{\rho\gamma} K^0_{S+-}$
B_{CP}	$\mu_{\rm core}$	0.0003 ± 0.0002	0.0001 ± 0.0002
	$\sigma_{\rm core}$	0.0058 ± 0.0003	0.0133 ± 0.0004
B_{CP} Pull	$\mu_{\rm core}$	0.0404 ± 0.0168	-0.0032 ± 0.0085
	$\sigma_{\rm core}$	0.9224 ± 0.0153	0.9381 ± 0.0080
Δt Pull	$\mu_{\rm core}$	-0.1819 ± 0.0226	-0.2323 ± 0.0110
	$\sigma_{\rm core}$	1.0706 ± 0.0231	1.0766 ± 0.0110

Table 8.28: Results for vertexing validation.

We made some checks in order to understand how the SXF events contribute to the CP asymmetry parameters. Because the vertexing reconstruction is made using the information on the η' meson, we study the Δt resolution for signal events with η' misreconstructed ($i.\ e.$ reconstructed with particles not belonging to the true η', denoted as SXF$_{\eta'}$ events) and with η' true or with permutated daughters. Due to the fact

that most of the SXF$_{\eta'}$ contributions come from the decays with $\eta'_{\eta(3\pi)\pi\pi}$, we decided to study these subdecays.

We show in figs. 8.3 and 8.4 the Δt and $\sigma_{\Delta t}$ distributions. There isn't any significant difference between the distributions.

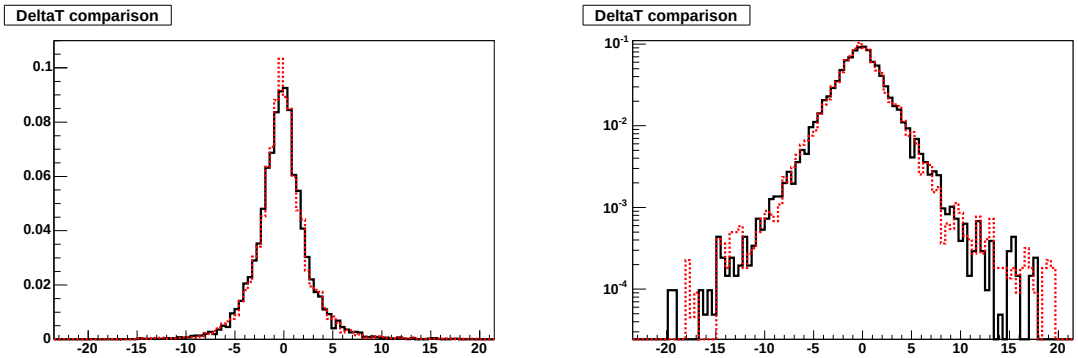

Figure 8.3: Δt distributions (left: linear, right: logarithmic) for true events (black continuos line) and SXF$_{\eta'}$ events (red dashed line) in $\eta'_{\eta(3\pi)\pi\pi} K^0_S$.

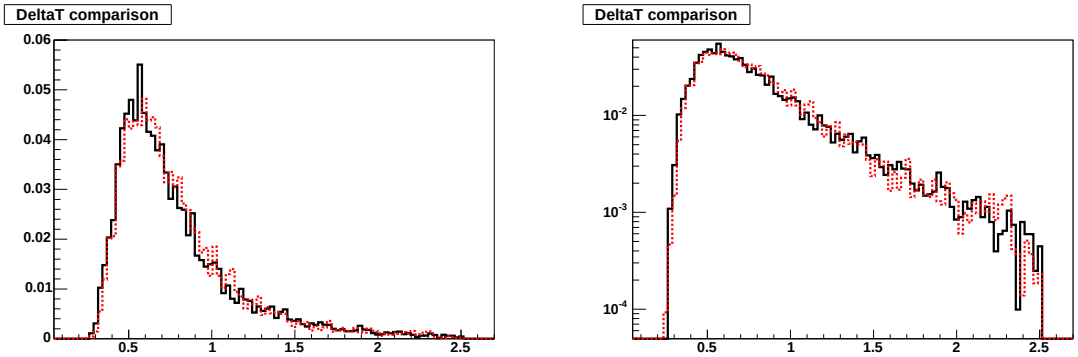

Figure 8.4: $\sigma_{\Delta t}$ distributions (left: linear, right: logarithmic) for true events (black continuos line) and SXF$_{\eta'}$ events (red dashed line) in $\eta'_{\eta(3\pi)\pi\pi} K^0_S$.

We calculate and fit with a double Gaussian the Δt pull in the channels with $\eta'_{\eta(3\pi)\pi\pi}$ for events with and without SXF$_{\eta'}$ contribution. The results are shown in tab. 8.29. The Δt pull distributions are shown in fig. 8.5.

We also check Δt residual for no $SXF_{\eta'}$ and $SXF_{\eta'}$ signal events. Both events are fitted using PDF defined as eq. 8.8. Results are shown in tab 8.30.

We calculate the CP parameters C and S for MC signal events, considering separately events with SXF and without SXF. The results are shown in tab. 8.31. As shown in the table, the CP asymmetry parameters are quite similar for the two categories, so the effect of the SXF events on S and C is negligible. For this reason we decide to fit the asymmetry parameters with the same S and C value for both kind of event.

		$\eta'_{\eta(3\pi)\pi\pi}K^0_S$
Δt Pull SXF	$\mu_{\rm core}$	-0.2080 ± 0.0184
Δt Pull no SXF	$\mu_{\rm core}$	-0.1994 ± 0.0104
Δt Pull SXF	$\sigma_{\rm core}$	0.9873 ± 0.0209
Δt Pull no SXF	$\sigma_{\rm core}$	0.9809 ± 0.0106

Table 8.29: Results for vertexing validation.

Parameter	$\eta'_{\eta(3\pi)\pi\pi}K^0_S$	
	no $SXF_{\eta'}$ events	$SXF_{\eta'}$ events
Scale (core)	1.1550 ± 0.0119	1.1802 ± 0.0242
$\delta(\Delta t)$ `Lepton` (core)	-0.0994 ± 0.0370	-0.1866 ± 0.0886
$\delta(\Delta t)$ `KaonI` (core)	-0.2209 ± 0.0348	-0.2182 ± 0.0790
$\delta(\Delta t)$ `KaonII` (core)	-0.2297 ± 0.0300	-0.1437 ± 0.0559
$\delta(\Delta t)$ `KorPI` (core)	-0.2668 ± 0.0335	-0.3994 ± 0.0613
$\delta(\Delta t)$ `Pions` (core)	-0.2665 ± 0.0321	-0.3457 ± 0.0586
$\delta(\Delta t)$ `Other` (core)	-0.2865 ± 0.0394	-0.1996 ± 0.0677
Scale (tail)	3.0 (fixed)	3.0 (fixed)
f (tail)	0.1009 ± 0.0075	0.1151 ± 0.0156
$\delta(\Delta t)$ (tail)	-1.3357 ± 0.1327	-1.1962 ± 0.2198
f (outlier)	0.0107 ± 0.0015	0.0260 ± 0.0038
Scale (outlier)	8.0 (fixed)	8.0 (fixed)
$\delta(\Delta t)$ (outlier) (ps)	0.0 (fixed)	0.0 (fixed)

Table 8.30: Δt residual parameters for no SXF signal and SXF events.

Decay mode	S	C
$\eta'_{\rho\gamma}K^0_{S00}$		
SXF events	0.744 ± 0.156	-0.022 ± 0.102
no SXF events	0.639 ± 0.058	0.046 ± 0.040
$\eta'_{\eta\pi\pi}K^0_{S00}$		
SXF events	0.648 ± 0.138	-0.006 ± 0.089
no SXF events	0.640 ± 0.062	0.027 ± 0.040
$\eta'_{\eta(3\pi)\pi\pi}K^0_S$		
SXF events	0.658 ± 0.068	0.011 ± 0.048
no SXf events	0.687 ± 0.031	0.003 ± 0.022

Table 8.31: CP asymmetry parameters for signal and SXF events.

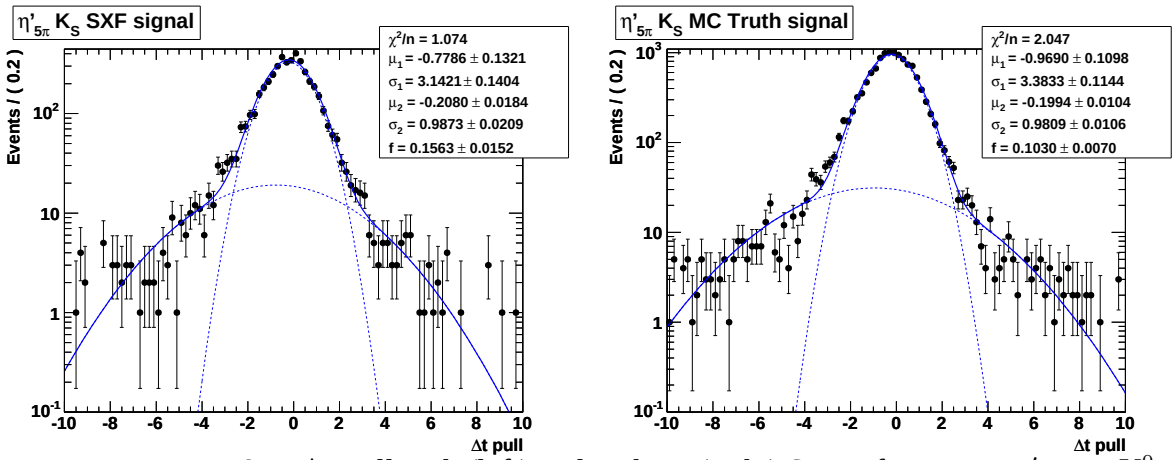

Figure 8.5: Δt pull with (left) and without (right) SXF$_{\eta'}$ fraction in $\eta'_{\eta(3\pi)\pi\pi} K^0_S$.

8.9.2 Vertexing Validation for K^0_L modes

Using the MC signal events and MC truth informations, we have that our MC signal sample in input to ML for $\eta'_{\eta\pi\pi} K^0_L$ is composed of:

- Events without B MC truth: 25.0% of total events
- Events without η' MC truth: 13.8% of total events

We think that for TD analysis is more important the percent of events without η' MC truth than the percent of events without B MC truth (because the vertex information comes from η' vertex). We show in the fig. 8.6 the distributions of the variables used in the ML fit and in the fig. 8.7 the residuals for Δt variable. We don't see an effect of misreconstruction for Δt distributions.

8.9.3 MC Toy experiments

We have generated 500 experiments for each decay mode in order to study any possible bias in the fit results. The events are taken from the MC for signal and $B\overline{B}$ background and generated from PDFs for continuum background. Numbers of signal events in each experiment are as measured in data, while $B\overline{B}$ and continuum are as expected in data. Number of embedded $B\overline{B}$ events are those shown in Tables 8.14- 8.17. Results of these toy experiments are shown in Tables 8.32–8.35. In these toys we use the MC BReco parameters (Tables 8.22 and 8.24).

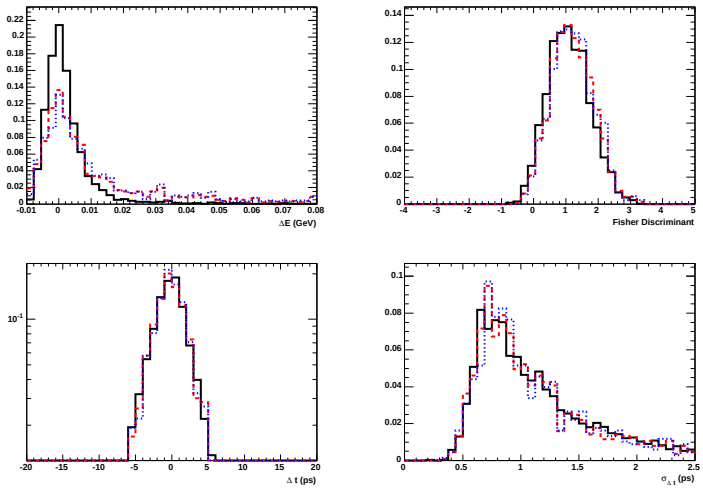

Figure 8.6: Comparison between the distributions of the variables used in the ML fit for $\eta'_{\eta\pi\pi}K^0_L$ mode: events with B MC truth (black solid line), events without B MC truth (red dashed line) and events without η' MC truth (blue dotted line).

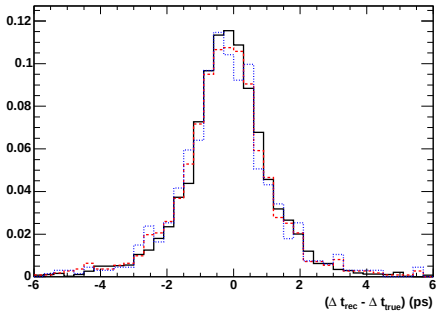

Figure 8.7: Comparison between the distributions of the residuals of the Δt variable used in the ML fit for $\eta'_{\eta\pi\pi}K^0_L$ mode: events with B MC truth (black solid line), events without B MC truth (red dashed line) and events without η' MC truth (blue dotted line).

In these tables we show results of fit of 500 toy experiments for all the decay modes. We give the number of embedded events of the type specified and the mean of the Gaussians used to fit the distributions of the fitted yield, S, and C with their corresponding errors. We show also the mean and sigma of the Gaussians used to fit the pull distributions of S and C. In the tables we show also the effect of embedding $B\overline{B}$ background and fitting with $B\overline{B}$ component.

We see that when we embed $B\overline{B}$ events in the decay modes $\eta'_{\rho\gamma}K^0_{S+-}$, $\eta'_{\rho\gamma}K^0_{S00}$, and $\eta'_{\eta\pi\pi}K^0_L$ the value for S is diluited and we observe a bias which we correct multiplicatively using the ratio of the value of S found fitting without embedding $B\overline{B}$ events and the value of S found fitting with $B\overline{B}$ embedded events. We will assign a systematic uncertainty.

Another kind of bias is present when we fit without embedding $B\overline{B}$ events. This bias has been studied extensively in the previous analysis (done in 2004) where it was finally considered as a fluctuation. In fact using MC samples that were ten times as large as before the effect disappeared. Furthermore this kind of bias is not present in pure toy experiments. For this reason we do not correct for this bias and we will assign a systematic uncertainty.

8.9.4 Pure Toy experiments

We have generated 500 experiments for each decay mode in order to study any possible bias in the fit results due to the fit itself. All events are generated from PDFs. We have done this check only for the $\eta'_{\eta(\gamma\gamma)\pi\pi}K^0_{S+-}$. The results are shown in tab. 8.36.

8.9.5 Fitting with CP asymmetry information in $B\overline{B}$ background

As a check we have used in the charmless $B\overline{B}$ background the CP model for the Δt PDF. We use the same CP model used in the signal Δt PDF, with proper S and C parameters (here called $S_{B\overline{B}}$ and $C_{B\overline{B}}$). We fit for all sub-modes (simultaneous fit). We have charmless $B\overline{B}$ component in $\eta'_{\rho\gamma}K^0_{S+-}$ and $\eta'_{\rho\gamma}K^0_{S00}$ modes. Results of this fit are shown in tab. 8.37, together with the results of the standard fit for comparison. As we can see the values of $S_{B\overline{B}}$ and $C_{B\overline{B}}$ are consistent with zero and the effect on S and C from the different parameterization of $B\overline{B}$ Δt PDF is negligible. For this reason we can consider adequate a triple Gaussian parameterization of $B\overline{B}$ Δt PDF. We assign a systematic uncertainty to S and C equal to the change in S and C when we use CP

Table 8.32: Mean values of CP violating parameters and their errors for 500 embedded toy MC experiments for neutral sub-decays. MC events are generated with $S = 0.7$ and $C = 0.0$.

$\eta'_{\rho\gamma}K^0_{S+-}$				
Signal events	566			
Bkg. events	11377			
$B\overline{B}$ events	0			
	Sg	$B\overline{B}$	S	C
Value	571.5 ± 0.7	-9.3 ± 1.2	0.704 ± 0.006	-0.002 ± 0.005
Value Error	28.6 ± 0.1	19.0 ± 0.2	0.129 ± 0.001	0.101 ± 0.001
Mean Pull	–	–	0.05 ± 0.05	-0.04 ± 0.05
Sigma Pull	–	–	0.95 ± 0.04	0.98 ± 0.04

$\eta'_{\rho\gamma}K^0_{S+-}$				
Signal events	566			
Bkg. events	11224			
$B\overline{B}$ events	153			
	Sg	$B\overline{B}$	S	C
Value	580.7 ± 0.9	118.8 ± 1.5	0.686 ± 0.007	-0.004 ± 0.005
Value Error	29.4 ± 0.1	30.5 ± 0.1	0.132 ± 0.001	0.102 ± 0.001
Mean Pull	–	–	-0.05 ± 0.06	-0.07 ± 0.05
Sigma Pull	–	–	1.06 ± 0.05	1.01 ± 0.05

$\eta'_{\eta(\gamma\gamma)\pi\pi}K^0_{S+-}$			
Signal events	224		
Bkg. events	440		
	Sg	S	C
Value	222.6 ± 0.3	0.694 ± 0.011	0.010 ± 0.007
Value Error	15.9 ± 0.1	0.211 ± 0.001	0.149 ± 0.001
Mean Pull	–	-0.07 ± 0.05	0.10 ± 0.05
Sigma Pull	–	1.03 ± 0.04	1.02 ± 0.04

$\eta'_{\eta(3\pi)\pi\pi}K^0_{S+-}$			
Signal events	73		
Bkg. events	104		
	Sg	S	C
Value	71.8 ± 0.2	0.717 ± 0.017	0.016 ± 0.016
Value Error	9.0 ± 0.1	0.371 ± 0.003	0.257 ± 0.001
Mean Pull	–	0.06 ± 0.05	0.09 ± 0.05
Sigma Pull	–	0.98 ± 0.04	1.06 ± 0.04

Table 8.33: Mean values of CP violating parameters and their errors for 500 embedded toy MC experiments for neutral sub-decays. MC events are generated with $S = 0.7$ and $C = 0.0$

$\eta'_{\rho\gamma} K^0_{s00}$				
Signal events	137			
Bkg. events	13778			
$B\overline{B}$ events	0			
	Sg	$B\overline{B}$	S	C
Value	148.0 ± 0.9	-6.6 ± 1.4	0.693 ± 0.017	-0.014 ± 0.013
Value Error	21.5 ± 0.1	27.7 ± 0.3	0.313 ± 0.002	0.254 ± 0.001
Mean Pull	–	–	0.02 ± 0.06	-0.09 ± 0.05
Sigma Pull	–	–	1.03 ± 0.05	1.08 ± 0.04
$\eta'_{\rho\gamma} K^0_{s00}$				
Signal events	137			
Bkg. events	13746			
$B\overline{B}$ events	32			
	Sg	$B\overline{B}$	S	C
Value	148.9 ± 0.9	14.3 ± 1.4	0.671 ± 0.015	-0.005 ± 0.012
Value Error	22.1 ± 0.1	30.3 ± 0.2	0.325 ± 0.002	0.261 ± 0.001
Mean Pull	–	–	-0.06 ± 0.05	0.00 ± 0.05
Sigma Pull	–	–	0.96 ± 0.04	1.03 ± 0.04
$\eta'_{\eta\pi\pi} K^0_{s00}$				
Signal events	52			
Bkg. events	438			
	Sg	S	C	
Value	51.7 ± 0.3	0.703 ± 0.015	0.019 ± 0.010	
Value Error	8.8 ± 0.1	0.524 ± 0.006	0.346 ± 0.003	
Mean Pull	–	0.10 ± 0.05	-0.10 ± 0.05	
Sigma Pull	–	0.95 ± 0.04	1.03 ± 0.04	

Table 8.34: Mean values of CP violating parameters and their errors for 500 embedded toy MC experiments for charged sub-decays. NOTE: these toys refer to a lower luminosity that used in analysis, $288.5\,\text{fb}^{-1}$. MC events are generated with $S = 0.0$ and $C = 0.0$.

$\eta'_{\rho\gamma}K^{\pm}$				
Signal events	1499			
Bkg. events	36708			
$B\overline{B}$ events	0			
	Sg	$B\overline{B}$	S	C
Value	1532.1 ± 1.1	-3.8 ± 1.8	0.008 ± 0.003	0.026 ± 0.003
Value Error	48.1 ± 0.1	35.7 ± 0.3	0.079 ± 0.001	0.062 ± 0.001
Mean Pull	–	–	0.06 ± 0.04	0.39 ± 0.04
Sigma Pull	–	–	1.00 ± 0.03	0.92 ± 0.03
$\eta'_{\rho\gamma}K^{\pm}$				
Signal events	1499			
Bkg. events	36237			
$B\overline{B}$ events	471			
	Sg	$B\overline{B}$	S	C
Value	1546.2 ± 1.6	387.9 ± 2.9	0.009 ± 0.004	0.022 ± 0.003
Value Error	49.2 ± 0.1	60.7 ± 0.1	0.080 ± 0.001	0.062 ± 0.001
Mean Pull	–	–	0.16 ± 0.05	0.34 ± 0.05
Sigma Pull	–	–	0.96 ± 0.03	1.00 ± 0.04
$\eta'_{\eta\pi\pi}K^{\pm}$				
Signal events	668			
Bkg. events	1024			
	Sg	S	C	
Value	667.2 ± 0.5	0.019 ± 0.005	0.010 ± 0.004	
Value Error	27.7 ± 0.1	0.112 ± 0.001	0.082 ± 0.001	
Mean Pull	–	0.15 ± 0.05	0.13 ± 0.05	
Sigma Pull	–	0.96 ± 0.03	1.00 ± 0.03	
$\eta'_{\eta(3\pi)\pi\pi}K^{\pm}$				
Signal events	194			
Bkg. events	298			
	Sg	S	C	
Value	191.7 ± 0.3	0.004 ± 0.010	0.002 ± 0.007	
Value Error	15.0 ± 0.1	0.209 ± 0.001	0.153 ± 0.001	
Mean Pull	–	0.02 ± 0.05	-0.01 ± 0.04	
Sigma Pull	–	1.06 ± 0.04	0.97 ± 0.03	

Table 8.35: Mean values of CP violating parameters and their errors for 500 SP8 embedded toy MC experiments for neutral sub-decays. MC events are generated with $S = 0.7$ and $C = 0.0$.

$\eta'_{\eta\pi\pi} K^0_L$			
Signal events	206		
Bkg. events	3993		
$B\overline{B}$ events	0		
	Sg	S	C
Value	204.6 ± 1.0	0.699 ± 0.014	-0.024 ± 0.010
Value Error	25.1 ± 0.1	0.318 ± 0.002	0.224 ± 0.001
Mean Pull	$-$	-0.01 ± 0.05	-0.09 ± 0.05
Sigma Pull	$-$	1.01 ± 0.04	0.97 ± 0.04
$\eta'_{\eta\pi\pi} K^0_L$			
Signal events	206		
Bkg. events	3985		
$B\overline{B}$ events	8		
	Sg	S	C
Value	208.3 ± 1.1	0.679 ± 0.016	-0.021 ± 0.012
Value Error	25.3 ± 0.1	0.317 ± 0.002	0.221 ± 0.001
Mean Pull	$-$	-0.04 ± 0.05	-0.10 ± 0.05
Sigma Pull	$-$	1.05 ± 0.04	1.00 ± 0.04

Table 8.36: Mean values of CP violating parameters and their errors for 500 Pure toy MC experiments for neutral sub-decays. NOTE: these toys refer to a lower luminosity that used in analysis, $288.5\,\text{fb}^{-1}$. Signal events are generated with $S = 0.7$ and $C = 0.0$.

$\eta'_{\eta(\gamma\gamma)\pi\pi}K^0_{S+-}$			
Signal events	206		
Bkg. events	406		
	Sg	S	C
Value	205.4 ± 0.6	0.704 ± 0.011	0.014 ± 0.008
Value Error	15.5 ± 0.0	0.230 ± 0.001	0.159 ± 0.000
Mean Pull	$-$	0.06 ± 0.05	0.08 ± 0.05
Sigma Pull	$-$	1.01 ± 0.04	0.98 ± 0.04

model for $B\overline{B}$ with respect to the standard fit.

We fit also the single $\eta'_{\rho\gamma}K^0_{S+-}$ mode with CP model for the charmless $B\overline{B}$ background Δt PDF. Results of this fit are in tab. 8.38. To validate this fit we have performed 500 MC toy experiments and the results are shown in tab. 8.39. In the same tab. 8.38 we show the results when we fit without the $B\overline{B}$ component. We have performed 500 MC toy experiments to validate the fit

Quantity	$\eta'_{\eta(\gamma\gamma)\pi\pi}K^0_{S+-}$	$\eta'_{\rho\gamma}K^0_{S+-}$	$\eta'_{\eta(3\pi)\pi\pi}K^0_{S+-}$	$\eta'_{\eta\pi\pi}K^0_{S00}$	$\eta'_{\rho\gamma}K^0_{S00}$	$\eta'_{\eta\pi\pi}K^0_{L}$
Standard fit						
Signal yield	224 ± 16	566 ± 30	73 ± 9	52 ± 9	133 ± 24	204 ± 24
$B\overline{B}$ yield	–	334 ± 41	–	–	159 ± 41	–
# Free parameters			93			
S			0.579 ± 0.100			
C			-0.158 ± 0.071			
Fit with CP model for charmless $B\overline{B}$ component						
Signal yield	224 ± 16	565 ± 30	73 ± 9	52 ± 9	129 ± 24	204 ± 24
$B\overline{B}$ yield	–	343 ± 41	–	–	176 ± 42	–
$S_{B\overline{B}}$	–	0.065 ± 0.236	–	–	0.023 ± 0.404	–
$C_{B\overline{B}}$	–	0.025 ± 0.234	–	–	0.055 ± 0.397	–
# Free parameters			97			
S			0.578 ± 0.101			
C			-0.162 ± 0.072			

Table 8.37: Summary of ML fit results for all the neutral decay modes.

Fit Configuration	Quantity	$\eta'_{\rho\gamma}K^0_{S+-}$
Standard Fit	Signal yield	566 ± 30
	$B\overline{B}$ yield	335 ± 39
	S	0.565 ± 0.141
	C	-0.237 ± 0.103
Fit with $S_{B\overline{B}}$ and $C_{B\overline{B}}$	Signal yield	565 ± 30
	$B\overline{B}$ yield	341 ± 39
	S	0.560 ± 0.145
	C	-0.245 ± 0.105
	$S_{B\overline{B}}$	0.069 ± 0.240
	$C_{B\overline{B}}$	0.066 ± 0.238
Without $B\overline{B}$ component	Signal yield	644 ± 30
	S	0.481 ± 0.126
	C	-0.227 ± 0.094

Table 8.38: ML fit results when we fit using for the $B\overline{B}$ Δt PDF a model like signal one with $S_{B\overline{B}}$ and $C_{B\overline{B}}$ free in the fit and when we fit without $B\overline{B}$ component.

$\eta'_{\rho\gamma}K^0_{S+-}$						
Signal events	565					
Bkg. events	11037					
$B\overline{B}$ events	341					
	Sg	$B\overline{B}$	S	C	$S_{B\overline{B}}$	$C_{B\overline{B}}$
Value	582.0 ± 0.9	285.9 ± 1.6	0.684 ± 0.007	-0.009 ± 0.004	-0.018 ± 0.013	0.000 ± 0.013
Value Error	30.0 ± 0.0	38.4 ± 0.1	0.139 ± 0.000	0.107 ± 0.000	0.318 ± 0.002	0.272 ± 0.002

Table 8.39: Mean values of CP violating parameters and their errors for 500 SP8 embedded toy MC experiments for $\eta'_{\rho\gamma}K^0_S(\rightarrow \pi^+\pi^-)$ mode with CP model for the charmless $B\overline{B}$ background Δt PDF. MC signal events are generated with $S = 0.7$ and $C = 0.0$. MC charmless $B\overline{B}$ events are listed in Table 8.14 (taken in the same proportion).

8.10 Systematic Errors

Contributions to the systematic uncertainties in S and C are estimated for the following:

- For PDF shapes, we estimate the errors by variation of the fit parameters. In tab. 8.40, we summarize all the variations and their results. For the signal and $B\overline{B}$ PDF we vary the MC/data corrections inside their errors. For the Fisher discriminat parameters we use the uncertanties described suggested by another group in *BABAR*. All changes are summed in quadrature to obtain an error which we round to 0.017 for S and 0.011 for C.

- We correct for a possible dilution of S due to embedded $B\overline{B}$ background. We have used a multiplicative correction for this bias. We fit with and without this correction and the difference in the results of S is assigned as systematic uncertainty. We find a systematic contribution on S of 0.014.

- Toy studies (section 8.9.3) show that there is a systematic bias in S and C related mainly to the limited statistics of MC toy experiment that we can perform. We take as systematic half of the maximum bias we find in toy experiments summed in quadrature with his uncertainty. We assign an uncertainty of 0.012 for S and 0.013 for C.

- We assign a systematics due to uncertanty of the CP content in the $B\overline{B}$ background (see section 8.9.5). For this reason we fit with CP model for the charmless $B\overline{B}$ Δt PDF. We find the values of S and C in $B\overline{B}$ background consistent with zero and we take as systematics the changes for S and C in signal when we use CP model for $B\overline{B}$ with respect to the standard fit. We find 0.001 for S and 0.004 for C.

- We have studied a systematic for the appropriateness of using Breco data for the $B^0 \to \eta' K^0$ signal. This is not quite as obvious as for ψK^0_S since the resolution on the signal side is not completely negligible so the resolution function could be slightly different. We take a systematic error of 0.004 for S and 0.012 for C.

- The systematic uncertainties related to the SVT alignment, beam-spot position and tag-side interference have been studied by another group in *BABAR* [113]. The systematic uncertainties due to the first two terms (SVT and beam-spot)

Table 8.40: Results of systematic variations. We show the nominal values, the amount that we vary these, the source of this variation amount, and the change of S and C for this amount of variation. We group similar quantities together after combining their variations in quadrature.

Quantity	Nominal	$\pm$ variation	Source of variation	Change in S	Change in C
$m_{\rm ES}$, ΔE, $\mathcal{F}$	PDF parameters, MC/data Corrections			$^{+0.019}_{-0.006}$	$^{+0.011}_{-0.004}$
Δm_d	0.507	0.005	PDG	$^{+0.007}_{-0.004}$	$^{+0.003}_{-0.002}$
τ_B	1.530	0.009	PDG	$^{+0.003}_{-0.001}$	$^{+0.001}_{-0.000}$
w	Table 8.21	Table 8.21	Table 8.21	$^{+0.004}_{-0.003}$	$^{+0.003}_{-0.001}$
Δw	Table 8.21	Table 8.21	Table 8.21	$^{+0.006}_{-0.001}$	$^{+0.007}_{-0.005}$
μ	Table 8.21	Table 8.21	Table 8.21	$^{+0.006}_{-0.000}$	$^{+0.002}_{-0.000}$
Signal $f_{\rm cat}$	Table 8.21	Table 8.21	Table 8.21	$^{+0.005}_{-0.000}$	$^{+0.002}_{-0.000}$
Signal Δt	Table 8.23	Table 8.23	Table 8.23	$^{+0.009}_{-0.006}$	$^{+0.005}_{-0.003}$
Total				$^{+0.025}_{-0.010}$	$^{+0.015}_{-0.007}$

are found negligible both for S and C while the systematic uncertainties for the interference with some tag-side B decays are 0.002 for S and 0.014 for C. We assume that all these systematic uncertainties are the same in all decay modes.

Summing all systematic errors in quadrature, we find 0.03 for both S and C as shown in tab. 8.41.

Table 8.41: Estimates of systematic errors.

Source of error	$\sigma(S)$	$\sigma(C)$
PDF Shapes	0.017	0.011
$B\overline{B}$ Background	0.018	0.013
CP content in $B\overline{B}$ Background	0.001	0.004
Breco signal shape	0.004	0.012
SVT alignment	0.001	0.001
Beam position/size	0.001	0.001
Tag-side interference	0.002	0.014
Total	0.025	0.025

8.11 Results

Results of ML fits for the 5 $B^0 \to \eta' K^0_S$ and the $B^0 \to \eta' K^0_L$ sub-decays are shown in tab. 8.42. We give the number of events to fit, the signal and $B\overline{B}$ yield, the number of free parameters in the fit, the correlation between S and C found in the fit, the dilution multiplicative bias correction for S due to $B\overline{B}$, and the parameters S and C. The same results for charged modes sub-decays are shown in tab. 8.43.

Incosistency of our result for S with CP conservation ($S = 0$) has a significance of 5.6 standard deviations (only statistical error contribution). Our result for the direct-CP violation parameter C is 2.2 standard deviations from zero (only statistical error contribution). The statistical significance is taken as the square root of

$$-2 \ln \frac{\mathcal{L}(x = 0)}{\mathcal{L}_{\max}}, \tag{8.9}$$

where x is the parameter for which we calculate the statistical significance (in our case is S or C), $\mathcal{L}(x = 0)$ is the likelihood function obtained fitting with $x = 0$, and $\mathcal{L}_{\max}$ is the likelihood function obtained when x is floating in the fit.

Considering statistical and systematic errors, incosistency of our result for S with CP conservation ($S = 0$) has a significance of 5.5 standard deviations. This represents the observation of mixing-induced CP in the rare decay mode $B^0 \to \eta' K^0$. For the direct-CP violation parameter C is 2.1 standard deviations from zero (statistical and systematics included). To include the systematics in the statistical significance calculation, we convolute the systematic error to the statistical $\mathcal{L}$, using a Gaussian approximation. In particular using the coefficient

$$f = \left(\frac{x_{\text{fitted}}}{\sigma_x^{\text{sys}}} \right)^2, \tag{8.10}$$

where x_{fitted} is the value of x obtained when it is floating in the fit and σ_x^{sys} is its systematic error, we correct the eq. 8.9 to include the systematics:

$$\frac{-2 \ln[\mathcal{L}(x = 0)/\mathcal{L}_{\max}]}{-2 \ln[\mathcal{L}(x = 0)/\mathcal{L}_{\max}] + f} f. \tag{8.11}$$

The statistical significance with systematics included is the root square of the eq. 8.11.

We measure a correlation of 3.2% between S and C in the fit.

Essentially in the fit for each mode we have as free parameters: S, C, signal yield,

$B\overline{B}$ background yield, continuum background yield and 5 fractions, background Δt and ΔE PDF parameters. Background $m_{\rm ES}$ and $\mathcal{F}$ PDF parameters for K^0_S modes are fixed in the fit for each single mode to the values found in the joint fit. When we combine different sub-decays, we have in common S, C, background $m_{\rm ES}$ and $\mathcal{F}$ PDF parameters for K^0_S modes. So, in the all sub-decays TD combined fit we have 93 free parameters: S, C, signal yields (6), $B\overline{B}$ background yield (2), continuum background yields (6) and fractions (30), background PDF parameters (47). For all fit we run HESSE and we check that its status is OK after fitting.

8.11.1 Projections

We draw the $m_{\rm ES}$, ΔE, and Δt projection plots for our decays. To reduce the contribution of background, we make a cut on the quantity:

$$R = \frac{P_{sig}}{P_{sig} + P_{bkg}} \tag{8.12}$$

where P_{sig} and P_{bkg} are the probability for the event to be signal or background, respectively. These probabilities are calculated from PDFs, excluding in the computation the variable being plotted. The projections of $m_{\rm ES}$ and ΔE are shown in fig. 8.8 for K^0_S and charged modes and fig. 8.9 for K^0_L mode. The projections of Δt and the raw asymmetries for K^0_S and K^0_L modes are shown in fig. 8.10. Fit curves shown are not a fit to the data in the histogram but the projection of the overall fit scaled to take into account the effect of the cut on R.

Quantity	$\eta'_{\eta(\gamma\gamma)\pi\pi}K^0_{S+-}$	$\eta'_{\rho\gamma}K^0_{S+-}$	$\eta'_{\eta(3\pi)\pi\pi}K^0_{S+-}$	$\eta'_{\eta\pi\pi}K^0_{S00}$	$\eta'_{\rho\gamma}K^0_{S00}$	$\eta'_{\eta\pi\pi}K^0_L$
Events into fit	664	11943	177	490	13915	4199
Signal yield	224 ± 16	566 ± 30	73 ± 9	52 ± 9	137 ± 24	206 ± 24
$B\overline{B}$ yield	–	335 ± 39	–	–	156 ± 39	–
# Free parameters	16	17	14	16	17	19
$S-C$ correlation (%)	11.8	3.8	-3.9	-13.9	-12.7	4.5
S correction	–	1.03 ± 0.01	–	–	1.03 ± 0.03	1.03 ± 0.03
S	0.61 ± 0.23	0.56 ± 0.14	0.89 ± 0.35	0.84 ± 0.42	0.56 ± 0.41	0.32 ± 0.28
C	-0.26 ± 0.14	-0.24 ± 0.10	0.14 ± 0.25	-0.26 ± 0.36	0.15 ± 0.27	0.08 ± 0.23
TD Combined fit:						
Signal yield	224 ± 16	565 ± 30	73 ± 9	52 ± 9	132 ± 24	
$B\overline{B}$ yield	–	335 ± 41	–	–	160 ± 41	
# Free parameters			76			
$S-C$ correlation (%)			3.4			
S			0.62 ± 0.11			
C			-0.18 ± 0.07			
TD all modes Combined:						
Signal yield	224 ± 16	566 ± 30	73 ± 9	52 ± 9	133 ± 24	204 ± 24
$B\overline{B}$ yield	–	334 ± 41	–	–	159 ± 41	–
# Free parameters			93			
$S-C$ correlation (%)			3.2			
S			$0.58 \pm 0.10 \pm 0.03$			
C			$-0.16 \pm 0.07 \pm 0.03$			

Table 8.42: Summary of ML fit results for all the neutral decay modes.

Quantity	$\eta'_{\eta(\gamma\gamma)\pi\pi}K^{\pm}$	$\eta'_{\rho\gamma}K^{\pm}$	$\eta'_{\eta(3\pi)\pi\pi}K^{\pm}$
Events into fit	1987	47942	581
Signal yield	804 ± 30	1826 ± 54	227 ± 16
$B\overline{B}$ yield	–	978 ± 68	–
# Free parameters	16	17	16
S	-0.06 ± 0.10	-0.07 ± 0.07	-0.17 ± 0.19
C	0.05 ± 0.07	0.04 ± 0.06	-0.15 ± 0.14
TD Combined fit:			
Signal yield	804 ± 30	1826 ± 54	228 ± 16
$B\overline{B}$ yield	–	978 ± 73	–
# Free parameters		49	
S		-0.08 ± 0.06	
C		0.03 ± 0.04	

Table 8.43: Summary of ML fit results for all the charged decay modes.

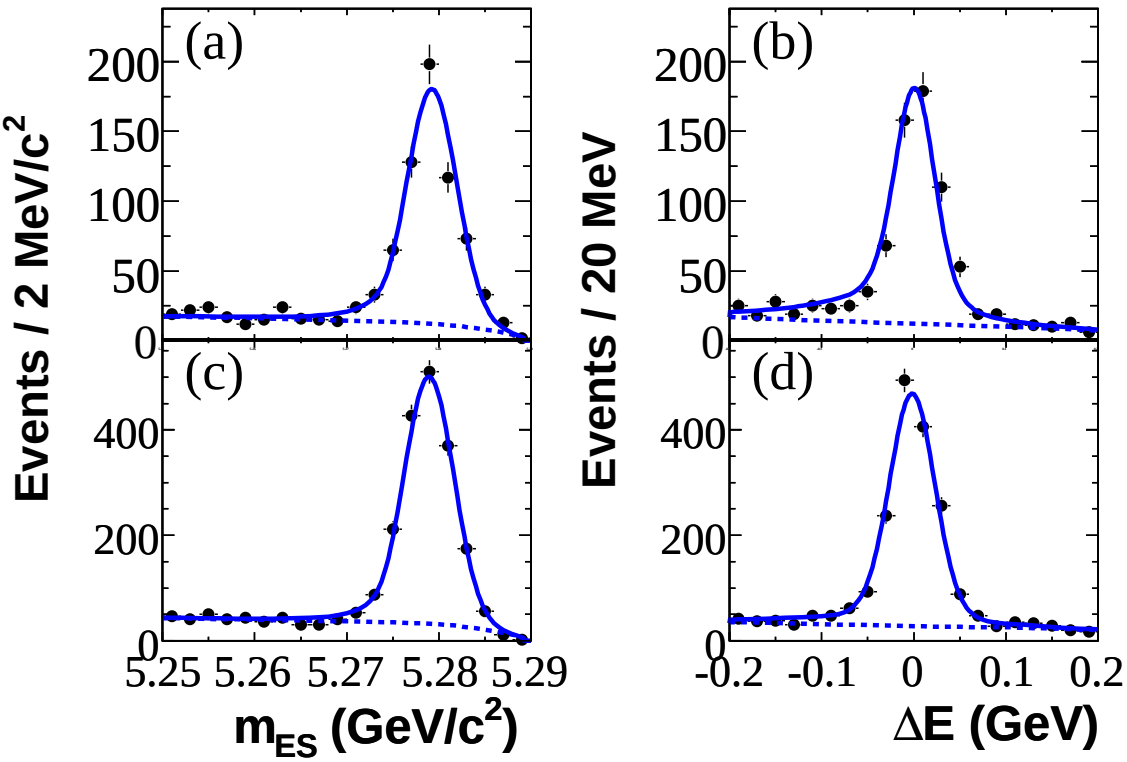

Figure 8.8: Projections on $m_{\rm ES}$ (left) and ΔE (right) in the dacays: (a, b) $\eta' K^0_S$, (c, d) $\eta' K^+$. We consider all sub-decays. Points with error bars (statistical only) represent the data, the solid line the full fit function, and the dashed line its background component.

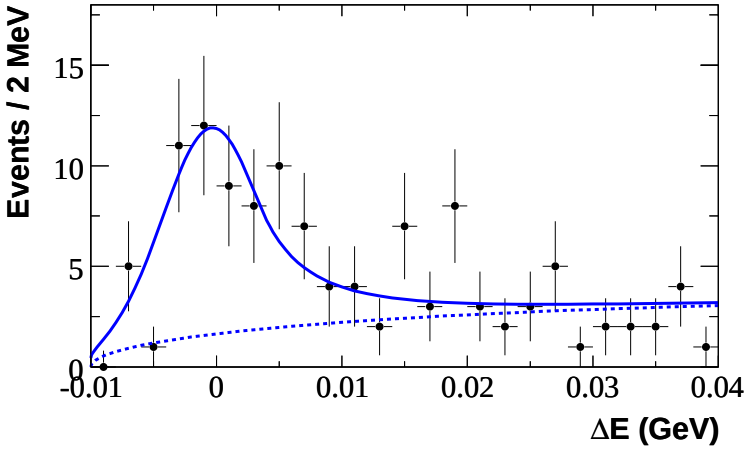

Figure 8.9: Projections on ΔE for $\eta' K^0_L$ mode. Points with error bars (statistical only) represent the data, the solid line the full fit function, and the dashed line its background component.

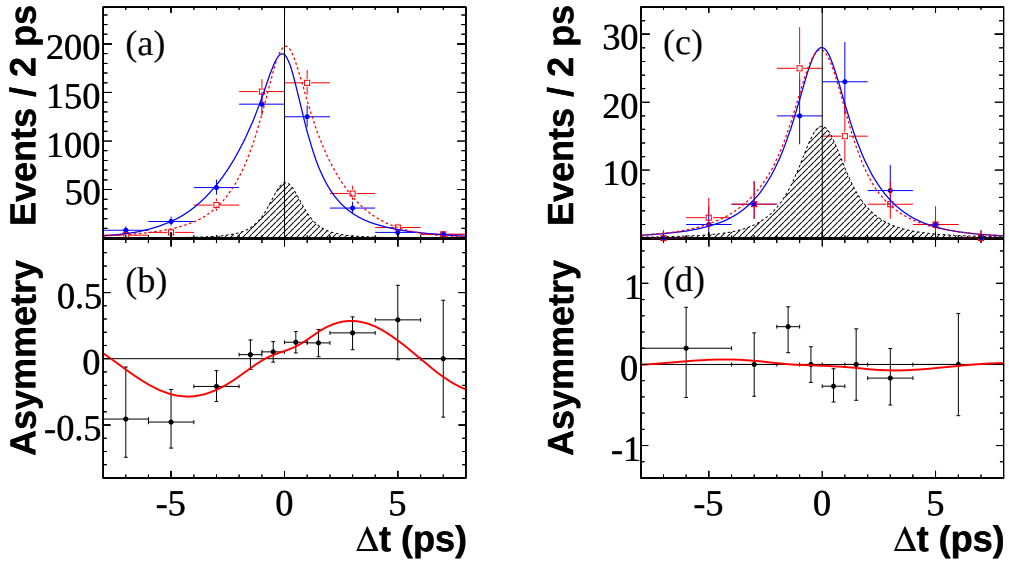

Figure 8.10: Projections onto Δt for (a) $\eta' K^0_S$ and (c) $\eta' K^0_L$ of the data (points with error bars for B^0 (blue solid circles) and $\overline{B}^0$ (red empty rectangles) tags), fit function (blue solid and red dashed lines for B^0 and $\overline{B}^0$ tagged events, respectively), and background function (black shaded regions), and the asymmetry between B^0 and $\overline{B}^0$ tags for (b) $\eta' K^0_S$ and (d) $\eta' K^0_L$.

8.11.2 Event Display

Using the *BABAR* Event Display, we draw one event of $\eta'_{\eta(\gamma\gamma)\pi\pi}K^0_{S+-}$. We require a tight cut on the probability ratio eq. 8.12 in order to extract a signal event in data. We show the event display in fig. 8.11. The tracks and clusters belonging to our signal event are shown in fig. 8.12.

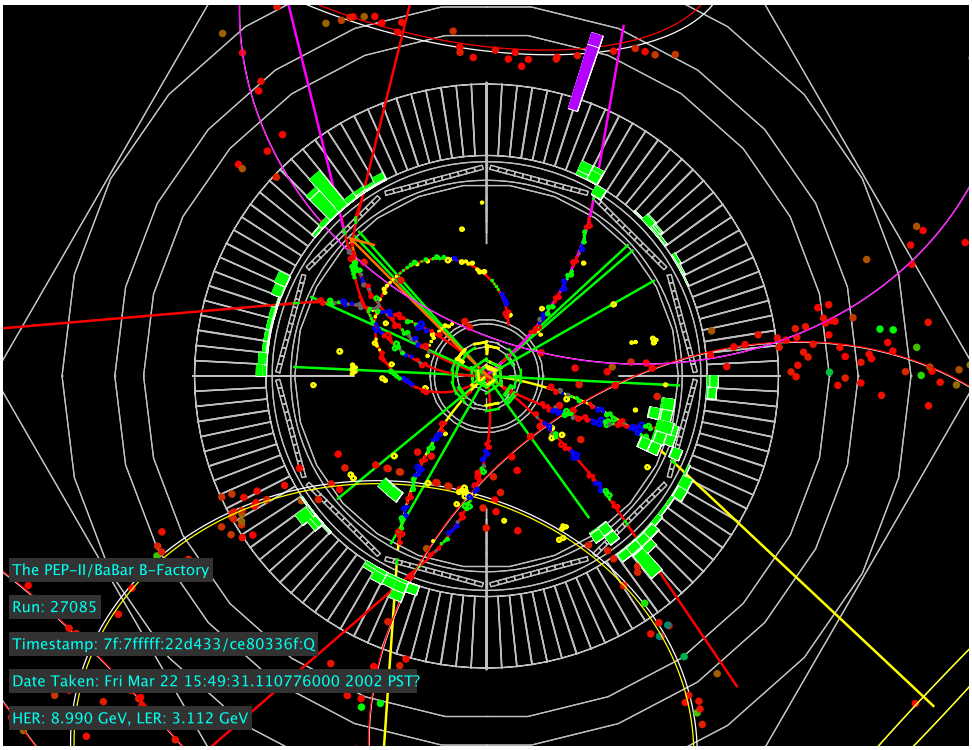

Figure 8.11: Event display of one events of $\eta'_{\eta(\gamma\gamma)\pi\pi}K^0_{S+-}$ data. We show all reconstructed tracks (magenta, red, and yellow lines), EMC clusters and the reconstructed photons (green lines).

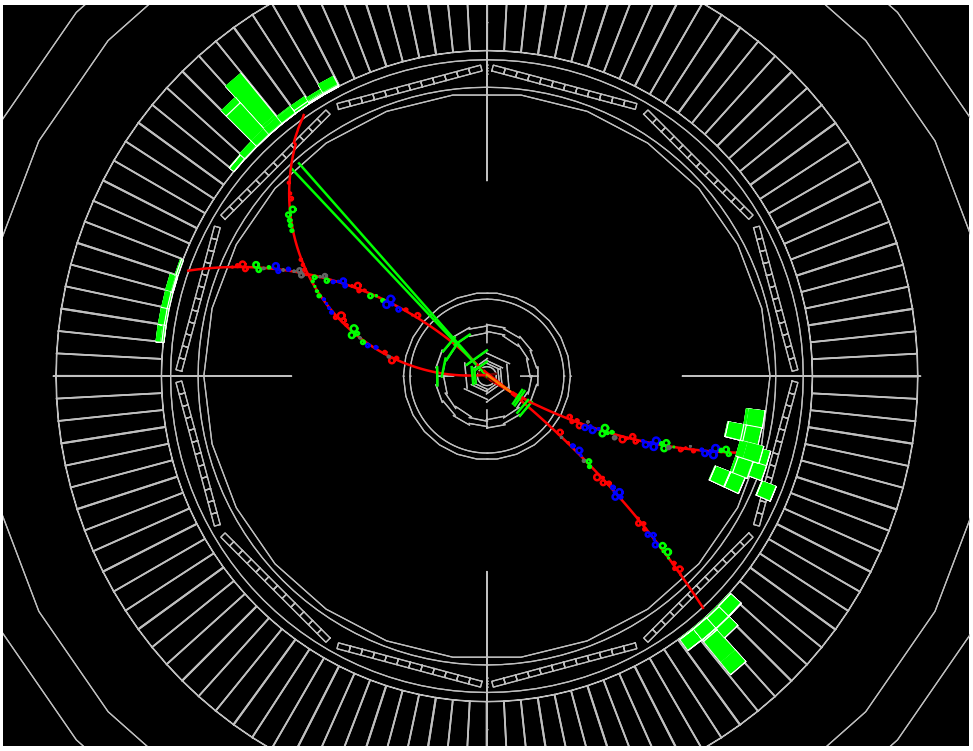

Figure 8.12: Event display of one events of $\eta'_{\eta(\gamma\gamma)\pi\pi} K^0_{S+-}$ data. We show only the tracks, photons and clusters belonging to our event. We distinguish on the left side the η' and on the right the K^0_{S+-}.

8.12 Comparison with previous results

We compare our previous published results, $S = 0.30 \pm 0.14$ [111] (obtained with data reconstructed with release 14, R14) with the new one $S = 0.58 \pm 0.10$ (R18). You should consider that in R14 we didn't use the K^0_L mode.

In tab. 8.44 we summarize the numbers of events common to both processings, and found to differ between both processings. Because in the R18 analysis we use only tagged events, this comparison refers only to tagged events. Table 8.45 reports the mean and RMS of the shifts observed for the fit variables for events common to both reprocessing cycles. Using these shifts for the fitting variables, we perform 500 toy-experiments where we generate and fit events using R18 PDF, we smear these events using the means and RMSs of the shifts and then we fit these new events with R14 PDFs. In this way we can compare results from the both reprocessing. This comparison is shown in fig. 8.13 for $\eta'_{\rho\gamma}K^0_{S+-}$ and fig. 8.14 for $\eta'_{\eta(\gamma\gamma)\pi\pi}K^0_{S+-}$. Of course this test assume that all events are common, whereas in reality the overlap fraction is less than unity.

Mode	Overlap	in R14 only (%)	in R18 only (%)
$\eta'_{\eta(\gamma\gamma)\pi\pi}K^0_{S+-}$	272	113 (29.4)	163 (37.5)
$\eta'_{\rho\gamma}K^0_{S+-}$	4124	2027 (33.0)	3438 (45.5)
$\eta'_{\eta(3\pi)\pi\pi}K^0_{S+-}$	60	46 (43.4)	63 (51.2)
$\eta'_{\eta\pi\pi}K^0_{S00}$	138	138 (50.0)	137 (49.6)
$\eta'_{\rho\gamma}K^0_{S00}$	3654	3494 (48.9)	4279 (53.9)

Table 8.44: R14-R18 overlap event comparison.

We fit the events for each mode for the Run 1-4 dataset, both R14 and R18 dataset, where R14 results are taken from the previous analysis. The results are shown in tab. 8.46. From th previous studies we can say that the differences between the two reprocessing releases are due to statistical fluctuations and different analysis approach.

Then we fit the common events for R14 analysis and R18 analysis and the results are summarized in tab. 8.47. We find that fitting on the common events $S = 0.273 \pm 0.153$ in R14 and $S = 0.356 \pm 0.155$ in R18. The common sample contains 511 signal events in R18. From tab. 8.42, we obtain that our full Run1-5 sample has an additional 741 signal events (unique to the reprocessing in Run1-4, added from Run5). Then, we calculate the probability to find $S = 0.58$ (our final result for Run1-5) or

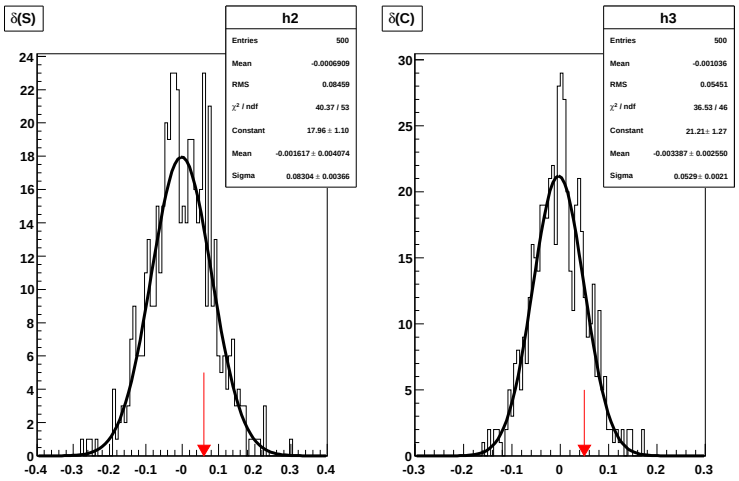

Figure 8.13: Distributions for $\eta'_{\rho\gamma} K^0_S$ mode of the shifts observed in S (left) and C (right) for 500 toy-experiments that have been smeared by the observed RMS for the R18 to R14 reprocessing. The arrows indicate the observed shifts in data. Note: these toys assume that all events are common, whereas in reality the overlap fraction is less than unity.

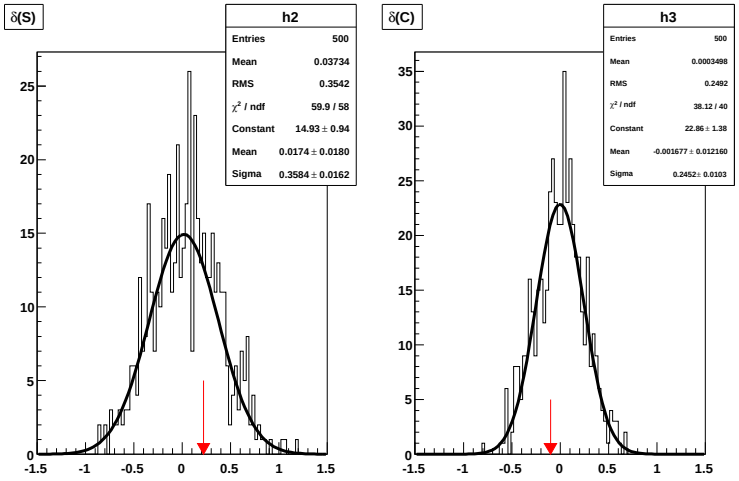

Figure 8.14: Distributions for $\eta'_{\eta\pi\pi} K^0_S$ mode of the shifts observed in S (left) and C (right) for 500 toy-experiments that have been smeared by the observed RMS for the R18 to R14 reprocessing. The arrows indicate the observed shifts in data. Note: these toys assume that all events are common, whereas in reality the overlap fraction is less than unity.

greater. The method is described in BAD 1509, section 14.13. Essentially we consider a Gaussian distribution of values for S with a mean of 0.273 and sigma of 0.153 for the 511 common events, and another Gaussian with mean of the "true value" of S with a sigma of 0.129 (rescaling 0.155 to the different number of events) for the 741 additional events. We add the two Gaussians, weighted for the numbers of events 511 and 741, respectively, to have the total distribution. We use this distribution to perform 100000 toy-experiments and then we calculate the fraction of S values greater than 0.58. This is our probability (actually we can also directly integrate analytically the distribution). Performing toys in two cases, with a true value of $S = 0.7$ and $S = 0.61$, where the latter is the current world average for S in $\eta' K^0$, we obtain a probability of 49.0% and 35.5%, respectively. A probability of nearly 50% is clearly a reasonable result consistent with statistics.

		$m_{\rm ES}$ (MeV)	ΔE (MeV)	$\mathcal{F}$	Δt (ps)	$\sigma_{\Delta t}$ (ps)
$\eta'_{\eta(\gamma\gamma)\pi\pi}K^0_{S+-}$	shift	-0.457	-3.095	0.028	-0.006	-0.002
	RMS	2.087	28.211	0.221	0.662	0.094
$\eta'_{\rho\gamma}K^0_{S+-}$	shift	-0.631	-0.116	-0.000	-0.007	-0.004
	RMS	1.492	19.112	0.186	0.557	0.119
$\eta'_{\eta(3\pi)\pi\pi}K^0_{S+-}$	shift	-0.897	-5.565	0.156	0.292	-0.015
	RMS	2.936	37.126	0.261	1.425	0.150
$\eta'_{\eta\pi\pi}K^0_{S00}$	shift	-0.850	-0.564	0.050	-0.008	-0.041
	RMS	3.071	45.465	0.200	0.789	0.141
$\eta'_{\rho\gamma}K^0_{S00}$	shift	-0.613	4.958	0.003	0.019	-0.037
	RMS	3.482	56.476	0.221	0.915	0.162
$\eta'_{\eta\pi\pi}K^0_{L}$	shift	–	1.143	0.001	-0.042	-0.058
	RMS	–	8.199	0.120	1.541	0.204

Table 8.45: R18-R14 shift and RMS in the fit variable values for common events.

	R14	R18
$\eta'_{\eta(\gamma\gamma)\pi\pi}K^0_{S+-}$		
Signal Yield	188 ± 15	132 ± 12
S	0.01 ± 0.28	0.13 ± 0.31
C	-0.18 ± 0.18	-0.26 ± 0.19
$\eta'_{\rho\gamma}K^0_{S+-}$		
Signal Yield	430 ± 26	365 ± 24
S	0.44 ± 0.19	0.60 ± 0.17
C	-0.30 ± 0.13	-0.31 ± 0.13
$\eta'_{\eta(3\pi)\pi\pi}K^0_{S+-}$		
Signal Yield	54 ± 8	47 ± 7
S	0.79 ± 0.47	0.64 ± 0.46
C	0.11 ± 0.35	0.01 ± 0.34
$\eta'_{\eta\pi\pi}K^0_{S00}$		
Signal Yield	44 ± 9	34 ± 7
S	-0.04 ± 0.57	0.31 ± 0.63
C	-0.65 ± 0.42	-0.43 ± 0.44
$\eta'_{\rho\gamma}K^0_{S00}$		
Signal Yield	94 ± 23	77 ± 19
S	-0.45 ± 0.68	0.61 ± 0.57
C	0.41 ± 0.40	0.42 ± 0.35

Table 8.46: Comparison of the results (Run1-4) between release 14 data (second column) and release 18 data (third column). Note that in R14 analysis we use also untagged events in the fit, which are not used in R18 analysis.

Quantity	$\eta'_{\eta(\gamma\gamma)\pi\pi}K^0_{S+-}$	$\eta'_{\rho\gamma}K^0_{S+-}$	$\eta'_{\eta(3\pi)\pi\pi}K^0_{S+-}$	$\eta' \to \eta\pi^+\pi^-K^0_{S00}$	$\eta'_{\rho\gamma}K^0_{S00}$
R14					
Signal yield	104 ± 11	297 ± 21	30 ± 6	28 ± 6	70 ± 17
S	-0.26 ± 0.32	0.50 ± 0.19	0.73 ± 0.53	0.11 ± 0.66	-0.54 ± 0.58
C	-0.27 ± 0.21	-0.24 ± 0.13	0.10 ± 0.39	-0.30 ± 0.45	0.58 ± 0.36
TD Combined fit:					
Signal yield	104 ± 11	297 ± 21	30 ± 6	28 ± 7	64 ± 17
S			0.273 ± 0.153		
C			-0.175 ± 0.104		
R18					
Signal yield	106 ± 11	292 ± 21	30 ± 6	24 ± 6	72 ± 17
S	-0.26 ± 0.34	0.52 ± 0.19	0.66 ± 0.57	0.19 ± 0.66	0.20 ± 0.58
C	-0.33 ± 0.21	-0.28 ± 0.14	0.10 ± 0.38	-0.23 ± 0.49	0.60 ± 0.30
TD Combined fit:					
Signal yield	105 ± 11	289 ± 21	30 ± 6	24 ± 6	63 ± 16
S			0.356 ± 0.155		
C			-0.177 ± 0.105		

Table 8.47: Summary of ML fit results for the neutral decay modes fitting on R14-R18 overlap events for R14 analysis and R18 analysis.

8.13 Cross Checks

We report here on a few checks we have done on the correctness and performance of the fitting procedure.

8.13.1 Likelihood ratio

In Figure 8.15 we show the likelihood ratio $\mathcal{L}(Sg)/[\mathcal{L}(Sg)+\sum\mathcal{L}(Bg)]$ for all modes.

8.13.2 Fits with $C = 0$

We fit the data for full fit with all subdecays for neutral modes with the constraint of $C = 0$. The value of S is 0.58 ± 0.10.

8.13.3 Consistency of Run1-3, Run4 and Run5 results

We fit Run1-3, Run1-4, Run4, and Run5 data, separately, for all neutral modes simultaneous fit. The three samples are chosen in order to correspond almost to the same integrated luminosity. The results for S and C are shown in tab. 8.48.

Data sample	S	C
Run1-3	0.400 ± 0.177	-0.127 ± 0.119
Run1-4	0.490 ± 0.130	-0.170 ± 0.090
Run4	0.660 ± 0.186	-0.258 ± 0.136
Run5	0.683 ± 0.153	-0.149 ± 0.112
Run1-5	0.579 ± 0.100	-0.158 ± 0.071

Table 8.48: ML fit results for all neutral modes simultaneous fit when we split data in different samples. The last row refers to the full sample.

We can compare these results with the previous ones obtained using R14 processing [110]:

$$\begin{aligned} S &= 0.36 \pm 0.13 \\ C &= -0.16 \pm 0.09 \end{aligned}$$

We see a movement in the S central value of about 1 σ due to the new processing of the data. Adding the Run5 data we see a further movement of the S central value and it becomes $S = 0.58 \pm 0.10$.

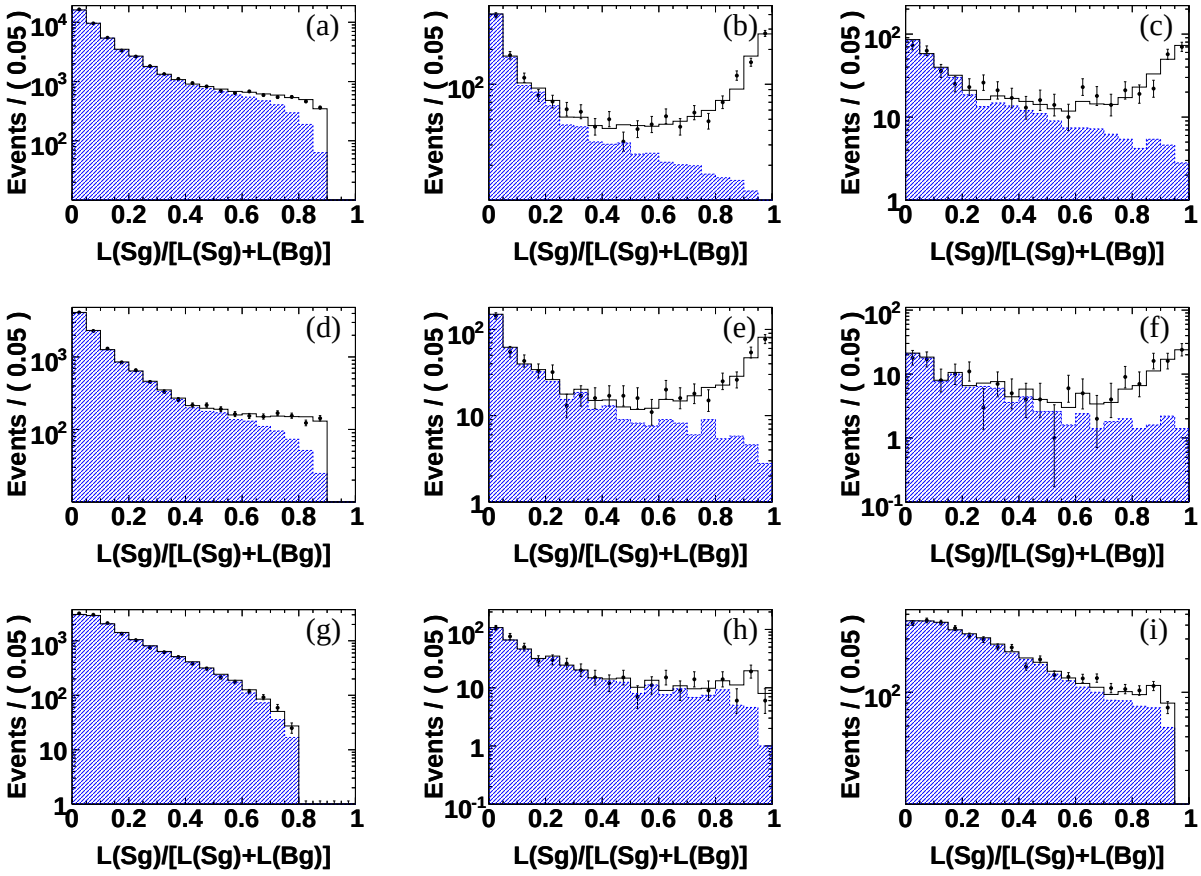

Figure 8.15: The likelihood ratio L(Sg)/[L(Sg)+ L(Bg)] for the all sub-decay modes: (a) $\eta'_{\rho\gamma}K^{\pm}$, (b) $\eta'_{\eta(\gamma\gamma)\pi\pi}K^{\pm}$, (c) $\eta'_{\eta(3\pi)\pi\pi}K^{\pm}$, (d) $\eta'_{\rho\gamma}K^0_{S+-}$, (e) $\eta'_{\eta(\gamma\gamma)\pi\pi}K^0_{S+-}$, (f) $\eta'_{\eta(3\pi)\pi\pi}K^0_{S+-}$, (g) $\eta'_{\rho\gamma}K^0_{S00}$, (h) $\eta'_{\eta\pi\pi}K^0_{S00}$, (i) $\eta'_{\eta\pi\pi}K^0_L$. The on-resonance data are shown as points with error bars; the sum of all simulated background samples is shown by the shaded (dashed-line) histograms; and the sum of these backgrounds plus the signal from the PDF model are given by the open (solid-line) histograms.

For only modes with K^0_S, we find for R18 Run1-4:

$$\begin{aligned} S &= 0.50 \pm 0.14 \\ C &= -0.22 \pm 0.10 \end{aligned}$$

We can compare these results with the previous published ones obtained using R14 processing [111]:

$$\begin{aligned} S &= 0.30 \pm 0.14 \\ C &= -0.21 \pm 0.10 \end{aligned}$$

We see a movement in the S central value of 0.20 due to the new processing of the data.

Conclusions

In this thesis work we have measured the following branching fractions or upper limits at 90% of confidence level, in the case where we do not see significant signal events, for B decays (in units of 10^{-6}):

$$\begin{aligned}
\mathcal{B}(B^0 \to \eta'\eta' K^0) &< 31 \quad [114] \\
\mathcal{B}(B^\pm \to \eta'\eta' K^\pm) &< 25 \quad [114] \\
\mathcal{B}(B^0 \to \eta' K^0) &= 68.9 \pm 2.0 \pm 3.2 \quad [111] \\
\mathcal{B}(B^\pm \to \eta' K^\pm) &= 67.4 \pm 3.3 \pm 3.2 \quad [111] \\
\mathcal{B}(B^0 \to \eta K^0 \gamma) &= 11.3^{+2.8}_{-2.6} \pm 0.6 \quad [115] \\
\mathcal{B}(B^\pm \to \eta K^\pm \gamma) &= 10.0 \pm 1.3 \pm 0.5 \quad [115] \\
\mathcal{B}(B^0 \to \eta' K^0 \gamma) &< 6.6 \quad [115] \\
\mathcal{B}(B^\pm \to \eta' K^\pm \gamma) &< 4.2 \quad [115] \\
\mathcal{B}(B^0 \to \eta K^0) &< 2.9 \quad [107] \\
\mathcal{B}(B^0 \to \eta\eta) &< 1.8 \quad [107] \\
\mathcal{B}(B^0 \to \eta\phi) &< 0.55 \quad [107] \\
\mathcal{B}(B^0 \to \eta'\phi) &< 0.98 \quad [107]
\end{aligned}$$

We have also measured the direct CP asymmetry for the charged modes where we see significan signal:

$$\begin{aligned}
\mathcal{A}_{ch}(B^\pm \to \eta' K^\pm) &= 0.033 \pm 0.028 \pm 0.005 \quad [111] \\
\mathcal{A}_{ch}(B^\pm \eta K^\pm \gamma) &= -0.086 \pm 0.120 \pm 0.010 \quad [115]
\end{aligned}$$

which are consistent with zero value.

All these results are published (see references) and they represent substantial improvements on the previous ones [91, 92, 93]. For the modes $\eta'\eta' K$ and $\eta' K\gamma$ we have the first measurements in the world.

For time-dependent analysis, we have reconstructed 1252 ± 50 flavor-tagged $B^0 \to \eta' K^0$ events. We use these events to measure the time-dependent asymmetry parameters S and C. We find $S = 0.58 \pm 0.10 \pm 0.03$, and $C = -0.16 \pm 0.07 \pm 0.03$. We measure a correlation of 3.2% between S and C in the fit. A non-zero value of C would represent a directly CP non-conserving component in $B^0 \to \eta' K^0$, while S would be equal to $\sin 2\beta$ measured in $B^0 \to J/\psi K^0_S$ [36], a mixing-decay interference effect, provided the decay is dominated by amplitudes of a single weak phase. The new measured value of S can be considered in agreement with the expectations of the "Standard Model", inside the experimental and theoretical uncertainties. Incosistency of our result for S with CP conservation ($S = 0$) has a significance of 5.5 standard deviations (statistical and systematics included). This represents the observation of mixing-induced CP in the rare decay mode $B^0 \to \eta' K^0$, which is the first observation of CP violation in a $b \to s$ mode. Our result for the direct-CP violation parameter C is 2.1 standard deviations from zero (statistical and systematics included). These results have been published on PRL [116].

Appendix A

PDF libraries for branching fraction and charge asymmetry measurements

We show for each decay modes the signal, self-crossfeed signal, continuum background and $B\overline{B}$ background PDFs used in ML fits. We show also tables of the correlations between fit discriminating variables and the values of the background PDF parameters which are floating in the fits. Signal PDFs are determined from MC signal events. For background continuum PDFs we have used on-peak sidebands. For $B\overline{B}$ background PDFs we have used MC events.

A.1 $B^0 \to \eta'_{\eta\pi\pi}\eta'_{\eta\pi\pi}K^0_S$

	$m_{\rm ES}$	ΔE	η' (1) mass	η' (2) mass	$\mathcal{F}$
$m_{\rm ES}$	1.000				
ΔE	0.040	1.000			
η' (1) mass	0.005	-0.003	1.000		
η' (2) mass	0.018	0.017	0.019	1.000	
$\mathcal{F}$	0.015	-0.001	0.011	0.015	1.000

Table A.1: Correlation matrix for signal MCtruth+PP events.

	$m_{\rm ES}$	ΔE	η' (1) mass	η' (2) mass	$\mathcal{F}$
$m_{\rm ES}$	1.000				
ΔE	0.064	1.000			
η' (1) mass	0.026	-0.005	1.000		
η' (2) mass	-0.028	0.002	-0.019	1.000	
$\mathcal{F}$	-0.021	-0.007	-0.029	0.010	1.000

Table A.2: Correlation matrix for signal MC SCF events.

	$m_{\rm ES}$	ΔE	η' (1) mass	η' (2) mass	$\mathcal{F}$
$m_{\rm ES}$	1.000				
ΔE	-0.003	1.000			
η' (1) mass	-0.021	-0.071	1.000		
η' (2) mass	0.079	-0.046	-0.014	1.000	
$\mathcal{F}$	0.078	0.016	-0.021	0.087	1.000

Table A.3: Correlation matrix in on-peak side band data.

```
deltaE_c1_bg_EPP_float = -0.412 +/- 0.073
mES_xi_bg_EPP_float = -0.646 +/- 1.374
fisher_Mu1_bg_EPP_float = 0.198 +/- 0.084
fisher_Sigma1_bg_EPP_float = 0.548 +/- 0.053
fisher_Sigma2_bg_EPP_float = 0.607 +/- 0.055
etapMass0_Frac_bg_EPP_float = 0.019 +/- 0.030
etapMass0_c1_bg_EPP_float = 0.461 +/- 0.073
etapMass1_c1_bg_EPP_float = 0.373 +/- 0.070
```

Final values for the parameters which were allowed to float in the fit.

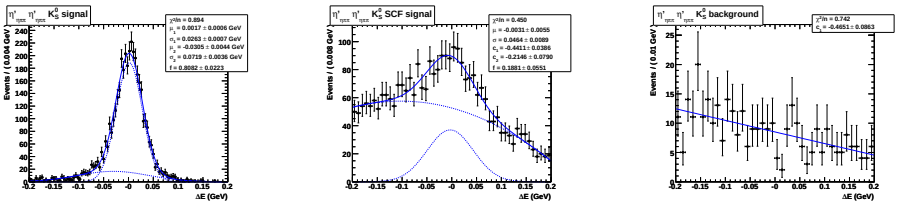

Figure A.1: ΔE PDFs: signal, double Gaussian; signal SCF, Gaussian plus Chebyshev second order polynomial; continuum background: Chebyshev first order polynomial.

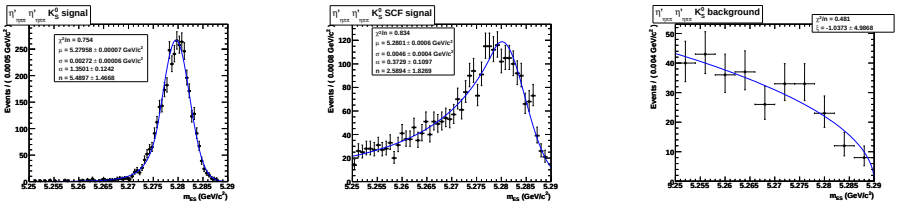

Figure A.2: $m_{\rm ES}$ PDFs: signal, Crystal Ball; signal SCF, Crystal Ball; continuum background: Argus function.

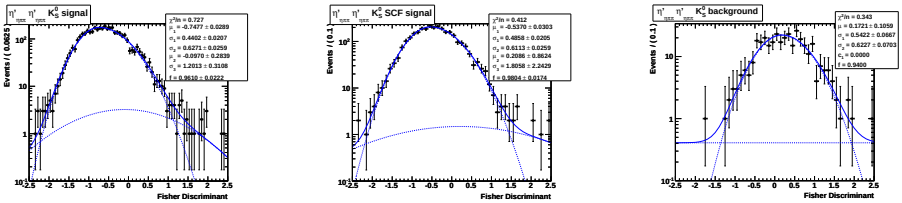

Figure A.3: $\mathcal{F}$ PDFs: signal, Gaussian plus asymmetric Gaussian; signal SCF, Gaussian plus asymmetric Gaussian; continuum background: asymmetric Gaussian plus Chebyshev first order polynomial.

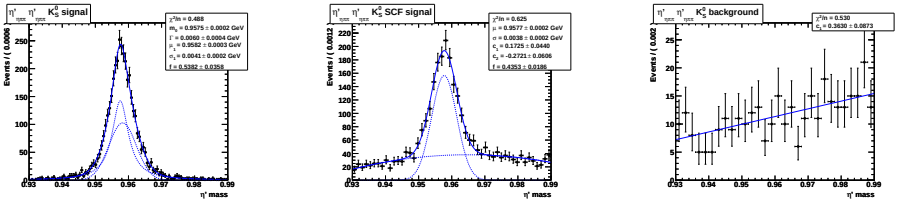

Figure A.4: η' (1) mass PDFs: signal, Breit-Wigner plus Gaussian; signal SCF, Gaussian plus Chebyshev second order polynomial; continuum background, Chebyshev first order polynomial.

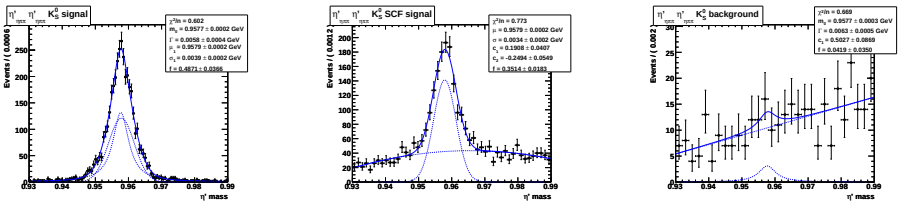

Figure A.5: η' (2) mass PDFs: Breit-Wigner plus Gaussian; signal SCF, Gaussian plus Chebyshev second order polynomial; continuum background: MC Breit-Wigner plus Chebyshev first order polynomial.

A.2 $B^0 \to \eta'_{\eta\pi\pi}\eta'_{\rho\gamma}K^0_S$

	$m_{\rm ES}$	ΔE	η mass	$\eta'_{\eta\pi\pi}$ mass	$\mathcal{F}$	$\mathcal{H}_\rho$
$m_{\rm ES}$	1.000					
ΔE	0.019	1.000				
η mass	-0.004	0.057	1.000			
$\eta'_{\eta\pi\pi}$ mass	-0.025	0.108	-0.005	1.000		
$\mathcal{F}$	0.008	-0.009	0.010	0.001	1.000	
$\mathcal{H}_\rho$	0.003	-0.006	0.021	0.028	-0.017	1.000

Table A.4: Correlation matrix for signal MCtruth+PP events.

	$m_{\rm ES}$	ΔE	η mass	$\eta'_{\eta\pi\pi}$ mass	$\mathcal{F}$	$\mathcal{H}_\rho$
$m_{\rm ES}$	1.000					
ΔE	0.041	1.000				
η mass	0.043	0.010	1.000			
$\eta'_{\eta\pi\pi}$ mass	-0.010	0.010	-0.040	1.000		
$\mathcal{F}$	$-0.0.13$	-0.006	0.013	-0.019	1.000	
$\mathcal{H}_\rho$	-0.003	0.0.13	0.008	-0.003	0.024	1.000

Table A.5: Correlation matrix for signal MC SCF events.

	$m_{\rm ES}$	ΔE	η mass	$\eta'_{\eta\pi\pi}$ mass	$\mathcal{F}$	$\mathcal{H}_\rho$
$m_{\rm ES}$	1.000					
ΔE	0.013	1.000				
η mass	0.001	0.019	1.000			
$\eta'_{\eta\pi\pi}$ mass	0.000	-0.011	-0.009	1.000		
$\mathcal{F}$	0.021	0.021	-0.005	-0.011	1.000	
$\mathcal{H}_\rho$	-0.021	0.010	-0.023	$-0.0.13$	0.015	1.000

Table A.6: Correlation matrix in on-peak side band data.

	$m_{\rm ES}$	ΔE	η mass	$\eta'_{\eta\pi\pi}$ mass	$\mathcal{F}$	$\mathcal{H}_\rho$
$m_{\rm ES}$	1.000					
ΔE	0.0.13	1.000				
η mass	0.027	0.005	1.000			
$\eta'_{\eta\pi\pi}$ mass	0.003	0.006	-0.013	1.000		
$\mathcal{F}$	$-0.0.13$	-0.009	-0.006	0.024	1.000	
$\mathcal{H}_\rho$	0.009	0.029	0.021	0.010	0.0.13	1.000

Table A.7: Correlation matrix in MC generic $B^0\overline{B}^0$.

	$m_{\rm ES}$	ΔE	η mass	$\eta'_{\eta\pi\pi}$ mass	$\mathcal{F}$	$\mathcal{H}_\rho$
$m_{\rm ES}$	1.000					
ΔE	0.001	1.000				
η mass	0.023	0.025	1.000			
$\eta'_{\eta\pi\pi}$ mass	0.015	$-0.0.13$	0.0.13	1.000		
$\mathcal{F}$	0.001	-0.023	-0.028	$-0.0.13$	1.000	
$\mathcal{H}_\rho$	0.036	0.018	0.0.13	0.000	-0.020	1.000

Table A.8: Correlation matrix in MC generic B^+B^-.

```
deltaE_c1_bg_RG_float = -0.325 +/- 0.026
deltaE_c2_bg_RG_float = 0.073 +/- 0.020
mES_xi_bg_RG_float = -11.640 +/- 3.145
fisher_Mu1_bg_RG_float = 0.277 +/- 0.030
fisher_Sigma1_bg_RG_float = 0.597 +/- 0.015
fisher_Sigma2_bg_RG_float = 0.643 +/- 0.015
fisher_Frac_bg_RG_float = 0.992 +/- 0.003
etaMass_Frac_bg_RG_float = 0.108 +/- 0.0.13
etaMass_c0_bg_RG_float = -0.238 +/- 0.023
etapMass0_Frac_bg_RG_float = 0.027 +/- 0.009
etapMass0_c0_bg_RG_float = 0.430 +/- 0.020
helicity1_c1_bg_RG_float = 0.005 +/- 0.021
```

Final values for the parameters which were allowed to float in the fit.

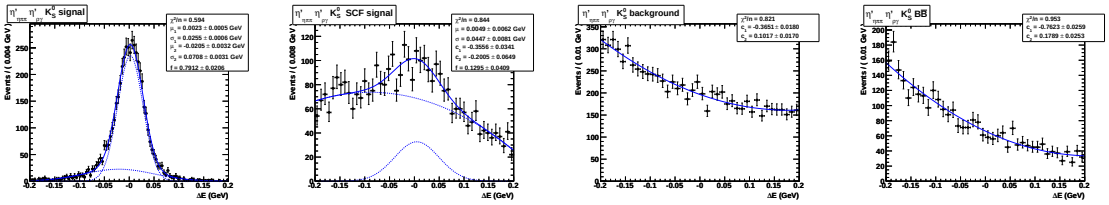

Figure A.6: ΔE PDFs: signal, double Gaussian; signal SCF, Gaussian plus Chebyshev second order polynomial; continuum background, Chebyshev second order polynomial; $B\overline{B}$ background, Chebyshev second order polynomial.

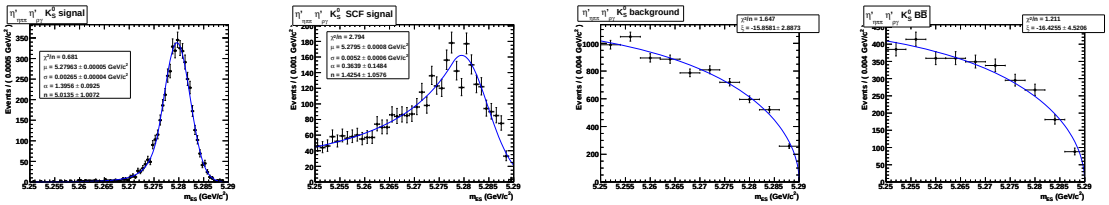

Figure A.7: $m_{\rm ES}$ PDFs: signal, Crystal Ball; signal SCF, Crystal Ball; continuum background, Argus function; $B\overline{B}$ background, Argus function.

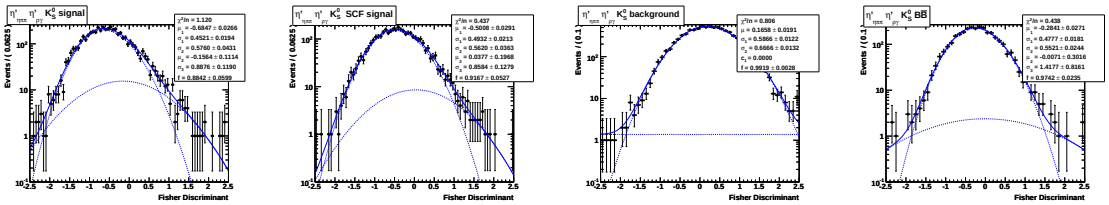

Figure A.8: $\mathcal{F}$ PDFs: signal, Gaussian plus asymmetric Gaussian; signal SCF, Gaussian plus asymmetric Gaussian; continuum background, asymmetric Gaussian plus Chebyshev first order polynomial; $B\overline{B}$ background, Gaussian plus asymmetric Gaussian.

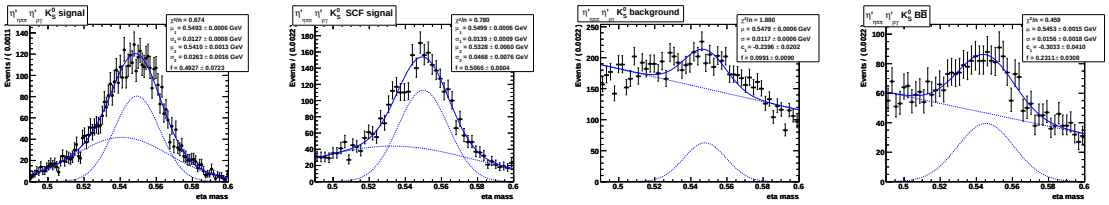

Figure A.9: η mass PDFs: signal, double Gaussian; signal SCF, double Gaussian; continuum background, MC Gaussian plus Chebyshev first order polynomial; $B\overline{B}$ background, Gaussian plus Chebyshev first order polynomial.

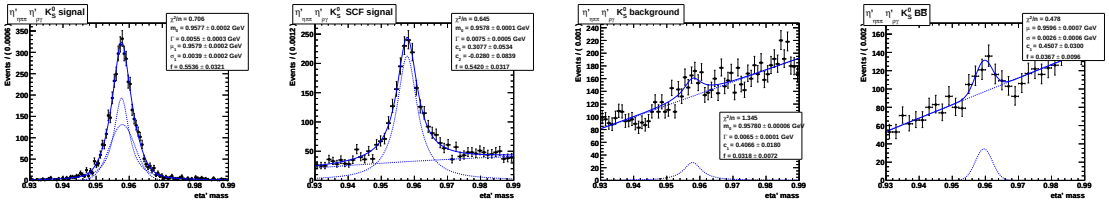

Figure A.10: $\eta'_{\eta\pi\pi}$ mass PDFs: signal, Breit-Wigner plus Gaussian; signal SCF, Breit-Wigner plus Chebyshev second order polynomial; continuum background, MC Breit-Wigner plus Chebyshev first order polynomial; $B\overline{B}$ background, Gaussian plus Chebyshev first order polynomial.

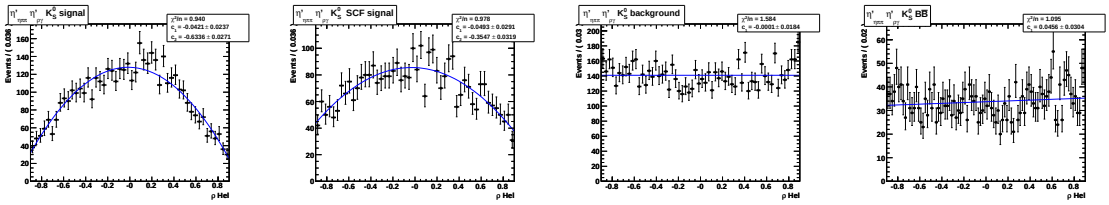

Figure A.11: $\mathcal{H}_\rho$ PDFs: Chebyshev second order polynomial; signal SCF, Chebyshev second order polynomial; continuum background, Chebyshev first order polynomial; $B\overline{B}$ background, Chebyshev first order polynomial.

A.3 $B^{\pm} \to \eta'_{\eta\pi\pi}\eta'_{\eta\pi\pi}K^{\pm}$

	$m_{\rm ES}$	ΔE	η' (1) mass	η' (2) mass	$\mathcal{F}$
$m_{\rm ES}$	1.000				
ΔE	0.018	1.000			
η' (1) mass	0.018	0.037	1.000		
η' (2) mass	-0.031	0.048	-0.015	1.000	
$\mathcal{F}$	-0.019	0.008	-0.015	0.000	1.000

Table A.9: Correlation matrix for signal MCtruth+PP events.

	$m_{\rm ES}$	ΔE	η' (1) mass	η' (2) mass	$\mathcal{F}$
$m_{\rm ES}$	1.000				
ΔE	0.019	1.000			
η' (1) mass	0.041	0.013	1.000		
η' (2) mass	-0.059	0.034	0.025	1.000	
$\mathcal{F}$	-0.054	0.020	-0.013	-0.006	1.000

Table A.10: Correlation matrix for signal MC SCF events.

	$m_{\rm ES}$	ΔE	η' (1) mass	η' (2) mass	$\mathcal{F}$
$m_{\rm ES}$	1.000				
ΔE	0.024	1.000			
η' (1) mass	0.000	-0.010	1.000		
η' (2) mass	-0.007	0.061	0.060	1.000	
$\mathcal{F}$	0.0.13	0.029	-0.004	0.033	1.000

Table A.11: Correlation matrix in data on-peak side band data.

```
deltaE_c1_bg_EPPK_float = -0.403 +/- 0.044
mES_xi_bg_EPPK_float = -7.823 +/- 6.879
fisher_Mu1_bg_EPPK_float = 0.134 +/- 0.045
fisher_Sigma1_bg_EPPK_float = 0.541 +/- 0.030
fisher_Sigma2_bg_EPPK_float = 0.688 +/- 0.031
etapMass0_Frac_bg_EPPK_float = 0.004 +/- 0.015
etapMass0_c1_bg_EPPK_float = 0.488 +/- 0.044
etapMass1_Frac_bg_EPPK_float = 0.049 +/- 0.014
etapMass1_c1_bg_EPPK_float = 0.497 +/- 0.043
```

Final values for the parameters which were allowed to float in the fit.

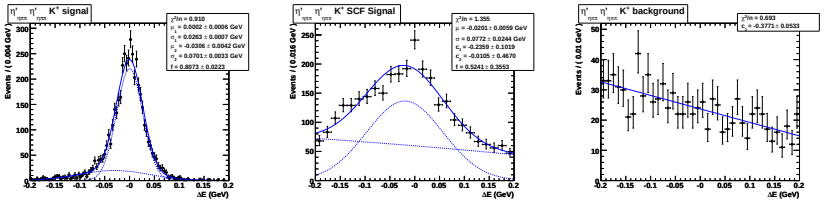

Figure A.12: ΔE PDFs: signal, double Gaussian; signal SCF, Gaussian plus Chebyshev second order polynomial; continuum background: Chebyshev first order polynomial.

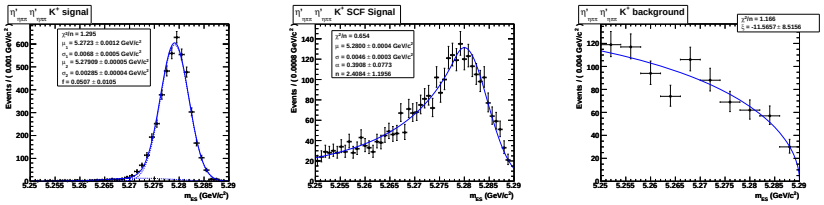

Figure A.13: $m_{\rm ES}$ PDFs: double Gaussian; signal SCF, Crystal Ball; continuum background, Argus function.

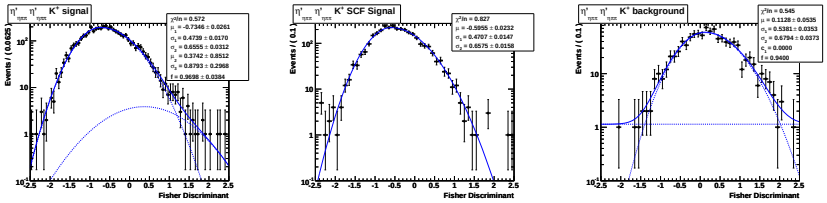

Figure A.14: $\mathcal{F}$ PDFs: signal, Gaussian plus asymmetric Gaussian; signal SCF, asymmetric Gaussian; continuum background, asymmetric Gaussian plus Chebyshev first order polynomial.

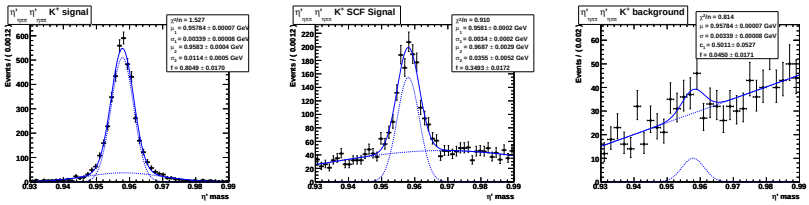

Figure A.15: η' (1) mass PDFs: signal, double Gaussian; signal SCF, double Gaussian; continuum background, MC Gaussian plus Chebyshev first order polynomial

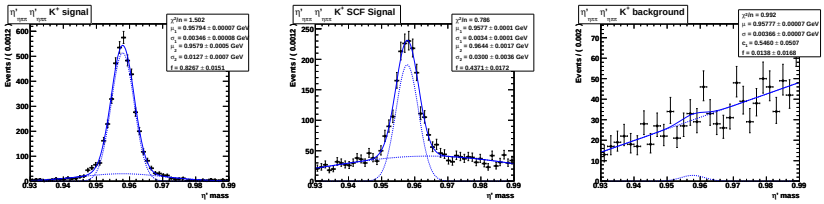

Figure A.16: η' (2) mass PDFs: signal, double Gaussian; signal SCF, double Gaussian; continuum background, MC Gaussian plus Chebyshev first order polynomial.

A.4 $B^{\pm} \to \eta'_{\eta\pi\pi}\eta'_{\rho\gamma}K^{\pm}$

	$m_{\rm ES}$	ΔE	η mass	$\eta'_{\eta\pi\pi}$ mass	$\mathcal{F}$	$\mathcal{H}_\rho$
$m_{\rm ES}$	1.000					
ΔE	-0.043	1.000				
η mass	0.028	0.045	1.000			
$\eta'_{\eta\pi\pi}$ mass	-0.009	0.014	-0.005	1.000		
$\mathcal{F}$	-0.001	0.0.13	0.0.13	0.009	1.000	
$\mathcal{H}_\rho$	0.0.13	0.000	0.015	0.007	0.000	1.000

Table A.12: Correlation matrix for signal MCtruth+PP events.

	$m_{\rm ES}$	ΔE	η mass	$\eta'_{\eta\pi\pi}$ mass	$\mathcal{F}$	$\mathcal{H}_\rho$
$m_{\rm ES}$	1.000					
ΔE	0.060	1.000				
η mass	0.015	-0.023	1.000			
$\eta'_{\eta\pi\pi}$ mass	0.005	0.009	-0.015	1.000		
$\mathcal{F}$	-0.019	-0.028	0.010	-0.005	1.000	
$\mathcal{H}_\rho$	0.011	-0.017	-0.009	0.007	0.0.13	1.000

Table A.13: Correlation matrix for signal MC SCF events.

	$m_{\rm ES}$	ΔE	η mass	$\eta'_{\eta\pi\pi}$ mass	$\mathcal{F}$	$\mathcal{H}_\rho$
$m_{\rm ES}$	1.000					
ΔE	0.013	1.000				
η mass	0.001	0.019	1.000			
$\eta'_{\eta\pi\pi}$ mass	0.000	-0.011	-0.009	1.000		
$\mathcal{F}$	0.021	0.021	-0.005	-0.011	1.000	
$\mathcal{H}_\rho$	-0.021	0.010	-0.023	$-0.0.13$	0.015	1.000

Table A.14: Correlation matrix in on-peak side band data.

	$m_{\rm ES}$	ΔE	η mass	$\eta'_{\eta\pi\pi}$ mass	$\mathcal{F}$	$\mathcal{H}_\rho$
$m_{\rm ES}$	1.000					
ΔE	0.0.13	1.000				
η mass	0.027	0.005	1.000			
$\eta'_{\eta\pi\pi}$ mass	0.003	0.006	-0.013	1.000		
$\mathcal{F}$	$-0.0.13$	-0.009	-0.006	0.024	1.000	
$\mathcal{H}_\rho$	0.009	0.029	0.021	0.010	0.0.13	1.000

Table A.15: Correlation matrix in MC generic $B^0\overline{B}^0$.

	$m_{\rm ES}$	ΔE	η mass	$\eta'_{\eta\pi\pi}$ mass	$\mathcal{F}$	$\mathcal{H}_\rho$
$m_{\rm ES}$	1.000					
ΔE	0.001	1.000				
η mass	0.023	0.025	1.000			
$\eta'_{\eta\pi\pi}$ mass	0.015	$-0.0.13$	0.0.13	1.000		
$\mathcal{F}$	0.001	-0.023	-0.028	$-0.0.13$	1.000	
$\mathcal{H}_\rho$	0.036	0.018	0.0.13	0.000	-0.020	1.000

Table A.16: Correlation matrix in MC generic B^+B^-.

```
deltaE_c1_bg_RGK_float = -0.087 +/- 0.046
fisher_Mu1_bg_RGK_float = -0.161 +/- 0.025
fisher_Sigma1_bg_RGK_float = 0.360 +/- 0.0.13
fisher_Sigma2_bg_RGK_float = 0.457 +/- 0.016
fisher_Frac_bg_RGK_float = 0.966 +/- 0.006
etaMass_Frac_bg_RGK_float = 0.081 +/- 0.019
etaMass_c0_bg_RGK_float = -0.221 +/- 0.038
etapMass0_Frac_bg_RGK_float = 0.025 +/- 0.014
etapMass0_c0_bg_RGK_float = 0.416 +/- 0.034
helicity1_c1_bg_RGK_float = 0.031 +/- 0.036
```

Final values for the parameters which were allowed to float in the fit.

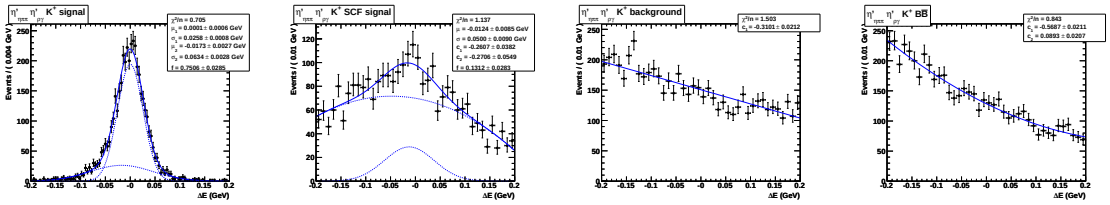

Figure A.17: ΔE PDFs: signal, double Gaussian; signal SCF, Gaussian plus Chebyshev second order polynomial; continuum background, Chebyshev first order polynomial; $B\overline{B}$ background, Chebyshev second order polynomial.

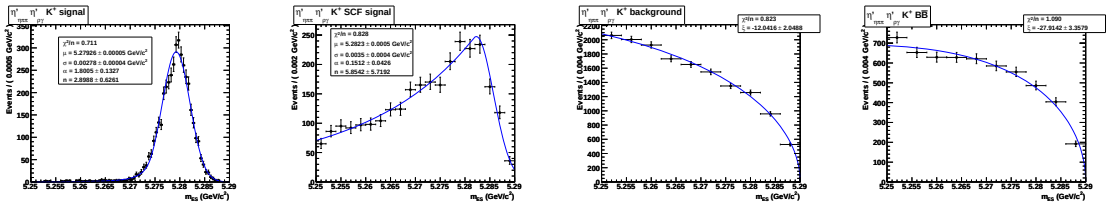

Figure A.18: $m_{\rm ES}$ PDFs: signal, Crystal Ball; signal SCF, Crystal Ball; continuum background, Argus function; $B\overline{B}$ background, Argus function.

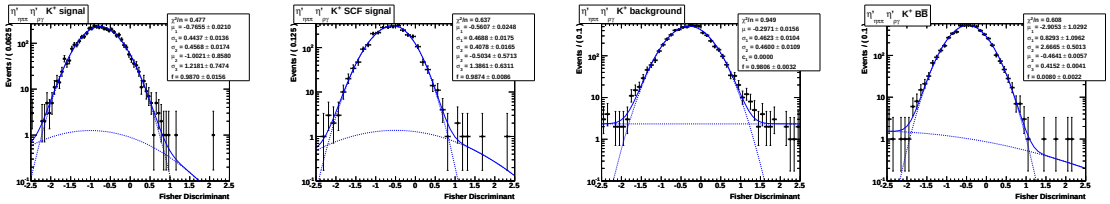

Figure A.19: $\mathcal{F}$ PDFs: signal, Gaussian plus asymmetric Gaussian; signal SCF, Gaussian plus asymmetric Gaussian; continuum background, asymmetric Gaussian plus Chebyshev first order polynomial; $B\overline{B}$ background, Gaussian plus asymmetric Gaussian.

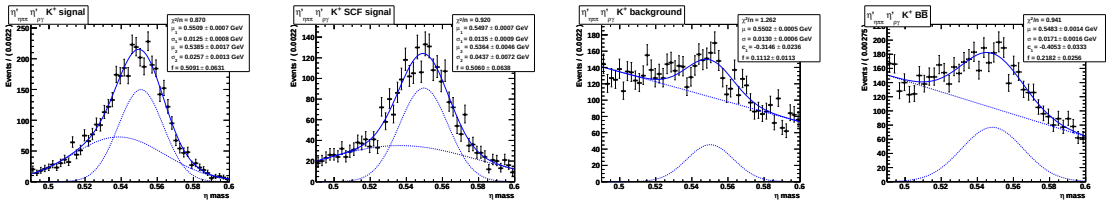

Figure A.20: η PDFs: signal, double Gaussian; signal SCF, double Gaussian; continuum background, MC Gaussian plus Chebyshev first order polynomial; $B\overline{B}$ background, Gaussian plus Chebyshev first order polynomial.

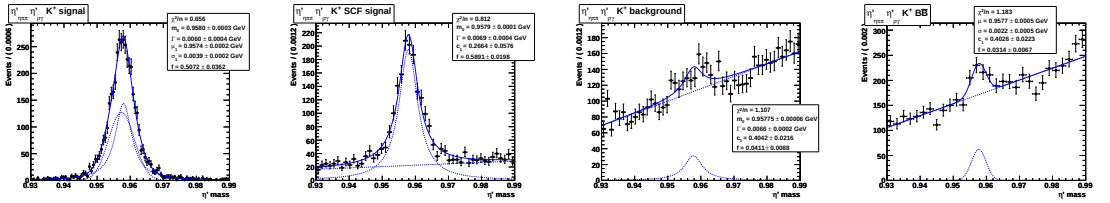

Figure A.21: $\eta'_{\eta\pi\pi}$ PDFs: signal, Breit-Wigner plus Chebyshev first order polynomial; signal SCF, Breit-Wigner plus Chebyshev first order polynomial; continuum background, MC Breit-Wigner plus Chebyshev first order polynomial; $B\overline{B}$ background, Gaussian plus Chebyshev first order polynomial.

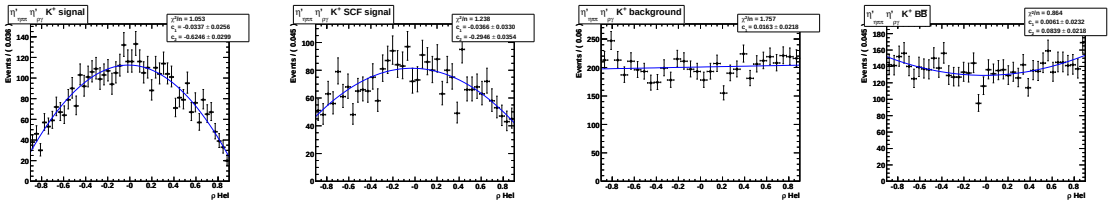

Figure A.22: $\mathcal{H}_\rho$ PDFs: signal, Chebyshev second order polynomial; signal SCF, Chebyshev second order polynomial; continuum background, Chebyshev first order polynomial; $B\overline{B}$ background, Chebyshev second order polynomial.

A.5 $B^0 \to \eta'_{\rho\gamma} K^0_{S+-}$

	$m_{\rm ES}$	ΔE	$\mathcal{F}$
$m_{\rm ES}$	1.000		
ΔE	0.029	1.000	
$\mathcal{F}$	−0.038	−0.017	1.000

Table A.17: Correlation matrix for MC signal events.

	$m_{\rm ES}$	ΔE	$\mathcal{F}$
$m_{\rm ES}$	1.000		
ΔE	−0.017	1.000	
$\mathcal{F}$	0.001	−0.013	1.000

Table A.18: Correlation matrix for on-peak side band data.

```
bMass_xi_bg_RG_float = -20.382 +/- 2.755 L(-45.000 - -10.000)
dE_c1_bg_RG_float = -0.319 +/- 0.018 L(-2.000 - 2.000)
fisher_Mu1_bg_RG_float = 0.344 +/- 0.018 L(-5.000 - 5.000)
fisher_Sigma1_bg_RG_float = 0.515 +/- 0.012 L(0.000 - 5.000)
fisher_Sigma2_bg_RG_float = 0.645 +/- 0.012 L(0.000 - 5.000)
fisher_Frac_bg_RG_float = 0.967 +/- 0.004 L(0.900 - 1.000)
deltaT_Mu2_bg_RG_float = 0.154 +/- 0.047 L(-10.000 - 10.000)
deltaT_Sigma2_bg_RG_float = 1.961 +/- 0.076 L(0.000 - 3.000)
deltaT_Mu1_bg_RG_float = 0.033 +/- 0.013 L(-10.000 - 10.000)
deltaT_Sigma1_bg_RG_float = 0.713 +/- 0.019 L(0.000 - 3.000)
deltaT_Frac1_bg_RG_float = 0.300 +/- 0.022 L(0.000 - 1.000)
deltaT_Frac2_bg_RG_float = 0.022 +/- 0.003 L(0.000 - 1.000)
```

Final values for the parameters which were allowed to float in the fit.

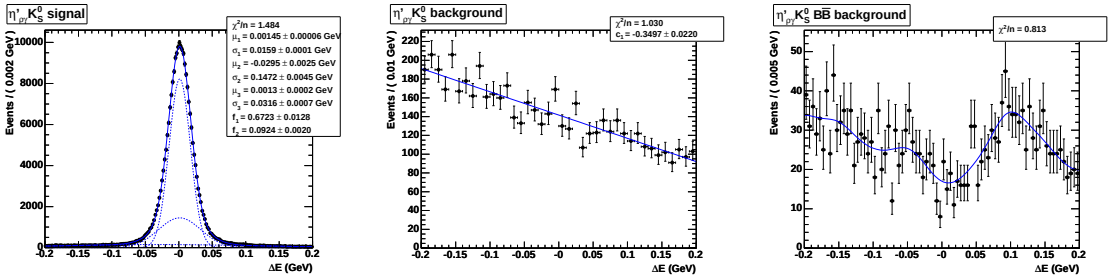

Figure A.23: ΔE PDFs: signal, triple Gaussian; continuum background, linear Chebyshev polynomial; $B\overline{B}$ background, KEYS.

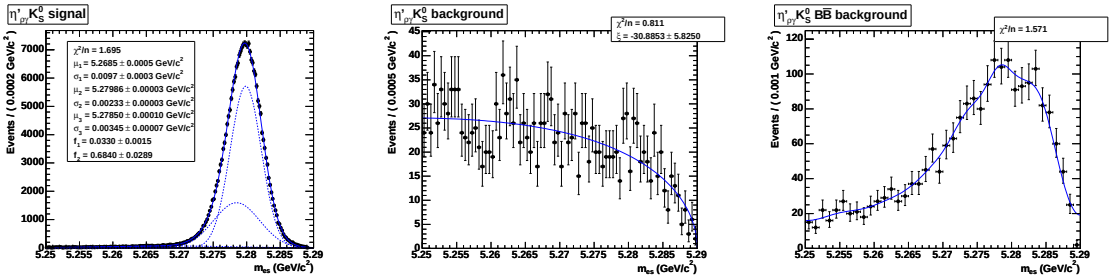

Figure A.24: $m_{\rm ES}$ PDFs: signal, triple Gaussian; continuum background, Argus function; $B\overline{B}$ background, KEYS.

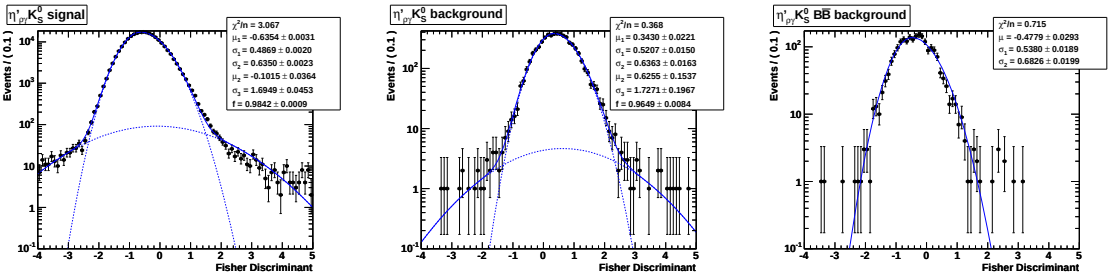

Figure A.25: $\mathcal{F}$ PDFs: signal, asymmetric Gaussian plus single Gaussian; continuum background, asymmetric Gaussian plus single Gaussian; $B\overline{B}$ background, asymmetric Gaussian.

A.6 $B^0 \to \eta'_{\eta\pi\pi} K^0_{S+-}$

	$m_{\rm ES}$	ΔE	$\mathcal{F}$
$m_{\rm ES}$	1.000		
ΔE	0.083	1.000	
$\mathcal{F}$	−0.026	−0.023	1.000

Table A.19: Correlation matrix for MC signal events.

	$m_{\rm ES}$	ΔE	$\mathcal{F}$
$m_{\rm ES}$	1.000		
ΔE	−0.030	1.000	
$\mathcal{F}$	0.054	−0.061	1.000

Table A.20: Correlation matrix for on-peak side band data.

```
bMass_xi_bg_EPP_float = -10.498 +/- 12.028 L(-45.000 - 0.000)
dE_c1_bg_EPP_float = -0.294 +/- 0.080 L(-2.000 - 2.000)
fisher_Mu1_bg_EPP_float = 0.388 +/- 0.077 L(-5.000 - 5.000)
fisher_Sigma1_bg_EPP_float = 0.558 +/- 0.049 L(0.000 - 5.000)
fisher_Sigma2_bg_EPP_float = 0.532 +/- 0.067 L(0.000 - 5.000)
fisher_Frac_bg_EPP_float = 0.957 +/- 0.030 L(0.600 - 1.000)
deltaT_Mu2_bg_EPP_float = 1.136 +/- 0.886 L(-10.000 - 10.000)
deltaT_Sigma2_bg_EPP_float = 1.836 +/- 0.292 L(0.000 - 3.000)
deltaT_Mu1_bg_EPP_float = -0.049 +/- 0.079 L(-10.000 - 10.000)
deltaT_Sigma1_bg_EPP_float = 0.904 +/- 0.096 L(0.000 - 3.000)
deltaT_Frac1_bg_EPP_float = 0.181 +/- 0.115 L(0.000 - 1.000)
```

Final values for the parameters which were allowed to float in the fit.

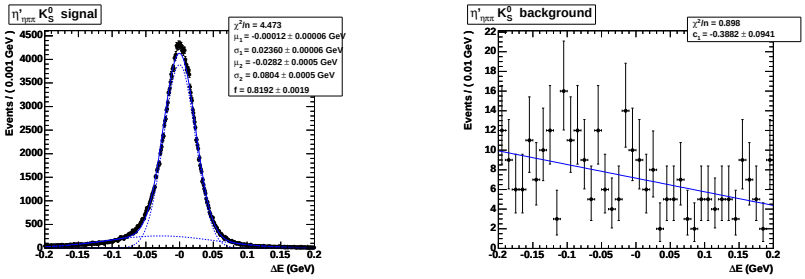

Figure A.26: ΔE PDFs: signal, double Gaussian; continuum background, linear Chebyshev polynomial.

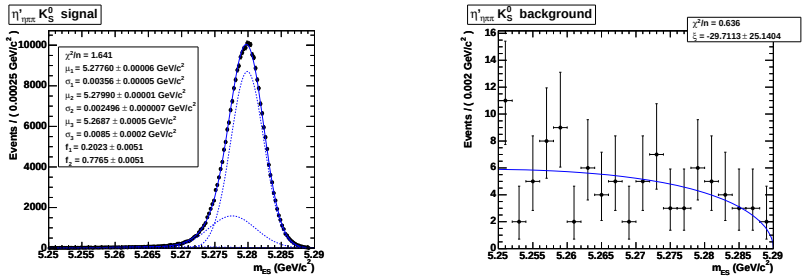

Figure A.27: $m_{\rm ES}$ PDFs: signal, triple Gaussian; continuum background, Argus function.

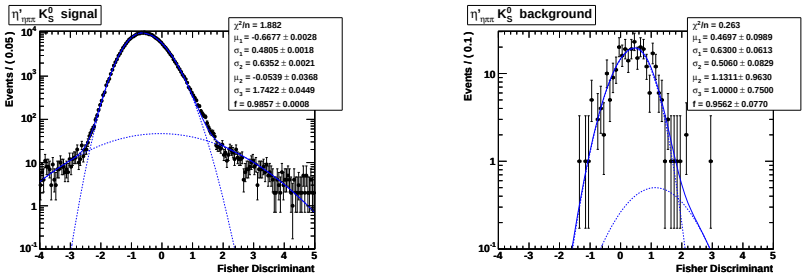

Figure A.28: $\mathcal{F}$ PDFs: signal, asymmetric Gaussian plus single Gaussian; continuum background, asymmetric Gaussian plus single Gaussian.

A.7 $B^{\pm} \to \eta'_{\rho\gamma} K^{\pm}$

	$m_{\rm ES}$	ΔE	$\mathcal{F}$
$m_{\rm ES}$	1.000		
ΔE	0.030	1.000	
$\mathcal{F}$	−0.043	−0.015	1.000

Table A.21: Correlation matrix for MC signal events.

	$m_{\rm ES}$	ΔE	$\mathcal{F}$
$m_{\rm ES}$	1.000		
ΔE	0.008	1.000	
$\mathcal{F}$	−0.003	−0.033	1.000

Table A.22: Correlation matrix for on-peak side band data.

```
bMass_xi_bg_RGK_float = -18.562 +/- 1.359 L(-45.000 - -10.000)
dE_c1_bg_RGK_float = -0.250 +/- 0.009 L(-2.000 - 2.000)
fisher_Mu1_bg_RGK_float = 0.388 +/- 0.009 L(-5.000 - 5.000)
fisher_Sigma1_bg_RGK_float = 0.536 +/- 0.006 L(0.000 - 5.000)
fisher_Sigma2_bg_RGK_float = 0.613 +/- 0.006 L(0.000 - 5.000)
fisher_Frac_bg_RGK_float = 0.978 +/- 0.001 L(0.000 - 1.000)
deltaT_Mu2_bg_RGK_float = 0.027 +/- 0.018 L(-10.000 - 10.000)
deltaT_Sigma2_bg_RGK_float = 1.499 +/- 0.030 L(0.000 - 3.000)
deltaT_Mu1_bg_RGK_float = 0.000 +/- 0.005 L(-10.000 - 10.000)
deltaT_Sigma1_bg_RGK_float = 0.579 +/- 0.008 L(0.000 - 3.000)
deltaT_Frac1_bg_RGK_float = 0.309 +/- 0.013 L(0.000 - 1.000)
deltaT_Frac2_bg_RGK_float = 0.012 +/- 0.001 L(0.000 - 1.000)
```

Final values for the parameters which were allowed to float in the fit.

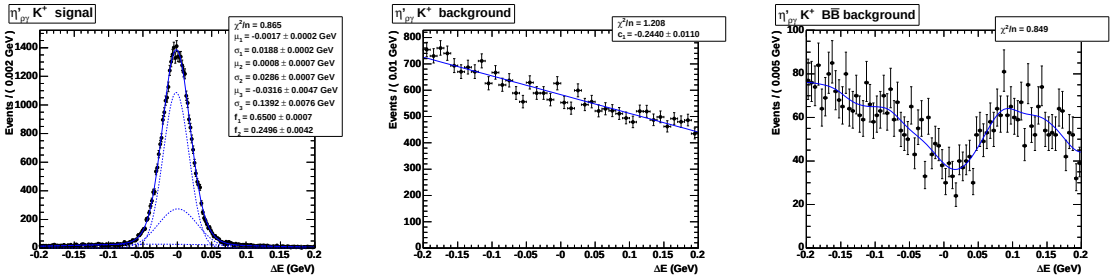

Figure A.29: ΔE PDFs: signal, triple Gaussian; continuum background, linear Chebyshev polynomial; $B\overline{B}$ background, KEYS.

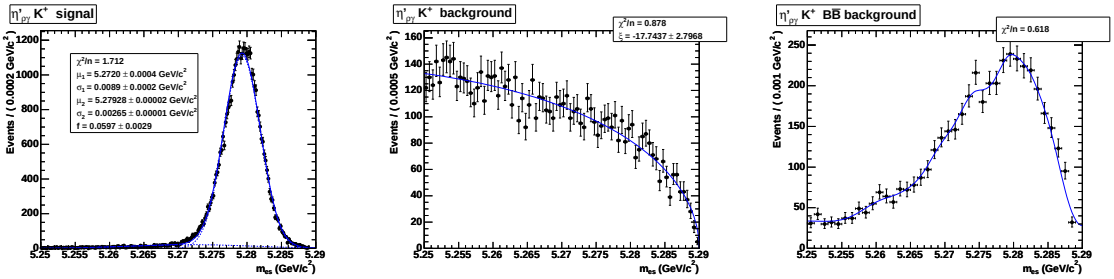

Figure A.30: $m_{\rm ES}$ PDFs: signal, double Gaussian; continuum background, Argus function; $B\overline{B}$ background, KEYS.

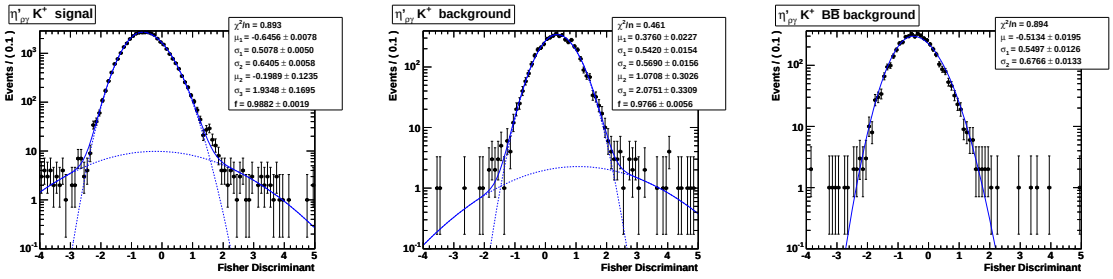

Figure A.31: $\mathcal{F}$ PDFs: signal, asymmetric Gaussian plus single Gaussian; continuum background, asymmetric Gaussian plus single Gaussian; $B\overline{B}$ background, asymmetric Gaussian.

A.8 $B^{\pm} \to \eta'_{\eta\pi\pi} K^{\pm}$

	$m_{\rm ES}$	ΔE	$\mathcal{F}$
$m_{\rm ES}$	1.000		
ΔE	0.001	1.000	
$\mathcal{F}$	-0.023	-0.008	1.000

Table A.23: Correlation matrix for MC signal events.

	$m_{\rm ES}$	ΔE	$\mathcal{F}$
$m_{\rm ES}$	1.000		
ΔE	0.006	1.000	
$\mathcal{F}$	-0.016	-0.011	1.000

Table A.24: Correlation matrix for on-peak side band data.

```
bMass_xi_bg_EPPK_float = -9.600 +/- 7.456 L(-45.000 - 5.000)
dE_c1_bg_EPPK_float = -0.238 +/- 0.049 L(-2.000 - 2.000)
fisher_Mu1_bg_EPPK_float = 0.244 +/- 0.045 L(-5.000 - 5.000)
fisher_Sigma1_bg_EPPK_float = 0.438 +/- 0.031 L(0.000 - 5.000)
fisher_Sigma2_bg_EPPK_float = 0.596 +/- 0.036 L(0.000 - 5.000)
fisher_Frac_bg_EPPK_float = 0.918 +/- 0.026 L(0.000 - 1.000)
deltaT_Mu2_bg_EPPK_float = 0.073 +/- 0.102 L(-10.000 - 10.000)
deltaT_Sigma2_bg_EPPK_float = 1.482 +/- 0.136 L(0.000 - 3.000)
deltaT_Mu1_bg_EPPK_float = -0.037 +/- 0.035 L(-10.000 - 10.000)
deltaT_Sigma1_bg_EPPK_float = 0.643 +/- 0.048 L(0.000 - 3.000)
deltaT_Frac1_bg_EPPK_float = 0.335 +/- 0.073 L(0.000 - 1.000)
```

Final values for the parameters which were allowed to float in the fit.

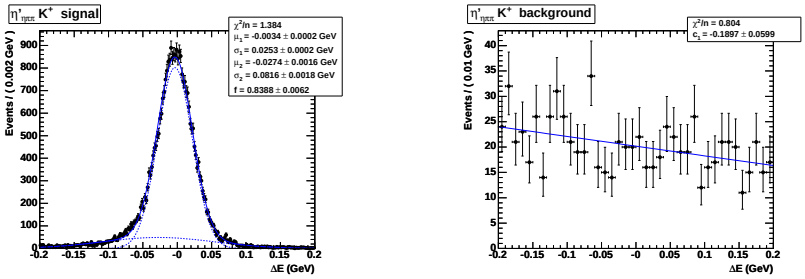

Figure A.32: ΔE PDFs: signal, double Gaussian; continuum background, linear Chebyshev polynomial.

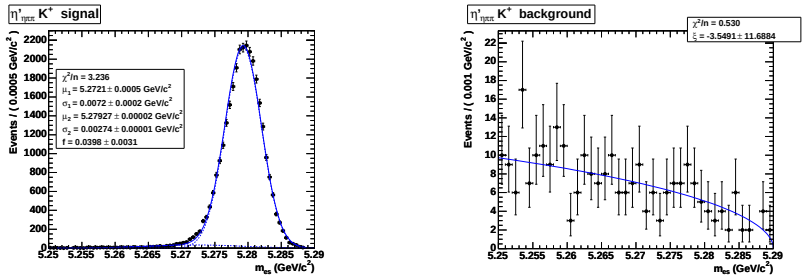

Figure A.33: $m_{\rm ES}$ PDFs: signal, double Gaussian; continuum background, Argus function.

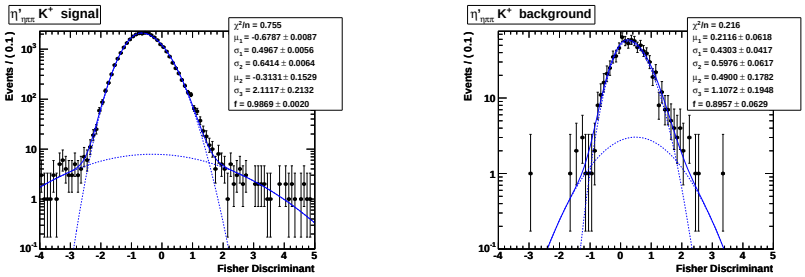

Figure A.34: $\mathcal{F}$ PDFs: signal, asymmetric Gaussian plus single Gaussian; continuum background, asymmetric Gaussian plus single Gaussian.

A.9 $B^0 \to \eta_{\gamma\gamma} K^0_S \gamma$

	$m_{\rm ES}$	ΔE	η mass	$\mathcal{F}$
$m_{\rm ES}$	1.000			
ΔE	0.039	1.000		
η mass	0.026	0.054	1.000	
$\mathcal{F}$	-0.029	-0.002	-0.003	1.000

Table A.25: Correlation matrix for signal MC events.

	$m_{\rm ES}$	ΔE	η mass	$\mathcal{F}$
$m_{\rm ES}$	1.000			
ΔE	0.024	1.000		
η mass	-0.049	0.024	1.000	
$\mathcal{F}$	-0.069	-0.009	0.006	1.000

Table A.26: Correlation matrix in on-peak side band data.

```
mES_xi_bg_float = -29.847 +/- 10.842
deltaE_c1_bg_float = -0.265 +/- 0.060
fisher_Mu1_bg_float = 0.202 +/- 0.057
fisher_Sigma2_bg_float = 0.589 +/- 0.039
etaMass_Frac_bg_float = 0.150 +/- 0.033
etaMass_c0_bg_float = -0.331 +/- 0.068
```

Final values for the parameters which were allowed to float in the fit.

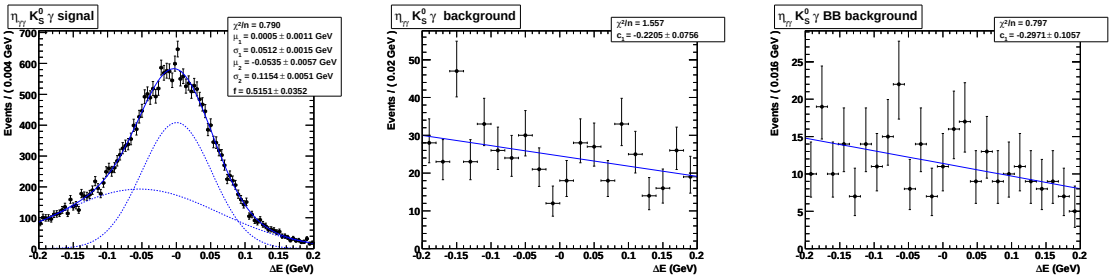

Figure A.35: ΔE PDFs: signal, double Gaussian; continuum background, Chebyshev first order polynomial; $B\overline{B}$ background, linear Chebyshev polynomial.

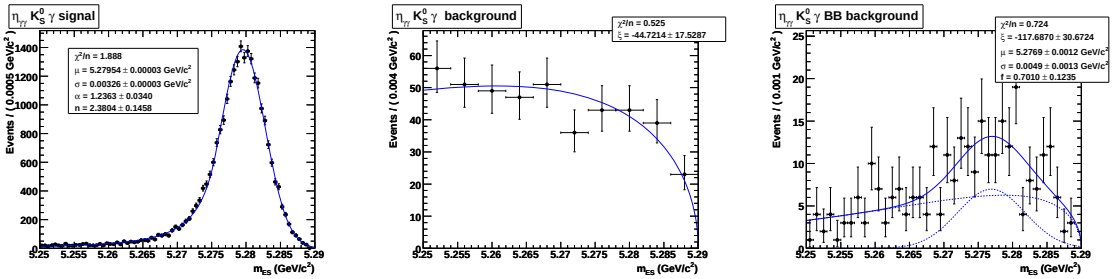

Figure A.36: $m_{\rm ES}$ PDFs: signal, Crystal Ball; continuum background, Argus function; $B\overline{B}$ background, Argus plus Gaussian.

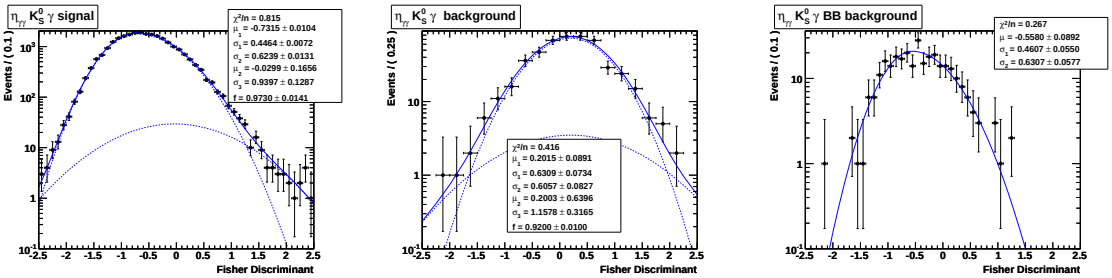

Figure A.37: $\mathcal{F}$ PDFs: signal, Gaussian plus asymmetric Gaussian; continuum background, Gaussian plus asymmetric Gaussian; $B\overline{B}$ background, asymmetric Gaussian.

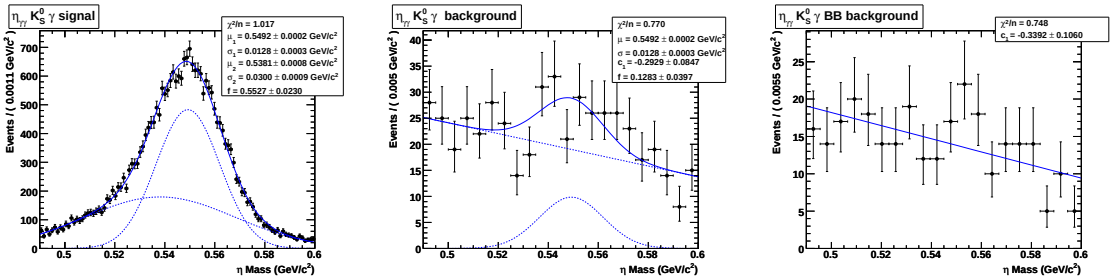

Figure A.38: η mass PDFs: signal, double Gaussian; continuum background, MC Gaussian plus Chebyshev first order polynomial; $B\overline{B}$ background, linear Chebyshev polynomial.

A.10 $B^{\pm} \to \eta_{\gamma\gamma} K^{\pm} \gamma$

	$m_{\rm ES}$	ΔE	η mass	$\mathcal{F}$
$m_{\rm ES}$	1.000			
ΔE	0.029	1.000		
η mass	0.028	0.040	1.000	
$\mathcal{F}$	-0.039	-0.004	-0.000	1.000

Table A.27: Correlation matrix for signal MC events.

	$m_{\rm ES}$	ΔE	η mass	$\mathcal{F}$
$m_{\rm ES}$	1.000			
ΔE	0.039	1.000		
η mass	-0.001	0.011	1.000	
$\mathcal{F}$	-0.070	-0.052	0.000	1.000

Table A.28: Correlation matrix in on-peak side band data.

```
mES_xi_bg_float = -22.929 +/- 6.868
deltaE_c1_bg_float = -0.295 +/- 0.036
fisher_Mu1_bg_float = 0.299 +/- 0.040
fisher_Sigma1_bg_float = 0.677 +/- 0.028
fisher_Sigma2_bg_float = 0.596 +/- 0.025
etaMass_Frac_bg_float = 0.205 +/- 0.021
etaMass_c0_bg_float = -0.275 +/- 0.042
```

Final values for the parameters which were allowed to float in the fit.

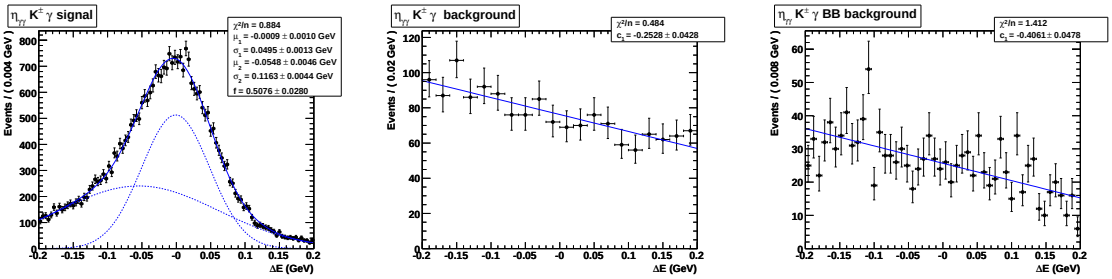

Figure A.39: ΔE PDFs: signal, double Gaussian; continuum background, Chebyshev first order polynomial; $B\overline{B}$ background, linear Chebyshev polynomial.

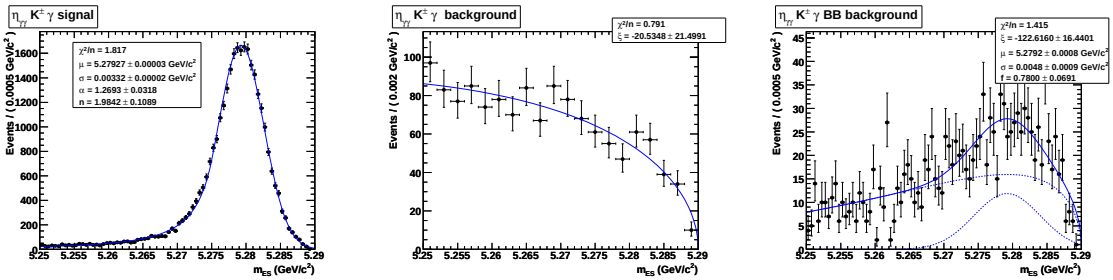

Figure A.40: $m_{\rm ES}$ PDFs: signal, Crystal Ball; continuum background, Argus function; $B\overline{B}$ background, Argus function plus Gaussian.

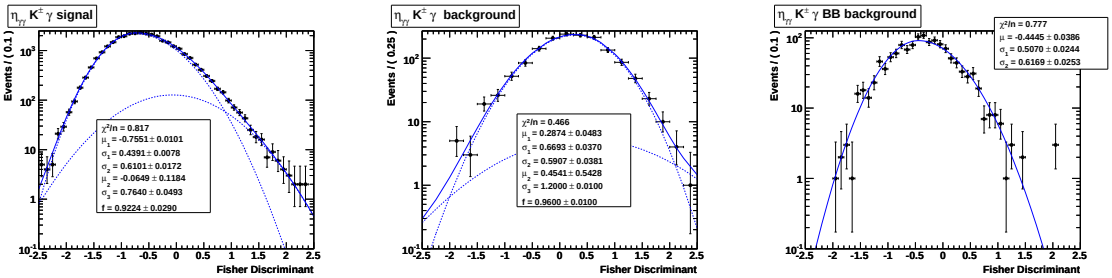

Figure A.41: $\mathcal{F}$ PDFs: signal, Gaussian plus asymmetric Gaussian; continuum background, Gaussian plus asymmetric Gaussian; $B\overline{B}$ background, asymmetric Gaussian.

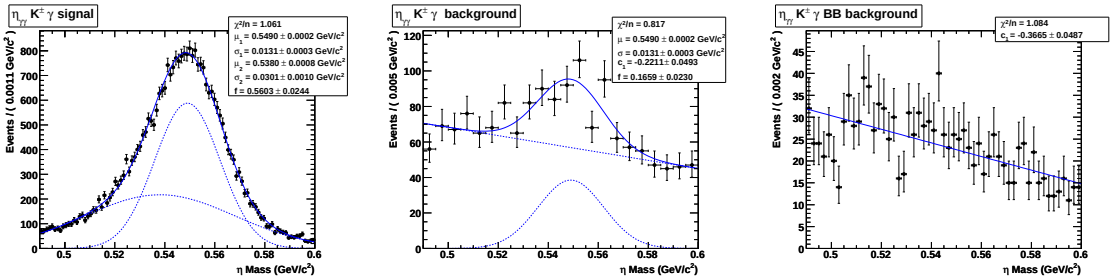

Figure A.42: η mass PDFs: signal, double Gaussian; continuum background, MC Gaussian plus Chebyshev first order polynomial; $B\overline{B}$ background, Chebyshev first order polynomial.

A.11 $B^0 \to \eta_{3\pi} K^0_S \gamma$

	$m_{\rm ES}$	ΔE	η mass	$\mathcal{F}$
$m_{\rm ES}$	1.000			
ΔE	0.047	1.000		
η mass	0.015	0.013	1.000	
$\mathcal{F}$	-0.023	-0.016	0.006	1.000

Table A.29: Correlation matrix in signal MC events.

	$m_{\rm ES}$	ΔE	η mass	$\mathcal{F}$
$m_{\rm ES}$	1.000			
ΔE	0.105	1.000		
η mass	-0.055	0.006	1.000	
$\mathcal{F}$	-0.150	-0.130	-0.005	1.000

Table A.30: Correlation matrix in on-peak side band data.

```
mES_xi_bg_float = -25.828 +/- 24.130
deltaE_c1_bg_float = -0.353 +/- 0.100
fisher_Mu1_bg_float = 0.193 +/- 0.108
fisher_Sigma1_bg_float = 0.576 +/- 0.072
fisher_Sigma2_bg_float = 0.543 +/- 0.076
etaMass_Frac_bg_float = 0.265 +/- 0.044
etaMass_c0_bg_float = 0.290 +/- 0.125
```

Final values for the parameters which were allowed to float in the fit.

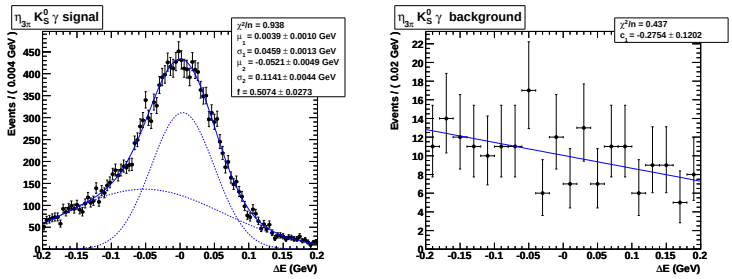

Figure A.43: ΔE PDFs: signal, double Gaussian; continuum background, Chebyshev first order polynomial.

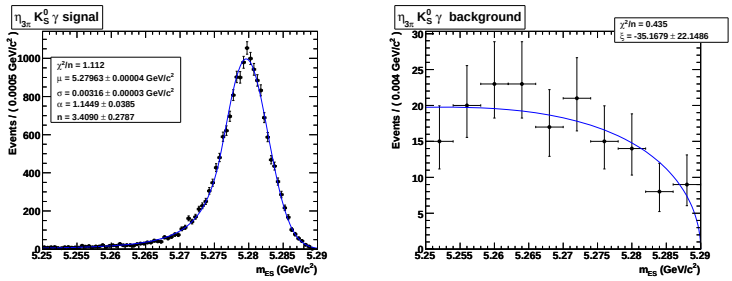

Figure A.44: $m_{\rm ES}$ PDFs: signal, Crystal Ball; continuum background, Argus function.

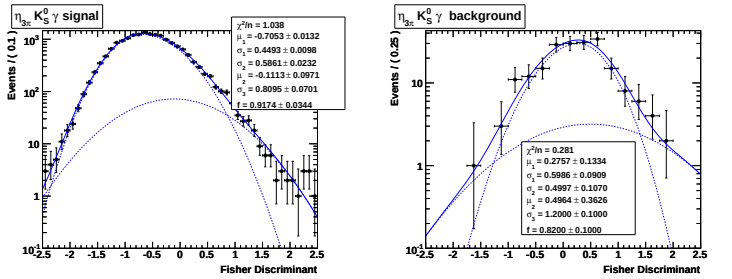

Figure A.45: $\mathcal{F}$ PDFs: signal, Gaussian plus asymmetric Gaussian; continuum background, Gaussian plus asymmetric Gaussian.

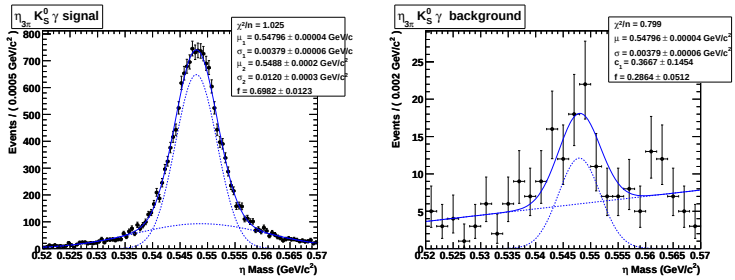

Figure A.46: η mass PDFs: signal, double Gaussian; continuum background, MC Gaussian plus Chebyshev first order polynomial.

A.12 $B^{\pm} \to \eta_{3\pi} K^{\pm} \gamma$

	$m_{\rm ES}$	ΔE	η mass	$\mathcal{F}$
$m_{\rm ES}$	1.000			
ΔE	0.051	1.000		
η mass	0.014	0.008	1.000	
$\mathcal{F}$	-0.025	-0.005	-0.008	1.000

Table A.31: Correlation matrix in signal MC events.

	$m_{\rm ES}$	ΔE	η mass	$\mathcal{F}$
$m_{\rm ES}$	1.000			
ΔE	0.032	1.000		
η mass	0.008	-0.024	1.000	
$\mathcal{F}$	-0.039	-0.020	-0.038	1.000

Table A.32: Correlation matrix in on-peak side band data.

```
deltaE_c1_bg_float = -0.298 +/- 0.052
fisher_Mu1_bg_float = 0.157 +/- 0.064
fisher_Sigma1_bg_float = 0.623 +/- 0.037
fisher_Sigma2_bg_float = 0.643 +/- 0.040
etaMass_Frac_bg_float = 0.241 +/- 0.024
etaMass_c0_bg_float = 0.278 +/- 0.064
```

Final values for the parameters which were allowed to float in the fit.

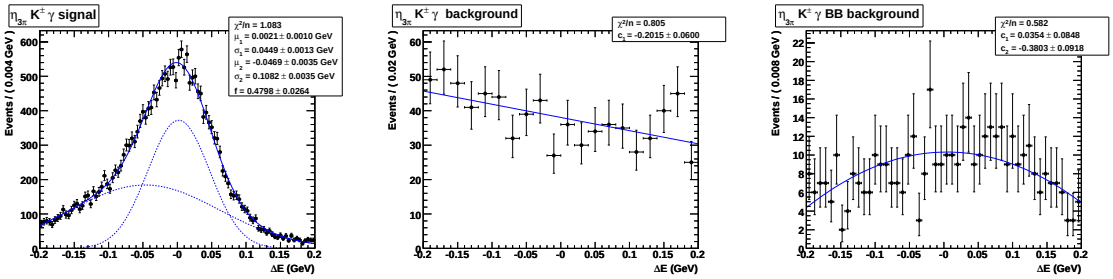

Figure A.47: ΔE PDFs: signal, double Gaussian; continuum background, Chebyshev first order polynomial; $B\overline{B}$ background, second order Chebyshev polynomial.

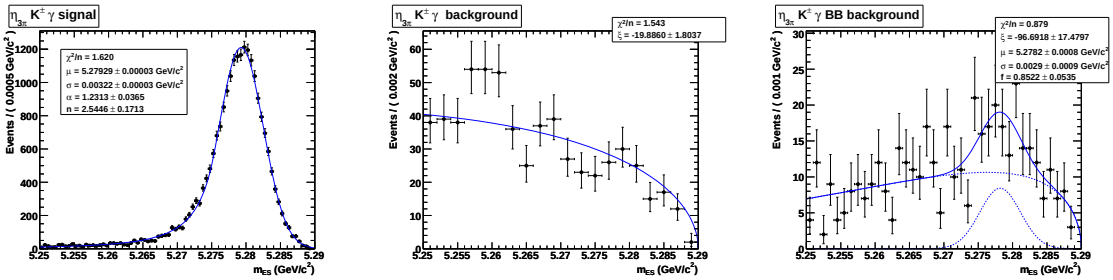

Figure A.48: $m_{\rm ES}$ PDFs: signal, Crystal Ball; continuum background, Argus function; $B\overline{B}$ background, Argus plus Gaussian.

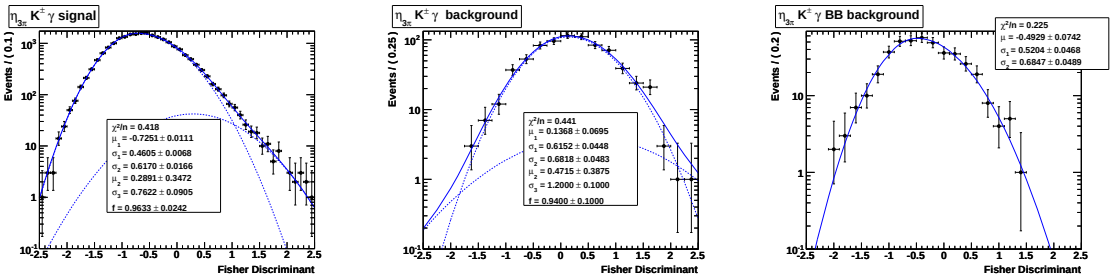

Figure A.49: $\mathcal{F}$ PDFs: signal, Gaussian plus asymmetric Gaussian; continuum background, Gaussian; $B\overline{B}$ background, asymmetric Gaussian.

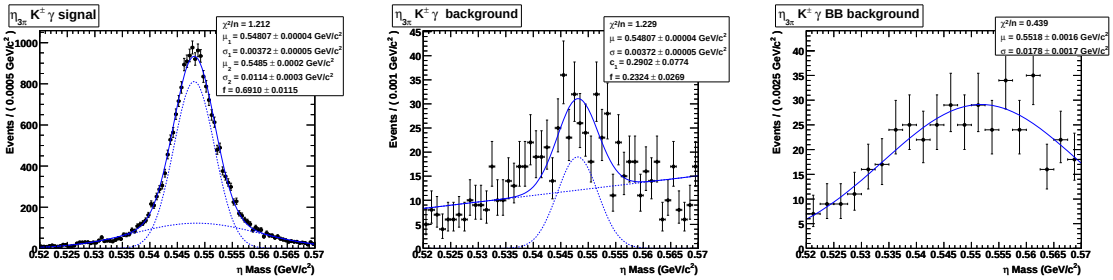

Figure A.50: η mass PDFs: signal, double Gaussian; continuum background, MC Gaussian plus Chebyshev first order polynomial; $B\overline{B}$ background, Gaussian.

A.13 $B^0 \to \eta'_{\eta\pi\pi} K^0_S \gamma$

	$m_{\rm ES}$	ΔE	η mass	η' mass	$\mathcal{F}$
$m_{\rm ES}$	1.000				
ΔE	0.044	1.000			
η mass	0.002	0.021	1.000		
η' mass	-0.011	-0.010	-0.009	1.000	
$\mathcal{F}$	-0.020	0.002	-0.014	-0.000	

Table A.33: Correlation matrix in signal MC events.

	$m_{\rm ES}$	ΔE	η mass	η' mass	$\mathcal{F}$
$m_{\rm ES}$	1.000				
ΔE	0.092	1.000			
η mass	0.073	0.166	1.000		
η' mass	0.008	0.050	0.002	1.000	
$\mathcal{F}$	-0.012	-0.088	-0.100	-0.036	

Table A.34: Correlation matrix in on-peak side band data.

```
deltaE_c1_bg_float = -0.465 +/- 0.135
fisher_Mu1_bg_float = -0.012 +/- 0.117
fisher_Sigma1_bg_float = 0.517 +/- 0.071
fisher_Sigma2_bg_float = 0.694 +/- 0.081
etaMass_c0_bg_float = -0.462 +/- 0.145
etapMass_c1_bg_float = -0.213 +/- 0.145
etapMass_c2_bg_float = -0.773 +/- 0.174
```

Final values for the parameters which were allowed to float in the fit.

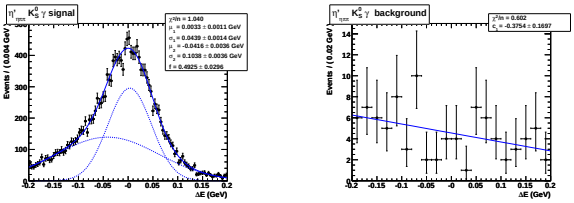

Figure A.51: ΔE PDFs: signal, double Gaussian; continuum background, Chebyshev first order polynomial.

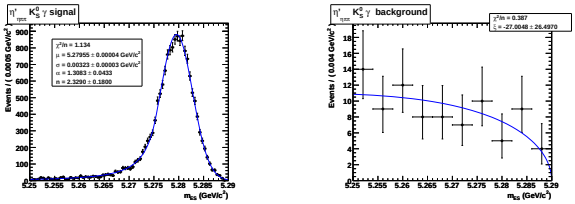

Figure A.52: $m_{\rm ES}$ PDFs: signal, Crystal Ball; continuum background, Argus function.

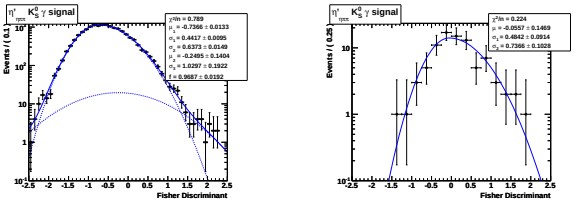

Figure A.53: $\mathcal{F}$ PDFs: signal, Gaussian plus asymmetric Gaussian; continuum background, Gaussian.

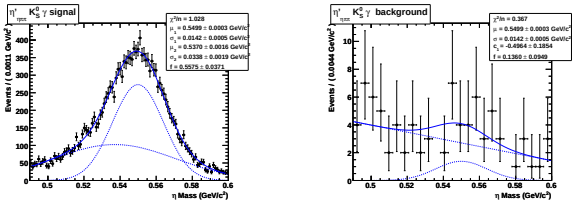

Figure A.54: η mass PDFs: signal, double Gaussian; continuum background, MC Gaussian plus Chebyshev first order polynomial.

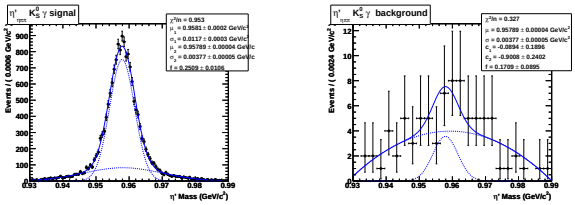

Figure A.55: η' mass PDFs: signal, double Gaussian; continuum background, MC Gaussian plus second order Chebyshev polynomial.

A.14 $B^{\pm} \to \eta'_{\eta\pi\pi} K^{\pm}\gamma$

	$m_{\rm ES}$	ΔE	η mass	η' mass	$\mathcal{F}$
$m_{\rm ES}$	1.000				
ΔE	0.019	1.000			
η mass	0.005	0.033	1.000		
η' mass	-0.013	-0.004	-0.010	1.000	
$\mathcal{F}$	-0.042	0.005	-0.022	-0.001	

Table A.35: Correlation matrix in signal MC events.

	$m_{\rm ES}$	ΔE	η mass	η' mass	$\mathcal{F}$
$m_{\rm ES}$	1.000				
ΔE	0.091	1.000			
η mass	0.010	-0.001	1.000		
η' mass	-0.017	0.081	0.082	1.000	
$\mathcal{F}$	0.009	-0.058	-0.073	-0.089	1.000

Table A.36: Correlation matrix in on-peak side band data.

```
deltaE_c1_bg_float = -0.153 +/- 0.091
fisher_Mu1_bg_float = 0.057 +/- 0.110
fisher_Sigma1_bg_float = 0.448 +/- 0.068
fisher_Sigma2_bg_float = 0.675 +/- 0.072
etaMass_Frac_bg_float = 0.208 +/- 0.049
etaMass_c0_bg_float = -0.157 +/- 0.103
etapMass_Frac_bg_float = 0.151 +/- 0.042
etapMass_c1_bg_float = 0.125 +/- 0.087
etapMass_c2_bg_float = -0.805 +/- 0.119
```

Final values for the parameters which were allowed to float in the fit.

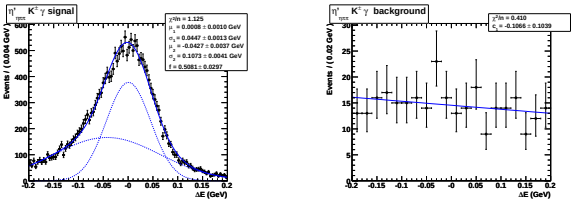

Figure A.56: ΔE PDFs: signal, double Gaussian; continuum background, Chebyshev first order polynomial.

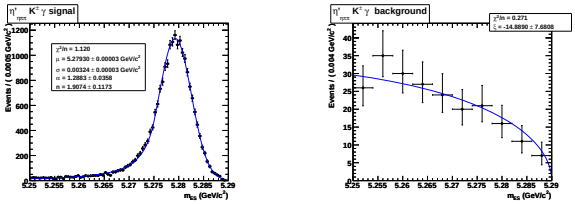

Figure A.57: $m_{\rm ES}$ PDFs: signal, Crystal Ball; continuum background, Argus function.

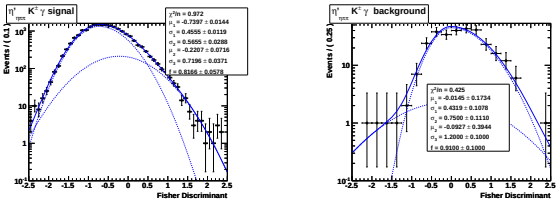

Figure A.58: $\mathcal{F}$ PDFs: signal, Gaussian plus asymmetric Gaussian; continuum background, Gaussian plus asymmetric Gaussian.

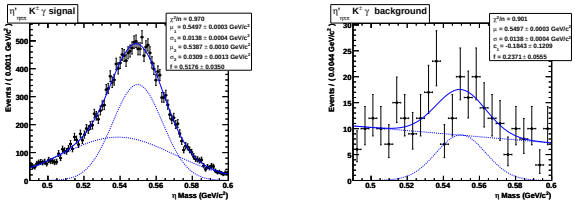

Figure A.59: η mass PDFs: signal, double Gaussian; continuum background, MC Gaussian plus Chebyshev first order polynomial.

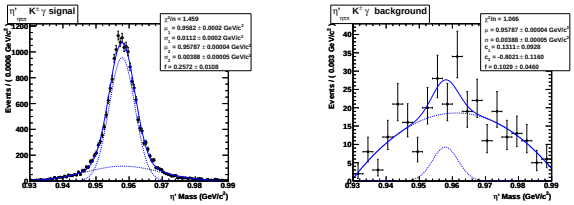

Figure A.60: η' PDFs: signal, double Gaussian; continuum background, MC Gaussian plus second order Chebyshev polynomial.

A.15 $B^0 \to \eta'_{\rho\gamma} K^0_S \gamma$

	$m_{\rm ES}$	ΔE	η' mass	$\mathcal{F}$	$\mathcal{H}_\rho$
$m_{\rm ES}$	1.000				
ΔE	-0.011	1.000			
η' mass	-0.012	0.174	1.000		
$\mathcal{F}$	-0.058	0.006	0.004	1.000	
$\mathcal{H}_\rho$	-0.011	-0.008	0.009	0.009	1.000

Table A.37: Correlation matrix in signal MC events.

	$m_{\rm ES}$	ΔE	η' mass	$\mathcal{F}$	$\mathcal{H}_\rho$
$m_{\rm ES}$	1.000				
ΔE	0.007	1.000			
η' mass	0.021	-0.006	1.000		
$\mathcal{F}$	-0.005	0.005	-0.005	1.000	
$\mathcal{H}_\rho$	-0.020	0.008	0.001	-0.026	1.000

Table A.38: Correlation matrix in on-peak side band data.

```
mES_xi_bg_float = -23.290 +/- 6.028
deltaE_c1_bg_float = -0.265 +/- 0.043
fisher_Mu1_bg_float = 0.118 +/- 0.045
fisher_Sigma1_bg_float = 0.597 +/- 0.025
fisher_Sigma2_bg_float = 0.655 +/- 0.027
helicity_c1_bg_float = -0.032 +/- 0.035
etapMass_Frac_bg_float = 0.026 +/- 0.014
etapMass_c1_bg_float = 0.058 +/- 0.036
```

Final values for the parameters which were allowed to float in the fit.

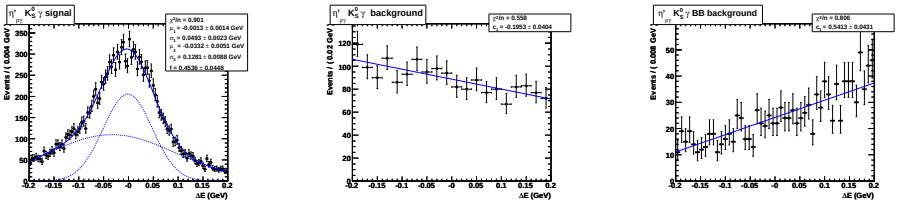

Figure A.61: ΔE PDFs: signal, double Gaussian; continuum background, Chebyshev first order polynomial; $B\overline{B}$ background, Chebyshev first order polynomial.

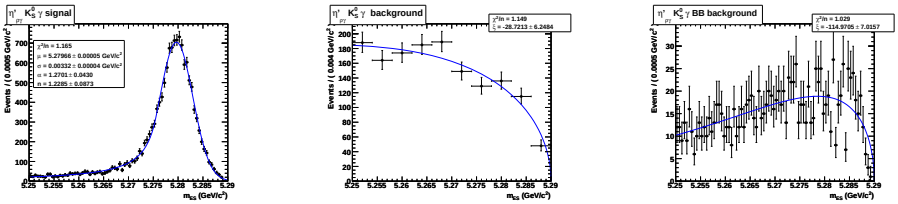

Figure A.62: $m_{\rm ES}$ PDFs: signal, Crystal Ball; continuum background, Argus function; $B\overline{B}$ background, Argus function.

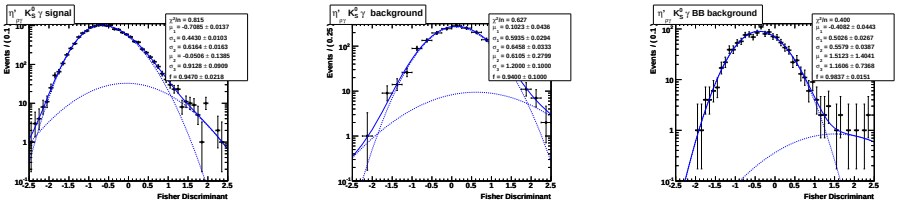

Figure A.63: $\mathcal{F}$ PDFs: signal, Gaussian plus asymmetric Gaussian; continuum background, Gaussian plus asymmetric Gaussian; $B\overline{B}$ background, asymmetric Gaussian plus Gaussian.

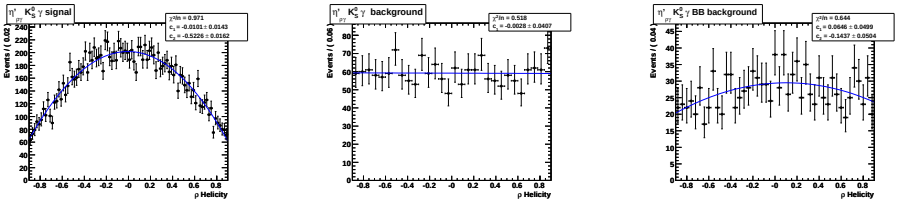

Figure A.64: $\mathcal{H}_\rho$ PDFs: signal, second order Chebyshev polinomial; continuum background, first order Chebyshev polynomial; $B\overline{B}$ background, Chebyshev second order polynomial.

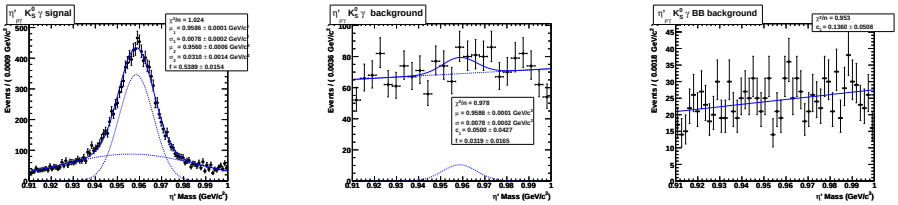

Figure A.65: η' mass PDFs: signal, double Gaussian; continuum background, Gaussian plus Chebyshev first order polynomial; $B\overline{B}$ background, Chebyshev first order polynomial.

A.16 $B^{\pm} \to \eta'_{\rho\gamma} K^{\pm} \gamma$

	$m_{\rm ES}$	ΔE	η' mass	$\mathcal{F}$	$\mathcal{H}_\rho$
$m_{\rm ES}$	1.000				
ΔE	-0.010	1.000			
η' mass	0.008	0.157	1.000		
$\mathcal{F}$	-0.055	-0.006	0.001	1.000	
$\mathcal{H}_\rho$	-0.001	-0.001	0.004	0.015	1.000

Table A.39: Correlation matrix in signal MC events.

	$m_{\rm ES}$	ΔE	η' mass	$\mathcal{F}$	$\mathcal{H}_\rho$
$m_{\rm ES}$	1.000				
ΔE	0.000	1.000			
η' mass	0.008	-0.017	1.000		
$\mathcal{F}$	-0.018	-0.012	-0.013	1.000	
$\mathcal{H}_\rho$	-0.010	-0.012	-0.000	-0.013	1.000

Table A.40: Correlation matrix in on-peak side band data.

```
mES_xi_bg_float = -20.419 +/- 3.231
deltaE_c1_bg_float = -0.277 +/- 0.024
fisher_Mu1_bg_float = 0.182 +/- 0.026
fisher_Sigma1_bg_float = 0.641 +/- 0.015
fisher_Sigma2_bg_float = 0.639 +/- 0.017
fisher_Mu2_bg_float = 0.718 +/- 0.184
helicity_c1_bg_float = -0.023 +/- 0.020
etapMass_Frac_bg_float = 0.018 +/- 0.008
etapMass_c1_bg_float = 0.099 +/- 0.020
```

Final values for the parameters which were allowed to float in the fit.

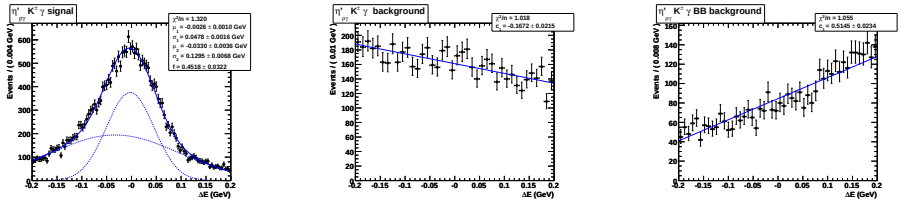

Figure A.66: ΔE PDFs: signal, double Gaussian; continuum background, Chebyshev first order polynomial; $B\overline{B}$ background, Chebyshev first order polynomial.

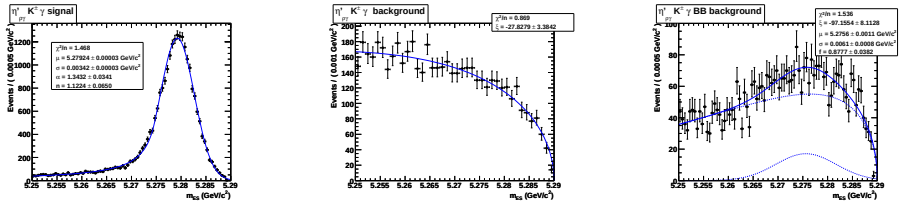

Figure A.67: $m_{\rm ES}$ PDFs: signal, Crystal Ball; continuum background, Argus function; $B\overline{B}$ background, Argus function plus Gaussian.

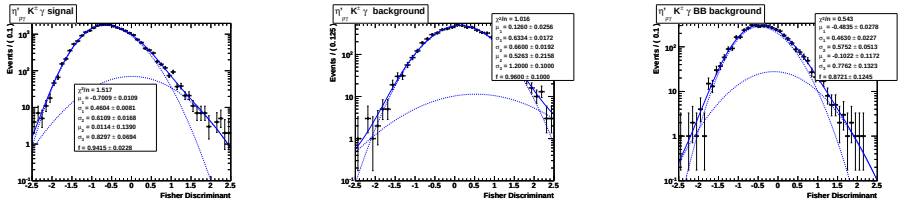

Figure A.68: $\mathcal{F}$ PDFs: signal, Gaussian plus asymmetric Gaussian; continuum background, Gaussian plus asymmetric Gaussian; $B\overline{B}$ background, Gaussian plus asymmetric Gaussian.

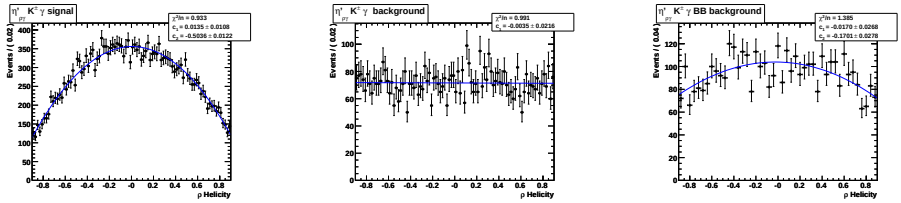

Figure A.69: $\mathcal{H}_\rho$ PDFs: signal, second order Chebyshev polinomial; continuum background, first order Chebyshev polynomial; $B\overline{B}$ background, Chebyshev second order polynomial.

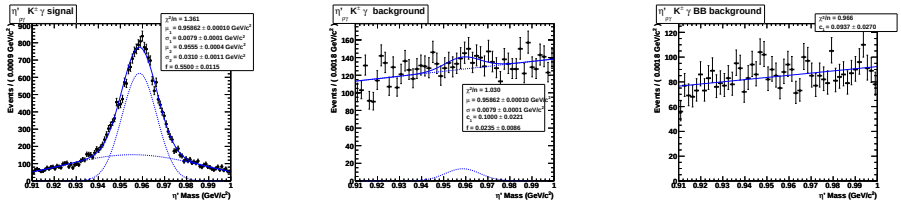

Figure A.70: η' mass PDFs: double Gaussian; continuum background, Gaussian plus Chebyshev first order polynomial; $B\overline{B}$ background, Chebyshev first order polynomial.

A.17 $B^0 \to \eta_{\gamma\gamma} K^0_S$

	$\mathcal{F}$	ΔE	$m_{\rm ES}$	η mass
$\mathcal{F}$	1.000			
ΔE	-0.004	1.000		
$m_{\rm ES}$	-0.007	0.013	1.000	
η mass	-0.003	0.186	0.026	1.000

Table A.41: Correlation matrix for MC signal events.

	$\mathcal{F}$	ΔE	$m_{\rm ES}$	η mass
$\mathcal{F}$	1.000			
ΔE	0.024	1.000		
$m_{\rm ES}$	-0.044	0.034	1.000	
η mass	-0.048	-0.010	0.038	1.000

Table A.42: Correlation matrix for on-peak side band data.

```
mES_xi_bg_float = -7.974 +/- 4.573
deltaE_c1_bg_float = -0.294 +/- 0.030
fisher_Mu1_bg_float = 0.351 +/- 0.027
fisher_Sigma1_bg_float = 0.565 +/- 0.019
fisher_Sigma2_bg_float = 0.621 +/- 0.017
etaMass_Frac_bg_float = 0.362 +/- 0.029
etaMass_c1_bg_float = -0.180 +/- 0.040
etaMass_c2_bg_float = 0.018 +/- 0.070
```

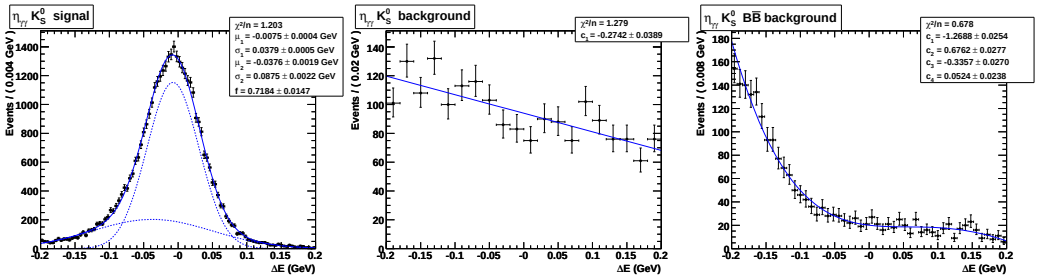

Figure A.71: ΔE PDFs: signal, double Gaussian; continuum background, linear polynomial; $B\overline{B}$ background, fourth order polynomial.

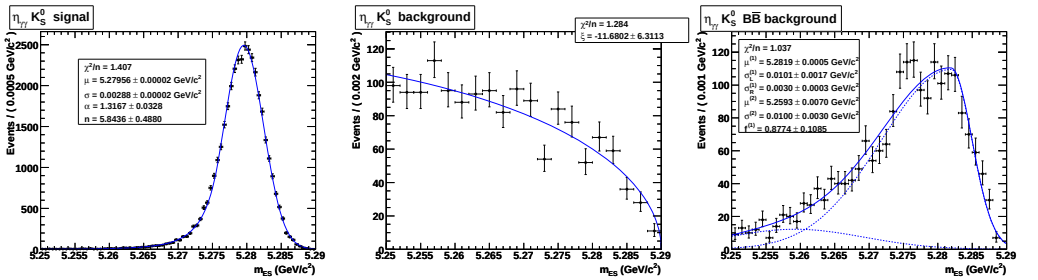

Figure A.72: $m_{\rm ES}$ PDFs: signal, Crystall Ball; continuum background, Argus function; $B\overline{B}$ background, asymetric Gaussian plus Gaussian.

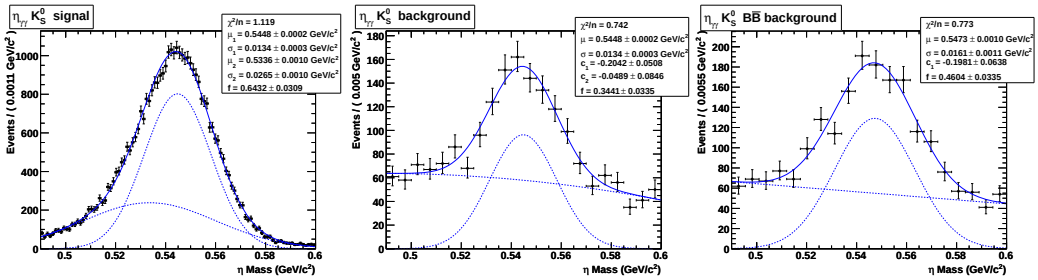

Figure A.73: η mass PDFs: signal, double Gaussian; continuum background, MC Gaussian plus a second order polynomial; $B\overline{B}$ background, Gaussian plus a linear polynomial.

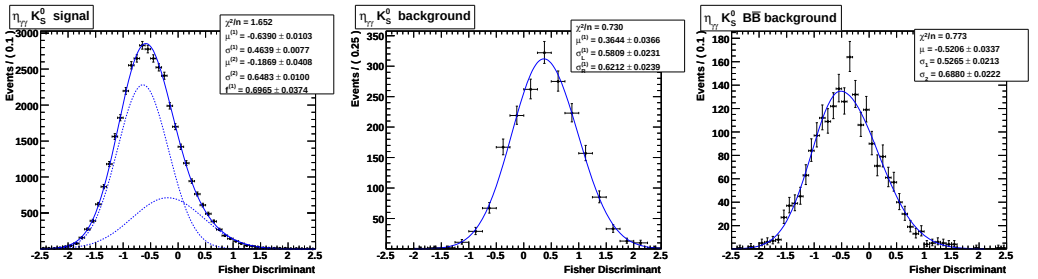

Figure A.74: $\mathcal{F}$ PDFs: signal, double Gaussian; continuum background, asymetric Gaussian; $B\overline{B}$ background, asymetric Gaussian.

A.18 $B^0 \to \eta_{3\pi} K^0_S$

	$\mathcal{F}$	ΔE	$m_{\rm ES}$	η mass
$\mathcal{F}$	1.000			
ΔE	-0.014	1.000		
$m_{\rm ES}$	-0.015	0.016	1.000	
η mass	-0.002	0.003	-0.008	1.000

Table A.43: Correlation matrix for MC signal events.

	$\mathcal{F}$	ΔE	$m_{\rm ES}$	η mass
$\mathcal{F}$	1.000			
ΔE	-0.025	1.000		
$m_{\rm ES}$	0.035	0.000	1.000	
η mass	0.018	-0.002	-0.002	1.000

Table A.44: Correlation matrix for on-peak side band data.

```
mES_xi_bg_float = -4.112 +/- 6.601
deltaE_c1_bg_float = -0.344 +/- 0.044
fisher_Mu1_bg_float = 0.369 +/- 0.043
fisher_Sigma1_bg_float = 0.582 +/- 0.028
fisher_Sigma2_bg_float = 0.640 +/- 0.028
etaMass_Frac_bg_float = 0.313 +/- 0.024
etaMass_c1_bg_float = 0.444 +/- 0.053
etaMass_c2_bg_float = -0.238 +/- 0.067
```

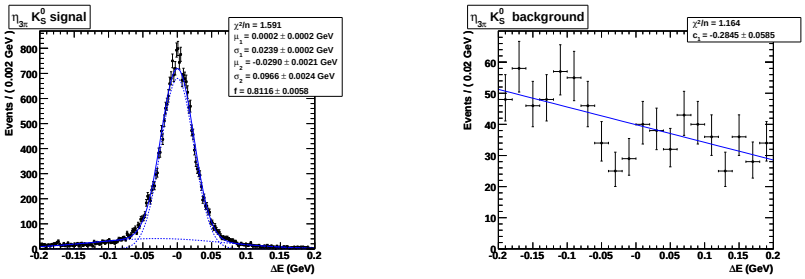

Figure A.75: ΔE PDFs: signal, double Gaussian; continuum background, linear polynomial.

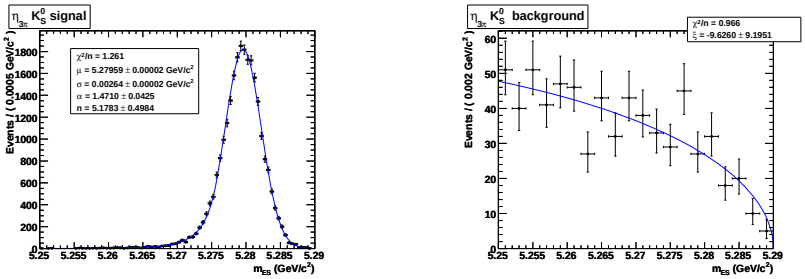

Figure A.76: $m_{\rm ES}$ PDFs: signal, Crystall Ball; continuum background, Argus function.

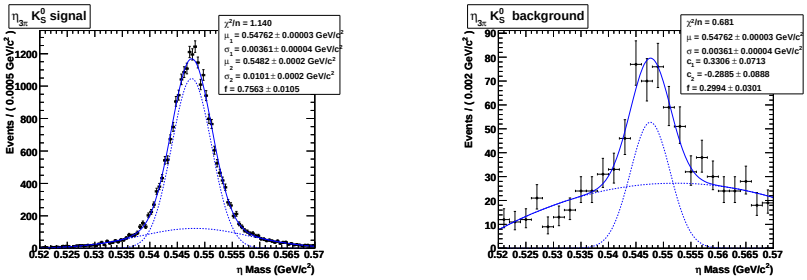

Figure A.77: η mass PDFs: signal, double Gaussian; continuum background, MC Gaussian plus a second order polynomial.

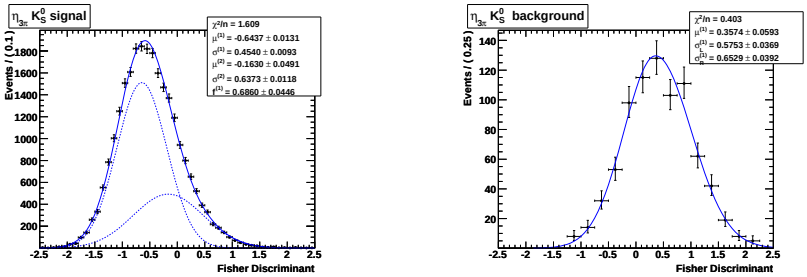

Figure A.78: $\mathcal{F}$ PDFs: signal, double Gaussian; continuum background, asymetric Gaussian.

A.19 $B^0 \to \eta_{\gamma\gamma}\eta_{\gamma\gamma}$

	$m_{\rm ES}$	ΔE	η (1) mass	η (2) mass	$\mathcal{F}$
$m_{\rm ES}$	1.000				
ΔE	-0.046	1.000			
η (1) mass	0.125	-0.077	1.000		
η (2) mass	0.094	0.105	0.028	1.000	
$\mathcal{F}$	-0.147	0.030	-0.062	-0.026	1.000

Table A.45: Correlation matrix for MC signal events.

	$m_{\rm ES}$	ΔE	η (1) mass	η (2) mass	$\mathcal{F}$
$m_{\rm ES}$	1.000				
ΔE	0.077	1.000			
η (1) mass	0.050	-0.044	1.000		
η (2) mass	0.037	-0.026	0.036	1.000	
$\mathcal{F}$	-0.032	0.007	-0.027	-0.003	1.000

Table A.46: Correlation matrix for on-peak side band data.

```
mES_xi_bg_float = -8.688 +/- 5.567
deltaE_c1_bg_float = -0.285 +/- 0.038
fisher_Mu1_bg_float = 0.502 +/- 0.033
fisher_SigmaL_bg_float = 0.586 +/- 0.026
fisher_SigmaR_bg_float = 0.574 +/- 0.021
etaMass0_Frac_bg_float = 0.368 +/- 0.020
etaMass0_c1_bg_float = -0.450 +/- 0.048
etaMass1_Frac_bg_float = 0.301 +/- 0.021
etaMass1_c1_bg_float = -0.330 +/- 0.046
```

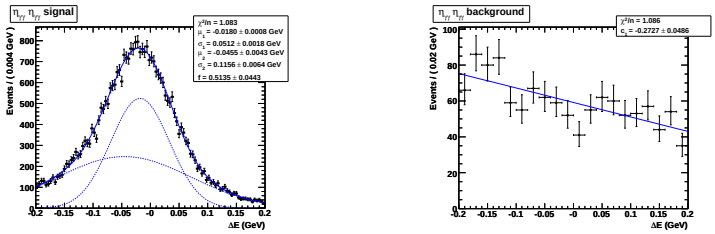

Figure A.79: ΔE PDFs: signal, double Gaussian; continuum background, Chebyshev linear polynomial.

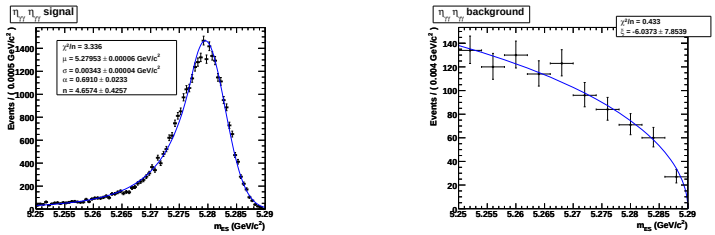

Figure A.80: $m_{\rm ES}$ PDFs: signal, Crystall Ball; continuum background, Argus function.

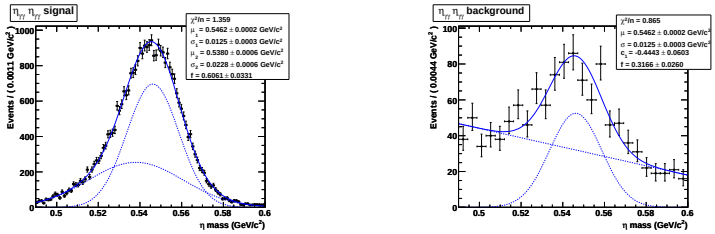

Figure A.81: η (1) mass PDFs: signal, double Gaussian; continuum background, MC Gaussian plus a Chebyshev linear polynomial.

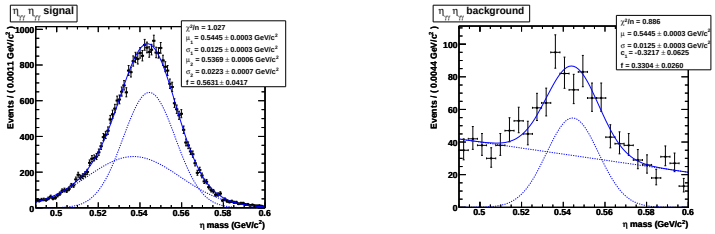

Figure A.82: η (2) mass PDFs: signal, double Gaussian; continuum background, MC Gaussian plus a Chebyshev linear polynomial.

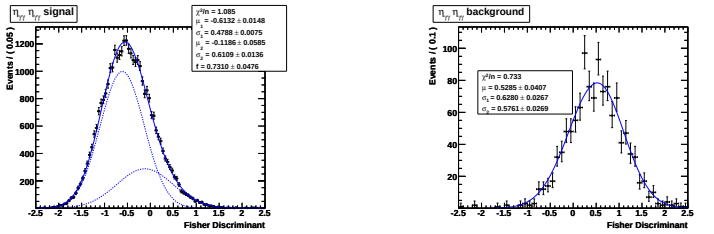

Figure A.83: $\mathcal{F}$ PDFs: signal, double Gaussian; continuum background, asymmetric Gaussian.

A.20 $B^0 \to \eta_{\gamma\gamma}\eta_{3\pi}$

	$m_{\rm ES}$	ΔE	$\eta_{\gamma\gamma}$	$\eta_{3\pi}$ mass	$\mathcal{F}$
$m_{\rm ES}$	1.000				
ΔE	0.031	1.000			
$\eta_{\gamma\gamma}$ mass	0.006	0.146	1.000		
$\eta_{3\pi}$ mass	0.010	0.033	1.000		
$\mathcal{F}$	-0.012	0.000	-0.001	-0.011	1.000

Table A.47: Correlation matrix for MC signal events.

	$m_{\rm ES}$	ΔE	$\eta_{\gamma\gamma}$ mass	$\eta_{3\pi}$ mass	$\mathcal{F}$
$m_{\rm ES}$	1.000				
ΔE	-0.052	1.000			
$\eta_{\gamma\gamma}$ mass	-0.037	-0.025	1.000		
$\eta_{3\pi}$ mass	0.090	-0.006	0.004	1.000	
$\mathcal{F}$	-0.021	-0.013	0.014	-0.013	1.000

Table A.48: Correlation matrix for on-peak side band data.

```
mES_xi_bg_float = -12.769 +/- 5.614
deltaE_c1_bg_float = -0.284 +/- 0.038
fisher_Mu1_bg_float = 0.448 +/- 0.034
fisher_SigmaL_bg_float = 0.567 +/- 0.023
fisher_SigmaR_bg_float = 0.601 +/- 0.022
etaMass0_Frac_bg_float = 0.295 +/- 0.021
etaMass0_c1_bg_float = -0.301 +/- 0.047
etaMass1_Frac_bg_float = 0.324 +/- 0.021
etaMass1_c1_bg_float = 0.419 +/- 0.044
etaMass1_c2_bg_float = -0.436 +/- 0.058
```

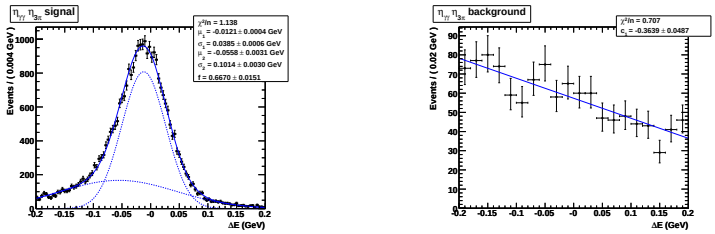

Figure A.84: ΔE PDFs: signal, double Gaussian; continuum background, Chebyshev linear polynomial.

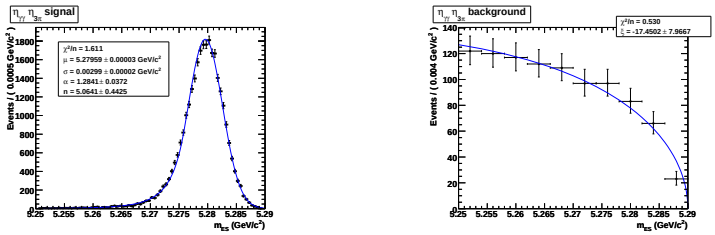

Figure A.85: $m_{\rm ES}$ PDFs: signal, Crystall Ball; continuum background, Argus function.

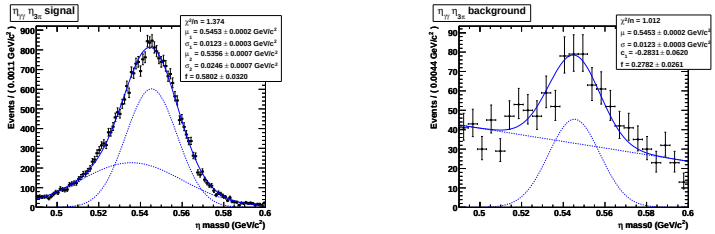

Figure A.86: $\eta_{\gamma\gamma}$ mass PDFs: signal, double Gaussian; continuum background, MC Gaussian plus a Chebyshev linear polynomial.

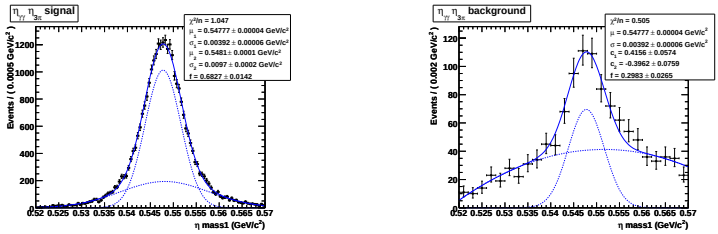

Figure A.87: $\eta_{3\pi}$ mass PDFs: signal, double Gaussian; continuum background, MC Gaussian plus a Chebyshev second order polynomial.

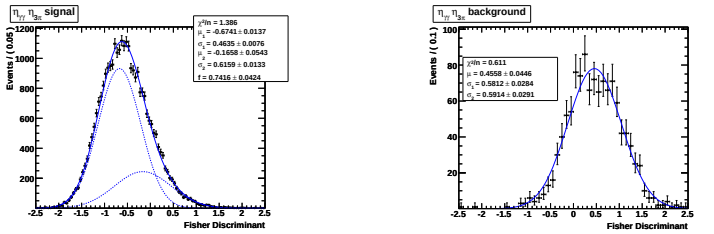

Figure A.88: $\mathcal{F}$ PDFs: signal, double Gaussian; continuum background, asymmetric Gaussian.

A.21 $B^0 \to \eta_{3\pi}\eta_{3\pi}$

	$m_{\rm ES}$	ΔE	η (1) mass	η (2) mass	$\mathcal{F}$
$m_{\rm ES}$	1.000				
ΔE	0.033	1.000			
η (1) mass	−0.001	0.013	1.000		
η (2) mass	0.002	0.033	0.002	1.000	
$\mathcal{F}$	−0.016	−0.009	−0.001	−0.004	1.000

Table A.49: Correlation matrix for MC signal events.

	$m_{\rm ES}$	ΔE	η (1) mass	η (2) mass	$\mathcal{F}$
$m_{\rm ES}$	1.000				
ΔE	−0.131	1.000			
η (1) mass	0.006	0.010	1.000		
η (2) mass	−0.056	−0.220	0.060	1.000	
$\mathcal{F}$	−0.019	−0.077	0.058	0.104	1.000

Table A.50: Correlation matrix for on-peak side band data.

```
mES_xi_bg_float = -11.074 +/- 11.474
deltaE_c1_bg_float = -0.317 +/- 0.080
fisher_Mu1_bg_float = 0.488 +/- 0.069
fisher_SigmaL_bg_float = 0.605 +/- 0.045
fisher_SigmaR_bg_float = 0.578 +/- 0.045
etaMass0_Frac_bg_float = 0.421 +/- 0.038
etaMass0_c1_bg_float = 0.552 +/- 0.110
etaMass1_Frac_bg_float = 0.400 +/- 0.037
etaMass1_c1_bg_float = 0.301 +/- 0.118
```

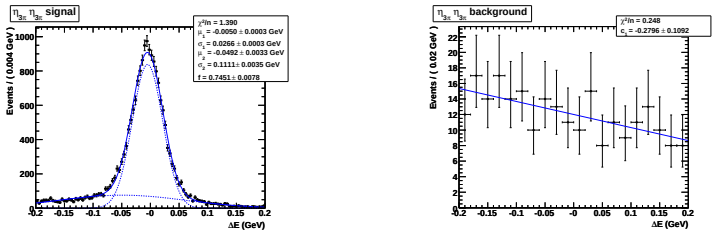

Figure A.89: ΔE PDFs: signal, double Gaussian; continuum background, Chebyshev linear polynomial.

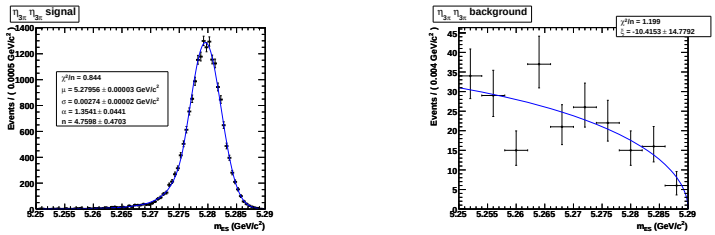

Figure A.90: $m_{\rm ES}$ PDFs: signal, Cristall Ball; continuum background, Argus function.

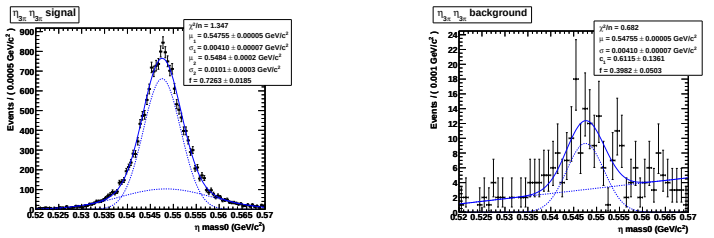

Figure A.91: η (1) mass PDFs: signal, double Gaussian; continuum background, MC Gaussian plus a Chebyshev linear polynomial.

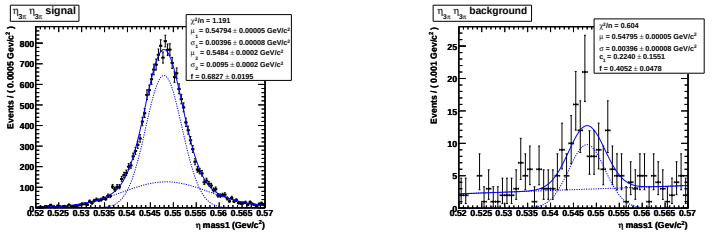

Figure A.92: η (2) mass PDFs: signal, double Gaussian; continuum background, MC Gaussian plus a Chebyshev linear polynomial.

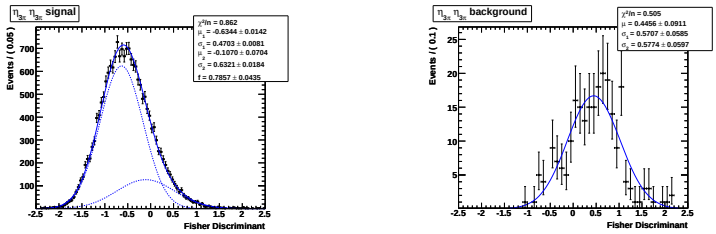

Figure A.93: $\mathcal{F}$ PDFs: signal, double Gaussian; continuum background, asymmetric Gaussian.

A.22 $B^0 \to \eta_{\gamma\gamma}\phi$

	$\mathcal{F}$	ΔE	$m_{\rm ES}$	η mass	$\mathcal{H}_\phi$
$\mathcal{F}$	1.000				
ΔE	-0.004	1.000			
$m_{\rm ES}$	0.011	-0.012	1.000		
η mass	0.007	0.179	0.021	1.000	
$\mathcal{H}_\phi$	0.003	0.007	0.006	-0.006	1.000

Table A.51: Correlation matrix for MC signal events.

	$\mathcal{F}$	ΔE	$m_{\rm ES}$	η mass	$\mathcal{H}_\phi$
$\mathcal{F}$	1.000				
ΔE	-0.028	1.000			
$m_{\rm ES}$	0.032	-0.002	1.000		
η mass	-0.019	-0.008	0.011	1.000	
$\mathcal{H}_\phi$	0.015	0.004	-0.027	-0.019	1.000

Table A.52: Correlation matrix for on-peak side band data.

```
deltaE_c1_bg_float = -0.326 +/- 0.023
mES_xi_bg_float = -14.704 +/- 3.527
fisher_Mu1_bg_float = 0.445 +/- 0.023
fisher_Sigma1_bg_float = 0.558 +/- 0.015
fisher_Sigma2_bg_float = 0.651 +/- 0.015
phiHel_c1_bg_float = -0.017 +/- 0.024
phiHel_c2_bg_float = 0.010 +/- 0.024
etaMass_Frac_bg_float = 0.279 +/- 0.020
etaMass_c1_bg_float = -0.319 +/- 0.029
etaMass_c2_bg_float = -0.078 +/- 0.048
```

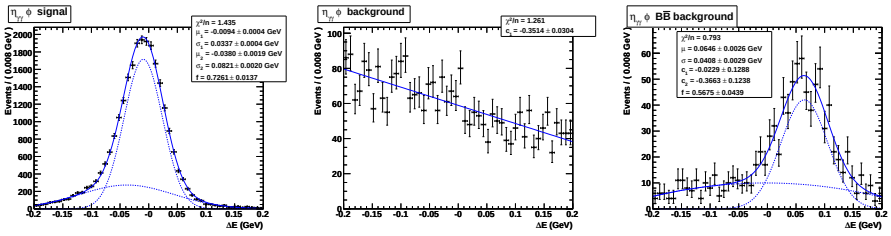

Figure A.94: ΔE PDFs: signal, double Gaussian; continuum background, Chebyshev linear polynomial; $B\overline{B}$ background, double Gaussian.

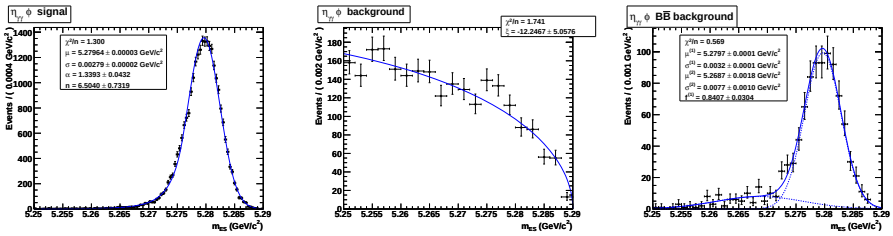

Figure A.95: $m_{\rm ES}$ PDFs: signal, Crystal Ball; continuum background, Argus function; $B\overline{B}$ background, double Gaussian.

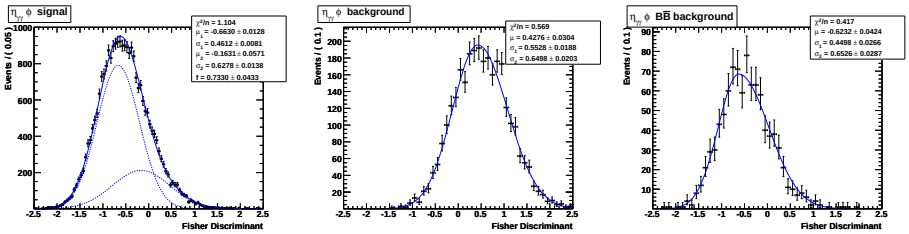

Figure A.96: $\mathcal{F}$ PDFs: signal, double Gaussian; continuum background, asymmetric Gaussian; $B\overline{B}$ background, asymmetric Gaussian.

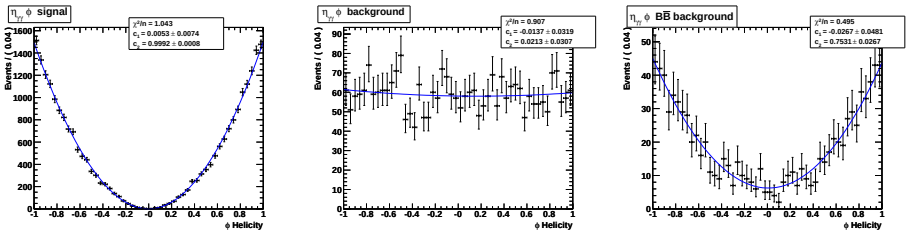

Figure A.97: $\mathcal{H}_\phi$ PDFs: signal Chebyshev 2^{rd} degree polynomial; continuum background, Chebyshev 2^{rd} degree polynomial; $B\overline{B}$ background, Chebyshev 2^{rd} degree polynomial.

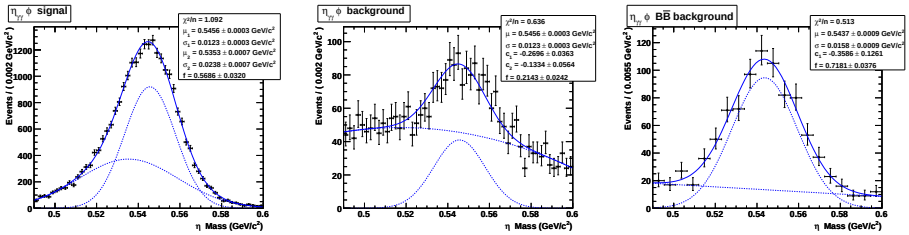

Figure A.98: η mass PDFs: signal, double Gaussian; continuum background, MC Gaussian plus Chebyshev 2^{rd} degree polynomial; $B\overline{B}$ background, Gaussian plus a Chebyshev linear polynomial.

A.23 $B^0 \to \eta_{3\pi}\phi$

	$\mathcal{F}$	ΔE	$m_{\rm ES}$	$\mathcal{H}_\phi$	η mass
$\mathcal{F}$	1.000				
ΔE	-0.019	1.000			
$m_{\rm ES}$	-0.027	0.013	1.000		
$\mathcal{H}_\phi$	0.013	-0.003	-0.001	1.000	
η mass	0.003	0.030	0.006	-0.007	1.000

Table A.53: Correlation matrix for MC signal events.

	$\mathcal{F}$	ΔE	$m_{\rm ES}$	$\mathcal{H}_\phi$	η mass
$\mathcal{F}$	1.000				
ΔE	-0.007	1.000			
$m_{\rm ES}$	0.023	-0.034	1.000		
$\mathcal{H}_\phi$	-0.018	0.019	0.005	1.000	
η mass	-0.047	-0.039	-0.023	0.036	1.000

Table A.54: Correlation matrix for on-peak side band data.

```
deltaE_c1_bg_float = -0.306 +/- 0.037
mES_xi_bg_float = -14.035 +/- 5.501
fisher_Mu1_bg_float = 0.486 +/- 0.032
fisher_Sigma1_bg_float = 0.587 +/- 0.021
fisher_Sigma2_bg_float = 0.591 +/- 0.021
phiHel_c1_bg_float = 0.010 +/- 0.038
phiHel_c2_bg_float = 0.059 +/- 0.036
etaMass_Frac_bg_float = 0.274 +/- 0.020
etaMass_c1_bg_float = 0.412 +/- 0.042
etaMass_c2_bg_float = -0.443 +/- 0.053
```

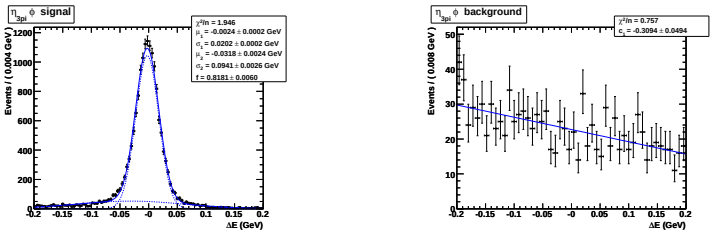

Figure A.99: ΔE PDFs: signal, double Gaussian; continuum background, Chebyshev linear polynomial.

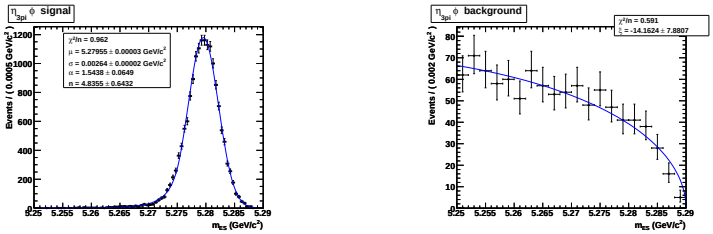

Figure A.100: $m_{\rm ES}$ PDFs: signal, Crystal Ball; continuum background, Argus function.

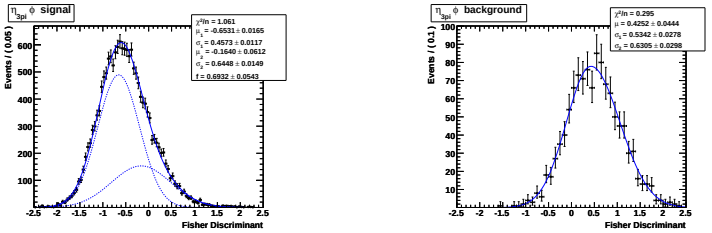

Figure A.101: $\mathcal{F}$ PDFs: signal, double Gaussian; continuum background, asymmetric Gaussian.

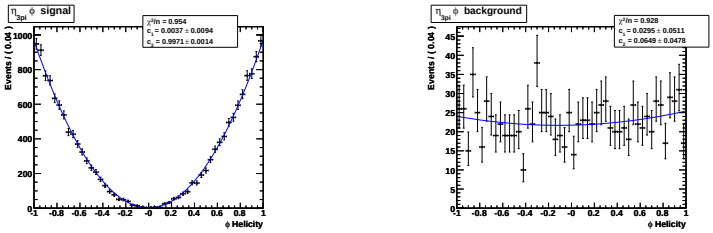

Figure A.102: $\mathcal{H}_\phi$ PDFs: signal, Chebyshev 2^{rd} degree polynomial; continuum background, Chebyshev 2^{rd} degree polynomial.

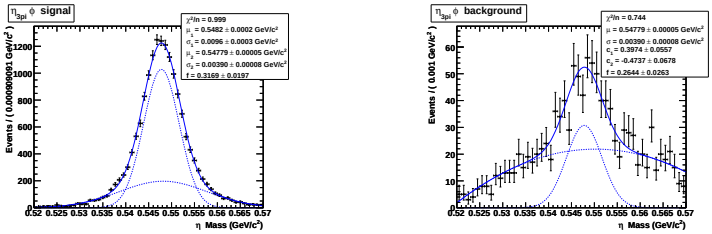

Figure A.103: η mass PDFs: signal, double Gaussian; continuum background, MC Gaussian plus Chebyshev 2^{rd} degree polynomial.

A.24 $B^0 \to \eta'_{\eta\pi\pi}\phi$

	$\mathcal{F}$	ΔE	$m_{\rm ES}$	η' mass	$\mathcal{H}_\phi$	η mass
$\mathcal{F}$	1.000					
ΔE	-0.013	1.000				
$m_{\rm ES}$	-0.012	0.044	1.000			
η' mass	0.001	0.002	-0.020	1.000		
$\mathcal{H}_\phi$	0.002	-0.007	-0.004	-0.007	1.000	
η mass	0.008	0.063	-0.007	0.013	-0.011	1.000

Table A.55: Correlation matrix for MC signal events.

	$\mathcal{F}$	ΔE	$m_{\rm ES}$	η' mass	$\mathcal{H}_\phi$	η mass
$\mathcal{F}$	1.000					
ΔE	0.024	1.000				
$m_{\rm ES}$	-0.001	-0.043	1.000			
η' mass	-0.054	0.049	0.035	1.000		
$\mathcal{H}_\phi$	0.028	0.006	-0.002	0.088	1.000	
η mass	-0.016	0.062	0.036	0.004	-0.079	1.000

Table A.56: Correlation matrix for on-peak side band data.

```
deltaE_c1_bg_float = -0.291 +/- 0.049
mES_xi_bg_float = -13.930 +/- 7.238
fisher_Mu1_bg_float = 0.421 +/- 0.044
fisher_Sigma1_bg_float = 0.608 +/- 0.029
fisher_Sigma2_bg_float = 0.599 +/- 0.029
phiHel_c1_bg_float = -0.003 +/- 0.051
phiHel_c2_bg_float = 0.076 +/- 0.046
etaMass_Frac_bg_float = 0.203 +/- 0.026
etaMass_c1_bg_float = -0.150 +/- 0.057
etapMass_Frac_bg_float = 0.152 +/- 0.024
etapMass_c1_bg_float = 0.010 +/- 0.048
etapMass_c2_bg_float = -0.829 +/- 0.060
```

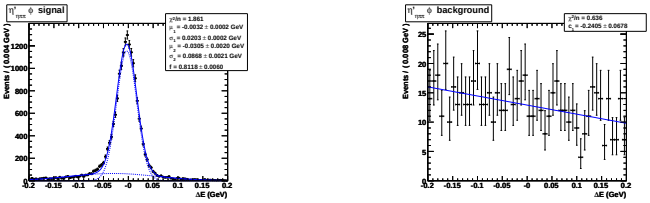

Figure A.104: ΔE PDFs: signal, double Gaussian; continuum background, Chebyshev linear polynomial.

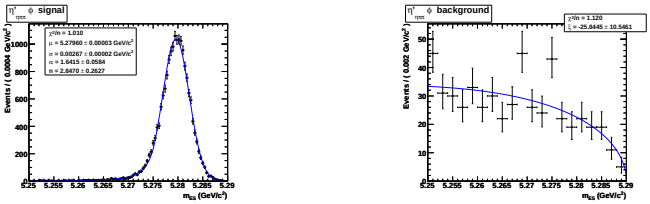

Figure A.105: $m_{\rm ES}$ PDFs: signal, Crystal Ball; continuum background, Argus function.

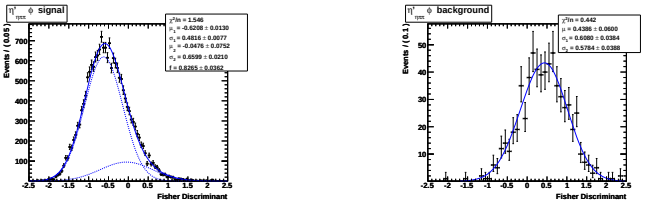

Figure A.106: $\mathcal{F}$ PDFs: signal, double Gaussian; continuum background, asymmetric Gaussian.

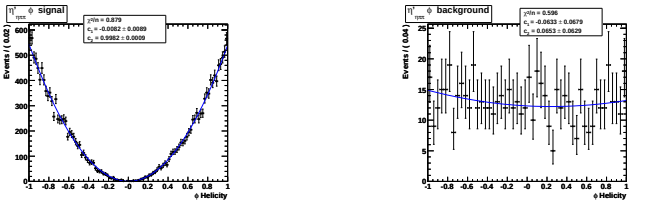

Figure A.107: $\mathcal{H}_\phi$ PDFs: signal, Chebyshev 2^{rd} degree polynomial; continuum background, Chebyshev 2^{rd} degree polynomial.

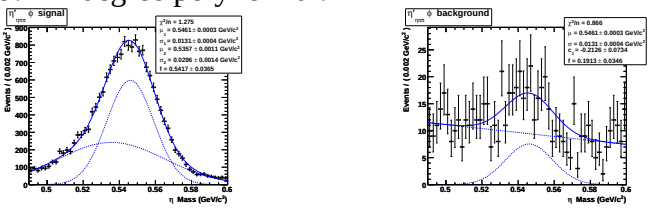

Figure A.108: η mass PDFs: signal, double Gaussian; continuum background, MC Gaussian plus Chebyshev 1^{rd} degree polynomial.

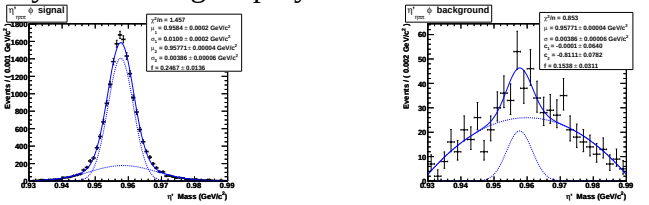

Figure A.109: η' mass PDFs: signal, double Gaussian; continuum background, MC Gaussian plus Chebyshev 2^{rd} degree polynomial.

A.25 $B^0 \to \eta'_{\rho\gamma}\phi$

	$\mathcal{F}$	ΔE	$m_{\rm ES}$	η' mass	$\mathcal{H}_\phi$	$\mathcal{H}_\rho$
$\mathcal{F}$	1.000					
ΔE	-0.024	1.000				
$m_{\rm ES}$	-0.027	-0.024	1.000			
η' mass	-0.006	0.046	0.021	1.000		
$\mathcal{H}_\phi$	-0.003	-0.001	-0.003	-0.003	1.000	
$\mathcal{H}_\rho$	0.004	-0.015	0.004	-0.011	-0.006	1.000

Table A.57: Correlation matrix for MC signal events.

	$\mathcal{F}$	ΔE	$m_{\rm ES}$	η' mass	$\mathcal{H}_\phi$	$\mathcal{H}_\rho$
$\mathcal{F}$	1.000					
ΔE	-0.004	1.000				
$m_{\rm ES}$	0.009	-0.005	1.000			
η' mass	-0.022	-0.030	-0.001	1.000		
$\mathcal{H}_\phi$	0.016	-0.022	0.007	0.010	1.000	
$\mathcal{H}_\rho$	-0.006	-0.011	0.001	-0.004	0.016	1.000

Table A.58: Correlation matrix for on-peak side band data.

```
deltaE_c1_bg_float = -0.280 +/- 0.013
mES_xi_bg_float = -15.585 +/- 1.919
fisher_Mu1_bg_float = 0.142 +/- 0.012
fisher_Sigma1_bg_float = 0.546 +/- 0.007
fisher_Sigma2_bg_float = 0.638 +/- 0.008
rho0Hel_c1_bg_float = 0.000 +/- 0.007
phiHel_c1_bg_float = -0.034 +/- 0.013
phiHel_c2_bg_float = 0.092 +/- 0.012
etapMass_c1_bg_float = 0.103 +/- 0.013
etapMass_c2_bg_float = -0.153 +/- 0.014
```

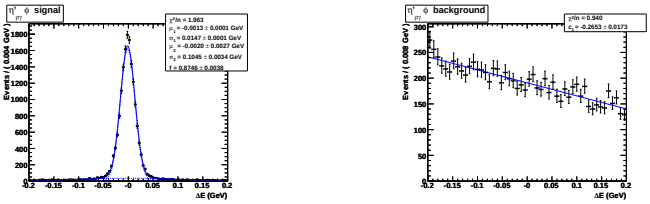

Figure A.110: ΔE PDFs: signal, double Gaussian; continuum background, Chebyshev linear polynomial.

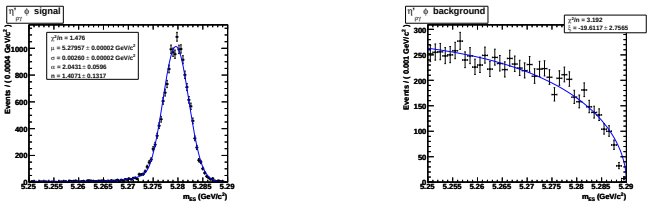

Figure A.111: $m_{\rm ES}$ PDFs: signal, Crystal Ball; continuum background, Argus function.

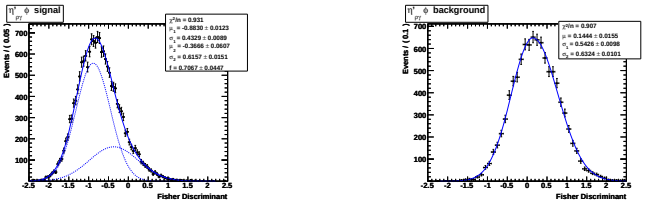

Figure A.112: $\mathcal{F}$ PDFs: signal, double Gaussian; continuum background, asymmetric Gaussian.

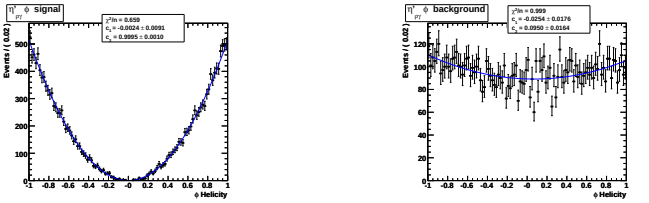

Figure A.113: $\mathcal{H}_\phi$ PDFs: signal, Chebyshev 2^{rd} degree polynomial; continuum background, Chebyshev 2^{rd} degree polynomial.

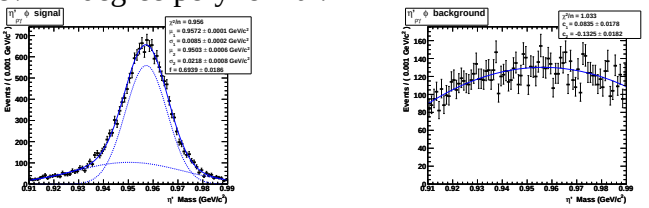

Figure A.114: η' mass PDFs: double Gaussian; continuum background, Chebyshev 2^{rd} degree polynomial.

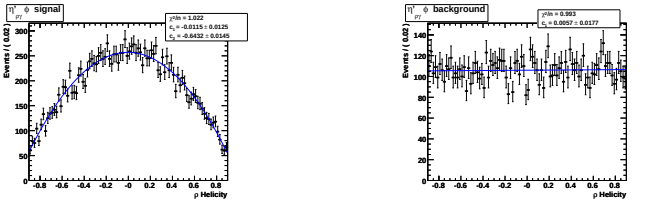

Figure A.115: $\mathcal{H}_\rho$ PDFs: Chebyshev 2^{rd} degree polynomial; continuum background, Chebyshev 1^{rd} degree polynomial.

Appendix B

PDF libraries for TD CP-asymmetries measurements

We show for each decay modes the signal, continuum background and $B\bar{B}$ background PDFs used in ML fits. We show also tables of the correlations among fit parameters. Signal PDFs are determined from MC signal events. For background continuum PDFs we have used on-peak sidebands. For $B\bar{B}$ background PDFs we have used MC events.

B.1 $B^0 \to \eta'_{\eta(\gamma\gamma)\pi\pi} K^0_{S+-}$

	$\mathcal{F}$	ΔE	Δt	$\sigma_{\Delta t}$	$m_{\rm ES}$
$\mathcal{F}$	1.000				
ΔE	-0.014	1.000			
Δt	-0.007	0.007	1.000		
$\sigma_{\Delta t}$	0.019	0.001	-0.018	1.000	
$m_{\rm ES}$	-0.013	0.021	-0.003	-0.014	1.000

Table B.1: Correlation matrix for MC signal $\eta'_{\eta(\gamma\gamma)\pi\pi} K^0_{S+-}$.

	$\mathcal{F}$	ΔE	Δt	$\sigma_{\Delta t}$	$m_{\rm ES}$
$\mathcal{F}$	1.000				
ΔE	0.050	1.000			
Δt	0.087	-0.002	1.000		
$\sigma_{\Delta t}$	-0.005	0.141	-0.025	1.000	
$m_{\rm ES}$	0.027	-0.021	0.021	0.015	1.000

Table B.2: Correlation matrix for on-peak side band data $\eta'_{\eta(\gamma\gamma)\pi\pi} K^0_{S+-}$.

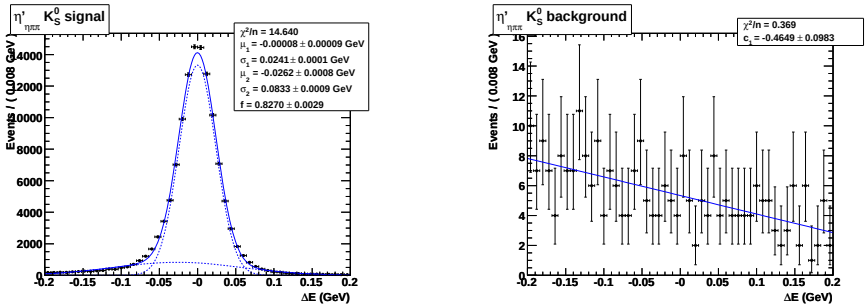

Figure B.1: Signal ΔE PDF (left): double Gaussian; Continuum Background ΔE PDF (right): linear polynomial.

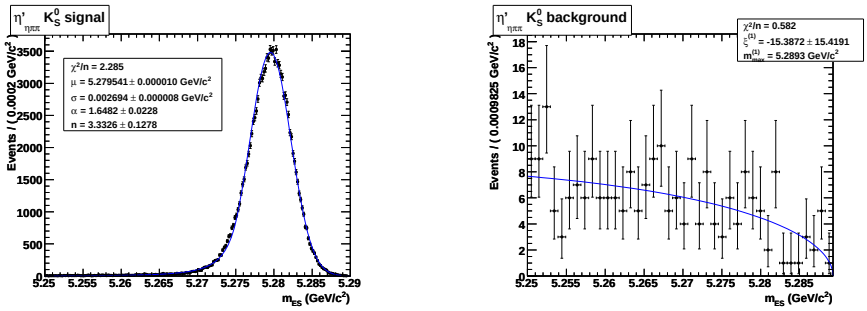

Figure B.2: Signal $m_{\rm ES}$ PDF (left): Crystal Ball; Continuum background $m_{\rm ES}$ PDF (right): Argus function.

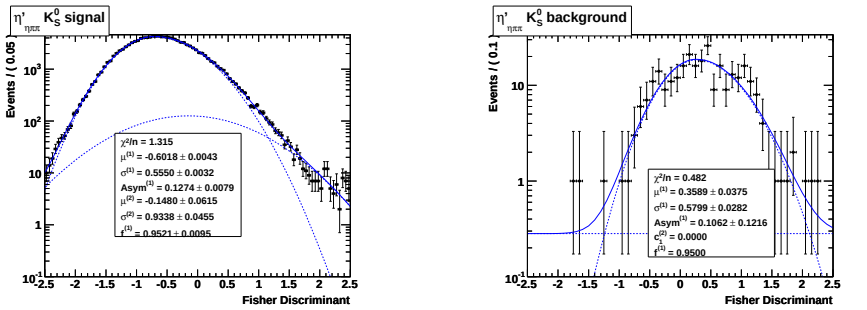

Figure B.3: Signal $\mathcal{F}$ Fisher PDF (left): asymetric Gaussian plus Gaussian; Continuum background $\mathcal{F}$ Fisher PDF (right): asymetric Gaussian plus linear polynomial.

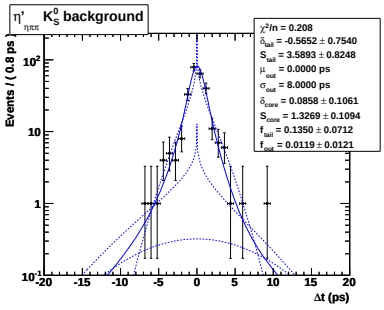

Figure B.4: Δt continuum background PDF: triple Gaussian where we use $\Delta t/\sigma_{\Delta t}$ as in signal Δt resolution model.

B.2 $B^0 \to \eta'_{\rho\gamma} K^0_{S+-}$

	$\mathcal{F}$	ΔE	Δt	$\sigma_{\Delta t}$	$m_{\rm ES}$
$\mathcal{F}$	1.000				
ΔE	-0.024	1.000			
Δt	-0.004	-0.003	1.000		
$\sigma_{\Delta t}$	0.010	-0.003	-0.019	1.000	
$m_{\rm ES}$	-0.013	0.021	-0.003	-0.014	1.000

Table B.3: Correlation matrix for MC signal $\eta'_{\rho\gamma} K^0_{S+-}$.

	$\mathcal{F}$	ΔE	Δt	$\sigma_{\Delta t}$	$m_{\rm ES}$
$\mathcal{F}$	1.000				
ΔE	-0.017	1.000			
Δt	0.036	0.035	1.000		
$\sigma_{\Delta t}$	-0.069	0.017	0.080	1.000	
$m_{\rm ES}$	0.013	-0.004	0.017	-0.012	1.000

Table B.4: Correlation matrix for on-peak data $\eta'_{\rho\gamma} K^0_{S+-}$.

	$\mathcal{F}$	ΔE	Δt	$\sigma_{\Delta t}$	$m_{\rm ES}$
$\mathcal{F}$	1.000				
ΔE	-0.098	1.000			
Δt	0.004	0.0019	1.000		
$\sigma_{\Delta t}$	0.060	0.004	0.069	1.000	
$m_{\rm ES}$	-0.044	0.091	-0.041	0.005	1.000

Table B.5: Correlation matrix for $B\overline{B}$ background $\eta'_{\rho\gamma} K^0_{S+-}$.

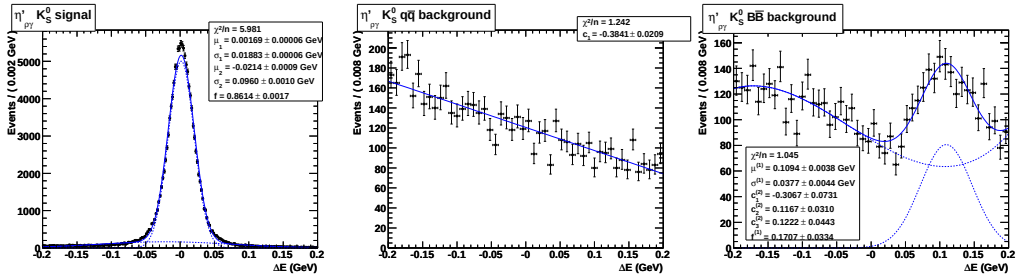

Figure B.5: Signal ΔE PDF (left): double Gaussian; Continuum Background ΔE PDF (center): linear polynomial; $B\overline{B}$ Background ΔE PDF (right): Gaussian plus third order polynomial.

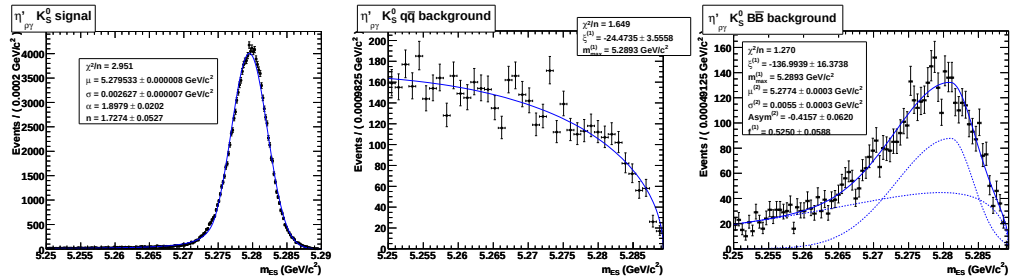

Figure B.6: Signal $m_{\rm ES}$ PDF (left): Crystal Ball; Continuum background $m_{\rm ES}$ PDF (center): Argus function; $B\overline{B}$ Background $m_{\rm ES}$ PDF (right): asymetric Gaussian plus Argus function.

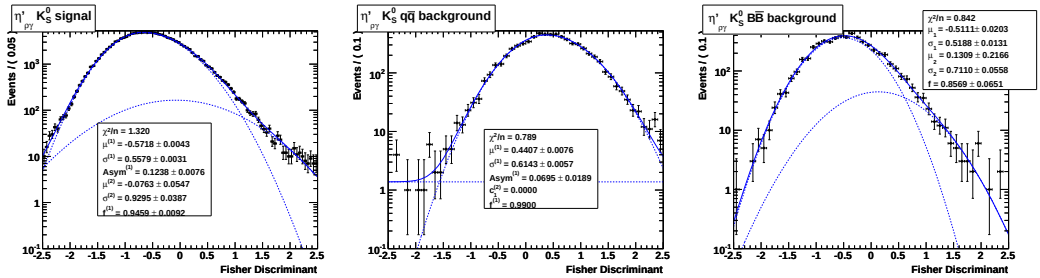

Figure B.7: Signal $\mathcal{F}$ Fisher PDF (left): asymetric Gaussian plus Gaussian; Continuum Background $\mathcal{F}$ Fisher PDF (center): asymetric Gaussian plus linear polynomial; $B\overline{B}$ Background $\mathcal{F}$ Fisher PDF (right): double Gaussian.

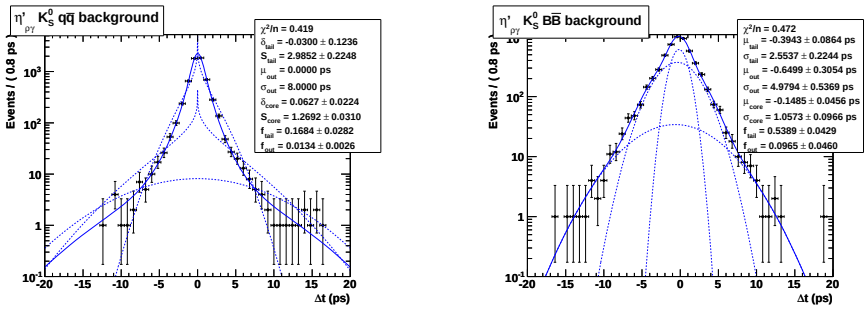

Figure B.8: Δt continuum background PDF (left): triple Gaussian where we use $\Delta t/\sigma_{\Delta t}$ as in signal Δt resolution model;Δt $B\overline{B}$ background PDF (right): triple Gaussian.

B.3 $B^0 \to \eta'_{\eta(3\pi)\pi\pi} K^0_{S+-}$

	$\mathcal{F}$	ΔE	Δt	$\sigma_{\Delta t}$	$m_{\rm ES}$
$\mathcal{F}$	1.000				
ΔE	-0.050	1.000			
Δt	-0.006	0.013	1.000		
$\sigma_{\Delta t}$	0.006	-0.018	-0.015	1.000	
$m_{\rm ES}$	-0.034	0.130	-0.012	-0.038	1.000

Table B.6: Correlation matrix for MC signal $\eta'_{\eta(3\pi)\pi\pi} K^0_{S+-}$.

	$\mathcal{F}$	ΔE	Δt	$\sigma_{\Delta t}$	$m_{\rm ES}$
$\mathcal{F}$	1.000				
ΔE	-0.021	1.000			
Δt	-0.092	0.094	1.000		
$\sigma_{\Delta t}$	-0.130	0.422	-0.015	1.000	
$m_{\rm ES}$	0.178	0.027	-0.121	-0.029	1.000

Table B.7: Correlation matrix for on-peak data $\eta'_{\eta(3\pi)\pi\pi} K^0_{S+-}$.

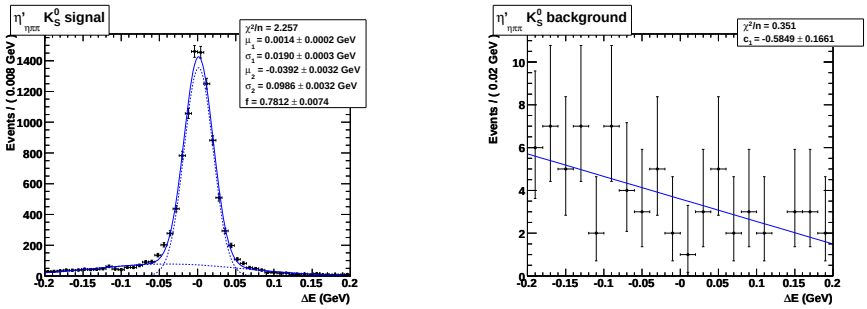

Figure B.9: Signal ΔE PDF (left): double Gaussian; Continuum Background ΔE PDF (right): linear polynomial

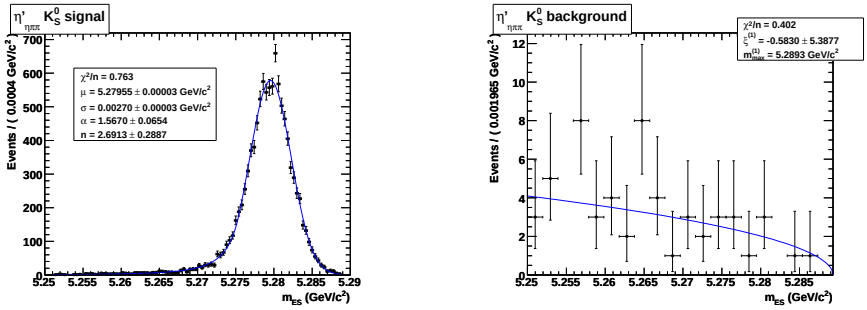

Figure B.10: Signal $m_{\rm ES}$ PDF (left): Crystal Ball; Continuum background $m_{\rm ES}$ PDF (right): Argus function

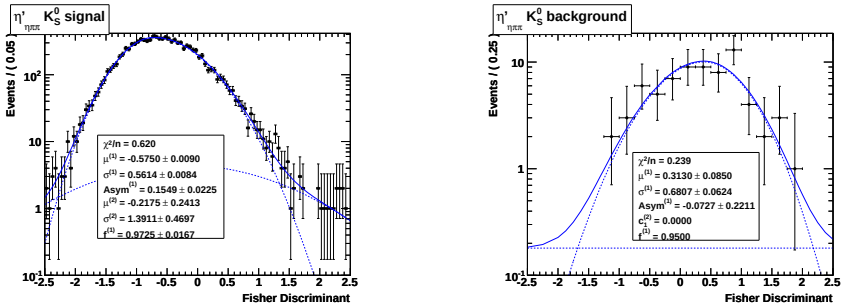

Figure B.11: Signal $\mathcal{F}$ Fisher PDF (left): Gaussian plus asymetric Gaussian; Continuum background $\mathcal{F}$ Fisher PDF (right): asymetric Gaussian plus linear polynomial.

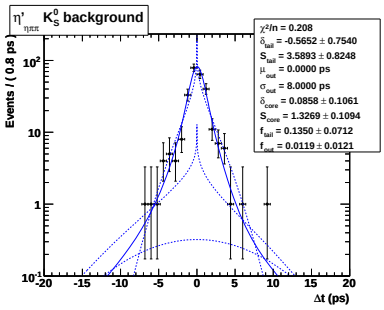

Figure B.12: Δt continuum background PDF: triple Gaussian where we use $\Delta t/\sigma_{\Delta t}$ as in signal Δt resolution model.

B.4 $B^0 \to \eta'_{\eta\pi\pi} K^0_{S00}$

	$\mathcal{F}$	ΔE	Δt	$\sigma_{\Delta t}$	$m_{\rm ES}$
$\mathcal{F}$	1.000				
ΔE	-0.010	1.000			
Δt	-0.006	0.004	1.000		
$\sigma_{\Delta t}$	0.028	-0.012	-0.016	1.000	
$m_{\rm ES}$	-0.017	0.081	0.006	-0.013	1.000

Table B.8: Correlation matrix for MC signal $\eta'_{\eta\pi\pi} K^0_{S00}$.

	$\mathcal{F}$	ΔE	Δt	$\sigma_{\Delta t}$	$m_{\rm ES}$
$\mathcal{F}$	1.000				
ΔE	-0.035	1.000			
Δt	0.127	0.051	1.000		
$\sigma_{\Delta t}$	-0.127	-0.055	0.092	1.000	
$m_{\rm ES}$	-0.084	-0.020	-0.033	0.034	1.000

Table B.9: Correlation matrix for on-peak data $\eta'_{\eta\pi\pi} K^0_{S00}$.

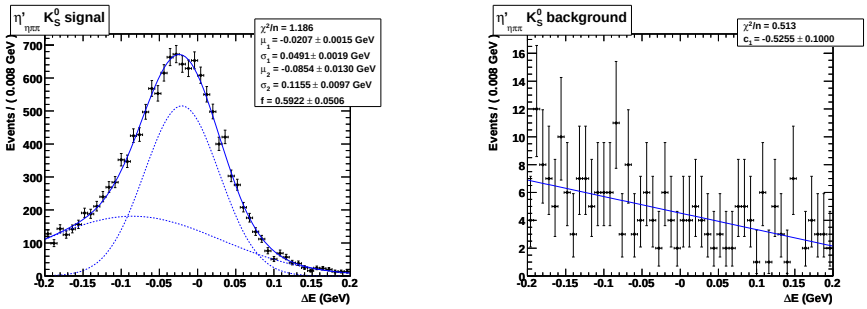

Figure B.13: Signal ΔE PDF (left): double Gaussian; Continuum Background ΔE PDF (right): linear polynomial.

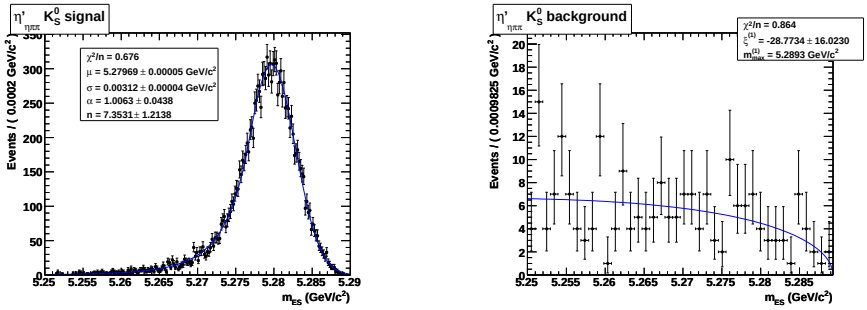

Figure B.14: Signal $m_{\rm ES}$ PDF (left): Crystal Ball; Continuum background $m_{\rm ES}$ PDF (right): Argus function.

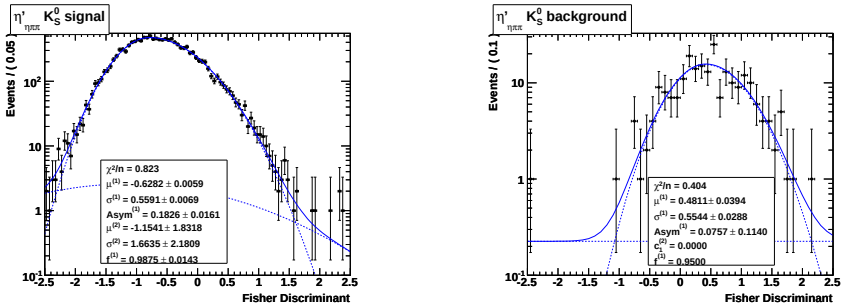

Figure B.15: Signal $\mathcal{F}$ Fisher PDF (left): Gaussian plus asymetric Gaussian; Continuum background $\mathcal{F}$ Fisher PDF (right): asymetric Gaussian plus linear polynomial.

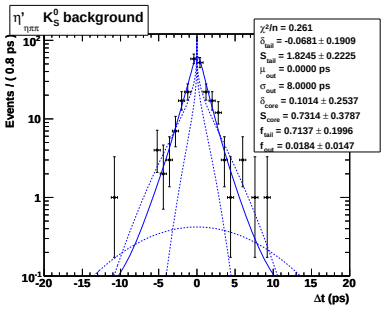

Figure B.16: Δt continuum background PDF: triple Gaussian where we use $\Delta t/\sigma_{\Delta t}$ as in signal Δt resolution model.

B.5 $B^0 \to \eta'_{\rho\gamma} K^0_{S00}$

	$\mathcal{F}$	ΔE	Δt	$\sigma_{\Delta t}$	$m_{\rm ES}$
$\mathcal{F}$	1.000				
ΔE	-0.019	1.000			
Δt	-0.002	-0.025	1.000		
$\sigma_{\Delta t}$	0.018	-0.037	-0.021	1.000	
$m_{\rm ES}$	-0.023	0.057	-0.002	-0.023	1.000

Table B.10: Correlation matrix for MC signal $\eta'_{\rho\gamma} K^0_{S00}$.

	$\mathcal{F}$	ΔE	Δt	$\sigma_{\Delta t}$	$m_{\rm ES}$
$\mathcal{F}$	1.000				
ΔE	-0.040	1.000			
Δt	0.006	0.020	1.000		
$\sigma_{\Delta t}$	-0.065	0.009	0.049	1.000	
$m_{\rm ES}$	0.001	0.005	0.017	-0.022	1.000

Table B.11: Correlation matrix for on-peak data $\eta'_{\rho\gamma} K^0_{S00}$.

	$\mathcal{F}$	ΔE	Δt	$\sigma_{\Delta t}$	$m_{\rm ES}$
$\mathcal{F}$	1.000				
ΔE	-0.019	1.000			
Δt	-0.032	-0.018	1.000		
$\sigma_{\Delta t}$	-0.003	-0.064	0.007	1.000	
$m_{\rm ES}$	0.018	0.002	0.018	0.033	1.000

Table B.12: Correlation matrix for $B\overline{B}$ background $\eta'_{\rho\gamma} K^0_{S00}$.

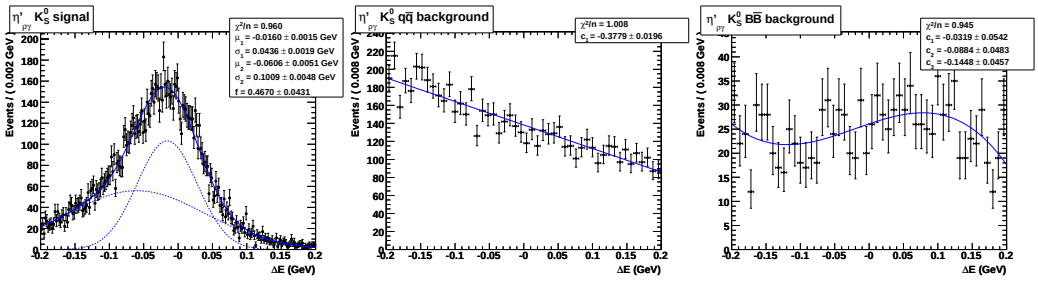

Figure B.17: Signal ΔE PDF (left): double Gaussian; Continuum Background ΔE PDF (center): linear polynomial; $B\overline{B}$ Background ΔE PDF (right): third order polynomial.

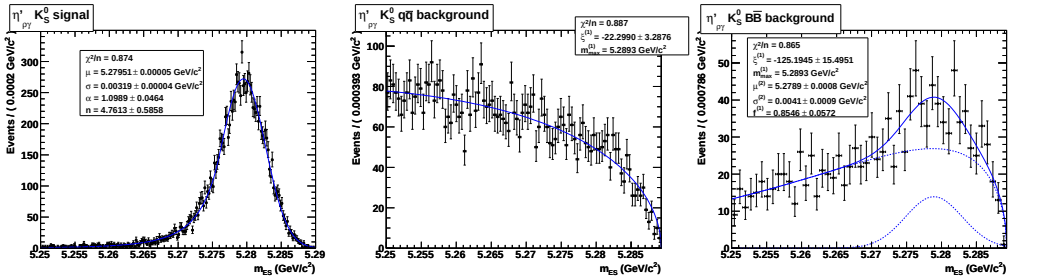

Figure B.18: Signal $m_{\rm ES}$ PDF (left): Crystal Ball; Continuum background $m_{\rm ES}$ PDF (center): Argus function; $B\overline{B}$ Background $m_{\rm ES}$ PDF (right): Gaussian plus Argus function.

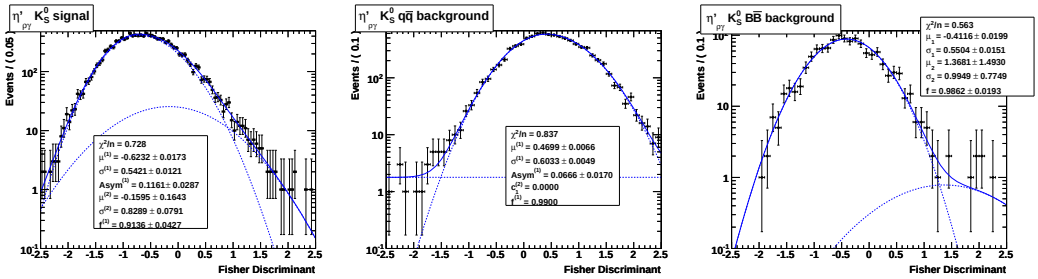

Figure B.19: Signal $\mathcal{F}$ Fisher PDF (left): asymetric Gaussian plus Gaussian; Continuum Background $\mathcal{F}$ Fisher PDF (center): asymetric Gaussian plus linear polynomial; $B\overline{B}$ Background $\mathcal{F}$ Fisher PDF (right): double Gaussian.

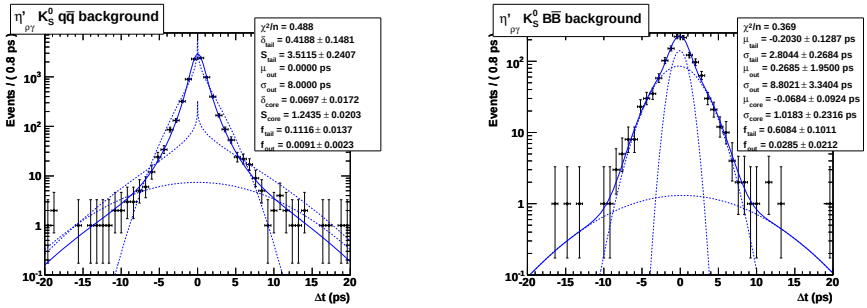

Figure B.20: Δt continuum background PDF (left): triple Gaussian where we use $\Delta t/\sigma_{\Delta t}$ as in signal Δt resolution model;Δt $B\overline{B}$ background PDF (right): triple Gaussian.

B.6 $B^{\pm} \to \eta'_{\eta(\gamma\gamma)\pi\pi} K^{\pm}$

	$\mathcal{F}$	ΔE	Δt	$\sigma_{\Delta t}$	$m_{\rm ES}$
$\mathcal{F}$	1.000				
ΔE	-0.003	1.000			
Δt	0.001	0.008	1.000		
$\sigma_{\Delta t}$	-0.005	-0.005	-0.017	1.000	
$m_{\rm ES}$	-0.007	-0.018	0.005	-0.009	1.000

Table B.13: Correlation matrix for MC signal $\eta'_{\eta(\gamma\gamma)\pi\pi} K^{\pm}$.

	$\mathcal{F}$	ΔE	Δt	$\sigma_{\Delta t}$	$m_{\rm ES}$
$\mathcal{F}$	1.000				
ΔE	-0.025	1.000			
Δt	-0.028	0.120	1.000		
$\sigma_{\Delta t}$	-0.105	0.007	-0.047	1.000	
$m_{\rm ES}$	-0.075	-0.020	-0.044	0.004	1.000

Table B.14: Correlation matrix for on-peak data $\eta'_{\eta(\gamma\gamma)\pi\pi} K^{\pm}$.

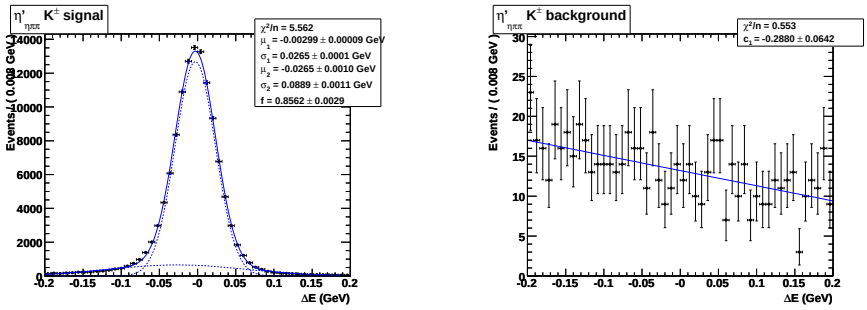

Figure B.21: Signal ΔE PDF (left): double Gaussian; Continuum Background ΔE PDF (right): linear polynomial.

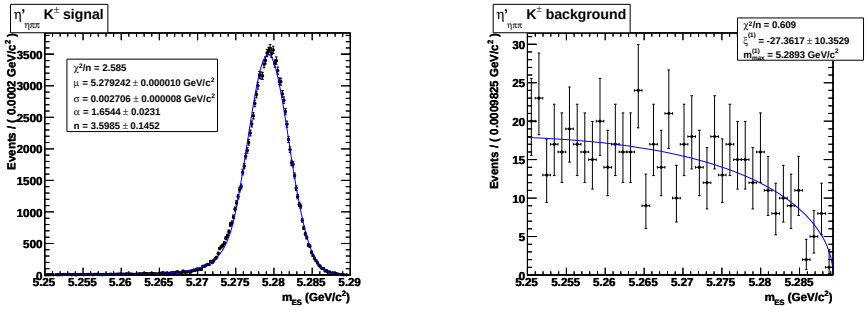

Figure B.22: Signal $m_{\rm ES}$ PDF (left): Crystal Ball; Continuum background $m_{\rm ES}$ PDF (right): Argus function.

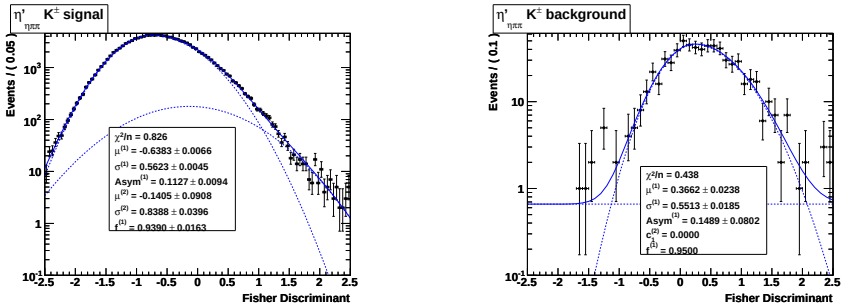

Figure B.23: Signal $\mathcal{F}$ Fisher PDF (left): asymetric Gaussian plus Gaussian; Continuum background $\mathcal{F}$ Fisher PDF (right): asymetric Gaussian plus linear polynomial.

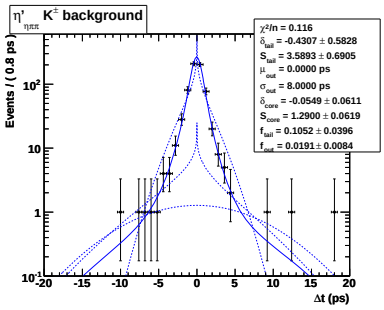

Figure B.24: Δt continuum background PDF: triple Gaussian where we use $\Delta t/\sigma_{\Delta t}$ as in signal Δt resolution model.

B.7 $B^{\pm} \to \eta'_{\rho\gamma} K^{\pm}$

	$\mathcal{F}$	ΔE	Δt	$\sigma_{\Delta t}$	$m_{\rm ES}$
$\mathcal{F}$	1.000				
ΔE	-0.015	1.000			
Δt	-0.000	0.001	1.000		
$\sigma_{\Delta t}$	-0.004	-0.017	-0.017	1.000	
$m_{\rm ES}$	-0.028	0.059	-0.004	-0.012	1.000

Table B.15: Correlation matrix for MC signal $\eta'_{\rho\gamma} K^{\pm}$.

	$\mathcal{F}$	ΔE	Δt	$\sigma_{\Delta t}$	$m_{\rm ES}$
$\mathcal{F}$	1.000				
ΔE	-0.034	1.000			
Δt	0.007	0.052	1.000		
$\sigma_{\Delta t}$	-0.087	0.033	0.029	1.000	
$m_{\rm ES}$	0.001	-0.005	-0.004	-0.020	1.000

Table B.16: Correlation matrix for on-peak data $\eta'_{\rho\gamma} K^{\pm}$.

	$\mathcal{F}$	ΔE	Δt	$\sigma_{\Delta t}$	$m_{\rm ES}$
$\mathcal{F}$	1.000				
ΔE	-0.021	1.000			
Δt	0.008	0.017	1.000		
$\sigma_{\Delta t}$	-0.002	-0.019	-0.029	1.000	
$m_{\rm ES}$	-0.044	0.063	-0.008	-0.023	1.000

Table B.17: Correlation matrix for $B\overline{B}$ background $\eta'_{\rho\gamma} K^{\pm}$.

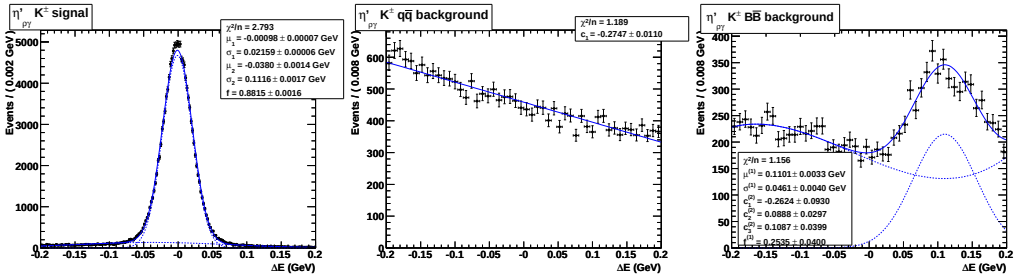

Figure B.25: Signal ΔE PDF (left): double Gaussian; Continuum Background ΔE PDF (center): linear polynomial; $B\overline{B}$ Background ΔE PDF (right): Gaussian plus third order polynomial.

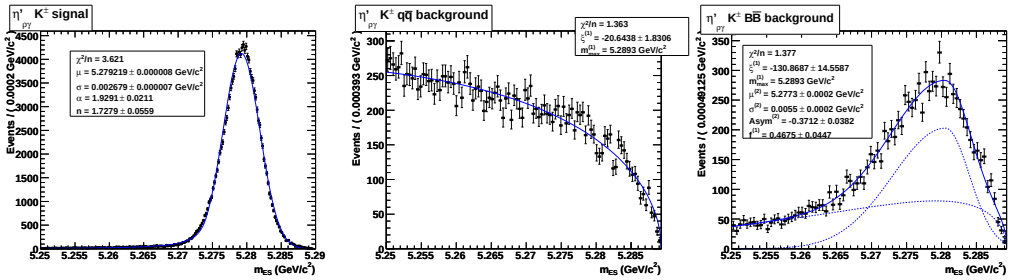

Figure B.26: Signal $m_{\rm ES}$ PDF (left): Crystal Ball; Continuum background $m_{\rm ES}$ PDF (center): Argus function; $B\overline{B}$ Background $m_{\rm ES}$ PDF (right): asymetric Gaussian plus Argus funtion.

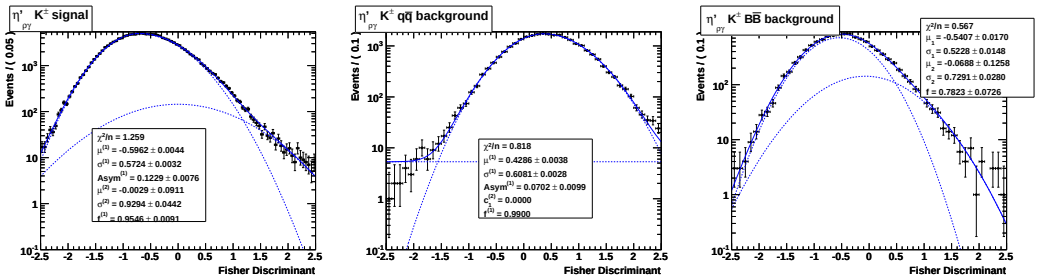

Figure B.27: Signal $\mathcal{F}$ Fisher PDF (left): asymetric Gaussian plus Gaussian; Continuum Background $\mathcal{F}$ Fisher PDF (center): asymetric Gaussian plus linear polynomial; $B\overline{B}$ Background $\mathcal{F}$ Fisher PDF (right): double Gaussian.

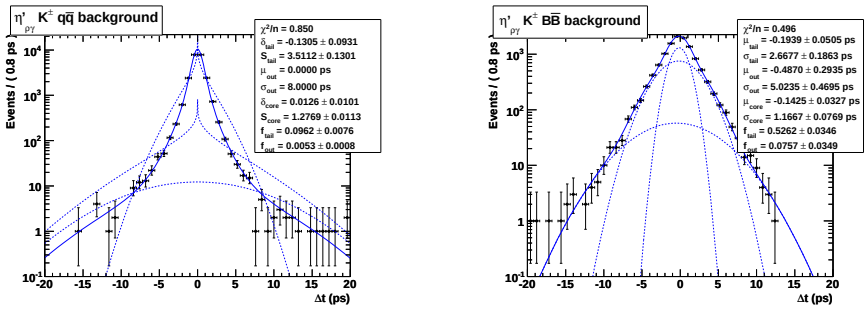

Figure B.28: Δt continuum background PDF (left): triple Gaussian where we use $\Delta t/\sigma_{\Delta t}$ as in signal Δt resolution model;Δt $B\overline{B}$ background PDF (right): triple Gaussian.

B.8 $B^{\pm} \to \eta'_{\eta(3\pi)\pi\pi} K^{\pm}$

	$\mathcal{F}$	ΔE	Δt	$\sigma_{\Delta t}$	$m_{\rm ES}$
$\mathcal{F}$	1.000				
ΔE	-0.036	1.000			
Δt	-0.006	-0.006	1.000		
$\sigma_{\Delta t}$	-0.004	0.001	-0.003	1.000	
$m_{\rm ES}$	-0.035	0.071	-0.001	-0.013	1.000

Table B.18: Correlation matrix for MC signal $\eta'_{\eta(3\pi)\pi\pi} K^{\pm}$.

	$\mathcal{F}$	ΔE	Δt	$\sigma_{\Delta t}$	$m_{\rm ES}$
$\mathcal{F}$	1.000				
ΔE	0.073	1.000			
Δt	0.027	0.145	1.000		
$\sigma_{\Delta t}$	-0.216	-0.013	-0.065	1.000	
$m_{\rm ES}$	-0.080	0.096	0.014	-0.067	1.000

Table B.19: Correlation matrix for on-peak data $\eta'_{\eta(3\pi)\pi\pi} K^{\pm}$.

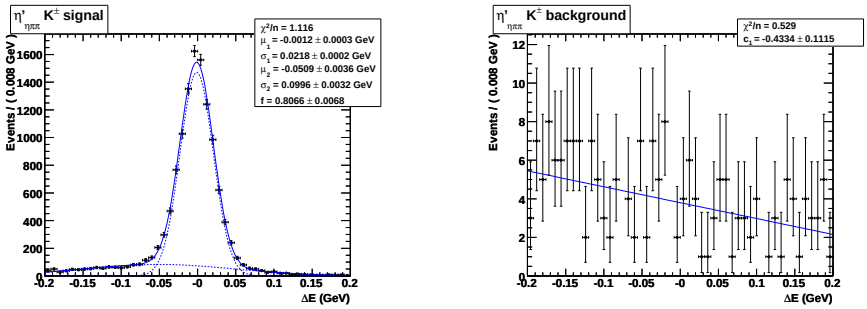

Figure B.29: Signal ΔE PDF (left): double Gaussian; Continuum Background ΔE PDF (right): linear polynomial.

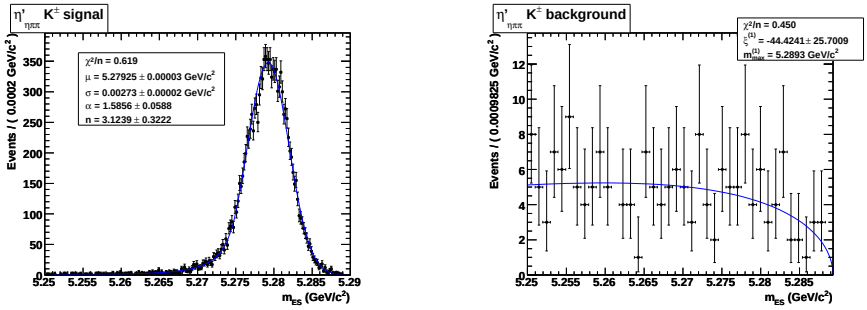

Figure B.30: Signal $m_{\rm ES}$ PDF (left): Crystal Ball; Continuum background $m_{\rm ES}$ PDF (right): Argus function.

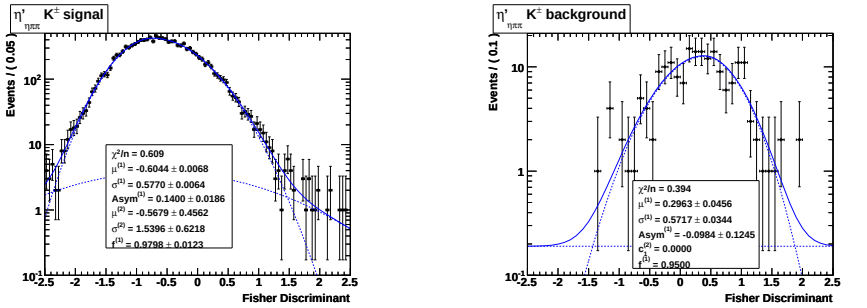

Figure B.31: Signal $\mathcal{F}$ Fisher PDF (left): asymetric Gaussian plus Gaussian; Continuum background $\mathcal{F}$ Fisher PDF (right): asymetric Gaussian plus linear polynomial.

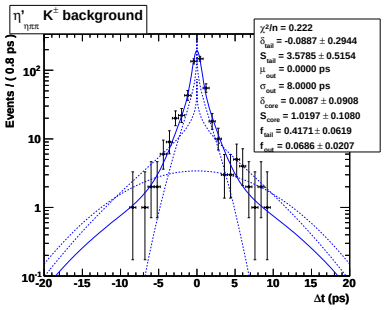

Figure B.32: Δt continuum background PDF: triple Gaussian where we use $\Delta t/\sigma_{\Delta t}$ as in signal Δt resolution model.

B.9 $B^0 \to \eta'_{\eta\pi\pi} K^0_L$

	$\mathcal{F}$	ΔE	Δt	$\sigma_{\Delta t}$
$\mathcal{F}$	1.000			
ΔE	0.074	1.000		
Δt	0.009	0.008	1.000	
$\sigma_{\Delta t}$	0.012	−0.013	−0.023	1.000

Table B.20: Correlation matrix for MC signal $\eta'_{\eta\pi\pi} K^0_L$.

	$\mathcal{F}$	ΔE	Δt	$\sigma_{\Delta t}$
$\mathcal{F}$	1.000			
ΔE	0.074	1.000		
Δt	0.009	0.008	1.000	
$\sigma_{\Delta t}$	0.012	−0.013	−0.023	1.000

Table B.21: Correlation matrix for off-peak data $\eta'_{\eta\pi\pi} K^0_L$.

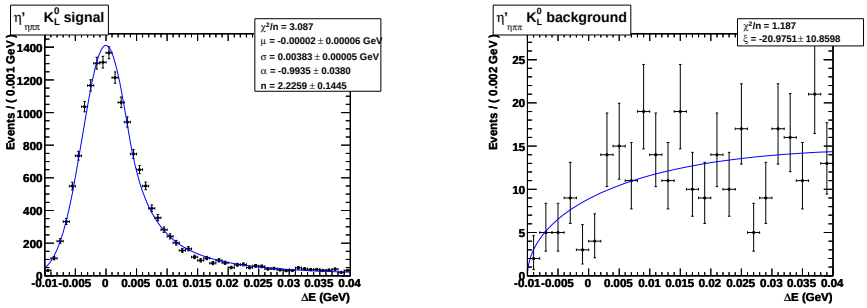

Figure B.33: Signal ΔE PDF (left): Crystal Ball function; Continuum Background ΔE PDF (right): Argus function.

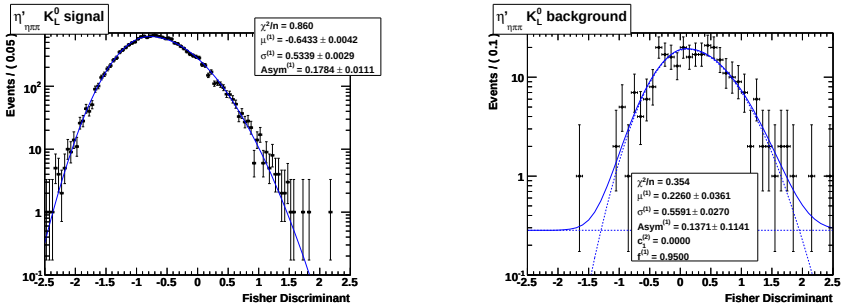

Figure B.34: Signal $\mathcal{F}$ Fisher PDF (left): asymetric Gaussian; Continuum background $\mathcal{F}$ Fisher PDF (right): asymetric Gaussian plus linear polynomial.

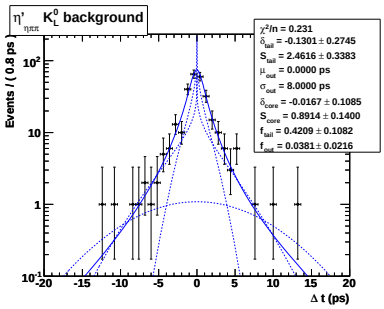

Figure B.35: Δt continuum background PDF: triple Gaussian where we use $\Delta t/\sigma_{\Delta t}$ as in signal Δt resolution model.

Bibliography

[1] J. H. Christenson *et al.*, Phys. Rev. Lett. **13**, 138 (1964).

[2] T. D. Lee, C. N. Yang, Phys. Rev. **104**, 254 (1956).

[3] C. S. Wu, E. Ambler *et al.*, Phys. Rev. **105**, 1413 (1957).

[4] N. Cabibbo, Phys. Rev. Lett. **10**, 531 (1963).

[5] M. Kobayashi, T. Maskawa, Prog. Th. Phys. **49**, 652 (1973).

[6] Fermilab E288 Collaboration, S. W. Herb *et al.*, Phys. Rev. Lett. **39**, 252 (1977); W. R. Innes *et al.*, Phys. Rev. Lett. **39**, 1240, 1640(E) (1977).

[7] CDF Collaboration, F. Abe *et al.*, Phys. Rev. D **50**, 2966 (1994); **51**, 4623 (1994); **52**, 2605 (1995); Phys. Rev. Lett. **73**, 225 (1994); **74**, 2626 (1995); D0 Collaboration, S. Abachi *et al.*, Phys. Rev. Lett. **72**, 2138 (1994); **74**, 2422 (1995); **74**, 2632 (1995); Phys. Rev. D **52**, 4877 (1995).

[8] NA48 Collaboration, V. Fanti *et al.*, Phys. Lett. B **465**, 335 (1999); KTEV Collaboration, A. Alavi-Harati *et al.*, Phys. Rev. Lett. **83**, 22, (1999).

[9] *BABAR* Collaboration, B. Aubert *et al.*, Phys. Rev. Lett. **89**, 201802 (2002); Belle Collaboration, K. Abe *et al.*, Phys. Rev. D **66**, 071102(R) (2002).

[10] *BABAR* Collaboration, B. Aubert *et al.*, Phys. Rev. Lett. **93**, 131801 (2004); Belle Collaboration, Y. Chao *et al.*, Phys. Rev. Lett. **93**, 191802 (2004).

[11] *BABAR* Collaboration, B. Aubert *et al.*, [hep-ex/0609052].

[12] Y. Grossman and M. P. Worah, Phys. Lett. B **395**, 241 (1997); D. Atwood and A. Soni, Phys. Lett. B **405**, 150 (1997); M. Ciuchini *et al.*, Phys. Rev. Lett. **79**, 978 (1997).

[13] Y. Grossman *et al.*, Phys. Rev. D **68**, 015004 (2003).

[14] C.-W. Chiang *et al.*, Phys. Rev. D **68**, 074012 (2003); M. Gronau *et al.*, Phys. Lett. B **596**, 107 (2004).

[15] M. Beneke and M. Neubert, Nucl. Phys. B **675**, 333 (2003).

[16] D. London and A. Soni, Phys. Lett. B **407**, 61 (1997).

[17] CLEO Collaboration, B. Behrens *et al.*, Phys. Rev. Lett. **80**, 3710 (1998).

[18] H. J. Lipkin, Phys. Lett. B **254**, 247 (1991).

[19] D. Atwood *et al.* Phys. Rev. D **71**, 076003 (2005).

[20] T. Gershon and M. Hazumi, Phys. Lett. B **596**, 163 (2004).

[21] S. Weinberg, Phys. Rev. Lett. **19**, 1264 (1967); A. Salam, *Elementary Particle Physics*, ed. by N. Svartholm (Almquist and Wiksells, Stockhol 1968), p. 367; S. Weinberg, Phys. Rev. Lett. **37**, 657 (1976).

[22] M. Gell-Mann and A. Pais, Phys. Rev. **97**, 1387 (1955).

[23] UA1 Collaboration, C. Albajar *et al.*, Phys. Lett. B **186**, 247 (1987).

[24] ARGUS Collaboration, H. Albrecht *et al.*, Phys. Lett. B **192**, 245 (1987).

[25] S.L. Glashow, J. Iliopoulos and L. Maiani, Phys. Rev. D **2**, 1285 (1970).

[26] L. L. Chau and W. Y. Keung, Phys. Rev. Lett. **53**, 1802 (1984).

[27] L. Wolfenstein, Phys. Rev. Lett. **51**, 1945 (1983).

[28] A.J. Buras, M.E. Lautenbacher and G. Ostermaier, Phys. Rev. D **50**, 3433 (1994).

[29] G. Buchalla, A.J. Buras and M.E. Lautenbacher, Rev. Mod. Phys. **68**, 1125 (1996).

[30] N. Isgur and M.B. Wise, Phys. Lett. B **237**, 527 (1990); Phys. Lett. B **232**, 113 (1989).

[31] A.V. Manohar and M.B. Wise, Camb. Monogr. Part. Phys. Nucl. Phys. Cosmol. **10**, 1 (2000).

[32] H. Georgi, Phys. Lett. B **240**, 447 (1990).

[33] J.D. Bjorken, Nucl. Phys. Proc. Suppl. **11**, 325 (1989).

[34] M.J. Dugan and B. Grinstein, Phys. Lett. B **255**, 583 (1991).

[35] C.W. Bauer, S. Fleming and M.E. Luke, Phys. Rev. D **63**, 014006 (2001); C.W. Bauer, S. Fleming, D. Pirjol and I.W. Stewart, Phys. Rev. D **63**, 114020 (2001); C.W. Bauer and I.W. Stewart, Phys. Lett. B **516**, 134 (2001); C.W. Bauer, D. Pirjol and I.W. Stewart, Phys. Rev. D **65**, 054022 (2002).

[36] W.-M. Yao *et al.*, J. Phys. G **33**, 1 (2006).

[37] CDF Collaboration, A. Abulencia *et al.*, [hep-ex/0609040].

[38] *BABAR* Collaboration, B. Aubert *et al.*, Phys. Rev. Lett. **96**, 251802 (2006); Belle Collaboration, K. Abe *et al.*, [hep-ex/0409012]; CLEO Collaboration, D.E. Jaffe *et al.*, Phys. Rev. Lett. **86**, 5000 (2001).

[39] ALEPH Collaboration, R. Barate *et al.*, Eur. Phys. J. C **20**, 431 (2001); OPAL Collaboration, G. Abbiendi *et al.*, Eur. Phys. J. C **12**, 609 (2000).

[40] M. Beneke, G. Buchalla, A. Lenz and U. Nierste, Phys. Lett. B **576**, 173 (2003) [hep-ph/0307344];
M. Ciuchini, E. Franco, V. Lubicz, F. Mescia and C. Tarantino, JHEP **0308**, 031 (2003) [hep-ph/0308029].

[41] The Heavy Flavor Averaging Group (HFAG) (E. Barberio *et al.*), Averages after the Summer 2006 conferences, ICHEP 2006, Moscow (Russia),
URL:`http://www.slac.stanford.edu/xorg/hfag/`.

[42] *BABAR* Collaboration, B. Aubert *et al.*, Phys. Rev. D **71**, 032005 (2005); Belle Collaboration, R. Itoh *et al.*, Phys. Rev. Lett. **95**, 091601 (2005).

[43] Belle Collaboration, P. Krokovny *et al.*, Phys. Rev. Lett. **97**, 081801 (2006).

[44] CKMfitter Group (J. Charles *et al.*), Results as of Summer 2006 (ICHEP06/BEAUTY06),
URL:`http://www.slac.stanford.edu/xorg/ckmfitter/`.

[45] M. Gronau and D. London, Phys. Rev. Lett. **65**, 3381 (1990).

[46] H.R. Quinn and A.E. Snyder, Phys. Rev. D **48**, 2139 (1993).

[47] *BABAR* Collaboration, B. Aubert *et al.*, Phys. Rev. Lett. **97** 051802 (2006). Belle Collaboration, K. Abe *et al.*, [hep-ex/0507096].

[48] M. Gronau and J. Zupan, Phys. Rev. D **73** 057502 (2006).

[49] Unitarity Triangle fit Group (M. Bona *et al.*), ICHEP'06 update, URL:`http://utfit.roma1.infn.it/`.

[50] M. Gronau and D. London, Phys. Lett. B **253**, 483 (1991); M. Gronau and D. Wyler, Phys. Lett. B **265**, 172 (1991).

[51] D. Atwood, I. Dunietz, and A. Soni, Phys. Rev. Lett. **78**, 3257 (1997); Phys. Rev. D **63**, 036005 (2001).

[52] A. Giri, Y. Grossman, A. Soffer and J. Zupan, Phys. Rev. D **68**, 054018 (2003); Belle Collaboration (A. Poluektov *et al.*), Phys. Rev. D **70**, 072003 (2004).

[53] *BABAR* Collaboration, B. Aubert *et al.*, Phys. Rev. D **71**, 112003 (2005); Belle Collaboration, K. Abe *et al.*, Phys. Rev. Lett. **93**, 031802 (2004) [Erratumibid. **93**, 059901 (2004)]; Belle Collaboration, T. Gershon *et al.*, Phys. Lett. B **624**, 11 (2005).

[54] G. Buchalla, G. Hiller, Y. Nir and G. Raz, JHEP **0509**, 074 (2005).

[55] M. Beneke, Phys. Lett. B **620**, 143 (2005).

[56] A. R. Williamson and J. Zupan, Phys. Rev. D **74**, 014003 (2006).

[57] M. Gronau *et al.*, hep-ph/0608085 (2006).

[58] D. Atwood, M. Gronau and A. Soni, Phys. Rev. Lett. **79**, 185 (1997).

[59] D. Atwood, T. Gershon, M. Hazumi and A. Soni, Phys. Rev. D **71**, 076003 (2005).

[60] B. Grinstein, Y. Grossman, Z. Ligeti and D. Pirjol, Phys. Rev. D **71**, 011504 (2005) [hep-ph/0412019].

[61] H.J. Lipkin, Y. Nir, H.R. Quinn and A. Snyder, Phys. Rev. D **44**, 1454 (1991).

[62] P. Oddone, in *Procedings of the UCLA Workshop: Linear Collider $B\overline{B}$ Factory Conceptual Design*, edited by D. Stork (World Scientific), 243 (1987).

[63] PEP-II, *An Asymmetric B-Factory: Conceptual Design Report*, SLAC-PUB-418 (1993).

[64] S. Kurokawa and E. Kikutani, Nucl. Instr. Methods Phys. Res., Sect. A **499**, 1 (2003).

[65] *BABAR* Collaboration, B. Aubert *et al.*, Nucl. Instr. Methods Phys. Res., Sect. A **479**, 1 (2002).

[66] Belle Collaboration, A. Abashian *et al.*, Nucl. Instr. Methods Phys. Res., Sect. A **479**, 117 (2002).

[67] C. M. Bishop, *"Neural Networks for Pattern Recognition"*, Oxford University Press.

[68] M.P. Perrone and L.N. Cooper, in *Artificial Neural Networks for Speech and Vision, pp 126-142*, Chapman & Hall. (1993).

[69] O. Long, M. Baak, R. N. Cahn, D. Kirkby, Phys. Rev. D **68**, 034010 (2003).

[70] S. Patton, *Object Oriented Programming (For a novice, by a novice)*, CSN 95-341 C3S 95-003 (1995).

[71] For a C++ language description see B. Stroustrup, *The C++ Programming Language (Third Edition)*, Addison-Wesley, ISBN 0-201-88954-4 (1997).

[72] S. Agostinelli *et al.*, Nucl. Instr. Methods Phys. Res., Sect. A **506**, 250 (2003).

[73] ROOT project web site:
`URL:http://root.cern.ch`.

[74] *BABAR* Collaboration, B. Aubert *et al.*, [hep-ex/0607107].

[75] *BABAR* Collaboration, B. Aubert *et al.*, Phys. Rev. D **66**, 032003 (2002).

[76] E. S. Raymond, *The Cathedral and the Bazaar*, O'Reilly and Associates Inc. (1999).

[77] See the web page the PAW project:
URL:http://wwwasd.web.cern.ch/wwwasd/paw.

[78] See the web page of the CINT project:
URL:http://root.cern.ch/root/Cint.html.

[79] See the web page of the RooFit project:
URL:http://roofit.sourceforge.net/.

[80] ARGUS Collaboration, H. Albrecht *et al.*, Phys. Lett. B **241**, 278 (1990); **254**, 288 (1991).

[81] F. James, *MINUIT - function minimization and error analysis*, CERN Program Library Long Writeup D506.

[82] M. Pivk and F. R. Le Diberder, Nucl. Instr. Methods Phys. Res., Sect. A **555**, 356 (2005).

[83] R. A. Fisher, *The use of multiple measurements in taxonomic problems*, Ann. Eugen. **7**, 179 (1936); *Contributions to Mathematical Statistics*, John Wiley, New York (1950).

[84] G. Cowan, *Statistical Data Analysis*, Oxford (1998).

[85] See the web page of the TNeuNet project:
URL:http://e.home.cern.ch/e/ernen/www/NN/.

[86] C. W. Chiang *et al.*, Phys. Rev. D **69**,034001 (2004); H. K. Fu *et al.*, Chin. J. Phys. 41, 601 (2003); H. K. Fu *et al.*, Phys. Rev. D **69**, 074002 (2004); H. K. Fu *et al.*, Nucl. Phys. Proc. Suppl. 115, 279 (2003).

[87] M. Bauer *et al.*, Z. Phys. C **34** 103 (1987); A. Ali and C. Greub, Phys. Rev. D **57** 2996 (1998); A. Ali, G. Kramer and C. D. Lu Phys. Rev. D **58** 094009 (1998); J. H. Jang *et al.*, Phys. Rev. D **59** 034025 (1999); Y. H. Chen *et al.*, Phys. Rev. D **60** 094014 (1999).

[88] G. P. Lepage and S. Brodsky, Phys. Rev. D **22** 2157 (1980); J. Botts and G. Sterman, Nucl. Phys. B **225** 62 (1989); Y. Y. Keum *et al.*, Phys. Lett. B **504** 6 (2001), Phys. Rev. D **63** 074006 (2001); Y. Y. Keum and H. N. Li, Phys. Rev. D **63** 054008 (2001).

[89] M. Beneke *et al.*, Phys. Rev. Lett. **83** 1914 (1999), Nucl. Phys. B **606** 245 (2001), Nucl. Phys. B **651**, 225 (2003).

[90] G. Kramer, W. F. Palmer, and H. Simma, Zeit. Phys. C **66** 429 (1995).

[91] The *BABAR* Collaboration, B. Aubert *et al.*, Phys. Rev. Lett. **91**, 161801 (2003).

[92] The *BABAR* Collaboration, B. Aubert *et al.*, Phys. Rev. Lett. **93**, 181806 (2004).

[93] The *BABAR* Collaboration, B. Aubert *et al.*, Phys. Rev. Lett. **95**, 131803 (2005).

[94] K. Lingel , T. Skwarnicki and James G. Smith, Ann. Rev. Nucl. Part. Sci. **48**, 253 (1998).

[95] Y. H. Chen *et al.*, Phys. Rev. D **60**, 094014 (1999).

[96] K. Abe *et al.*, Phys. Lett. B **610**, 23 (2005).

[97] A. Kagan and N. Neubert, Eur. Phys. Jour.7, 5 (1999).

[98] The Heavy Flavor Averaging Group (HFAG) (E. Barberio *et al.*), Averages after the Summer 2004 conferences,
URL:`http://www.slac.stanford.edu/xorg/hfag/`.

[99] S. Eidelman *et al.* Phys. Lett. B **592**, 1 (2004).

[100] The Heavy Flavor Averaging Group (HFAG) (E. Barberio *et al.*), Averages after the Winter 2005 conferences,
URL:`http://www.slac.stanford.edu/xorg/hfag/`.

[101] F. Blanc *et al.*, *BABAR* Analysis Document # 744 (2004).

[102] A. Ali, G. Kramer, and C. D. Lü, Phys. Rev. D **58**, 094009 (1998); Y. H. Chen *et al.*, Phys. Rev. D **60**, 094014 (1999).

[103] M. Gronau and J. L. Rosner, Phys. Rev. D **53**, 2516 (1996); A. S. Dighe, M. Gronau, and J. L. Rosner, Phys. Rev. Lett. **79**, 4333 (1997); M. R. Ahmady, E. Kou, and A. Sugamoto, Phys. Rev. D **58**, 014015 (1998); D. Du, C. S. Kim, and Y. Yang, Phys. Lett. **B426**, 133 (1998).

[104] I. Halperin and A. Zhitnitsky, Phys. Rev. D **56**, 7247 (1997); E. V. Shuryak and A. Zhitnitsky, *ibid.* **57**, 2001 (1998).

[105] G. Engelhard *et al.*, Phys. Rev. D **72**, 075013 (2005).

[106] *BABAR* Collaboration, B. Aubert *et al.*, Phys. Rev. D **73**, 071102 (2006).

[107] *BABAR* Collaboration, B. Aubert *et al.*, Phys. Rev. D **74**, 051106 (2006).

[108] We thank Denis for providing us with his program.

[109] H. Y. Cheng *et al.*, Phys. Rev. D **71**, 014030 (2005), Phys. Rev. D **72**, 014006 (2005); S. Fajfer *et al.*, Phys. Rev. D **72**, 114001 (2005).

[110] *BABAR* Collaboration, B. Aubert *et al.*, [hep-ex/0507087].

[111] *BABAR* Collaboration, B. Aubert *et al.*, Phys. Rev. Lett. **94**, 191802 (2005).

[112] *BABAR* Collaboration, B. Aubert *et al.*, Phys. Rev. Lett. **94**, 161803 (2005).

[113] F. Blanc *et al.*, B.A.D. # 1509, 2006.

[114] *BABAR* Collaboration, B. Aubert *et al.*, Phys. Rev. D **74**, 031105 (2006).

[115] *BABAR* Collaboration, B. Aubert *et al.*, Phys. Rev. D **74**, 031102 (2006).

[116] *BABAR* Collaboration, B. Aubert *et al.*, it will appear on Phys. Rev. Lett. **98** on Jannuary 2, 2007, [hep-ex/0609052].

Acknowledgements

First of all I would like to thank Fernando. Many thanks to Vincenzo, my PhD collaborator. With Vincenzo the working life has been much easier.

I would like to thank all my *BABAR* collaborators, in particular Fred Blanc, Bill Ford, Keith Ulmer, and Jim Smith from Colorado Boulder Group. I thank my AWG conveners Adrian Bevan and Jim Smith for their suggestions and comments in the analyses. The PhD work has been an exciting period. Many thanks to everybody helped its realization.

I would like to thank for interesting discussions the *BABAR* Milan undergraduate students Giordano Cerizza, Riccardo Pellegrini, Domenico delle Cave, Alessandra Colnago, Simone Stracka.

Many thanks to my friends who supported me during the three PhD years: Giordano, Angelo, Andrea, Paola, Riccardo, Laura. Thanks to everybody.

Ringraziamenti

Quante cose sono successe in questi tre anni di dottorato!!! Molte sono le persone che mi hanno aiutato, anche a loro insaputa, a portare a termine questo lavoro. Ognuno con cui ho parlato anche minimimante di cosa facevo ha dato un contributo per me fondamentale. Sarebbe mia intenzione ringraziare tutti, anche se sono sicuro che dimenticherò qualcuno. Il mio piccolo ricordo su un documento che riassume il lavoro durato un decimo della mia attuale vita. Mi scuso con quanti non riuscirò a ringraziare, per i quali riservo qui uno speciale ringraziamento cumulativo.

Tre anni intensi in cui in certi momenti una giornata sembra durare troppo poco! Mi alzavo la mattina pensando che a quello che dovevo fare e a notte fonda (già, bisogna anche dormire qualche ora!) non mi ricordavo cosa avevo fatto (forse perché avevo fatto una piccolissima parte di quello che speravo di fare!). Tempi duri, frammisti alle vincende della vita. Qualche volta sono stati tristi, altri (la maggior parte) allegri. Non sono mancate le soddisfazioni, i premi, le sorprese, le belle istantanee conservate nei ricordi. Verrebbe di ricominciare da capo... per fortuna non è possibile!

Ed ora i ringraziamenti.

Ringrazio Vincenzo, collega e amico durante i tre anni. Quante ne abbiamo passate, Vincenzo! Dalle trasferte in giro per il mondo, alle giornate passate a lavorare a SLAC come matti. Ricordo quando a Denver per chiedere dove comprare le sigarette ci ritrovammo in un ufficio con un certo Mike che ci spiegava che lì lavoravano tutte donne!!! Vincenzo è il perfetto fisico, che unisce la fisica al pensiero tutto, e che prende la vita con i suoi tempi. A proposito, quando hai tempo dammi le foto.

Ringrazio Marco per il periodo passato insieme a SLAC quando il pager era l'incubo peggiore della giornata. Devo dire che qualcuno dall'alto ci ha guardati perché poteva andare molto peggio. Alla fine il pager è stato un sorriso. Non so di quanto siamo "responsabili" dell'incidente (chiaramente in modo indiretto), ma è successo e questo ci ha semplificato la vita. Con Marco abbiamo condiviso la casa, nelle sere passate a

cucinare e a guardare la TV mentre la signora, sorda, dormiva. Il momento che ricordo e che mi fa ancora ridere e quando provammo ad azionare la lavastoviglie con il detersivo liquido. Risultato, la schiuma veniva fuori da tutte le parti! Ma Marco, con un colpo di reni, ha risolto tutto prima che la signora si accorgesse (infatti subito dopo ha acceso lei la lavastovigle con il giusto detersivo).

Ringrazio gli amici e collaboratori Antonio, David, Loredana ed Emanuele. Siete stati più amici che collaboratori.

Ringrazio i ragazzi del gruppo di Milano: Giordano, il perfetto braccio destro ed amico; Riccardo, con il quale abbiamo lottato per portare a termine l'analisi; Simone, il migliore tra tutti per impegno e con il quale ho fatto tutto via skype (perfino la discussione della sua tesi); Domenico e Alessandra, che hanno completato con me le ultime analisi.

Ringrazio gli amici conosciuti al collegio, la vera linfa dei momenti passati fuori dall'ufficio. Un ringraziamento all'amica Paola, punto di riferimento in molte occasioni; Riccardo, la persona su cui puoi contare; Laura, la perfetta amica con cui parlare e a cui auguro di raggiungere quello che desidera; Fabio e Dimitri per gli incontri del gruppo di divulgazione; Andrea T., con cui è sempre un piacere parlare e bere (grande astrofisico).

Ringrazio i miei amici del sud: Elena, Angelo, Filippo, Salvo A. and Salvo C.. La Sicilia è casa mia, e gli amici del sud sono un riferimento indiscutibile per chi ha deciso di vivere oltre lo Stretto.

Un ringraziamento ulteriore alla mia famiglia. A mio padre e mia madre che ancora si chiedono che cosa in realtà faccio come lavoro. A mia sorella Maria Grazia, il suo compagno Giuliano e mio nipote Claudio, per la loro ospitalità a Milano e perché molte delle vicende personali successe in questi tre anni mi legono profondamente a loro. A mia sorella Rita, mio cognato Andreas e alle mie due splendide nipotine Sophie e Carolina, che sono la vera sorpresa dei tre anni. A mio fratello Orazio e sua moglie Cinzia per il loro supporto. E a Lilli per essermi stata ad ascoltare mentre faceva le fusa.

Un ultimo ringraziamento ad una persona molto speciale. Hai rappresentato per me un faro nella notte. L'impegno e la forza d'animo che dimostri nelle cose che fai mi hanno spinto a continuare nei momenti difficili. È anche grazie a te, soprattutto direi, che alla fine tutto è andato bene. Spero che anche per te succeda quanto di meglio è successo a me. Sei stata il pensiero dolce, felice, a volte meno felice, triste, rabbioso.

Ma ci sei sempre stata nei tre anni, e ci sarai ancora. So che saprai riconoscerti tra queste parole. Ti ho ringraziato più volte e se dovessi farlo ora impigherei molte parole ancora. Ma io alle parole preferisco i fatti, lo sai, quindi per te l'ultima parola della tesi: grazie.

This thesis is written in LaTeX 2_ε
Milan, November 15th 2006.